Proceeding of JSPS-CAS Core University Program Seminar on Production and Control of High Performance Plasmas with Advanced Plasma Heating and Diagnostic Systems 1-4 November, 2010, Guilin, China

Edited by
Xiang GAO and Shigeru MORITA

Abstract

The JSPS-CAS Core University Program (CUP) seminar on "Production and control of high performance plasmas with advanced plasma heating and diagnostic systems" took place in Guilin Bravo Hotel, Guilin, China, 1-4 November 2010. This seminar was organized in the framework of CUP in the field of plasma and nuclear fusion. Two special talks and 46 oral talks were presented in the seminar including 36 Chinese, 18 Japanese and 4 Korean attendees.

Production and control of high performance plasmas is a crucial issue for realizing an advanced nuclear fusion reactor in addition to developments of advanced plasma heating and diagnostics. This seminar was motivated along the issues. Results in the field of fusion experiments obtained through CUP activities during recent two years were summarized. Possible direction of future collaboration and further encouragement of scientific activity of younger scientists were also discussed in this seminar with future experimental plans in both countries.

Key words: magnetically confined devices, toroidal plasmas, high performance plasmas, improved confinement, H-mode, steady state operation, MHD stability, high beta plasmas, advanced plasma heating, advanced plasma diagnostics.

Organization Committee

Xiang GAO (Chairperson, Institute of Plasma Physics, Chinese Academy of Sciences, China)

Shigeru MORITA (Chairperson, National Institute for Fusion Science)

Program Committee

China

Xuantong DING (Southwestern Institute of Physics, China)

Xiang GAO (Institute of Plasma Physics, Chinese Academy of Sciences, China)

Kongjia WANG (Institute of Plasma Physics, Chinese Academy of Sciences, China)

Longwen YAN (Southwestern Institute of Physics, China)

Japan

Kazuaki HANADA (Kyushu University, Japan)

Shunsuke IDE (Japan Atomic Energy Agency, Japan)

Takashi MAEKAWA (Kyoto University, Japan)

Shigeru MORITA (National Institute for Fusion Science, Japan)

Kazuo TOI (National Institute for Fusion Science, Japan)

Conference Secretariats

Shaohua DONG (Secretary, Institute of Plasma Physics, Chinese Academy of Sciences, China)

Liqun HU (Scientific secretary, Institute of Plasma Physics, Chinese Academy of Sciences, China)

Mayumi KATO (Secretary, National Institute for Fusion Science, Japan)

Preface

The JSPS-CAS Core University Program (CUP) seminar on "Production and control of high performance plasmas with advanced plasma heating and diagnostic systems" took place in Guilin Bravo Hotel, Guilin, China, 1-4 November 2010. This seminar was organized in the framework of CUP in the field of plasma and nuclear fusion.

Production and steady state operation of high performance plasmas and developments of advanced plasma heating and diagnostics are crucial issues for realizing an advanced nuclear fusion reactor. Education of younger scientists becomes also extremely important for future progress of the fusion research. Many CUP collaboration programs have been carried out along such important issues in the category of "improvement of core plasma properties". Scientific progresses in the field of fusion experiment obtained from CUP activities during recent two years were summarized in this seminar. In the seminar two special talks and 46 oral talks were presented including 36 Chinese, 18 Japanese and 4 Korean attendees. In addition, 11 PHD students were presented their results as an oral talk and submitted papers to Journal of Plasma Science and Technology. The presentations were mainly focused on the following topics which are very important in the fusion research, regardless of the difference in magnetic configurations such as tokamaks and helical devices.

1. Production and steady state operation of high-performance plasmas
3. MHD stability of high-beta plasmas
4. Particle and energy transport of core and edge plasmas
5. Advanced heating scenarios and plasma diagnostics
5. Present status of planning and constructing fusion devices

This seminar was closed with great success, clarifying remarkable progresses in researches related to these important topics obtained through CUP and contributing the fostering of younger scientists and the education of PHD students. The organizing and program committees are grateful to all participants for their supports and corporation to this seminar.

Xiang GAO and Shigeru MORITA
Chairpersons of the Organizing Committee

Contents


桂林宾馆
Guilin Bravo Hotel

JSPS-CAS Core University Program Seminar on
Production and Control of High Performance Plasmas
with Advanced Plasma Heating and Diagnostic Systems
1 - 4 November, 2010, Guilin, China

MHD Spectroscopy in Toroidal Plasmas using Various MHD Instabilities

K. Toi, K. Ogawa, M. Isobe, M. Osakabe, D.A. Spong*

National Institute for Fusion Science, Toki, Japan
Oak Ridge National Laboratory, Oak Ridge, U.S.A.

Abstract

A possibility to MHD spectroscopy where information of MHD equilibrium is extracted by means of monitoring energetic ion driven MHD instabilities is discussed in toroidal plasmas such as stellarator/helical and tokamak plasmas. This technique is very important for a fusion reactor where sophisticated diagnostic systems for internal plasma measurements will be considerably limited, and only simpler diagnostics such as magnetic probe arrays and microwave diagnostics will be available. Some promising examples of MHD spectroscopy in the Large Helical Device are shown and are compared with those in tokamaks.

1. Introduction

In a fusion reactor, high performance plasma having higher beta value will be produced and sustain near stability boundary. Installation of internal plasma diagnostics will be strongly limited in harsh condition near a fusion reactor. It is important to know MHD plasma equilibrium by simpler diagnostics and reflect plasma operation. Magnetic probes and a few microwave diagnostics can be effectively employed for this purpose. A promising approach in this situation of a fusion reactor is to establish “MHD spectroscopy” which is an approach to extract global quantities describing MHD events such as the rotational transform ($\iota/2\pi$) or safety factor ($1/q=\iota/2\pi$) profile by monitoring global mode frequencies and their time evolutions. In a tokamak plasma, several candidate MHD modes are thought to be useful for MHD spectroscopy, that is, reversed shear Al;fven eigenmodes (RSAEs)[1-3], core localized toroidal Alfven eigenmodes (C-TAEs,)[4], energetic ion-driven geodesic acoustic modes (GAMs) [5-7] and so on. In an experimental reactor such as ITER, these energetic ion driven MHD modes would be destabilized [8] and if necessary they are expected to exist having benign level under controlled condition. Some usual ideal and resistive MHD instabilities also may be useful candidates for MHD spectroscopy. It is interesting and important to extend the ideas of MHD spectroscopy in tokamak plasmas to 3D plasmas such as stellarator/helical plasmas[9]. The LHD has a three

dimensional magnetic configuration having large toroidal period number N=10. In this configuration, toroidal mode coupling is not important for TAE, although the gap frequency decreases slightly (typically, less than 10%) from the case without toroidal mode coupling [9-11]. Accordingly, TAEs have no essential differences in tokamak and LHD plasmas, but some differences in Alfven eigenmodes (AEs) will result from the differences in the rotational transform profile [9]. Figure 1 shows comparisons of the rotational transform profiles between tokamak and LHD plasmas in monotonic and non-monotonic (or reversed-shear) profile cases. In a monotonic profile case, the magnetic shear is negative (q'<0) in a whole minor radius of an LHD plasma while it is positive (q'>0) in a standard tokamak plasma. In a reversed-shear (RS-) profile case, the curvature of the safety factor q"(r_o) at the zero-shear layer (r=r_o) away from the plasma center is respectively negative and positive in reversed-shear LHD and tokamak plasmas. When the toroidal beta value is increased in LHD, the rotational transform profile changes from the above-mentioned monotonic profile to the reversed-shear profile with q"(r_o)<0. Core localzed TAEs, global Alfven eigenmodes (GAEs) and RSAEs can exist, corresponding to the changes of the rotational transform profiles [9-11]. In LHD, the RS plasma was also generated by counter neutral beam current drive and RSAEs were detected [12]. In the plasma, energetic ion driven geodesic acoustic mode (GAM) was also detected [12]. These global modes such as AEs and GAMs can be employed for "MHD spectroscopy" in LHD. In Section 2, the rotational transform at the plasma center is predicted from the transition behavior from C-TAE to GAE observed in LHD. Section 3 describes the evaluation of the minimum value of the rotational transform profile from the time evolution of the RSAE frequency in LHD. An application of GAM observed in the RS plasma to MHD spectroscopy is discussed. Section 4 summarizes the results of MHD spectroscopy in LHD.

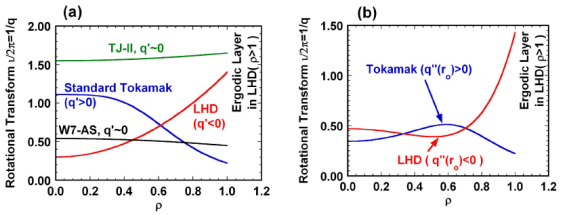

Fig.1 *Comparison of typical rotational transform profiles in tokamak and stellarator/helical plasmas in the cases of monotonic (a) and reversed shear (b) profiles.*

2. Prediction of the rotational transform profile from C-TAE to GAE transition

Figure 2(a) shows an example of n=1shear Alfven spectra in very low beta plasma of LHD, and the TAE gap is formed by poloidal mode coupling between m=2 and m=3 spectra. When the beta increases slightly, the central value of the rotational transform increases and exceeds a value related to a TAE gap position: [ι(0)/2π]*=2n/(2m+1), for instance, [ι(0)/2π]*=0.4 for m=2

(a) (b)

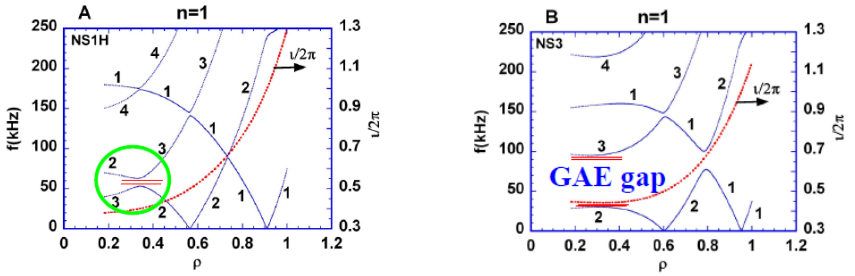

Fig.2 *Shear Alfvén spectra of low toroidal mode number n=1 for the profiles of very low (a) and slightly higher (b)beta plasmas in LHD without toroidal mode coupling. The numerals nearby the continua indicate the poloidal mode number m. In very low beta case A shown in Fig.(a), the TAE gap (shown by a green circle) is formed by poloidal mode coupling between m=2 and m=3 Fourier modes. If the plasma beta increases slightly, the TAE gap disappears and a GAE gap is newly generated, as shown in Fig.(b).*

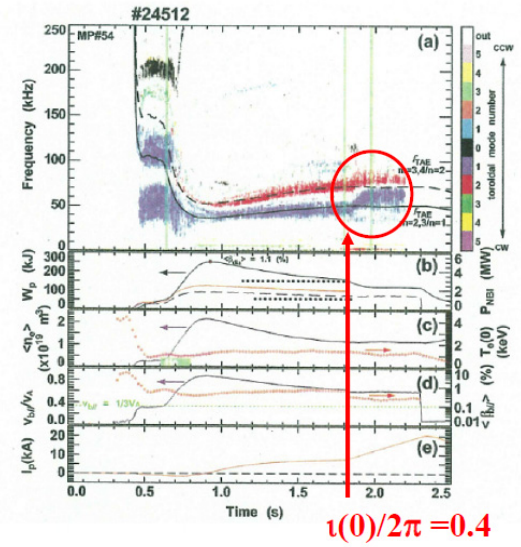

Fig. 3 *(a)Time evolution of the frequencies of various coherent magnetic fluctuations. The color code indicates the toroidal mode number: n=1(blue) and n=2 (red). Solid and broken curves indicate the n = 1 TAE gap frequency related to m = 2 and m = 3 coupling and the n = 2 one for m = 3 and m = 4 coupling, respectively. (b) Time evolution of the plasma stored energy together with absorbed NBI powers. (c) Time evolution of line-averaged electron density (black) and electron temperature at the magnetic axis (red). (d) Time evolution of the velocity ratio, $V_{b//}/V_A$(black), and the volume-averaged beam beta, $<\beta_{b//}>$(red), where $V_{b//}$ is the initial velocity of energetic beam ions, parallel to the toroidal field and V_A is the Alfven speed. (e) Time evolution of net plasma current.*

and n=1. This leads to remove the TAE gap and generate GAE gap, as shown in Fig.2(b). This event was observed in an LHD plasma where plasma current was increased by switching of neutral beam injection from balanced injection to co-injection [9, 11]. At t=1.8s in Fig.3, core localized n=1 TAE disappeared and m=3/n=1 GAE was clearly excited. Note that m=2/n=1 GAE was quickly damped due to continuum damping.

In the shear Alfven spectra shown in Fig.2(b), four GAEs are predicted by ideal MHD theory to exist just below m=3 continuum [9, 11]. A reason why only one m=3/n=1 GAE was detected experimentally may be due to differences in the details of $\iota/2\pi$ profile, where the shear profile may be somewhat different between the calculation and experiment. Observation of multiple modes may give useful information on the magnitude of the magnetic shear around the GAE gap formed in the plasma center.

3. MHD spectroscopy using RSAE and GAM in RS plasmas of LHD

A reversed shear plasma can be produced by counter NBCD in relatively low density regime, where energetic ion content is fairly high. In this plasma, RSAEs are observed having a characteristic frequency sweeping. The typical wave form of the discharge is shown in Fig.4(a). The electron temperature measured by electron cyclotron emission (ECE) in the central region of the normalized minor radius $\rho \leq 0.49$ exhibits sharp drops during the plasma current rise by counter NBCD. In this shot RSAEs with m~3/n=2, m~2/n=1 and m~3/n=1 mode structure are sequentially observed, as shown in Fig.4(b)[9]. The frequencies of m~2/n=1 and m~3/n=1 RSAEs evolves chirping down and chirping up via the minimum. The comparison of these experimental data with RSAE theory indicates that the minimum value of the rotational transform at the zero shear layer passes the rational values of 1/2 and 1/3 at each time of the minimum frequency, that is, t=2.0s and t=2.72s, respectively. At these timings, ECE signals show a sharp dip. These data also support this fact and are similar to those observed in a RS plasma in DIII-D[13]. In Fig.4(b), m~3/n=2 RSAE is also observed and induces the sharp drop in ECE signals shown in Fig.4(a). The time evolution of RSAE frequency provides the precise information on the evolution of the reversed shear rotational transform as same as in tokamak RS plasmas. Moreover, the minimum frequency depends on the GAM frequency and the effective frequency due to the gradients of bulk and energetic ion pressures[12]. The minimum frequency provides information of energetic ion content if bulk electron and ion temperatures are known by other diagnostics. It is concluded that RSAEs in LHD plasma are promising candidate modes for “MHD spectroscopy”.

In the RS plasma, a peculiar coherent mode is excited, of which toroidal mode number is n=0 (Fig.4(b)). This frequency agrees well with the GAM frequency including a small fraction of energetic ion components. This mode grows gradually with the decrease in the minimum

value of the rotational transform in the RS plasmas of LHD. This mode accompanies strong magnetic perturbations as well as density and potential fluctuations. In conclusion, this is thought to be energetic ion driven GAM [12] and to be a global mode in contrast to GAMs excited through nonlinear mode coupling among drift waves. This is similar to energetic ion driven GAMs observed in tokamaks, although the mode frequencies have some differences [5-7]. The GAM frequency is proportional to ion sound wave having a dependence on the rotational transform. This global type GAM instability is a candidate for "MHS spectroscopy". It should be noted that the frequency of this energetic ion driven GAM can be affected by energetic ion contents and more experimental and theoretical studies are needed [7].

(a) (b)

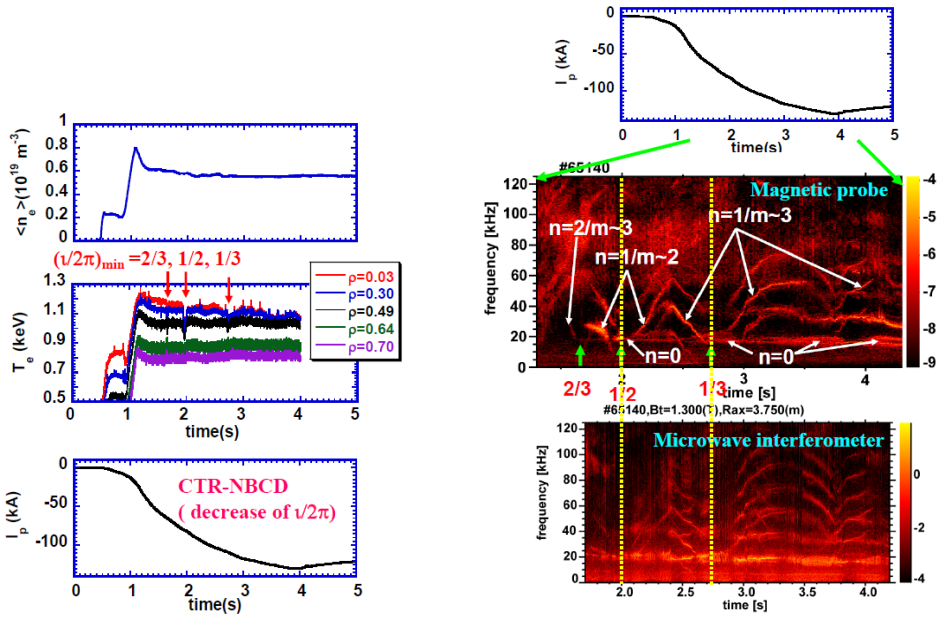

Fig.4 *(a) Time evolutions of line averaged electron density, ECE electron temperature measured at ρ=0.03 to 0.70 and plasma current. (b) Spectrogram of magnetic probe and microwave interferometer signals in an RS-plasma. The frequency sweeping modes of n=2/m~3, n=1/m~2 and n=1/m~3 are RSAE and the n=0 mode is GAM destabilized by energetic ions.*

4. Summary and outlook

In this presentation, we have discussed a possibility of MHD spectroscopy in stellarator/helical plasmas as well as tokamak ones, where various quantities related to MHD equilibrium can be derived using the time evolution of the mode frequency. If other diagnostics such microwave diagnostics provides the radial information, MHD spectroscopy will be more powerful in operation of a fusion reactor. Extension of MHD spectroscopy to 3D

plasmas from 2D tokamak type plasmas would contribute to develop an inexpensive and useful tool for a fusion reactor. It should be noted that MHD spectroscopy also provide precise information on MHD phenomena such as a sawtooth crash [3].

Acknowledgements

The authors acknowledge T. Tokuzawa, K. Ida, T. Ido, S. Morita, K. Nagaoka, K. Narihara, A. Shimizu and K. Tanaka, Y. Todo, F. Watanabe (Kyoto Univ.) and S. Yamamoto (Kyoto Univ.) for their excellent supports and useful discussions in this research. This work is supported in part by the Grant-in-Aid for Scientific Research from MEXT, No. 16082209 and from JSPS, No. 12480127, No. 16656287 and No. 21360457, and the LHD project budget (NIFS09ULHH508). This research is also supported by the JSPS-CAS Core-University Program in the field of "Plasma and Nuclear Fusion".

References

[1] S.E. Sharapov et al., Nucl. Fusion **46**, S868 (2006).

[2] M. Van Zeeland et al., Nucl. Fusion **46**, S880 (2006).

[3] E.M. Edlund et al., Phys. Rev. Lett. **102**, 165003 (2009).

[4] G.J. Kramer et al., Plasma Phys. Control. Fusion **40**, 863 (1998).

[5] H.L. Berk et al., Nucl. Fusion **46**, S888 (2006).

[6] R. Nazikian et al., Phys. Rev. Lett. **101**, 185001 (2008).

[7] G.Y. Fu, Phys. Rev. Lett. **101**, 185002(2008).

[8] A. Fasoli et al**.,** Nucl. Fusion **47**, S264 (2007).

[9] K. Toi et al., "Energetic-ion-driven Global Instabilities in Stellarator/Helical Plasmas and Comparison with Tokamak Plasmas", a cluster paper of *Physics at Stellarator-Tokamak interface,* to be published in Plasma Phys. Control. Fusion.

[10] K. Toi et al., Nucl. Fusion **40**, 1349 (2000).

[11] S. Yamamoto et al., Nucl. Fusion **45**, 326 (2005).

[12] K. Toi et al., Phys. Rev. Lett. **105**, 145003 (2010).

[13] M.E. Austin et al., Phys. Plasmas **13**, 082502 (2006).

A dip structure in the intrinsic toroidal rotation near the edge of the EAST Ohmic plasmas

G. S. Xu[1, a], V. Naulin[2], B. N. Wan[1], H. Y. Guo[3], W. Zhang[1], J. F. Chang[1], N. Yan[1], S. Y. Ding[1], L. Zhang[1], L. Wang[1], S. C. Liu[1], P. Liu[1], M. Jiang[1], H. Q. Wang[1], H. Xiong[1], J. Juul Rasmussen[2], A. H. Nielsen[2], C. J. Xiao[4], X. Gao[1], S. Z. Zhu[1], Z. W. Wu[1], J. P. Qian[1], Y. J. Shi[1], X. Z. Gong[1]

[1] Institute of Plasma Physics, Chinese Academy of Sciences, Hefei 230031, China

[2] Association Euratom-Risø DTU, DK-4000 Roskilde, Denmark

[3] Tri Alpha Energy, P.O. Box 7010, Rancho Santa Margarita, CA 92688, USA

[4] Plasma Physics Laboratory, University of Saskatchewan, Saskatoon, SK S7N 5E2, Canada

E-mail: gsxu@ipp.ac.cn

Abstract

The main ion toroidal velocity, v_t, in the outermost 4 cm of the confined region and in the scrap-off layer of Ohmic L-mode plasmas in the EAST superconducting tokamak was measured using Mach probes. At about 1 cm inside the separatrix a local minimum in v_t was observed, from where a cocurrent rotation increased towards the plasma center and towards the separatrix. The radial width of the v_t dip was 1~2 cm, situated at the same location of a dip structure in radial electric field and steep gradients in density and electron temperature profiles. It was observed in both divertor and limiter configurations. Similar dip structure in v_t was recently observed near the H-mode plasma edge of the ASDEX-U and DIII-D tokamaks. The velocity in our experiments amounts to ~20 km/s, which is at the same level of those from ASDEX-U and DIII-D H-mode, suggesting that it is not an exclusive feature of the H-mode. To find out its origin, the toroidal torques induced by neutral friction, neoclassical viscosity, collisional perpendicular shear viscosity, ion orbit loss and turbulent Reynolds stress were estimated using the measured parameters. Our results indicate that in this particular parameter regime the neutral friction was the dominant damping force. The calculated cocurrent toroidal torque by the neoclassical viscosity dominates over those from the collisional perpendicular shear viscosity, ion orbit loss and turbulent Reynolds stress. These results are potentially important for the understanding of boundary conditions for the intrinsic toroidal momentum in tokamak plasmas.

PACS numbers: 52.55.Fa, 52.25.Fi, 52.25.Ya, 52.35.Ra

(Some figures in this article are in color only in the electronic version)

[a] Author to whom any correspondence should be addressed.

1. Introduction

Rotation and velocity shear can have a strong impact on plasma stability and confinement of fusion plasmas. In future fusion reactors, the available neutral beam injection (NBI) power is not high enough to drive significant rotation due to the high injection energy needed for the beam to penetrate deep into the plasma [1]. Thus, there has been a growing interest in the 'intrinsic rotation' in tokamak plasmas, i.e. plasma rotation in the absence of any auxiliary momentum source [2]. Recent experiments indicate that a toroidal momentum pinch is necessary to explain the measured momentum transport [3]. While it seems relatively robust that rotation profiles will be peaked in ITER thanks to the pinch term, its absolute value remains very challenging to predict with the present knowledge of momentum sources and sinks at the plasma edge, and the uncertainties in the rotation boundary condition. New data from DIII-D showed that the intrinsic velocity is measured to scale roughly linearly with the local ion temperature, $v_t \propto T_i$, in the pedestal [4]. The mechanism driving the cocurrent intrinsic rotation near the edge is not yet well understood.

The measurements of the main-ion rotation were achieved long time ago [5], but only with the recent advent of high-resolution spectroscopy more detailed structures were observed. A dip structure in the toroidal rotation at the H-mode edge transport barriers (in the outermost 5 cm of the confined plasma) was observed in ASDEX-U [6] and DIII-D [4] tokamaks. At about 1 cm inside the separatrix the rotation exhibited a local minimum. From there, the rotation of the main ions and the impurity ions in cocurrent direction increased towards the plasma center and towards the separatrix. In our recent experiments similar structure in v_t was observed in Ohmic L-mode plasmas, suggesting that it is not an exclusive feature of the H-mode. This phenomenon has been observed in both divertor and limiter discharges and perfectly reproducible on EAST.

2. Experiment setup

The experiments were carried out on the EAST tokamak [7] in Ohmic heated deuterium L-mode plasmas using two fast reciprocating Langmuir probes. The two probes are located both on the outer midplane, toroidally separated by 90°. The fast reciprocating motion was driven by an AC servo motor system capable of scanning a range of 50 cm at a speed up to 2 m/s.

A Langmuir-Mach probe was used to provide simultaneous measurements of plasma profiles and ion parallel flows as shown in figure 1(a). The upstream and downstream graphite electrodes, which were embedded in a boron nitride ceramic body, sampled plasma from opposite directions along the

same field line, forming a 'Mach probe pair' in which the parallel Mach number was estimated from the ratio of ion saturation current signals, $M_{\parallel} = 0.4 \ln\left(I_{up}/I_{down}\right)$. The other five tips on top of the probe head were operated as triple probe, allowing simultaneous measurements of electron density $n_e = \alpha_s I_s / c_s$, electron temperature $T_e = \left(\Phi_{pb} - \Phi_f\right)/\ln 2$, and plasma potential $\Phi = 2.8 T_e + \Phi_f$, where I_s is ion saturation current measured by Tip4, $c_s \equiv \left(2T_e/m_i\right)^{1/2}$ is ion sound speed, α_s is a constant coefficient, Φ_f is floating potential measured by Tip1, 3 and 5, and Φ_{pb} is the potential on Tip2 which was positively biased at 250 V. The parallel flow velocity was then estimated as $v_{\parallel} = M_{\parallel} c_s$. The toroidal rotation velocity is approximately equal to the parallel flow velocity in a low-β tokamak, $v_t \cong v_{\parallel}$, since the toroidal field is much stronger than the poloidal field, $B_t \gg B_p$.

The turbulent Reynolds stress was measured using a 3-tip probe array as shown in figure 1(b). Tip 1 and 2, poloidally separated by 6.6 mm, $L_{12} = 6.6mm$, were used to measure fluctuations in the poloidal electric field $\tilde{E}_y = \left(\tilde{\Phi}_{f1} - \tilde{\Phi}_{f2}\right)/L_{12}$ which was then used to calculate radial **E×B** velocity fluctuations $\tilde{v}_r = \tilde{E}_y / B$. Tip3 radially protruded by 5 mm, $L_3 = 5mm$, and was shielded by a graphite tube with 5 mm in length. Fluctuations in the radial electric field were estimated as $\tilde{E}_r = \left(\tilde{\Phi}_{f3} - \tilde{\Phi}_{f12}\right)/L_3$, where $\tilde{\Phi}_{f12} = \left(\tilde{\Phi}_{f1} + \tilde{\Phi}_{f2}\right)/2$ is approximately the floating potential fluctuation at the midpoint of Tip1 and 2. The poloidal **E×B** velocity fluctuations were then computed as $\tilde{v}_y = \tilde{E}_r / B$. In this way the radial and poloidal components of the electric field fluctuations were estimated at the same location, providing a local measurement of the electrostatic Reynolds stress, $\Pi_{RS} \equiv \left\langle \tilde{v}_r \tilde{v}_y \right\rangle$ where $\langle \cdots \rangle$ denotes the flux surface average. All the probe tips were made of graphite with 1.8 mm in diameter and 2 mm in length. The probe data were simultaneously sampled at 2 MHz with 12-bit resolution using a multichannel digitizer.

To exclude the influence of ballooning-transport-driven scrap-off layer (SOL) flows on the rotation boundary condition [8], we chose balanced double-null (BDN) and limiter configurations for these experiments. A typical BDN Ohmic heated L-mode discharge #22111 was used for this study, with plasma current I_p = 250 kA, the location of magnetic axis R_0 = 1.88 m, toroidal magnetic field on the magnetic axis B_0 = 1.8 T, poloidal magnetic field on the separatrix of the outer midplane B_p =

0.1 T, horizontal minor radius a = 0.45 m, plasma elongation κ = 1.7. The safety factor at the plasma edge was very high, q_{95} ~ 10, due to the low plasma current. The electron density and electron temperature measured by Thomson scattering at the plasma centre in a similar discharge (there was no Thomson scattering data in this discharge) was $n_{e0} \sim 1.5\times10^{19}\mathrm{m}^{-3}$ and T_{e0} ~ 500 eV, respectively. The Ohmic heating power was ~200 kW. In such low power Ohmic discharges the graphite probes can provide reliable measurement in the outermost 4 cm of the confined region and in the SOL where electron temperature was usually less than 60 eV. The experiments were conduced in 'normal B' direction which was defined as B_t clockwise ($\boldsymbol{B}\times\nabla B$ pointing down) and I_p counterclockwise, viewed from the top. Gas puff location was at the outer midplane.

3. Inversed shear in the intrinsic toroidal rotation near the edge

At about 1 cm inside the separatrix a local minimum in parallel Mach number, $M_{||}$, was observed, from where a cocurrent rotation increased towards the plasma center and towards the separatrix, as shown in figure 2(b). The radial width of the $M_{||}$ dip was 1~2 cm, situated at the same location of a dip structure in radial electric field, E_r, and steep gradients in density and electron temperature profiles. The density and electron temperature profiles are displayed in figure 2(a). Figure 3 shows the profile of poloidal **E×B** velocity $v_{Ep} = E_r / B_t$, where the E_r was calculated as the radial gradient of plasma potential $\Phi = 2.8T_e + \Phi_f$. The floating potential profile Φ_f is displayed in figure 2(b). In figure 3 we also plot the poloidal phase velocity of floating potential fluctuations calculated using the standard two-point correlation technique. It is roughly at the same velocity of v_{Ep} outside the edge E_r shear layer, but inside the edge E_r shear layer the fluctuations propagated in the electron diamagnetic direction in the plasma frame of reference.

The distance from this dip to the separatrix was ~1cm, which was close to the poloidal ion gyroradius $\rho_{pi} = m_i v_{thi} / eB_p$ and the banana orbit width of thermal ions. The normalized ion collisionality $\nu_{PSi} = \nu_{ii} / \omega_{tri}$ was larger than 5 at the plasma edge so that the plasma was in the deep Pfirsch-Schlüter regime, where $\omega_{tri} = v_{thi} / q_{95} R_0$ is the ion transit frequency. The parallel velocity $v_{||} = M_{||} c_s$ in our experiments amounts to ~20 km/s, as shown in figure 4. The calculated neoclassical

'offset' parallel velocity $v_{\|}^{Neo} \cong \left(E_r - \partial_r p_i / en + k\partial_r T_i / e\right)/B_p$ was more than two times larger than the measured parallel flow velocity at the plasma edge, where T_i was assumed to be equal to T_e and the collisionality coefficient k was ~ –2 in this case. A dip structure in $v_{\|}^{Neo}$ can also be seen at the same radial location of the dip structure in the measured parallel flows, and clearly this dip structure was mainly contributed by the E_r, as indicated by the toroidal **E×B** velocity $v_{Et} = E_r / B_p$ profile in figure 4.

4. Toroidal torques near the edge

To explain how this dip structure in v_t gets formed, the toroidal torques were estimated using the measured parameters. Momentum transport and rotation sources/sinks at the plasma edge are usually more complicated than those in the core region since several processes could play roles in determining the rotation profiles, and in different plasma scenarios or collisionality regimes the dominating processes could be different. The important processes include charge-exchange (CX) neutral friction, turbulent Reynolds stress, collisional perpendicular shear viscosity, ion orbit loss, and neoclassical viscosity. Each of these processes is in association with a nonambipolar radial current, J_r, and a toroidal torque, $\mathrm{T}_t = \left\langle \mathbf{J}_f \cdot \nabla \psi \right\rangle = \left\langle J_r R B_p \right\rangle$ [9], where ψ is the poloidal flux function and $\mathbf{J}_f$ is the free current. The net (total) radial free current consists of

$$J_r = J_{Neo} + J_{CX} + J_{IOL} + J_{CV} + J_{RS} + \tilde{J}_B + J_{other} \quad (1)$$

which are induced by the neoclassical toroidal viscosity (J_{Neo}), the CX neutral friction (J_{CX}), the ion orbit loss (J_{IOL}), the collisional perpendicular shear viscosity (J_{CV}), the turbulent Reynolds stress (J_{RS}, i.e. the so-called nonlinear polarization current [10]), the curvature and grad-B drift ($\tilde{J}_B$), and other unknown mechanisms (J_{other}), respectively. Among them the radial current induced by curvature and grad-B drift, $\tilde{J}_B = \left(RB_p B\right)^{-1} \left(p_\perp \mathbf{b} \times \nabla \ln B + p_{\|} \nabla \times \mathbf{b}\right) \cdot \nabla \psi$, is responsible for the oscillating component of E_r in association with the geodesic acoustic mode [11]. Its time average is assumed to be negligible in this paper.

The toroidal momentum equation can be written as

$$\partial_t L_t - \varepsilon_0 \partial_t \left\langle \mathbf{E} \cdot \nabla \psi \right\rangle = \mathrm{T}_t \tag{2}$$

where $L_t - \varepsilon_0 \left\langle \mathbf{E} \cdot \nabla \psi \right\rangle \cong L_t$ is the total toroidal angular momentum density, $L_t \equiv \left\langle m_i n v_t R \right\rangle \sim I_t \omega_t$ is the mechanical toroidal angular momentum density of ions, $I_t \equiv \left\langle m_i n R^2 \right\rangle$ is the moment of inertia density, $\omega_t \equiv -\partial\Phi/\partial\psi - (en)^{-1} \partial p_i/\partial\psi \sim \left\langle v_t / R \right\rangle$ is the toroidal angular frequency, $-\varepsilon_0 \left\langle \mathbf{E} \cdot \nabla \psi \right\rangle$ is the toroidal angular momentum density in the electromagnetic field which is negligible in a low-β plasma where the Alfvén speed is much smaller than the speed of light $v_A \ll c$, and ε_0 is the dielectric constant of vacuum. The E_r evolution is governed by the radial Ampère's law.

$$\varepsilon \partial_t \left\langle \mathbf{E} \cdot \nabla \psi \right\rangle = -\left\langle \mathbf{J}_f \cdot \nabla \psi \right\rangle \tag{3}$$

Here $\varepsilon = \varepsilon_\perp + \varepsilon_0 \cong \varepsilon_\perp$ is the dielectric coefficient and $\varepsilon_\perp$ is the perpendicular dielectric coefficient which is enhanced by a geometry factor $1 + 2q^2$ in a torus, $\varepsilon_\perp \cong \left(1 + 2q^2\right) \left\langle m_i n B^{-2} \right\rangle$ [9].

In a torus the toroidal rotation and the E_r are coupled through the well-known ion radial force balance equation.

$$E_r - \frac{\partial_r p_i}{en} = B_p v_t - B_t v_p = -B v_\perp = R B_p \omega_t \tag{4}$$

Here the perpendicular velocity $v_\perp = v_E + v_{di}$ is composed of the **E×B** velocity $v_E = -E_r / B$ and the diamagnetic velocity $v_{di} = \partial_r p_i / enB$. The nonambipolar radial currents are generally functions of E_r and/or plasma temperature and density gradients. Therefore, each of these nonambipolar radial currents has a dependence on the toroidal rotation. In a steady state the balance in the toroidal torques, $\mathrm{T}_t = 0$, or equivalently, the vanishment in the net radial free current, $\left\langle J_r \right\rangle = 0$, determines the structure of the toroidal rotation as a function of the plasma profiles. Based on these understandings the toroidal torques in the edge region of EAST were estimated using the measured parameters.

4.1. Charge-exchange neutral friction

Neutral particles usually only play a role in the edge region since, in general, the plasma is considered to be impermeable to neutrals with the penetration depth limited to a few centimeters [12]. Neutral density is typically of the order of 10^{16}~10^{17} m^{-3} at the tokamak edge but decreases steeply

by one order of magnitude over just several centimeters inside the separatrix. Neutral particles are unbound by the magnetic field and multiple CX interactions can redistribute energy, particles and momentum. To determine the magnitude of CX momentum losses, the neutral density profile was modeled in this work using a 1.5D fluid neutral transport code FRANTIC [13] embedded in TRANSP code, performing neutral gas transport calculation for tokamak plasmas in the confined region, taking into account multiple CX interactions and impact ionization atomic reactions in a simplified nested cylindrical flux surface geometry. This code was also recently employed on JET to study momentum losses by CX neutral friction [14]. The modeled neutral density profiles has been benchmarked against the flux-surface averaged neutral density profiles calculated with 2D Monte Carlo neutral transport code EIRENE implemented in B2SOLPS code. The absolute value of neutral density estimated by the codes was then validated against the Dα/Hα emission intensity measured by Dα/Hα photodiode arrays (PDA) installed on the EAST device. Two arrays of 35-channal Dα/Hα, viewing the inner target and dome surfaces of both upper and lower divertors from the outer midplane through the in-vessel reflection mirrors; and 18-channel Dα/Hα, viewing the lower outboard divertor from the top of the machine. The PDAs were absolutly calibrated using an integrating sphere standard light source (PHOTO RESEARCH LRS-455). The input parameters into the FRANTIC/TRANSP code include:

(1) Magnetic equilibrium data from EFIT;

(2) Edge n_e and T_e profiles measured by the fast reciprocating probes;

(3) Electron cyclotron emission (ECE) in combination with Thomson scattering was used to obtain T_e profile in the core. Core n_e profile was provided by Thomson scattering;

(4) Core T_i profile, based on the broadening of line emission from trace amount of highly ionized argon, was measured by a high resolution imaging x-ray crystal spectrometer;

(5) The ratio of H/(H+D), obtained through an analysis on the Dα/Hα spectral lineshape, was measured using an optical multi-channel analysis system (OSM) [15], which was equipped with a high-resolution Acton Research Spectrometer (SP-750) and ICCD (EEV 384×578 pixels) cooled by a multistage Peltier element. The 2400gr/mm grating was used with a spectral resolution of 0.01 nm. The working gas was deuterium, but there was a hydrogen concentration of about 30% for these experiments. The hydrogen mainly came from the first wall;

(6) The particle confinement time $\tau_p \sim 40ms$ was estimated based on recycling particle flux deduced from Dα/Hα emmision intensity measured by the Dα/Hα PDAs;

(7) The neutral population on the separatrix, which is one of the boundary conditions in the code, is split into two contributions with their percentage and energy obtained through an analysis on the Dα/Hα spectral lineshape [15]. There were roughly 50% 'warm' Franck-Condon particles at temperature 3 eV and 50% 'cold' molecules at temperature 0.03 eV from the wall and gas puff;

(8) The fraction of escaping neutrals to return as 'warm' recycling neutrals was set as 50%, and the remainder was supposed to return as 'cold' neutrals.

The modeled neutral density profile was then used to calculate the Dα/Hα emission profiles along the lines of sight of Dα/Hα PDAs on EAST. The obtained line integral photon fluxes were then validated against the measured photon fluxes. The modeled flux-surface averaged profiles of deuterium neutral density n_{0D}, hydrogen neutral density n_{0H}, the total neutral density $n_0 = n_{0D} + n_{0H}$ as well as the averaged neutral density estimated based on the measurement of Dα/Hα emission intensity for EAST discharge #22111 are shown in figure 5(a) for comparison. The averaged neutral density was determined from the calibrated Dα/Hα data by assuming that the light arises from electron excitation of neutral atoms according to the relation $I_{D\alpha} = n_e n_0 \langle \sigma v_e \rangle_{EXC}$, where $I_{D\alpha}$ is the intensity from the Dα/Hα PDAs, and $\langle \sigma v_e \rangle_{EXC}$ is the photon emissivity coefficient obtained from the ADAS atomic data base. The estimated neutral density at the plasma edge is $n_0(\rho = 1) \sim 3 \times 10^{16} m^{-3}$, as shown in figure 5(a). Since most of the neutrals were from wall recycling or gas puff, their toroidal velocity is expected to be small, $v_0 \sim 0$, such that the neutral friction is always a drag force which damps the rotation. It produced a radial return current, J_{CX} [9]. This return current must be balanced by a driving current or currents in a steady state. The toroidal torque associated with CX neutral friction can be computed as [14]

$$\mathrm{T}_{tCX} = \langle J_{CX} R B_p \rangle \sim -\nu_{i0} m_i n R_0 \langle v_t \rangle \tag{5}$$

where $\nu_{i0} = n_0 \langle \sigma v_i \rangle_{CX}$ is a momentum loss rate and $\langle \sigma v_i \rangle_{CX}$ is the CX rate coefficient. Using the obtained neutral density profile, figure 5 (b) shows the calculated CX neutral friction torque per unit velocity, indicating that the CX neutral friction is significant in the vicinity of the separatrix.

4.2. Turbulent Reynolds stress

The plasma fluctuation levels associated with microturbulence were observed to be of the order of unity at the plasma edge but typically only of the order of 1% in the core region, so that turbulent momentum transport could play a more important role in the edge than in the core [9]. The turbulent Reynolds stress has long been proposed as a suspect in driving poloidal rotation [16], toroidal rotation [17,18] or L-H transition [19]. Recently the potential role of turbulent momentum transport in generating the 'intrinsic rotation' was proposed [20]. The profiles of turbulent Reynolds stress, $\Pi_{RS} \equiv \left\langle \tilde{v}_r \tilde{v}_y \right\rangle$, measured using the 3-tip probe array shown in figure 1(b) on the outer midplane of EAST in several Ohmic discharges are displayed in figure 6. Similar Π_{RS} magnitude and profiles were also reported previously from ISTTOK [16] and JET [21] tokamaks. The radial gradient of Π_{RS} is small in the SOL but more significant in the vicinity of the separatrix. The induced toroidal torque can be estimated as

$$\mathrm{T}_{tRS} = \left\langle J_{RS} R B_p \right\rangle \sim \alpha_{ballooning} R_0 B_p B_0^{-1} m_i n r^{-1} \partial_r \left(r \Pi_{RS} \right) \tag{6}$$

where $\alpha_{ballooning}$ is a ballooning factor. Since the measurement was conducted on the outer midplane where usually one expects to see the highest fluctuation levels, a reasonable value for the ballooning factor is ~1/5 [8]. The radial gradient length of Π_{RS} was of the order of ρ_{pi}. The calculated torque profile at the edge is shown in figure 5(c), $\mathrm{T}_{tRS} \sim 0.01 N/m^2$, suggesting that although the ambipolar component of anomalous transport induced by microturbulence clearly dominates in the Ohmic L-mode plasmas, the nonambipolar component, i.e. the so-called nonlinear polarization current due to the turbulent Reynolds stress [10], is relatively small.

4.3. Collisional perpendicular shear viscosity

The collisional perpendicular shear viscosity is generally negligible in the hot plasma core region but could be significant in the high-collisionality edge. Momentum transport by this process is usually included in the sophisticated edge 2D fluid transport codes, such as B2SOLPS, UEDGE and EDGE2D. The collisional perpendicular shear viscosity is a classical effect, which is usually a small

contribution and has some effect only in high-shear regions. The induced toroidal torque can be estimated as [22]

$$\mathrm{T}_{tCV} = \left\langle J_{CV} R B_p \right\rangle \sim -\left(1+2q^2\right) R_0 B_p B^{-2} \eta_{i\perp} \partial_r^2 E_r \tag{7}$$

where $\eta_{i\perp} = (3/10) n T_i \nu_{ii} / \omega_{ci}^2$ is the Braginskii perpendicular viscosity coefficient [23], ν_{ii} is the ion-ion collision frequency and ω_{ci} is the ion cyclotron frequency. The appearance of an enhancement factor $1+2q^2$ in expression (7) is due to the well-known toroidal effect [9]. Using the approximation $\partial_r^2 E_r \sim |E_r| / \rho_{pi}^2$, we can make an estimation of the toroidal torque at the edge, as shown in figure 5(c), $\mathrm{T}_{tCV} \sim 0.01 N/m^2$, indicating that the contribution from the collisional perpendicular shear viscosity is small.

4.4. Ion orbit loss

The ion orbit loss has long been proposed as a candidate mechanism for the L-H transition [24, 25]. It is a typical boundary effect. Ion orbits with large radial excursions or falling into the loss cone in the vicinity of an X-point tend to intersect the material boundary or divertor targets and are lost from the confinement region. The ion orbit loss mechanism in tokamaks results from the coupling between the configuration-space diffusion and the velocity-space scattering. In this work the model by Shaing [26] were used to give an estimation of the toroidal torque induced by ion orbit loss.

$$\mathrm{T}_{tIOL} = \left\langle J_{IOL} R B_p \right\rangle \sim R_0 B_p G e n \nu_{ii} \rho_{pi} \left(\nu_{*i}^{1/4} + |X|\right)^{-1} \exp\left[-\left(\nu_{*i}^{1/4} + |X|\right)^2\right] \tag{8}$$

Here $\nu_{*i} = \nu_{ii} / \omega_{tri} \varepsilon^{3/2}$ is the standard collisionality parameter. The E_r parameter, X, is defined as

$$X = M_p (r-a) / \rho_{pi} \sqrt{2\varepsilon} \tag{9}$$

where $M_p \equiv E_r / B_p v_{thi}$ is the poloidal **E×B** Mach number. $G \sim O(1)$ is a geometry factor. The ion orbit loss enhancement due to the X-point effect [27] is simplified by just introducing this geometry factor. The X-point effect was previously investigated by Chankin [28], Miyamoto [29], Heikkinen [30], and recently by Chang and coworkers [27]. More recently the X-point effect was employed to explain the nearly linear scaling of the intrinsic toroidal velocity with the pedestal ion temperature, $v_t \sim T_i$, observed in DIII-D H-mode [4]. Here we simply set $G = 1$. The ion orbit loss enhancement due

to the X-point effect is left for future investigations.

The ion orbit loss process becomes important when ions are collisionless, so that they can intersect the material boundary if it appears in their trajectories. The collisionality in the plasma edge region was very high in our case, which could be a reason for the very small contribution from ion orbit loss as indicated in figure 5(c). In figure 5(c) one can see there are two peaks in the torque T_{tIOL} at the radial location where E_r crosses zero. This is mainly due to the exponential term in expression (8). The small ion orbit loss contribution in our case does not mean it is unimportant in the L-H transition, since the ion orbit loss rate is very sensitive to the local collisionality. When approaching the L-H transition, the increase of edge temperature can significantly enhance the ion orbit loss rate due to the exponential dependence in expression (8). Therefore, it is still possible to play an important role during the L-H transition.

4.5. Neoclassical viscosity

The neoclassical viscosity could have significant contribution to the rotations in both core and edge regions, but the core and edge plasmas are usually in different collisionality regimes. The plasma core is usually in the collisionless regimes where the neoclassical toroidal viscosity is expected to introduce a torque to accelerate the plasma towards the 'offset' toroidal velocity [31], while the plasma edge is usually in the plateau or collisional regimes in medium or small size tokamaks. The orbit squeezing effect was neglected here since it is thought to be only relevant to the banana regime, which is not the case in our experiments.

A conventional Maxwellian neoclassical theory [32] with large gradient scale length, i.e. much larger than banana width, expresses the poloidal rotation in terms of the radial temperature gradient.

$$v_p^{Neo} = v_{\|}^{Neo} B_p / B + v_{\perp} B_t / B = \left(\left\langle B v_{\|}^{Neo} \right\rangle - F \omega_t \right) B_p \Big/ \left\langle B^2 \right\rangle = B_t k \partial_r T_i \Big/ e \left\langle B^2 \right\rangle \tag{10}$$

Here $F(\psi) \equiv RB_t = R_0 B_0$ is a flux surface constant, and k is a collisionality coefficient which was given in Ref. [33] for arbitrary collisionality and aspect ratio. It is equal to 1.17 in the banana, –0.5 in the plateau, and –2.1 in the collisional regime [32]. In our case $k \sim -2$. Substituting the poloidal velocity into the ion radial force balance equation (4), we obtain the neoclassical 'offset' parallel flow

$$B_0 U_{\|}^{Neo} \equiv \left\langle B v_{\|}^{Neo} \right\rangle = \left(B_t / B_p \right) \left(E_r - \partial_r p_i / en + k \partial_r T_i / e \right) \cong F \left\langle v_t^{Neo} / R \right\rangle \tag{11}$$

where v_t^{Neo} is the neoclassical toroidal rotation velocity. The flows are naturally ordered to be much smaller than the ion thermal speed in the standard neoclassical theory [32]. To make an estimation of the toroidal torque induced by the neoclassical viscosity, we employ the neoclassical transport model by Connor and Stringer for the transition region from the plateau regime to the collisional regime [34,35]. In this model the drift kinetic equation with a BGK collision operator was used.

$$\mathrm{T}_{tNeo} = \left\langle J_{Neo} R B_p \right\rangle \sim 2 D_i \rho_{pi}^{-2} m_i n R_0 \left(U_{\|}^{Neo} - U_{\|} \right) \mathrm{Im}\, Z \tag{12}$$

Here in the collisional regime $\nu_{PSi} > M_p$, we have $\mathrm{Im}\, Z = \pi^{-1/2} \nu_{PSi} \left(\nu_{PSi}^2 + M_p^2 \right)^{-1}$ [36], $\nu_{PSi} = \nu_{ii} / \omega_{tri}$ is the normalized ion collisionality, and D_i is the neoclassical ion diffusivity which is given by [32]

$$D_i = \left(\sqrt{\pi} / 4 \right) \rho_{pi}^2 \omega_{tri} \left(\varepsilon^2 + N q_{95} \delta^2 \right) \tag{13}$$

where δ is the ripple in the toroidal magnetic field and N is the number of toroidal field coils. EAST has 16 toroidal magnetic field coils and, therefore, $N = 16$, and a ripple amplitude δ up to 1.5% at the plasma edge on the outer midplane. The ripple is largest on the outboard side where the plasma is close to the toroidal magnetic field coils. Since the ripple breaks the toroidal symmetry, the motion of individual particles may lead to nonambipolar transport that can affect the plasma rotation through the neoclassical toroidal viscosity [31]. The enhancement in the neoclassical ion diffusivity due to ripple effect was estimated in expression (13) by simply introducing a factor $N q_{95} \delta^2$ [37]. This factor is comparable to ε^2 at the plasma edge on the outboard side, such that the ripple effect is important, especially in the outboard plasma edge region.

The calculated toroidal torque profile induced by neoclassical viscosity is shown in figure 5(c). It dominates over those from the turbulent Reynolds stress, collisional perpendicular shear viscosity and ion orbit loss. It accelerated the plasma rotation in the cocurrent direction. In a steady state, our data showed that it was mainly balanced by the drag force by the CX neutral friction. A comparision of the calculated toroidal velocity due to the balance between the neoclassical viscosity and the neutral friction, $\left\langle v_t \right\rangle = \mathrm{T}_{tNeo} / \left(\mathrm{T}_{tCX} / \left\langle v_t \right\rangle \right)$, versus the measured parallel flow velocity, $v_{\|} B_t / B_0$, shows remarkable agreement in the plasma edge region, as indicated in figure 5(d).

5. Summary

The main ion toroidal velocity in the outermost 4 cm of the confined region and in the scrap-off layer of Ohmic L-mode plasmas in the EAST tokamak was measured using Mach probes. At about 1 cm inside the separatrix a local minimum in v_t was observed, from where a cocurrent rotation increased towards the plasma center and towards the separatrix. The radial width of the v_t dip was 1~2 cm, situated at the same location of a dip structure in radial electric field and steep gradients in density and electron temperature profiles. It was observed in both divertor and limiter configurations. Similar dip structure in v_t was recently observed near the H-mode plasma edge of the ASDEX-U [6] and DIII-D [4] tokamaks. The velocity in our experiments amounts to ~20 km/s, which is at the same level of those from ASDEX-U and DIII-D H-mode, suggesting that it is not an exclusive feature of the H-mode.

To explain how this dip structure in v_t get formed, the toroidal torques induced by neutral friction, neoclassical viscosity, collisional perpendicular shear viscosity, ion orbit loss and turbulent Reynolds stress were estimated using the measured parameters. Our results indicate that in this particular parameter regime the neutral friction was the dominant damping force. The calculated cocurrent toroidal torque by the neoclassical viscosity dominates over those from the collisional perpendicular shear viscosity, ion orbit loss and turbulent Reynolds stress. These results are potentially important for the understanding of mechanisms driving cocurrent 'intrinsic rotation' near the edge in tokamak plasmas.

Acknowledgments

This work is supported by the National Natural Science Foundation of China under contracts 11075181, 10725523, 10721505, 10990212, 10605028 and the ITER project of China under contract 2010GB104001. This work was partially supported by the JSPS-CAS Core-University program in the field of'Plasma and Nuclear Fusion'.

References

[1] M. N. Rosenbluth and F. L. Hinton, Nucl. Fusion 36, 55 (1996).

[2] J. E. Rice et al., Nucl. Fusion 47, 1618 (2007).

[3] T. Tala et al., Phys. Rev. Lett. 102, 075001 (2009).

[4] J. S. deGrassie, et al., Nucl. Fusion 49, 085020 (2009).

[5] J. Kim et al., Phys. Rev. Lett. 72, 2199 (1994).

[6] T. Pütterich et al., Phys. Rev. Lett. 102, 025001 (2009).

[7] B. N. Wan, Nucl. Fusion 49, 104011 (2009).

[8] B. LaBombard et al., Nucl. Fusion 44, 1047 (2004).

[9] K. Itoh and S-I Itoh, Plasma Phys. Control. Fusion 38, 1 (1996).

[10] P. H. Diamond and Y. B. Kim, Phys. Fluids B 3, 1626 (1991).

[11] N. Winsor, J. L. Johnson and J. M. Dawson, Phys. Fluids 11, 2448 (1968).

[12] B. A. Carreras et al. Phys. Plasmas 3, 4106 (1996).

[13] M. Valovič et al., Plasma Phys. Control. Fusion 46, 1877 (2004).

[14] T. Versloot et al., 37th EPS Conference on Plasma Physics, Dublin, Ireland, 21-25 June 2010.

[15] J. Huang et al., Chinese Physics B 17, 4562 (2008).

[16] C. Hidalgo et al., Phys. Rev. Lett. 83, 2203 (1999).

[17] C. Hidalgo et al., Phys. Rev. Lett. 91, 065001 (2003)

[18] B. Gonçalves et al., Phys. Rev. Lett. 96, 145001 (2006).

[19] P. H. Diamond et al., Phys. Rev. Lett. 72, 2565 (1994).

[20] Ö. D. Gürcan et al. Phys. Plasmas 14, 042306 (2007).

[21] G. S. Xu et al., Nucl. Fusion 49, 092002 (2009).

[22] J. A. Heikkinen, T. P. Kiviniemi and A. G. Peeters, Contrib. Plasma Phys. 40, 431 (2000).

[23] S. I. Braginskii, Reviews of Plasma Physics (New York: Consultants Bureau, 1965) Vol.1.

[24] S-I. Itoh and K. Itoh, Phys. Rev. Lett. 60, 2276 (1988).

[25] K. C. Shaing and E. C. Crume, Jr., Phys. Rev. Lett. 63, 2369 (1989).

[26] K. C. Shaing, Phys. Fluids B 4, 3310 (1992).

[27] C. S. Chang, S. Kue and H. Weitzner, Phys. Plasmas 9, 3884 (2002).

[28] A. V. Chankin and G. M. McCracken, Nucl. Fusion 33, 1459 (1993).

[29] K. Miyamoto, Nucl. Fusion 36, 927 (1996).

[30] J. A. Heikkinen, T. P. Kiviniemi and A. G. Peeters, Phys. Rev. Lett. 84, 487 (2000).

[31] K. C. Shaing et al., Nucl. Fusion 50, 025022 (2010).

[32] F. L. Hinton and R. D. Hazeltine, Rev. Mod. Phys. 48, 239 (1976).

[33] Y. B. Kim, P. H. Diamond and R. J. Groebner, Phys. Fluids B 3, 2050 (1991).

[34] J. W. Conner and T. E. Stringer, Phys. Fluids 14, 2184 (1971).

[35] T. E. Stringer and J. W. Conner, Phys. Fluids 14, 2177 (1971).

[36] T. E. Stringer, Nucl. Fusion 33, 1249 (1993).

[37] K. C. Shaing, S. P. Hirshman and J. D. Callen, Phys. Fluids 29, 521 (1986).

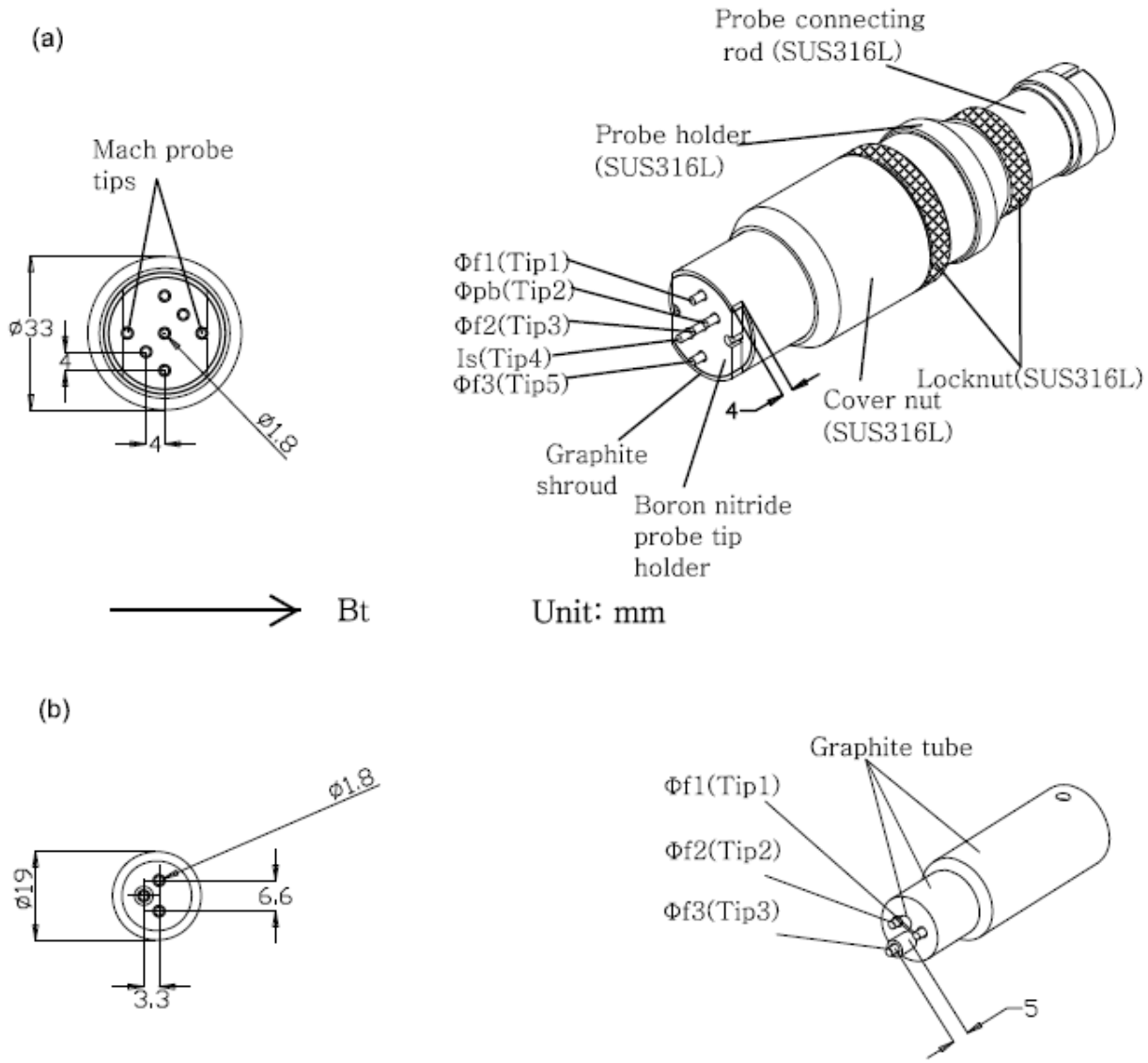

Figure 1. (a) The layout of 7-tip Langmuir-Mach probe array on the EAST tokamak. Two tips were oriented along the same magnetic field line for the measurement of parallel flows. The other five tips on top of the probe head were operated as triple probe with two additional floating potential tips. (b) The layout of 3-tip Langmuir probe array which was used for the measurement of turbulent Reynolds stress. The Tip3 protruded by 5 mm and was shielded by a graphite tube. All the probe tips were made of graphite with 1.8 mm in diameter and 2 mm in length. The plasma facing surface of the probe heads were made of graphite to stand high heat load.

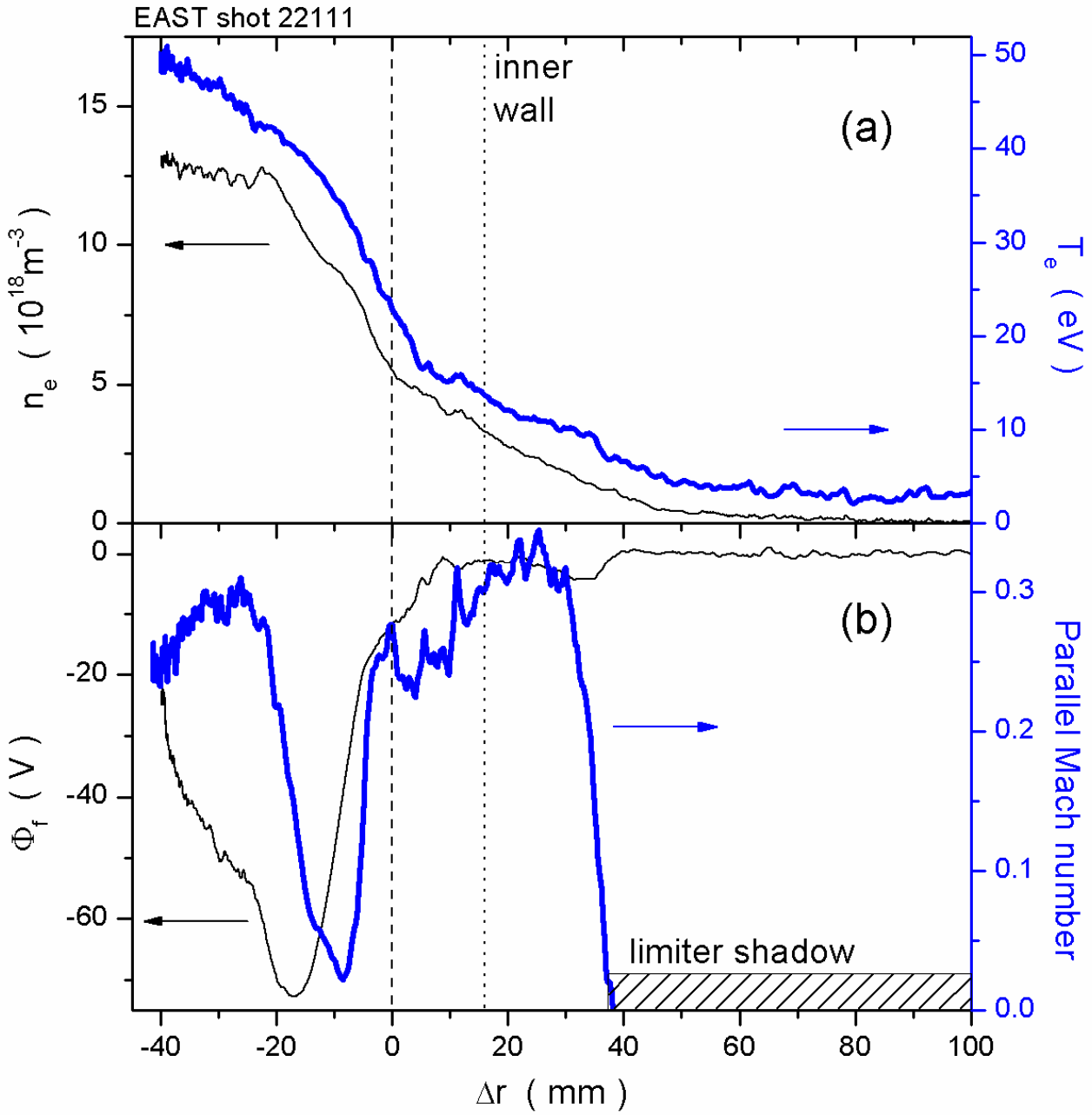

Figure 2. (a) left: electron density profile ne, right: electron temperature profile T_e, (b) left: floating potential profile Φ_f, right: parallel Mach number profile $M_{||}$, measured using a fast reciprocating Langmuir-Mach probe on the outer midplane of EAST, where $\Delta r = r - a$ is the distance to separatrix on the outer midplane. The shadow region of outer limiter and the inner wall location are also indicated. (Colour online.)

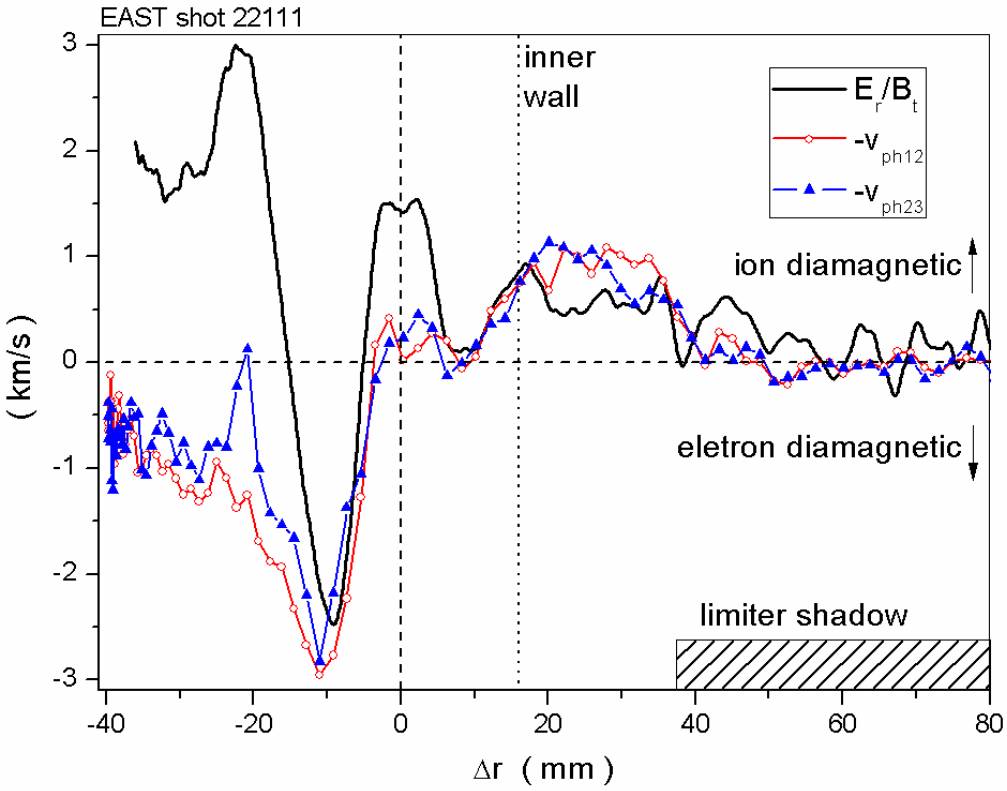

Figure 3. Profiles of poloidal **E×B** velocity $v_{Ep} = E_r / B_t$ and poloidal phase velocity of floating potential fluctuations calculated using the standard two-point correlation technique, measured using fast reciprocating probes on the outer midplane of EAST. Positive is in the ion diamagnetic direction. v_{ph12} and v_{ph23} were calculated through the correlation between $\tilde{\Phi}_{f1} / \tilde{\Phi}_{f2}$ and $\tilde{\Phi}_{f2} / \tilde{\Phi}_{f3}$, respectively. The radiel electric field was calculated as the radial gradient of plasma potential $\Phi = 2.8T_e + \Phi_f$. The shadow region of outer limiter and the projection of inner wall location are also indicated. (Colour online.)

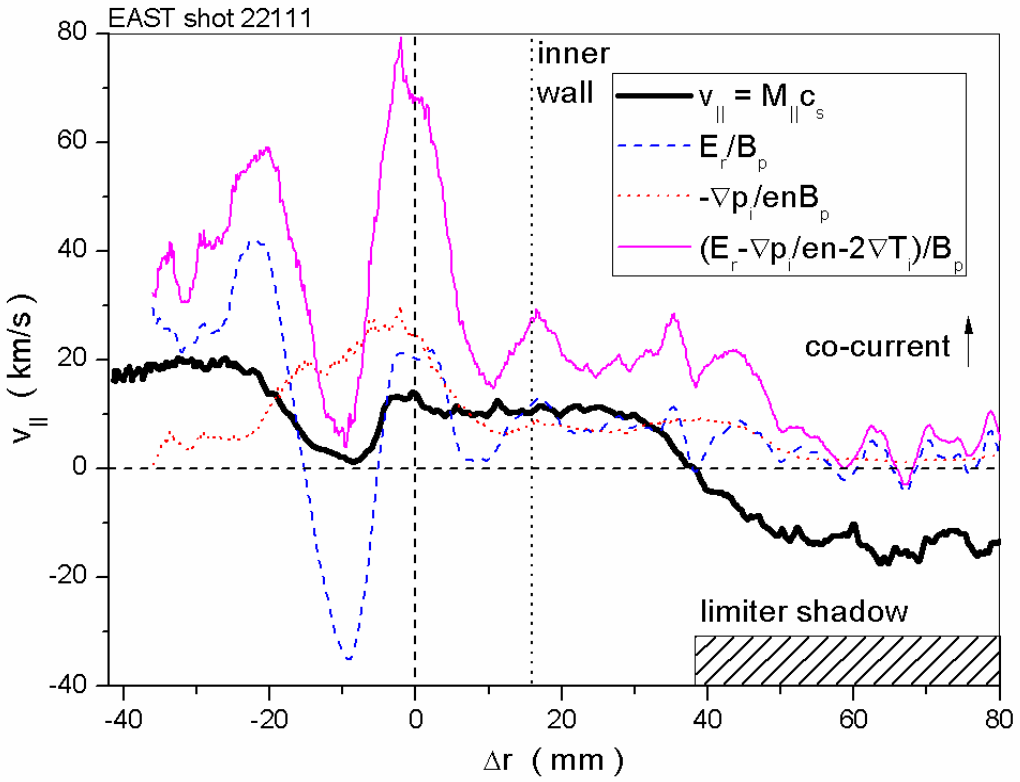

Figure 4. Profiles of parallel flow velocity $v_{\|} = M_{\|} c_s$ measured using a Mach probe on the outer midplane of EAST, toroidal **E×B** velocity $v_{Et} = E_r / B_p$, toroidal diamagnetic velocity $v_{dit} = -\partial_r p_i / enB_p$ and the neoclassical 'offset' parallel velocity $v_{\|}^{Neo} = \left(E_r - \partial_r p_i / en - 2\partial_r T_i / e\right) / B_p$. Positive is in the cocurrent direction. (Colour online.)

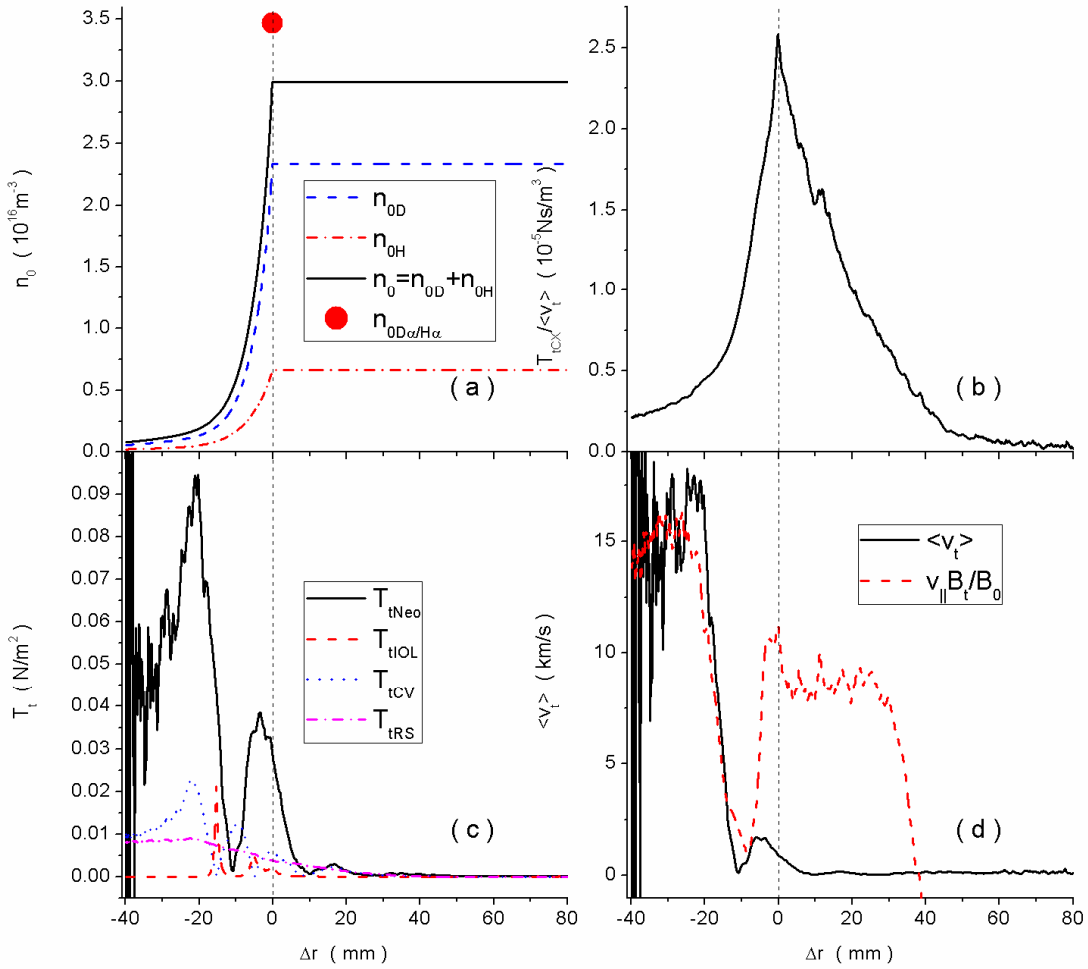

Figure 5. (a) Flux-surface averaged profiles of deuterium neutral density n_{0D}, hydrogen neutral density n_{0H}, the total neutral density $n_0 = n_{0D} + n_{0H}$, and the averaged neutral density estimated based on the measurement of Dα/Hα emission intensity for EAST discharge #22111. (b) Profile of toroidal torque per unit velocity induced by charge-exchange neutral friction. (c) Torque profiles induced by neoclassical viscosity T_{tNeo}, ion orbit loss T_{tIOL}, collisional perpendicular shear viscosity T_{tCV}, and turbulent Reynolds stress T_{tRS}, respectively. (d) Comparision of the calculated toroidal velocity due to the balance between the neoclassical viscosity and the neutral friction, $\langle v_t \rangle = T_{tNeo} / \left(T_{tCX} / \langle v_t \rangle \right)$, versus the measured parallel flow velocity, $v_{\|} B_t / B_0$, showing remarkable agreement in the edge region. (Colour online.)

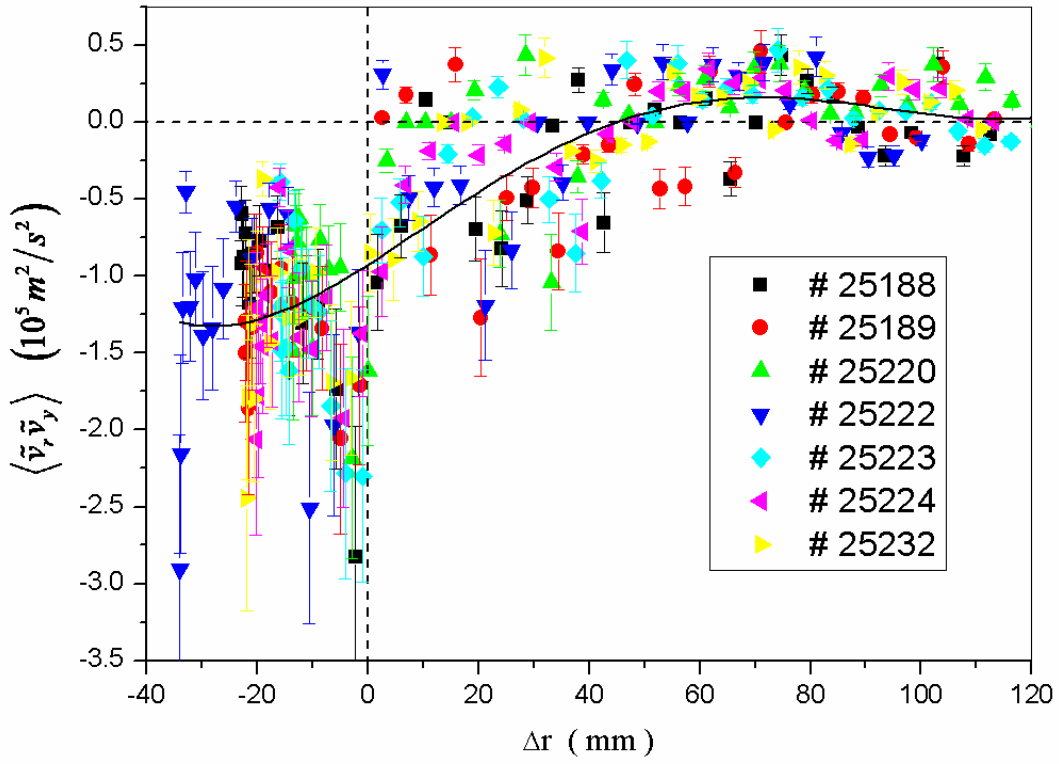

Figure 6. Profiles of turbulent Reynolds stress measured using a fast reciprocating probe array on the outer midplane of EAST in several Ohmic discharges. (Colour online.)

Present status of JT-60SA project and development of heating systems for JT-60SA

Y. Ikeda[1)] and the JT-60SA Team (JT-60SA Project Team[2)], JT-60 JA-Home Team[1)] and JT-60SA EU-Home Team[3)])

1) JT-60SA JA-Home Team and 2) JT-60SA Project Team, Japan Atomic Energy Agency, 801-1 Mukoyama, Naka, Ibaraki, 311-0193 Japan, 3) JT-60SA EU-Home Team, Fusion for Energy, Boltzmannstr 2, Garching, 85748, Germany

E-mail contact of main author: ikeda.yoshitaka@jaea.go.jp

Abstract

This paper describes the present statue of the JT-60SA (JT-60 Super Advanced) project which has been implemented jointly by Europe and Japan since 2007. Design of the main tokamak components were completed in late 2008, where all the scientific missions are preserved to contribute to ITER and DEMO reactors. The construction of the JT-60SA has began with procurement activities for the superconducting magnet systems, vacuum vessel, in-vessel components and other components under the relevant procurement arrangements between the implementing agencies of JAEA (Japan Atomic Energy Agency) in Japan and Fusion for Energy in Europe. Designs and developments of the auxiliary heating systems for JT-60SA have been progressed at JAEA so as to provide the total injection power of 41 MW for 100s.

1. Introduction

The JT-60SA project is a combined project of JAEA's program for national use and JA-EU Satellite Tokamak Program collaborating with Japan and EU fusion community [1]. The main mission of the JT-60SA project is to contribute to early realization of fusion energy by supporting the exploitation of ITER [2] and by complementing ITER in resolving key physics and engineering issues for DEMO reactors [3]. The JT-60SA device is capable of confining high temperature deuterium plasma of break even equivalent class for a duration longer than the time scales characterizing key plasma processes, such as current diffusion and particle recycling, using superconducting toroidal and poloidal field coils. The maximum plasma current is 5.5 MA. The device is to be pursue fully non-inductive steady-state operations with high values of the plasma pressure exceeding the non-wall ideal MHD stability limits. The JT-60SA experiments are expected to explore ITER and DEMO-relevant plasma regimes in terms of non-dimentional plasma parameters.

In order to satisfy these requirements, the JT-60SA device has been designed to realize a flexible plasma configurations for extrapolating ITER and DEMO. JT-60SA is also featured by powerfull heating

systems to allow variety of heating, current-drive, and momentum- input combination. This paper summarizes the present status of JT-60SA project and the recent R&D activities of heating systems for JT-60SA.

2. Objectives and Design requirements

The JT-60SA will be capable of confining break-even equivalent class high-temperature deuterium plasmas at a plasma current I_p of 5.5 MA, a major radius of ~3 m and a toroidal field of 2.25 T lasting for a duration longer of ~100 s than the timescales characteristic of plasma processes such as current diffusion. JT-60SA also pursues full non-inductive steady-state operation with high plasma beta close to and exceeding no-wall ideal stability limits, and establish ITER-relevant high density plasma regimes well above the H-mode power threshold [4]. High β_N regime to be pursued is shown with possible DEMO and ITER regimes in Fig.1. The cross-section of the JT-60SA tokamak is shown in Fig.2.

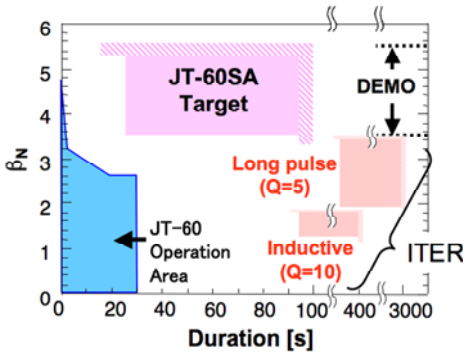

Fig.1 High β_N target of JT-60SA

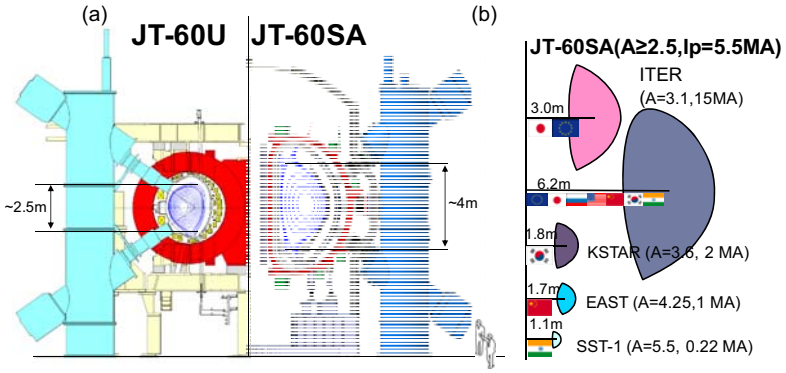

Fig.2 (a) Cross-section of JT-60U and JT-60SA. (b) plasma cross-section of superconducting tokamaks

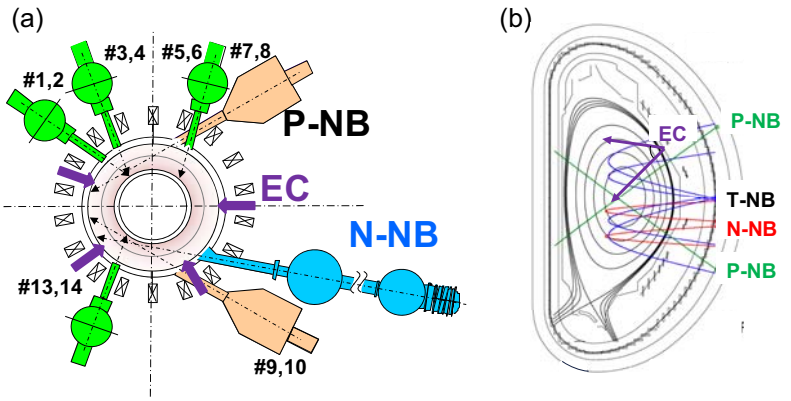

Fig.3 (a) Layout of heating systems in JT-60SA. (b) beam trajectories of NB injectors and EC waves

Table 1 Typical plasma parameters of JT-60SA

Scenario	Case 1	Case 2	Case 3	Case 4	Case 5
Parameters	Full Current Inductive DN, 41MW	Full Current Inductive SN,41MW	Full Current Inductive SN, 30MW High density	ITER like inductive	High β_N Full-CD
Plasma current, I_p (MA)	5.5	5.5	5.5	4.6	2.3
Toroidal field, B_t (T)	2.25	2.25	2.25	2.28	1.71
q_{95}	~3	~3	~3	~3	~5.7
R/a (m/m)	2.96/1.18	2.96/1.18	2.96/1.18	2.93/1.14	2.97/1.11
Aspect ratio, *A*	2.5	2.5	2.5	2.6	2.7
Elongation, κ_x	1.95	1.87	1.86	1.81	1.92
Triangularity, δ_x	0.53	0.50	0.50	0.41	0.51
Shaping factor, *S*	6.7	6.3	6.2	5.7	6.9
Normalised beta, β_N	3.1	3.1	2.6	2.8	4.3
Electron density, n_e (10^{19} m^{-3})	6.3	6.3	10.	9.1	5.0
P_{add} (MW) (N-NB/P-NB/EC)	41 (10/24 /7)	41 (10/24/7)	30 (10/20/0)	34 (10/24/0)	37 (10/20/7)
Thermal confinement time, $\tau_{E,th}$ (s)	0.54	0.54	0.68	0.52	0.23
$H_{H98(y,2)}$	1.3	1.3	1.1	1.1	1.3
V_L (V)	0.06	0.06	0.15	0.12	
Available flux at flat-top (W_b)	<~9	<~9	<~9	<~17	
Neutron production rate, S_n (n/s)	1.3×10^{17}	1.3×10^{17}	6.5×10^{16}	6.6×10^{16}	4.5×10^{16}

In order to satisfy the these requirements, the machine has been coherently designed to cover: a wide range of plasma equilibria with divertor configurations at high plasma shaping factor of S ($=q_{95}I_p/(aB_t)$) ~ 7. The typical parameters of JT-60SA are shown in Table 1. The maximum plasma currents are 5.5 MA with highly shaped configurations (in case of the double null (DN) case, and 4.6 MA for an ITER-shaped configuration. Inductive operations at Ip=5.5 MA for the flat top duration of 100 s are possible. The heating system provides 24 MW/85 keV NB injection, 10 MW/500 keV co-tangential injection and 7 MW of EC wave with steerable injection. The 24 MW/85 keV injectors consist of 2 units of co-tangential beams (4 MW), 2 units of counter-tangential beams (4 MW), and 8 units of near perpendicular beams (16 MW). The EC system consists of 9 gyrotrons, each of which generates the output power of 1MW for 100 s. Effects of non-inductive current drive, electron heating fraction and plasma rotation are clarified by changing combinations of these heating systems. Figure 3 shows the layout of the heating systems and their beam trajectories. With these capabilities, JT-60SA enables explorations in ITER- and DEMO-relevant plasma regimes in terms of the non-dimensional parameters (such as the normalized poloidal gyro radius ρ*, the normalized collisionality ν* together with high densities in the range of $1\times10^{20}/m^3$ as shown in Fig.4. In DEMO reactors, it is required to sustain high values of the energy confinement improvement factor (the HH-factor), the

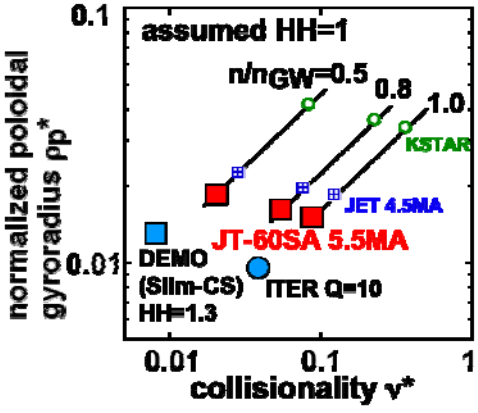

Fig.4 Non dimensional parameter regime in normalized poloidal gyroradius and normalized collisonality

normalized beta β_N, the bootstrap current fraction f_{BS}, the non-inductively driven current fraction, the plasma density normalized to the Greenwald density, the fuel purity, and the radiation power normalized to the heating power simultaneously in the steady-state [5]. The most important goal of JT-60SA for DEMO is to demonstrate and sustain such a high integrated performance. JT-60SA allows exploitations of full non-inductive steady-state operations with 10MW/ 500keV tangential injection and 7 MW of ECCD. Assuming HH=1.3, a full non-inductive operation up to 2.3 MA with f_{BS} =0.68, β_N =4.3 and f_{GW} (=n_e/n_{GW})=1 is expected. These plasma regimes satisfy the research goal of the highly integrated performance as shown in Fig.5.

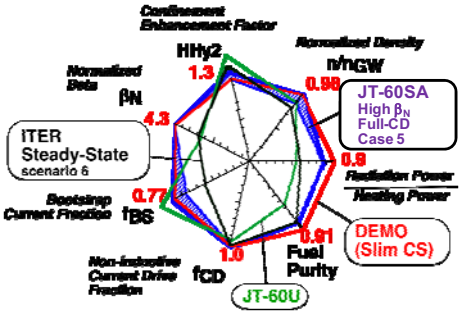

Fig.5 Integrated plasma performance of JT-60SA compared with DEMO Slim-CS, ITER steady-state and a JT-60U simultaneous achievement.

3. Design and Procurement activities of main tokamak components

The JT-60SA will be build jointly by Europe and Japan at the Naka site. Sharing of in-kind contributions by Japan and Europe, including those procured by the Japanese national program, is schematically illustrated in Fig.6. Existing JT-60 facilities will be utilized as much as possible.

Since design activities for each component are made in distributed institutes in Europe and in Japan, design integration, configuration and interface management, is key for the project. In order to define the scope of contribution of each parties and make sure that systems match each other, a single distributed organization put in place for the international implementation of the project is established as an "Integrated Project Team", built by the union of the Project Team, the EU Home Team, and the JA Home Team. Once the design is completed, the Procurement Arrangements (PAs) is to be concluded between JAEA and Fusion for Energy. Up to date, the PAs of the main tokamak components have been concluded. According to the PAs, industrial contracts have been launched when in place. The present status of the design and manufacturing of the main tokamak components, such as the superconducting magnet systems, vacuum vessel and invessel components are described.

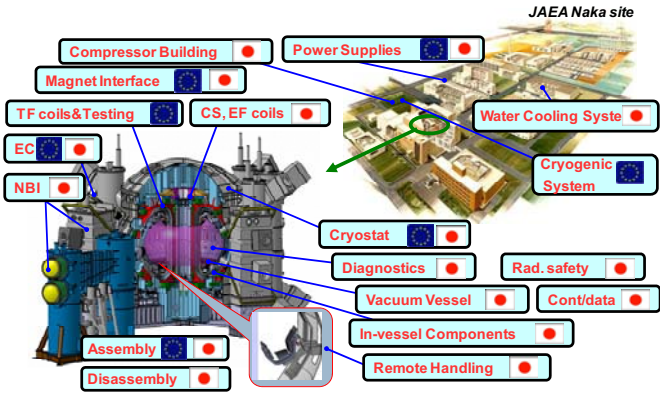

Fig.6 Sharing of contributions from Europe and Japan for JT-60SA

1) Superconducting magnet systems

The superconducting magnet system consists of 18 Toroidal Field (TF) coils, a Central Solenoid (CS) with four modules, 6 Equilibrium Field (EF) coils as shown in Fig.7 [6]. All conductors are cooled by a forced flow of supercritical helium. The total weight of the magnetic systems is ~ 700 ton. Each TF coil uses a rectangular steel-jacketed NbTi cable-in conduit conductor to produce the maximum magnetic field of 5.65 T. The TF coil casing is supported by a gravity support which is bolted to the cryostat ring. The gravity support of each coil is enveloped in a thermal shield and includes a cryogenically-cooled thermal barrier. In accordance with the PA for the TF coil concluded in 2010, manufacturing procedure of TF coils has started at EU Home Team.

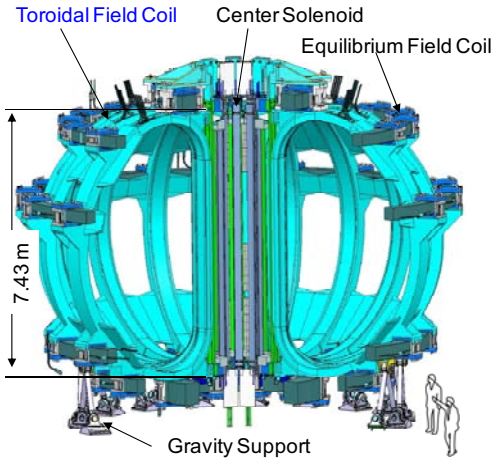

Fig.7 Superconducting magnet systems for JT-60SA

The PF magnet is composed of the CS and EF coils using Nb_3Sn and NbTi cable-in conduit conductors, respectively. The CS is a vertical stack consisting of four independently winding pack modules. The stack is hung from the top of the TF coils through flexible supports and is provided at the bottom with a locating mechanism which acts as a support against dynamic horizontal forces. High-temperature-superconducting-current-leads, which is delivered by EU, is to be used for all SC coils to reduce cryogenic loads. The six EF coils are attached to the TF coil cases through supports which include flexible plates allowing radial displacements. The PF coils are optimized to provide suitable magnetic fields for the plasma equilibrium and control and their position and size have been optimized accordingly, within the constraints imposed by the access to the in-vessel components. New buildings were completed in 2009 at the Naka site in Japan to manufacture the EF and CS superconducting coil. The jacketing of the superconducting cables of PF coils has started there.

2) Vacuum vessel

The vacuum vessel (VV) of JT-60SA is composed of 18 toroidal sectors constructed out of SS316L with low cobalt content of < 0.05 wt%, to reduce activation levels [7]. The overall vessel parameters are the torus inside and outer diameter of 2.86 m and 9.95 m, respectively, and the torus hight of 6.63 m, the main vessel body weight of ~150 ton and one turn resistance of ~16 μΩ. The VV gravity support with 9 legs is designed with the rigidity of the laminated leaf spring and the joint against the seismic motion of 1 G. The vacuum vessel can be baked up to 200°C using nitrogen gas after draining the borated water. Baking at 200°C will be done to keep the Thermal Shield at 100 K. The temperature of the vacuum vessel in normal operation is kept at ~50°C. In 2010, Development of a trial upper half of the 20 degree sector of

the VV has been completed in Japan, where welding processes are successfully finished as shown in Fig.8. Thus manufacturing of actual VV has started.

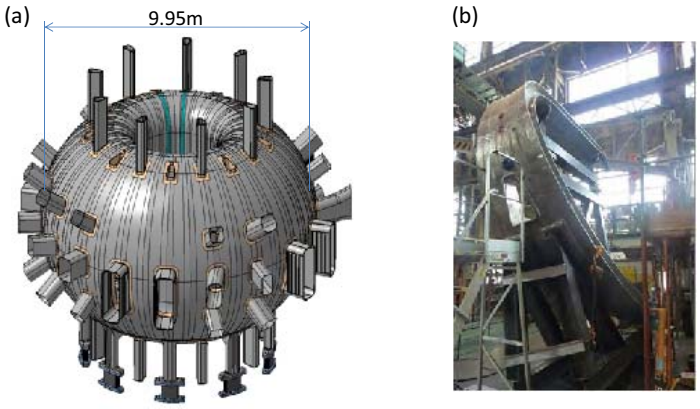

Fig.8(a) Vacuum vessel of JT-60SA (b) prototype of upper half of the 20 degree sector.

3) In-vessel components

The divertor consists of inner and outer vertical targets with a V-shaped corner to enhance particle recycling and reduce target heat flux in to a private flux region dome as shown in Fig. 9 [8]. CFC monoblock targets for the divertor cassettes is to be installed to allow high heat flux (up to 15 MW/m^2) operation lasting for 100 s. The divertor cassettes are designed to be compatible with remote handling maintenance for the preparation of future increase in radioactivation. The inner and outer first wall is to be covered with bolted armour tiles on cooled heat sink. Bolted graphite tiles on cooled heat sink withstand the heat flux of 0.1-0.3 MW/m^2 for ~100 s. All plasma-facing components including the divertor target, baffle plates and inner/outer first wall will be water-cooled at 40°C. Cryopanels will be installed below the divertor cassette for particle control. The divertor pumping speed can be changed by 8 steps up to 100 m^3/s for the lower divertor. In order to allow exploitations of high beta regimes, JT-60SA is equipped with the stabilizing shell matched to the high shape factor configurations, the resistive wall mode (RWM) stabilizing coils, and the error field correction/generation coils [9]. Design of divertor cassettes and first wall materials have been completed for the PA, and other in-vessel components are under final design phase.

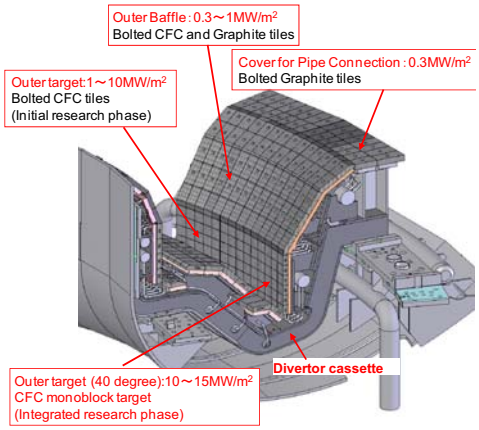

Fig.9 Lower divertor cassette of JT-60SA.

4. Developments of Heating systems

High power heating systems are a key to achieve the JT-60SA mission, such as high integrated plasma

performance. The heating systems for JT-60SA are to be set maximum utilization of JT-60U. Both NB injectors and EC systems are employed to inject the total power of 41 MW for 100s, which consist of 34 MW of NB injection and 7 MW of EC wave. The positive ion source based neutral beams (P-NBs) consist of 12 units, each of which injects 2 MW at 85 keV. The negative ion source based neutral beam (N-NB) system provides 10 MW/500 keV for strong electron heating and current drive. The 7 MW/110GHz EC system, which is composed of 9 transmission lines with 9 gyrotrons, allows a real time control of the deposition location by steerable mirrors with high frequency modulation capability (>5 kHz).

Since the achieved performances of these heating systems were 2 MW, 30 s for P-NB unit [10], 3 MW, 30 s for N-NB system [11] and 3MW, 5 s for EC system [12] on JT-60U, further improvements of the heating systems have been required to satisfy the specifications for JT-60SA.

1) NB injector system

The original injection time of the positive-ion-based injectors was 10 s on JT-60[13]. In 2004, the P-NB injector unit was upgraded to extend the injection time to 30 s at 85 keV [10]. Electric parts in the power supply was replaced with the higher heat-capacity ones, and the leading edge shape of the beam limiters was modified to increase the heat receiving area. These allowed to extend the injection time to 30 s at the injection power of 2 MW/unit as that before the modification. In this operation, the cooling capability of the beamline components such as an ion source and a residual ion dump was verified to sustain the 100 s operation. Therefore, a long pulse injection up to 100 s is expected by employing the same electric modifications and upgrade of the active cooling of the beam limiters on the P-NB injector.

One of the key issues for realization of the N-NB injector for JT-60SA is the improvement of the voltage holding capability of the ion source with three acceleration stages because the achieved accelecation voltage was 416 keV at the pulse duration less than several 100 ms due to breakdowns [13]. Although the voltage holding capability can be readily improved by the extension of the gap length, an excess extension of the gap length causes the degradations of beam optics and the stripping losses of negative ions due to collisions with residual gas molecules in the large gap. The original gap length of the N-NB ion source was designed on the database on the vacuum gap insulation obtained in the small sample electrodes (surface area:S_a= ~ 0.02 m^2). However, the low voltage holding capability of the N-NB ion source (S_a = ~2 m^2) indicates that the database obtained in the small sample is insufficient to extrapolate the

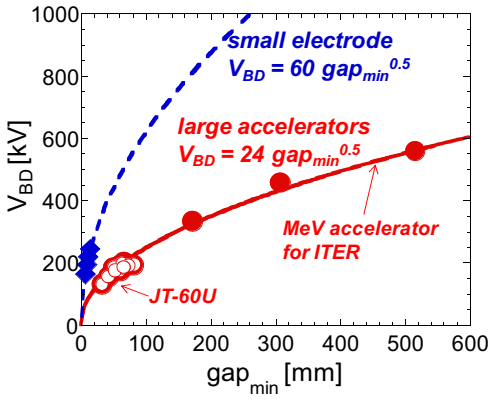

Fig.10 Breakdown voltage as a function of the gap length obtained in the large accelerators (S_a = ~2 m^2) and small electrode (S_a = ~0.02 m^2).

vacuum gap insulation for the large grids. Then the breakdown voltage was examined by varying the gap length in the JT-60 negative ion source and the MeV accelerator for ITER [14]. The breakdown voltages obtained in all three stages were plotted as a function of the minimum cathode-anode distance in each of gaps as shown in Fig.10. In this figure, the breakdown voltages obtained in the small sample electrodes are also shown for comparison. Each of the breakdown voltages were obtained after sufficient conditioning. The breakdown voltages seem to increase with the square root of gap length. Based on this result, the gap lengths for each acceleration stage were extended from 55-75mm to 85mm in order to target 200 kV for each of the acceleration stage under the condition that no significant degradations of the beam optics and the beam losses are indicated by computational calculations. The voltage holding capability of the modified ion source is drastically improved from 400 kV to 500 kV. Long pulse duration of 40 s at 490 kV, which was the power supply limitation, was also stably sustained without breakdowns .

After the improvement of the voltage holding capability, the high beam acceleration was achieved on the N-NB injector using the JT-60U test facility, where the available pulse length and the accelerated beam current were limited to be < 1s and < 10 A, respectively. The beam energy was given by sum of acceleration and extraction voltages. The hydrogen negative ion beams were produced through 20% of an ion extraction area to fit the available beam current. Figure 11 shows the beam performances before and after modification. The negative ion beams of 2.8A, 490 keV and 1A, 510 keV have been stably produced. This is the first demonstration of a high-energy negative ion acceleration of more than one-ampere to the beam energy of 500 keV in the world [14]. The power loading measurements of the acceleration grids and beamline components showed no significant degradations of the beam optics and the beam losses. The power loading measurements of the acceleration grids and beamline components showed no significant degradations of the beam optics and the beam losses. The beam current density is 85A/m^2 and 65% of the design value of 130 A/m^2 for JT-60SA. This was limited by poor ion extraction voltage (< ~5 kV) due to a misalignment of feed-through for the extraction voltage in this test campaign. New feed-through is designed for JT-60SA so as to avoid the misalignment in setting. These successful results indicate feasibility of high energy beam injection up to 500 keV for JT-60SA.

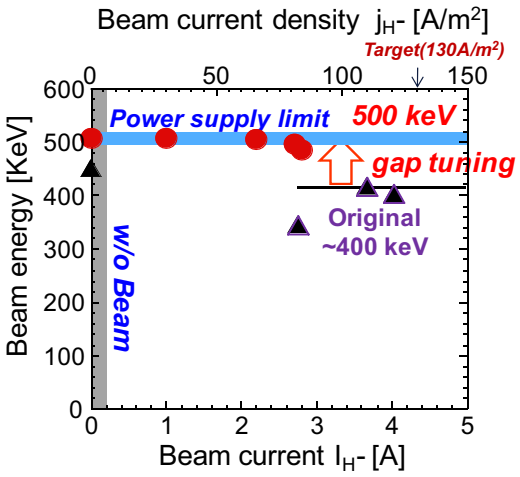

Fig.11 Beam performances before and after the gap tuning of the JT-60 negative ion source.

2) EC system

A 110 GHz gyrotron used in JT-60U was originally designed for obtaining 1 MW output power with a

pulse length of up to 5 s. After achieving the target output power of 1 MW for 5 s [12], improvements of the gyrotron for obtaining longer pulse length and higher power had been continued. The longest pulse length of 30 s was successfully achieved in an experimental campaign of JT-60U in 2007, however, the output power should be reduced from 1 MW to 0.4 MW to avoid the overheating on the DC ceramic between body electrode and collector electrode due to diffracted power in the gyrotron [12]. The diffracted power might be caused by poor mode convertion efficiency at the internal mode convertor in the gyrotron. For reducing the diffracted power in the gyrotron, an improved 110 GHz gyrotron was fabricated with equipping a newly designed built-in mode convertor. The design technique, so called Launcher Optimization Tool [15], was employed to optimize the shape of the mode convertor. The diffraction loss was improved from 6.8 % to 3.5 % in calculation. This was the same level as that of the 170 GHz gyrotron for ITER, which had already installed the new mode convertor and achieved an oscillation of 1 MW for 800 s at JAEA [16]. On the new gyrotron, the pulse length at an output power of 1 MW has been reached to 31 s. Since the temperature of the cooling water on the DC ceramic is saturated at 35°C within 10 s [17], further long pulse up to 100 s at 1MW is expected after sufficient conditioning.

Other progress on the gyrotron development is to increase the output power more than 1 MW by enhancing the oscillation efficiency. For high efficiency, it is a key to achieve the gyrotron oscillation at the lowest possible magnetic field on the cavity. The higher pitch factor of the electron beam ($=V_{perpendicular}/V_{parallel}$) is required to start the gyrotron oscillation at lower magnetic field, however, the operation at higher pitch factor increases the trapped electrons between the mirror magnetic field and the potential of the electron gun and finally prevents the oscillation. On the development of ITER 170 GHz gyrotron at JAEA, it was found that a transition from low to high efficient oscillation was obtained by gradually reducing the magnetic field. This high efficient operational regime is the so-called hard-excitation one, where the oscillation can be excited only after the gyrotron oscillation is established [16]. On the development of 110 GHz gyrotron, a new approach to the hard-excitation was pursued by quickly changing the pitch factor. In this technique, the magnetic field on the cavity was set at just below the normal operation level, where the gyrotron oscillation cannot be excited at the normal pitch factor. Then, the electron beam is turned on and accelerated with the higher pitch factor than the normal operation so as to start the gyrotron oscillation at low magnetic field. Once the gyrotron oscillation with high efficiency was established, the pitch factor is quickly reduced so as to avoid the increase of the trapped electrons and to keep the oscillation for long pulse. This technique was applied on the original gyrotron. A high power up to 1.5 MW for 4 s was obtained [17]. The pulse duration was limited by the overheat on the DC ceramic due to large diffracted power of the original gyrotron. Longer pulse duration is expected on the new gyrotron in which the temperature of the cooling water on the DC ceramic is to be saturated at ~50°C at the output power of 1.5 MW. Figure 12 shows the recent progress on the gyrotron at JAEA. A high frequency modulation of 10 kHz, which is required to efficiently suppress the NTM for JT-60SA, was

also demonstrated by modulating the pitch factor at the power level of 1 MW.

EC antenna is featured by the movable mirrors to control the local heating and current drive location during plasma operation. Indeed, in JT-60U, antennas with motor driven rotation mirror without active cooling [18] brought actual results in various ECCD/ECH experiments. For JT-60SA, it is required to employ active cooling for movable mirrors because of the long pulse duration up to 100 s. A new concept with a mirror driven in the linear motion was proposed [19], where the antenna eliminates the flexible tube for coolant supply and the link mechanism in the vacuum. There is a tradeoff between "poloidal angle range" and "beam radius" in choosing curvature radius of the second curved mirror. Curvature radius of 0.7 m enables the wide control of the poloidal injection angle of -40° to +20° with the beam radius of 0.1 m or less. Low power measurements of the mock-up antenna are consistent with the design values [20]. Figure 14 shows the conceptual design of JT-60SA antenna with two beam lines, each of which has the linear motion mirror to control the poroidal injection angle. Concerning with the toroidal injection angle, it is possible to control the injection angle ±15° by rotating the drive shaft.

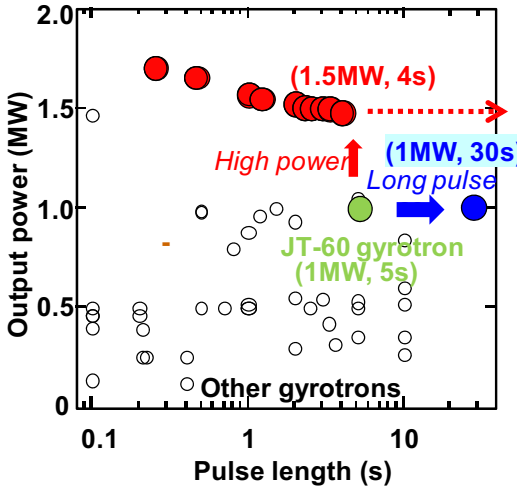

Fig.12 Progresses of the 110 GHz gyrotron for JT-60SA

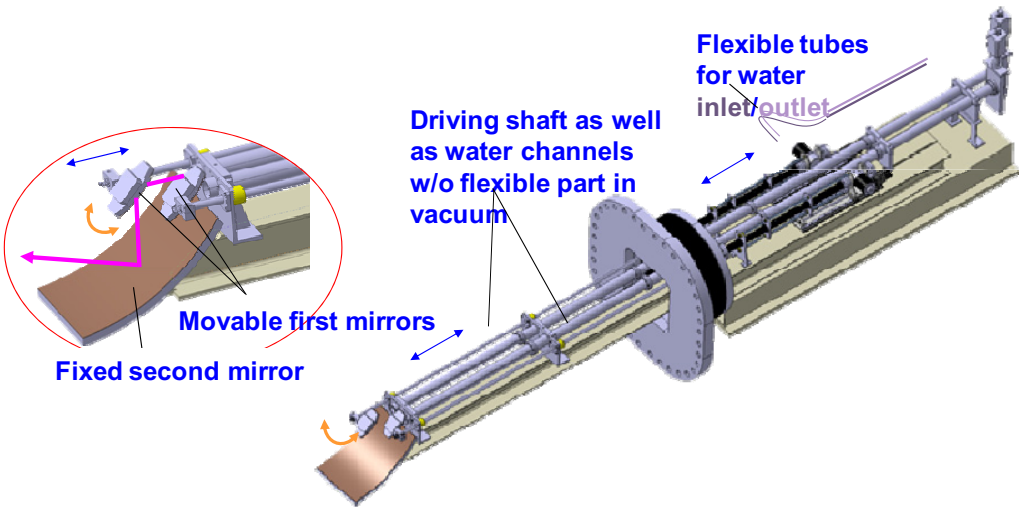

Fig.13 EC antenna with linear motion mirror for JT-60SA

5. Schedule

The project schedule is shown in Fig.15, which was approved by the Broader Approach Steering Committee in late 2008 taking into account a more detailed analysis of the manufacturing and assembly schedule. As a result, the milestone of "First Plasma" is foreseen in 2016. Other main milestones are set out as "Start Tokamak Assembly" in 2012, "Complete Tokamak Assembly" in 2015. The JT-60SA facilities such as heating systems will be upgraded step by step according to the phased operation plan as shown in Table 2, where the operational phase is correspondingly shown as an initial research phase (hydrogen phase and deuterium phase), an integrated research phase, and an extended research phase. Experiences and achievements in JT-60SA in these research phases are indispensable for an efficient and reliable start-up of ITER operation and for optimizations of discharge scenarios in H/He, DD and DT phases of ITER operation.

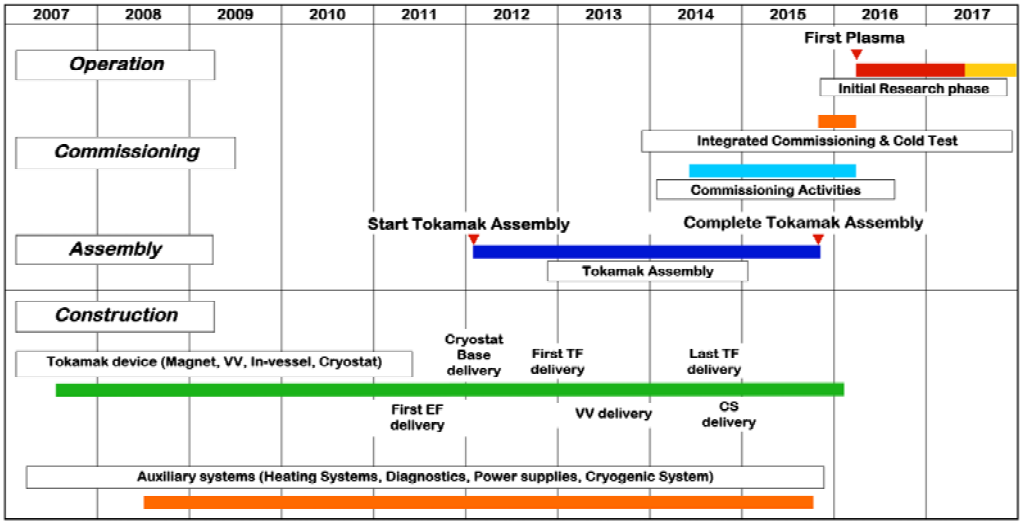

Fig.14 Present schedule of JT-60SA project

Table 2 Operation phases and status of key components

	Phase	Expected Duration		Annual Neutron Limit	Remote Handling	Divertor	P-NB	N-NB	EC	Max Power	Power x Time
Initial Research Phase	phase I	1-2 y	H/D	-	R&D	LSN partial monoblock	10MW	10MW	1.5MW x100s + 1.5MW x5s	23MW	NB: 20MW x 100s 30MW x 60s duty = 1/30 EC: 100s
	phase II	2-3y	D	4E19			Perp. 13MW Tang. 7MW			33MW	
Integrated Research Phase	phase I	2-3y	D	4E20		LSN full-monoblock			7MW	37MW	
	phase II	>2y	D	1E21	Use						
Extended Research Phase		>5y	D	1.5E21		DN	24MW			41MW	41MW x 100s

Acknowledgements

The author would like to thank all persons who have contributed to the JT-60SA project. The presentation was also partially supported by the JSPS-CAS Core-University program in the field of 'Plasma and Nuclear Fusion'.

References

[1] S. Ishida et al., Proc. of the 23rd Fusion Energy Conf., 2010, OV/P-4.

[2] 'Progress in the ITER Physics Basis', Nucl. Fusion 47 (2007) S1.

[3] K. Tobita et al., Nucl. Fusion 49 (2009) 075029.

[4] Y. Kamada et al., Journal of Plasma and Fusion Research SERIES Vol. 9 (2010) 641.

[5] Y. Kamada and JT-60 Team, Nucl. Fusion 41 (2001) 1311.

[6] M. Peyrot et sl, Proc. of the 23rd Fusion Energy Conf., 2010, FTP/P6-29.

[7] S. Sakurai et al., Fusion Engineering and Design, **84**, (2009), 1684.

[8] S. Sakurai et al, Proc. of the 23rd Fusion Energy Conf., 2010, FTP/P1-29.

[9] M. Takechi et al., Proc. of the 23rd Fusion Energy Conf., 2010, FTP/P6-30.

[10] Y. Ikeda et al., Fusion Engineering and Design **82,** (2007) 701-707.

[11] M.Hanada et al., Rev. Sci. Instrum.**77,** (2006), 03A515.

[12] S. Moriyama et al., Nucl. Fusion 49 (2009) 085001.

[13] M.Kuriyama et al., Fusion Science and Technology **42,** (2002) 410.

[14] A. Kojima et al., Proc. of the 23rd Fusion Energy Conf., 2010, FTP/1-1Ra.

[15] R. Minami et al., J. Infrared. Millim. Waves 27, (2006) 13.

[16] K. Sakamoto et al., Nature Phys. 3, (2007) 411.

[17] T. Kobayashi et al., Proc. of the 23rd Fusion Energy Conf., 2010, FTP/P6-13.

[18] Y. Ikeda et al., Fusion Science and Technology **42,** (2002) 435.

[19] S. Moriyama et al., Fusion Eng. Des. 82, (2007) 757.

[20] T. Kobayashi et al., J. Plasma Fusion Res. SERIES, Vol. 9 (2010) 363.

Recent results of H-mode experiments in HL-2A*

HL-2A Team (Presented by YAN, Longwen)

Southwestern Institute of Physics, Chengdu, China

e-mail: lwyan@swip.ac.cn

H-mode discharges have been achieved in HL-2A by combining the heating power of NBI (P_{NBI} <0.8 MW) and ECRH (P_{EC} <1.6 MW) with 2nd harmonic X-mode [1], which are strongly dependent on the optimized discharge conditions, including good wall conditioning and divertor configuration, SMBI fuelling, and suitable density range with feedback, titanium gettering in divertor, et al. Typical ELM periods are 1-3 ms, which can sustain more than ten times of energy confinement time with enhanced confinement factor H_{89} > 1.5. Some have more than 10 ms.

The SMBI is used to fuel plasma because it has higher fueling efficiency, deeper penetration depth, and lower recycling than normal gas puffing. An H-mode discharge is shown in Fig. 1. There are 6 SMBI pulses injected into the plasma. The first pulse makes the D_α in divertor decrease slightly even if the density increases. The ECRH power of 450 kW added at t = 425 ms lets central electron density drop and radiation power rise obviously. The beam power of 460 kW is injected into plasma at t = 510 ms. Immediately, stored energy and radiation power gradually rise. Plasma density begins to rise at t = 530 ms after the second SMBI pulse and then discharge enters H-mode phase from t = 550 ms. The available data indicate that power threshold is reduced about 10% by the SMBI fueling in comparison with gas puffing.

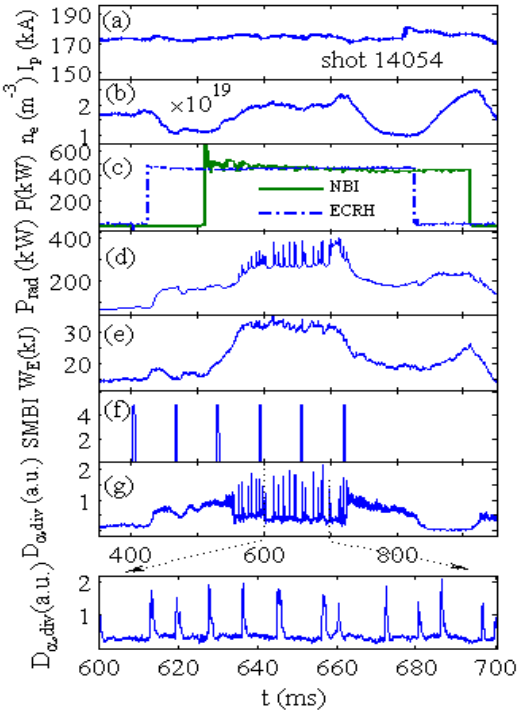

Fig. 1. The H-mode fuelled by the SMBI fueling in discharge 14054.

The waveforms from top to bottom are, the plasma current (a), central line-averaged density (b), NBI and ECRH powers (c), radiation power in main chamber (d), stored energy (e), SMBI pulses (f), D_α emissions in divertor (g) and a zoomed part of it, respectively.

The parameter space of H-mode discharges is extended. The initial plasma density is a rather important parameter, which is limited in (1.2-1.8) $\times 10^{19}$ m^{-3} due to the use of ECRH method. The ECRH power will be deviated or reflected if density over 2.2×10^{19} m^{-3}. The L-H transitions mainly depend on total heating power. They are almost independent of heating ways. The longest

*Presentation for a CUP seminar on plasma control, heating and diagnostics, 1-4 Nov. 2010, Guilin, China

H-mode duration is 550 ms, which is only limited by the heating time. Pedestal density width in discharge 14052 is about 3.5 cm, measured by microwave reflectometry of O-mode, and the pedestal density is 1.2×10^{19} m^{-3}.

This work was partially supported by the JSPS-CAS Core-University program in the field of'Plasma and Nuclear Fusion'.

[1] Duan X.R., Dong J.Q., Yan L.W., et al. Nucl. Fusion 50 (2010) 095011.

Recent experiments towards steady state operation of spherical tokamak QUEST

K.Hanada[a)], H.Zushi [a)], H.Idei [a)], K.Nakamura [a)], M.Ishiguro [b)], S.Tashima [b)], E.I.Kalinnikova[b)], M.Sakamoto [a)], M.Hasegawa [a)], A.Fujisawa [a)], A.Higashijima [a)], S.Kawasaki [a)], H.Nakashima [a)], H.Liu [b)], O.Mitarai [c)], T.Maekawa [d)], A.Fukuyama [e)], Y.Takase [f)], J. Qian[g)]

a): Research Institute for Applied Mechanics, Kyushu University, Japan,

b):Interdisciplinary Graduate School of Engineering Science, Kyushu University, Japan,

c): School of Industrial Engineering, Tokai University, Japan

d):Graduate School of Energy Science, Kyoto University, Japan,

e): Graduate School of Technology, Kyoto University, Japan

f): Graduate School of Frontier Science, University of Tokyo, Japan

g): Institute of Plasma Physics, Chinese Academy of Sciences, China.

Abstract

Plasma start-up and its maintenance were successfully done by fully non-inductive current drive using a microwave of 8.2 GHz. Plasmas current of 15kA was achieved for 1 s. Magnetic surface reconstruction shows a plasma shape with the aspect ratio of less than 1.5. The plasma current depended significantly on the injected microwave power, vertical magnetic field strength, however was not affected by the injected wave mode and the refractive index to toroidal magnetic field. Hard X-ray (HXR) emitted from energetic electrons accelerated by the microwave was observed and the plasma current over 4kA followed with the number of photons of 10-12 keV. This suggests that the plasma current may be driven by energetic electrons. Based on the experimental conditions, the candidates how the plasma current could be driven are discussed.

1. Introduction

Non-inductive plasma start-up and maintenance can provide an attractive way towards cost-effective fusion power plants such as spherical tokamaks (STs) without ohmic heating (OH) coils. Recently experiments on plasma start-up using microwaves were successfully executed on the various STs such as CDX-U [1], LATE [2], TST-2 [3], MAST [4] and CPD [5]. Even in tokamaks, many experiments were also done on WT-2 [6], JIPPT-IIU [7], WT-3 [8], PLT [9], TRIAM-1M [10] with various frequencies of microwaves in the range of 2-170GHz. These results indicate the plasma start-up using the microwaves is a promising way to get the plasma start-up for making a tokamak configuration.

In the tokamaks, lower hybrid wave (LHW), which is a powerful tool for accelerating electrons along the magnetic field line, can accessible to the core part of plasmas and the effective combination of LHW and electron cyclotron wave (ECW) played an essential role in the

achievement of non-inductive plasma start-up. However as ST has been operated in the similar density under significant lower toridal magnetic field, LHW cannot provide a valid way anymore. In ST, electron Bernstain wave (EBW) is expected for a candidate to drive the plasma current instead of LHW. EBW is a kind of electro-static wave in plasmas and direct excitation of the wave is not expected. Mode-conversion process plays an essential role in the wave excitation [11]. This is a key issue for driving plasma current in ST with high density.

QUEST [11] is a ST constructed in Kyushu University to aim steady state operation under controlled plasma wall interaction (PWI) and it has been running from 2008. A main purpose of the research locates on non-inductive current drive using microwaves and several results on non-inductive current drive in QUEST are reported in this paper. In the successive section, a brief introduction of the experimental apparatuses is described and experimental results are shown in the section 3. Discussion on how plasma current is driven in the plasma is done in the section 4. The contents of this paper are summarized in the section 5.

2. Experimental Apparatus

The QUEST project will be developed in increment step such as, I. low β steady state operation in limiter configuration, II. low β steady state operation in divertor configuration, III relatively high β steady state operation in closed divertor configuration. Now QUEST is in the phase I. Specifications and major planned parameters of QUEST are listed in Table 1.

The maximum toroidal field is 0.5T within 1sec and 0.25T in steady state at R=0.64m. Both the height and the diameter of the vacuum vessel is 2.8m. The schematic view of QUEST is shown in Fig. 1. QUEST has several pairs of PF coils including PF4-1/4-3, PF4-2, which is suitable to put in magnetic flux into the plasma via ohmic heating (OH). These have the capability to supply the magnetic flux by 200 mVs. The vertical magnetic field required to make an equilibrium can provide from two pairs of PF1-7, PF2-6 which are referred in Fig. 1 and any other poloidal field (PF) coils were not operated in the non-inductive current drive experiments described in this paper. The PF1/7 and PF2/6 coils can provide the vertical magnetic field of 85 G and 145 G per 1kA at R=64cm. Two kinds of microwaves of 2.45GHz, 50kW and 8.2GHz, 400kW are available to drive plasma current and heat plasmas and they have the capability to operate in steady state. A system of 8.2GHz has the well-designed antenna to adjust injection mode, polarization, injection angle [12]. The dependence of the injection mode and angle on driving plasma current is studied using the antenna.

The inner part of the vacuum vessel is completely covered by stainless steel of 3mm in thickness coated by W. Moreover four fixed water-cooled limiters made of W are installed around only mid-plane on the inner part of the vessel. The lower divertor is composed of W-coated 16 panels made of stainless steel and the upper one is composed of non W-coated 16 panels. Four fixed limiters which made of stainless steel are installed on the outer part of the vessel. 67 flux loops are

installed along the inner side of the vacuum vessel and a Rogosky coil to reconstruct magnetic flux surface.

3. Experimental results

Typical waveforms of plasma current, I_P, injected microwave power, P_{RF}, currents of the vertical field coil, PF1/7 and PF2/6, and H_α signal on non-inductive current drive experiment are shown in Fig. 2. The plasma current of 15kA could be achieved and it maintained for 1 s. It should be noted that no loop voltage to the plasma was supplied from the PF coils in their steady state condition more than the time constant to penetrate magnetic field through the vacuum vessel, which is about 10ms. This indicates the plasma current could be maintained by the only injected microwave in a fully non-inductive manner. Fueling was only done for the plasma production just before the discharge and no more fueling was done during the discharge. This shows the fuel can be supplied through recycling process. The plasma current was significantly reduced by excessive out-gassing from the wall, which emerged as a rise in H_α signal. Although no diagnostics for density was installed on QUEST except three sets of probes, low density may be required to obtain high current. The density measurements by a scanning probe were done and a density profile could be obtained on the peripheral region of plasma of 5 kA. The density of $3x10^{17}m^{-3}$ was obtained at the edge of the core plasma.

Two ways for reconstruction of magnetic flux surfaces are executed. EFIT is used for the purpose and this is one of the world standard code to reconstruct magnetic flux surfaces. Parabolic current fitting (PCF) method is also applied for the purpose and this was proposed by Yoshinaga on LATE [13]. EFIT gives the best result to satisfy the Grad-Shafranov equation from the measured data. PCF provides the best current density profile to fit the measured magnetic data to assumed parabolic-shaped-profile [13]. EFIT does not permit any plasma current located outside of the last closed flux surface (LCFS). On QUEST, only 67 flux loops and a Rogosky coils could be available in every reconstruction. Therefore the assumed current profile in EFIT is the simplest one. As PCF makes effort to fit the measured magnetic data based on the parabolic-shaped-profile with 11 fitting-parameters, the accuracy of the resultant current profile is better than EFIT. However the resultant current profile is not considered to satisfy the Grad-Shafranov equation. A comparison of the magnetic surfaces reconstructed by two above-described ways in #9119 is shown in Fig. 3. The target plasma had 12kA in plasma current and used as a standard operation due to the good reproducibility. The structure of LCFS is similar each other and the current profile by PCF is broader than that by EFIT. The aspect ratios of the reconstructed LCFS are 1.47 in EFIT and 1.45 in PCF and this clearly indicate that a spherical tokamak configuration has been obtained by a fully non-inductive current drive on QUEST.

Hard X-ray (HXR) radiated via bremsstrahlung process from plasmas was monitored by

two detectors (CdTe, CdZnTe), which can detect X-ray in the range of 3-200 keV [14]. Lower energy X-ray than 10keV can be detected, however considerable correction is required because of the drastic change of the detection efficiency. Detected X-ray was investigated using pulse-height analysis (PHA) to obtain energy spectrum and it was found that the plasma current more than 4kA was almost proportional to the number of photons in the range of 10-12keV as shown in Fig. 4. Plasma current below 4kA did not have clear relation with the detected HXR. This suggests that the non-inductive current more than 4kA may be driven by energetic electrons with around 10keV. Figure 4 shows the plasma current is almost proportional to the strength of the vertical magnetic field at R=0.64m where is the center of the vacuum vessel. The plasma current also increased with the injected power. While the excessive energetic electrons were observed as the plasma current grew up and they directly attacked to a vacuum wall on low field side and produced hot spots on the wall. Consequently, out-gassing from the hot spots prevent from maintaining plasmas.

4. Discussion

As fully non-inductive current drive can be obtained on QUEST as described above, we should discuss how the plasma current was driven. The antenna for 8.2GHz has the capability to inject the microwave as well-controlled mode [12] and the amount of driven current was investigated as the function of the injection angle to the toroidal magnetic field in the experiments. As the result, the plasma current did not depend on the injection angle to the toroidal field and the wave mode such as O and X modes. Well-controlled wave injection will be required to excite EBW in the plasma [11] and the efficiency of mode conversion to EBW significantly depends on the density profile. In the O-X-B scenario, a wave as O-mode injected into the plasma and the wave is reflected at the O-mode cut-off and the wave as O-mode converted to slow X-mode via the reflection at the O-mode cut-off. The efficiency for the mode-conversion is significantly influenced by the injection angle of the wave, that is the refractive index along the magnetic field, $N_{//}$ [15]. The mode-converted wave propagates as slow X-mode for the low-field side and the wave approaches the upper hybrid resonance (UHR) layer from high field side. The next mode-conversion from slow X-mode to EBW can be expected. The excited EBW propagates to the higher density side and it reaches to the ECR layer and absorbs into the plasma. In X-B scenario, a tunneling effect to penetrate unpropagated layer for the wave as fast X-mode plays an essential role in the excitation of EBW. The tunneling effect has the strong dependence on the density gradient at UHR, because the density gradient is the decisive parameter of the thickness of unpropagated layer [11]. Anyway the most important thing in each scenario is the presence of well-fitted density profile to excite EBW. Lower density than O-mode cut-off leads to no mode conversion to EBW, and it is natural that the current drive by EBW does not work well. These things suggest that the current driven by EBW could not be expected in the experiments, because higher density prevented from higher current.

Electron cyclotron current drive (ECCD) is the alternative candidate to drive the plasma current. ECCD drives the plasma current via electrons accelerated by electron cyclotron wave (ECW) at the ECR layer. The resonance condition of ECW depends on the energy of the electron via relativistic effect and the velocity along the magnetic field via Doppler effect. When ECW with positive $k_{//}$ is injected from low field side, the wave resonates to electrons with positive $v_{//}$ at first, where $k_{//}$ shows the components along the magnetic field of the wave number vector and $v_{//}$ means the velocity of electron along the magnetic field. After passing the cold ECR, the wave resonate again to electrons with negative $v_{//}$. This effect tends to cancel the driven current by ECCD and especially week one-pass-absorption enhances the cancelling effect. In the experiments, the expected one-pass absorption is less than 10% even for energetic electron of 10keV, the cancelling effect may prevent from driving the plasma current. When right hand cutoff locates just high field side of the cold ECR layer, the wave as X-mode cannot reach to the resonance for the electrons with negative $v_{//}$ [16], the effective current drive can be expected. In this case, the amount of driven current depends strongly on the wave mode. However the current drive efficiency does not depend on the wave mode.

The most plausible explanation of current drive is spontaneous current drive based on the precession motion of trapped electrons and the asymmetric electron orbit with positive and negative $v_{//}$. This effect was proposed in the neo-classical theory and a quantitative analysis was done on open magnetic field in a spherical tokamak [17]. The current drive based on the precession motion is quite effective on open magnetic surafce (OMS) before the formation of closed magnetic surface (CMS) which is essential to make a tokamak configuration. The current induced by the asymmetry of electron orbit can be driven on even CMS and may play an important role in a rise of plasma current. The details of the spontaneous current are under investigation.

5. Summary

On QUEST, the spherical tokamak configuration with the aspect ratio of less than 1.5, the plasma current up to 15kA could be obtained for 1s by fully non-inductive current drive using the well-controlled microwave of 8.2GHz. The plasma current was almost proportional to the number of photons emitted from energetic electrons. This suggests that the non-inductive current may be driven by energetic electrons accelerated by the microwave. The plasma current was reduced by the increment of out-gassing caused by the presence of the hot spots made by direct attack the energetic electrons on the wall. The driven current did not depend significantly on the injected wave mode and angle to the magnetic field. This suggests that the expected current drive such as EBW and ECCD does not play a dominant role in a rise of the plasma current. Discussion on how the plasma current could be driven is still under investigation.

Acknowledgements

This work is performed with the support and under the auspices of the NIFS Collaboration Research Program (NIFS05KUTR014, NIFS08KUTR022). This work is partially supported by a Grant-in-aid for Scientific Research from Ministry of Education, Science and Culture of Japan. This work was also partially supported by the JSPS-CAS Core-University program in the field of 'Plasma and Nuclear Fusion' and the Collaborative Research Program of Research Institute for Applied Mechanics, Kyushu University.

References

[1] C. B Forest. *et al.*, Phys. Plasmas **1**, 1568 (1994).
[2] M. Uchida *et al*., PRL **104**, 065001 (2010)
[3] A. Ejiri. et al, Nucl. Fusion **46**, 709 (2006).
[4] V. E. Shevchenko et al., Nucl. Fusion 50, 022004 (2010)
[6] S.Kubo, et al., PRL **50** (1983) 1994-1997
[7] K.Toi, et al., Nucl. Fusion, **28** (1988) 147-156.
[8] K.Ogura, et al., Nucl. Fusion, **30** (1990) pp. 611-624.
[9] F.Jobes, et al., PRL **52** (1984) pp.1005-1008.
[10] K.Hanada, et al., Nuclear Fusion, Vol.44 (2004), pp.357-361
[11] A.K. Ram, S.D. Schultz. Phys. Plasma, Vol. 7 (2000) pp.4084-4093.
[12] H. Idei et al., Proc. 34th International Conference on Infrared, Millimeter, and Terahertz Waves, Busan, Korea, (2009).
[13] T. Yoshinaga et al., Nucl. Fusion, Vol. 47 (2007), pp.210.
[14] S.Tashima et al., Journal of Plasma and Fusion Research Series, Volume 9 (2010), pp.316-321.
[15] H. Idei et al., Journal of Plasma and Fusion Research SERIES, Vol.8 (2009), pp. 1104-1107.
[16] T. Maekawa et al., Phys. Rev. Lett. Vol. 70, No. 17 (1993) 2561-2564.
[17] A. Ejiri and Y. Takase, Nucl. Fusion **47**, 403 (2007).

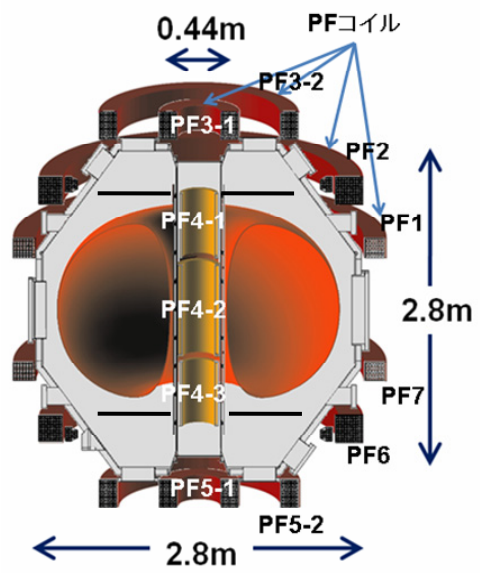

Fig. 1 Schematic view of QUEST is shown. Six pairs of PF coils (PF1/7, 2/6, 3-1/5-1, 3-2/5-2, 4-1/4-3, 4-2) are installed for double null configuration. Each coil can operate individually to form single null configuration. Flat divertor plates are installed in upper and lower side of the vacuum vessel (the positions are indicated by black lines on the figure.).

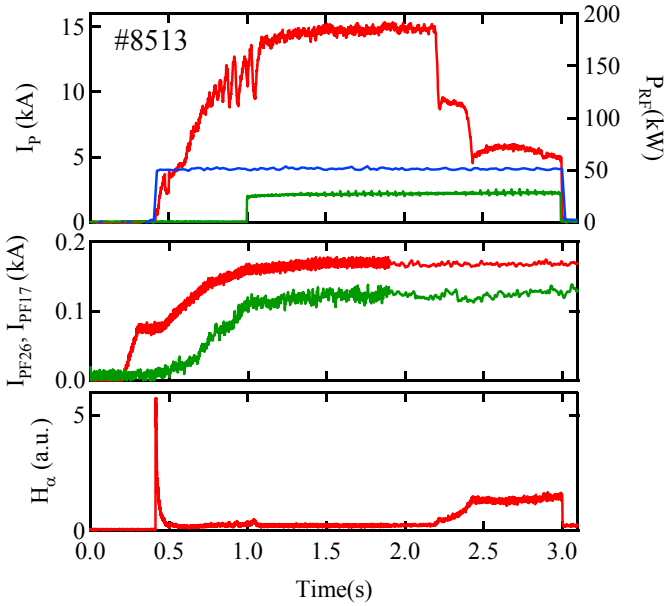

Fig. 2 Typical waveforms of plasma current, I_P, injected microwave power, P_{RF} (two systems were running in this shot) in top figure, currents of PF1/7 and PF2/6 in middle one, and H_α signal in bottom one on non-inductive current drive experiment are shown. Sampling rate of PF1/7, PF2/6 coil currents for data acquisition was changed around 1.8 sec.

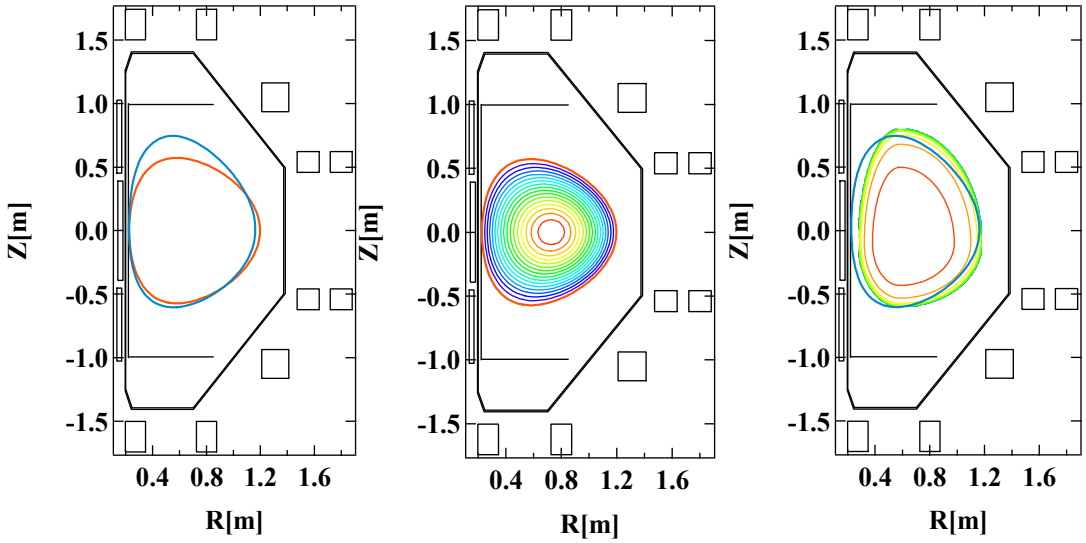

Fig. 3 The comparison of the reconstructed LCFSs using EFIT and PCF in #9119 is shown in the left figure (EFIT; Red line, PCF; Blue line). The middle figure shows the reconstructed current profile by EFIT and the right one also shows the reconstructed current profile by PCF.

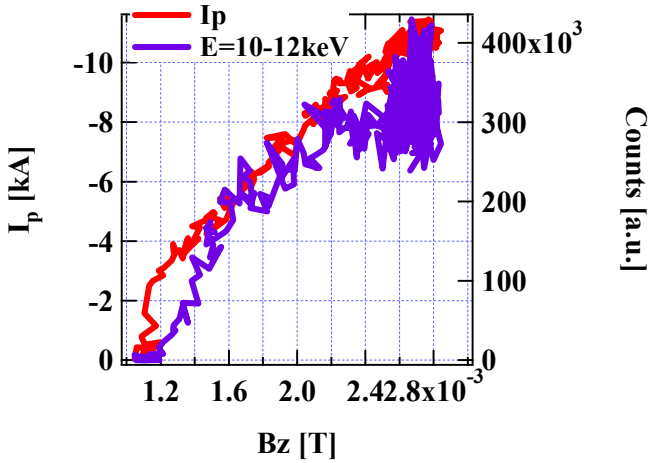

Fig. 4 Plasma current, I_p and the detected number of X-ray with 10-12keV are shown as the function of the strength of vertical magnetic field, B_z.

	Phase I	Phase II		Phase III
	Steady	Pulse	Steady	Steady
R(m)	0.68			
a(m)	0.4			
B_T (T)	0.25	0.5	0.25	0.25
I_P (kA)	20	300	100	300
P_{RF}(MW)	0.45	1	1	1

Table 1: Specifications and major planned parameters of QUEST, where R and a show the major and minor radii in a standard configuration and B_T shows the toroidal magnetic field at R=0.64m. I_P and P_{RF} mean the expected plasma current and injection microwave power in each phase, respectively.

Recent Progress on Plasma Control Studies to Improve Plasma Performance in Heliotron J

T. Mizuuchi[1],K. Nagasaki[1], H. Okada[1], S. Kobayashi[1], S. Yamamoto[1], T. Minami[1],S. Ohshima[2], M. Takeuchi[1],K. Mukai[3], H.Y. Lee[3],L. Zang[3], K. Nomura[3], M. Suwa[3], K. Yamamoto[3], H. Yashiro[3], H. Yoshino[3], S. Arai[3], T. Kagawa[3], T.Y. Minami[3], K. Mizuno[3], Y. Wada[3], Y. Watada[3], N. Nishino[4], Y. Nakashima[5], K, Hanatani[1], Y. Nakamura[3], S. Konoshima[1] and F. Sano[1]

1) Institute of Advanced Energy, Kyoto Univ., Gokasho, Uji, 611-0011 Japan.
2) Kyoto Univ. PioneeringResearch Unit for Next Generation, Gokasho, Uji, Japan.
3) Graduate School of Energy Science, Kyoto Univ., Gokasho, Uji, Japan.
4) Graduate School of Engineering, Hiroshima Univ., Higashi-Hiroshima, Japan.
5) Plasma Research Center, Univ. of Tsukuba, Tsukuba, Japan.

E-mail contact of main author: mizuuchi@iae.kyoto-u.ac.jp

Abstract. This paper reviews recent progress on plasma control studies to improve plasma performance in Heliotron J.The SMBI fueling is successfully applied to Heliotron J plasma. A supersonic H_2-beam is effective to increase fueling efficiency and make a peaked profile. Local fueling with a short pulse by SMBI can increase the core plasma density avoiding the degradation due to the edge cooling.Second harmonic ECCD experiments have been performed by injecting a focused Gaussian beam with $-0.05 \leq N_{\|} \leq 0.6$. The experimental results show that the EC driven current is determined not only by $N_{//}$ but also by local magnetic field structure where the EC power is deposited. The detailed analysis of the observed $\boldsymbol{N}_{\|}$ and B dependencesis in progress with a ray-tracing simulation using TRAVIS code.Fast ion velocity distribution has been investigated using fast protons generated by ICRF minority heating. In the standard configuration in Heliotron J, CX-NPA measurements show the higher effective temperature of fast minority protons in the on-axis resonance case than that in the HFS (high field side) off-axis resonancecase. However, the increase of the bulk ion temperature in the HFS resonance case is larger than that in the on-axis resonance.

1. Introduction

Heliotron J[1, 2]is a medium sized helical device ($\langle R_0 \rangle / \langle a_p \rangle$ = 1.2/0.17m, $\langle B_0 \rangle \leq$ 1.5T) based on the helical-axis heliotron concept [3, 4]with an L/M = 1/4 helical coil. Here, L and M are the pole number of the helical coiland its helical pitch number, respectively.In the helical-axis heliotron concept, the bumpiness ε_b is introduced as the third measure to control the neoclassical transport in addition to the other major harmonics in the Boozer coordinates, helicity ε_h and toroidicity ε_t. One of the main goals of the Heliotron J project is to experimentally explore the potential of this advanced concept as an attractive fusion device and to expand the operation regimes of the helical system.

In the previous experiments, the configuration effects on various aspects of plasma performance (bulk plasma confinement, high-energy particle confinement, plasma current control, particle fuelling, MHD, etc.) were mainly investigated in the parameter range of ($\iota/2\pi$, ε_b) [5]. Recently, experiments in the expanded investigation range in ($\varepsilon_t/\varepsilon_h$, $\varepsilon_b/\varepsilon_h$)-space have been performed. In addition to such configuration studies, survey of effective heating and fuelling scenarios has been conducted for better plasma performance. By using ICRF minority heating, the fast ion formation and confinement has been investigated in a low-density condition ($\sim 4\times10^{18}$ m^{-3}) by changing the resonance position. The ECCD experiment have been carried out by controlling $N_{//}$ at several conditions of the magnetic field ripple. These results are compared with expectations from numerical simulations. The NBI experiments with two tangential beam lines (Co and CTR) have been performed not only to

control plasma performance in higher density region but also to study high-energy particle loss mechanism and relating MHD phenomena in a helical-axis heliotron. The optimization of fuelling scenario is also in progress. A gas fuelling by supersonic molecular beam injection (SMBI) was successively applied to ECH/NBI plasmas [6]. An interesting discharge mode, similar to the re-heat mode in CHS [7], is observed for high power NBI with short-pulse intensive gas-puffing.

This paper briefly reviewsthe recent progress on plasma control studies to improve plasma performance in Heliotron J.

2. Experimental Set-up

Figure 1 schematically shows a layout of main heating, fueling and some diagnostic equipment. The initial hydrogen or deuteriumplasma is usually produced by using second harmonic X-mode ECH (70GHz, <0.40MW). The hydrogen beam is injected for NBI experiments by using one or two tangential beam-lines(BL-1 and BL-2). The acceleration voltage of NB is < 30kV and the beam power is<0.7MW/beam-line). For density control, apiezoelectric-valvesystem is usually used as a conventional gas-puffing (GP) system, which are installed at four inboard-side ports at ≈ 90° intervals around the torus (indicated by"Gas" in Fig. 1). Due to the space limitation, the nozzles of these valves do not directly see the plasma. The amount of H (or D) atomsfrom the GP system is pre-programmed to control the line-averaged density $\bar{n}_e$. Two SMBI systems of hydrogenareequippedon two horizontal outboard-sideports (the port number: #3.5, #11.5). The SMBI system at #11.5 consists of a fast solenoid-valve with a short (~ 4 mm) conic-nozzle. The diameter of its orifice is 0.2 mm$^{\phi}$ for this experiment. To reduce the stray field effect on the fast valve action, a soft-magnetic-iron cylinder covers it as a magnetic shield. The other system at #3.5 consists of a fast piezoelectric valve with a short conic-nozzle (0.2 mm$^{\phi}$ orifice).In front of the #3.5-SMBI nozzle, a movable shutter plate is installed to protect a viewing window at the same port.The amount of H atoms injected with these SMBIs is controlled by changing the pulse width of each SMBI valve under a fixed plenum pressure (P_{pl}~1-2 MPa).

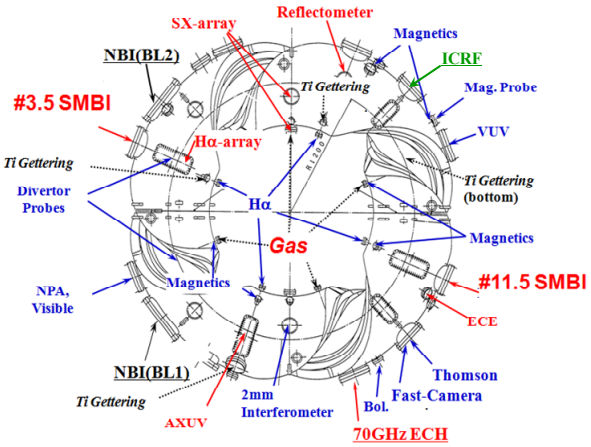

Fig. 1 *Experimental Set-up.A layout of main heating, fueling and diagnostic equipment.*

3. Effects of SMBI Fueling

Fueling and recycling control is one of the key issues to obtain high density and high performance plasma in magnetic confinement devices from two aspects; (1) profile control of core plasma and (2) reduction of neutrals in the peripheral region. A supersonic molecular-beam injection (SMBI) technique isconsidered to be not only an effective fueling method for deeper penetration of neutral particles into the core plasma compared to the conventional gas-puffing (GP)[8]but also an effective edge modification technique in fusion devices [9, 10, 11]. In Heliotron J, fueling control studies have been performed with high-pressure SMBI. In a

combination heating condition of ECH and Co-NBI, the stored energy reached ~ 4.5kJ, which is about 50% higher than the maximum one achieved so far under the similar heating condition with conventional gas-puff fueling in Heliotron J[6].

The speed of injected H_2-beam is evaluated by a "time of flight" method, where the distance from the nozzle to the last closed flux surface (LCFS) is divided by the delay time from the SMBI trigger to the start of Hαincrease monitored at almost the same toroidal position with the injector. The beam speed of 1.3-1.6 km/s is evaluated for P_{pl} ~ 1.0-1.5 MPa [12].Since the beam speed itselfis not so fast compared to that for H_2introduced by normal GP (i.e. thermal speed at room temperature), a key of SMBI fueling, which cause the peculiar plasma performance in SMBI, should be the directional motion of the injected gas and the small area of plasma-beam interaction. If the high neutral density areais small enough and localized in SMBI, it could useful to avoid the degradation of plasma performance through the increase of CX-loss, convection, etc.

Direct comparison between the beam (directional) gas injection and non-directional gas injection was performed by using the shutter plate in front of the #3.5-SMBInozzle. When the shutter is open, the injected beam can reach directly to the plasma, while the beam is stopped at the shutter and then diffuses to the plasma when the shutter is closed. Figure 3 shows time traces of the stored energy W_p and the line-averaged density $\bar{n}_e$and the intensity of Hα emission at #3.5 (indicating the SMBI timing, t≈ 208.5 ms) $H_\alpha^{\#3.5}$ for two discharges under the same experimental condition except for the shutter condition; the shutter is open (Fig. 3(a)) and closed (Fig. 3(b)). The SMBI timing is indicated by a rapid increase of $H_\alpha^{\#3.5}$. As shown in Fig. 3(a), $\bar{n}_e$ shows quick increase just after SMBI and then gradually increases up to ~ 2.6×10^{19} m^{-3} during ~30 ms in the directly injected case (the open shutter case). The stored energy also shows rapid increase with a slight delay, keeps the elevated value for ~10 ms and then starts to decrease when the increase of $\bar{n}_e$ becomes saturated.In the case of closed shutter (Fig. 3(b)), on the other hand, the increases of $\bar{n}_e$ and W_p are slow and mild. The density already saturates at ~1.4×10^{19} m^{-3} and starts to decrease at ~15 ms after SMBI. The change of density profile for these two discharges measured with a microwave reflectmeter [13] at #15.5 section. In the open shutter case, the density profile, which is rather flat before SMBI, rapidly changes to a peaked one after SMBI, while the profile change is slow and mild in the closed shutter case [14]. This observations indicate that the injected beam well penetrate to core plasma region in the open shutter case. Since the amount of injected gas is the same for these two cases, the difference of the attainable $\bar{n}_e$ after the SMBI indicates the effectiveness of SMBI in the over-all fueling efficiency perhaps including the confinement improving effect.

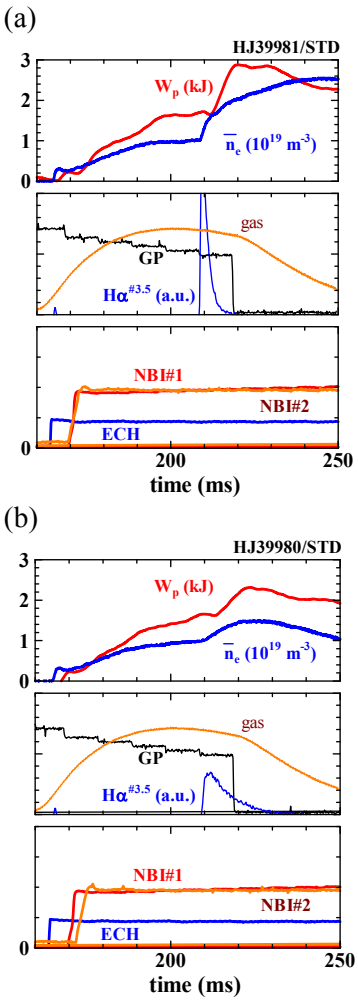

Fig. 3 *Time traces of line-averaged density, stored energy for ECH+NBI plasmas between two cases of open (a) and closed (b) conditions of the shutter in front of SMBI.*

4. Second Harmonic Electron Cyclotron Current Drive

In stellarators/heliotrons, non-inductive current can change the rotational transform profile, affecting equilibrium and MHD activities as well as tokamaks. In a low magnetic shear configuration, moreover, non-inductive current also can modify the edge field topology and divertor performance [15]. Electron cyclotron current drive (ECCD) is expectedas an effective method to control such non-inductive current effects caused by finite-plasma pressure and neutral beams.

The ECCD experiments inHeliotron J revealedstrong dependence of the magnetic fieldconfiguration onthe EC current(Fig. 4) [16, 17]. This suggests that the ECCD is determined by the balance between two current drive mechanisms; the Fisch-Boozer and the Ohkawa effects.To deepen understanding in the ECCD physics and to extend the controllability of ECCD in a helical-axis heliotron, a launching systemwitha focusingmirror and a steering mirrorhas been installed recently [18]. By using this system,a focused Gaussian beam is injected with the parallel refractive index of -0.05 $\leq N_{||} \leq$ 0.6.The position of the EC injection port and the available toroidal injection angle are also shownin Fig. 5 withthemagnetic field strength along the magnetic axis for different three ε_b configurations (i.e. different field ripple ratio).

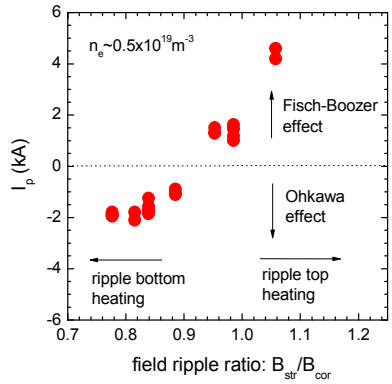

Fig. 4.*Dependence of measured toroidal current on magneticfield ripple.* [17]

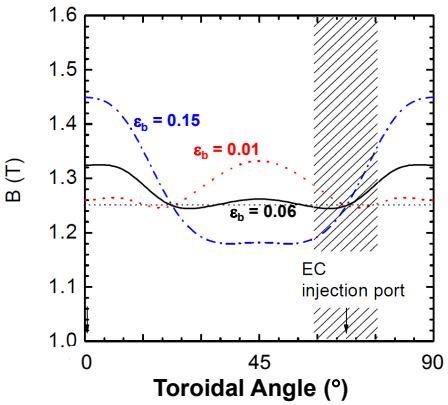

Fig. 5.*Magnetic field strength along the magnetic axis for different three $\varepsilon_b$configurations.The shaded span denotes the available toroidal injection*

Theexperimental resultswith this new launching system have revealed the $N_{||}$dependence of EC driven current in different field ripple configurations [19]. The maximum EC driven current is attained at $N_{||}$=0.5 when theEC power is deposited nearly at the ripple top, while the EC driven current is nearlyzero independent of $N_{||}$ when the EC power is deposited near the ripple bottom.Animportant role of high-energy electrons is indicated from the strong correlation between EC current and ECE signals. The detailed analysis of the experimental results including the B and $N_{||}$dependences is in progress with simulation using the TRAVIS code [20, 21].

5. Resonance Position Dependence of Fast-IonEnergy Spectra Generated by ICRF

In order to study the effect of the magnetic field rippleon fast-ion behavior and to optimize theICRF heating condition in the three dimensional magnetic field configurationof the helical-axis heliotron,fast ion velocity distribution has been investigated using fast protons generated by ICRF minorityheating in Heliotron J [22]. The cyclotron-resonancelayer is located near the axis with a frequency of 19 MHz in the STD configuration. Changing the frequency, the resonance layer can be shifted to theselected position (Fig. 6).

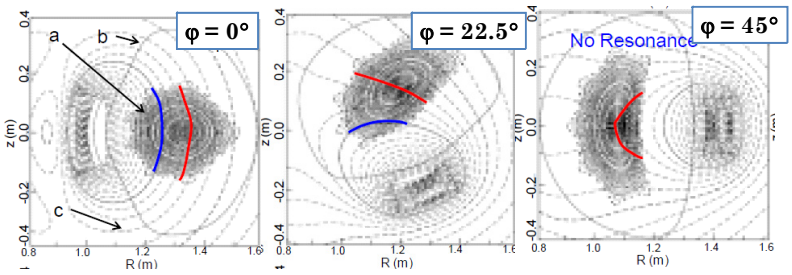

Fig. 6.*The magneticflux surfaces (a), vacuumchamber (b),mod-B surfaces (c), thefundamental cyclotronresonance layer ofminority proton for 19 MHz (red) and 23.2 MHz (blue) at the various toroidalangle (φ). The antennasare installed in thepoloidal cross section atφ=0°. Resonance layer for 19MHz is in the confinement region for any toroidal angle, while that for 23.2MHz is only in limited toroidal positions.*

The pitchangle ψ_{pitch} dependences of ion energy spectra for two resonance positions, on-axisand HFS(inner-side) off-axis resonance, are investigated by using a CX-NPA [22]. For both the cases, the effective temperature of the minority protons $T_{\mathrm{eff.}}^{\mathrm{H}^+}$, shows the pitch angle dependence andthe peak of $T_{\mathrm{eff.}}^{\mathrm{H}^+}$ is observed at ~ 120° in the pitch angle.Higher $T_{\mathrm{eff.}}^{\mathrm{H}^+}$ is observed in the on-axis resonance case compared tothe HFS resonance case. The number of fast ions is also large in theon-axis case compared to the HFS resonance case. However, the increaseof the bulk ion temperature in the HFS resonance case is larger than that that in the on-axis case.In order to understand these observations, three-dimensional waveanalyses have been performed by using TASK/WM code[23].

6. Summary

This paper reviewed recent progress of Heliotron J experiments from a viewpoint of plasma control to improve plasma performance in Heliotron J.

1. The SMBI fueling is successfully applied to Heliotron J plasma. A supersonic H2-beam is effective to increase fueling efficiency and make a peaked profile. Local fueling with a short pulse by SMBI can increase the core plasma density avoiding the degradation due to the edge cooling. A large increment of plasma stored energy after a short pulse intense gas fueling from a conventional piezoelectric-valve system has been observed in NBI (or NBI+ECH) plasma. The physics under the observation would give us a new insight into more preferable plasma operation conditions.
2. Second harmonic ECCD experiments have been performed.A focused Gaussian beam is injected with -0.05 ≤$N_{\|}$≤ 0.6. The experimental results showthat the EC driven current is determined not only by $N_{//}$ but also by local magnetic field structure where the EC power is deposited. A large increase in ECE signals has been observed when the EC current was driven, indicatingthe important role of high-energy electrons on the ECCD. The detailed analysis of the experimental results on the $N_{\|}$and B dependences is in progress with a ray tracing simulation using TRAVIS code.
3. Fast ion velocity distribution has been investigated using fast protons generated by ICRF minorityheating. In the standard configuration in Heliotron J, the larger fast minority protons are observedin the on-axis resonance case than in the HFSresonance case. However, the increase of thebulk ion temperature in the HFS resonance case is larger. The change of the absorption ratiois one candidate for the explanation of the experimental result.

Acknowledgements

The authors are grateful to the Heliotron J supporting group for their excellent arrangement of the experiments. One of the authors (T. M.) gives special thanks to Profs. L. Yao, Q.W. Yang and their colleagues in Southwestern Institute of Physics for kind instruction of SMBI experiments and fruitful discussions.This work is performed with the support and under the auspices of the JSPS-CAS Core University Programin the field of "Plasma and Nuclear Fusion", the Collaboration Program of the Laboratory for Complex Energy Processes, IAE, Kyoto University, the NIFS Collaborative Research Program (*NIFS10KUHL030, etc.*) and the NIFS/NINS project of Formation of International Network for Scientific Collaborations, as well as the Grant-in-Aid for Sci. Research, MEXT.

References

[1] SANO F., et al., J. Plasma Fusion Res. SERIES **3**(2000) 26.
[2] OBIKI T., et al., Nucl.Fusion **41**(2001)833.
[3] WAKATANI M., et al., Nucl.Fusion **40**(2000) 569.
[4] YOKOYAMA M., et al., Nucl.Fusion **40** (2000)261.
[5] MIZUUCHI T., et al., in Proc. 17th IAE ISHW (Princeton, 2009), I24.
[6] MIZUUCHI T., et al., Contrib. Plasma Phys. **50**(2010) 639.
[7] MINAMI T., et al., Journal of Physics: Conference Series **123**(2008) 012006.
[8] YAO L., in "New Developments in Nuclear Fusion Research" (Nova Sci. Pub., 2006)) pp. 61-87.
[9] YAO L.and BALDZUHN J., Plasma Sci. Tech.**5**(2003) 1933.
[10] GIRUZZI G., et al., Nucl.Fusion **49**(2009) 104010.
[11] TAKENAGA H., et al., Nucl.Fusion **49**(2009) 075012.
[12] MIZUUCHI T., et al., in Proc. 19th PSI Conference (San Diego, 2010) P2-70.
To be published in J. Nucl. Mater.
[13] MUKAI K., et al., Contrib. Plasma Phys. **50**(2010) 646.
[14] MIZUUCHI T., et al., in Proc. 23rd IAEA FEC (2010, Deajeon) IAEA-CN-180/EXC/P8-11
[15] MIZUUCHI T., et al., Nucl.Fusion **47** (2007) 395.
[16] MOTOJIMA G., et al., Nucl.Fusion **47** (2007) 1045.
[17] NAGASAKI K., et al., Nucl.Fusion **50** (2010) 025003.
[18] NAGASAKI K., et al., Contrib. Plasma Phys. **50**(2010) 656.
[19] NAGASAKI K., et al., in Proc. 23rd IAEA FEC (2010, Deajeon) IAEA-CN-180/EXW/P7-19.
[20] MARUSHCHENKO N.B., et al., Plasma Fusion Res. **2** (2007) S1129.
[21] MARUSHCHENKO N.B., et al., Nucl.Fusion **48** (2008) 054002.
[22] OKADA H., et al., in Proc. 17th IAE ISHW (Princeton, 2009) P03-18.
[23] FUKUYAMA A., et al., in Proc. 19th IAEA FEC (2002) IAEA-CN-94/TH/P3-14.

The verification of real time plasma shape reconstruction on EAST

B.J. Xiao, Z.P. Luo, A.S. Welander*, D.A. Humphreys*,
Y. Guo, Q.P. Yuan, R.R. Zhang and S.K. Yang

Institute of Plasma Physics, Chinese Academy of Sciences,
P.O.Box 1126, Hefei, China

**General Atomics, DIII-D National Fusion Facility, San Diego, CA, USA*

Correspondent author email: bjxiao@ipp.ac.cn

Plasma shape control using isoflux algorithm and real time equilibrium reconstruction (rtEFIT code) [1] has been implemented on the Experimental Advanced Superconducting Tokamak (EAST) [2]. The real time equilibrium reconstruction provides the flux at points on the desired plasma boundary, which are used as the input to the isoflux shape control. The accuracy of plasma shape control largely depends on the accuracy of the real time plasma shape reconstruction.

In this paper, the verification of real time plasma shape reconstruction is presented. Firstly, the simulated values on magnetic diagnostics given by TSC code [3] are used as the input to offline plasma equilibrium reconstruction (offline EFIT code) [4]. Consistent results are given. A real time plasma shape reconstruction running in simulation mode, based on the same input diagnostic values and same fitting settings, has a good fitting accuracy. Then, a random error, i.e., 3%-5% was added to the TSC simulated signal to model the real experimental diagnostics. The reconstruction was repeated with these data to check the reliability of the reconstruction. The comparison shows that the reconstruction scheme used in current EAST plasma control has the sufficient accuracy if the magnetic signals uncertainty is below 3%.

Finally, a selected experimental discharge data are used as input to both the offline and real time reconstruction. Consistent results can be obtained. Further improvement of the reconstruction relies on the improvement of the model data such as the exact position and tilt angle of the magnetic probes and the coil dimensions and the inclusion of the vessel eddy current into the real time reconstruction.

This work was partially supported by the JSPS-CAS Core-University program in the field of 'Plasma and Nuclear Fusion'.

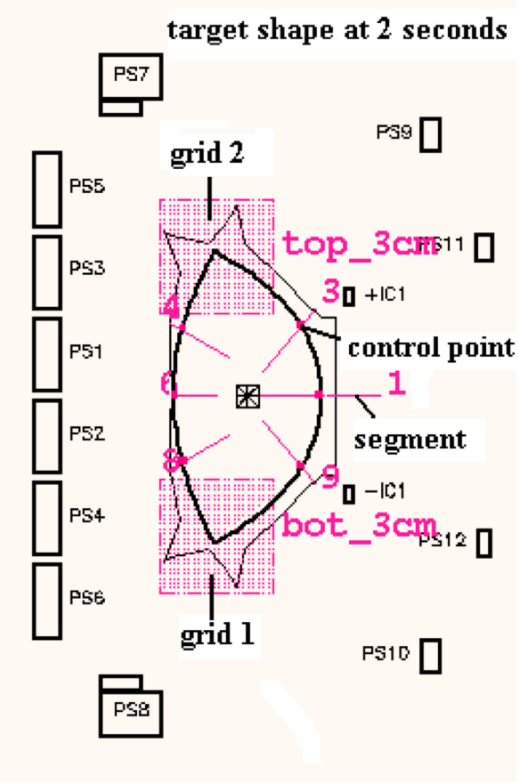

References:
[1] J.R. Ferron, M. L. Walker, et al. Real time equilibrium reconstruction for tokamak discharge control. Nuclear Fusion **38**(7) (1998) 1055-1066.
[2] B.J. Xiao. EAST plasma control system, Fusion Engineering and Design 83 (2008) 181-187.
[3] S.C. Jardin, N. Pomphrey, J. DeLucia. Dynamic modeling of transport and position control of tokamaks. Journal of Computational Physics (1986) 66: 481.
[4] L.L. Lao, H. E. ST. John, Q. Peng, et al. MHD equilibrium reconstruction in the DIII-D tokamak. Fusion Science and Technology 48 (2004) 968-977.

Study of Electron Orbits for Formation of Toroidal Closed Flux Surface by ECH

T. MAEKAWA[1], T. YOSHINAGA[2], H. TANAKA[1], M. UCHIDA[1] and F. WATANABE[1]
[1] Graduate School of Energy Science, Kyoto University, Kyoto 606-8502, Japan
[2] National Institute for Fusion Science, Toki, Japan
E-mail:maekawa@energy.kyoto-u.ac.jp

Abstract. Electron orbits under the external vertical field (B_V) and the self poloidal field from the toroidal plasma current are investigated by using analytic model fields for them in order to search for appearance of appropriate confinement asymmetry of electrons along the field line to ensure closing of field lines in ECH-started plasmas in large devices. It is shown analytically that the characteristics depends on the product of the major radius and the external vertical field. The results suggest that in large devices B_V should be lowered and also quickening of pitch angle scattering for higher energy range of electrons is needed.

1. Introduction

Removal of central solenoid from the core of tokamak reactors is beneficial [1]. They would be reduced in size, simplified in structure and improved in plasma performance via reduction of the aspect ratio, and, therefore, the construction cost could be reduced. Without the central solenoid, however, alternative methods for plasma initiation and current start up are required. The EC heating (ECH) is potentially an attractive candidate for this purpose in reactors since the microwaves for ECH can be launched with a simple small launcher positioned remote from the plasma surface.

Recently, a closed flux surface was found to be formed via current jump by ECH under a weak vertical field B_v in small and low-aspect-ratio torus devices, the LATE device [2] and the CPD device [3]. Furthermore, the plasma current was ramped up by EC current drive (ECCD) after the formation of closed flux surface in the LATE device [4, 5]. Then a question arises; whether such a closing of flux surface by ECH is also possible or not in large devices. In other words what is needed in the large devices to ensure closing of the field lines.

A model for closing of flux surface via current jump was briefly proposed in [2]. The model predicts that unidirectional confined orbits of electrons which arise upon the change of the magnetic field from open to closed structure generate a quick increase of current, that is, current jump. However, there has been done no study how the model depends on the scale of the device. In the present paper we investigate the scale dependence of the model and discuss the implications of the results.

2. Electron orbits and discussions

We employ cylindrical coordinates as shown in figure 1. In a simple toroidal field electrons drifts vertically by the curvature and gradient of the field by the velocity. Therefore, there is no confined orbit.

When a weak vertical field B_V is superposed to the toroidal field B_ϕ, another vertical velocity component arises from parallel drift velocity along the helical field lines in addition to the above vertical charge separation drift. Both drifts compensate each other for some electrons as follows. The total vertical drift velocity is given by

$$V_Z = v_{//}\frac{B_V}{B_\phi} - \frac{m\gamma\left(v_{//}^2 + v_\perp^2/2\right)}{qRB_\phi} \quad . \tag{1}$$

Here γ is the relativistic factor, q and m are electron mass and charge, respectively, and the subscripts // and $\perp$ denote parallel and perpendicular components of the electron velocity to the magnetic field, respectively. The electrons which satisfy the condition V_Z=0 are confined. This condition reduces

$$\left[1+\left(\frac{R\Omega_V}{c}\right)^2\right]\left(\frac{v_{//}}{c}\right)^4 + \left\{\left[1+\left(\frac{R\Omega_V}{c}\right)^2\right]\left(\frac{v_\perp}{c}\right)^2 - \left(\frac{R\Omega_V}{c}\right)^2\right\}\left(\frac{v_{//}}{c}\right)^2 + \frac{1}{4}\left(\frac{v_\perp}{c}\right)^4 = 0 \quad , \tag{2}$$

where $\Omega_V = eB_V/m$. In the non relativistic case,

$$\frac{\left(v_{//} - \frac{R\Omega_V}{2}\right)^2}{\left(\frac{R\Omega_V}{2}\right)^2} + \frac{{v_\perp}^2}{2\left(\frac{R\Omega_V}{2}\right)^2} = 1 \tag{3}$$

This relationship makes an ellipse in the electron velocity space that is referred as Vz ellipse. It is noted that the product RB_V solely determines the characteristics given by equations (2) and (3).

Some examples of V_Z ellipses are plotted in figure 2, manifesting asymmetric confinement along the field line in the particle orbit picture. Current generation by this asymmetry by the superposition of B_V was used in numerical study for ECH current start-up [6]. Another mechanism of toroidal current generation was the current circulation along the helical field line driven by the vertical charge separation in the toroidal field. The current density is proportional to the electron pressure as follows,

$$j_\phi = -\frac{2P_e}{RB_V} \tag{4}$$

This was originally proposed as an equilibrium current by the fluid picture [7] and recently confirmed experimentally [8].

Thus a toroidal current is generated in the toroidal plasma under B_V. In order to study characteristics of electron orbits under B_V and the self poloidal field from the toroidal plasma current, we have developed analytic models for the B_V and the self field.

The flux function of B_V field may be given by,

$$\Psi_{ext} = R_0 X B_{V0} + \frac{1-n}{2}X^2 B_{V0} + \frac{n}{2}Z^2 B_{V0} + \left(\frac{1}{6}\Psi_{XXX}X^3 + \frac{1}{2}\Psi_{XZZ}XZ^2\right) \tag{5}$$

where $X = R - R_0$, $\Psi_{XXX} = \partial^3\Psi_{ext}/\partial X^3\big|_{R=R_0,Z=0}$, $\Psi_{XZZ} = \partial^3\Psi_{ext}/\partial X\partial Z^2\big|_{R=R_0,Z=0}$,

B_{V0} is the vertical field at R=R_0, and n is the decay index of B_V at R=R_0, $n = -\left(R_0/B_{V0}\right)\partial B_V/\partial R\big|_{R=R_0}$. Using normalized forms of $\psi = \Psi_{ext}/R_0^2 B_{V0}$, $x = X/R_0$ and

$z = Z/R_0$, equation (5) reduces to

$$\psi_{ext} = x + \frac{1-n}{2}x^2 + \frac{n}{2}z^2 + \left(\frac{1}{6}\psi_{xxx}x^3 + \frac{1}{2}\psi_{xzz}xz^2\right) \tag{6}$$

While this form generates finite toroidal current density inside the minor radius, it becomes negligible by setting $\psi_{xxx} = -n$ and $\psi_{xzz} = 0$.

The plasma current profile assumes the following form,

$$j_\phi = \begin{cases} \frac{1}{h}\frac{2I_P}{\pi a^2}\left[1-\left(\frac{r}{a}\right)^2\right] & at\ r \le a \\ 0 & at\ r > a \end{cases} .$$

Here, $h = 1 + r\cos\theta/R_0$ and $r = \sqrt{X^2 + Z^2}$. Then the poloidal field takes the form, $\mathbf{B} = B_\theta\hat{\theta}$, where

$$B_\theta = \begin{cases} 2B_a\left[\frac{r}{a} - \frac{1}{2}\left(\frac{r}{a}\right)^3\right] & at\ r \le a \\ B_a\left(\frac{r}{a}\right)^{-1} & at\ r > a \end{cases}$$

Here, $B_a = I_P/2\pi a$ is the field strength at the current boundary at $r = a$.

The flux function of this self field in the normalized form is given by

$$\psi_{\text{int}} \equiv \frac{\Psi_{\text{int}}}{R_0^2 B_{V0}} = \begin{cases} \frac{a}{R_0}\frac{B_a}{B_{V0}}\left[\left(\frac{r/R_0}{a/R_0}\right)^2 - \frac{1}{4}\left(\frac{r/R_0}{a/R_0}\right)^4\right] & at\ r \le a \\ \frac{a}{R_0}\frac{B_a}{B_{V0}}\left[\frac{3}{4} + \log\left(\frac{r/R_0}{a/R_0}\right)\right] & at\ r > a \end{cases} \tag{7}.$$

There are three constants of motion for the motion of the electron in above axisymmetric fields; angular momentum, magnitude of velocity and magnetic moment as follows,

$$P_\phi = m\gamma R v_\phi + q\left(\Psi_{ext} + \Psi_{\text{int}}\right) \cong m\gamma R v_{//} + q\left(\Psi_{ext} + \Psi_{\text{int}}\right)$$

$$W = v_\perp^2 + v_{//}^2$$

$$\mu = \frac{m\gamma v_\perp^2}{2B} \cong \frac{m\gamma v_\perp^2}{2B_\phi}$$

Then,

$$W = \frac{2}{m\gamma}\mu B_\phi + \frac{m\gamma}{2}\left[\frac{P_\phi - q\left(\Psi_{ext} + \Psi_{\text{int}}\right)}{m\gamma R}\right]^2 . \tag{8}$$

When the starting point of the orbit is the center of the current, R=R_0 and Z=0 and we write the initial values of velocity components as $v_{//} = v_{//0}$ and $v_{\perp} = v_{\perp 0}$,

$$\mu B_{\phi} = \frac{m\gamma v_{\perp 0}^2}{2B_0}\frac{B_0 R_0}{R} = \frac{m\gamma v_{\perp 0}^2}{2}(1+x)^{-1}, \tag{9}$$

and

$$\frac{P_{\phi} - q(\Psi_{ext} + \Psi_{\text{int}})}{m\gamma R} = \frac{m\gamma v_{//0} - qR_0 B_{V0}(\psi_{ext} + \psi_{\text{int}})}{m\gamma(1+x)} \quad . \tag{10}$$

By substituting equations (9) and (10) with (6) and (7) into equation (8), it is found that W has the following functional form,

$$W = W\left(R_0 B_{V0}, \frac{R_0}{a}, \frac{B_a}{B_{V0}}, n, v_{//0}, v_{\perp 0}; x, z\right) \tag{11}$$

We now can calculate the trajectory of electron projected on the poloidal cross section that starts from x=0 and z=0. The coordinates x and y are functions of the distance ℓ along the trajectory from the starting point. Then the following deferential equations describe the evolutions of x and y, that is, electron trajectory in terms of normalized coordinates x and z.

$$\frac{dx}{d\ell} = \frac{\frac{\partial W}{\partial z}}{\sqrt{\left(\frac{\partial W}{\partial x}\right)^2 + \left(\frac{\partial W}{\partial z}\right)^2}} \quad \text{and} \quad \frac{dz}{d\ell} = -\frac{\frac{\partial W}{\partial x}}{\sqrt{\left(\frac{\partial W}{\partial x}\right)^2 + \left(\frac{\partial W}{\partial z}\right)^2}} \tag{12}$$

The functional form of W shown in equation (11) indicates that the normalized trajectories that start from the center of the current profile are completely determined by the set of parameters; $R_0 B_{V0}$, R_0/a, B_a/B_{V0}, n, $v_{//0}$ *and* $v_{\perp 0}$. It is straightforward to show that if the starting point is different from the centre the same statement holds for the same set of parameters.

Figure 2 shows mapping of classification of electron orbits into passing, trapped and lost areas on the space of initial velocities of $v_{//0}$ *and* $v_{\perp 0}$ for various parameters of $R_0 B_{V0}$ *and* B_a/B_{V0}. Aspect ratio of current cross section is taken to be $R_0/a = 3$ and decay index is n=0.1. It is noted that the characteristics depend on the product of the major radius and the external vertical field $R_0 B_{V0}$. When we assume B_{V0}=50 Gauss, the left, center and right columns correspond the cases of R_0=0.3m, 0.9m and 2.7 m, respectively. When we assume R_0=3m, the left, center and right columns correspond the cases of B_{V0}=5 Gauss, 15 Gauss and 45 Gauss, respectively. When we assume R_0=0.3 m, the left, center and right columns correspond the cases of B_{V0}=50 Gauss, 150 Gauss and 450 Gauss, respectively.

Let us begin with the case shown in the left column in figure 2. The decay index of Bv field is n=0.1 and there is a weak mirror effect. Therefore, some electrons located near the Vz = 0 ellipse in the

velocity space are also confined. The passing area expands toward lower energy region when the plasma current Ip starts to flow and increases as shown in the second mapping from top. In this initial stage, Ip is the equilibrium current that is proportional to the electron pressure as shown by equation (4). It is noted that the passing area at this stage is in high energy range and the electrons in this area may be few since it is difficult to fill the passing area with electrons by pumping up them through a narrow path of passing area from bulk electrons. When Ip increases further up to a certain level (third mapping), the passing area expands up to the tail region of the bulk Maxwellian distribution. Here the current generation due to the asymmetric confinement would begin in full scale since the electron population becomes significant and the pitch angle scattering from perpendicularly EC heated electrons becomes frequent. The resultant current increase enlarges the passing area further and current increase would be quickly accelerated since both the electron population and pitch angle diffusion rate increase drastically towards the thermal bulk, resulting in the current jump. ECCD may also start to work at this stage and finally a closed flux surface is formed (bottom mapping).

When we move to the center column, we notice that even if the self poloidal field increases to amount 80 % of the Bv field, the passing area does not expand to the vicinity of the bulk thermal tail. This means that when the product $R_0 B_{V0}$ increases current jump becomes difficult to take place. It was reported that more ECH power was needed when B_{V0} was increased [2] for current jump. This result implies that in the large devices B_V should be lowered. Furthermore, quickening of pitch angle scattering for higher energy range of electrons is needed to ensure positive feedback of current increase by asymmetric confinement as shown in the third mapping in this column. A superposition of a weak radial magnetic field Br might be effective for such purpose.

Summary

Electron orbits under the external vertical field (B_V) and the self poloidal field from the toroidal plasma current are investigated by using analytic model fields for them in order to search for appearance of appropriate confinement asymmetry of electrons along the field line to ensure closing of field lines in ECH-started plasmas in large devices. The orbit characteristics depend on the product of the major radius and the external vertical field. This result implies that in large devices B_V should be lowered. Furthermore, quickening of pitch angle scattering for higher energy range of electrons is needed to ensure positive feedback of current increase by asymmetric confinement.

Acknowledgement- This work was also partially supported by the JSPS-CAS Core-University program in the field of ‘Plasma and Nuclear Fusion'.

References

[1] NISHIO, S. et al., Proc. of 20th Fusion Energy Conf., IAEA-CN-116/FT/P7-3.
[2] YOSHINAGA, T., et al., Phys. Rev. Lett. **96** (2006) 125005.
[3] YOSHINAGA, T., et al., J. Plasma Fusion Res. SERIES **8** (2009) 100.
[4] MAEKAWA, T. Et al., Plasma Science and Technology **11** (2009) 394.

[5] UCHIDA, M. et al., Phys. Rev. Lett. **104** (2010) 065001.
[6] SHIMOZUMA, T. et al., J. Phys. Soc. Jpn, **54** (1985) 1360.
[7] ZAKHAROV, L.E. and PEREVERZEV, G.V., Sov. J. Plasma Phys. **14** (1988) 75.
[8] NISHI, S. Et al., Plasma Phys. Control. Fusion **52** (2010) 125004.

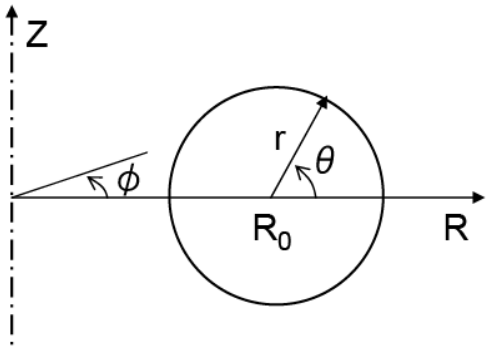

Figure 1. Coordinates

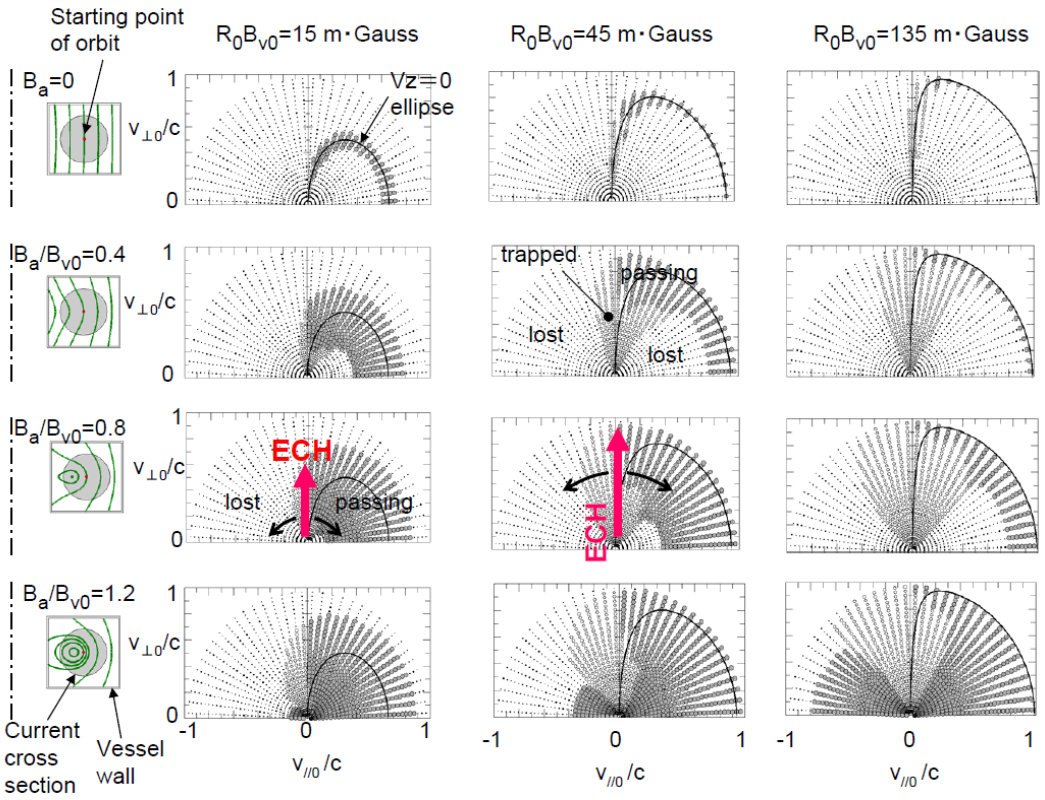

Figure 2. Mapping of electron orbits as passing, trapped and lost area on the space of initial velocities of $v_{//0}$ *and* $v_{\perp 0}$ for various parameters of $R_0 B_{V0}$ *and* B_a / B_{V0} . Here, $B_a = I_P / 2\pi a$. Aspect ratio of current cross section is $R_0 / a = 3$ and decay index is n=0.1. When the electron orbit crosses the vessel wall, it is classified to be lost.

Neutral Density Estimate of Edge Plasma with Double Null Configuration on EAST Tokamak*

ZHANG Ling(张凌), XU Guosheng(徐国盛), DING Siye(丁斯晔), GAO Wei(高伟),
WU Zhenwei(吴振伟), CHEN Yingjie(陈颖杰), HUANG Juan(黄娟),
LIU Xiaoju(刘晓菊), ZANG Qing(臧庆), CHANG Jiafeng(常加峰),
ZHANG Wei(张炜), LI Yingying(李颖颖), QIAN Jinping(钱金平)

Institute of Plasma Physics, Chinese Academy of Science, Hefei 230030, China

E-mail: gsxu@ipp.ac.cn

Abstract The neutral density plays an important role in the low to high (L-H) confinement mode transition. In this work, population coefficients of hydrogen's n=3 excited state from hydrogen collisional-radiative (CR) model (from DEGAS 2 data file) are used to calculate the photon emissivity coefficients (PECs) of hydrogen Balmer-α (n=3→2) (H_alpha). The results are compared with the PECs from Atomic Data and Analysis Structure (ADAS) database and fit well. 1.5-D fluid transport code FRANTIC gives magnetic surface-averaged neutral density profile of typical doublenull (DN) plasma of EAST. It is found that the sum of integral D_alpha and H_alpha emission intensity calculated via the neutral density agrees with the measurement from the absolutely calibrated multi-channel poloidal photodiode array systems viewing the lower divertor at the last closed flux surface (LCFS). This fact indicates that the typical magnetic surface-averaged neutral density at LCFS is about $3.5\times10^{16}m^{-3}$.

Keywords: neutral density, photon emissivity coefficients, collisional-radiative (CR) model, edge plasma

1. Introduction

The low to high (L-H) confinement mode transition is important in tokamak because of the significantly improved global energy confinement time, τ_E, and significantly higher plasma pressure that can be sustained. The prediction L-H transition threshold power for ITER is P_{LH}=40-50MW [1].

There is evidence that neutrals play an important role in the L-H transition. High neutral pressure was observed to increase the L-H transition threshold power on Alcator C-mod [2]. The underlying effect of the plasma or divertor configuration on the L-H transition threshold power is often related to the influence of the neutral density at the plasma boundary. The compression of neutral particles near the X-point was observed with W shape pumped divertor and to reduce the threshold power on JT-60U[3]. This was confirmed by the reduction of the threshold power using high field side gas puff fuelling rather than low field side on COMPASS-D, MAST [4] and NSTX [5] .

The prevailing model is that during the L-H transition, radial electric field in the edge increases sharply and causes a sheared poloidal rotation of the plasma ions[6][7]. The principal effect of neutrals on the transition is the damping of this rotation via charge exchange [8][9]. EAST tokamak is to achieve steady state operation in high confinement mode, thus it is necessary to obtain the neutral density level of EAST plasma.

In this work, the population coefficients of hydrogen's n=3 excited state with electron temperature and density from hydrogen collisional-radiative (CR) model (from DEGAS 2 data file) are used to calculate the photon emissivity coefficients (PECs) of hydrogen Balmer-α (n=3→2) (H_α) both from excitation and recombination process. The results are compared with the PECs from ADAS database. The neutral density profile was modeled in this work using the FRANTIC code [10] implemented into TRANSP code. FRANTIC is a 1.5-D fluid code, performing neutral gas transport calculation for tokamak plasmas in the confined region, taking into account charge exchange and impact ionization atomic reactions in a simplified nested cylindrical flux surface geometry. The boundary conditions for the FRANTIC code in TRANSP use the experimental gas valve rate with efficiency unity for neutrals entering the separatrix and the integrated D_α/H_α photon flux. The neutral density profile is checked by absolutely calibrated multi-channel poloidal photodiode array systems viewing the lower divertor[11] through comparing the chord integral D_α/H_α emission intensity.

This paper is organized as follows: Collisional-Radiation Model of hydrogen is introduced in section 2. The experimental setups are presented in section 3. Results from experiment and simulation are discussed in section 4.

2. Collisional-Radiative Model of Hydrogen

The rate equation constructed in C-R Model is to describe the temporal development of the p excited level population in the plasma [12][13] :

$$\frac{\mathrm{d}}{\mathrm{d}t}n(p) = -\left\{\sum_{q<p}A(q,p) + \sum_{q\neq p}C(q,p)n_e + S(p)n_e\right\}n(p) + \sum_{q>p}A(p,q)n(q) + \sum_{q\neq p}C(p,q)n_e n(q) + \left\{\alpha(p)n_e + \beta(p)\right\}n_i n_e \quad (1)$$

A(q,p) is spontaneous transition probability from excited level q to p, C(q,p) is excitation or deexcitation rate coefficient by electron impact. S(p) is ionization rate coefficient, α(p) is three-body recombination rate coefficient, β(p) is radiative recombination rate coefficient. n_e and n_i are electron and ion density respectively. Population coefficient is obtained assuming the quasi-steady state of the excied-level population.

Photon emission coefficients (PECs) contributed by excitation process (with superscript 'e') and recombination process (with superscript 'r') is calculated via population coefficient (as D_α for example):

$$P_{D_\alpha} = P^e_{D_\alpha} + P^r_{D_\alpha} = A_{23}\left(\frac{n^e_3}{n_1}\right)/n_e + A_{23}\left(\frac{n^r_3}{n_i}\right)/n_e \quad (2)$$

Assuming total neutral density n^0 equals to ground state density n_1 for excitation process, the line emission intensity of D_α is :

$$\varepsilon_{D_\alpha} = n_3 A_{23} h\nu/4\pi = h\nu\left(P^e_{D_\alpha} n_e n^0 + P^r_{D_\alpha} n_e n_i\right)/4\pi \qquad \left(W/m^3/Sr\right) \quad (3)$$

The chord integral intensity measured by an absolutely calibrated system is:

$$I_{D_\alpha} = \int \varepsilon_{D_\alpha}\,\mathrm{d}l \qquad \left(W/m^2/Sr\right) \quad (4)$$

Studies on C-R model of hydrogen are maturely with tiny difference of rate coefficients in databases between each other. Fig. 1 compares the PECs calculated from DEGAS 2 data file of population coefficients with ones directly from ADAS database. Fig. 1 shows that the two databases fit well.

3. Experiment Setup

In this work, the typical double null configuration of ohmic discharge, shot

number 22111, of the last experimental campaign in spring 2010 is used to calculate the neutral density. The main plasma parameters of this shot are: plasma current I_p=250kA, toroidal magnetic field B_t =2.0T, and line average density n_{el}= (0.9-1.2)×$10^{19}$$m^{-3}$. Major radius R=1.88 m, minor radius r=0.44 m, the elongation κ=1.665 were calculated by EFIT plasma equilibrium reconstruction. In this shot, fast reciprocating probe was inserted from outer mid-plane into the plasma inside the LCFS 0.04m at 1.8s to obtain the edge plasma electron temperature and density with 1mm space resolution [14]. The electron temperature of main plasma were from 25-channel Thomson scatting system covering the upper half poloidal plane (at geometry coordinate R=1.89m) [15] and the electron cyclotron emission system [16]. The density of main plasma were from Thomson scatting system and far infrared laser interferometer system[17]. The working gas on EAST is deuterium and the density feedback controlling gas puff fuelling is from the low field side midplane inlet. But there was a hydrogen concentration H/(H+D) of about 30% for these experiments. The hydrogen mainly came from the first wall. The D_α/H_α spectral lineshape was measured by using an optical multi-channel analysis (OMA) system with a spectral resolution of 0.01 nm[18], The lineshape also determined the ratio of 'warm' and 'cold' component of neutral particle. There were roughly 50% 'warm' Franck-Condon particles at temperature 3eV and 50% 'cold' molecules at temperature 0.03eV from the wall and gas puffing. The fraction of escaping neutrals to return as 'warm' recycling neutrals was set as 50%, and the remainder was supposed to return as 'cold' neutrals. The particle confinement time τ_p~40ms was estimated based on the recycling particle flux deduced from the D_α/H_α emmision system. The experimental condition and plasma characteristics mentioned above are the input of FRANTIC code. The absolute value of the neutral density estimated by the codes was calibrated against D_α/H_α emmision intensity measurement obtained by 35-channel D_α/H_α photodiode arrays (PDA) and interference filter (with center wavelength at 659.3nm and FWHM 10nm) viewing the inner target and dome surfaces of lower divertors from the outer midplane through the in-vessel reflection mirrors on the EAST , the system was calibrated by means of an integrating sphere standard light source (PHOTON RESEARCH LRS-455).

The plasma equilibrium reconstruction of shot 22111 at 1.8s, the Thomson scatting observasion point, the fast reciprocating probe location inserted, and the D_α/H_α PDA viewing chords are shown schematically in Fig.2(a). The inserted probe

enhanced the intensity of D_α/H_α, thus D_α/H_α measurements of another shot 20566 at 2.0s with the same plasma parameters, configuration and similar wall condition is displayed in Fig.2(b).

4. Results and Discussion

Fig. 3(a) displays the T_e and n_e profile from experiment. Neutral density profiles of deuterium and hydrogen at r<a region were simulation results of the FRANTIC code, and for the region of r>a, they were assumed to be equal to the value at r=a, which are plotted at Fig. 3(b). Fig.3(c) displays the D_α/H_α line emission intensity profile by both excitation process and recombination process via expression (3) assuming $n_i \sim n_e$. The simulation results illustrate that the neutral (including deuterium and hydrogen) density at the LCFS of typical DN configuration on EAST is about $3.47\times10^{16}m^{-3}$. The D_α/H_α line emission intensity profile is mapped to the geometry (R, Z) coordinate via normalized flux Ψ(R, Z) coordinate, where $\Psi(R, Z)= [\Psi_{core}-\Psi(R, Z)]/ [\Psi_{core}-\Psi_{separatrix}]$ as the Fig.4 (a) shows, and then mapped to 35 chords, the Fig.4 (b) plotes the profile on chord 23 for example.

The neutral density from FRANTIC simulation is calibrated by integrating the D_α/H_α line emission intensity along the viewing chords as expression (4). The results are compared to experimental data in Fig. 5. The simulation and experiment results fit to each other in the vicinity of X-point, which shows that $n^0 \sim 3.5\times10^{16}m^{-3}$ at LCFS as that obtained from simulation. Integral D_α Intensity in the region of r>a from experiment is larger than that from simulation, which indicates that the neutral density is larger than $3.5\times10^{16}m^{-3}$ there, and the neutral particle would come from the fist wall. From the X-point to the inner target, the T_e would decrease from 20eV to about 3eV, and the PEC decreases two orders of magnitude. Thus the n^0 above the inner target is about 500 times of $3.5\times10^{16}m^{-3}$ due to D_α intensity there being 5 times of that from simulation. Low field side mid-plane gas puff fuelling, more ion flux arriving at the outer target because of the magnetic equilibrium causing the n^0 and T_e above the outer target is higher than inner target and finally results in larger D_α intensity around the outer target.

The neutral density obtained in this work is barely magnetic-averaged one, however the local neutral density in the vicinity of X-point is more important, therefore the diagnostics for local T_e, n_e profile in divertor and 2-D simulation (such

as DEGAS 2) are necessary, and at the same time, more complicated molecule reactions should be considered in the future.

Acknowledgments

This work is supported by the National Natural Science Foundation of China under Grant No. 11075181, 10605028 and 11075180. And the authors would like to acknowledge the members of the EAST Team and especially the valuable discussion with Dr. LIU Yong and Dr. FU Jia. This work was partially supported by the JSPS-CAS Core-University program in the field of 'Plasma and Nuclear Fusion'.

References

[1] Doyle E J, Houlberg W A, Kamada Y, et al. 2007, Nucl. Fusion 47:S18
[2] Snipes J A, Hubbard A E, Garnier D T, et al. 1996, Plasma Phys. Control. Fusion 38:1127
[3] Fukuda T, Takizuka T, Tsuchiya K, et al. 2000, Plasma Phys. Control. Fusion 42:A289
[4] Akers R J, Ahn J W, Antar G Y, et al. 2003,Plasma Phys. Control. Fusion 45:A175
[5] Bush C E, Bell M G, Bell R E, et al. 2003, Phys. Plasmas, 10:1755
[6] Groebner R J, Burrell K H, Seraydarian R P. 1990,Phys. Rev. Lett. 64:3105
[7] Burrell K H, Carlstrom T N, Doyle E J, et al. 1990, Phys. Fluids B, 2: 1405
[8] Carreras B A, Owen L W, Maingi R, et al. 1998, Phys. Plasmas 5:2623
[9] Colchin R J, Maingi R, Fenstermacher M E, et al. 2000,Nucl.Fusion 40: 175
[10] Valovič M, Budny R, Garzotti L, et al., 2004, Plasma Phys. Control. Fusion, 46:1877
[11] Gao W. 2009, Study of MARFE Instability and Impurity Behavior in AC Discharge on HT-7 Tokamak. [PhD]Hefei: Hefei Institutes of Physical Science
[12] Fujimoto T. 2004, Plasma Spectroscopy. United Stated: Oxford University Press
[13] Stotler D, Karney C, Kanzleiter R, User's Guide for DEGAS 2 Release V.4.3
[14] Zhang W, Chang J F, Wan B N, Fast Reciprocating Probe System on the EAST Superconducting Tokamak, to be published in Rev. Sci. Instrum.
[15] Hu L Q. 2010, Diagnostics Development on the EAST Superconducting Tokamak. 37th EPS Conference on Plasma Physics, Dublin Ireland
[16]Sajjad S, Gao X, Ling B L, et al. 2008, Meas. Sci. Technol., 19:075701
[17] Xu Q, GAO X, JIE Y X, et al. 2008, Plasma Science and Technology, 10:519
[18]Huang J. 2007, Behaviors of Impurity and Edge Recycling towords Long Pulse Discharges in the HT-7 Tokamak. [PhD]Hefei: Hefei Institutes of Physical Science

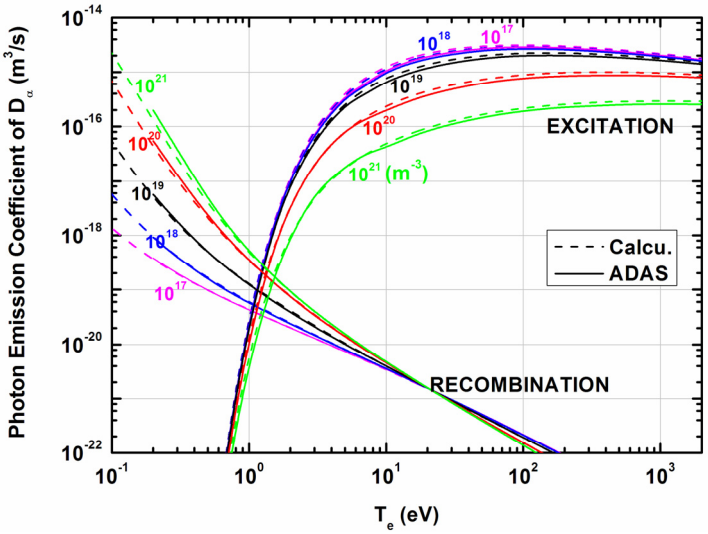

Fig.1 The photon emissivity coefficient calculated from DEGAS 2 data file of population coefficients (dash line) and from ADAS database (solid line) with T_e and $n_e(10^{17}$-$10^{21}m^{-3})$ by both excitation and recombination process.

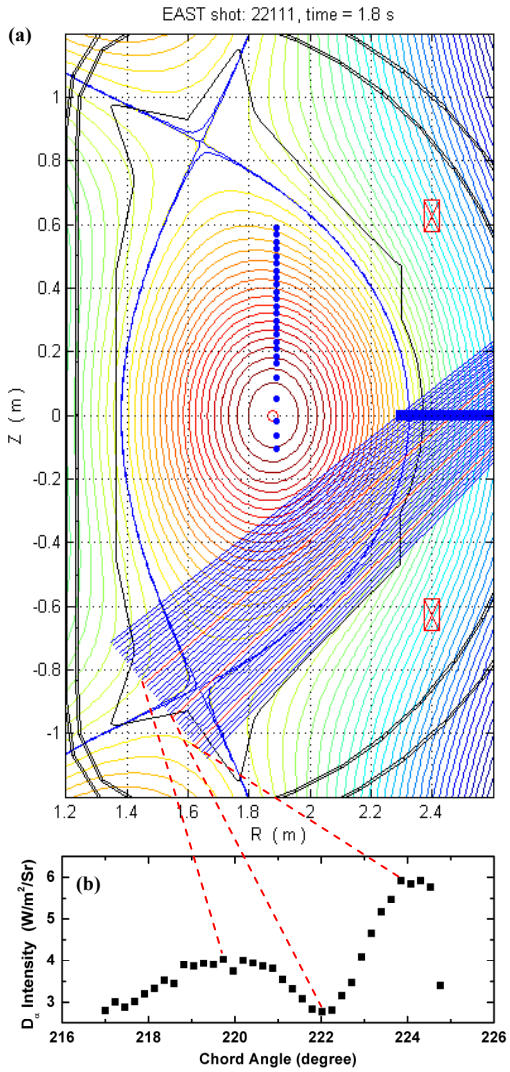

Fig.2 (a) Cross-section of EAST showing the EFIT equilibrium reconstruction, Thomson scatting observasion point and the fast reciprocating probe location inserted, (b) chord integral D_α/H_α line emission intensity measured by PDA system

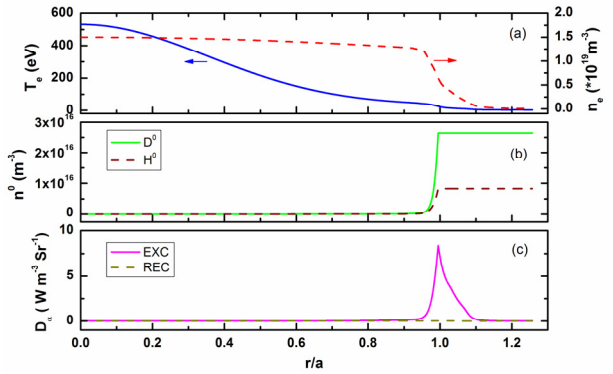

Fig.3 (a) T_e and n_e profile, (b) FRANTIC simulation results of neutral density profile (assuming the value at r/a>1 equals to that at r/a=1), (c) D_α/H_α line emission intensity profile

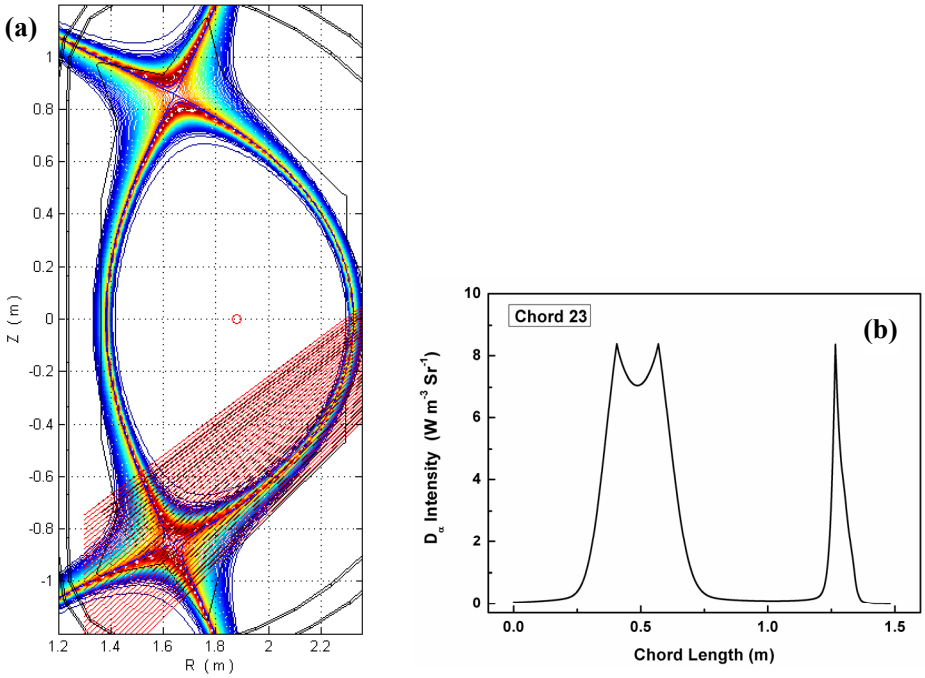

Fig.4 (a) Calculated D_α/H_α line emission intensity profile mapping to the (R, Z) coordinate and the integrating chords, (b) D_α/H_α line emission intensity profile on chord 23 (with chord angle 222˚)

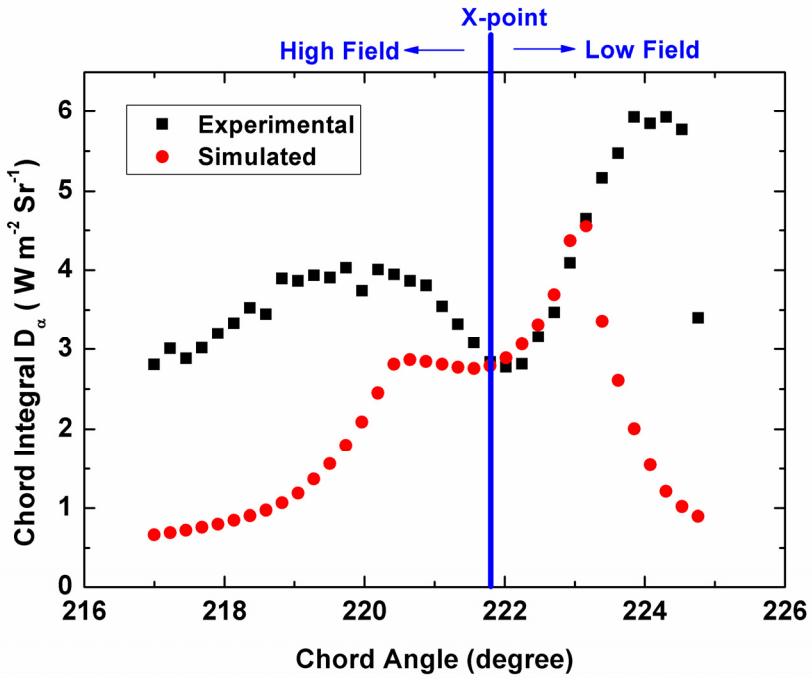

Fig.5 Chord integral D_α/H_α line emission intensity from simulation results comparing to the experiment data

The Experimental Platform of Magnetic Reconnection in Laboratory Plasma

ZHANG Shoubiao(张寿彪)1,2, XIE Jinlin(谢锦林)1, LIU Wandong(刘万东)1, YU Changxuan(俞昌旋)1, Gaoxiang(高翔)2

1、CAS Key Laboratory of Basic Plasma Physics, Department of Modern Physics, University of Science and Technology of China, Hefei 230027, China

2、Institute of Plasma Physics, Chinese Academy of Sciences, Hefei 230031, China

Email: bszhang@ipp.ac.cn

Abstract: A laboratory experiment on the reconnection of magnetic field lines in plasmas has been performed. The plasma is produced by RF discharge, a time-varying magnetic field is applied to two copper plates and the magnetic field exhibits an X-type neutral point in vacuum. The profile of magnetic field is measured by magnetic probe built in 2D moving platform.

Keywords: magnetic reconnection, LMP

PACS:

1、Introduction

Magnetic reconnection is an important process in plasmas, it plays an important role in the evolution of solar flares, during interaction of solar winds with the earth's magnetosphere, and in astrophysical plasmas[1-3]. It also appears as the self-organization process in fusion plasmas[4]. During these process magnetic energy is converted to kinetic energy by the acceleration or heating of charged particles. For a long time it has been considered as a possible mechanism for generation of fast particles in solar flares and magnetospheric substorms [5]. In space plasmas it is often difficult to resolve global and microscopic processes simultaneously. But in laboratory, it is easy to control the plasma parameter, plasma parameter and magnetic field parameter can measure easier, so we can understand simpler physical mechanism of magnetic reconnection in laboratory.

Recently a number of experimental program have been active to investigate the basic mechanisms of magnetic reconnection, include LCD[6]、MRX[7]、VTF[8]、CS-3D [9]et al. Because the decoupling of ions from the magnetized electrons in the current sheet, the Hall effect appears and it can speed up the reconnection. The Hall effect leads to the formation of a two-scale structure in the reconnection region, an electron diffusion region embedded in a much broader ion diffusion region. The Hall effect and electron diffusion region are observed in MRX and other device[10]. The experiments in MRX and TS-3 measured the acceleration and heating of ion[11-13], but the exact mechanism for the heating and acceleration is still open question. Recently simulation indicate, the fluctuations in electron diffusion region is a possible mechanism.

2、The Constructed of Experimental Setup

The experiments were performed in the Linear Magnetized Plasma Device (LMP) at USTC[14]. The LMP vacuum vessel has a radius 25cm and length 2m. Magnetic fields are produced by a total of ten water-cooled solenoidal magnetic coils and the producing steady state B<=1kG. The argon plasma was produced by RF helicon discharge and radially confined by uniform axial magnetic field. The helicon antenna has around a 10cm diameter 80cm long Pyrex tube. The glass tube, sealed at one end, is attached to one end of the LMP vacuum chamber using an o-ring seal. A sketch of the experimental setup is shown in Fig. 1. The plasma parameter was controlled mainly by the discharge power W, the argon pressure P_{Ar} and the axial magnetic field B_0. The typical discharge parameters were as follows: the argon pressure $1X10^{-1}$Pa, electron density $5X10^{11}cm^{-3}$, electron temperature 5eV. And the electron inertial length from those parameters is 1.68cm, the Lundquist number is 50, so the characteristic of reconnection is collisionless reconnection, and the

study region is around electron diffusion region.

Copper plates and pulse current source

The magnetic field configuration for reconnection produced by external current through the plates, in vacuum the field topology exhibits has been an X-type point. The two copper plates was installed in vacuum, and the plates parallel to the plasma column (See Fig.1). The plate current returns through the metallic chamber walls to the current sources. The dimension of plates is width 10cm, length 120cm, spacing 10cm and thickness 0.5cm.

The circuit used to produce the magnetic field for reconnection is shown in Fig. 2. A 500μF capacitor bank stores the electrical energy used to produce the current, and this bank is connected the loading through a semiconductor switch. The semiconductor switch consists of insulated gate bipolar transistors (IGBTs 1700V3600A). Once the switch is energized, the current begins to build up on the plates, a typical wave form is shown in Fig. 3. After an exponential rise phase, this current reaches its desired peak value. This peak current is determined by lead resistance and capacitor bank voltage. And at last the IGBT switch is turned off. The flyback diode serves to prevent the inductive voltage transient that would be caused at this time by the sudden decrease in current flowing in the leads. One of the main issue in the design of high current switching circuits is the management of voltage transients . If a circuit is conducting 6000A and turns off in 5μs, even 2μH of inductance can result in a voltage transient of 2400V, enough to destroy the transistor. So we design the cushion circuit to make use of capacitance、resistance and fast recovery diode (FRD), and parallel connection non-linear resistance, at last the discharge voltage can maintain at 1000V when the peak current attain to 6000A.

Fig. 3 shows the maximum current is 2600A in one plate, so the magnetic field for reconnection is 100G at r=5cm. During the period of current rise, an inductive electric field $-\partial A/\partial t$ is generated along the plasma column. This field drives the plasma and produce the magnetic reconnection.

2D precision moving platform and diagnostic tools

Because the magnetic reconnection happens in the section of LMP, so we need measure the two-dimensional parameter of reconnection. Additionally, the plasma parameters are repeatable ($\Delta n/n<5\%$), so after measure parameter of every point in two-dimensional section we can obtain the profile of plasma parameter. Therefore, in order to investigate reconnection process in experiment, we need a precision moving platform to move the various probes.

Figure 4 shows the 2D precision moving platform at LMP. It is a two-axis positioning system capable of locating a probe head with better than 0.5mm accuracy in a 12X20 cm2 plane. The system consists of five linear slideway and five silder, all components installed in vacuum. The probe head drive by two stepping motors in two different directions.

So we have designed and constructed a small, three-axis, high-frequency magnetic probe and supporting electronics to measure magnetic field. The enameled wire of 0.1mm diameter toroidally wound as 70 turn at ceramic of 1.2mm diameter, through the calibration of standard solenoid , the effective area of probe is about $90mm^2$. Three magnetic probe orthogonality install in epoxy resin, they measure the three dimensional magnetic field at some point.

3、Preliminary Results

A large amount of quality data has been obtained since LMP device construction was completed. We can obtain the time variation of magnetic field at every point in repeatedly discharge, at the certain time, we can obtain the distribution of magnetic field through the magnetic field of various points. At the condition of 1200W discharge power and 0.1Pa argon pressure, we was obtained the magnetic field configuration as shown Fig. 5. The configuration exist one x-point, be appropriate to studying for magnetic reconnection.

In summary, we have constructed the LMP device to investigate the fundamental physics of magnetic reconnection in a well-controlled laboratory setting, a more detailed study would carry out in the next place. In upcoming LMP research, we plan to investigate (1) how magnetic energy is transformed into plasma energy, and (2) what is physical mechanism of fast reconnection.

Acknowledgments

The authours are grateful to Mr. G. L. Huang and Mr. X. G. Wang for their support.

This work was partly supported by the National Nature Science Foundation of China with contract No: 10303003, 40390155, 10605025. This work was partially supported by the JSPS-CAS Core-University program in the field of'Plasma and Nuclear Fusion'.

REFERENCES

1 Tsuneta S, Astrophys. J., 1996, 840: L63

2 Russell C T, Elphic R C, Geophys. Res. Lett., 1979, 6: 33

3 Taylor J B, Rev. Mod. Phys., 1986, 28: 243

4 Yamada M, Levinton F M, Pomphrey N et al., Phys. Plasmas, 1994, 1:3269

5 Dungey J W, Phys. Rev. Lett., 1953, 91: 766

6 Stenzel R L, Gekelman W, Journal of Geophysical Research, 1981, 86: 649-658

7 Yamada M, Ji Hantao, Hsu Scott et al., Phys. Plasmas, 1997, 4: 1936-1944

8 Egedal J, Fasoli A, Tarkowski et al. , Phys. Plasmas, 2001, 8: 1935-1943

9 Frank A G, Plasma Phys. Control. Fusion, 1999, 41: A687-A697

10 Ren Yang, Yamada M, Ji Hantao, et al., Phys. Plasmas 2008, 15: 082113

11 Ono Y, Yamada M, Akao T, PRL, 1996, 76: 3328

12 Hsu S C, Fiksel G, Carter T A, et al. PRL, 2000, 84: 3859

13 Hsu S C, Carter T A, Fiksel G, et al. Phys. Plasmas, 2001, 8: 1916

14 Xie Jinlin, Yu Zhi, Yu Changxuan et al., Plamsa Science and Technology, 2006, 8: 99

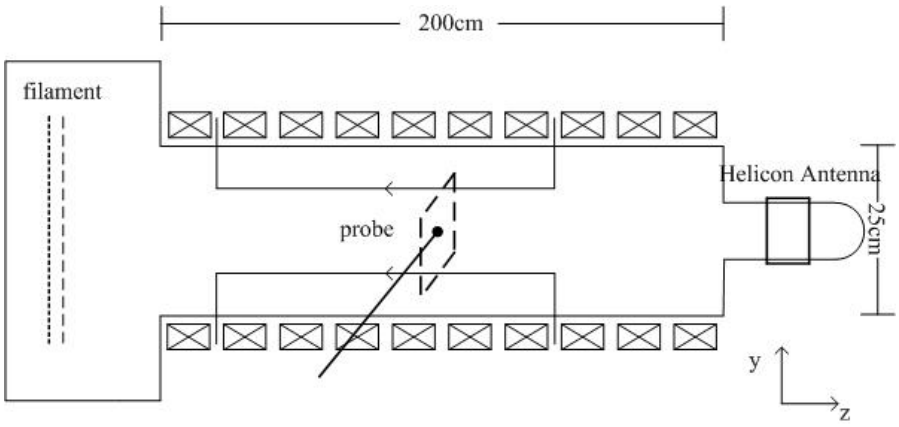

Fig. 1：LMP experimental device

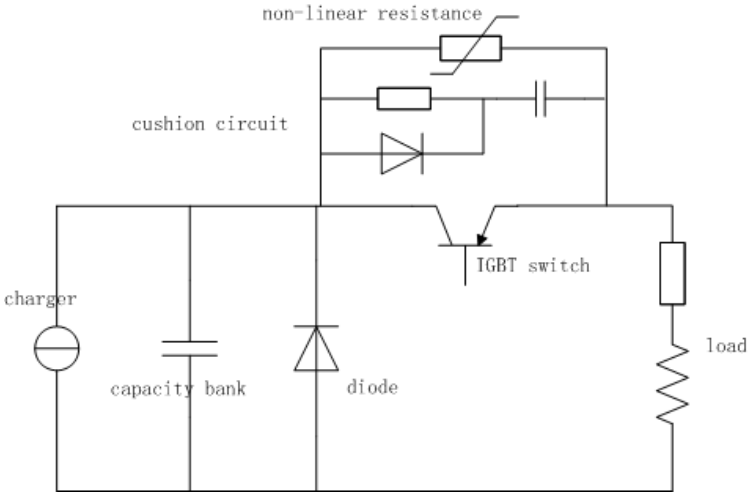

Fig. 2 The circuit diagram of pulse current source

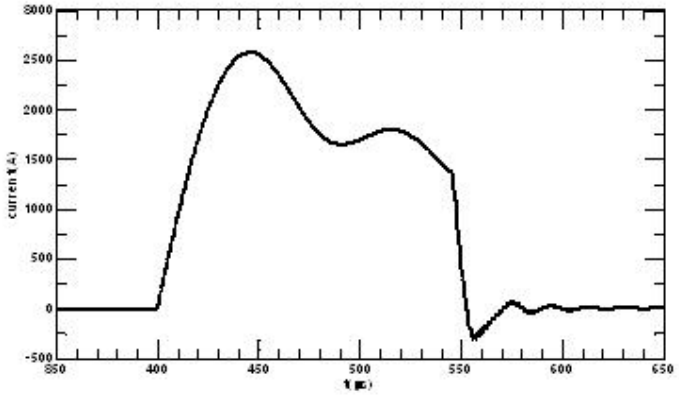

Fig. 3 the current waveform

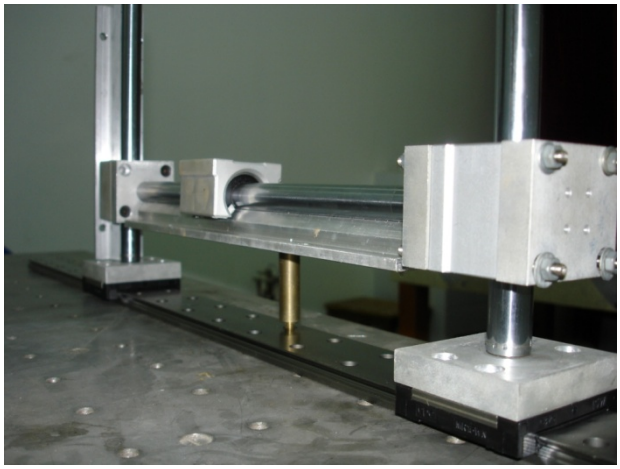

Fig. 4 the 2D moving platform for probe

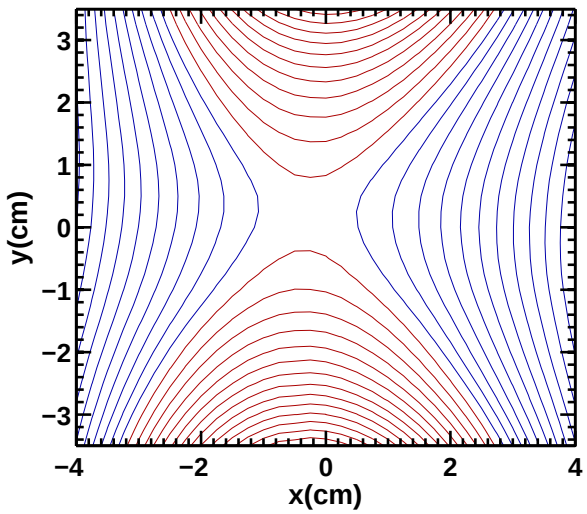

Fig. 5 The distribution of magnetic filed line

Recent results of LHCD experiments in EAST

B J Ding1), E H Kong 1), M H Li 1), Y L Qing1), L Zhang 1), A Ekedahl 2), Y Peysson 2), M Wang 1), H D Xu 1), H C Hu 1), G S Xu 1), J F Shan 1), F K Liu 1), Y P Zhao 1), X Gao 1), B N Wan 1), J G Li 1), and EAST Group1)

1) Institute of Plasma Physics, Chinese Academy of Sciences, P R China, Hefei 230031

2) CEA/IRFM Cadarache 13108, Saint Paul Lez Durance, France

Abstract LHW-plasma coupling and lower hybrid current drive (LHCD) experiments in both divertor configuration and limiter plasma have been performed systematically in EAST. In normal experiment, LHW can be coupled into plasma with RC less than 10% and the current drive efficiency is about $0.6\sim0.9\times10^{19}\mathrm{Am}^2\mathrm{W}^{-1}$. The maximum of incident LHW power is up to 1.4MW and the obtained plasma current with LHCD is about 830kA. Studies indicate that the best coupling is obtained in the limiter case, followed by the single null, and the last one is the double null configuration. Current drive efficiency investigated by a least squares fit shows that there is no obvious difference in the drive efficiency between the double null and the single null cases, whereas the efficiency is a little small in the limiter configuration. Current drive efficiency is affected by plasma density, mainly due to influence of density on impurity concentration.

1. Introduction

Lower hybrid current drive (LHCD) has become an effective means to sustain tokamak plasma current and control plasma profile. A good LHW-plasma coupling is the first necessary condition for LHCD experiment and a high current drive efficiency is important for driving plasma current and controlling plasma current profile. Nuclear fusion experiments have made a rapid progress since 1980's in many tokamaks by using LHCD[1-8]. A 2MW 2.45GHz lower hybrid wave (LHW) system has been installed and run in Experimental Advanced Superconducting Tokamak (EAST), in which LHW-plasma coupling and LHCD experiments have been preliminary performed systemically recently.

Steady state operation and high performance are two main goals of EAST. In order to pursue these tasks, it is necessary to investigate LHW-plasma coupling and LHCD experiment in different configurations in EAST so as to optimize the parameters of LHCD experiments.

2. Description of LHW setup

In EAST, a LHW is launched into the tokamak plasma by a multi-junction grill[9] type of antenna with 5 modules arranged by 5 rows in the poloidal direction. The power spectrum of the launched wave can be adjusted in the range of $1.85 \le N_{//}^{peak} \le 2.6$ when the phase difference between the adjacent waveguides of the coupler is feedback controlled at $-90^0 \le \Delta\Phi \le 180^0$, where $N_{//}^{peak}$ is the peak index of parallel refraction of the launched wave.

3. Experiments and results

3.1 LHW-plasma Coupling Characteristic

The LHW-plasma coupling experiments were performed in the DN configuration, the SN

configuration and the limiter plasma (as shown in Fig. 1) with parameters of a plasma current (Ip) ~ 250kA, a toroidal magnetic field (Bt)~2T, a central line averaged density (n_e) ~ 1.0~1.3×10^{19} m^{-3}, and a peak value of parallel refractive index of $N_{//}^{peak}$ = 2.1. The coupling is investigated by analyzing the input power (P_{in}), the reflected power (P_{re}), both of which are measured by directional couplers, and the averaged reflection coefficient (RC = P_{re}/P_{in}) over all the waveguides. The experiments were performed by changing the distance between the LHW grill and the last closed flux surface (LCFS) of plasma and investigating the coupling at different rows. The experimental results are shown in Fig. 2. It is seen that when the distance is less than 11cm, the averaged RCs over all rows with different configurations are almost the same (about 10%), suggesting that they have similar coupling characteristics. With the distance increase, there exists a turning point from which RC increases quickly, indicating the coupling deteriorates. Furthermore, the turning point value where RC increases is the smallest in the double null configuration, then followed by the single null configuration, and the largest one is the limiter case. The corresponding slope of RC increment with the distance exhibits the same variation tendency with RC. All the results suggest that the coupling in the limiter case is the best and the one in the DN case is the worst.

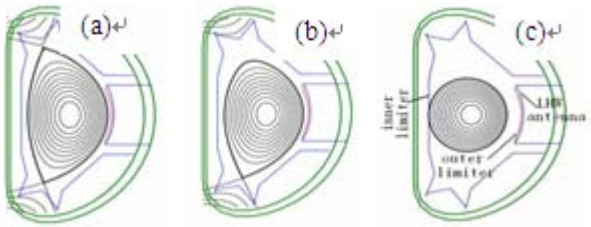

Fig. 1 Three configurations used in experiments
a. double null b. single null c. limiter

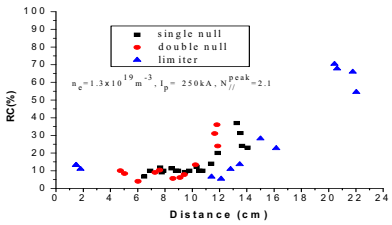

Fig. 2 Averaged RC vs distance between LHW antenna and LCFS

The different coupling characteristics at 3 configurations can be interpreted by the different magnetic connection length L. For an identical d between LCFS and grill mouth, $n_{e,grill}$ is determined by the decay length in the scrape-off layer (λ_{SOL}), which is dependent of magnetic connection length L ($\lambda_{SOL} \propto L$). For an identical plasma current and B_T, the length of L in the DN case is nearly twice of that in the SN case. Among the 3 cases, L in the limiter case is the largest. As a result, λ_{SOL} in this case is the largest, then the single null case, lastly the double null configuration. Therefore, the best coupling is obtained in the limiter case and the worst one is in the double null case. This can be seen from the edge density profile (see Fig.3) measured by Langmuir probes, showing that the density at the grill mouth (located at about Distance~5cm) in the limiter plasma is higher than that in the DN configuration.

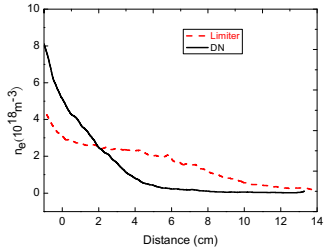

Fig. 3 Edge density profile measured by Langmuir probe

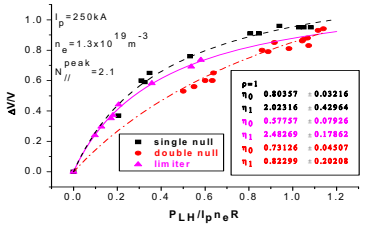

Fig.4 Relative change of loop voltage vs normalized LHW power

3.2 Analysis of LHCD Efficiency

Based on the above coupling experiments, the current drive experiments have also been carried out for the three configurations (SN, DN and limiter) with B_t~2T. Since LHW power is insufficient to sustain plasma current in the experiments, the plasma current is mainly sustained by LHW driven current, Ohmic current, and LHW-Ohmic driven current. In this case, current drive efficiency at zero loop voltage (η_0) is estimated by the method [10,11].

For the 3 configurations, the experimental dependence of the relative drop of loop voltage ($\Delta V/V_{OH}$) on the normalized LHW power (P_{LH}/Ipn_eR) are plotted in Fig.4 (I_p~250kA, n_e~1.0~1.3×10^{19} m^{-3}, $N_{//}^{peak}$ = 2.1), from which the non-inductive current drive efficiency has been obtained by the least squares fit. It is seen that there is no obvious discrepancy in the current drive efficiencies between SN (0.80×$10^{19}$$Am^2W^{-1}$) and DN (0.73×$10^{19}$$Am^2W^{-1}$) configurations, whereas the efficiency is a little small in the limiter case (0.58×$10^{19}$$Am^2W^{-1}$), suggesting the drive effect in the divertor configuration is better than that in the limiter case.

The different current efficiencies are in agreement with the simulated ray tracing and power deposition by LUKE/C3PO code. Figure 5 shows the parallel refractive index ($N_{//}$) evolutions during the ray propagation, in which the wave accessibility [12] and the Landau damping condition ($6.5/T_e^{0.5}$) are also plotted. Where, s is the ray length and the black region means Landau damping through which the wave energy is transferred to electrons. It is seen that the Landau damping occurs after much longer ray path in the limiter case than that in the SN and DN plasmas, meaning the much slower absorption in the limiter plasma. As a result, no obvious difference in the power deposition between SN and DN configuration, and in the limiter case, the power deposition is near to core region with a little smaller power density, which can be seen in Fig.6, where r is the radial position and a is the minor radius.

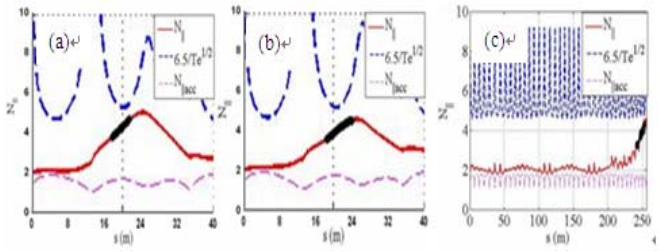

Fig. 5 Evolution of parallel refractive index

(a. double null b. single null c. limiter)

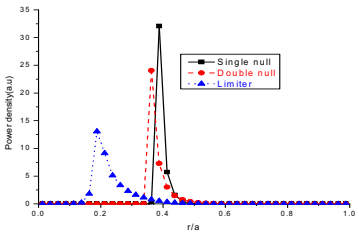

Fig. 6 Calculated power deposition

The current drive efficiency was also investigated with I_p~250kA and $N_{//}^{peak}$ = 2.1 at different density of 0.8×10^{19} m^{-3}, 1.0×10^{19} $m^{-3}$and 1.3×10^{19} m^{-3}. The obtained drive efficiencies are shown in Fig. 7, showing that the efficiency increases with the density increase. Simple estimation indicates the wave satisfies the accessibility condition. Invoked from $\eta_0^{theor} = 1240\alpha/[\ln\Lambda(5+Z_{eff})(\beta^2 N_{//}^{\ 2})]$, Z_{eff} is a possible candidate for the dependence of drive efficiency on density since Z_{eff} will decrease with the density increase. Seen from Fig. 8, the data normalized by 5+Z_{eff} with the three densities are in line and it can be fitted by one curve. Therefore, the impurity concentration is the main reason for the discrepancy in the drive efficiency.

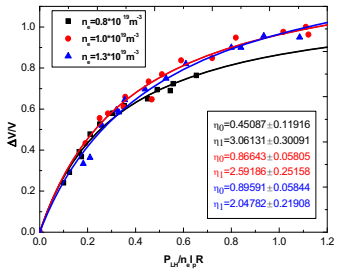

Fig. 7 CD efficiency vs n_e

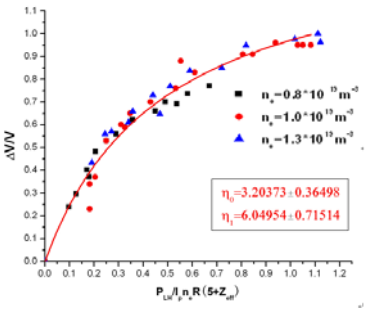

Fig. 8 Normalized CD efficiency

4. Large Current and High Power Experiment

To achieve EAST goals, enough coupled LHW power is necessary to obtain large plasma current. Up to now, the maximum incident LHW power is up to 1.4MW (Fig. 9) with RC less than 10% and the maximum of plasma current is about 830kA (Fig. 10) with the help of LHCD, whose two main contributions is assisting current up and plasma shaping in the experiments. Further physics investigation is on the way.

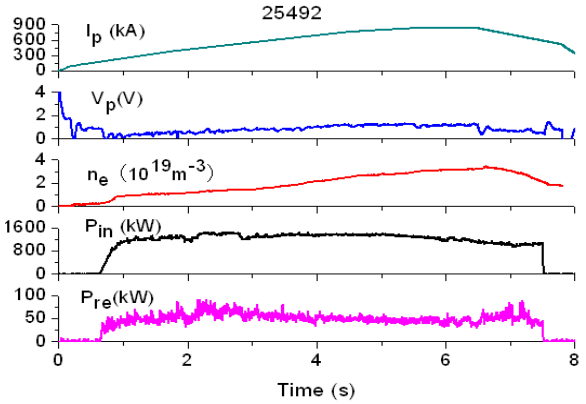

Fig.9 Waveform of maximum incident LHW power

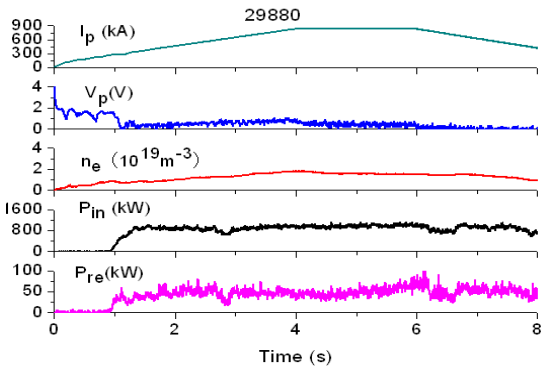

Fig. 10 Waveform of maximum plasma current

5. Discussion and Conclusion

Wave-plasma coupling and current drive experiments in EAST suggest that LHW can be effectively coupled into plasma and drive plasma current with present LHW system. Preliminary studies indicate that LHW-plasma coupling and current drive efficiency are both affected by plasma configurations. The best coupling is obtained in limiter configuration, then SN plasma, and the worst is DN plasma. The CD efficiency in limiter plasma is lower than those in divertor configurations. The current drive efficiency is affected by density due to the contribution of impurity concentration.

In the present parameters in EAST, the current drive efficiency is relative low. This is mainly due to low plasma temperature, since the experimentally obtained current drive efficiency in JT-60U and JET much depends on plasma temperature [13]. This could be improved with the improvement of plasma parameter in future.

Acknowledgements: This work is supported by the National Natural Science Foundation of China under Grant No. 10875149 and 10928509, the ITER Relevant Foundation in China (Grant No 2010GB105000), Core University Program between Japan and China, and the Dean Foundation of Hefei Institute of Physical Science, Chinese Academy of Science.

References:

[1] Jobes F.C. *et al* 1985 *Phys. Rev. Lett.* **55** 1295
[2] Leuterer F. *et al* 1985 *Phys. Rev. Lett.* **55** 75
[3] Takase Y. *et al* 1987 *Phys. Fluids* **30** 1169
[4] Leuterer F. *et al* 1991 *Nucl. Fusion* **31** 2315
[5] Hoang G T, Gil C, Joffrin E, *et al* 1994 *Nucl. Fusion* **34** 75.
[6] Ide S, Fujita T, Naito O *et al* 1996 *Plasma Phys. Control. Fusion* **38** 1645.
[7] Pamela J and JET EFDA Contributors 2003 *Nucl. Fusion* **43** 1540.
[8] Romanelli F. FTU Team and ECRH Team 2002 *Overview of the FTU results* Fusion Energy 2002 (*Proc. 19th Int. Conf. Lyon, 2002)* (Vienna: IAEA) CD-ROM file OV/4-5 and http://www.iaea.org/programmes/ripc/physics/fec2002/html/fec2002.htm
[9] Brambilla M. 1976 *Nucl. Fusion* 16 47
[10] Fisch N J, 1985 *Phys. Fluids* **28** 245.
[11] Gituzzi G, Barbato E, Bernabei S, Cardinali A, 1997, *Nucl. Fusion* **37** 673.
[12] STIX T. H. The Theory of Plasma Waves, McGraw-Hill, New York(1962).
[13] SHI B.R. 1999 *Magnetic Confinement Fusion Principles and Practice* Atomic Energy Press, Beijing (in Chinese).

Progress of Positive-Ion-Based NBI for LHD

Katsuyoshi Tsumori, Masaki Osakabe, Ken-ichi Nagaoka, Yasuhiko Takeiri,
Katsunori Ikeda, Haruhisa Nakano, Masashi Kisaki, Osamu Kaneko,
Eiji Asano, Mamoru Sato, Masayuki Shibuya, Tomoki Kondo,
Seiji Komada and Haruo Sekiguchi

National Institute for Fusion Science, 322-6 Oroshi Toki, Gifu 509-5292, Japan

Abstract:

Two positive-ion-based neutral injectors for Large Helical Device (LHD), which are LHD-NBI #4 and #5, are overviewed. Those injectors are installed to enhance the ion temperature of LHD plasmas by producing low-temperature ions. Each beamline has four ion sources, and the injection power of NBI #4 is 6 MW at the energy of 40 keV. The NBI #5 is designed to provide the beam power of 6 MW at 45 keV for hydrogen beam and 9 MW at 80 keV for deuterium beam.

Beam injection with NBI #4 has started with two ion sources in 2004 and with full of four sources in 2005. The maximum power of NBI #4 has reached 7 MW. The injector contributes to increase ion temperature, and is also applied to a diagnostic beam using charge exchange recombination spectroscopy (CXRS). The NBI #5 has been operational in 2010. After tuning a ratio of acceleration and deceleration voltages, the injection power reaches 5.8 MW at 40 keV so far.

Key word:

NBI, positive ion source, arc efficiency, beam optics, perveance, H^+, D^+, LHD

1. Introduction

Neutral beam injection (NBI) is a most reliable method to heat the target plasmas and has been widely applied to fusion experimental devices [1-9]. Neutral beams are also applied for increasing the density of target plasmas and neutral-beam current drive [10-17]. The positive-ion-based injectors have long history of researched and developed, and they are one of the surely established heating devices in the nuclear fusion research [18-20]. Many fruitful results in plasma physics, for instance H-mode, internal thermal barrier (ITB) and Alfven eigenmodes (AE), have been obtained with neutral injections in Tokomaks and Helical systems [21-30].

The neutral beams in LHD had been injected in LHD with three tangential negative-ion-based NBI systems, initially. The maximum beam energies increased more than 170 keV and the injection power became more than 10 MW. The ion temperature of LHD plasma was, nevertheless, insensitive to the injection power of those neutral injectors. That is because the beam energy is mainly consumed by electrons in LHD plasma above the energy range of 100 keV. Low energy beams transfer the power to plasmas effectively and increase ion temperature efficiently. It is, however, difficult to obtain high current density with negative-ion-based beams. Consequently positive NBI systems are planed to construct to increase the ion temperature of LHD plasmas.

Here, we report an overview of progress in the positive-ion-based NBI systems for LHD. In following sections, outline, the design and experimental studies on arc plasmas, beam accelerator, actual beam conditioning and injection concerning positive NBI systems are described.

2. Scheme of Positive-ion-Based NBI for LHD

Arrangement of two positive-ion-based NBI systems for LHD is schematically shown in Fig. 1(a) and (b) together with negative NBI systems. The positive NBI systems inject the beams in perpendicular directions to the magnetic axis of LHD torus. As shown in Fig. 2(a) and 2(b), main components of the positive NBI are four (horizontally two and vertically two) ion sources, gas neutralizer, ion-deflection coil magnet with an iron core, residual beam dumps, neutral beam dump with calorimeter array, and injection port. Taking into account of the proton / deutron neutralization efficiencies [31], the maximum beam energies are kept lower than 40 keV for proton (H^+) and 80 keV for deutron (D^+) beams in those systems. In order to obtain the injection power over 6 MW per beamline, the beam current of 250 – 300 A is necessary to achieve the power. In this range of current density, the beam divergence becomes 12 – 14 mrad due to the space charge. On the other hand, the area and length of the injection port is already fixed. Therefore, the combination of beam transparency, arrangement of ion sources and distance between ion source and injection port has been comprehensively optimized with use of numerical calculation.

In the case of NBI #4, a large cylindrical chamber is set at the downstream of four gas neutralizers, and an ion-deflection magnet with iron core is installed in the chamber. The magnet bends non-neutralized beams horizontally to residual ion dumps (RID) assembled with two panels of stacking swale tubes. The ions collide to the beam-dump

panels with shallow angles to spread the heat load; i.e. the beam axis is along the long side of the panel and is parallel to water flow lines. In spite of the high heat removal of the swale tubes, ion beam concentrates at a certain part of the RID panel. The beam concentration damages to the panel. By changing applied current to the coil of ion-deflection magnet, residual ion beams are swung on the RID panel to avoid the localization of the beam peak. Five cryo-sorption pumps are installed in the NBI #4 vessel. Evacuation abilities of four of those pumps are 375 litter / sec, and that of another pump, added later, is 500 litter /sec. In the neutral beam dump, four sets of 11(H) x 9 (V) thermocouple tips, calorimeter arrays, are installed to monitor each beam profile during beam conditioning. Perveance matching is analyzed with the arc power, extraction voltage and beam width at the calorimeter array. The neutral dump is lifted vertically and moves out of the beam center during beam injection.

The final specification values of NBI #4 and #5 are shown in Table 1. The NBI #4 was designed for H^+ acceleration, while the NBI #5 is available to accelerate both of H^+ and D^+ ions as its original plan.

3. Arc Efficiency

The ion source of positive NBI #4 and #5 are common except for the accelerators with their insulators. Inner size of the arc chamber is 330 mm (W) x 740 mm (H) x 250 mm (D). The beam extraction area is 210 mm (W) x 550 mm (H), and 20 x 17 apertures with the diameters of 7 or 8 mm are arranged. Filament-arc discharge is applied to generate the plasma to obtain positive ion beam. Arc efficiency, which is defined as a ratio of accelerated beam current to input arc power, is one of the important parameter to decide the capacity of filament and arc power supplies.

In the ion sources with high arc efficiency, stable plasma generation is achieved in high input arc power, and the filament lifetime becomes longer. It was clear that the ion source with high arc efficiency has an advantage to provide stable beam injection. However, there was no definite guiding principle to improve the arc efficiency at the planning period of the positive NBI for LHD. Since the comparison of several large-scaled ion sources with different magnetic configuration spends time and cost, systematic survey of the efficiency is not practical. In consequence, alternative method to decide the efficiency was required. The arc efficiency can be interpreted how many ionizations occur with single electron. In other words, the efficiency depends on how long the electrons stay in the chamber until reaching the chamber wall or thermalization after emitted from filaments. We, therefore, tried to characterize the efficiency with aid

of trajectory calculation of the electrons by changing the magnetic structure inside the arc chamber [32].

In this calculation, the electrons are emitted from filaments with 75 eV of the energies, which is the typical voltage of the arc discharge in our ion source. Collision-less model is adopted to make clear the drift motions of non-themalized electrons in the arc chamber. The magnetic field is calculated to the all cusp magnets, and the field induced by filament current is taken into account. Twenty types of magnetic configurations were examined using magnetic and trajectory simulation, and two typical configurations are described here. The short-side cross sectional view of two types of cusp configurations are schematically indicated together with the magnetic field in Fig. 3(a) and 3(b). Here, the ion sources of Fig 3(a) and 3(b) are named type (a) and type (b) ion sources, respectively. The former is a basic configuration, whose sidewall is surrounded with 6 lines of cusp magnets. Another line of cusp magnet is added in the configuration of type (b) source. In the later configuration, more magnetic field lines intersect the plasma grid, which is indicated as a line at z origin than former case. On the other hand, in the former case, a tent-like fields running across the inner part of arc chamber trap electrons from filaments. The electron distribution in former case is shown in Fig. 4, which indicates the view from the back-plate. The electrons are emitted from two filaments at 50 mm in y, and they circulate in the direction of counter clockwise due to the drifts caused by the structure of the tent-like field; they are curvature and $\nabla |B|$ drifts. The simulation result shows that the electron lifetime is longer in type (a) source, and more plasma flux flow onto the grid along the magnetic lines in the configuration of type (b) [32].

To confirm which configuration has better arc efficiency, actual efficiencies are compared with the experiment by changing the magnetic configurations shown in Figures 3. The beam current of subtracting deceleration current form acceleration current with respect to input arc power is indicated in Fig. 5 to compare those two magnetic configurations. The beam current is defined as the difference of drain currents of acceleration power supply and deceleration one, *Iacc* – *Idec*, which corresponds accelerated positive ion current approximately. Better arc efficiency of 0.45 A / kW and linearity of beam current is obtained in the type (a) source. Determination of the arc efficiency only from simulation result is indirect. Comparing the simulation result to experimental data, however, the efficiency is considered correlative to the lifetime of high-energy electron. This does not contradict the ionization efficiency of high-energy electrons, and the numerical simulation has a

possibility to be an aid to design the magnetic configuration of ion sources.

4. Proton Ratio

Positive hydrogen beams include molecular ion components. After passing though the neutralizer, those ions become neutral hydrogen-atomic (H^o) beams. Since the energies per nuclei are a half in H_2^+ and one-third in H_3^+, the penetration depths in target plasma are shorter in H^o beams originated in those molecular ions. Neutral beams with higher proton ratio have the more efficiency of energy transfer and they deposit at core part of the target plasma.

Charge exchange spectroscopy (CXS) is an apposite method to measure the beam components and is utilized to many positive-NBI systems [33-36]. The detail description on an apparatus and processing method of are described elsewhere [37]. The spectra of Hα originated from accelerated proton, H_2^+, H_3^+ ions as well as background hydrogen gas are indicated in Fig. 6. Gaussian-fits of the spectra are shown as dotted curves in this figure. Doppler shifted spectra of beam components have wider widths than the width emitted by background gas, and the widths is caused by the beam divergences. The width of proton having fundamental energy of E_o is about square root of 2 times as wide as that of the spectrum with energy of $E_o/2$. The CXS is applicable to obtain the minimum beam width during the beam injection without use of calorimeter

Beam compositions as functions of arc power are shown in Fig. 7. The proton ratio is 80 % at the arc power of 50 kW, and reaches 88 % at the nominal arc power of 100 kW. As increasing the arc power, the H_3^+ component exponentially decreases. The H_2^+ component settles at a constant value of ~9 %.

5. Beam Optics

Before installing the ion sources of positive NBI systems, the acceleration characteristics are investigated at a NBI test stand. To monitor beam profiles, a cross-type calorimeter array is installed in the test stand, and the array is set at 4.3 m apart from the grounded grids of the ion sources. Two types of the plasma grids are tested for the accelerator of the positive ion source. Figures 8(a) and 8(b) show the three-dimensional cut view of two types of accelerators consisting of plasma grid (PG), deceleration grid (DG) and grounded grid (GG). The accelerators in Fig. 8(a) and 8(b) are here named type (a) and (b). All the grids are initially made of oxygen free copper with water-cooling channels. In PG shown in Fig. 8(a), the water-cooling channels meander between the nearest neighbor horizontal rows of PG apertures. The

water-channel grooved on the lower side of grid plate, and another plate is brazed on the grooved plate. Total grid thickness is reduced 3.3 mm. The grid is tested to increase the plasma density at beam extraction region. All the accelerator grids are made of oxygen free copper (OFC). In case of the grid in Fig. 8(b), straight copper tubes are welded along the PG ditches dug horizontally between the rows of the apertures. The thickness of the grid is 4.5 mm, and the grid is prepared for the test of high heat removal.

Changes of horizontal and vertical beam widths with respect to beam perveance are shown in Fig. 9. The widths are measured using the calorimeter array. The perveance is defined as $Iacc / Vacc^{3/2}$, where Iacc is the drain current of acceleration power supply in ampere and applied acceleration voltage in kV. The minimums beam widths in horizontal and vertical directions are designed at the same perveance of 0.3, and the experimental minimums are obtained at lower perveance of 0.25 – 0.26 as shown Fig. 9. The difference was acceptable from the point of view in the beam focusing of actual injection. However, the perveance condition has gradually changed in relatively long period of LHD experiment. The beam profiles monitored with calorimeter array installed in the NBI beamline distorted clearly, and focal length also changed. That was because PG made of OFC was warped due to the strong irradiation of arc plasma. A distortion in the type (a) PG was serious, and even the type (b) PG was distorted slightly. After that, the material of PG has been replaced to molybdenum to avoid the problem. The perveance curve is reproductive in the molybdenum grid with high heat removal cooling tubes, and beam optics becomes much better then the case of the previous OFC grid.

6. Beam Injection

The NBI #4 has installed at LHD with two positive ion sources and has stared the injection in 2004. Full four sources have been equipped in 2005 [32,38]. The maximum beam power reaches 7 MW at the energy of 40 keV. The power is well over the nominal value of 6 MW. The injector is also utilized to measure the ion temperature and radial electric field of LHD plasmas. The beam is on/off-modulated with the acceleration voltage and charge exchange recombination spectroscopy (CXRS) is applied for the diagnostics [39].

Newest positive NBI #5 has installed at LHD and started the injection in 2010. Beam conditioning is usually done before beam injection. Trend of the beam power in the conditioning period is shown in Fig. 10(a). A deceleration voltage, Vdec, of 5 kV has been applied to the DG at first, and the increase of beam power was unexpectedly

slow. Sharp peak also could not be observed at calorimeter array. By reducing Vdec down to 2.5 - 3.0 kV, the beam power jumps up steeply at a shot count of ~4100, and beam power reaches 6 MW. The beam current as a function of voltage ratio, *Vacc / Vdec*, is categorized with the Vdec as shown in Fig. 10(b). Since breakdowns occur frequently near the maximum current, it was impossible to increase the acceleration voltage in Vdec of 5 kV. On the other hand, more current is obtained to the breakdown limit after decreasing Vdec. The beam profiles have usual Gaussian shapes in case of lower Vdec. The maximum beam current of 280 A is obtained from four ion sources at the voltage ratio of 15 in this accelerator having the acceleration and deceleration gaps of 4.5 and 4.0 mm, respectively. This is interpreted the beam optics is worse with higher Vdec in this accelerator configuration.

A plasma response to the injected beam of NBI #5 is indicated in Fig. 11. In this scenario, plasma is initiated by ECH and is heated with NBI and ICH. As shown in this figure, the electron density of LHD plasma indicated with FIR signal increases during NBI and ICH injections, and is maintained by NBI only. The energy confinement time of neutral beam is the order of 0.3 sec, and thus the FIR signal remains after beam-finishing time at 5.1 sec.

7. Conclusion

Two positive-ion-based NBI systems are designed and constructed to transfer the beam power to LHD plasmas efficiently and to increase the ion temperature of LHD plasmas.

Arc efficiency of designed arc chamber is examined with aid of numerical simulation including magnetic calculations and trajectory calculation of high-energy electrons. The result is confirmed with practical experiment, and it is considered the efficiency relates to electron lifetime.

Proton ratio has been measured with charge exchange spectroscopy. The arc chamber having long electron lifetime performs the ratio of 88 %.

Beam optics has been investigated using two different accelerators. Horizontal and vertical beam widths are obtained as functions of beam perveance. The widths indicate the minimums at 0.27 of optimal perveance, which is close to the designed values. The plasma grid made of oxygen-free copper was distorted after irradiated by arc plasma, and the thermal distortion had a strong influence to beam optics. The problem has been resolved by replacing the grid material to molybdenum.

The beam injection with NBI #4 with full installation of four ion sources has started

since 2005. The maximum power of 7 MW has been achieved at the injection energy of 40 keV. A new NBI #5 has constructed and installed on 2010. Due to the mismatching of beam optics the beam power was considerably low initially. Later the deceleration voltage has been reduced from 5 kV to lower than 3 kV, and the beam power increased drastically, and the power reached 6 MW so far.

Acknowledgements

The authors would like to express their thanks to the continuous encouragement of the present Director general Prof. A. Komori and previous Director general Prof. O. Motojima. This work is supported with the NIFS05ULBB501 and NIFS10ULRR703, and is also partially supported by the JSPS-CAS Core-University program in the field of 'Plasma and Nuclear Fusion'.

Table 1. Specification values of NBI #4 and #5.

	NBI #4	NBI #5
Beam energy	40 keV	60 keV (H), 80 keV (D)
Beam current / ion source	75 A	60 A (H), 65 A (D)
Total number of ion sources	4	4
Beam power	6 MW	6 MW (H), 9 MW (D)
Beam duration	10 sec	10 sec
Focal length	8.3 m	10.5 m
Transparency of PG	35 %	35 %

References

[1] SM. Kaya, M.G. Bell, K. Bol et al, 1984, Journal of Nuclear Materials, 121:115

[2] P. G. Carolan, B. P. Duval, A. R. Field et al, 1987, Phys. Rev. A, 35:3454

[3] JET Team, 1992, Nuclear Fusion, 32:187.

[4] M.G. Bell, K.M. McGuire, V. Arunaslam et al, 1995, Nucl. Fusion, 35:1429.

[5] T. Stevenson, O'Connor, V. Garzotto et al. 1995, Fusion Engineering, 16th IEEE/NPSS Symposium, SOFE'95. 1:537

[6] K. D. Zastrow, W.G.F. Core, L. G. Eriksson, et al. 1998, Nucl. Fusion, 38:257.

[7] X.R. Duan, X.T. Ding, J.Q. Dong et al, 2000 Nucl. Fusion 40:1897

[8] S. Matsuda, M. Akiba, M. Araki, et al, 1987. Fusion Eng. and Design, 5:85

[9] Y. Ohara, 1998. Rev. Sci. Instrum, 69:908.

[10] F. Wagner, G. Becker, K. Behringer et al, 1982, Phy. Rev. Lett, 49:1408.

[11] S. Okamura, K. Matsuoka, K. Nishimura et al, 1995, Nucl. Fusion, 35:283

[12] S. Sakakibara, H. Yamada, K.Y. Watanabe et al, 2001, Nucl. Fusion, 41:1177.

[13] M. Murakami,1,b_ M. R. Wade,2 C. M. Greenfield et al, 2006, Phys. of Plasmas, 13:056106-1

[14] F.X. SOLDNER, R. BARTIROMO, F. LEUTERER et al, 1993, Nucl. Fusion, 33:333.

[15] T. Oikawa, K. Ushigusa, C.B. Forest et al, 2000, Nucl. Fusion, 40:435.

[16] T. Oikawa, Y. Kamada, A. Isayama et al, 2001, Nucl. Fusion, 41:1575.

[17] N. C. Hawkes,1 B. C. Stratton,2 T. Tala et al, 2001, Phys. Rev. Lett, 87:115001-1

[18] Y. Ohara, 1978. Japanese Journal of Appl. Phys, 18:351.

[19] R. Hong, A. P. Colleraine, D. H. Ke;;man et al, 1992, Internal report of General Atomics, GA-A-21034

[20] Y. Ohara, 1998. Rev. Sci. Instrum, 69:908.

[21] M. F. F. Nave, P. Lomas, C. Gowers, et al,. 2000, *Plasma Phys. Control.Fusion,* 42:A89

[22] T. H. Osbone, et al, 1994, Plasma Phys. Control. Fusion, 36:A237.

[23] A. Sykes, R. J. Akers, L. C. Appel et al, 2000, Phys. Rev. Let, 84:495

[24] C. Gormezano, Y. F. Baranov, C. D. Challis et al, 1998, Phys. Rev. Lett, 80:5544.

[25] T. Fujita, Y. Kamada, S. Ishida et al, 1999, Nucl. Fusion, 39:1627

[26] O. Gruber, R. Arslanbekov, C. Atanasiu et al, 2001, Nucl. Fusion, 41:1369.

[27] A. Welter, D. A. Spong, R. Jaenicke et al, 1994, Phys. Rev. Lett, 72:1220.

[28] S. Ali-Arshad and D. J. Campbell, 1995, Plasma Phys. Control. Fusion 37:715.

[29] E. D. Fredrickson, N. Gorelenkov, C. Z. Cheng et al, 2001, Phys. Rev. Lett, 87:145001-1.

[30] K. Toi, S. Ohdachi, S. Yamamoto et al, 2004, Nucl. Fusion 44:217

[31] K. H. Berkner, R.V. Pyle and J. W. Stearns, 1975, *Nucl. Fusion*, 15:249.

[32] M. Osakabe, K. Nagaoka, K. Tsumori et al, 2007, Proceedings of ITC/ISHW2007

[33] Y. Okumura, H. Horiike, and K. Mizuhashi, 1982, Rev. Scl.lnstrum. 55:1.

[34] M. Akiba, M. Araki, H. Horiike et al, 1982, Rev. Sci. Instrum. 53:1964

[35] R. Uhlemann, R. S. Hemsworth, G. Wang et al, 1993, Rev. Sci. Instrum, 64:974

[36] Y. Li-Ming, L. Guang-Jiu, C. Jian-Yong et al, 2010, *Chinese Phys. Lett.* **27**:042901

[37] K. Nagaoka, K. Ikeda, M. Osakabe et al, 2007, Plasma and Fusion Research, 2:S1051

[38] Y. Takeiri, O. Kaneko, K. Tsumori et al, 2010, Fusion Sci. and Tech, 58:482.

[39] K. Ida, H. Funaba, S. Kado et al, 2001, Phys. Rev. Lett, 86:5297

[40] K. Ida, T. Shimozuma, H. Funaba et al, 2003, Phys. Rev. Lett, 91:085003

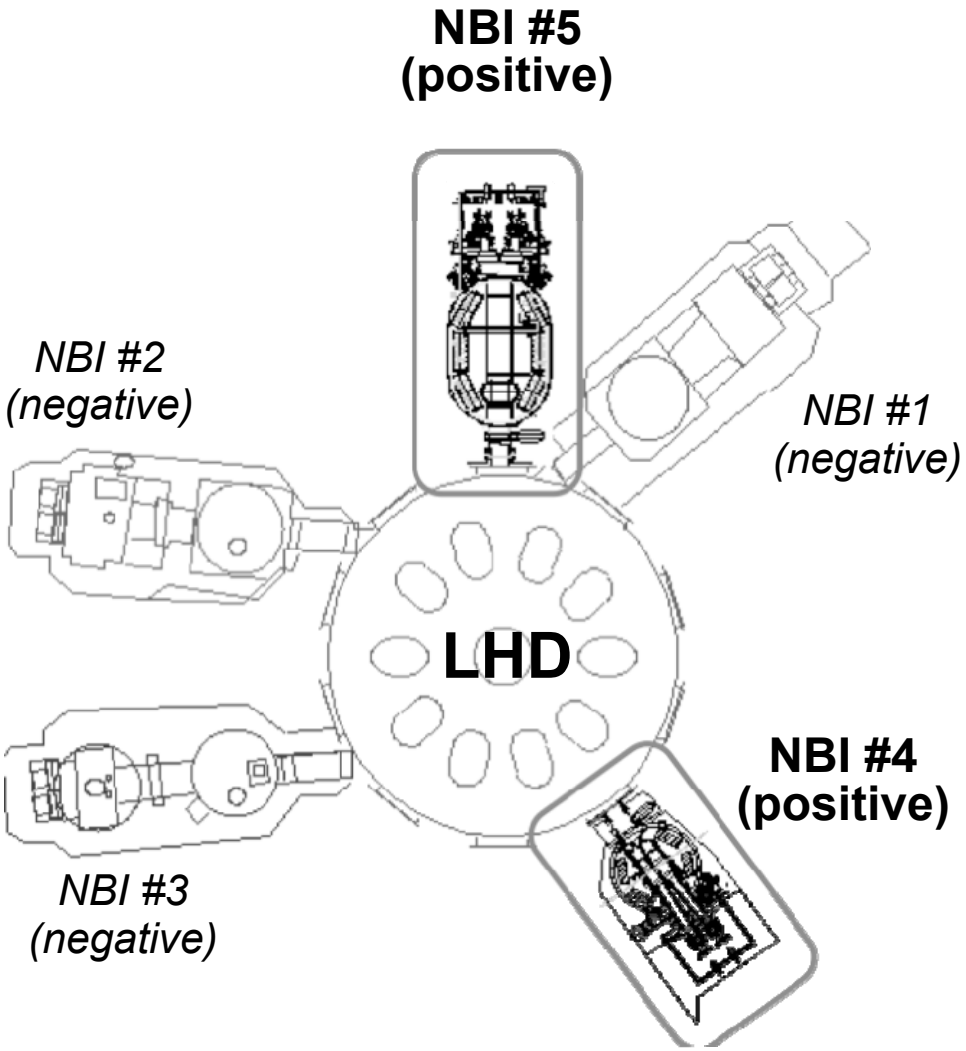

Fig. 1. Arrangement of LHD and NBI systems. The NB1 #1 to #3 are negative-ion-based and tangential beamlines. The NBI #4 and #5 are of positive-ion- based and perpendicular ones.

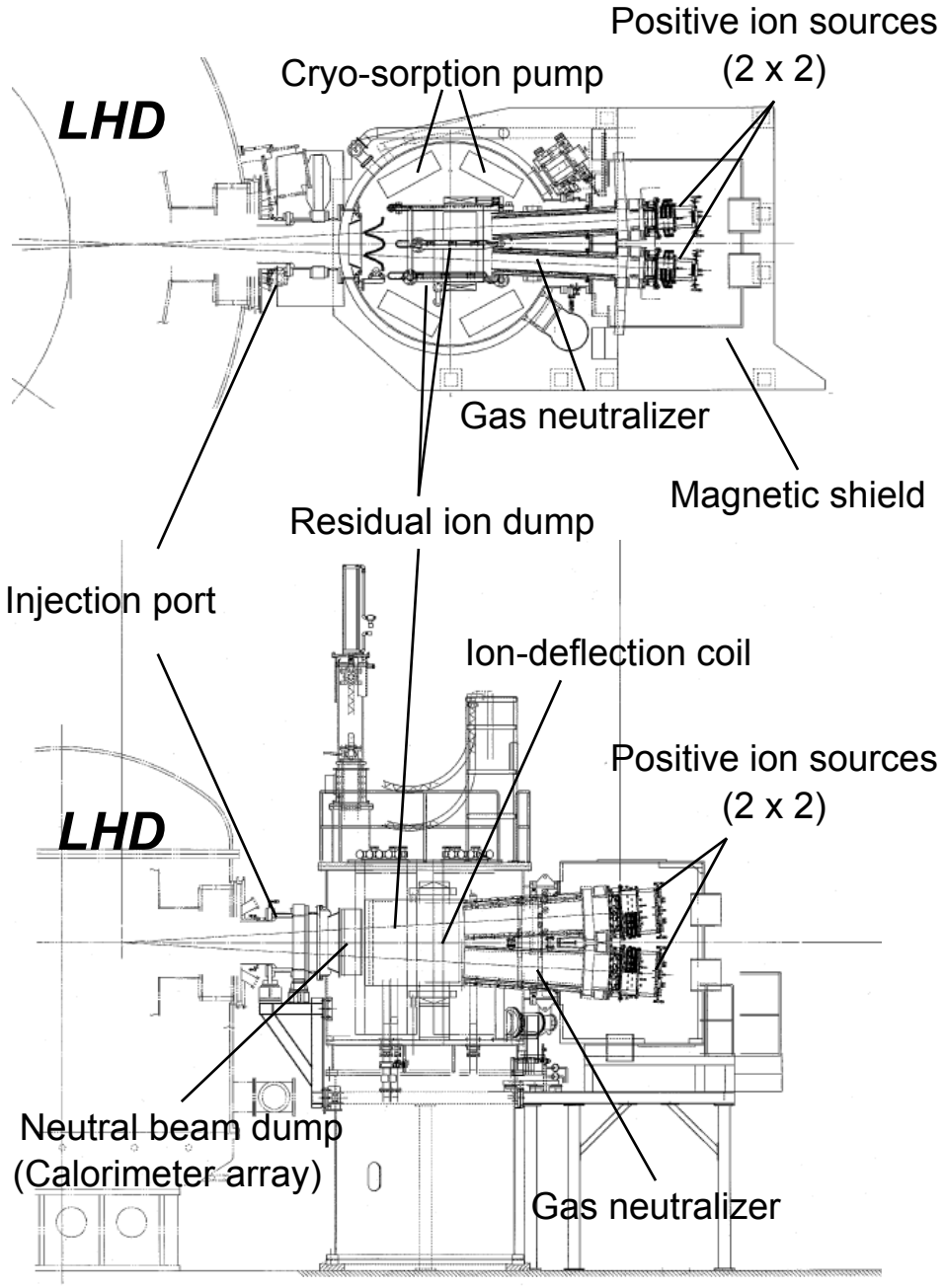

Fig. 2. Schematic top and side views of positive-ion-based LHD-NBI #4.

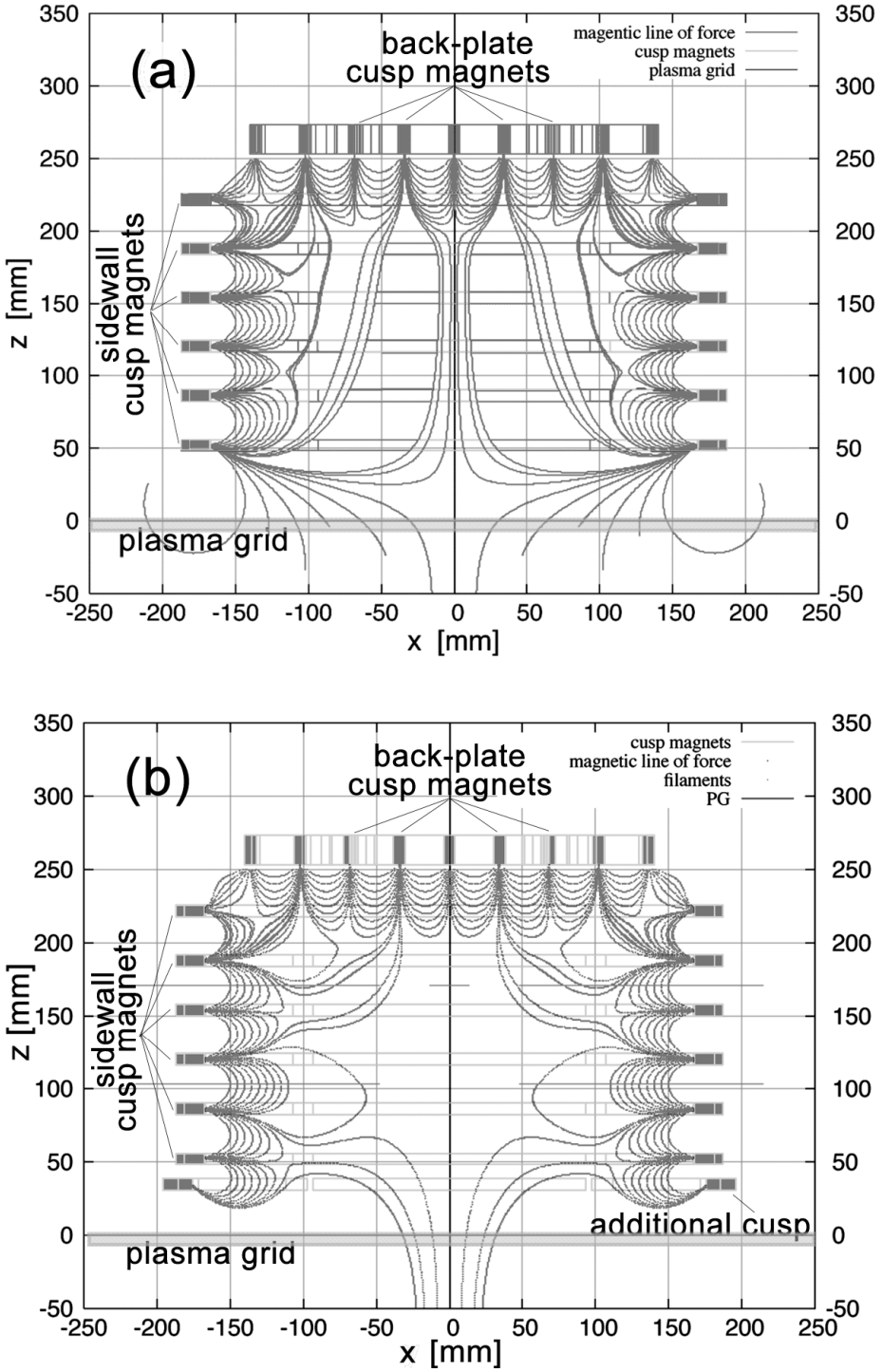

Fig. 3. Configurations of magnetic field induced with two cusp-magnet arrangement. A basic configuration (a) and a variation with additional cusp magnet between the lowest cusp magnet and plasma grid (b) are shown in the short chamber direction, x-z plane.

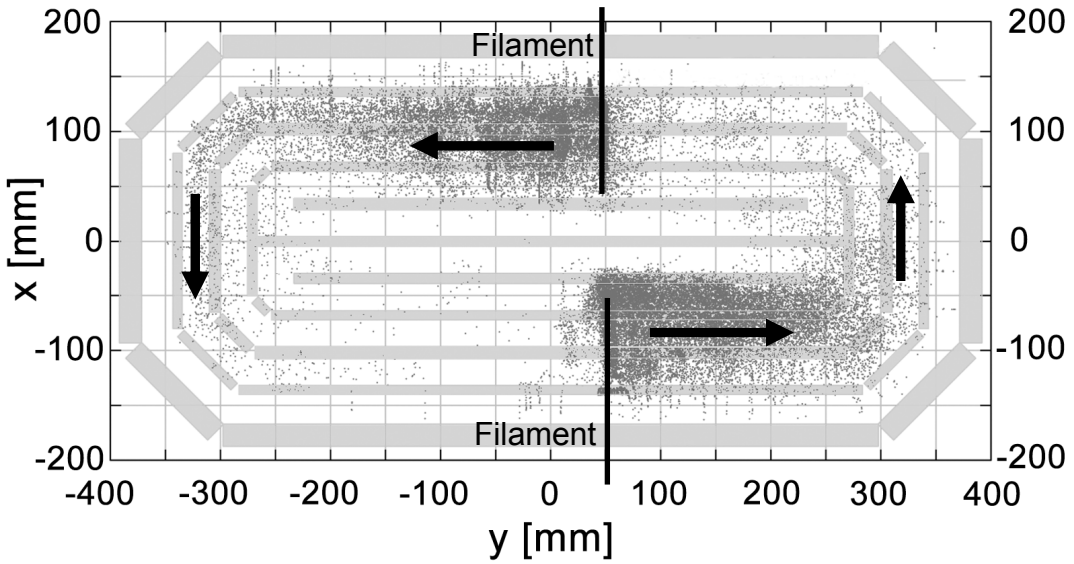

Fig. 4. Electron motion inside arc chamber of Fig. 3(a). Electrons are emitted from a pair of filaments at y of 50 mm circulate along the sidewall of arc chamber due to gradient |B| and curvature drifts.

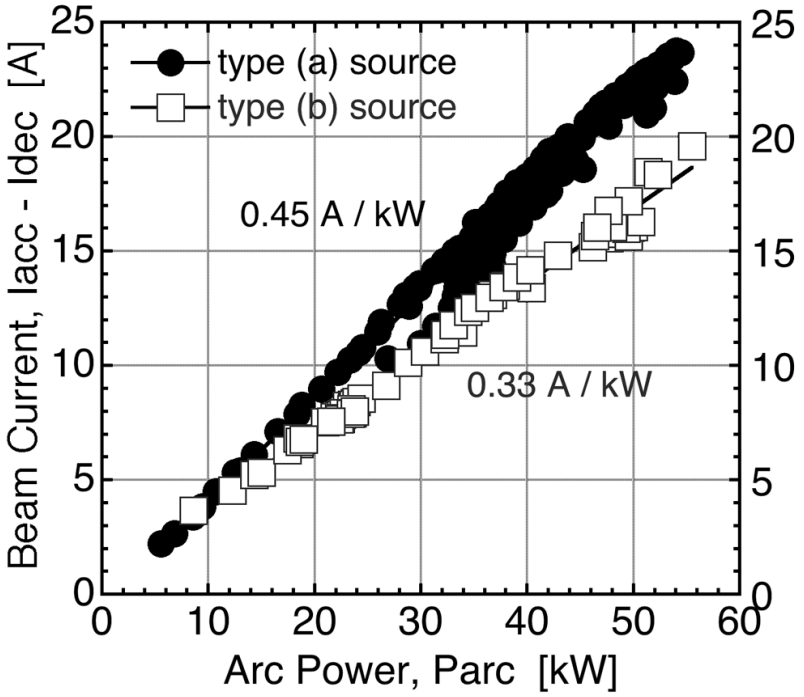

Fig. 5. Arc efficiency in the ion sources with the magnetic configurations of Fig. 3(a) and 3(b).

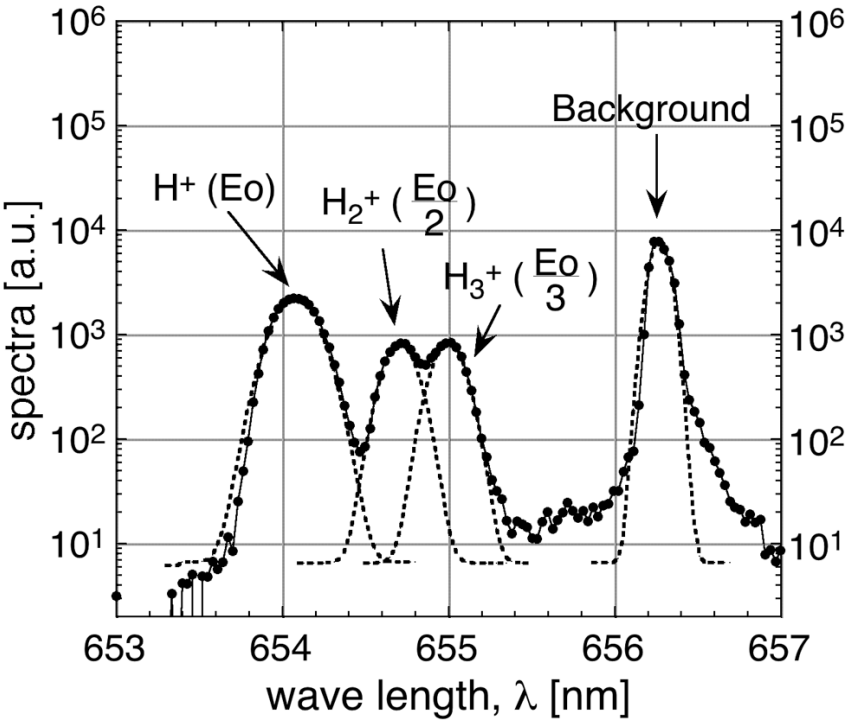

Fig. 6. Comparison of arc efficiencies between the magnetic fields indicating Fig. 5 (a) and (b) corresponding to the type (a) and type (b) sources, respectively.

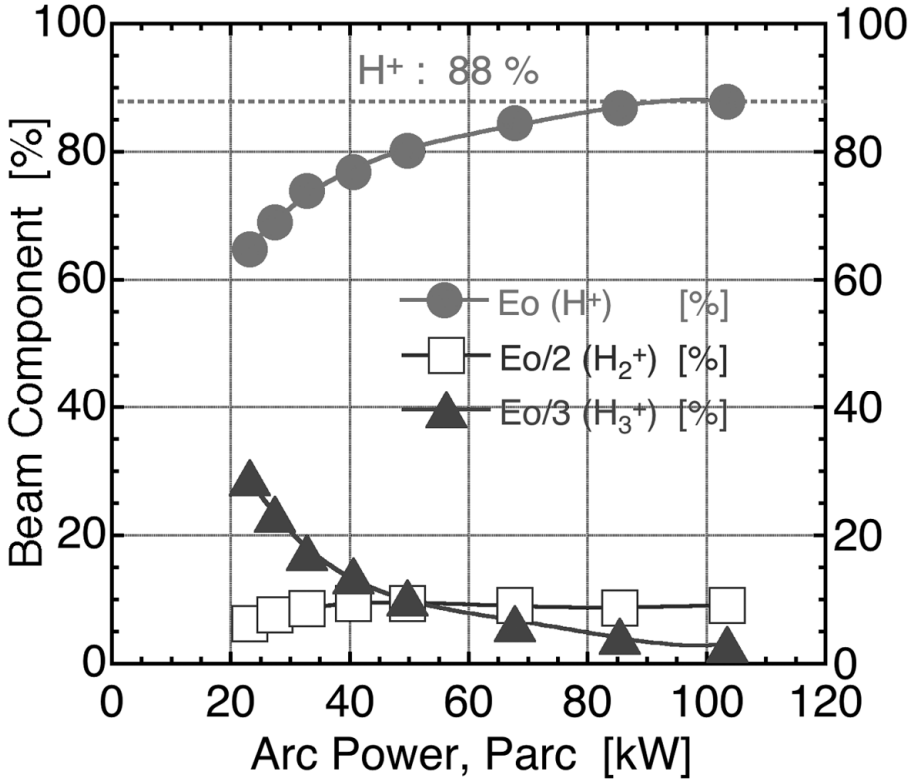

Fig. 7. Distribution of charge-exchange Hα spectra of hydrogenous positive ions (H^+, H_2^+ and H_3^+) and emitted from background gas.

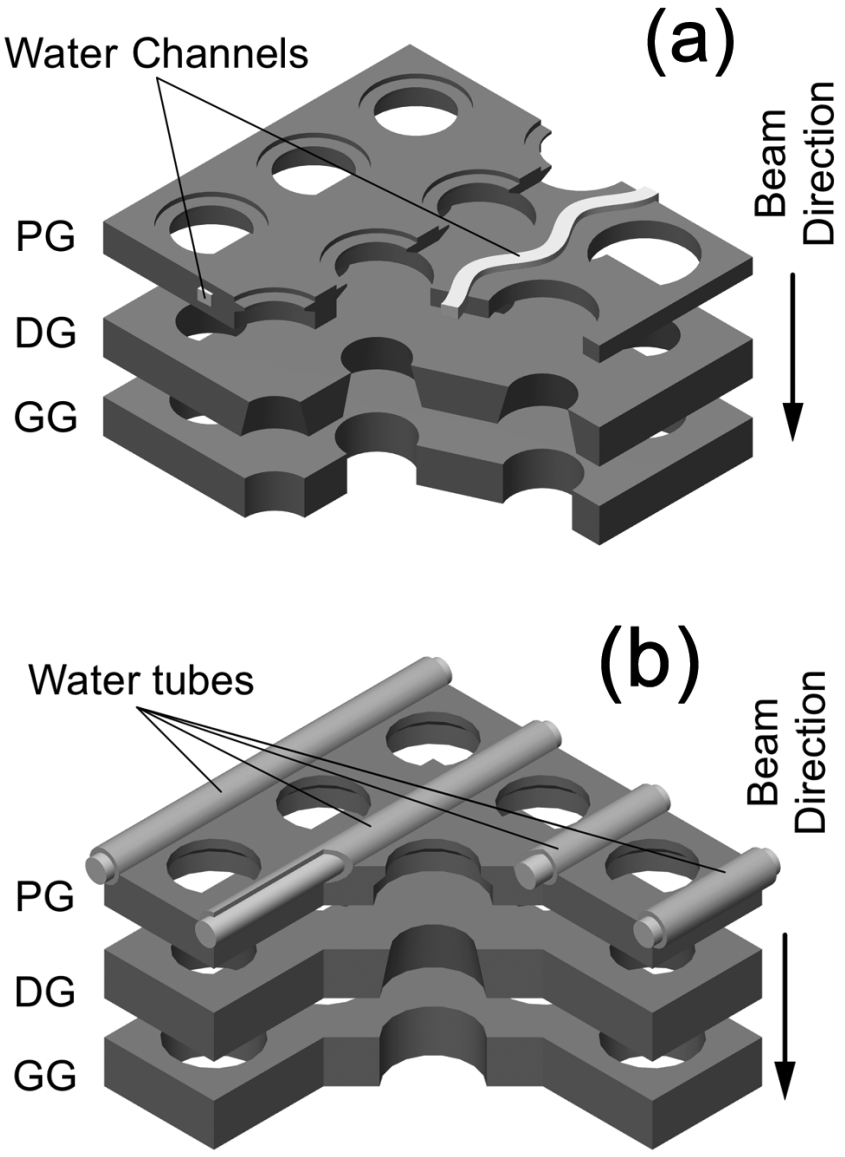

Fig. 8. Three-dimensional cut view of accelerator electrodes. One has a plasma grid with immersed water-cooling channels (a), and another has a grid welded cupper tubes (b)..

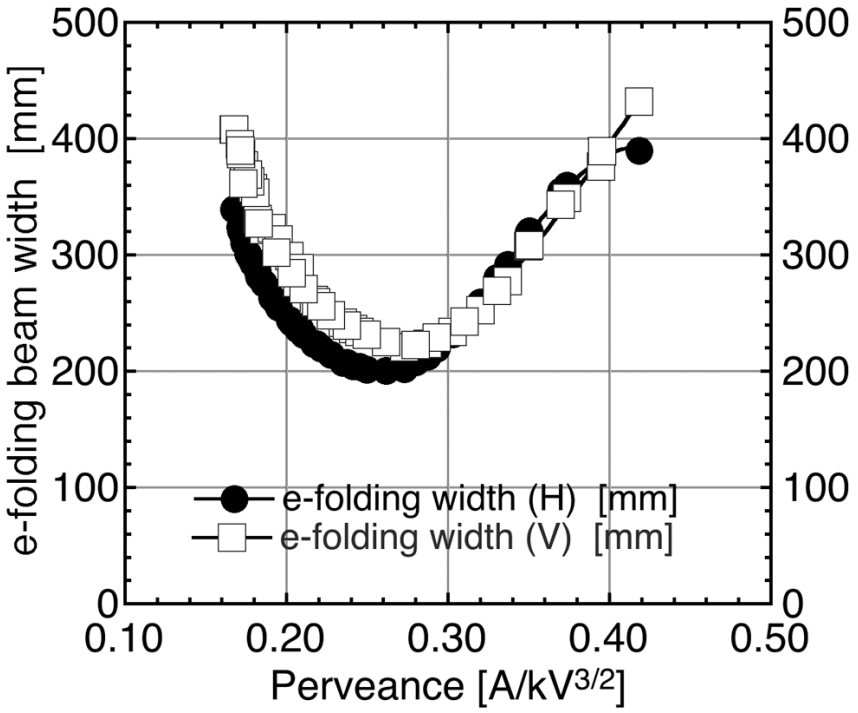

Fig. 9. Horizontal and vertical perveance curves indicating beam widths of the both directions as functions of beam perveance, which is acceleration drain current divided by the two-third power of acceleration voltage.

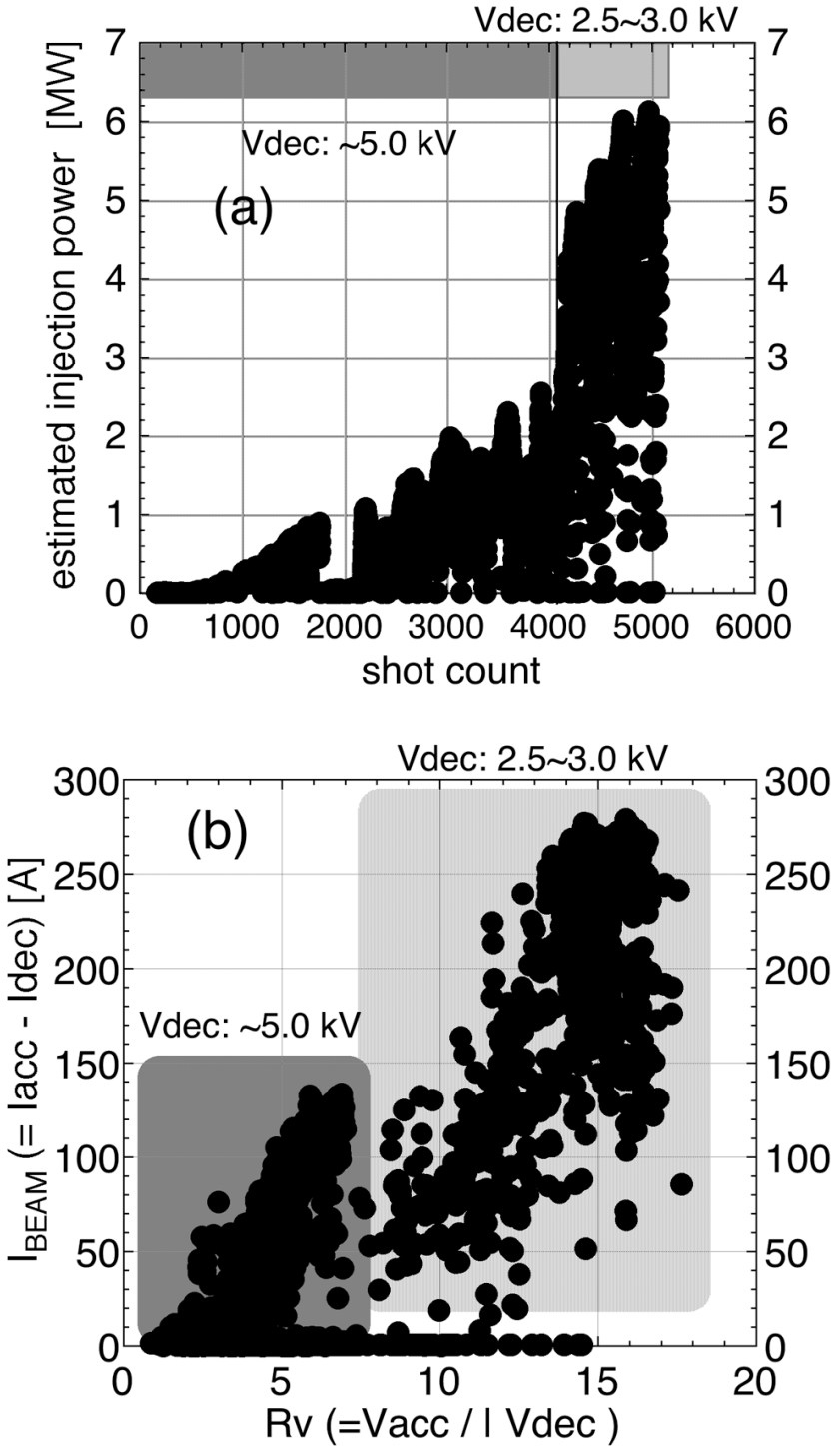

Fig. 10. (a) Trend of injection power as a function of shot count, which corresponds to the conditioning time, and (b) beam current with respect to voltage ratio of acceleration to deceleration voltages Vacc / Vdec.

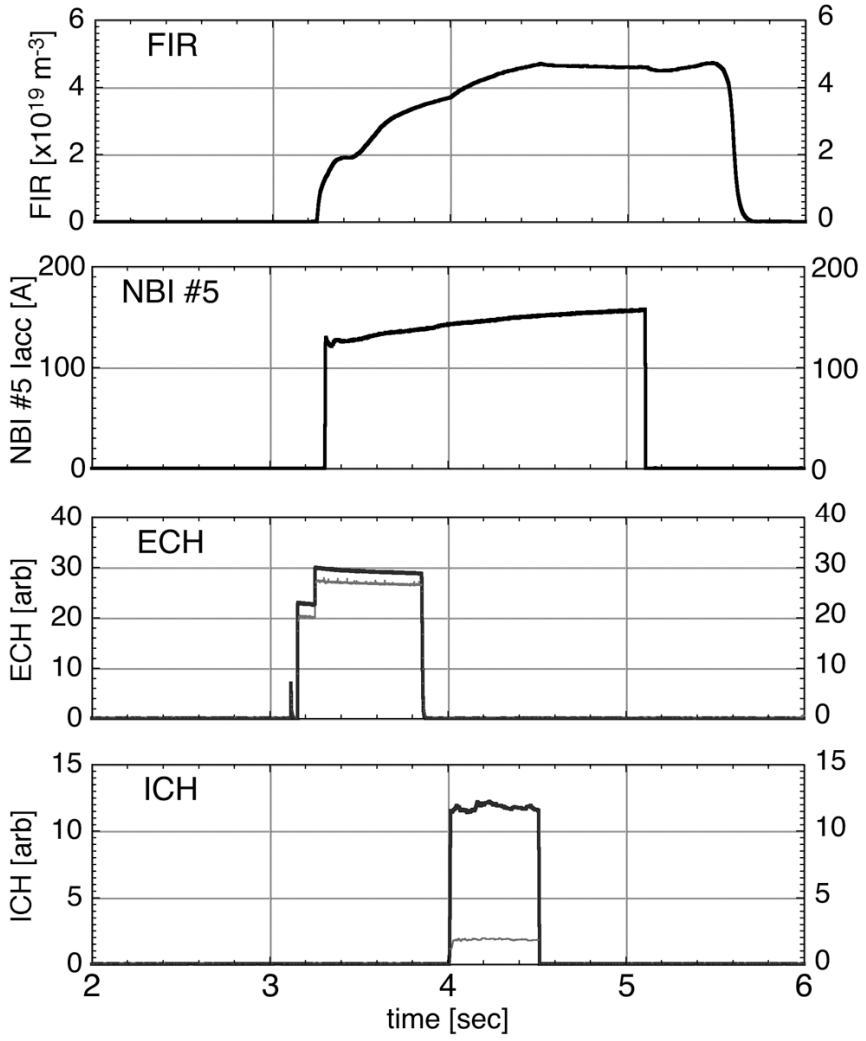

Fig. 11. Waveforms of FIR, acceleration current of NBI #5, ECH and ICH powers. The FIR signal indicates the time changing electron density of LHD plasma.

Present Status of ICRF System on EAST

X. J. Zhang 1), Y. P. Zhao 1), C. M. Qin 1), Y. Z.Mao 1), S. Yuan 1), D. Y. Xue 1),L. Wang 1), J.Y. Ding1),S.Q. Ju 1), Y. Chen 1),C. H. Wang 1), J.S. Shen1),Y. T .Song 1), Y. Lin 2),J. G. Li 1),B. N. Wan 1),and EAST Group

1) Institute of Plasma Physics, Chinese Academy of Sciences, P R China, Hefei 230031
2) MIT Plasma Science and Fusion Center, Cambridge, MA 02139, USA

Email contact of main author: xjzhang@ipp.ac.cn

Abstract: Radio frequency (RF) power in the ion cyclotron range of frequencies (ICRF) will be one of the primary auxiliary heating techniques for Experimental Advanced Superconducting Tokamak (EAST). The ICRF system provides 6 MW power in primary phase and will be capable of 10MW later. Three 1.5 MW ICRF systems in the range of 25-70 MHz have been put into operation.The ICRF launchers are designed to have two current straps and each strap is driven by an independent 1.5MW RF power source. This paper gives brief introduction of the EAST ICRF system capability and especially first primary results on the EAST tokamak during 2010 spring campaign.

1. Introduction

The research objectives of EAST are to perform advanced tokamak research in high performance regime and to explore methods for achieving a steady-state operation for a tokamak fusion reactor.EAST is a fully superconducting tokamak (R = 1.75m, a = 0.4m, Bt = 3.5T, pulse length <= 1000 sec) being commissioned at ASIPP. Since the first plasma in 2006, much significant progress has been achieved [1, 2]. Radio frequency (RF) power in the ion cyclotron range of frequencies will be one of the primary auxiliary heating techniques for EAST. The ICRF systemswill be capable of 10MW of RF power to the plasma.

ICRF system has been designed to operate in the range of 25-70MHz and operate for long pulse length up to 1000s. The main objectives of EAST ICRF are: 1) to study coupling issue with different plasma edge; 2) to study heating and plasma flow generation with different scenarios; 3) to study profile control by on-axis and off-axis heating schemes for electrons and ions; 4) to study the technology of ICRF hardware and launching systems; 5) to investigate combination of ICRH and LHCD for high performance regime for long pulse plasma discharges.

Figure 1 shows the variation of cyclotron resonance frequency of various ion species across the plasma radius. The ICRF heating scenarios for EAST are as follows:

1. H minority heating in D majority plasma. The frequency of 37MHz is good for H minority with 2.5T of the magnetic field.

2. Helium 3 minority heating in D majority plasma. The frequency of 27MHz can be used with 2.5T of the magnetic field.

3. D-Helium 3 mode conversion heating in D majority plasma. The frequency of 26MHz with 3.0T may be possible for the electron heating by using mode conversion.

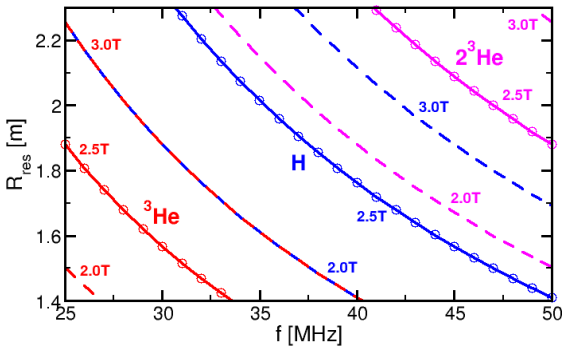

Figure 1 Variation of Cyclotron resonance frequencies of various ion species across the plasma radius

2. The main technical feature of ICRF Systems on EAST

There are four ICRF systems on EAST. Three 1.5MW ICRF systems have put into operationin 2010 experimental campaigns and another 1.5MW ICRF system is under way of construction [3]. ICRF system includes High-power and wide-frequency radio amplifier, the phase shifter system, the matching system and the 2-straps antenna.

Thetransmission line size is 9 inch. The characteristic impedance is 50 Ω. The dry nitrogen gas is filled at the pressure of 3 atmbetween innerand outer conductor. In order tosatisfy the CW operation the inner and outer conductor can be cooled by the pure water.DC breaker has been used in order to isolate the grounds between RF transmitter and theantenna. The matching system consists of three stub tuner. There are four triple liquid stub tuners for EAST 6.0 MW ICRF heating system. Phase between the straps is controlled in the low power parts of the RF system. The ICH launcher is designed to have two current straps and each strap will be driven by an independent 1.5MW RF power source. Three 1.5 ICRF systems have been employed for RF heating experiment on the EAST in 2010 spring experimentalcampaign. Maximum of the injected RF power reached to 1.6MW on EAST.

There are two ports for ICRF in EAST, as shown in figure 2.The EAST ICRH systems consist of two port-mounted antennas that have two current straps, each of which at I port is grounded at the center, and have a coaxial feed line connected to each end of the current strap Fig2 (left). After going through two vacuum feedthroughs, the top and bottom coax feed lines of each current strap are connected to each other in a resonant loop configuration. The length of the current strap that coupled power to plasma is 700mm. The antenna at O port are folded, end grounded with a central current feed, as shown in Fig2 (right). The length of the current strap is 750mm. A 1.5MW RF transmitter is attached to the antenna through a matching system. The matching system consists of three stub tuner. Phase between the straps is controlled in the low power parts of the RF system.The phase between the current straps can be change in 0-360.

For long pulse operation, the antennas have many cooling channels inside the current strap, cavity wall, the faraday screen and vacuum transmission line. In order to adjust the coupling of the antenna to plasma, the antenna can be moved a little in radial direction. The current straps located 10mm from the back surface of the Faraday screen. The front surface of the faraday screen is located 8mm from the limiter. There are two current straps per antenna arranged in a toroidal array. They are spaced with the gap of 14.2cm. The each current strap is 108mm wide and 10mm thick, and its edge is rounded to reduce the electric field strength around the current straps. The polodially curvature of the current strap is 767mm. The material of the strap is stainless steel 316L. The faraday screen is designed as water cooled and single layered tube. The material of the tube is also stainless steel 316. Each of two screens consist 42 tubes. There are four 8 inch vacuum transmitter lines (VTL) and vacuum feedthroughs for I port and two 8 inchfor O port. Its characteristic impedance is 50Ω.

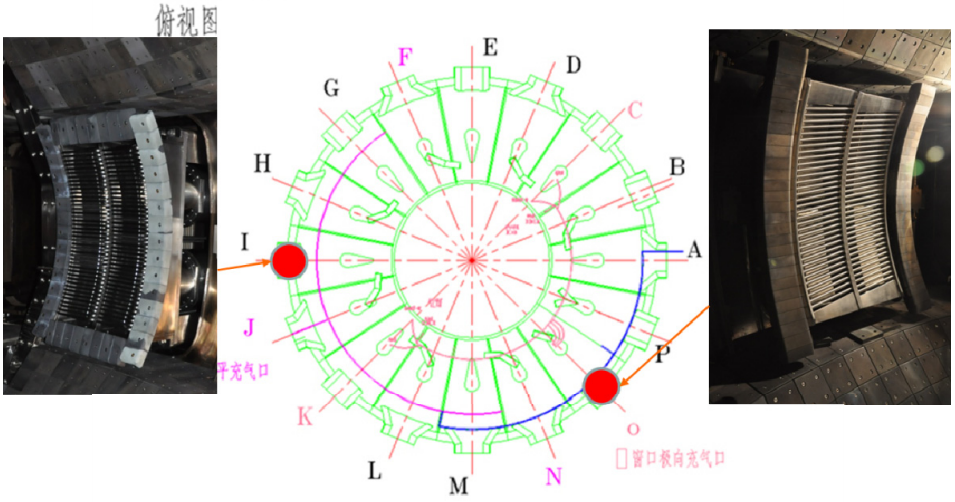

Figure 2 the ICRF Antenna system on EAST

3. ICR Heating Experiments on EAST During 2010 Autumn Campaign

Fig. 3(Right) shows data from a typical ICRF shot in 2010 autumn campaign with atoroidal magnetic field of 2 T. The deuterium was used as the working gas. As ICRF frequency of the transmitter was set up as 27 MHz and it corresponded to hydrogen minority heating mode at 2 T. 1.5MW ICRF power were injected to the double null plasma with LHW. Up to 200eV increase of electron temperature and 10KJ increase of stored energy have been observed. A significant improvement was done compared with 2010 springexperiments [3]. This was believed to be due to the decreased distance between the plasma and the antenna as well as decreasedH/(H+D) ratio. The distance from the last closed flux surface to the limiter was decreased from 50 mm to 20 mm. Hydrogen minority heating is the main ion heating scheme on EAST and the control of minority hydrogen concentrationis very important for the efficient ICRF heating. EAST in vessel components were covered by graphite tiles and graphite tiles could absorb a lot of the hydrogen due to their high absorption characteristics.

H/(H+D) ratio was very high in 2010 Spring campaign. H/(H+D) ratio did not decrease below 30 % over the whole spring campaign. After lithium coating, H/(H+D) gradually decreases up to 10%in 2010 Autumn campaign, as shown in Fig3 (left).

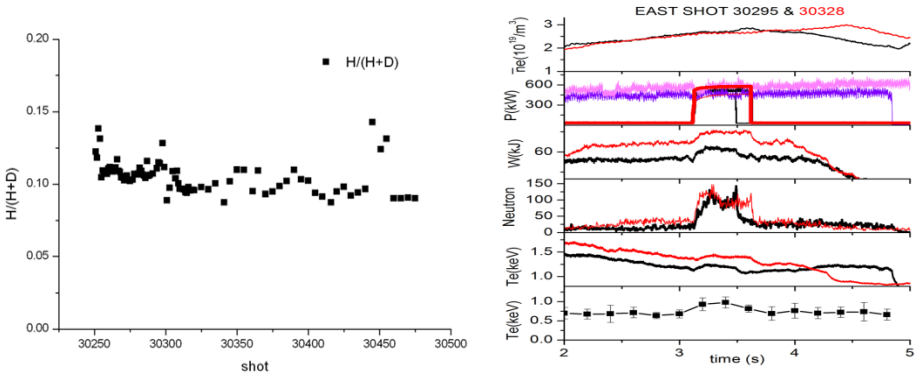

Fig.3 evolution of H/(H+D) (Left) and typical ICRF shot(Right)

4. Summary

We presented the brief introduction of the EAST ICRF system capability. Since 2006, the EAST ICRF system has been designed and fabricated. Three 1.5MW ICRF systems have put into operation in 2010 spring campaign. Up to a 1.6MW RF power was coupled to the D shape plasma with O port antennain the spring campaign.A significant improvement was done compared with 2010 spring experiments. At the beginning of 2010 autumn campaigns, up to 200eV increase of electron temperature and 10KJ increase of stored energy have been observedwith 1.5MW RF power injection in the hydrogen minority heating mode, which wasdue to the decreased distance between the plasma and the antenna as well as decreased H/(H+D) ratio.We expect the ICR Heating experiments to be better for the 2010 autumn campaign by reducing furtherHydrogen concentrations on the shaped plasmas starting with higher plasma parameters and good confinement.

Acknowledgments

We are grateful to the EAST operation and diagnostics group. This work was supported by the ITER Relevant Foundation in China (Grant No 2010GB110000). This work is supported partly by the National Natural Science Foundation of China under Grant No. 10928509 and by the Knowledge Innovation Program of the Chinese Academy of Sciences No. Y05FCQ0126. This work was partially supported by the JSPS-CAS Core-University program in the field of‘Plasma and Nuclear Fusion’.

References

1) Baonian Wan, etc., 22nd IAEA Fusion Energy Conference, October 13-18, 2008, Switzerland
2) Baonian Wan, 3rd EAST IAC meeting, Hefei, China, May 14-15, 2009
3) Xinjun Zhang, etc., 23nd IAEA Fusion Energy Conference, October 11-16, 2010, Korea

Study on overall operation features of tokamak plasma with lower hybrid current drive*

ZHU Tingru（朱廷儒）[1] , ZHAO Xiaoming （赵小明）[1], PENG Xiaodong（彭晓东）[2], and TANG Changjian（唐昌建）[1†]

E-mail: zhutingyan66@163.com

[1]college of Physical Science and Technology, Sichuan University, Chengdu, 610064, China

（四川大学物理科学与技术学院，邮编610064）

[2] Southwest Institution of Physics Center for Fusion Science, Chengdu, 610041, China

（四川成都核工业西南物理研究院，邮编610041）

Abstract

We apply the C-S-D model to analyze the overall consistency features between the core plasma operation and the SOL-divertor plasma operation of tokamak plasma with lower hybrid current drive. The basic property of the overall operation for tokamak plasma is printed. And a numerical analysis for the primary characteristics was done. The influences of

* Project supported by National Magnetic Confinement Fusion Science Progam (Code number 2009GB105002)

† Corresponding author. E-mail: 542160287@sina.com

impurity seeding, gas puffing in the edge of the device and bootstrap current for the consistency operation are investigated. Results show that increasing the impurity radiation, gas puffing in edge region and raising the bootstrap current fraction are effective methods for improving the overall operation region for the tokamak plasma.

Keywords: operation features, impurity seeding, gas puffing, bootstrap current

PACC: 5225F，5255G

1. Introduction

Traditionally, the tokamak plasma is divided into three regions to study solely in accordance with physical features and conditions. A core region is the main one for fusion reaction of deuterium-tritium, which possesses very high temperature (~keV). The region of scrape-of -layer (SOL) separates the core plasma from the wall of vessel, which possesses lower temperature (~eV). Another region is called divertor. Generally, we hope the core plasma in the high-mode (H-mode) operation and the operation of SOL plasma in the detached condition when the tokamak plasma runs in steady-state, which is suggested in the International Thermonuclear Experimental Reactor (ITER) device. Therefore，there must be available total heating power for sustaining the core plasma and the total heating power should meet the requirements of the H-mode operation. Also, we consider the lower hybrid current drive mode (LHCD), the available LHCD power is limited and the LHCD heating power can not be larger than total heating power. In addition, the heat flux and particle fluxes coming from the SOL or the core will be absorbed by divertor targets and drawn out by pumping. So, we have to consider the heat flux to the edge region so as not to damage the

divertor targets. Thus, the three regions are strongly dependent each other. Considering above discussions, it is very necessary to investigate the overall operation features of the tokamak plasma between the SOL-Divertor plasma and the core plasma. A multi dimensional transport code such as B2-Eirene or Uedge was employed to analyze this issue accurately[1, 2]. But the demerit of the multi dimensional transport codes is that they are generally massive, and it requires divertor geometry and large calculation cost. Prior to such detailed and massive calculations, it is necessary to understand qualitatively the overall features based on the state of the three regions.

In the present paper, we employ a Core-SOL-Divertor (CSD) model[3], which is suggested by Doctor Hiwatari and proved to be useful in analyzing the basis operating rules of a tokamak device[4, 5], to study the overall operation features of the tokamak plasma with LHCD. The total heating power for sustaining the core plasma, the threshold condition for the transition of low mode to high mode (L-H), the available LHCD power, and the heat flux to the divertor region can form a closed region, which is called operation space, in the phase space of the particle flux and the heat flux across the separatrix surface of a tokamak. The influences of impurity seeding, gas puffing and bootstrap current on the overall operation features (or operation space) are investigated in some detail.

2. Review of the CSD model

The CSD model integrates the 0-D core plasma transport model based on ITER physics guidelines and the two-point model of SOL-divertor plasma[6].

In the core region of a tokamak, the dynamics of plasma energy W_{th} and density n_j is

determined by

$$\frac{dW_{th}}{dt} = -\frac{W_{th}}{\tau_E} + P_{OH} + P_{\alpha} + P_{aux} - P_{Brad} - P_{sync}, \tag{1}$$

$$\frac{dn_j}{dt} = -\frac{n_j}{\tau_{Pj}} + S_{nj}^{core}. \tag{2}$$

Here τ_E and τ_{Pj} are energy confinement time and j-component particle confinement time, respectively. One can adopt ITER scaling laws or a special device scaling law. P_{OH}, P_{α}, P_{aux}, P_{Brad} and P_{sync} denote Ohmic heating power, α-particle heating power, auxiliary heating power, bremsstrahlung radiation power, and synchrotron radiation power. S_{Pj}^{core} is the particle source of j-component. Eqs.(1) and (2) describe the 0-D core plasma transports.

The two-point model[7] under steady state conditions can be applied with a time dependent core transport model, because the time scale of core plasma transport is much longer than that of SOL-divertor plasma. Basic equations of the usual two-point model are defined by momentum balance, energy balance, radial energy transport, and electron thermal transport along the field lines as follows:

$$(1 - f_{mom}^{div}) n_s T_s = (1 + M_d^2) n_d T_d, \tag{3}$$

$$(1 - f_{imp}) L_s q_{\perp} = n_d M_d C_s(T_d) \Delta_E [\varepsilon + (\gamma + M_d^2) T_d], \tag{4}$$

$$q_{\perp} = \left(\frac{\chi_{\perp}}{\Delta_T} + \frac{3D_{\perp}}{\Delta_n} \right) n_s T_s, \tag{5}$$

$$(1 - f_{imp}) L_s^2 q_{\perp} = \frac{4\kappa_0 \Delta_T}{49} (T_s^{7/2} - T_d^{7/2}). \tag{6}$$

Here *n* and *T* are density and temperature, and subscript *s* and *d* denote the upstream SOL and divertor region, respectively. The heat flux from the core plasma, temperature decay length, power decay length, density decay length, and Mach number at the divertor target are defined

by $q_\perp$, Δ_T, Δ_E, Δ_n, and M_d, respectively. Usually, there is $\Delta_E = 2\Delta_T/7$ and $M_d = 1$ is assumed. $C_s(T_d) = \sqrt{T_d/m}$ is the ion sonic speed. The coefficients f_{mom}^{div} and f_{imp} are the fraction of momentum loss and impurity radiation loss. The coefficient $\gamma \approx 7.0$ is the sheath energy transmission coefficient, and the heat load $\varepsilon \approx 21.8$ eV on the target comes from the recombination and radiation process. The SOL length $L_s = \pi a q_{eff}$ is defined by the plasma minor radius *a* and plasma safety factor q_{eff}. In order to integrate the core and edge plasma model, the upstream SOL density n_s should be given in a self-consistent manner both for the core plasma and for the edge plasma. For this purpose, the particle balance equation in the SOL and divertor regions must be considered. We assume that all neutral particles originate at the divertor plate at the rate proportional to the total particle flux onto the divertor plate. Consequently, total neutral source rate at the edge region N_n including gas puff term N_{puff} reads as

$$N_n = C_n \frac{1}{2}(1-\frac{1}{e^2}) n_d M_d C_s(T_d) 2\pi R \Delta_n \sin\psi + N_{puff}, \tag{7}$$

where ψ is the angle of the magnetic field to the divertor plate. The coefficient C_n is a calibration factor and $C_n = 1$ is assumed. By using this simple neutral particle model and the particle flux $\Gamma_\perp$ across the separatrix, the particle balance equation for the SOL-divertor region becomes

$$\Gamma_\perp S_p + N_n^{SOL-DIV} = C_n \frac{1}{2}(1-\frac{1}{e^2}) n_d M_d C_s(T_d) 2\pi R \Delta_n \sin\psi, \tag{8}$$

where $N_n^{SOL-DIV} = \{1-\{f_{ion}^{DIV} + f_{ion}^{SOL}(1-f_{ion}^{DIV})\}\}N_n$, f_{ion}^{DIV} and f_{ion}^{SOL} are the ionization fraction in the divertor and the SOL region, respectively. S_p is the core plasma surface normal to the particle flux. R is the major radius of the tokamak. The ionization fraction in the divertor region is modeled by[8]

$$f_{ion}^{DIV} = 1 - \exp\left(- \frac{L_d \sin\psi}{\lambda_{ion}^{DIV}} \right), \tag{9}$$

where L_d is the divertor length and the ionization mean free path $\lambda_{ion}^{DIV} = v_n / (n_d < \sigma v >_{ion})$ is defined by the ionization cross section $< \sigma v >_{ion}$, which is the strong function of the divertor plate temperature T_d, and the neutral velocity $v_n = \sqrt{T_n / m}$. The ionization fraction in the SOL region f_{ion}^{SOL} are assumed to be mainly dependent on geometrical parameters as follows

$$f_{ion}^{SOL} = \frac{A_{SOL}}{A_{core} + A_{SOL} + A_{pump}}, \tag{10}$$

where $A_{core} = 2\pi Ra$ is the effective area for the core plasma, $A = 2\pi R\Delta_n$ is the effective area for the SOL plasma. The effective area A_{pump} is defined by $A_{pump} = C_{pump} / (v_n / 4)$, where C_{pump} is the speed of the pumping system[9].

Employing the particle flux $\Phi_p = \Gamma_\perp S_p$ and the heat flux $Q_{in} = q_\perp (S_p / 2) / 0.33$ across the separatrix, one can obtain n_s, T_s, n_d, T_d, and Δ_T as the functions of (Φ_p, Q_{in}) by solving equations (3)~(8).

3. Study on basic trade-off conditions of a tokamak plasma operation

3.1.Main trade-off conditions

Considering core and SOL plasma operation and material and energy process in the divertor range, there exist four trade-offs as mentioned above, i.e., 1) available total heating power in the core plasma; 2) threshold power for L-H transition; 3) available current drive power; and 4) heat flux in the divertor range. We try to discuss the integral operation feature in the four conditions for the main operating characteristics of the three ranges which can be

express with these conditions. The total particle flux and the total heat flux across the separatrix, which comes from the core plasma and reachs the divertor region eventually, can serve as a bridge links the three ranges. So we can study the overall operation features of core and edge plasma in the phase space of the total particle flux Φ_p and the total heat flux Q_{in} across the separatrix. Next, we want to express the above four conditions with Φ_p and Q_{in}.

Based on the particle and the power balance of the core plasma [3, 4], the total particle flux Φ_p and the total heat flux Q_{in} across the separatrix are $\Phi_p = n_{20} V_p / \tau_E$ and $Q_{in} = 0.048 n_{20} T V_p / \tau_E$, respectively. Here V_p is the plasma volume. Using ITER scaling laws, we can express the temperature and density of the core plasma as $T = C_T Q_{in} / \Phi_p$ and $n_{20} = C_n \Phi_p^{10/9} / Q_{in}^{5/9} = n_{20}(\Phi_p, Q_{in})$, respectively. With these parameter relations, we can write the above four constraints, or trade-offs, as the functions of $((\Phi_p, Q_{in}))$ and discuss the plasma trade-off for core and SOL-Divertor plasma on (Φ_p, Q_{in}).

First, the scaling law of the threshold power for L-H transition can be written as the function of (Φ_p, Q_{in}), i.e.,

$$P_{thr} = 2.75 B_t^{0.96} R^{1.23} a^{0.76} M_i^{-1} C_n^{0.77} (\Phi_p^{7.7} / Q_{in}^{3.85})^{1/9}, \tag{13}$$

where M_i is the average ion mass (amu).

Then, the heat flux to the divertor target can be written as

$$q_{div} = [\varepsilon + (\gamma + M_d^2) T_d] n_d M_d C_s(T_d) \sin\psi \sin\theta, \tag{14}$$

The n_d and T_d can be obtained by solving equations (3)~(8). Where θ denotes the inclination angle of the divertor plate to the magnetic lines force in the poloidal plane. Eq.(14) can also be expressed by Φ_p and Q_{in} defined above.

The available current drive power (1) and available heating power in the core plasma (3)

depend on heating or current driven method. We can express the current driven power as the function of (Φ_p, Q_{in}) by using some experiential formulae such as the ITER scaling law. The power required for LHCD is estimated by the following model[10]

$$P_{LHCD} = \frac{I_{CD} R \ln \Lambda}{0.122\, j^* / p^*} \frac{n_{20}}{T}. \tag{15}$$

So it can be written as

$$P_{LHCD} = \frac{I_{CD} R \ln \Lambda}{0.122\, j^* / p^*} C_n \Phi_p^{19/9} C_T^{-1} Q_{in}^{-14/9}. \tag{16}$$

Where j^* / p^* =15 is assumed in the present paper. Then, the available heating power is the following relationship,

$$P_{LHCD}(\Phi_p, Q_{in}) \le Q_{in}. \tag{17}$$

Employing the following conditions, $P_{LHCD}(\Phi_p, Q_{in}) \le P_{LHCD}^{\max}$, $P_{LHCD}(\Phi_p, Q_{in}) \le Q_{in} < P^{total}$, $q_{div}(\Phi_p, Q_{in}) \le q_{\max}$, and $Q_{in} \ge P_{thr}(\Phi_p, Q_{in})$. For HL-2A device, the LHCD power limit is $P_{LHCD}^{\max} = 2$ MW, the total heating power is set to be $P^{total} = 7.5$ MW, for the heat flux in the divertor range, it may be constraint by the material physical and chemical properties of the target plates so as the divertor target not to damage by the high heat load, Usually, the $q_{\max}$ is taken to be3.5MW$/m^2$, which corresponds to the averaged value estimated [11], the plasma current is $I_p = 0.45$ MA, major radius $R = 1.65$ m, minor radius $a = 0.40$ m. With these parameters and constraints, we can examination the basic feature of overall operation Using numerical methods.

We explore the possible trade-offs process in the (Φ_p, Q_{in}) space as shown in Fig.1 in the numerical methods. Each boundary is the operation condition as mentioned above. Fig.1 indicates that the upper boundary of Q_{in} is limited to 3.0-3.5 MW by $q_{div} \le 3.5$ MW$/m^2$.

So the heat flux in the divertor region is a key factor for the constraint of the upper boundary of Q_{in}. For the $Q_{in} \le 3.0$ MW, the boundary of $q_{div} \le 3.5$ MW$/m^2$ implies a decrease of q_{div} by the transition from low to high recycling state. The upper boundary of the particle Φ_p is dominated by the power balance for the low Q_{in} region, while it is limited by the available LHCD power for higher Q_{in}. From the analysis, we can reach a conclusion that the upper boundary of Φ_p is dominated by power balance constraint and LHCD power constraint, while the lower boundary of Φ_p is confined by divertor heat flux constraint. The available power for the LHCD tends to be a key parameter for extending the operation density of core plasma in this high regime. The painted is operational region constrained by basic trade-off conditions. In this exploration, no gas puffing is assumed. The sudden changes in the curve for the required LHCD power and the power balance are caused by the L-H transition.

3.2.Impurity seeding case

We investigate the effect of impurity seeding in the SOL-divertor region for the overall operation of tokamak plasma in the qualitative sense when the remaining parameters are kept the same values as those in Fig.1. The f_{imp} is given as the input parameter in the two-point model, and f_{imp} can be expressed as follows:

$$f_{imp} = \frac{2\pi R \Delta_E L_d f_C L(T_d) \sin\psi}{q_\perp S_p} n_d^2, \tag{18}$$

where f_C is the ratio of carbon impurity to the plasma density, and a constant cooling rate $L(T_d) = 1.0 \times 10^{-31}$ Wm^{-3} for carbon is applied. So the heat load on the target plates will be change with changes of f_{imp}. When the value of f_{imp} is taken as 0.3, 0.5, 0.6(similar to that of the ITER divertor design), we can clearly see that the heat load on the target plates is significantly inflected with the increase of f_{imp} as shown in Fig.2. , and the possible

operation region may be extend. From the physical sense, when increasing the impurity seeding in the SOL-divertor region, the particle fluxes coming from the SOL or the core will be more opportunities for collision with impurity, and the heat flux will be exchanged for impurity or scattering by impurity. So the same particle fluxes into the edge region will have smaller heat flux. Thus, the heat flux into the divertor region will be smaller, one have not to warry about the fault of divertor caused by the excessive heat load.

3.3.Gas puffing case

Based on the particle balance equation in the SOL and divertor regions as mentioned above, all neutral source rate at the edge region N_n including gas puff term N_{puff} is as Eq.(7). Some neutral particles ionize in the divertor region by the fraction of f_{ion}^{DIV}. Other neutral particles go into core, SOL, and pumping regions by the fraction of f_{ion}^{CORE}, f_{ion}^{SOL} and f_{ion}^{PUMP}, respectively. Fig.3 is the simple model of particle balance. Where $N_{\mathrm{n}}^{\mathrm{sol}}$ and $N_{\mathrm{n}}^{\mathrm{div}}$ was given above as $N_n^{SOL-DIV}$. Here , $N_{\mathrm{n}}^{\mathrm{core}}$ is ionization rate in the core region

$$N_{\mathrm{n}}^{\mathrm{core}} = f_{\mathrm{ion}}^{\mathrm{core}}\left(1 - f_{\mathrm{ion}}^{\mathrm{div}}\right) N_{\mathrm{n}} . \tag{19}$$

The ionization fraction in the core region is modeled by:

$$f_{\mathrm{ion}}^{\mathrm{core}} = \frac{A_{\mathrm{core}}}{A_{\mathrm{core}} + A_{\mathrm{sol}} + A_{\mathrm{pump}}} . \tag{20}$$

The pumping effect is defined by:

$$N_{\mathrm{n}}^{\mathrm{pump}} = f_{\mathrm{ion}}^{\mathrm{pump}}\left(1 - f_{\mathrm{ion}}^{\mathrm{div}}\right) N_{\mathrm{n}} . \tag{21}$$

With

$$f_{\mathrm{ion}}^{\mathrm{pump}} = \frac{A_{\mathrm{pump}}}{A_{\mathrm{core}} + A_{\mathrm{sol}} + A_{\mathrm{pump}}} \tag{22}$$

In view of particle balance, we consider the influence of the element of gas puffing for the operation region. the particle balance equation is an important factor in solving the two-point model, the gas puff term N_{puff} will affect the heat flux and particle fluxes in the edge region.

The three curves of figure4 correspond the N_{puff} as $0.5\times10^{21}s^{-1}$(which come up to 2.5% of the total neutral source rate N_n), $1.0\times10^{21}s^{-1}$, $1.5\times10^{21}s^{-1}$. We can see clearly that the operation region will be extended. When the particle flux is fuelled in the divertor region, the heat load that hit to the target decrease with increasing of gas puffing. For the energy of particle fluxes coming from the SOL or the core is absorbed partly by the puffing gas or the neutral gas hold up the particle fluxes, the average heat fluxes in edge region is weaken.

The heat flux and particle fluxes absorbed by divertor target will be drawn out by pumping finally. The speed of the pumping system (C_{pump}) may be one of the candidates for swaying the divertor temperature. When augment the speed of pumping, the impurity and particle will be reduction in the edge region, so that the particle fluxes coming from the SOL or the core are easier to reach the edge of the region without loss of energy. Obviously, the heat load arrived at divertor target will be larger. That is the operation region is reduced. We can see the effect of C_{pump} for the plasma operation in Fig.5(in which the N_{puff} is fixed as $1.0\times10^{21}s^{-1}$)intuitively: the heat load of divertor target is significant change with the raise of the speed of the pumping system when the particle fluxes are not large. So, we clearly to see that gas puffing is an effective method to extend the plasma operation. Maybe, we should reduce the speed of the pumping system for increasing the speed will compress the operation. Actually, it is qualitative analysis on the two factors.

3.4.Bootstrap current case

Taking the bootstrap current into account, the noninductive current may be obtained by

$$I_{CD} = I_p - I_{BS}, \tag{23}$$

where I_{BS} is plasma current. The bootstrap current size and distribution are strongly

dependent on the plasma density, temperature, and pressure. The empirical fit for bootstrap current is

$$I_{BS} = C_{bs}(\varepsilon^{1/2}\beta_{pa})I_p , \tag{24}$$

Where C_{bs} is constant, $\varepsilon = a/R$ and $\beta_{pa} \propto < p > / I_p^2$. $< p >$ is average plasma pressure, and $< p > \propto n_{20}T$, so we have

$$I_{BS} = C_m \Phi_p^{1/9} Q_{in}^{4/9} I_p . \tag{25}$$

C_m is defined as the coefficient of the bootstrap current, which is modifiable. Then, Eq.(16) and Eq.(17) should be modified, and we can write Eq.(16) as

$$\begin{aligned} P_{LHCD} &= \frac{R \ln \Lambda}{0.122\, j^* / p^*} C_n \Phi_p^{19/9} C_T^{-1} Q_{in}^{-14/9} (I_p - I_{BS}) \\ &= \frac{R \ln \Lambda}{0.122\, j^* / p^*} C_n \Phi_p^{19/9} C_T^{-1} Q_{in}^{-14/9} (I_p - C_m \Phi_p^{1/9} Q_{in}^{4/9} I_p) \end{aligned} \tag{26}$$

That is the change of bootstrap current will cause the alteration of available current drive power and available heating power in the core plasma.

The bootstrap current will be reduce the noninductive current fraction in the total plasma current such that the current drive power(P_{LHCD}) should be down for the I_{CD} is falling with the raising of I_{BS} . But the value of P_{LHCD} is fixed, so the particle fluxes will augment in the case of the same heating power. That is the equal heating power will accompany the larger particle fluxes in the core plasma. Figures 6~7 display this property by changing the bootstrap current coefficient C_m from 0.1 to 0.2. and contrasting to C_m =0, the particle fluxes Φ_p is gradually increasing with the accretion of $C_m = 0.2$. the bootstrap current I_{BS} is very close the plasma current When $C_m = 0.2$, we can see the growth trend of particle fluxes is more significant. In theory, Bootstrap current generation is due to the exiting of plasma density or

pressure gradients. When raising the proportion of bootstrap current, the imbalance of density and pressure of the plasma is more pronounced, so that there will be greater particle fluxes in the same heat power. From the mathematical point of view, the drive current decreases when the bootstrap current increases, so the smaller drive power is required. In fact, the drive power is unchanged. Thus, the particle fluxes Φ_p is increasing for the same heat fluxes when the bootstrap current increases. The dependence of core plasma operation on the change of the bootstrap current to the total plasma current have been made clear for the LHCD operation.

4. Summary

The basic features of integrated operational of tokamak plasma have been examined for the LHCD steadystate tokamak plasma operation including core and edge plasma in the phase space of the total particle flux and the total heat flux across the separatrix. The impact of different factors, which comprise impurity seeding, gas puffing and bootstrap current, for the constraint condition are investigated. The qualitatively properties of the impurity seeding and gas puffing for the heat flux in the divertor region is investigated. What is important, we have confirmed that the consistent operational of core and edge plasma have potential to be expanded by raising the bootstrap current fraction of the total plasma current and the increasing of the speed of the pumping system of a device may narrow the overall plasma operation for it can increase the heat flux that hitting into the divertor target. Of course, the relative parameters including coefficient C_{pump}, c_m must be certain by experiments in detail. We hope that these results can provide some basis for the next experiment and the future fusion device.

Acknowledgments

The authors gratefully acknowledge the support by the JSPS-China core-university program on Plasma and Nuclear Fusion.

References

[1] A. S. Kukushkin, H. D. pacher, G. W. Pacher et al, IAEA-CN77/CT/P-07, Proc. 19th IAEA Fusion Enery Conf. (Lyon, France, 2002).
[2] G.W. Pacher, H. D. Pacher, A. S. Kukushkin et al., Nucl. Fusion **43,** 188 (2003).
[3] R. Hiwatari, Y. Kuzuyama, A. Hatayama and el al, Contrib. Plasma Phys. **44**, 76(2004).
[4] R. Hiwatari, Y. Kuzuyama, A. Hatayama and el al, J. Nucl. Mater. **337-339**, 386(2005).
[5] R. Hiwatari, A. Hatayama, Zhu Sizheng and el al, Plasma Science & Technology 1, 110(2006).
[8] N. Hayashi, T. Takizuka, A. Hatayama, et al. J. Phys. Soc. Japan, 1997, 66:3815
[9] M. Sugihara, T. Amano, D. Boucher, et al. J. Nucl. Mater.,1997, 241-243:299-304
[6] N. Uckan, ITER Physics Group, 1990 ITER Physics Design Guidelines: 1989 ITER Documentation Series No. 10.
[7] K.Borrass, Nucl. Fusion, 1999, 31: 1035.
[10] S.Takamra, Plasma heating basis. Nagoya:university of nagoya press, 1986 (in japanese)
[11] S.Zhu, Contrib. Plasma Phy., 2000, 40:322.

低杂波电流驱动托卡马克等离子体整体操作性质的研究

摘要：我们利用CSD模型，在粒子流和热流的相空间，分析了低杂波电流驱动芯部和边缘托卡马克等离子体一致性操作的整体性质。文章给出了低杂波电流驱动托卡马克等离子体整体操作的基本特性，对这些特性做了数值的分析。同时，本文还审查了杂质辐射，在装置边缘区域喷入气体和自举电流对托卡马克等离子体一致性操作的影响，并做了相应的分析。结果显示，增加杂质辐射，在装置边缘区域喷入中性气体和增加芯部等离子体自举电流的比重都是改善托卡马克等离子体整体操作的有效方法。

关键词：操作性质，杂质辐射，喷气，自举电流

图表：

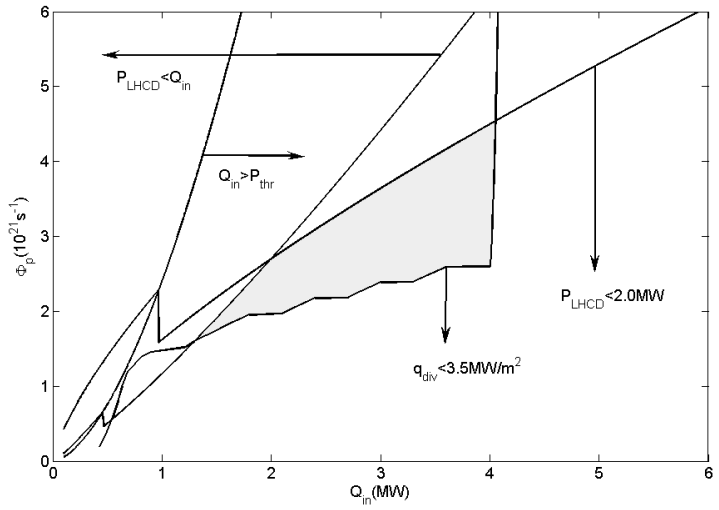

Figure1. Qualitative feature on overall operation of tokamak plasma.

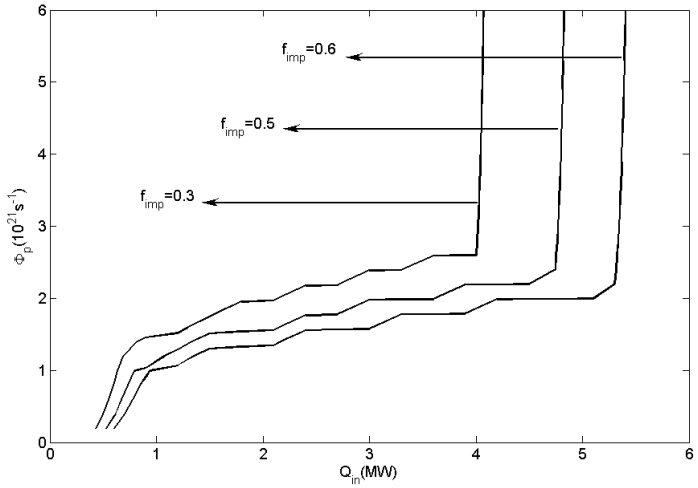

Figure2. The effect of impurity seeding on the tokamak plasma operation.

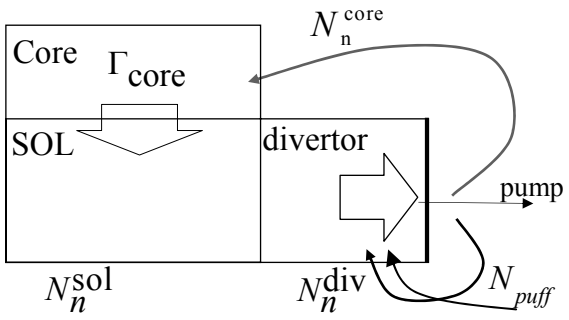

Figure3. A simple model of the steady state particle balance.

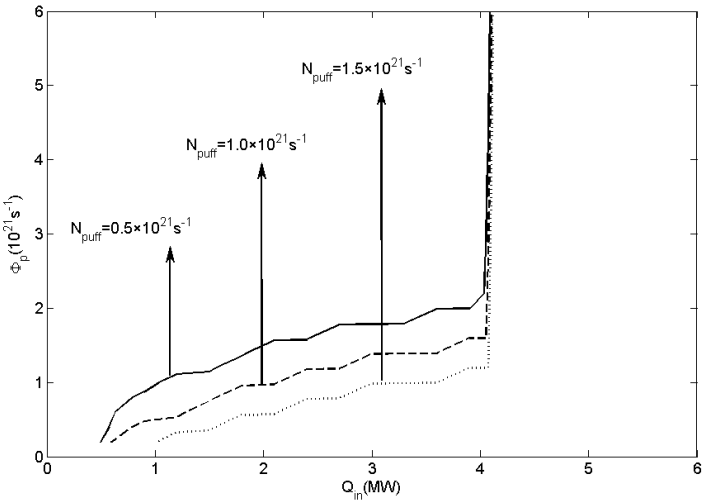

Figure4. The effect of gas puffing on the tokamak plasma operation.

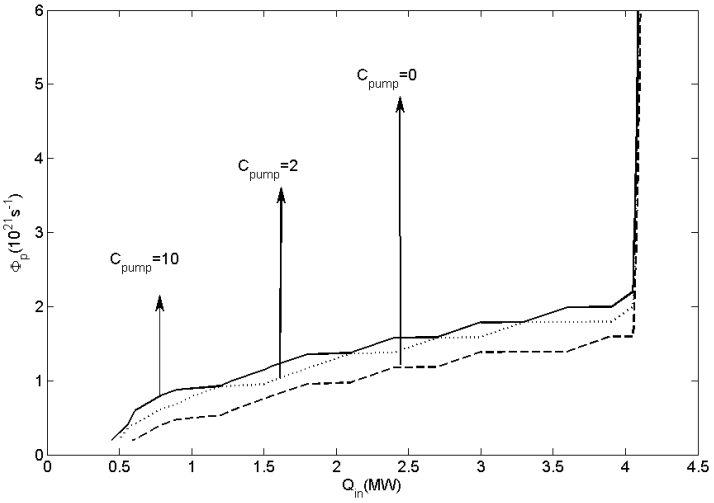

Figure5. The effect of the speed of the pumping system on heat flux in the edge region.

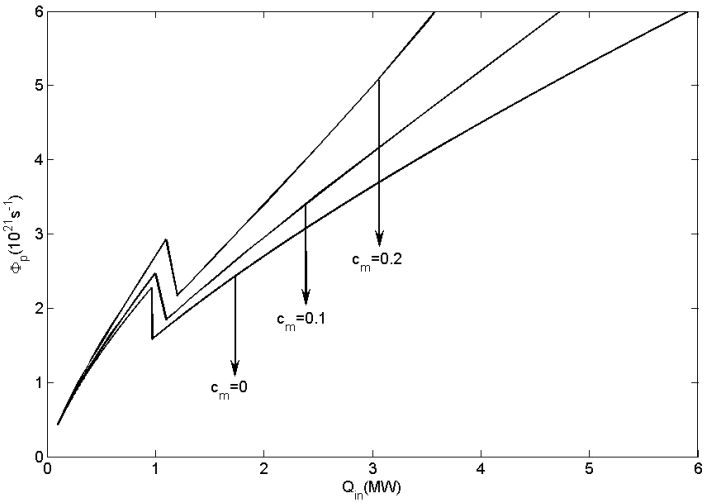

Figure6. The influence of raising the bootstrap current on current drive power.

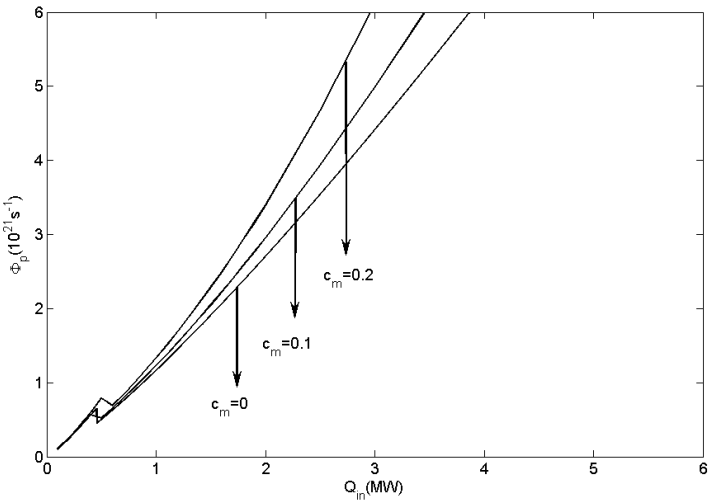

Figure7. The influence of raising the bootstrap current on available heating power

Sawtooth suppression by LHCD on HT-7 tokamak

Zixi LIU*, Xiang Gao, Yinxian Jie, Bojiang Ding, Yao Yang, HT-7 team and EAST team

Institute of Plasma Physics, Chinese Academy of Sciences,

P.O.Box 1126, Hefei, Anhui 230031, P.R.China

***E-mail**: zxliu316@ipp.ac.cn

Abstract

Sawtooth control by low hybrid wave current drive (LHCD) Experiments has been studied with a limiter configuration on HT-7 and with a double null configuration on Experimental Advanced Superconducting Tokamak (EAST). Sawtooth behavior diagnosed by soft X-ray has been observed. Simulation of LHCD power deposition has been studied using the ray tracing code. The sawtooth behavior in different plasma current on HT-7 has been studied. The critical power of LHCD for sawtooth stabilization and the power deposition of LHCD are different between the two tokamaks.

Keywords: LHCD, sawtooth

PACS: 52.50.Sw, 52.55.Fa

1. Introduction

A sawtooth crash triggered by NTMs is a violent event that about 15% of the stored energy leaves the plasma [1,2]. This energy loss is not vital to the first wall in the highβ ELMy H-mode discharge at present tokamaks, but it will become a crucial problem when it comes to the ITER which contains about 350MJ of stored plasma energy. Sawtooth control remains an important

unresolved issue for ITER operation.

The initial thoughts of sawtooth control contain five aspects: safe factor in the centre, localised current drive, heating deposition, rotation, shaping, Unbalanced passing fast ions, Trapped fast ions. Electron cyclotron current drive (ECCD) often controls the sawtooth by localized current drive. LHCD and ion cyclotron current drive (ICCD) often affect the central safe factor by changing the current profile. Neutral beam injection (NBI) usually can change the rotation, Unbalanced passing fast ions, Trapped fast ions.

Although there are mainly four ways to control the sawtooth oscillation, only two effective ways have been widely accept, which is ECCD and ICCD. Experiments on Tore Supra showed that ECCD can destabilize long sawteeth induced by core ICRF heating, when the deposition of ECCD is precisely inside the q = 1 surface [1]. JET experiment shows that ICRF power was launched with +90° phasing and a hydrogen minority cyclotron resonance close to the magnetic axis to establish fast-ion-induced long sawteeth. Thereafter, ICRF power with -90° phasing was applied for ICCD with a hydrogen minority cyclotron resonance close to the q = 1 surface on the high field side. A clear destabilization of the sawteeth occurred a short period after ICRF power for ICCD was turned on [2]. Through the experiments, it is observed that the deposition position of the wave is the most important fact to the sawtooth suppression.

Sawtooth suppression by LHCD was studied both on HT-7 and EAST recently. In this paper, the LHCD experiment in sawtooth control is summarized.

2. Experiment setup

The HT-7 superconducting tokamak has a major radius of R = 1.22 m and a minor radius of a = 0.27 m in the circular cross-section [3,4]. There are two layers of thick copper shells, and between them are located 24 superconducting coils which can create and maintain a toroidal magnetic field (Bt) of up to 2.5 T. The HT-7 tokamak with the limiter configuration is normally operated under the basic parameters: Ip = 100–170 kA, the toroidal magnetic field B_T = 1.8 T, the central line-averaged plasma density is 1.5×10^{19} m^{-3}, central electron temperature T_e = 0.5–1.0 keV. The plasma current, position and central line averaged electron density were feedback controlled during discharges. A stainless-steel liner was installed in the vacuum chamber at the radius of 0.32

m [4].

There are five soft X-ray arrays on the HT-7 machine as shown in Figure 1. The maximum sampling rate of the soft X-ray diagnostic system is 250 kHz, correspond to the temporal resolution is 4 μs. The spatial resolution is changed from 0.6 to 1.5 cm. This diagnostic equipment is used to analysis the radius of sawtooth reversal surface (r_s) and to generate tomographic reconstruction in the HT-7 tokamak. During the sawtooth suppression by LHCD experiments in this paper, the injected power of LHW is scanned from 100 kW to 500 kW with the same plasma current of Ip = 120 kA.

Experimental Advanced Superconducting Tokamak, as a full superconducting tokamak, is aimed at long pulse (60–1000 s) high performance operation. The device parameters includes a major radius of R = 1.75 m, minor radius of a = 0.4 m, aspect ratio of 4.25, an elongation range of 1.2–2, and multi-configurations of single null divertor, double-null divertor and circular configurations with a limiter. The main operational parameters used for EAST experiments are: an ohmic heated hydrogen discharge with plasma current Ip = 100–500 kA, a toroidal field of 2 T at R = 1.75 m, a line averaged density of 0.5–4 × 10^{19} m^{-3}, an edge value of safety factor of 2–10 [5].

The RF systems with maximum output powers of 1.5MW in the ion cyclotron resonant frequency range 30–110MHZ and 2MW in the lower hybrid frequency range at 2.45 GHz are available for heating and current drive, as well as wall conditioning and discharge pre-ionization. It consists of twenty klystron amplifiers, which can each deliver 100kW with CW capacity at 2.45 GHz. A multijunction coupler consists of 5 column×4 row main waveguides as shown in figure 2. Each main waveguide is split into eight sub-waveguides and powered by individual klystron amplifiers. The coupler can launch the LHCD power with parallel refractive index $N_{//}$ of 1.6–3.2 and typical FWHM of 0.2 at $N_{//}^{peak}$ = 2.3. The spectra of $N_{//}$ can be changed within a fast response time of 0.1 ms during one discharge, which provides a possible tool for the control of the plasma current density profile.

3. Sawtooth suppression by LHCD on HT-7

Figure 2 shows the sawtooth duration time with different LHW power from 100 kW to 500 kW with Ip=120kA. When the injected LHW power is increased, the sawtooth duration time is

postponed and increased. The critical power of LHCD for sawtooth stabilization is 450 kW on HT-7. In Tore Supra the critical LHW power is 1.8 MW [6]. Figure 3 shows the waveform of a sawtooth discharge with plasma current, loop voltage, average electron density, LHW power, the measured position of magnetic axis R(0), and the soft X-ray signal during the sawtooth discharge. The radius of the sawtooth reversal surface increased during the two discharges (r_s is from 6 to 9 cm in 107260). The magnetic axis R(0) calculated from the SXR is shifted to the low field side from the centre of device (R = 122cm).

Figure 4 shows the soft X-ray signal at different time. Figure 4(a) is before LHCD injects at time=0.48s~0.52s, and figure 4(b) is after LHCD injects at time=0.73s~0.77s. In figure 4 (a), strong sawtooth oscillation is observed with reverse surface (at R=-5.67cm and R=7.23cm). In figure 4 (b), all the signals become synchronous after time=0.76s, and reverse surface disappears. It indicates that the sawtooth is suppressed. The LHCD power is mainly deposited at the position around $\rho \approx 0.1$ at the discharge 107260 (using a ray tracing code [7]) as shown in figure 5. The dash line shows the q=1 reverse surface, so the deposition of LHCD is on-axis near the reverse surface.

Sawtooth suppression experiment is carried out by LHCD with Ip=120kA, but it can not be suppressed with Ip=170kA using the same LHCD power. Figure 5 shows the peaking factor of hard X-ray (HXR) profile for different LHW power with two different plasma current discharges (Ip=120 kA and Ip=170 kA) on the HT-7 tokamak. It is observed that hard X-ray profile with the low Ip is more peeking than with the high Ip. It implies that the deposition of LHW with the lower Ip is more close to the magnetic axis on HT-7.

4. Sawtooth suppression by LHCD on EAST

Same experiment has also studied on EAST tokamak with Ip=250kA. Figure 7 shows the sawtooth duration time with different LHW power from 100 kW to 250 kW, and critical power of LHCD for sawtooth stabilization is 250kW. Figure 8 shows the waveform of a sawtooth discharge with plasma current, loop voltage, average electron density, LHW power, and the sawtooth period diagnosed by soft X-ray signal during the sawtooth discharge. Figure 9 shows the soft X-ray signal at different time. Figure 9 (a) is time=3s~3.2s, and figure 9 (b) is at time=5s~5.2s. In figure 4(a), strong sawtooth oscillation is observed. In figure 4 (b), no sawtooth is found. The LHCD

power is mainly deposited at the position around $\rho \approx 0.5$ at the discharge 11830 as shown in figure 10. The dash line shows the q=1 reverse surface, so the deposition of LHCD is off-axis far away from the reverse surface. The configuration of the discharge is double null as shown on the right side of figure 10.

5. Summary

Sawtooth suppression experiment is carried out by LHCD with Ip=120kA in the HT-7 tokamak, but sawtooth can not be suppressed with Ip=170kA using the same LHCD power. Experiment trying to enhance the LHCD power with Ip=170kA has been taken, but the strong LHW reflection appeared when the LHCD power was upon 450kW. The LHCD deposition of the Ip=120kA discharge might be closer to the magnetic axis than the Ip=170kA discharge, so the profile of the current driven by the LHCD would be different during the two discharge. It might be the reason of the different sawtooth behavior.

The critical power of LHCD for sawtooth stabilization for HT-7 is 450kW with Ip=120kA while the critical power of LHCD for EAST is 250kW with Ip=250kA. From the simulation, the power deposition of LHCD on HT-7 tokamak is on-axis (near the reverse surface) and the power deposition of LHCD on EAST tokamak is off-axis (far away from the reverse surface). Changing the magnetic shear by the localised current drive by LHCD might be the reason of the sawtooth stabilization on HT-7 tokamak. The current profile broadening which make the central safe factor above zero has been clearly proved to be the reason of the sawtooth stabilization on EAST tokamak. The difference of the configuration between HT-7 and EAST might be another key to the reason of the different critical powers.

Acknowledgments

This work was partially supported by the JSPS-CAS Core-University program in the field of 'Plasma and Nuclear Fusion'. This paper has been supported by National Magnetic Confinement Fusion Science Program (Code number 2010GB106000, and 2010GB106001). This work was funded by National Nature Science Foundation of China with contract No: 10721505.

References

[1] M.Lennholm et al., Phys. Rev. Lett. 102, 115004 (2009)

[2] M.J.Mantsinen et al., AIP Conf. Proc. Volume 933, pp. 35-42(2007)

[3] G.L.Kuang et al., Nucl. Fusion 39, 1769 (1999)

[4] X.Gao, Plasma Phys. Control. Fusion 50, 035006 (2008)

[5] Baonian Wan et al Nucl. Fusion 49, 104011 (2009)

[6] D.Moreau et al., Plasma Phys. Control. Fusion 33, 1621 (1991)

[7] Bojiang Ding, Guangli Kuang, Jiafang Shan, et al Plasma Phys. Control. Fusion 43, 558 (2003)

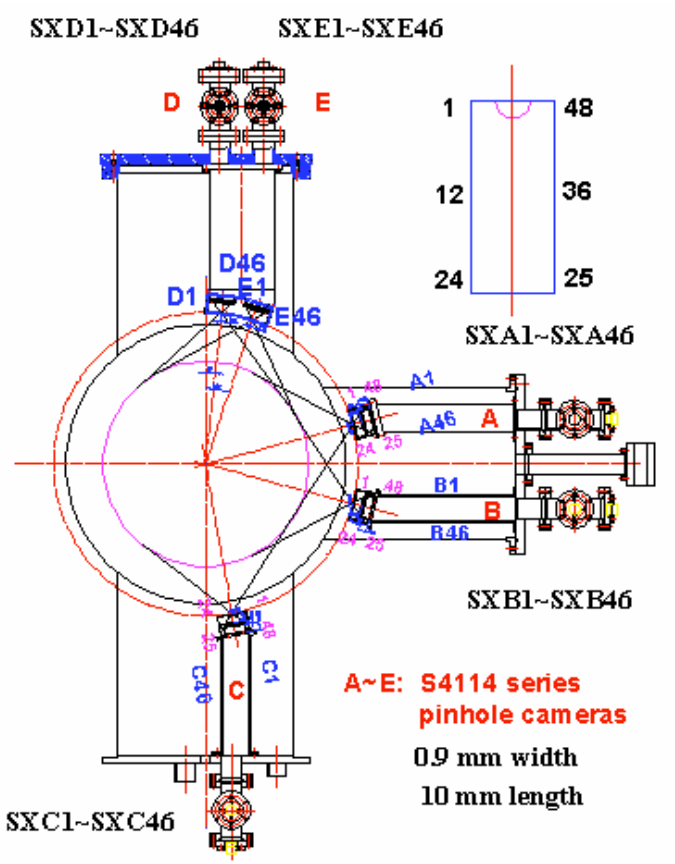

Fig.1 The soft X-ray diagnostic system on HT-7 tokamak.

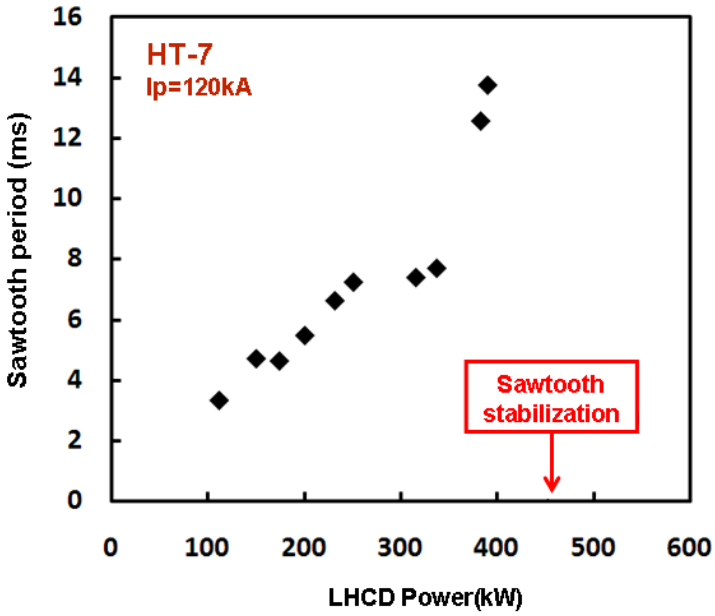

Fig.2 The sawtooth period with different LHCD power from 100 kW to 500 kW, and the sawtooth is stabilized at P_{LHW} = 450 kW on HT-7 tokamak.

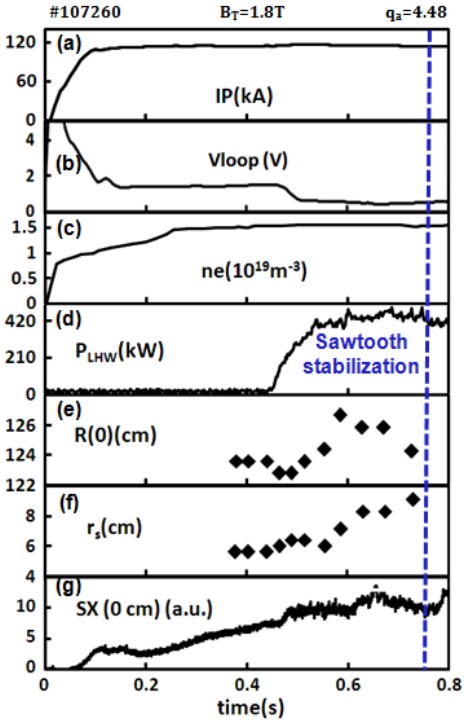

Fig.3 Waveform of a sawtooth suppression discharge with plasma current, loop voltage, average electron density, LHW power, the measured position of magnetic axis R(0) during the sawtooth discharge, and the soft X-ray signal on HT-7 tokamak

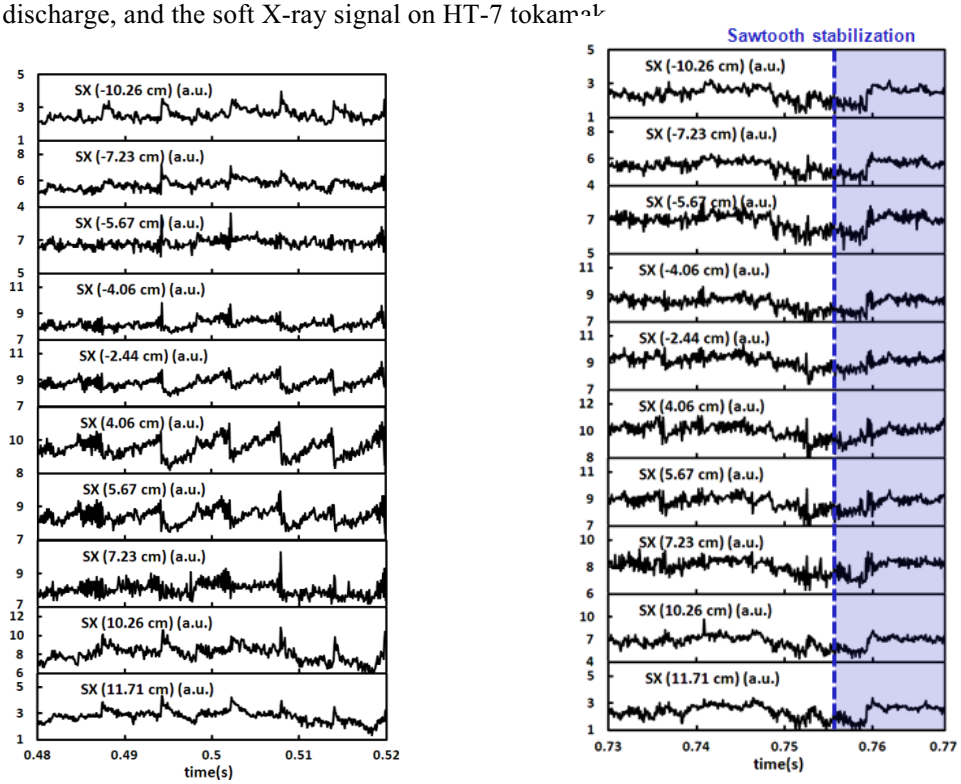

(a) (b)

Fig.4 Soft X-ray signal, (a) is at time=0.48s~0.52s, and (b) is at time=0.73s~0.77s on HT-7 tokamak

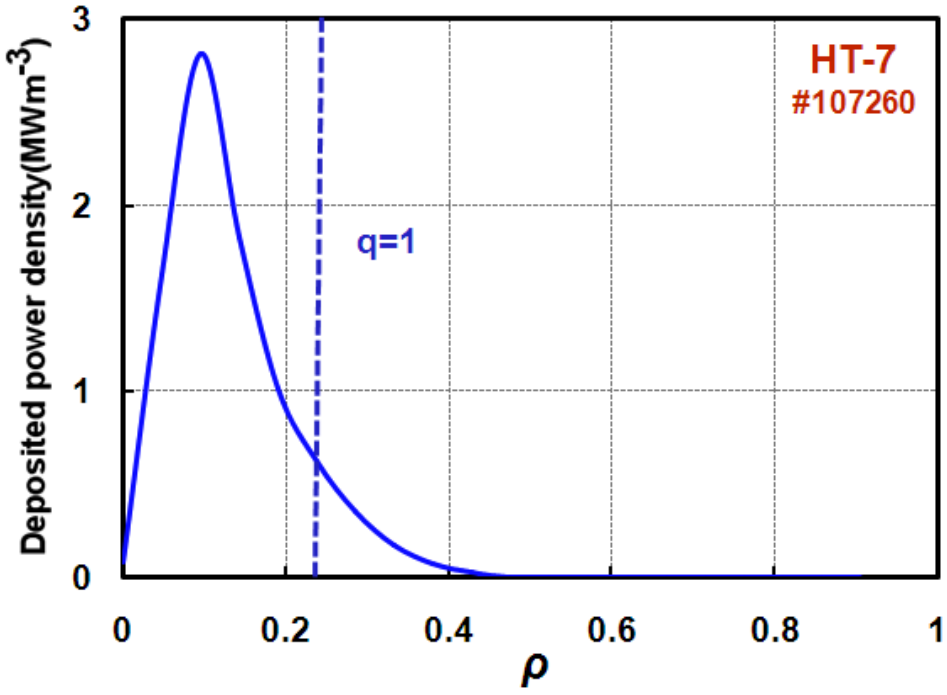

Fig.5 The power deposition of LHCD in discharge 107260, and the deposition is inside the q=1 surface on HT-7 tokamak.

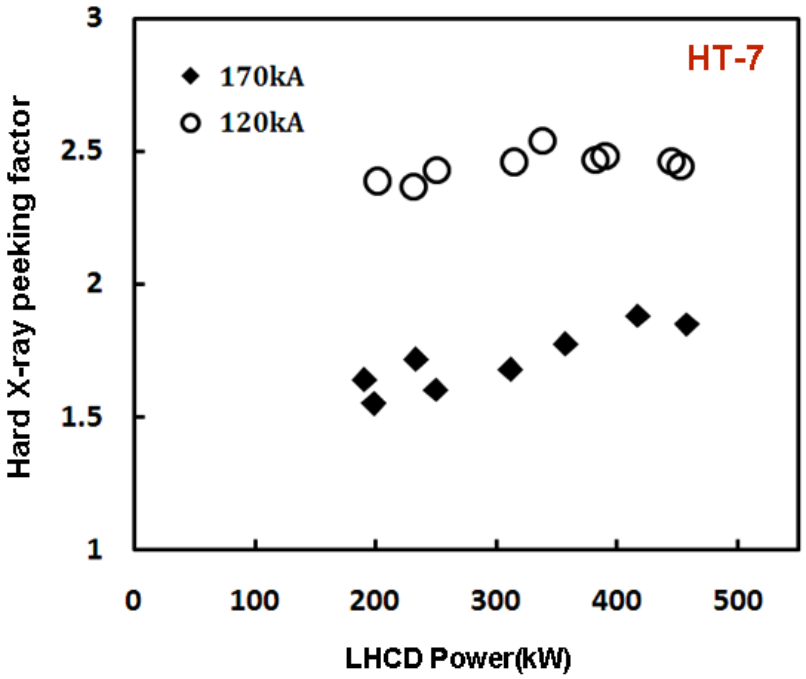

Fig.6 The hard X-ray peeking factor in two teams of discharges which have different Ip (120kA and 170kA) on HT-7 tokamak.

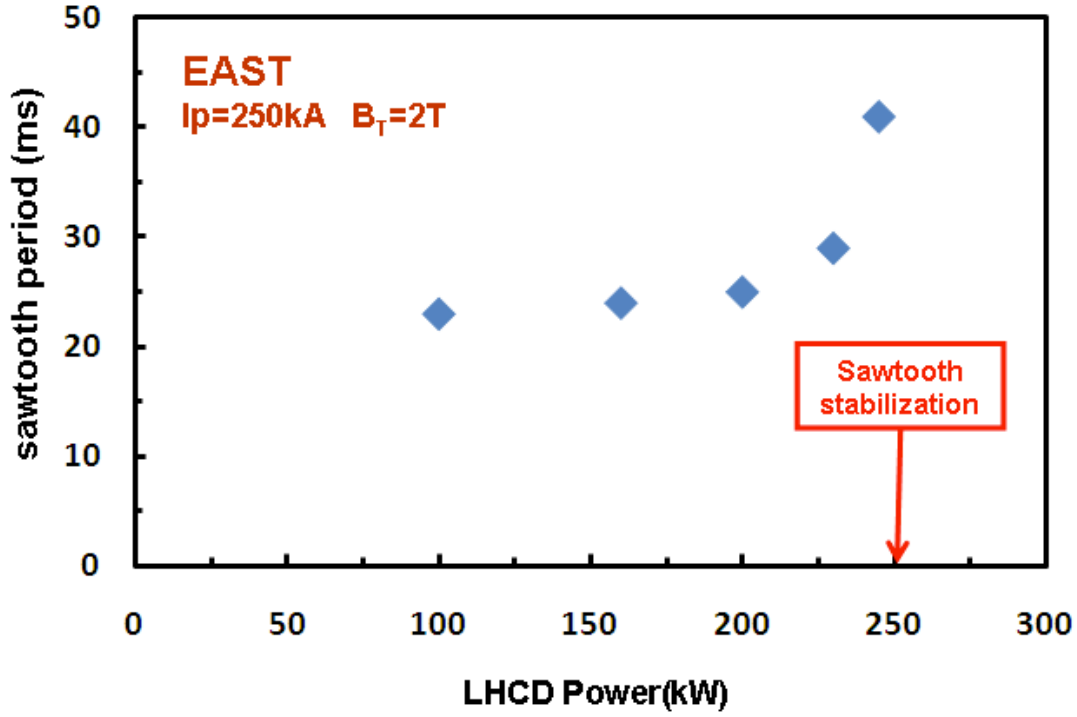

Fig.7 The sawtooth period with different LHCD power from 100 kW to 250 kW, and the sawtooth is stabilized at P_{LHW} = 250 kW on EAST tokamak.

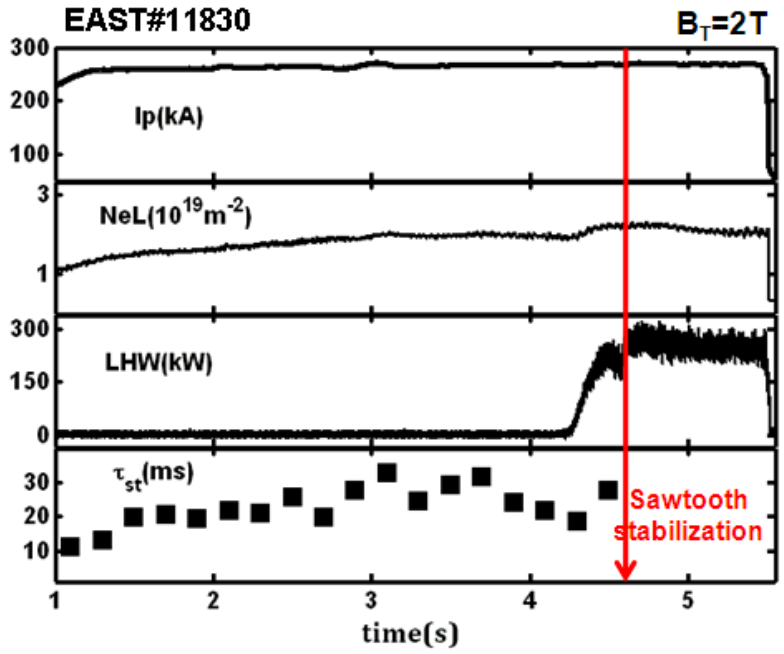

Fig.8 Waveform of a sawtooth suppression discharge with plasma current, loop voltage, average electron density, LHW power, and the sawtooth period on EAST tokamak.

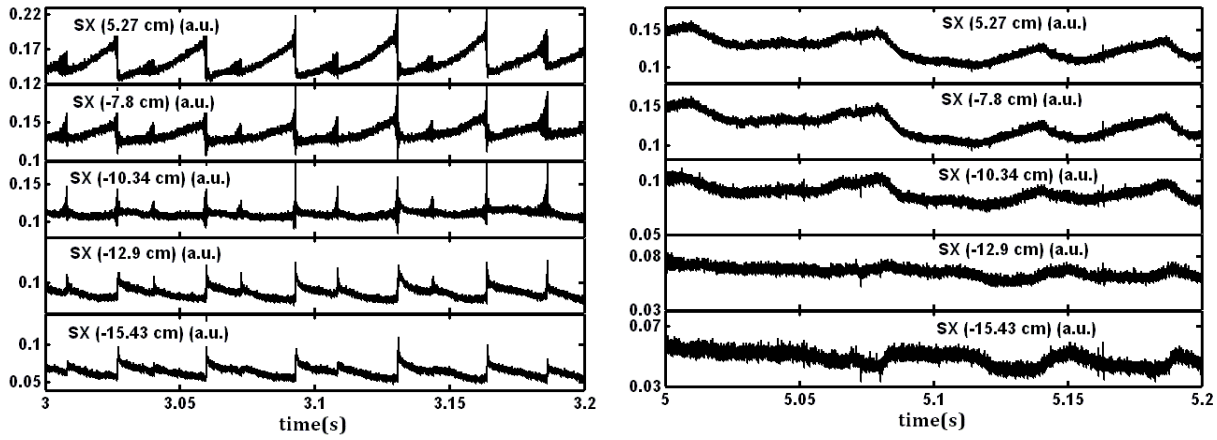

(a) (b)

Fig.9 Soft X-ray signal. (a) is at time=3s~3.2s, and (b) is at time=5s~5.2s on EAST tokamak.

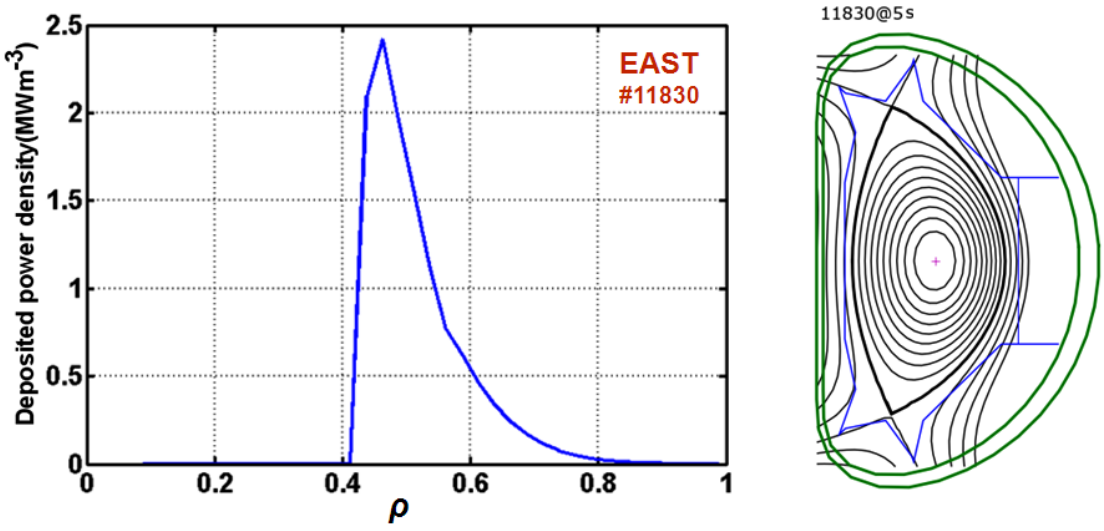

Fig.10 The power deposition of LHCD in discharge 11830, and the deposition is outside the q=1 surface on EAST tokamak.

Suppression of runaway electrons during disruption in HT-7

LIN Shiyao (林士耀), WAN Baonian (万宝年), HU Liqun (胡立群), LU Hongwei (卢洪伟),

ZHANG Jizong (张继宗), MHD&Disruption group

Institute of Plasma Physics, Chinese Academy of Sciences, Hefei 230031, China

E-mail of corresponding author: linsy@ipp.ac.cn

Abstract: One of the important problems of a large tokamak such as ITER is the disruption generated runaway electrons, which impinge the plasma facing components (PFC) and damage them. The experiments for mitigating and avoiding the current quench and runaway electrons during disruption have been carried out in HT-7 by lower hybrid wave (LHW), massive gas injection and magnetic perturbation. The plasma current quenching time is typically 1~2ms for a major disruption in HT-7. When LHW was injected, the post-disruption current with a plateau can be sustained up to a soft termination of discharge. Current carried by LHCD driven electrons plays an important role in this operation scenario. Another way tried in HT-7 to suppress runaway electrons generated during major disruption is by magnetic oscillations. Radiation of runaway electrons nearly disappeared when strong magnetic oscillations exist. It seems to be the most effective way to suppress runaway electrons in HT-7.

Keywords: tokamak, runaway electron, LHW, magnetic oscillation

PACS: 52.55Fa, 52.50Sw, 52.30Cv

1. Introduction

One of the outstanding problems of a large tokamak such as ITER is the possible damage caused by disruption generated runaway electrons. [1,2]. The electric field in the current quench could generate runaway currents of several mega-amps with runaway energies that are predicted to be as high as several tens Mev. [3]. Intense runaway electrons with high energies of several tens of MeV generated at a major disruption would significantly reduce the lifetime of the first wall [4]. In consequence, there is a great concern about the damage that these energetic runaway electrons might cause if they impact on the first wall structures, which might be critical for larger devices such as the ITER tokamak [5]. In spite of the fact that considerable progress has been made in recent experiments based on massive gas jets and pellet injection ([6,7]) the problem of runaway suppression is still considered to be one of the primary task for a reliable tokamak operation[8]. The experiments for mitigating and avoiding the current quench by LHCD and ECRH have been

carried out [5,9, 10]. In these experiments, runaway electrons can also be generated. The experiments for mitigating the current quench and suppressing runaway electrons simultaneously should be further carried out to enhance reliability of a tokamak safe operation.

The experiments for mitigating disruption generated runaway electrons have been carried out in HT-7 by LHW, massive gas injection and magnetic perturbation.

The observations and interpretations of the production and loss of the runaways during disruptions in HT-7 Tokamak are investigated in this paper. This paper is organized as follows. In section 2, the experimental set-up is introduced. Disruption in LHCD plasmas is presented in section 3. The mitigation of runaway electrons with gas puffing in LHCD plasmas is presented in section 4. In section5, the mitigation of runaway electrons with strong magnetic oscillations in LHCD plasmas is presented. Finally, conclusions are presented in section 6.

2. Experimental set-up

HT-7 is a medium-sized tokamak with superconducting toroidal coils and water-cooled graphite limiters. The machine runs normally with plasma current I_p=100-250kA, the toroidal magnetic field B_T=1.5-2T, the central line-averaged plasma density n_e =(1-4)×$10^{19}m^{-3}$, major radius R=122cm, minor radius a=27cm, central electron temperature T_e=0.5-3.0keV, central ion temperature T_i =0.3-1.5keV, with circular cross section [11]. The plasma current, position and central line-averaged electron density were feedback controlled during discharges. A lower hybrid wave (LHW) power up to 1.2MW at 2.45GHz is available in the HT-7 tokamak. LHCD was used not only for sustaining the plasma discharges but also for current density profile control.

The high energy hard X-ray diagnostics and fast electron bremsstrahlung (FEB) diagnostics [12] have been used as the main tool to investigate the behavior of runaway electrons. The high energy hard X-ray emission in the energy of 1.0-10.0MeV was detected by the NaI scintillator detectors. It provides the considerable information on the hard X-ray emission resulting from the thick target bremsstrahlung when runaway electrons are lost from the plasma and impinge on the vessel walls or plasma facing components. The hard X-ray in the energy of 30-300kev was measured FEBwith the CdTe detectors array. It provides considerable information on the LHW power deposition profile and the spatial and velocity distribution of the fast electrons. It also provides information on runaway electrons inside of the plasmas. Based on the above diagnostics, phenomena of runaway electrons during disruptions of discharges in HT-7 were studied.

3. Current quench in LHCD plasmas

HT-7 is a medium-sized tokamak, usually the plasma current quenched rapidly during current quench phase. Current plateau can not be sustained and nearly no runaway electrons can be detected. To study disruption generated runaway electrons in HT-7, we tried to inject LHW before disruption.

A typical LHCD discharge is shown in figure 1. I_p is plasma current, V_{loop} is the parallel loop voltage, n_e is line-averaged electron density, P_{LHW} is the power of LHW, Ra is the intensity of high energy hard X-ray, and HX is the intensity of FEB. The plasma current was 120kA, the line-averaged density n_e was $0.9\times10^{19}m^{-3}$; 400kW LHW was launched into the plasma.

The plasma current quenching time is typically 1~2ms for a major disruption in HT-7 ohmic discharges. When LHW was injected, the post-disruption current with a plateau can be sustained up to a soft termination of discharge. As shown in Figure 1, the loop voltage was not significantly increased during application of LHW, which leads runaway electrons with limited energy indicated by low radiation level of high energy hard X-ray. Current carried by LHCD driven fast electrons plays an important role in this operation scenario.

4. Mitigation of runaway electrons with gas puffing in LHCD plasmas

Above experiments shows clearly that LHCD can be used to mitigate the current quench of a disruption, but runaway electrons were still generated, although the energy of runaway electrons is not so high. Furthermore, to suppress runaway electrons, massive deuterium is injected into plasma together with injection of LHW in HT-7, as shown in Figure 2. Gas is the signal of gas puff. The plasma current was 120kA, the line-averaged density n_e was $0.9\times10^{19}m^{-3}$, the power of LHW was 300kW.

In the shot 89680, massive deuterium was injected into plasma together with LHW during disruption phase. The post-disruption current with a plateau can be sustained and the loop voltage was not significantly increased. The plasma density is significantly increases with gas puff during the post-disruption current plateau. The amount of runaway electrons in this scenario is reduced compared to the discharge without gas injection after major disruption. Furthermore, large increase of plasma density during disruption can lower the plasmas temperature and thus mitigate effects of thermal damage.

5. Mitigation of runaway electrons with strong magnetic oscillations in LHCD plasmas

LHCD can be used to mitigate the current quench of a disruption, but runaway electrons were still generated. Another way to suppress runaway electrons generated during major disruption is by magnetic oscillations. It has been tried in HT-7 shown in Figure 3. I_p is plasma current, V_{loop} is the parallel loop voltage, n_e is line-averaged electron density, P_{LHW} is the power of LHW, Ra is the intensity of high energy hard X-ray, HX is the intensity of FEB, and dB/dt is the intensity of magnetic oscillation.. The plasma current was 120kA, the line-averaged density $n_e=0.9\times10^{19}m^{-3}$, the power of LHW was 250kW.

In the shot 89720, radiation of runaway electrons nearly disappeared when strong magnetic oscillations exist, and the post-disruption current with a plateau can be sustained up to a soft termination of discharge. It seems to be the most effective way to suppress runaway electrons in HT-7.

6. Conclusions

The experiments for mitigating and avoiding the current quench have been carried out in HT-7 by LHW, massive gas injection and strong magnetic oscillation.

When LHW was injected, the post-disruption current with a plateau can be sustained up to a soft termination of discharge. Current carried by LHCD driven electrons plays an important role in this operation scenario.

To suppress runaway electrons, massive deuterium is injected into plasma together with injection of LHW in HT-7. The plasma density is significantly increases with gas puff during the post-disruption current plateau. The amount of runaway electrons in this scenario is reduced compared to the discharge without gas injection after major disruption.

Another way to suppress runaway electrons generated during major disruption is by magnetic oscillations. Radiation of runaway electrons nearly disappeared when strong magnetic oscillations exist. It seems to be the most effective way to suppress runaway electrons in HT-7.

The underlying physical mechanisms from these experiments is being analyzed and discussed in detail. These techniques for suppressing runaway electrons during major disruptions will be further verified in EAST, which is equipped with more diagnostics and has more capability for these investigations. This work was partially supported by the JSPS-CAS Core-University program in the field of‘Plasma and Nuclear Fusion’. This paper has been supported by National Magnetic Confinement Fusion Science Program (Code number 2010GB106000, and

2010GB106004).

References

[1] R. Jaspers, et al, study of disruption generated runaway electrons in TEXTOR-94., 25thEPS Conference on Plasma Phys. (1998). http://www.ipp.ac.cn/gjhy/EPS/25th(1998)/WEB/98ICPP_W/B068PR.PDF

[2] Y. Kawano, et al, 32nd EPS Conference on Plasma Phys. Tarragona, 27 June - 1 July ECA Vol.29C (2005) P-2.068

[3] R. Jaspers, et al, Nucl. Fusion **36** (1996) 367

[4] R.Yoshino, et al Nuclear Fusion **40** (2000) 1293.

[5] J.R. Martin-Solis, et al, Phys.Rev.Lett. **97** (2006) 165002

[6] ITER Physics Expert Group on Disruptions, Plasma Control and MHD, ITER Physics Basis Nucl. Fusion **39** (1999) 2251

[7] V.V. Plyusnin, et al Nucl. Fusion **46** (2006) 277

[8] P.V. Savrukhin, Plasma Phys. Control. Fusion **48** (2006) B201–B210

[9] R.D. Gill,et al, Nucl. Fusion **42** (2002)1039

[10] R. Yoshino, et al, Nucl. Fusion **39** (1999)151

[11] W. Baonian, et al, Phys. Plasma **11** (2003) 2543

[12] Lin shiyao, et al, Plasma Science & Technology **8** (2006) 261

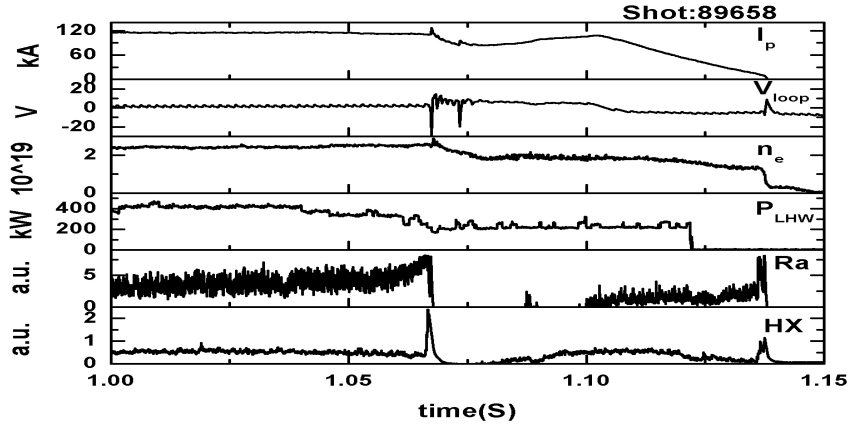

Figure 1. LHW injected into plasma during major disruption

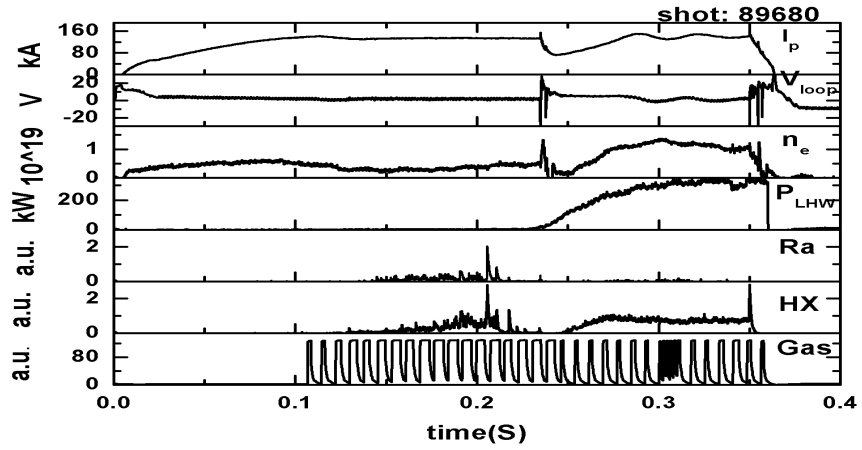

Figure 2. Gas puffing together with LHW during major disruption

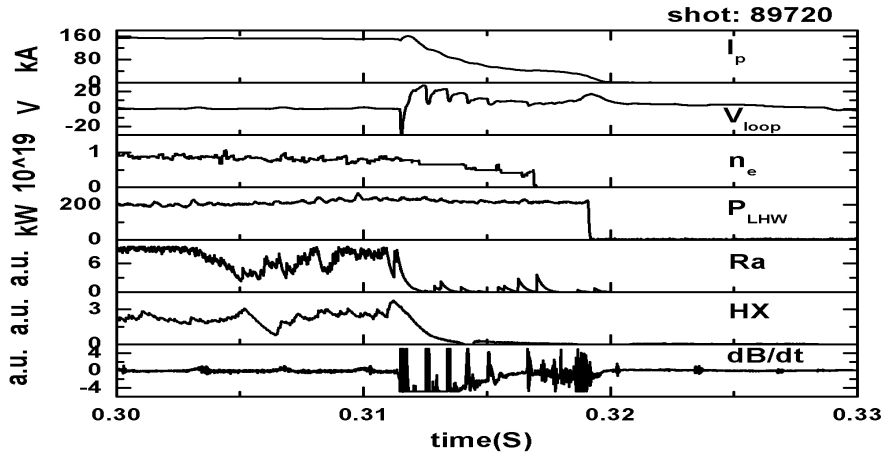

Figure 3. Strong magnetic oscillations kill runaway electrons

This paper has been supported by National Magnetic Confinement Fusion Science Program (2010GB106000&2010GB106004), National Natural Science Foundation of China (No. 10775041).

Turbulence and Zonal Flow Study in Edge Plasmas of HL-2ATokamak

K. J. Zhao [1], J. Q. Dong [1,2], L. W. Yan [1], W. Y. Hong [1], A. Fujisawa [3], Q. Li [1], J. Qian [1], J. Cheng [1], T. Lan [4], A. D. Liu [4], H. L. Zhao [4], D. F. Kong [4], Y. Huang [1], Yi Liu [1], X. M. Song [1], Q. W. Yang [1], X. T. Ding [1], X. R. Duan [1] and Yong Liu [1]

[1]Southwestern Institute of physics, P. O. Box 432, Chengdu, China
[2]Institute for Fusion Theory and Simulation, Zhejiang University, Hangzhou, China
[3]Research Institute for Applied Mechanics Kyushu University 6-1 Kasuga-kouen, Kasuga, 816-8580, Japan
[4]Department of Modern Physics, University of Science and Technology of China, Hefei, China

Correspondent author email: kjzhao@swip.ac.cn

Measurements with a toroidally and poloidally displaced three dimensional set of Langmuir probe arrays have revealed details of turbulence, geodesic acoustic modes (GAMs), zonal lows and their interactions in edge region of HL-2A tokamak plasmas. The coexistence of intensive low frequency zonal flows (LFZFs) of f< 4 kHz and the GAMs of 7 kHz<f_{GAM}<20 kHz has been unambiguously demonstrated. The poloidal and toroidal symmetries of the flows, including the GAMs, are verified experimentally. In particular, the coherency of the flows over a large toroidal scale of 2100 mm at a magnetic flux surface is emphasized. The LFZF packets are shown to propagate outwards and inwards as equally likely events, whereas predominantly outward propagation of the GAM packets is analyzed. The nonlinear three wave coupling of the flows with the ambient turbulence (AT) is shown with bicoherency analysis and envelope modulation of the latter by the former. The intensity of the LFZFs is observed to increase and decrease with increases of ECRH power (~ 300-700 kW) and safety factor q ~(3.5-6.2), respectively, whereas the intensity of the GAMs increases with increases of both ECRH power and q.

The coexistence of intensive LFZF and GAM were observed, and the radial wave numbers demonstrated the linear dispersion relation. LFZF intensity sharply goes up ~ 2.5 cm inside the LCFS, GAM has a maximum in the region of ~1-2 cm inside the LCFS. GAMs modulate AT dominantly near the LCFS. Both LFZF and GAM modulate AT in deeper plasma.

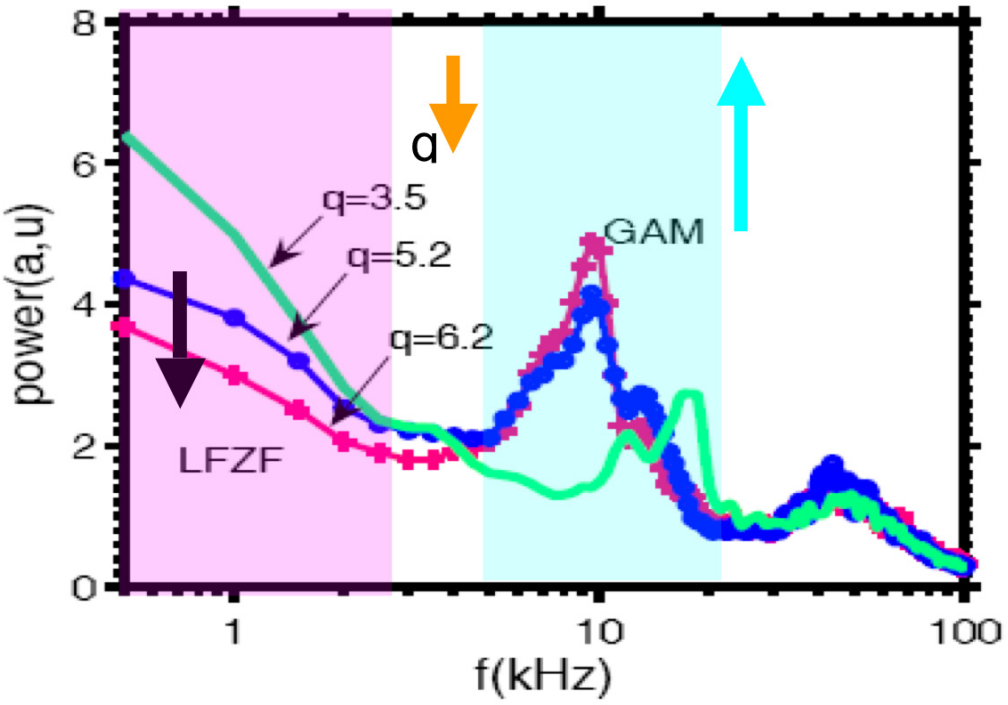

Fig.1 Dependence of LFZF and GAM intensity on edge safety factor

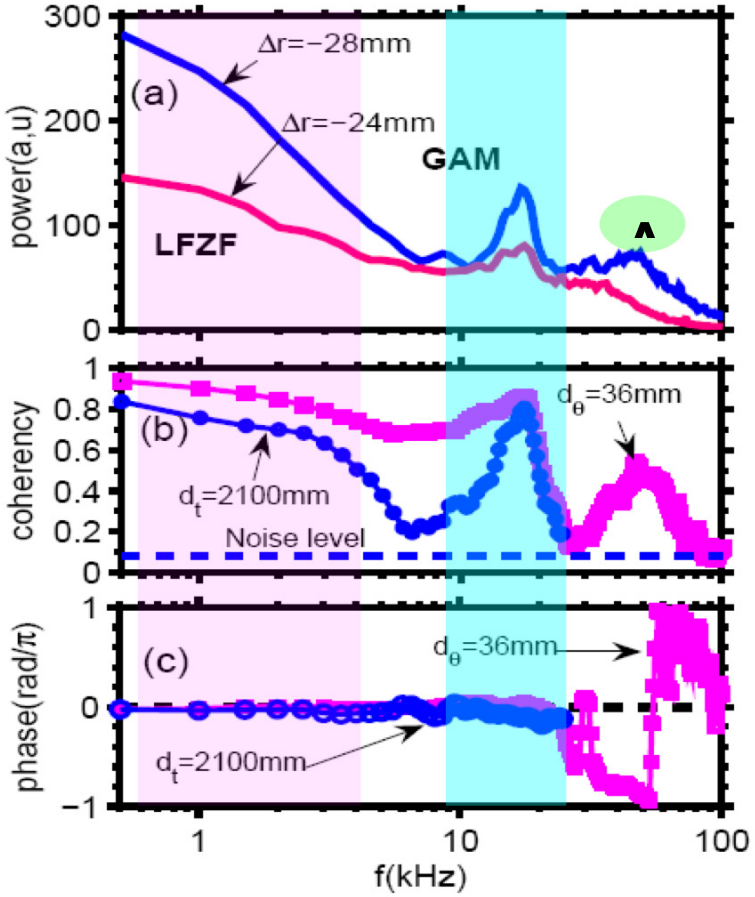

Fig.2 Coexistence of intensive LFZFs and GAMs

The intensity of LFZF/GAM decreases/increases with edge safety factor increase. The intensity of LFZF and GAM increases with ECRH power. The toroidal coherency of LFZF and GAM increases with ECRH power.

This work was partially supported by the JSPS-CAS Core-University program in the field of 'Plasma and Nuclear Fusion'.

Gyro-kinetic linear response function for zonal flows

T.Watari and Y.Hamada
National Institute for Fusion Science
e-mail:" watari.tetsuo@toki-fs.jp"

Abstract
A linear response function for zonal flows is obtained solving the gyro-kinetic equation. This is an extension of the previous work which adopted the method of "integrating along particle orbit" to solve the drift kinetic equation. The formula derived in this paper is used to calculate the dispersion relation of geodesic acoustic mode, which is compared with that of the gyro-kinetic analytic formula

I. Introduction

Zonal flows are important players determining the level of turbulence and anomalous transport and, therefore, many papers are dedicated to this subject: The high-frequency part of zonal flow is referred to as GAM (geodesic acoustic mode) and the steady-flow part is referred to as RZF (residual zonal flow). The presence of GAM oscillation was theoretically predicted in the early work by Winsor et al [1] based on the MHD (magneto-hydro dynamic) equation. Novakovskii [2] and Lebedev [3] introduced kinetic effects by using the DKE (drift kinetic equation). In these works, the dispersion relation was obtained in the form of $DI(\omega)=\omega^2-\omega_G^2(T_i(r),T_e(r),q(r))=0$. Therefore, a frequency of GAM oscillation is determined for each flux surface with given local temperatures, $T_e(r)$ and $T_i(r)$ .With such theoretical background, various aspects of GAM were studied: In reference [4], matrices were first introduced in the formulation suggesting the shape effect of GAM in tokamaks and possible existence of GAM in helical systems. It was also suggested that the GAM damping is lowered when the ratio Ti/Te is small. This prediction changed the prevailing common understanding that GAM is observed only in the large minor radius area where the safety factor q is large. Ref [5] pointed out the possible existence of another branch of GAM in the lower frequency range.

A notable step was made in independent works by Sugama [6], Gao [7], Watari [8], and Zonca[9], when the dispersion relation was solved in second order in $k_\perp\rho_i$,i.e., $DII(\omega)=a(\omega)+b(\omega)(k_\perp\rho_i)^2=0$: the Gyro-kinetic equation (GKE) was solved analytically in Ref.[6], Ref.[7] and Ref.[9]. The Drift kinetic equation (GKE) was used in Ref.[8] by adopting the method of IAPO (integrating along particle orbit).

In this paper, we apply this new method to GKE and address the difference between

GKE and DKE.

II. Formulation

We start with the standard form of the GKE (Gyro-Kinetic Equation):

$$(\frac{\partial}{\partial t}+\upsilon_{\parallel}\vec{b}\cdot\vec{\nabla}+\vec{\upsilon}_d\cdot\vec{\nabla})g_k=-i\omega\frac{e\phi}{T}F_0J_0(k_\perp\rho_i) \quad (1)$$

with an assumed wave form $\phi=\phi_k e^{ik_\psi\psi+il\theta-i\omega t}$. Equation (1) is associated with the following formula relating the distribution function to density perturbation:

$$\delta n_k=\int d^3\upsilon(J_0(k_\perp\rho_i)g_k-\frac{e\phi_k}{T}F_0(\vec{\upsilon})) \quad (2)$$

Equations (1) and (2) reduce to the DKE when $J_0(k_\perp\rho)$ is replaced by unity.

$$(\frac{\partial}{\partial t}+\upsilon_{\parallel}\vec{b}\cdot\vec{\nabla}+\vec{\upsilon}_d\cdot\vec{\nabla})f_k=-i\omega\frac{e\phi}{T}F_0 \quad (3)$$

The density perturbation is then calculated by

$$\delta n_k=\int d^3\upsilon(f_k+f_c) \quad (4)$$

with the classical polarization f_c defined by

$$f_c=(J_0^2(k_\perp\rho_i)-1)\frac{e\phi}{T}F_0 \quad (5)$$

Applying the method IAPO to the GKE, we calculate the distribution function with the following formula:

$$f_k=-F_0\frac{e\phi_k}{T}e^{ik_\psi\psi+il\theta-i\omega t}-i\omega\frac{e\phi_k}{T}e^{ik_\psi\psi-i\omega t}\int_{-\infty}^{t}F_0J_0(\mu,w,B(\vec{r}'))e^{ik_\psi(\psi'-\psi)+il\theta'-i\omega(t'-t)}dt' \quad (6)$$

Since the particle orbits have periodic nature, we consider a temporal Fourier expansion of integrand:

$$FT_m[g(t')]=\frac{1}{\tau_b}\int_{t-\tau_b}^{t}g(t')e^{im\omega_b t'}dt'=\frac{1}{\tau_b}\int_{-\tau_b}^{0}g(t')e^{im\omega_b t'}dt'$$
$$g(t')=\sum_m FT_m e^{-im\omega_b t'} \quad (7)$$

Consecutively, it is spatially Fourier Transformed: For nay function $g(\theta)$,

$$FS_l[g(\theta)]=\frac{1}{2\pi}\int_{-\theta_0}^{\theta_0}g(\theta)e^{-il\theta}d\theta$$
$$g(\theta)=\sum_l FS_l e^{-il\theta} \quad . \quad (8)$$

In Eq.(8), $\theta_0 = \pi$ for passing particles and $\theta_0 = \theta_t$ for trapped particles, θ_t is the turning point angle. See Ref. [9] for a detailed calculation scheme of Eq.(7) and Eq.[8]. In performing this calculation, we expand all the perturbed quantities in powers of $\varepsilon_p = \sqrt{2}(q/\varepsilon)k_\perp \rho_i$ with $\rho_i = \sqrt{T_i / M_i} / \omega_{c,i}$:

$$\phi_l = \phi_l^{(0)} + \varepsilon_p \phi_l^{(1)} + (\varepsilon_p)^2 \phi_l^{(2)} + \cdots \text{and} \quad \rho_l = \rho_l^{(1)} \varepsilon_p^1 + \rho_l^{(2)} \varepsilon_p^2 + \cdots \quad (9)$$

where the polarization is defined by $\rho = \sum_s 4\pi e_s \delta n_s$ and $\rho_l^{(n)} = 4\pi \sum_s e_s \delta n^{(n)}$. The subscript, s, denotes the species of plasma, ion or electron.

We obtain the polarization in response to the potentials of various order and poloidal mode numbers:

$$\rho_l^{(n)} = \sum_{ns \geq 0} (\vec{\vec{\alpha}}_{l,l'}^{(ns)}) \cdot \vec{\phi}_{l'}^{n-ns} \quad (10)$$

We find that the $l \neq 0$ component of Eq. (10) gives the recurrence formula

$$\vec{\phi}^{(n)} = \vec{\vec{M}} \cdot \sum_{s, ns \neq 0} \vec{\vec{\alpha}}_s^{(ns)} \cdot \vec{\phi}^{(n-ns)}$$
$$\vec{\vec{M}} = \sum_s \vec{\vec{\alpha}}_s^{(ns=0)} \quad (11)$$

For the $l = 0$ component, we equate the induced charge with the external charge $-\rho_{ext,l=0}$, i.e., the charge neutrality condition is applied to the total charge. We obtain the excited potential:

$$\sum_{n=0,2,4} \varepsilon_p^{(n)} \rho_{l=0}^{(n)} \phi^{(0)} = \rho_{ext,l=0}$$
$$\phi^{(0)} = \frac{-\rho_{ext,l=0}}{\sum_{n=0,2,4} \varepsilon_p^{(n)} \rho_{l=0}^{(n)}} = \frac{-\rho_{ext,l=0}}{\varepsilon_p^{(2)} \rho_{l=0}^{(2)} + \varepsilon_p^{(4)} \rho_{l=0}^{(4)}} \quad (12)$$

The dispersion relation is obtained from the denominator of Eq.(8)

$$D = \varepsilon_p^{(2)} \rho_{l=0}^{(2)} + \varepsilon_p^{(4)} \rho_{l=0}^{(4)} \quad (13)$$

III. Numerical Calculation and Comparison with other works:

In the previous section, we obtained the dispersion equation:

$$D = \varepsilon_p^{(2)} \rho_{l=0}^{(2)} + \varepsilon_p^{(4)} \rho_{l=0}^{(4)} = k_D^2 (2(k_\perp \rho_i)^2 \rho_{l=0}^{(2)} + 4(k_\perp \rho_i)^4 \rho_{l=0}^{(4)}) = 0 \quad (14)$$

We compare this result with that obtained from the analytic formula derived by Zonca

[7]: Using the same notations as used in Ref. [7], we reconstruct the dispersion relation in the following form

$$D_{Zonca} = \Lambda_0 - (k_\perp \rho_i)^2 \Lambda_1 = 0 \quad (11)$$

Then, the assigned correspondences are $\rho_{l=0}{}^{(2)} = -\frac{1}{2}(\frac{\varepsilon}{q})^2 \Lambda_0$ and $\rho_{l=0}{}^{(2)} = -\frac{1}{2}(\frac{\varepsilon}{q})^2 \Lambda_0$. The squared wave number is thus given by

$$\varepsilon_p^2 = -\frac{\rho_{l=0}{}^{(2)}}{\rho_{l=0}{}^{(4)}} \quad . (12)$$

The key quantities $\rho_{l=0}{}^{(2)}$, $\rho_{l=0}{}^{(4)}$, and ε_p^2 are calculated for the parameters of $q = 1.5$, $\varepsilon = 0.1$, and $T_i / T_e = 0.2$; this set of parameters corresponds to the inner region of a plasma.

In the top column of Fig.1, the real and imaginary parts of the second order polarization $\rho^{(2)}$ are shown: (a) the one obtained in this paper and (b) the one obtained from Zonca formula , $\rho^{(2)}{}_{Zonca} = -(1/2)(\varepsilon / q)^2 \Lambda_0$. We find a fairly good agreement between the two as far as $\rho^{(2)}$ is concerned.

In the middle column, the fourth order polarizations $\rho^{(4)}$ are shown: (b) the one obtained in this paper and (c) the one obtained from the Zonca formula, $\rho^{(4)}_{Zonca} = (1/4)(\varepsilon / q)^4 \Lambda_1$. In all of the figures, $\zeta = qR\omega / \upsilon_T$ is taken for the abscissa and the ordinates are non-dimensional.

We find qualitative agreement between the two $\rho^{(4)}$. However, they are different quantitatively: In (b) the real part of $\rho^{(4)}$ has a change in sign at high frequency while in (c) the imaginary part changes in sign. The difference is also found in the low frequency range $2 < \zeta = qR\omega / \upsilon_T < 4$, particularly in the imaginary part. In the bottom column of Fig.1, the squared wave numbers $\varepsilon_p^2 = (q / \varepsilon)^2 (k_\perp \rho_i)^2$ are shown versus the frequency $\zeta = q\omega / \upsilon_T$. (d) shows the one obtained from $\rho^{(2)}$ and $\rho^{(4)}$ in this paper and (f) shows the one obtained from Λ_0 and Λ_1. An outstanding difference is found in the frequency range above $\zeta = 6$, which is attributed to the fact that $\rho^{(4)}$ changes sign in Zonca formula and does not in the formula in this paper. They show quite different behavior in the lowest frequency range, $\zeta < 2$ as they should do; in Ref. [9] and in the present paper, the method of " IAPO " is employed abolishing the use of approximations so that the obtained formula is extended to the residual zonal flow [10] frequency range. Though the difference is smaller in the GAM frequency range $2 < \zeta < 4$, this

quantitative difference may cause significant differences in determining GAM potential spectrum. A comparison of the two schemes in this regard will be published elsewhere as a separate paper.

Conclusion:

A gyro-kinetic linear response function was obtained in this paper, using the method of "integrating along particle orbit". This method was used in the previous work based on the drift kinetic equation. Since approximations are minimally used, other analytic formulae may be obtained as reductions from ours with clarification of used approximations. The analytic formula shows qualitative agreement with the present analysis: It agrees in the second order polarization term but some differences are found in forth order term. Though, these differences are not large, they may cause significant differences in determining the GAM spectrum.

Acknowledgement

This work was partially supported by the JSPS-CAS Core-University program in the field of ‘Plasma and Nuclear Fusion'

[1]Winsor N. et al. *Physic Fluids* **11**,2448 (1968)

[2] Novakovskii C.S. et al, *Physic Plasmas*, **4** 4272 (1997)

[3] Lebedev V.B. et al, *Phys. Plasmas* **3** 3023 (1996)

[4] Watari T. et al, *Phys. Plasmas* **12** 062304 (2005)

[5] Sugama H. and Watanabe T.-H, *Phys. Plasmas,* **13** 012501(2006)

[6] Watari T. et al , *Phys. Plasmas,* **13** 062504 (2006)

[7] Zonca F. and Chen L. *Euro. Phys. Lett.* , **83** 35001,(2008)

[8] Gao Z. et al, *Phys. Plasmas* **15** 072511 (2008)

[9] Watari T. et al, *Phys. Plasmas* **14** 112512 (2007)

[10]Rosenbluth M.N. and Hinton F.L., *Phys. Rev. Letts*, **80** 724(1998)

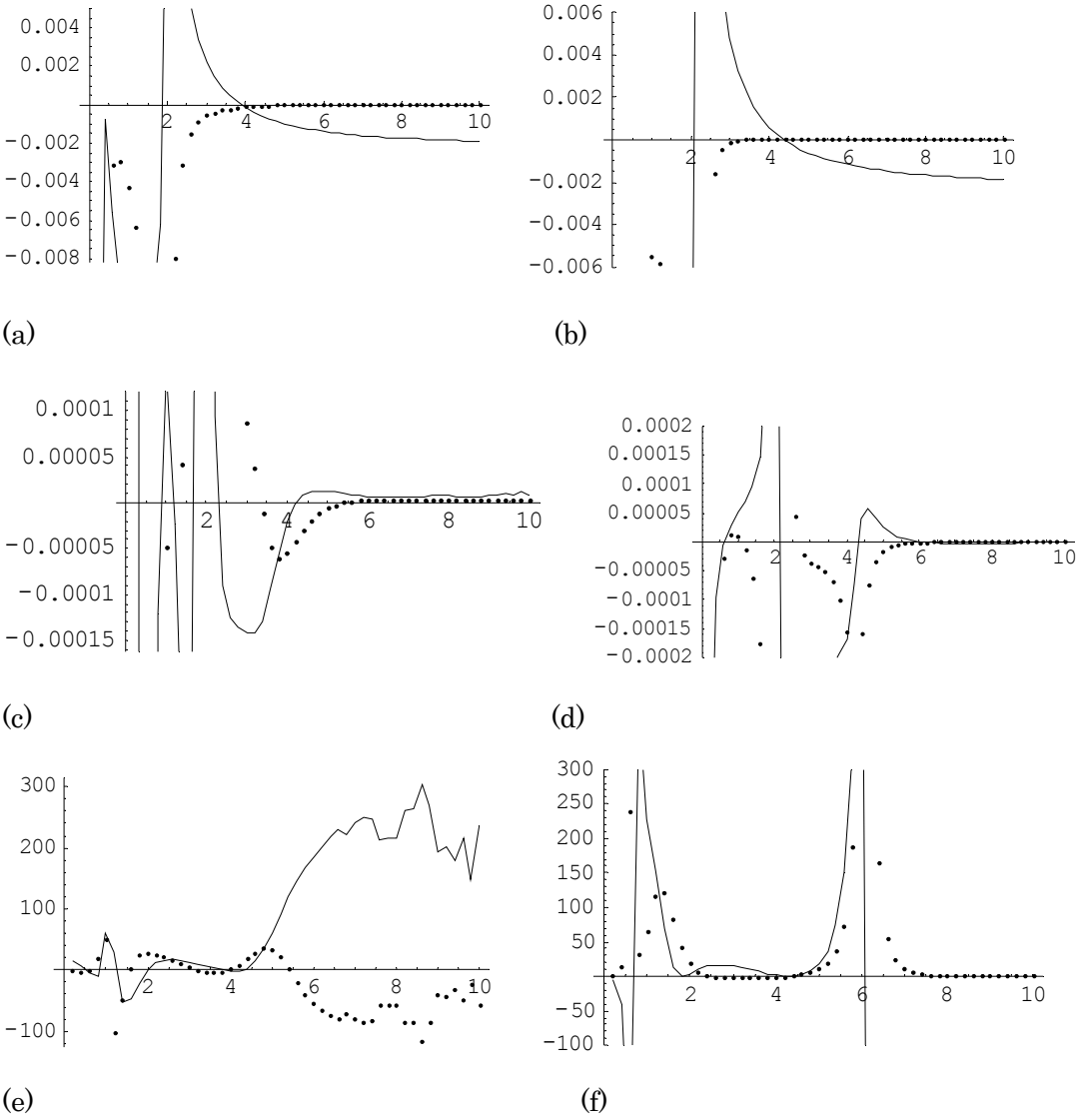

Fig.1: (a) The second order polarization $\rho^{(2)}$ in this paper and (b) corresponding one in Ref. [7], $-(1/2)(\varepsilon/q)^2\Lambda_0$. (c) The fourth order polarization $\rho^{(4)}$ in this paper and (d) corresponding one in Ref.[7], $(1/4)(\varepsilon/q)^2\Lambda_1$. $\zeta = qR\omega/\upsilon_T$ is taken for the abscissa, and the ordinate is non-dimensional . (e) The $\varepsilon_p^2 = (q/\varepsilon)^2(k_\perp\rho_i)^2$ is shown versus frequency, $\zeta = qR\omega/\upsilon_T$. (f) The corresponding one from Zonca formula.

Magnetic-island-induced ion temperature gradient mode

Z. X. Wang,[1,a)] J. Q. Li,[2] Y. Kishimoto[2] and J. Q. Dong[3,4]

1, Key Laboratory of Materials Modification by Beams of the Ministry of Education, School of Physics and Optoelectronic Technology, Dalian University of Technology, Dalian 116024, China

2, Graduate School of Energy Science, Kyoto University, Gokasyo, Uji, Kyoto 611-0011, Japan

3, Southwestern Institute of Physics, P.O. Box 432, Chengdu 610041, China

4, Institute for Fusion Theory and Simulation, Zhejiang University, Hangzhou 310027, China

Characteristics of ion temperature gradient (ITG) instability in the presence of a magnetic island are investigated numerically using a gyrofluid model. It is shown that when the magnetic island is wide enough to produce a broad distribution of rational surfaces near the O-point region, the ITG perturbations at these rational surfaces form a radially global-type eigenmode with a fast growth rate, which is referred to as the magnetic-island-induced ITG (MITG) mode. Moreover, the magnetic island also causes both radial and poloidal mode couplings, which play a stabilizing role. This work was partially supported by the JSPS-CAS Core-University program in the field of 'Plasma and Nuclear Fusion'.

[a)] Electronic mail: zxwang@mail.dlut.edu.cn

Observation of blobs and holes in the boundary plasma of EAST tokamak

N. Yan[1], G. S. Xu[1], W. Zhang[1], J. F. Chang[1], L. Wang[1], S. C. Liu[1], P. Liu[1], H. Q. Wang[1], M. Jiang[1], H. Xiong[1] ,S. Y. Ding[1], L. Zhang[1], B. N. Wan[1], S. Z. Zhu[1], H. Y. Guo[1], X. Gao[1], V. Naulin[2], J. Juul Rasmussen[2], A. H. Nielsen[2]

[1]*Institute of Plasma Physics, Chinese Academy of Sciences, Hefei 230031, China*

[2]*Association Euratom-Risø DTU, DK-4000 Roskilde, Denmark*

e-mail:" yanning@ipp.ac.cn"

Abstract:

Intermittent convective transport has been investigated in the edge and the scrape-off layer (SOL) of EAST by fast reciprocating Langmuir probe measurements. Plasma structures, holes have been detected for the first time inside the shear layer .The amplitude probability distribution function of the turbulence is strongly skewed, with positive skewed events ("blobs") prevailing in the SOL region and negative skewed events ("holes") dominant inside the shear layer. The statistical properties coincide with previous observations from the JET tokamak [G. S. Xu et. al, Nuclear Fusion 49, 092002 (2009)]. The generation mechanism of blobs and holes is also discussed. Moreover, burst structure and dynamics character of them are presented in this paper.

Keywords: intermittent, blobs, holes, generation mechanism, dynamics character

Introduction

The intermittency in the fusion plasma is generally attributed to the creation and propagation of filamentary (magnetic-field aligned) structures .Large amplitude events in Langmuir probe, beam-emission spectroscopy, and gas puff imaging measurements are therefore due to the passage of high-density structures through the low-density edge region. The outward propagation of these structures results in significant particle transport in the edge of magnetic confinement devices, a process referred to as anomalous transport. These filamentary coherent structures extended along the magnetic field lines, often called "blobs", were believed to be responsible for a strong intermittency of the SOL plasma turbulence observed with probes. The study of plasma blobs /filaments and holes is one of the most active research areas within plasma physics. Blobs /filaments will lead to serious wall erosion, impurity and recycling problems for future fusion reactors. Statistical features of these objects appear to be universal in many magnetized fusion device, regardless of the magnetic (tokamaks, stellarators, reversed field pinches) or geometrical configuration (toroidal or linear devices), Holes exist as a mechanism for inward transport of impurities Nevertheless, experiment evidence of holes are very limited.[1,2,3].

Experimental observations of intermittent convective transport in the SOL plasma have spawned a rapidly growing literature addressing the theory and simulation of these phenomena. So far several mechanisms have been proposed for

the generation of these structures. Generally, these objects are believed to be the results of complex nonlinear mechanisms which arise from free energy sources, e.g. the density gradient in the case of drift-type vortices described by Hasegawa–Mima-like equations or from magnetic field inhomogeneities as is the case of interchange turbulence. The latter mechanism has been recently invoked in order to explain the presence of radially propagating coherent structures in the scrape-off layer of toroidally magnetized plasmas. Recently, blobs are observed to originate at the crest of a coherent drift-interchange wave in TORPEX [4,5]. Simulation results also support this viewpoint [6,7]. However, how blobs and holes are generated remains an open question.

In this paper, intermittent convective transport has been investigated in the edge and the scrape-off layer (SOL) of EAST by fast reciprocating Langmuir probe measurements. Plasma structures, holes have been detected for the first time inside the shear layer (see figure 1(a)), where plasma pressure profiles change steep gradients. The amplitude probability distribution function of the turbulence is strongly skewed, with positive skewed events ("blobs") prevailing in the SOL region and negative skewed events ("holes") dominant inside the shear layer. The presence of the negative skewness region coincides with previous observations from the JET tokamak [2], where it was reported that this region was inside the shear layer. With the conditional averaging technique, the burst pattern of holes and blobs are presented. Blobs propagate outward in the SOL with excess density a compared with the background plasma, while holes are of lower density than background plasma, and it propagate inward from the inner shear layer (Δr<-28mm). Moreover, experimental probe measurements also provide dynamic character of blobs and holes, and the velocity, lifetime, radial size and poloidal size are computed respectively. The observation on EAST may indicate the mechanism of generation of blobs and holes.

Experimental setup and plasma parameters

Experiments were performed on the EAST, which is a fully superconducting tokamak with a major radius R0=1.75 m, a minor radius a=0.4m and a graphite rail limiter defining a plasma radius aL=0.0.44 m. The experiments were performed in deuterium ohmic plasma discharge with plasma current Ip=250KA, a toriodal field $\mathbf{B_0}$=2.0T at major axis, and line- average electron density ne=$1.5\times10^{19}m^{-3}$.The data presented below were obtained in double null（DN）magnetic configuration. The poloidal cross-section calculated by EFIT is shown in Figure 1(*a*)

Measurements of the edge plasma parameters were performed using reciprocating Langmuir probe at the outer mid-plane. The probe scans horizontally from the outside wall to the edge plasma. A typical position trace is shown in figure 1(b). Here $\triangle r$ is the radial position from the separatrix. Radial profiles of the plasma parameters measured by probe are produced by plotting a corresponding time series averaged over a short time interval (typically 1 ms) against the distance from the separatrix .Probe array is divided to two groups according to their function. One group is constituted by five separated tips in the middle part of probe array（Fig1(c). They can sense ion saturation current I_{sat} ,which is proportional to density,floating

potential V_f. $I_{sat} = 1/2 A_{eff}\, en_e C_s = 1/2 A_{eff} / en_e (kT_e + kT_i/m_i)^{\frac{1}{2}}$, ($T_e$ and T_i are the electron temperatures, A_{eff} is effective receiving area of tips and n_e is electron density) .The plasma temperature was estimated with the formula $T_e = T_i \approx V_+ - V_f / \ln 2$, where V_+ is the potential of positively baised probe and V_f is taken as the average of V_{f1} and V_{f2} avoiding polodial phase delay error . n_e was estimated directly from the ion saturation current neglecting the electron temperature fluctuation effect ,and plasma potential was calculated as $\phi_P = 3T_e + V_f$, with $3T_e$ being probe sheath potential drop for a deuterium plasma. The probe scans radially from the outside wall in approximately 200 ms along the path indicated in Fig. 1（b）. E_θ was deduced from the floating potentials measured with two tips separated by d_θ in the poloidal direction assuming that the temperatures and the sheath drops are identical in both the probes and that the plasma structures are larger than the separation between the probes (i.e. $E_{\theta 12} = (V_{f1} - V_{f2})/d_\theta$ $E_{\theta 23} = (V_{f2} - V_{f3})/d_\theta$) .Accordingly, The arrangement of the tips also allows the simultaneous measurements of the turbulent (electrostatic) particle, convective heat and conductive heat fluxes given respectively by

$$\Gamma_r^{ES} = \frac{1}{B_\varphi} < n_e E_{\theta 23} >$$

$$Q_r^{ES} = Q_{conv} + Q_{cond} = \frac{3}{2} kT_e \Gamma_r^{ES} + \frac{3}{2} n_e < kT_e E_{\theta 12} >$$

$E_{\theta 23}$ (aligned with the Isat tip) is then used to correlate with I_{sat} to obtain the turbulent particle flux and convective heat flux, while $E_{\theta 12}$ (aligned with the Te (V+)tip) is used to correlate with Te for the conductive heat flux measurements[8]

The other group tips located on the both sides of ceramics podium are the field aligned Mach probe pairs, from which the parallel flow Mach number is obtained. Experiments results from Mach probe will be covered elsewhere. The fluctuation data was digitized at 2 MHz with 12-bit resolution using a multi-channel digitizer.

Experimental results

Fluctuations are ubiquitous characteristics of signals measured in magnetized plasmas. They are the manifestation of turbulence. The frequency and wave-number power spectrum, probability distribution function (PDF) and its moments; skewness (*S*) and kurtosis (F) are always involved to describe fusion plasmas [9]. Statistical analysis of EAST experimental data has generally proved that the PDF of the signals

possesses large non-Gaussian tails, Such behavior can be explained in terms of intermittent events sticking out of the fluctuations; As is shown in figure 1 (a), the floating potential profile show a strong shear character in the region (-28<△r<0).The skeness turn to be negative when the probe reached the left shoulder of the shear layer .and skeness decrease to below three. Such features are an indication of the holes propagation. The position where S=0 (△r≈-28) is believed to be the production region of blobs and holes. The skewness profile indicated that the deviation of the signals from Gaussian statistics clearly increases from the plasma edge to the SOL and the intermittency became stronger in SOL. The problems turn to the definition of a suitable threshold to identify the fluctuations responsible for intermittency .Conditional average method (CA) is used to distinguish these burst from the background turbulence. Fluctuation events exceeding the threshold are treated as intermittent events. In the figure 3(b), the bursts which are larger than 2 times the standard deviation value of ion saturation current fluctuation component are detected by CA approach. The time evolutions of busty structures display an asymmetric pattern. The decay time is much longer than the raising time. It may imply blobs have over-dense front followed by a light tail (like a comet) .CA has also been performed to detect the negative density bursts -holes, i.e. density dropping below the mean level (figure 3 (e)) with the same threshold of blobs. The asymmetric is also demonstrated with sharp raise and slow decay. The probability distribution function of blobs and holes are presented in figure 3(c) and (f) respectively, along with the Gaussian distributions fitted with the Isa fluctuation. It is clear that the PDF of fluctuations data with blobs and holes has deviated from the Gaussian distribution, and the influence of blobs on the PDF of fluctuation signal seems more distinct than holes.

Figure 4 (a) present average poloidal velocity of background turbulence, one can find strong shear flow (~3km/s) has developed in the shear layer. The phase different of density and floating potential is investigated. As is illustrated in shadow region of figure 4 (b), the phase different between ion saturation current and floating potential is around 0.4π, which is close to prediction of interchange driven turbulence. In the corresponding region, the pressure profile changes the sharp steep tendency and became gentle. It may be caused by ejection of blobs and accumulation of holes in this area, in which process amount particle was taken away. In Refs [10], a first qualitative theory of individual blob dynamics has been suggested. Combined it with observation on EAST ,the dynamics of these coherent structure may can be understood that due to interchange turbulent processes in the steep region of plasma pressure, a coherent filament with large plasma density is peeled off the bulk plasma, Then, plasma polarization (i.e. charge separation) caused by effective gravity drifts at the outer side of the torus (curvature and ▽B drifts in tokamaks), results in a radial $\boldsymbol{E}\times\boldsymbol{B}$ convection ,the coherent structures (blobs and holes) move radially according to the $\boldsymbol{E}\times\boldsymbol{B}$ drift velocity. The magnitude of the electric field and, therefore, the convection speed are determined from the balance of polarization and parallel currents. As is shown in figure 5(a), the radial velocity of blobs decrease outwards

along the radial radius, It is because in this case parallel current is free to flow along the field lines, which will relieve the polarization effect.

Beside the radial movement of these plasma structures mentioned in last part, They are also able to propagate poloidally in the two-dimensional poloidal cross section .The radial velocity and poloidal velocity are presented in figure 5 (a) .radial velocity of blobs is positive, It means blobs propagate outwards from the shear layer to far SOL .While holes, from which the induced charge polarization, and hence propagation direction, is reversed from that of blobs. The inward propagation of holes worked as a mechanism for inward transport of impurities .using two-point correlation method, polodial movement of blobs and holes are identified. Blobs propagate from Vf2 to Vf1, which is consistent with ion diamagnetic drift direction, while holes propagate from Vf1 to Vf2, which is consistent with electron drift direction. What's more, the poloidal velocity of them is almost consistent with background poloidal velocity. To gain further insight into the nature of the intermittency fluctuations, the auto correlation function (ACF) which show them local decorrelation time of the density fluctuations is adopted to present the life time of them. As is shown in figure 5 (b), the life time τ_c of the coherent structures is increase with radius except in the middle part of the shear layer. The radial size and poloidal size are calculated as $\delta r \sim V_r \tau_c$ and $\delta r \sim V_p \tau_c$ respectively. Figure 5 (c) shows the spatial dimension of the blobs and holes. In order to distinguish blobs and holes, here the dimension of holes is expressed in negative value. Similar to the life time distribution, both the dimension of them also decreased in the middle of shear layer, which is due to the decorrelation effect of shear layer.

Concluding remarks

In this work we have presented statistical features of boundary turbulence of EAST under DN magnetic configuration. The results presented in this paper allow one to conclude that

(1) The blobs and hoes are produced in the shear layer, where shear flow has developed. It may imply that the shear flow shear off the coherent structure and eject it as blobs and holes.

(2) Blobs propagate from the shear layer to the SOL region, while holes travel on the contrary direction. The statistical features of them are different: S<0 for holes and S>0 for blobs. What's more, they turn out to be opposite burst structure: blobs are positive density pulses, whereas holes are negative.

(3) Blobs and hole formed in the steep region where the phase difference of density and floating potential are close to $\pi/2$. Therefore, the drift-interchange drive mechanism may be the main reason for the formation of blobs and hole, which is consistent with the simulation result from reference [5]

Acknowledgments

. The authors wish to acknowledge fruitful discussion with colleagues. This research was supported by the National Nature Science Foundation of China under Grant Nos 10605028，10675127, 10675126,10675124 ,11075181 and National Basic Research Program of China under Grant No.2010GB104001. This work was partially supported by the JSPS-CAS Core-University program in the field of'Plasma and Nuclear Fusion'.

References

[1] Boedo J.A. et al, Phys. Plasmas **10** 1670 (2003)
[2] G. S. Xu et. al, Nuclear Fusion 49, 092002 (2009)
[3] T. A. Carter. Phys. Plasmas **13**, 010701 (2006)
[4] S. H. Mŭller A. Diallo, A. Fasoli, *et al.*, Phys. Plasmas 14, 110704 (2007)
[5] I. Furno, B. Labit, M. Podesta`, et al PRL 100**,** 055004 (2008)
[6] O. E. Garcia, J. Horacek, R. A. Pitts *et al.*, Plasma Phys. Controlled Fusion 48, L1 (2006),
[7] N. Bisai, A. Das, S. Deshpande *et al.*, Phys. Plasmas 12, 072520 (2005)
[8] D L Rudakov1, J A Boedo1, R A Moyer1,et al, Plasma Phys. Control. Fusion 44 717–731(2002)
[9] Serianni G , et al., Plasma physics Control. Fusion, 49:B267-CB28 （2007）
[10] Krasheninnikov S, Phys. lett. A, 83,368 .（2001）

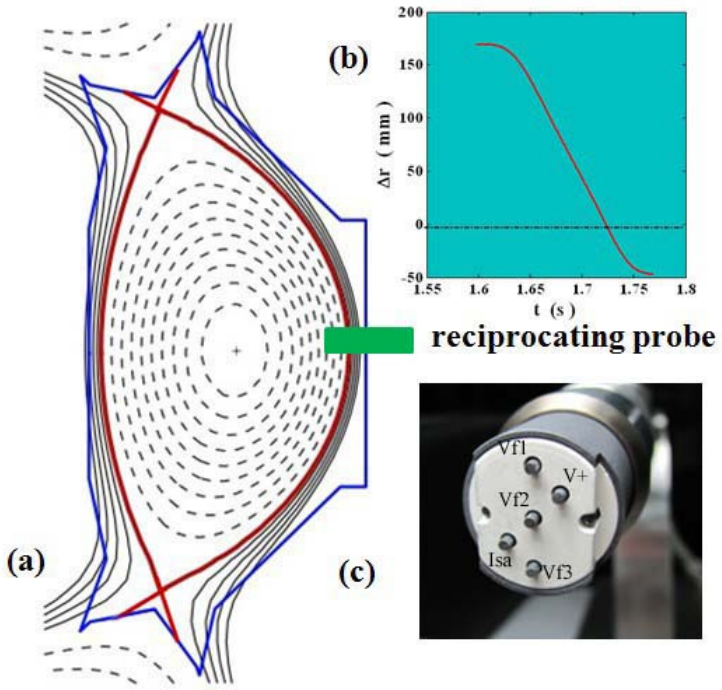

Figure 1 (a) Magnetic configuration of the discharge calculated by EFIT
(b) The trace of probe movement for single trip.
(c) Probe head used in the EAST experiment documented in this paper

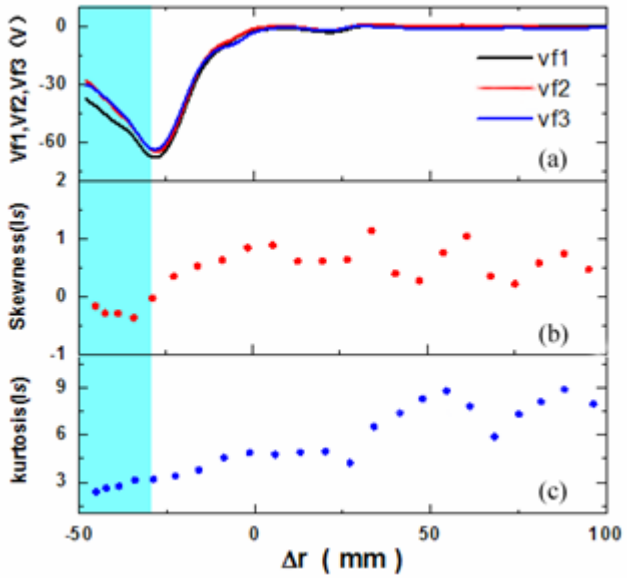

Figure 2 (a) Radial profiles of floating potential $V_{f1,}$ $V_{f2,}$ V_{f3}
(b) Radial profile of skewness of ion saturation current
(c) Radial profile of kurtosis of ion saturation current

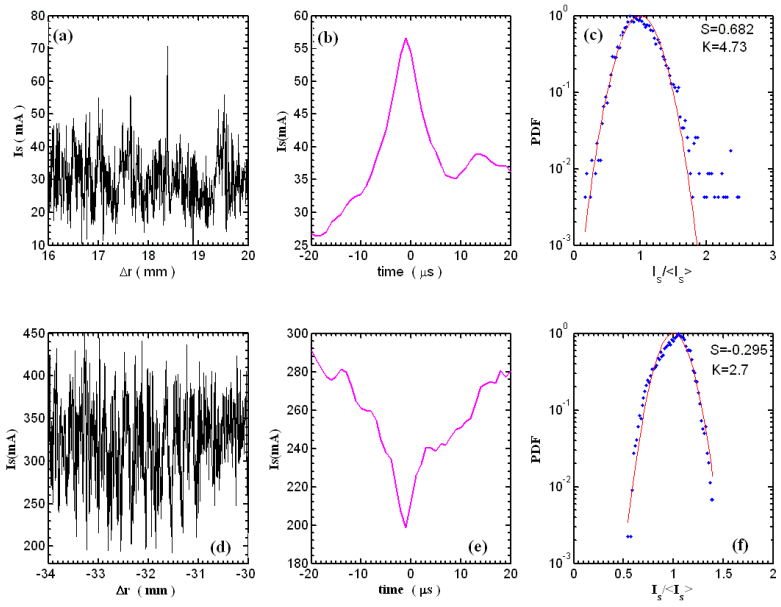

Figure 3

(a) Ion saturation current signal in the SOL region (16mm<△r<20mm).

(b) Burst structure of blobs abstracted in ion saturation current (16mm<△r<20mm)

(c) The PDF of ion saturation current and fitted Gaussian function in the region (16mm<△r<20mm).

(d) Ion saturation current signal in the SOL region (-34mm<△r<-30mm).

(e) Burst structure of blobs abstracted in ion saturation current (-34mm<△r<-30mm).

(f) The PDF of ion saturation current and fitted Gaussian function in the region (-34mm<△r<-30mm).

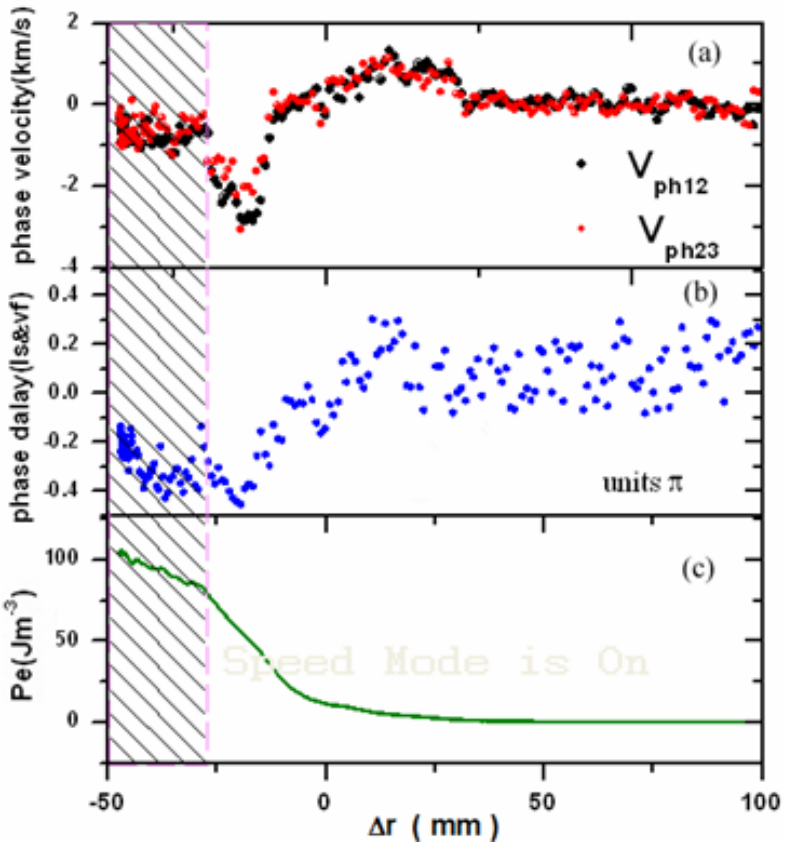

Figure 4

(a) Radial profile of average phase velocity

(b) Radial profile of phase difference between ion saturation current I_{sat} floating potential V_f.

(c) Radial profile of plasma pressure

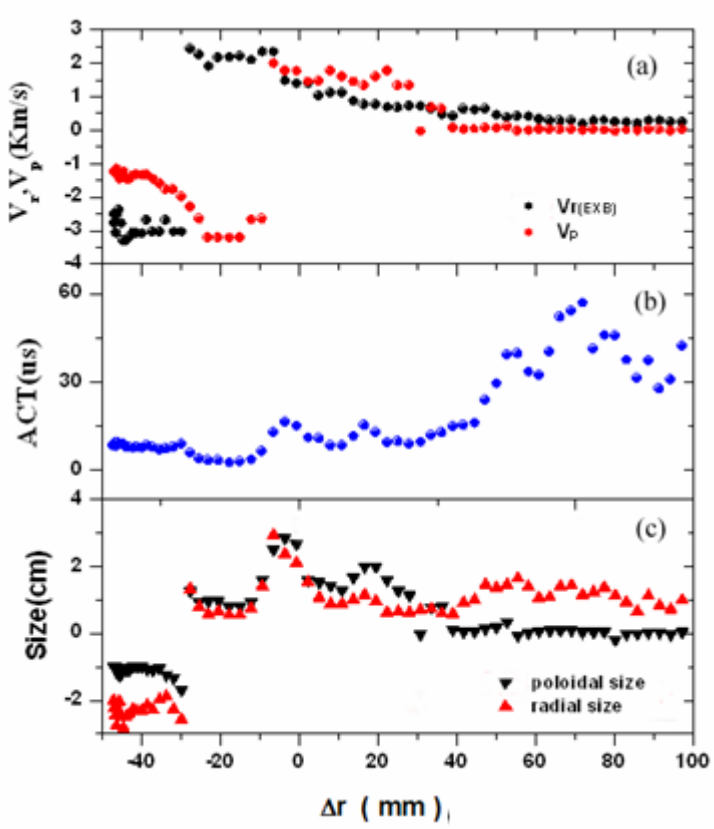

Figure 5 (a) Radial profile of radial and poloidal velocity of blobs and holes
(b) Radial profile of lifetime of coherent structures
(c) Radial profile of radial size and poloidal size of blobs and holes.

Developments of Doppler reflectometer system for the investigation of the electron density propagation in LHD

T. Tokuzawa, K. Kawahata, and LHD Experiment Group
National Institute for Fusion Science, Toki, Japan
A. Ejiri
Graduate School of Frontier Sciences, The University of Tokyo, Kashiwa 277-8561, Japan

Doppler reflectometry is a unique technique combined with the backscattering method and reflectometry. It can measure the perpendicular velocity of electron density fluctuations $v_\perp$, the radial electric field E_r, and the perpendicular wave number spectrum $S(k_\perp)$ in magnetized confinement plasmas [1-8]. Especially, the E_r and its shear are one of the important parameter for the understanding of plasma turbulence and confinement transition phenomena.

The principle of Doppler reflectometry can be explained by the grating reflection model with small sinusoidal corrugation characterized by a wave number $k_\perp$. The signal wave is launched and received under a non-zero tilt angle θ_{tilt} with respect to the normal onto the reflecting layer. This selects perturbations with a finite wave vector component in the reflecting layer $k_\perp$ via microwave scattering into diffraction order -1. This condition determines the probed wave number to $k_\perp$=-2k_i, where k_i is the local wave vector of the incident beam. For a plasma slab, the Bragg condition k_i=k_0 sin(θ_{tilt}), where k_0 is the wave number of the microwave in vacuum. By an actuation of θ_{tilt}, the $k_\perp$-spectrum of the density perturbations can be scanned. The unwanted strong 0th order reflection used in conventional reflectometry is at least partially suppressed as it is shifted out of the receiving antenna pattern. For the high-curvature LHD plasma, $k_\perp$=-2k_i has to be used for determining the perpendicular wave number. To calculate k_i, a 3D ray-tracing code LHDGAUSS[9] is employed.

The Doppler shift of the received signal depends on the velocity of the plasma turbulence and on its wave number

$$\omega_D = \mathbf{v} \cdot \mathbf{k} = v_\perp k_\perp + v_\parallel k_\parallel + v_r k_r \ . \qquad (1)$$

In magnetically confined plasmas it is usually assumed that $k_\perp >> k_\parallel$ and $v_\perp < v_\parallel$, in a way that the second term is negligible with respect to the first one. If in addition the turbulence does not displace itself radially, the third term vanishes and $\omega_D = v_\perp k_\perp$ is obtained. Therefore, the propagation velocity $v_\perp(k_\perp)$ of the selected perturbations can be calculated.

The perpendicular velocity measured by Doppler reflectometry is a composition of the plasma background ExB velocity v_{ExB} and the intrinsic phase velocity of the density fluctuations v_{ph},

$$v_\perp = v_{E\times B} + v_{ph} \ . \qquad (2)$$

In the plasma edge, $v_{ph} << v_{ExB}$ is usually satisfied in magnetically confined devices. Then, the radial electric field E_r can be deduced from the measurement of the perpendicular velocity through $E_r = v_\perp B$, where B is the absolute value of the magnetic field.

The schematic of *ka*-band Doppler reflectometer system is shown in Fig. 1. A microwave synthesizer is used as a source, because its phase noise is low enough to apply the density fluctuation measurements. The utilized frequency range is from 13 to 20 GHz and its output frequency is easily changed by the external GPIB control. For obtaining the complex frequency components and also the phase fluctuation strength, the single side-band (SSB) modulation is utilized. The source output is split into the probe and the reference signal. The probe signal is doubled followed by an active multiplier to bring the launching frequency up to 26-40 GHz (*ka*-band). The microwave launches from the outboard side along inverse the major radius direction on equatorial plane with slightly tilting angle. The polarization of launching wave is selectable on the ordinary mode or extraordinary mode. The returning wave

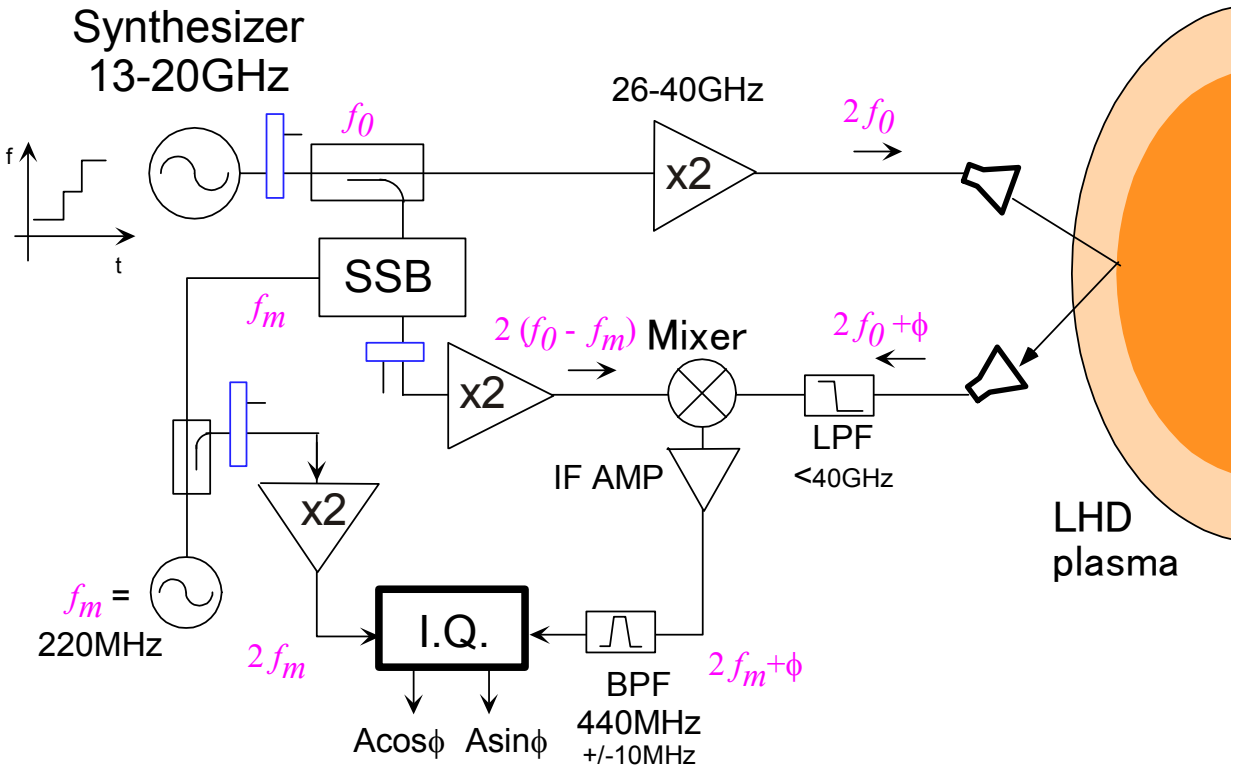

Figure 1 Schematic of the *ka*-band Doppler reflectometer system.

is received and mixed with reference wave. The SSB modulator driven by 220 MHz (f_m) quartz oscillator shifts the frequency of the reference signal for the heterodyne I-Q detection. The suppression levels of image sidebands are less than -20dB in this system. The intermediate frequency (IF) signal is amplified and filtered by band pass filter (BPF) which the pass frequency component is 440±10 MHz. Then, the IF signal and the modulation signal are led to I-Q detection. The output signals of I-Q demodulator, which are described by $A\cos\phi$ and $A\sin\phi$, are acquired by real-time data acquisition system[10] based on a compact PCI digitizer and the sampling rate is usually 1 and/or 10 MHz during the whole plasma discharge. Also, the part of the IF signal is monitored by the spectrum analyzer for checking the frequency shift.

Here, we show a preliminary experimental result of this Doppler reflectometer system with tilting angle antenna setup in the LHD plasma. The experiment is carried out the magnetic axis position is 3.60 m, the axial magnetic field strength is 2.75 T, and neutral beams and ECRH are injected. The plasma parameters, which are stored energy, plasma current, ion temperature, and averaged electron density, are shown in Fig. 2. Complex frequency spectra at the times t=3.9s and 4.2s are shown in Fig. 3. As the density profiles are almost same at both times, the scattered position is also almost same, which you can see in Fig. 4(a). The estimated poloidal velocity is about 4 km/s at t=3.9s and zero km/s at t=4.2s. The radial profiles of poloidal velocity which is measured by CXRS are shown in Fig. 4(b). The scattered position, which is hatched in the figure, is around R=4.5-4.6m. The value of poloidal velocity measured by CXRS is 3±2 km/s and

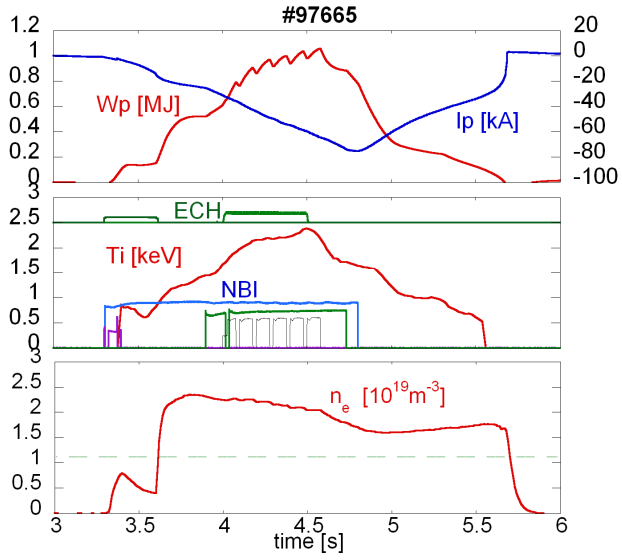

Figure 2 Temporal behavior of plasma parameter and heating source. (a) stored enegy (Wp: red) and plasma current (Ip: blue). (b) ion temperature (Ti: red) and (c) electron density (n_e).

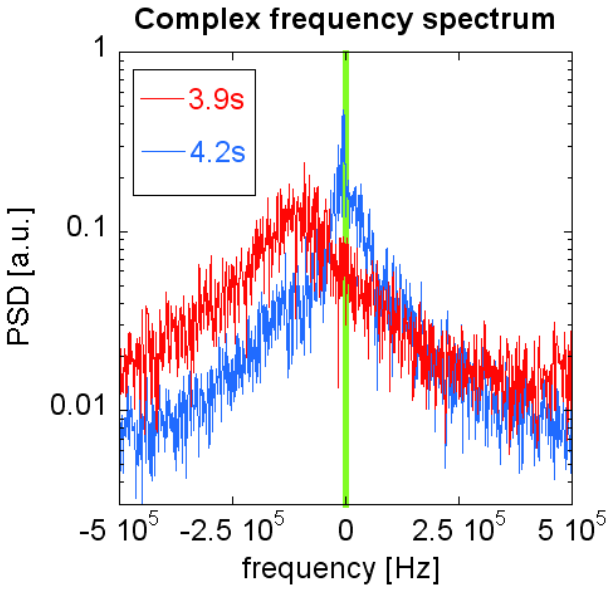

Figure 3 Complex frequency spectra measured by Doppler reflectometer in the same discharge of Fig. 2. Red and blue lines are t= 3.9s and 4.2s, respectively.

0.5±2.5 km/s at corresponding both times. These results are same order and considerable values. Because the measured position is located in a quite sensitive area which the shear of poloidal flow and its temporal change are large, we need to care about the estimated scattered position and improve the spatial resolution. Figure 5(a) shows the frequency spectrum of temporal behavior of Doppler shifted frequency which is calculated by the weighted-frequency method. We can observe the coherent frequency components of 2.2 kHz at t=3.9s and 3.7 kHz at t=4.2s. It is found that these frequencies are the same as the density fluctuation. It is likely that the background flow is modulated by the bulk plasma.

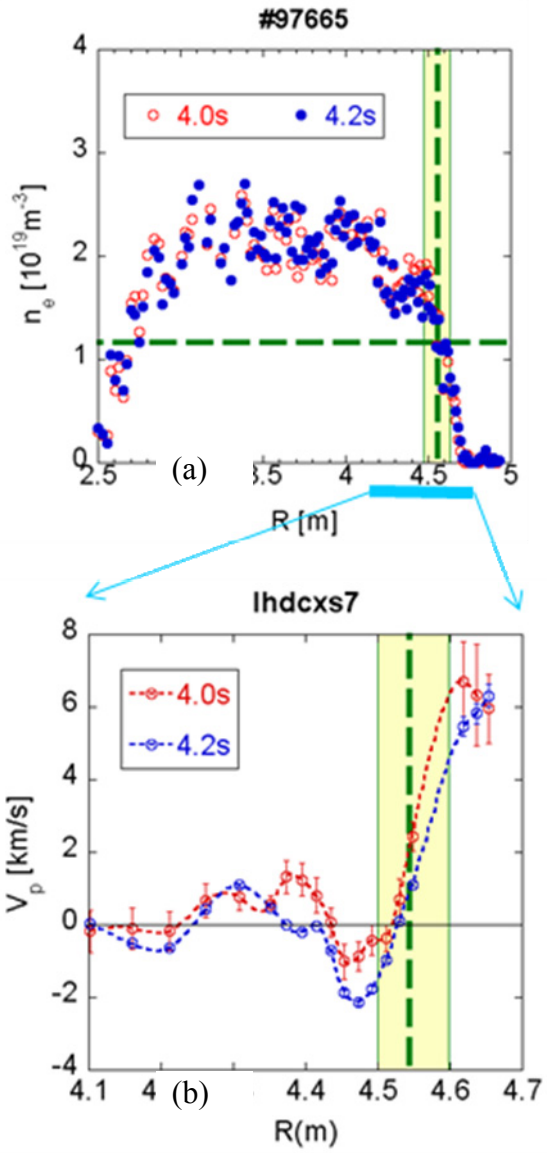

Figure 4 Radial profiles of (a) electron density obtained by Thomson scattering measurement and (b) poloidal velocity measured by CXRS. Scattered position is estimated around R=4.5 – 4.6m.

Acknowledgement

This work was specially supported by a Grant-in-Aid from the Ministry of Education, Culture, Sports, Science, and Technology of Japan, “Priority area of Advanced Burning Plasma Diagnostics” (Nos.18035015 and 20026010). Also, this work was partially supported by KAKENHI (Nos. 18686075, 22360394, and 22017007), a budgetary Grant-in-Aid from

National Institute for Fusion Science (NIFS10ULHH010), Japan / U.S. Cooperation in Fusion Research and Development. This research was also supported by the JSPS-CAS Core-University Program in the field of “Plasma and Nuclear Fusion”.

References

[1] V.V.Bulanin, *et al.*, Plasma Phys. Rep. **26**, 813 (2000).

[2] M. Hirsch, *et al.*, Rev. Sci. Instrum. **72** 324 (2001).

[3] M. Hirsch, *et al.*, Plasma Phys.Controlled Fusion **43**,1641 (2001).

[4] P. Hennequin, *et al.*, Rev.Sci.Instrum.**75**, 3881 (2004).

[5] G.D.Conway, *et al.*, Plasma Phys. Controlled Fusion **46**, 951 (2004).

[6] G. D. Conway, *et al.*, Nucl. Fusion **46**, S799 (2006).

[7] J. Schirmer *et al.*, Plasma Phys. Controlled Fusion 49 1019 (2007).

[8] J. C. Hillesheim et al., Rev. Sci. Instrum. **80**, 083507 (2009).

[9] S.Kubo, H.Idei, T.Shimozuma, Y.Yoshimura, T.Notake, K.Ohkubo, S.Inagaki, Y.Nagayama, K.Narihara and LHD experimental group "ECH Power Deposition Study in the Collisonless Plasma of LHD" in Proceedings of 11th Int. Congress on Plasma Physics (July 2002, Sydney, Australia) p.133 (2002).

[10] H. Nakanishi *et al.*, Fusion Eng. Design 66-68 827(2003).

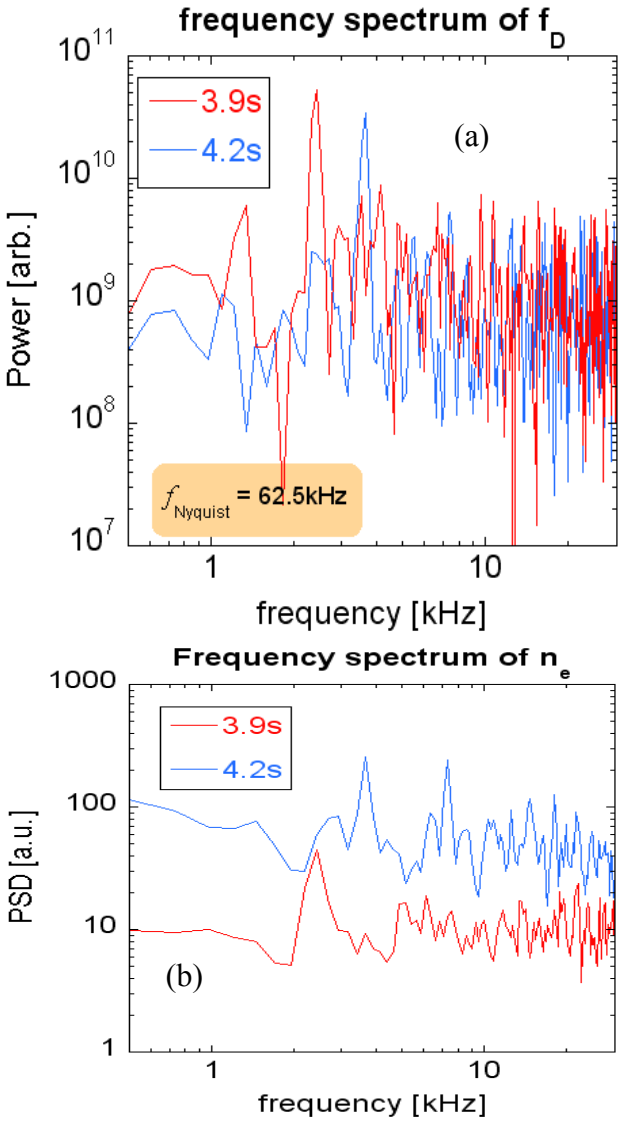

Figure 5 Frequency spectra of (a) Doppler shifted frequency and (b) electron density. (The fluctuation amplitude of electron density at t= 4.2s is shown with 10 times multiplying one).

Basic features on $E \times B$ convection nonlinearity in tokamak plasmas

Peng Xiaodong and Qiu Xiaoming

Southwestern Institute of Physics, P. O. Box 432, Chengdu 610041, China

Abstract

Basic features on $E \times B$ convection nonlinearity in tokamak plasmas, especially, large-scale coherent structures, are studied on the basis of both the model of three coupled modes and the model of four coupled modes. The diversity with most current models is that we deal with a nonlinearly unstable system such as the ion-temperate-gradient driven turbulence in tokamaks. Two types of coherent structure are identified with spatio-temporal characteristics called a zonal flow (ZF), and an oscillating shearing flow (OSF), respectively. In the meantime, the anomalous heat fluxes relevant to them are analyzed in some detail. Results show that the two types of coherent structure play different roles in both plasma turbulent fluctuations and related anomalous transports. Moreover, only the large-scale coherent structure with zero frequency, namely, the zonal flow, can suppress the turbulent fluctuations remarkably and hence benefits tokamak plasma confinements.

PACS: 52.35.Mw，52.35.Ra，52.35.Kt

Email: pengxd@swip.ac.cn

In recent years, the physics of large-scale coherent structures (LSCSs) in tokamak plasmas, such as zonal flows (ZFs), has attracted a great deal of interests of both theoretical and experimental researchers [1-12]. It is believed that zonal flows, which are defined as modes that are radial localized and sheared [12], and poloidal uniform [1-4, 13], play an important role in tokamak confinements. Firstly, it is well known that the ZF have strong shearing stabilization effects on plasma turbulences [1-3, 14, 15] which are mainly responsible for the anomalous transports observed in tokamaks. Secondly, experiments [16] show that the formation of transport barriers is always companied by the onset of the ZF or a shearing flow. Thirdly, the intermittency [17] of the ZF may be regarded as some behaviors such as edge localized modes (ELMs) in tokamaks. In addition, nonlocal transport phenomena [18] observed in tokamaks may be connected to the generation of the LSCS，such as the ZF.

It is widely accepted that the ZF is generated by nonlinear modulations among small-scale turbulence modes, which means that the ZF is a type of LSCSs. At present, there are some analytical models [4, 7, 9, 13, 19-22] to explain the generation of the ZF in the drift wave turbulence. Therein, a model of four coupled modes [4, 13, 19, 22], which include a zonal flow mode, a pump mode, and two sidebands, has been used successfully to obtain the growth rate of the ZF by many theoretical researchers. In fact, a model of three coupled modes [23-25] with only an upper sideband of two sidebands can also represent the generation of the ZF. In the present Letter, a model of three coupled modes and a corresponding model of four coupled modes are applied to study the basic features on $\boldsymbol{E}\times\boldsymbol{B}$ nonlinear convection in tokamak plasmas on the basis of the low-dimensional approach (LDA) suggested by Horton and Hu [23, 24] for studying ITG turbulence and used by Peng *et al*. [25] for studying electron-temperature-gradient (ETG) turbulence. It is natural that a comparison between the two models for the generation and development of the LSCS will be presented in the Letter, too.

To illustrate the basic features on $\boldsymbol{E}\times\boldsymbol{B}$ nonlinear convection in tokamak plasmas, we study the simplest possible model of curvature driven ITG turbulence. Its basic equations are [1, 29]

$$\partial_t(\widetilde{\phi} - \nabla_\perp^2\phi) + [\bar{\phi}, \widetilde{\phi}] - [\phi, \nabla_\perp^2\phi] + v_{*n}\partial_y\phi - v_B\partial_y p + \mu_0\nabla_\perp^4\phi = 0, \quad (1)$$

$$\partial_t p + [\phi, p] + v_{*P}\partial_y\phi - \chi_0\nabla_\perp^2 p = 0. \quad (2)$$

Here we have used notations ϕ, p, μ_0 and χ_0 to denote electrostatic potential, plasma pressure, viscosity, and heat conductivity, respectively. The Poisson bracket $[\phi, f] = \mathbf{z}\times\nabla\phi\cdot\nabla f$ arises from the $\mathbf{E}\times\mathbf{B}$ convection; a quantity f can be expressed as the sum of a flux-surface averaged part $\bar{f}$ and a contribution $\widetilde{f}$ depending on a flux-surface; $\nabla_\perp \equiv \hat{x}\partial_x + \hat{y}\partial_y$, where x and y represent the radial and poloidal coordinate in tokamaks, respectively. The left hand side of Eq. (1) has been modified due to the consideration that the flux-surface averaged part of the electron density does not respond adiabatically, which means that the electron density $n_e = \widetilde{\phi}$. The equations are de-dimensionalized by $x/\rho_i \to x$ ($k_x\rho_i \to k_x$), $y/\rho_i \to y$ ($k_y\rho_i \to k_y$), $\Omega_i t \to t$, $e\phi/T \to \phi$, and $p/p_0 \to p$, so that $v_{*n} = \rho_i/L_n$, $v_{*p} = \rho_i/L_p$, and $v_B = \rho_i/L_B$, where ρ_i is the ion Larmor radius, Ω_i ion gyro-frequency; L_n, L_p, and L_B are plasma density, pressure, and magnetic field gradient length, respectively.

The LDA analysis [24] on the ITG turbulence has demonstrated that there exists an L-mode attractor. In the analysis, it has been assumed that $\bar{\phi} = 0$, $\widetilde{\phi} = \phi_0^s \sin k_x x \sin k_y y + \phi_0^c \sin k_x x \cos k_y y$, $\widetilde{p} = p_0^s \sin k_x x \sin k_y y + p_0^c \sin k_x x \cos k_y y$, and $\bar{p} = p_0' \sin 2k_x x$ which plays a key role in the generation of the L-mode attractor. Figure. 1 depicts the L-mode attractor for the ITG turbulence in the case of a wave-vector $\mathbf{k} = (0.6, 0.3)$. It is clearly shown that the saturated level of the perturbation $|\phi|$ increases with a control parameter χ_N, which replaces the heat conductivity χ_0 in the dynamical equation about p_0', and the corresponding heat flux does, too.

The L-mode attractor can be used to construct the model of three coupled modes for the ITG turbulence. We express the perturbations of the potential ϕ and the pressure p as follows

$$\bar{\phi} = \phi_q \sin qx\,, \tag{3}$$

$$\begin{aligned}\tilde{\phi} = {} & \phi_0^s \sin k_x x \sin k_y y + \phi_0^c \sin k_x x \cos k_y y \\ & + \phi_1^s \sin(k_x + q)x \sin k_y y + \phi_1^c \sin(k_x + q)x \cos k_y y\end{aligned}, \tag{4}$$

$$\begin{aligned}p = {} & p_q \sin qx + p_0^s \sin k_x x \sin k_y y + p_0^c \sin k_x x \cos k_y y + p_0' \sin 2k_x x \\ & + p_1^s \sin(k_x + q)x \sin k_y y + p_1^c \sin(k_x + q)x \cos k_y y + p_1' \sin 2(k_x + q)x\end{aligned}. \tag{5}$$

Here we have used $\bar{\phi}$ to represent the ZF potential whose amplitude is ϕ_q and wave-number is q. When $q = k_x$ expressions (3)-(5) reduce to those in Ref. 24. (ϕ_0, p_0) denotes the pump wave with the wave-vector $\mathbf{k} = (k_x, k_y)$, and (ϕ_1, p_1) is the upper sideband with the wave-vector $\mathbf{k} = (k_x + q, k_y)$. Substituting equations (3)-(5) into (1) and (2), the mode dynamic equations can then be deduced

$$q^2 \partial_t \phi_q = (qk_y/4)(k^2 - k_1^2)(\phi_0^s \phi_1^c - \phi_0^c \phi_1^s) - \mu_N q^4 \phi_q\,, \tag{6}$$

$$(1 + k^2)\partial_t \phi_0^s = (qk_y/2)(1 + k_1^2 - q^2)\phi_q \phi_1^c + k_y v_{*n} \phi_0^c - k_y v_B p_0^c - \mu_0 k^4 \phi_0^s\,, \tag{7}$$

$$(1 + k^2)\partial_t \phi_0^c = -(qk_y/2)(1 + k_1^2 - q^2)\phi_q \phi_1^s - k_y v_{*n} \phi_0^s + k_y v_B p_0^s - \mu_0 k^4 \phi_0^c\,, \tag{8}$$

$$(1 + k_1^2)\partial_t \phi_1^s = (qk_y/2)(1 + k^2 - q^2)\phi_q \phi_0^c + k_y v_{*n} \phi_1^c - k_y v_B p_1^c - \mu_0 k_1^4 \phi_1^s\,, \tag{9}$$

$$(1 + k_1^2)\partial_t \phi_1^c = -(qk_y/2)(1 + k^2 - q^2)\phi_q \phi_0^s - k_y v_{*n} \phi_1^s + k_y v_B p_1^s - \mu_0 k_1^4 \phi_1^c\,, \tag{10}$$

$$\partial_t p_q = (qk_y/4)(\phi_0^c p_1^s - \phi_0^s p_1^c - p_0^c \phi_1^s + p_0^s \phi_1^c) - \chi_N q^2 p_q\,, \tag{11}$$

$$\partial_t p_0' = (k_x k_y/2)(\phi_0^s p_0^c - \phi_0^c p_0^s) - 4\chi_N k_x^2 p_0'\,, \tag{12}$$

$$\partial_t p_1' = [(k_x + q)k_y/2](\phi_1^s p_1^c - \phi_1^c p_1^s) - 4\chi_N (k_x + q)^2 p_1'\,, \tag{13}$$

$$\partial_t p_0^s = (qk_y/2)(\phi_q p_1^c - p_q \phi_1^c) + k_x k_y \phi_0^c p_0' + k_y v_{*p} \phi_0^c - \chi_0 k^2 p_0^s\,, \tag{14}$$

$$\partial_t p_0^c = (qk_y/2)(p_q \phi_1^s - \phi_q p_1^s) - k_x k_y \phi_0^s p_0' - k_y v_{*p} \phi_0^s - \chi_0 k^2 p_0^c\,, \tag{15}$$

$$\partial_t p_1^s = (qk_y/2)(\phi_q p_0^c - p_q \phi_0^c) + (k_x + q)k_y \phi_1^c p_1' + k_y v_{*p} \phi_1^c - \chi_0 k_1^2 p_1^s\,, \tag{16}$$

$$\partial_t p_1^c = (qk_y/2)(p_q\phi_0^s - \phi_q p_0^s) - (k_x+q)k_y\phi_1^s p_1' - k_y v_{*p}\phi_1^s - \chi_0 k_1^2 p_1^c . \qquad (17)$$

Here we have, in equations (6) and (11)-(13), replaced the collisional dissipations μ_0 (viscosity) and χ_0 by control parameters μ_N and χ_N, respectively. $k^2 = k_x^2 + k_y^2$ and $k_1^2 = (k_x+q)^2 + k_y^2$. Employing this group of equations we can study the basic features on $\boldsymbol{E}\times\boldsymbol{B}$ nonlinear convection and behaviors of the generation and development of the LSCSs in the ITG turbulence. So we choose the pump wave-vector $\mathbf{k} = (0.6, 0.3)$, which is located at the neighbor of the unstable separatrix, the collisional dissipations $\mu_0 = 0.015$ and $\chi_0 = 0.1$.

The numerical calculation results of equations (6)-(17) show that the LSCSs strongly depend on the wave-number q. First, there exists a threshold q_c for the given plasma gradient lengths such as the pressure one L_p and the density one L_n. The LSCS with the wave-number $q \geq q_c$ does not appear. Then, the LSCS with only space period structure，which is called a zonal flow, is observed for a moderate wave-number q. And finally the LSCS with spatio-temporal period structure, which is called an oscillating shearng flow (OSF), is discovered for a lower wave-number q.

Plotted in figure 2 is that both the saturated level of the LSCS and the corresponding heat flux change with the wave-number q. Here the heat flux is defined as $q_r = -<p\partial_y\phi> = k_y(\phi_0^c p_0^s - \phi_0^s p_0^c + \phi_1^c p_1^s - \phi_1^s p_1^c)/4$. The threshold wave-number q_c is about 0.45. It is worthwhile to emphasis that there exists a turning point for the heat flux curve, which is the point for the wave-number $q \approx 0.1$. On the right hand side of this point, the LSCS is the ZF and the higher the level of the ZF is the lower the corresponding heat flux is. However, on the left hand side of this point, the LSCS is the OSF and the higher the level of the OSF is the greater also the corresponding heat flux is. It implies that only the ZF plays a suppressive role of the plasma anomalous transports.

The parameters μ_N and χ_N (as above-mentioned, physically they act as viscosity and heat conductivity, respectively) affect the saturated potential level and the corresponding heat flux level of the L-mode attractor. We study dependences of the LSCS on the parameters μ_N and χ_N such that it is possible to control the development of the turbulences and the ZFs in experiments.

Figure 3 depicts the dependence of the ZF and the corresponding heat flux on the control parameter μ_N. From figure 3 we can clearly see that the saturated level of the ZF increases from 0.25 to 0.69 with μ_N descending from 0.0135 to 0.0015, but the corresponding heat flux drops from 0.0028 to 0.0009. It means that the parameter μ_N plays a damping role of the ZF. The effects of the other parameter χ_N on the ZF and the corresponding heat flux are shown in figure 4. It is easily found that the saturated level of the ZF increases (from 0.17 to 0.42) with χ_N (from 0.012 to 0.040), and corresponding heat flux rises from 0.0013 to 0.0024. It is well known that χ_N is a source of the L-mode attractor. So the larger χ_N is the higher the saturated level of the turbulence is. It is natural that the saturated level of the ZF is raised, too. Although the ZF ascends the corresponding heat flux also rises because that the heat flux of the corresponding L-mode attractor increases greatly. In addition, the calculations also show that the saturated time of the turbulence advances greatly due to χ_N increase.

In expressions (4) and (5), we consider the lower sideband (ϕ_2, p_2) with the wave-vector $\mathbf{k} = (k_x - q, k_y)$, that is

$$\begin{aligned}\widetilde{\phi} = {} & \phi_0^s \sin k_x x \sin k_y y + \phi_0^c \sin k_x x \cos k_y y + \phi_1^s \sin(k_x + q)x \sin k_y y \\ & + \phi_1^c \sin(k_x + q)x \cos k_y y + \phi_2^s \sin(k_x - q)x \sin k_y y + \phi_2^c \sin(k_x - q)x \cos k_y y\end{aligned}, \quad (4')$$

$$\begin{aligned}p = {} & p_q \sin qx + p_0^s \sin k_x x \sin k_y y + p_0^c \sin k_x x \cos k_y y + p_0' \sin 2k_x x \\ & + p_1^s \sin(k_x + q)x \sin k_y y + p_1^c \sin(k_x + q)x \cos k_y y + p_1' \sin 2(k_x + q)x \\ & + p_2^s \sin(k_x - q)x \sin k_y y + p_2^c \sin(k_x - q)x \cos k_y y + p_2' \sin 2(k_x - q)x\end{aligned}. \quad (5')$$

Then the model of four coupled modes for the ITG turbulence can be built similar to

that of three coupled modes. A set of mode dynamic equations for 17 variables (ϕ_q, p_q, ϕ_0^s, ϕ_0^c, ϕ_1^s, ϕ_1^c, ϕ_2^s, ϕ_2^c, p_0', p_1', p_2', p_0^s, p_0^c, p_1^s, p_1^c, p_2^s, and p_2^c) can be easily obtained.

Figure 5 shows that the saturated levels of both the LSCS and the corresponding heat flux with wave-number q in the model of four coupled modes. Here the contribution of the lower sideband to the heat flux must be included. Similar to the case of three coupled modes, we find that the wave-number q of LSCS plays an important role in determining its spatio-temporal pattern in the model of four coupled modes and there exists a turning point (the wave-number q = 0.18) for the heat flux curve. On the right hand side of this point, due to the generation of the ZF, the higher the level of the LSCS is the lower the corresponding heat flux is. However, on the left hand side of the point, due to the generation of the OSF, the higher the level of the LSCS is the higher the corresponding heat flux is, too. It is obvious that the wave-number q of the turning point in the model of four coupled modes is higher than that ($q \approx 0.1$) of the case of three coupled modes. Howbeit, there is no threshold q_c in the model of four coupled modes. The linear instability of the upper sideband is governed by its wave-number or the wave-number q of the LSCS if the wave-number of the pump wave is given. But the lower sideband is always linearly unstable. So it is understandable that there is no ZF threshold wave-number in the model of four coupled modes because there always exist wave-wave interactions in the case of four coupled modes.

Figures 6 and 7 depict the dependence of the ZF and the corresponding heat flux on the control parameters μ_N and χ_N in the model of four coupled modes, respectively. From figure 6 we clearly see that the saturated level of the ZF increases (from 0.78 to 1.81) with μ_N descending from 0.0135 to 0.0015, but the corresponding heat flux drops from 0.0043 to 0.0021. For the other control parameter χ_N, from figure 7 it is easily found that the saturated level of ZFs increases (from

0.64 to 1.09) with χ_N (from 0.010 to 0.040), and the corresponding heat flux rises from 0.0017 to 0.0042, too. These results, in qualitatively, are in agreement with those in the model of three coupled modes.

We have investigated the basic features on $\boldsymbol{E}\times\boldsymbol{B}$ convection nonlinearity based on both the model of three coupled modes and model of coupled modes. The results of the both are discussed and compared. The LSCS generation in plasma turbulences represents one of intrinsic characteristics of the $\boldsymbol{E}\times\boldsymbol{B}$ convection nonlinearity. At least, there exist two kinds of the LSCS in a tokamak plasma system.

The large-scale space coherent structure, namely ZF, plays a key role in the tokamak confinement improvement. The anomalous heat transport flux decreases obviously when the ZF occurs in the system. The control parameters μ_N and χ_N affect the saturated levels of both the ZF and corresponding heat flux. The larger the parameter μ_N is, the lower the saturated level of the ZF is; the larger the parameter χ_N is, the higher the saturated level of the ZF is. These properties provide a direction for experimental control of the ZF. On the other hand, the large-scale spatio-temporal coherent structure, namely OSF, has been verified in the present Letter. The role of the OSF in reducing the anomalous heat flux is obviously weaker than that of the ZF. Detailed discussions will be published in another full paper.

This work was supported by the National Natural Science Foundation of China under Grant No. 10775043 and National Magnetic Confinement Fusion Science Program (Code number 2010GB106000 and 2010GB106006). This work was partially supported by the JSPS-CAS Core-University program in the field of‘Plasma and Nuclear Fusion’.

References

[1] Diamond P H, Champeaux S, Malkov M, and *et al.* 2001 Nuclear Fusion **41**, 1067.

[2] Diamond P H, Itoh S -I, Itoh K, and Hahm T S 2005 Plasma Phys. Controlled Fusion **47**, R35.

[3] Itoh S -I and Itoh K 2001 Plasma Phys. Controlled Fusion **43**, 1055.

[4] Chen L, Lin Z, and White R B 2000, Phys. Plasmas **7**, 3129.

[5] Lin Z, Hahm T S, Lee W W, Tang W M, and White R B 1998 Science **281**, 1835.

[6] Melkov M A, Diamond P H, and Smolyakov A I 2001 Phys. Plasmas **8**, 1553.

[7] Smolyakov A I, Diamond P H, and Medvedev M V 2000 Phys. Plasmas **7**, 3987.

[8] Smolyakov A I, Diamond P H, and Medvedev M V 2000 Phys. Rev. Lett. **84**, 491.

[9] Anderson J and Kishimoto Y 2007 Phys. Plasmas **14**, 012308.

[10] Fujisawa A, Itoh K, Iguchi H, and *et al.*2004 Phys. Rev. Lett. **93** 165002.

[11] Fujisawa A, Shimizu A, Nakano H, and *et al.*2007 Plasma Phys. Controlled Fusion **49,** 211.

[12] Sugama H, Watanabe T -H, and Horton W 2007 Phys. Plasmas **14**, 022502.

[13] Manfredi G, Roach C M, and Dendy R O 2001 Plasma Phys. Controlled Fusion **43**, 825.

[14] Biglari H, Diamond P H, and Terry P W 1990 Phys. Fluids **B 2**, 1.

[15] Li J and Kishimoto Y 2003 Phys. Plasmas **10**, 683.

[16] Bell R E, Levinton F M, Batha S H, and *et al.* 1998 Phys. Rev. Lett. **81**, 1429.

[17] Miki K, Kishimoto Y, Li J, and Miyato N 2008 Phys Plasmas **15**, 052309.

[18] Miyato N, Kishimoto Y, and Li J Q 2006 Plasma Phys. Controlled Fusion **48**, A335.

[19] Anderson J, Nordman H, Singh R, and Weiland J 2002 Phys. Plasmas **9**, 4500.

[20] Guzdar P N, Kleva R G, and Chen L 2001 Phys. Plasmas **8**, 459.

[21] Singh R, Tangri V, Kaw P, and *et al*. 2005 Phys. Plasmas **12**, 092307.

[22] Watanabe T -H, Sugama H, and Sato T 2000 Phys. Plasmas **7**, 984.

[23] W. Horton, G. Hu, and G. Laval, Phys. Plasmas **3**, 2912 (1996).

[24] Hu G and Horton W 1997 Phys. Plasmas **4**, 3262.

[25] Peng X D, Tang C J, and Qiu X M 2007 Phys. Plasmas **14**, 010703.

[26] Horton W, Choi D I, and Tang W M 1981 Phys. Fluids **24**, 1077.

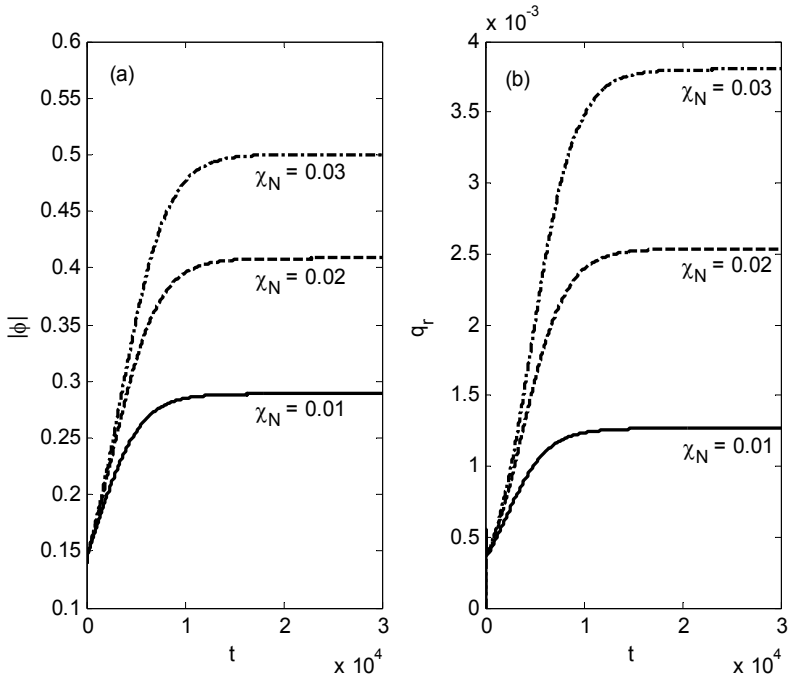

Fig. 1. Plot of L-mode attractor. (a) Evolution of potential amplitude $|\phi|=\sqrt{\phi_0^{s2}+\phi_0^{c2}}$ and (b) Evolution of heat flux $q_r = k_y(\phi_0^c p_0^s - \phi_0^s p_0^c)/4$. Both the saturated potential perturbation and the corresponding heat flux increase with the control parameter χ_N.

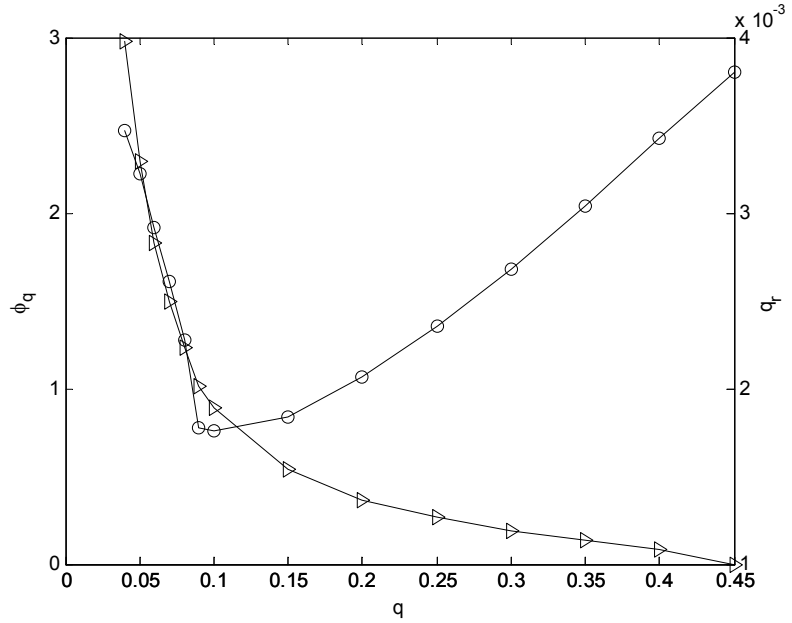

Fig. 2. The LSCS (curve with triangle) and the corresponding heat flux (curve with circle) change with wave-number q (three coupled modes) for $\mu_N = 0.0075$, $\chi_N = 0.03$. The LSCS is the ZF when $q > 0.1$, and the LSCS is the OSF when $q < 0.1$.

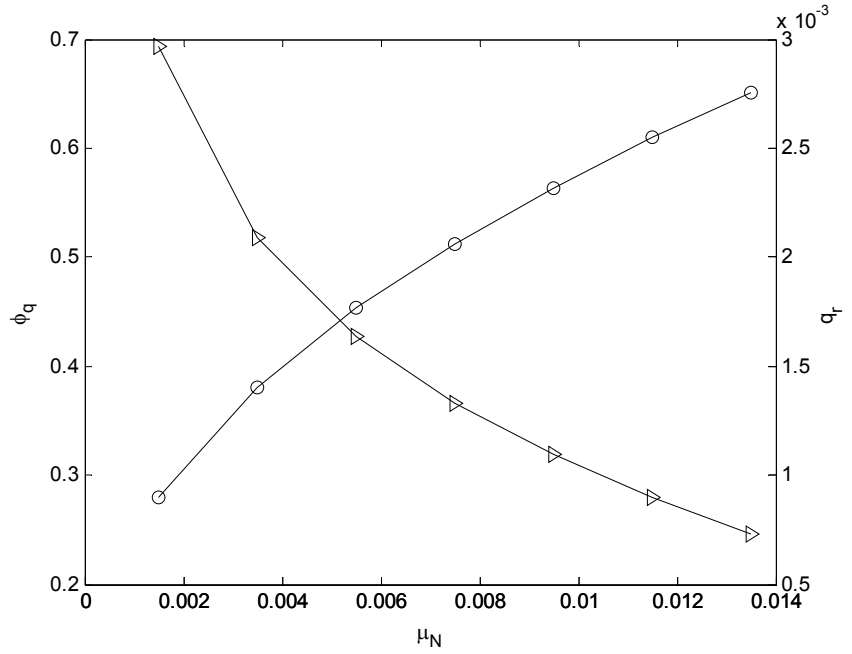

Fig. 3. The ZF (curve with triangle) and corresponding heat flux (curve with circle) change with μ_N (three coupled modes) for $q = 0.20$, $\chi_N = 0.03$.

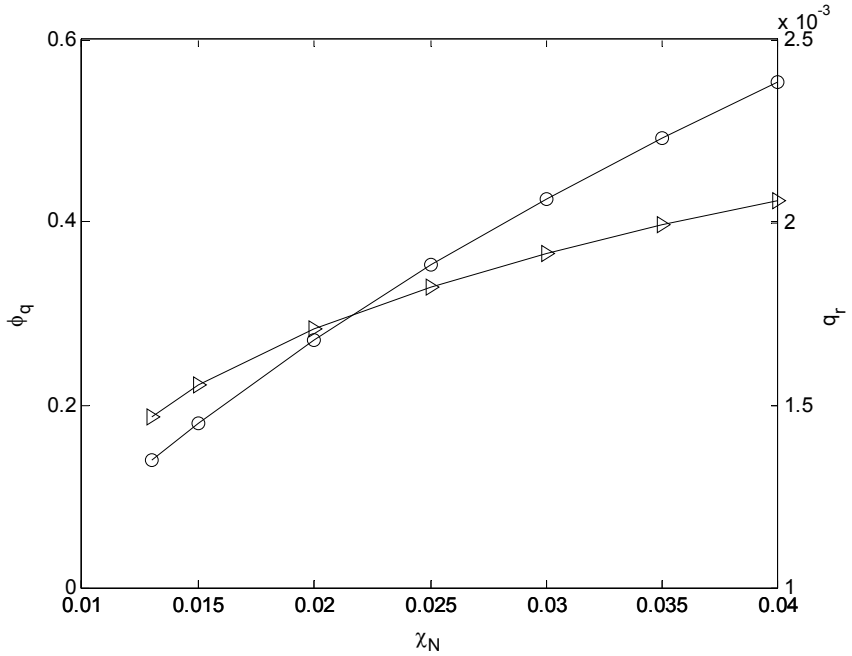

Fig. 4. The ZF (curve with triangle) and corresponding heat flux (curve with circle) change with χ_N (three coupled modes) for $q = 0.20$, $\mu_N = 0.0075$.

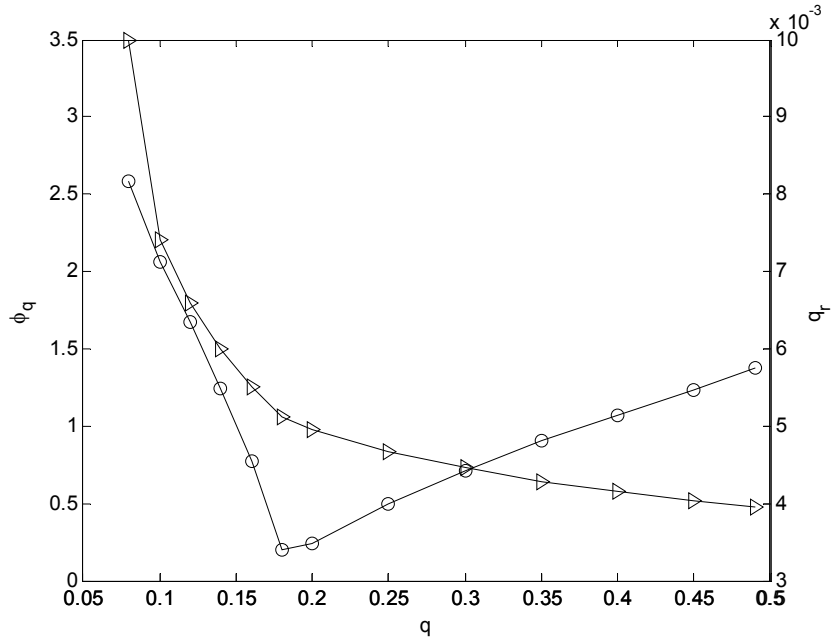

Fig. 5. The LSCS (curve with triangle) and corresponding heat flux (curve with circle) change with wave-number q (four coupled modes). $\mu_N = 0.0075$, $\chi_N = 0.03$. The LSCS is the ZF when $q > 0.18$, and the LSCS is the OSF when $q < 0.18$.

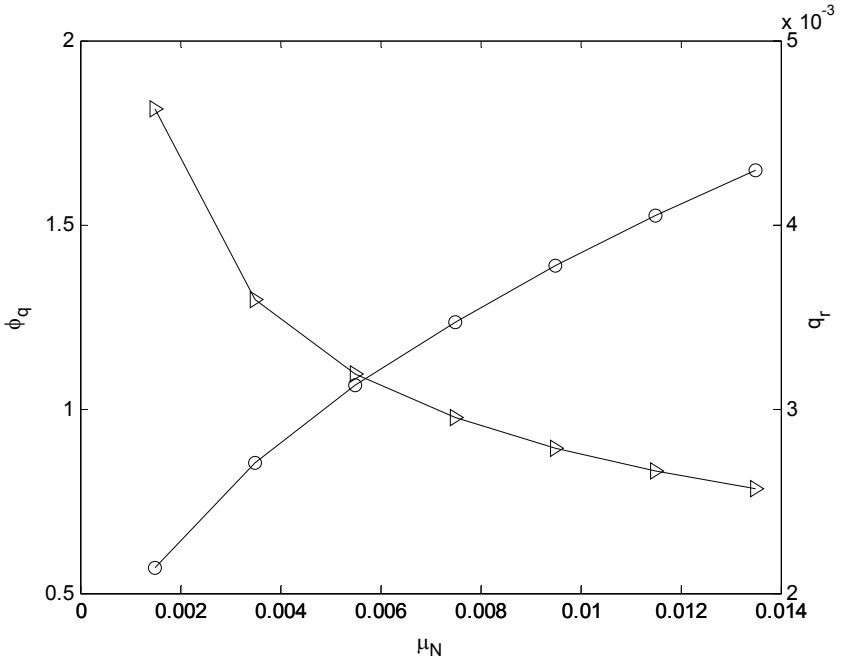

Fig. 6. The ZF (curve with triangle) and corresponding heat flux (curve with circle) change with μ_N (four coupled modes) for $q = 0.20$, $\chi_N = 0.03$.

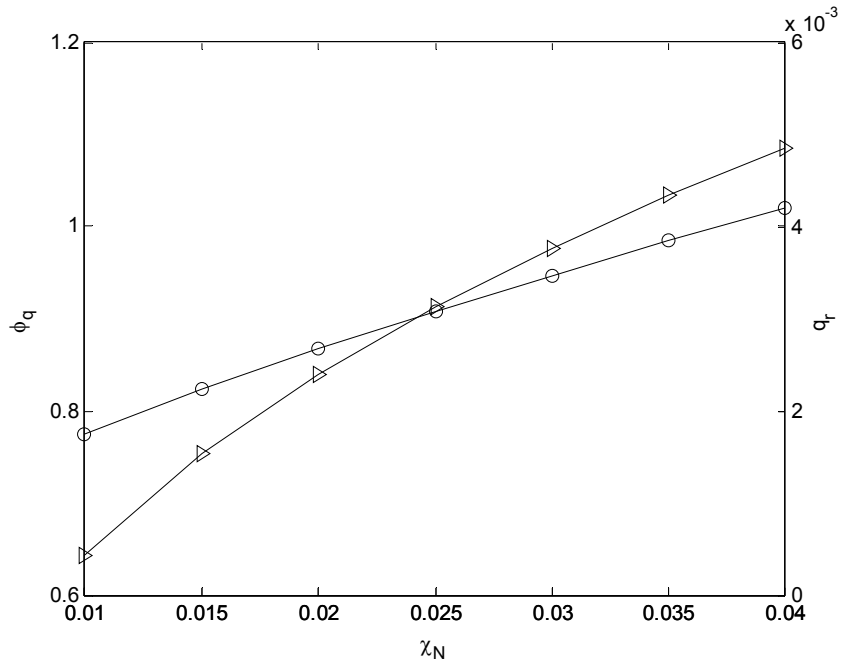

Fig. 7. The ZF (curve with triangle) and corresponding heat flux (curve with circle) change with χ_N (four coupled modes) for $q = 0.20$, $\mu_N = 0.0075$.

The present state of the electron cyclotron emission measurements on HT-7 and EAST*

Liu Yong (刘永)†, Ti Ang (提昂), Han Xiang (韩翔), Wang Yumin (王嵎民), Li Erzhong (李二众), Ling Bili (凌必利), Hu Liqun (胡立群) and Gao Xiang (高翔)

Institute of plasma physics, Chinese Academy of Sciences, Hefei 230031, China

(Dated: October 31, 2010)

This paper presents the present state of the diagnostics for electron cyclotron emission (ECE) measurements on HT-7 and EAST. Two ECE measurement systems have been installed on HT-7 and EAST, and they are separately a 16-channel heterodyne radiometer system and a 20-channel grating polychromator. A 32-channel heterodyne radiometer system is being built, which has a wider frequency coverage and better spatial resolution. Quasi-optical antenna is employed to improve the poloidal resolution. To reduce the transmission loss, corrugated waveguide is used. In the past few experimental campaigns, the ECE measurement has provided the evolution of the electron temperature profiles. Researches on the electron heat transport and the anomalous Doppler resonance have been performed.

PACS numbers: 52.70.Gw, 52.25.Fi

Keywords: Electron cyclotron emission, electron temperature profile, heterodyne radiometer, grating polychromator.

1. INTRODUCTION

The Experimental Advanced Superconducting Tokamak (EAST) [1] is a full superconducting tokamak with a non-circular cross-section vacuum vessel, which is a upgrade of the HT-7 [2]. The main parameters of these two machines are listed in Table 1.

Electron cyclotron emission (ECE) measurement has been widely used in tokamak plasmas since the 1960s [3], to provide the temporal evolution of local electron temperature [4, 5] and the information on the electron velocity distribution [6–8]. Two ECE measurement systems have been developed on HT-7 and EAST: a 16-channel heterodyne

* This work was supported by the Knowledge Innovation Program of the Chinese Academy of Sciences.
† liuyong@ipp.ac.cn

TABLE I: Main parameters of HT-7 and EAST.

	HT-7	EAST
Toroidal field, B_0	2.5 T	3.5 T
Plasma current, I_p	250 kA	1 MA
Major radius, R	1.22 m	1.7 m
Minor radius, a	4	4.25
Elongation, K_x	1	1.6-2

radiometer system (HRS) [9–11] and a 20-channel grating polychromator (GPC) [12]. The coverage range of the 16-channel HRS is 98.5-126 GHz, and the radial resolution is around 2 cm. The GPC covers frequency range from 90-250 GHz, and it has a radial resolution of around 2.5 cm. A 32-channel HRS, which covers the frequency range of 104-168 GHz and has a better radial resolution, is being built now. This paper is organized as follows. The section two introduces the ECE measurement systems on HT-7 and EAST. The calibration method employed now is introduced in this section as well. Related researches performed on HT-7 and EAST are exampled in section three. Section four is the summary.

2. INSTRUMENTS

2.1. 16-channel heterodyne radiometer system (HRS)

A 16-channel HRS has been in operation since 2005. This radiometer receives emission from the plasma in the range of 98.5-126 GHz. Figures 1 illustrates the schematic of the system. Emission from plasma is received by a combination of TPX lens and corrugated horn, and the spot size of this system is around 10 cm. A 3 dB directional coupler is employed to split the emission into two units, and each unit has a high pass filter to ensure single side band operation of the mixer. One unit has a local oscillator of frequency 95 GHz, and the other 108.5 GHz. A low pass filter is employed to overcome the intermediate frequency (IF) due to the residual harmonics. Each of the two 2-18 GHz signals is amplified and split into 8 channels. Each channel is then filtered by band pass filters of 1 GHz bandwidth, and the central frequency is designated in Figure 1. Schottky diode detectors are used to detect signal of each channel. Finally, the output of the detector is amplified and digitalized.

2.2. 20-channel grating polychromator (GPC)

A 20-channel GPC was transferred from Princeton plasma physics laboratory (PPPL) in 2008, and had been re-planted on EAST [13]. Figure 2 is the schematic of the system, which is based on the Ebert-Fastie grating monochro-

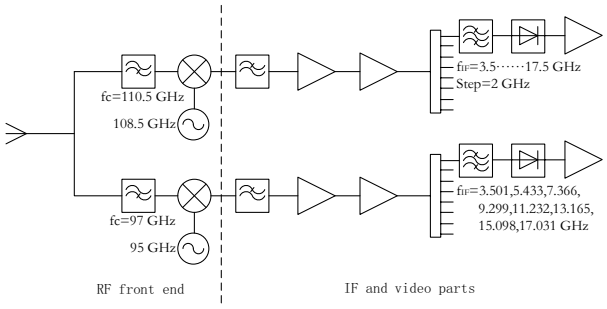

FIG. 1: Schematic of 16-channel heterodyne radiometer system.

mator and some other grating instruments used for plasma diagnostics. Electron cyclotron emission from plasma is diffracted at the entrance aperture, which is located at the focal point of the spherical collimating mirror M1. The grating disperses the plane wave reflected by M1 according to the grating equation. Then, the diffracted light is focused by the camera mirror M2 to the exit apertures. The spectral coverage of this system is very wide, and covers the frequency range of 90-250 GHz, which corresponds to a central toroidal magnetic field of 2-3.5 T in EAST. The frequency bandwidth of each channel is around 1.5 GHz, and it is determined by the spectral resolution of the system.

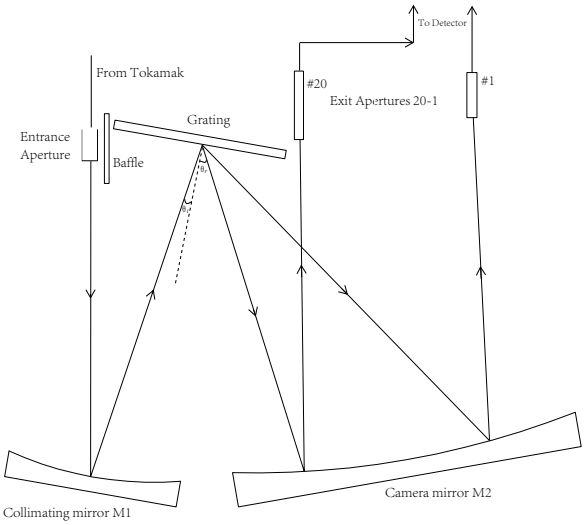

FIG. 2: Schematic of the 20-channel grating polychromator.

The emission from plasma is collected by a quasi-optical antenna, which is composed of an ellipsoidal mirror and a flat mirror. Then, the emission is introduced by the low-loss corrugated waveguides into the polychromator. The spot size of this quasi-optical system is around 5 cm, which is equivalently the poloidal resolution of the measurement.

2.3. 32-channel HRS

A 32-channel HRS is building under the collaboration with the University of California at Davis (UC Davis). The frequency range of the system is 104-168 GHz, and the RF frequencies are equally spaced every 2 GHz from 105 to 167 GHz. Each channel has an RF bandwidth of 500 MHz, and this corresponds to a smaller radial resolution than the present two ECE measurement instruments on HT-7 and EAST.

The RF front end of this system is different from the present system, and it is shown in Figure 3. ECE radiation from the plasma is optically separated into four beams using a combination of beamsplitters and mirrors. High density polyethelene (HDPE) lenses, specially designed for this application, focus each of the four beams into harmonic mixers, with LO signals supplied by dedicated Gunn oscillators. The position of each lens will be adjusted to form a beam waist in the vicinity of the ECE radiation layer for that receiver, thereby minimizing Doppler broadening of the emission layers. Rather than using waveguide filters to ensure that each mixer receives single sideband radation, dichroic plates are employed, serve as excellent high pass filters. The IF part is more or less the same as the present 16-channel HRS one, and this will not be described here.

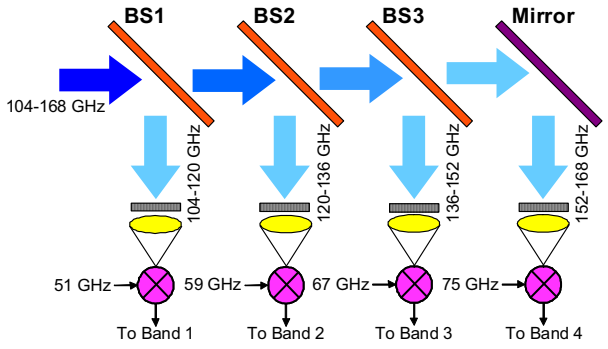

FIG. 3: The RF front end of the 32-channel heterodyne radiometer system.

2.4. Calibration

The relative calibration method is employed to obtain the relative coefficients for the 16-chanal HRS [11]. Two discharges of the same plasma parameters except the toroidal magnetic field, are needed for the relative calibration. The toroidal magnetic field of these two discharges is chosen so that the adjacent channels observers the almost same volume of plasma. Then the relative coefficient can be deduced from the relative intensity of the adjacent two channels. To obtain the absolute electron temperature, the value of the central channel is cross calibrated with the value deduced from the soft x ray diagnostic [14].

An in-situ absolute calibration system is currently being built, and the layout is shown in Figure 4. This calibration system will employ a Dicke [15] calibration technique that uses a chopped liquid nitrogen-cooled Eccosorb CV source/SiC hot source and a lock-in amplifier.

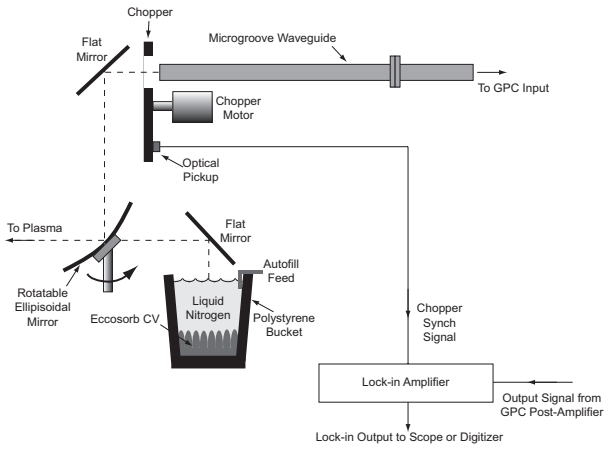

FIG. 4: The layout of the absolute calibration system.

3. RELATED PHYSICS

In the past few experimental campaigns, the second harmonic ECE in HT-7 and EAST has been measured. On one hand, the evolution of the electron temperature profile is deduced with the relative and cross calibration method. On the other hand, some related physics are performed based on the ECE measurement. Two examples of the related physics performed on HT-7 and EAST are introduced in the following subsections.

3.1. Electron heat transport

Electron heat diffusivity is inferred from the sawtooth propagation [16]. Perturbative method (time to peak method and fast Fourier transform method) and power balance method are separately used to deduce the electron heat diffusivity for different discharge conditions. The results obtained from time to peak method and fast Fourier transform method agree fairly well. The values deduced from the perturbative method is larger than the one from the power balance method by a factor of 2-10, and this phenomenon is explained by the non-linear behavior. Further researches employing the power modulation method will be performed on EAST, when ICRH or ECRH is prepared.

3.2. Anomalous doppler resonance (ADR) effect

An abrupt increase of the ECE intensity happens during the current ramp down in some discharges on HT-7 and EAST [17]. This phenomenon is explained by the ADR effect. Results from discharges of different plasma parameters show the existence of a threshold of ω_{pe}/ω_{ce} for triggering this phenomenon.

3.3. Flux surface reconstruction

2-D flux surface is reconstructed from the ECE measurements based on plasma rigid rotation which is confirmed by the Mirnov diagnostic [18]. With the reconstructed flux surface, the classical m/n=3/2 mode is identified during some discharges on HT-7.

4. CONCLUSIONS

Two ECE measurement instruments have been installed on HT-7 and EAST, and they are separately a 16-channel HRS and a 20-channel GPC. A 32-channel HRS is going to be installed on EAST, and it has a wide frequency range and better radial resolution.

With the relative and cross calibration method, the ECE measurement has provided the evolution of electron temperature profile. An absolute calibration system is being built now. Related researches based on ECE measurement have been performed on HT-7 and EAST.

5. ACKNOWLEDGEMENTS

The authors are grateful to Dr. Gary Taylor for the helpful discussion in the reconstruction of the 20-channel GPC on EAST. We also are grateful to Prof. N. C. Luhmann, Dr. Calvin W. Domier and X. Y. Kong in the 32-channel HRS, Dr. Perry Phillips and Dr. Huang He for the support in the 16-channel HRS.

References

[1] Wu S, EAST Team. 2007, Fusion Engineering and Design, 82:463–471.

[2] Li J G, Wan B N, Mao J S, et al. 2000, Plasma Phys. Control. Fusion, 42:135–146.

[3] Lichtenberg A J, Sesnic S, Trivelpiece A W. 1964, Phys. Rev. Lett., 13:387–388.

[4] TFR group. 1975, in Controlled Fusion and Plasma Physics (Proc. 7th Europ. Conf. Lausanne, 1975), 1:14b.

[5] Hutchinson I H, Komm D S. 1977, Nucl. Fusion, 17:1077–1084.

[6] Kato K, Hutchinson I H. 1986, Phys. Rev. Lett., 56:340–343.

[7] Kato K, Hutchinson I H. 1987, Phys. Fluids, 30:3809–3820.

[8] Sozzi C, Luna E D L, Farina D, et al. 2008, Buring plasma diagnostics. 73–80.

[9] Ling B L, Xu Y C, Wan B N. 2005, Journal of microwaves, 21:66–69 (in Chinese).

[10] Ti A, Ling B L, Fei Q S, et al. 2007, Int. J. Infrared Milli. Waves, 28:243–249.

[11] Sajjad S, Gao X, Ling B, et al. 2008, Meas. Sci. Technol., 19:075701.

[12] Cavallo A, Cutler R C, McCarthy M P. 1988, Rev. Sci. Instrum., 59:889–894.

[13] Liu Y, Li E Z, Ling B L, et al. 2010, Fusion Sci. and Technol., (Accepted).

[14] Xu P, Lin S Y, Hu L Q, et al. 2009, Plasma Sci. and Technol., 11:468–471.

[15] Dicke R H. 1946, Rev. Sci. Instrum., 17:268–275.

[16] Du Q, Ling B L, Ti A, et al. 2008, Plasma Sci. and Technol., 10:681–684.

[17] Li E Z, Hu L Q, Ling B L, et al. 2010, Nuclear Instruments and Methods in Physics Research A, 621:566–569.

[18] Li E Z, Hu L Q, Ling B L, et al. 2010, Rev. Sci. Instru., 81:073506.

Study of SOL width in Ohmic and LHCD heating Double-Null divertor plasmas on EAST tokamak

L. Wang[1*], G. S. Xu[1], J. F. Chang[1], W. Zhang[1], N. Yan[1], S. Y. Ding[1], S. C. Liu[1], T. F. Ming[1], P. Liu[1], H. Q. Wang[1], M. Jiang[1], H. Xiong[1], B. N. Wan[1], X. Gao[1], H. Y. Guo[1,2], Z. W. Wu[1], S. Z. Zhu[1], G. N. Luo[1], V. Naulin[3], J. Juul Rasmussen[3], A. H. Nielsen[3]

[1] *Institute of Plasma Physics, Chinese Academy of Sciences, Hefei 230031, China*

[2] *Tri Alpha Energy, P.O. Box 7010, Rancho Santa Margarita, CA 92688, USA*

[3] *Association Euratom-Risφ DTU, DK-4000 Roskilde, Denmark*

Abstract: In this work, the edge plasma profiles in Ohmic and LHCD heating discharges on EAST are presented and comparisons are made with predictions from theoretical models of SOL width scaling. The edge plasma parameters are diagnosed by divertor triple probe diagnostic system and fast reciprocating probes at the outer mid-plane. The experimental results show that the SOL width of DN divertor plasmas in EAST appear to exhibit a negative dependence on the power crossing the separatrix (P_{SOL}), consistent with collisional SOL scalings, *i.e.,* $\Delta_h \propto P_{SOL}^{-2/5}$ or $P_{SOL}^{-4/17}$, with perpendicular thermal diffusivity $\chi_\perp \propto T^{1/2}/n$, as observed on JET and Alcator C-Mod[1, 2]. This work will provide useful information for the extrapolation to ITER SOL width scaling for power deposition.

I. INTRODUCTION

In tokamak plasmas, the width of the scrap-off layer (SOL) characterizes the impacted target area, and thus affects the peak power load onto the divertor plates or limiters[3–5]. The SOL width is determined by the competition between cross-field transport and parallel transport along magnetic field[6–8]. The power that heats a tokamak plasma must ultimately be exhausted from the confinement system. The radiation fraction is spread over the surrounding walls and does not pose a serious problem, while the remainder is transported across the separatrix and hence goes into the divertor or limiter targets, where the energy is deposited. This impacts choices of target material, shape, and the upper limit of the heat flux to avoid material damage. Therefore, the investigation on the heat flux in SOL is of fundamental importance. Even in ITER, the divertor target lifetime, which is governed by the peak heat flux and radial heat flux width of SOL in steady-state operation, will be a significant issue. At present, the SOL width scaling has been carried on a range of divertor tokamaks, such as JET, Alcator C-Mod, ASDEX-U, MAST and so on[1, 2, 7, 9–11]. However, a thorough understanding of the transport mechanisms that set SOL width remains a problem.

The Experimental Advanced Superconducting Tokamak (EAST) is a non-circular advanced steady-state experimental device with major radius R of 1.75m and minor radius a of 0.4m. It can realize the limiter and three divertor configurations of plasma, including the lower-single-null (LSN), the upper-single-null (USN) and the double-null (DN) divertor geometry. In the last EAST campaign, DN divertor geometric experiments were performed under Ohmic, Lower Hybrid Current Drive (LHCD) and Ion Cyclotron Range Frequency (ICRF) heating techniques. In this paper, the edge plasma parameter profiles in Ohmic and LHCD heating experiments are presented and compared with the theoretical models of SOL width scalings. The edge plasma parameters are diagnosed by divertor triple probe diagnostic system and fast reciprocating probes at the outer mid-plane.

*Email: wliang@ipp.ac.cn

II. ANALYTIC TRANSPORT MODEL AND WIDTH SCALINGS OF SOL

The importance of SOL and divertor plasmas for core plasma confinement has been recognized and the basic process in the SOL and divertor region was widely studied. Simple models for the tokamak SOL are usually based on a balance of parallel (along the SOL flux tube to the divetor target) and perpendicular transport (from the plasma core into the SOL) on the open field lines. The models are distinguished by the SOL collisionality, which determines the parallel transport, and the choice of cross-field diffusivity. An (upstream) SOL collisionality parameter is defined[12]:

$$\begin{aligned}\nu^*_{SOL} &\equiv L_\parallel/\lambda_{mfp} \\ &\approx 10^{-16} n_{eu} L_\parallel / T^2_{eu}\ ,\end{aligned} \tag{1}$$

where λ_{mfp} is the electron-electron collisional mean free path, $L_\parallel = \pi R q_{95}/2\ (m)$ is the parallel connection length for DN diveror geometry with q_{95} the safety factor at the 95% flux surface. The upstream n_{eu} is in units of m^{-3} and T_{eu} in eV.

In the collisional SOL ($\nu^*_{SOL} \gg 1$), parallel transport is dominated by the collisional diffusion and can be treated by classical Spitzer-Härm theory[13]

$$q_\parallel = -n\chi_{\parallel 0} T^{5/2} \nabla_\parallel T, \tag{2}$$

where $q_\parallel$ is the parallel heat flux density along the SOL, $\chi_\parallel = \chi_{\parallel 0} T^{5/2}$ is the parallel heat diffusivity, n the electron density and T the electron temperature. On the other hand, in the collisionless case ($\nu^*_{SOL} <\sim 1$), the parallel transport results from the heat streaming and $\chi_\parallel \propto L_\parallel T^{1/2}$. Similarly, the cross-field heat flux

$$q_\perp = -n\chi_\perp \nabla_\perp T \approx n\chi_\perp T_b/\lambda_T \tag{3}$$

with $\chi_\perp$ the perpendicular heat diffusivity, T_b the mid-plane separatrix temperature and λ_T the radial gradient length of the temperature. And different models of $\chi_\perp$ are investigated in developing SOL width scalings in terms of key operating parameters, such as q_{95}, $\bar{n}_e$ and P_{SOL} (the power crossing the separatrix into SOL from core plasma)[2, 3, 6].

$$P_{SOL} = q_\parallel A_\parallel = q_\perp A_\perp, \tag{4}$$

where $A_\parallel$ is the projected area perpendicular to the field line of an annulus width Δ_h at the outer mid-plane and $A_\perp$ is the surface area of the plasma boundary. Δ_h is the SOL heat flux width. In the large aspect ratio ($a \ll R$) of circular cross-section approximation, $A_\perp = 2\pi R \cdot 2\pi a = 4\pi^2 Ra$ and $A_\parallel = 2\pi(R+a)\Delta_h \sin(\alpha) \approx 2\pi R\Delta_h B_p/B$, where α is the field line angle at the outer mid-plane, B_p and B are the polodial and total fields respectively. Making the simplifying assumption $\nabla_\parallel T \approx T/L_\parallel$ with Eq. (2), thus the parallel and perpendicular energy balance equation of Eq. (4) gives

$$-n\chi_\parallel T/L_\parallel = \frac{B}{B_p}\frac{P_{SOL}}{2\pi R\Delta_h}, \tag{5}$$

$$n\chi_\perp T/\lambda_T = \frac{P_{SOL}}{4\pi^2 Ra}. \tag{6}$$

Taking $q \approx aB/RB_p$ and $L_\parallel \propto Rq_{95}$ into account, Eqs (5) and (6) yield $\Delta_h \propto \sqrt{\chi_\perp L_\parallel^2 / \chi_\parallel}$. Thus one can extimate the SOL width as

$$\Delta_h \propto L_\parallel \sqrt{\chi_\perp n / T^{5/2}} \tag{7}$$

in the collisional SOL and

$$\Delta_h \propto \sqrt{\chi_\perp L_\parallel / T^{1/2}} \tag{8}$$

in the collisionless case.

However, the radial diffusivity $\chi_\perp$ is anomalous and is crucial for modelling the SOL in divertor plasmas. There are considerable theoretical models for the scaling of $\chi_\perp$ and thus the SOL width Δ_h. In the scalings of SOL width presented by Connor and Counsell[1, 2], the models that better fit both the experimental data in the collisional SOL of JET and Alactor C-Mod all relate cross-field diffusion to $\chi_\perp \propto T^{1/2}/n$. These models of perpendicular

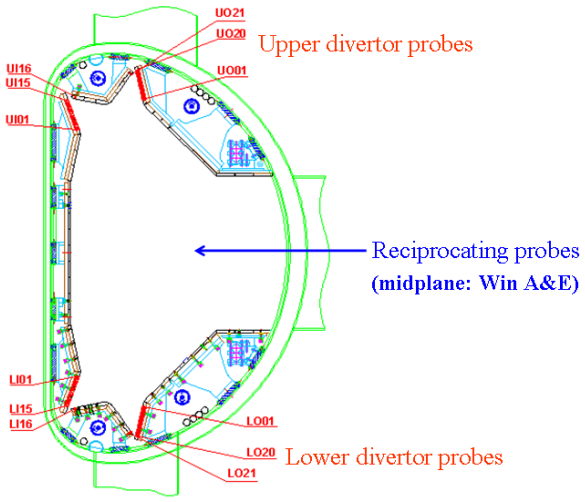

FIG. 1: The poloidal view of divertor and mid-plane reciprocating probes of EAST.

thermal diffusivity yield a strong negative dependence of collisional SOL width on the power crossing the separatrix, that is $\Delta_h \propto P_{SOL}^{-2/5}$ or $P_{SOL}^{-4/17}$. However, in the collisionless SOL of COMPASS-D tokamak, most of the better fitting scalings exhibit a positive dependence on P_{SOL}. And the Scrap-off Layers of EAST DN plasmas shown in this work are collisional, both in Ohmic and LHCD experiments (see Section 3).

III. EXPERIMENTS AND DISCUSSION

In the divertor regions of EAST tokamak, 222 probe tips are embedded in the lower and upper inboard, outboard and dome plates, which consist into the divertor triple probe diagnostic system on EAST. These 222 tips are assembled into 74 groups of poloidal triple probes with spatial resolution of 10-15mm at the target surfaces, and 4 groups of which are domed ones (UI16, UO21, LI16 and LO21). Moreover, the three probes in each group are spaced toroidally to ensure the plasma uniformity. Figure 1 shows the poloidal layout of the divertor probes in the EAST chamber with UI01-15 locating at the upper inner targets, UO01-20 locating at the upper outer targets, LI01-15 locating at the lower inner targets and LO01-20 locating at the lower outer targets respectively. Using divertor probes it was possible to derive an accurate over a much wider range of discharge conditions than would have been possible using the fast reciprocating probes at the outer mid-plane, which is also shown in Fig. 1 and can be employed to obtain edge parameters of upstream plasma.

The plasma of Shot #22942 is of DN divertor configuration with normal $B = 2T$ ($B \times \nabla B$ downwards), and the time evolution of the discharge paramaters are shown in Figure 2. The discharge gas is deuterium. The dashed

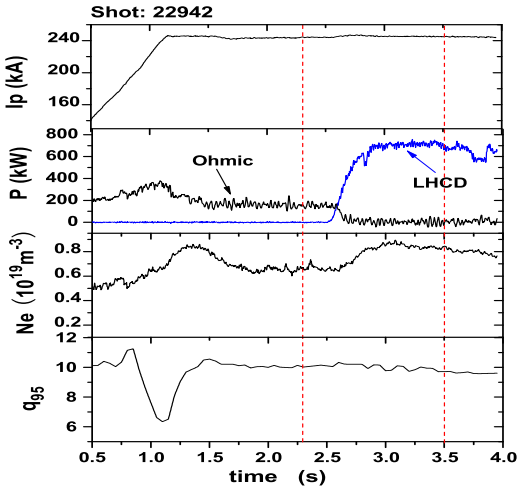

FIG. 2: Time evolution of key parameters in the discharge of Shot #22942.

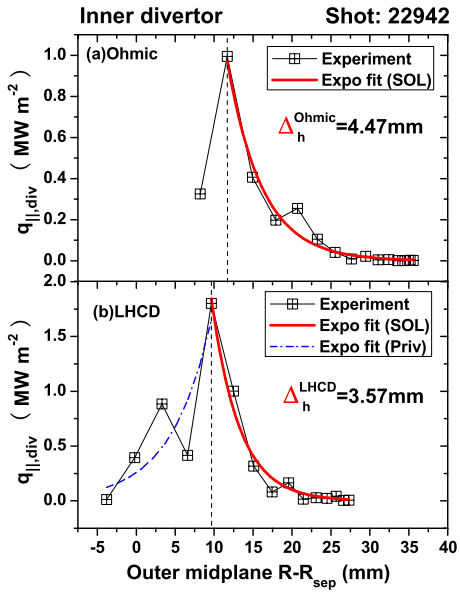

FIG. 3: Profiles of parallel power flux at the inner divertor target, mapped to the outer mid-plane with EFIT, in (a) Ohmic and (b) LHCD-driven discharges. The bounded crosses are experimental data and the bold curves are exponential fittings.

vertical lines indicate the time with upsteam probe measurements. The heating power increased greatly ($P_{LHCD}/P_{Ohmic} \approx 4.4$), while the average line density and the safety factor at the 95% flux surface changes little ($Ne_{_{LHCD}}/Ne_{_{Ohmic}} \approx 1.2$, $q_{95_{LHCD}}/q_{95_{Ohmic}} \approx 1$). Taking the radiation part of the heating power into account, the power crossing the separatrix of LHCD is also greatly enhanced compared with that of Ohmic discharge.

Figures 3 and 4 compare the profiles of parallel heat flux of Shot #22942, mapped to the outer mid-plane with EFIT magnetic equilibrium reconstruction codes, between Ohmic and LHCD heating plasmas with the double-null (DN) divertor configuration, at inner and outer divertor plates, respectively. The scattering points represent the experimental data, and the exponential fittings to the profiles are illustrated with bold lines. $q_{\|,div} = n_t c_{st} \gamma T_t$[3, 4], where γ is the sheath heat transmission coefficient approximately $\gamma = 7$, n_t and $c_{st} = (2T_t/m_i)^{1/2}$ (assuming $T_i = T_e$) are the density and ion acoustic speed at the target plate and m_i is the mass of an ion.

It is shown that the SOL width of LHCD plasma is narrower than that of Ohmic heating, *i.e.*, the SOL width decreases with the power crossing the separatrix, both at inner and outer divertor targets. It is to be noted that the strike points mapped to the outer mid-plane have an obvious shift from the sepatrix. This results from the different precision of EFIT code and divertor probes on EAST at present. Figure 5 displays the discrepancy of UO strike point between EFIT code and divertor probes at 3.5s, a magnification of the outer mid-plane region is shown inset.

As known, the plasma of downstream SOL has strong relationship with mid-plane SOL[3, 4, 14]. Figure 6 illustrates the profiles of upstream electron pressure measured by fast reciprocating probes at the phases of the

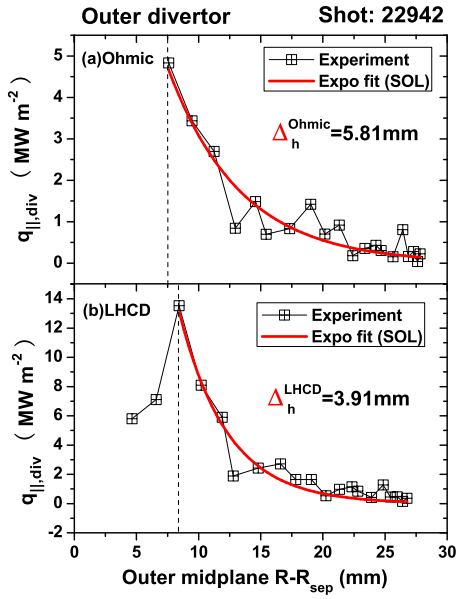

FIG. 4: Profiles of parallel power flux at the outer divertor target, mapped to the outer mid-plane with EFIT, in (a) Ohmic and (b) LHCD-driven discharges. The bounded crosses are experimental data and the bold curves are exponential fittings.

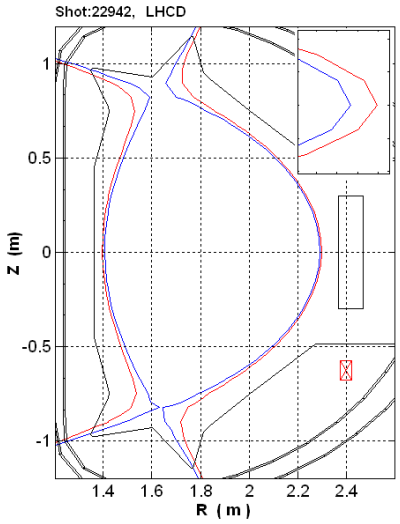

FIG. 5: The discrepancy of UO strike point between EFIT codes and divertor probes at 3.5s, inset is a magnification of the outer mid-plane region.

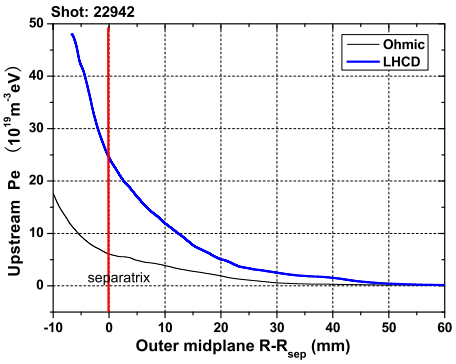

FIG. 6: Comparison of upstream electron pressure profiles between Ohmic and LHCD plasmas.

two different heating mechanisms. We can learn that the decay length of electron pressure at upstream SOL is also narrower in LHCD plasma than that of Ohmic heating plasma. This result is consistent with the divertor data shown above.

As described in Section 2, the collisionality in the SOL is an essential parameter for the SOL width scaling. Figure 7 compares the collision frequency of Ohmic and LHCD heating plasmas of Shot #22942, which are calculated from the data of upstream reciprocating probes. The results show that both Ohmic and LHCD plasmas exhibit collisional SOL ($\nu^*_{SOL} \gg 1$), as in JET and Alcator C-Mod divertor plasmas[1, 2]. Therefore, our investigation qualitatively confirmed the SOL width scalings for power in the collisional SOL. The collisional SOL width has a negative dependence on the power crossing the separatrix.

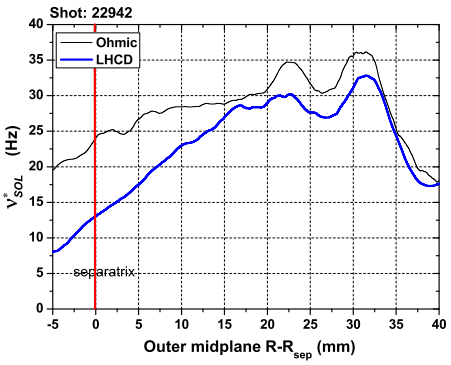

FIG. 7: The radial profiles of electron-electron collision rate in Ohmic and LHCD SOL.

IV. CONCLUSIONS

The width of Scrap-off-Layer (SOL) in Ohmic and LHCD heating double-null divertor plasmas on EAST tokamak is investigated experimentally. The theoretical models of SOL transport and width scalings are presented, which reveal that the SOL width is determined by a nbalance between the perpendicular transport and the one parallel to the field lines. The experimental results show that the SOL width of EAST DN divertor plasma exhibit an inverse dependence on the power crossing the separatrix (P_{SOL}), consistent with the scaling models of collisional SOL ($\Delta_h \propto P_{SOL}^{-2/5}$ or $P_{SOL}^{-4/17}$). These models are all associated with perpendicular thermal diffusivity $\chi_\perp \propto T^{1/2}/n$. Both the measurements carried out in Ohmic and LHCD plasmas of this work are in collisional SOL.

Acknowledgements

This work was supported by National Nature Science Foundation of China with grant No. 11075181 and National Basic Research Program of China with grant No. 2010GB104001.

[1] Connor J W, Counsell G F, et al. 1999, Nucl. Fusion, 39: 169
[2] Counsell G F, Connor J W, et al. 1999, J. Nucl. Mater., 266-299: 91
[3] Stangeby P C, 2000, "The Plasma Boundary of Magnetic Fusion Devices", IOP Publishing Ltd.
[4] Pitcher C S, Stangeby P C, 1997, Plasma Phys. Control. Fusion, 39: 779
[5] Loarte A, Lipschultz B, et al. 2007, Nucl. Fusion, 47: S203
[6] Itoh S-I, Itoh K, 1994, Plasma Phys. Control. Fusion, 36: 1845
[7] Ahn J W, Counsell G F, Kirk A, 2006, Plasma Phys. Control.

Fusion, 48: 1077
[8] ITER Physics Expert Group on Divertor, et al. 1999, Nucl. Fusion, 39: 2391
[9] Loarte A, Bosch S, Chankin A, et al. 1999, J. Nucl. Mater., 266-299: 587
[10] Pitcher C S, Herrmann A, et al. 1997, Plasma Phys. Control. Fusion, 39:1129
[11] McCormick K, Asakura N, et al. 1999, J. Nucl. Mater., 266-269: 99
[12] Erents S K, Stangeby P C, LaBombard B, et al. 2000, Nucl. Fusion, 40: 295
[13] Spitzer L, Härm R, 1953, Phys. Rev. 89: 977
[14] Ahn J W, Boedo J A, et al. 2008, Phys. Plasmas, 15: 122507

Asphericalizing the Light Collection Mirror for the 200-Point Thomson Scattering Diagnostic Installed on the Large Helical Device

Kazumichi Narihara and Hiroshi Hayashi

National Institute for Fusion Science, Toki, 592-5292, Japan

Abstract This paper shows numerically that it is possible to make the image of a laser beam over 2.5 m distance, formed by the spherical multi-segment mirror installed on the Large Helical Device, twice sharper by suitably adjusting the inclination of each segment mirror, which is equivalent to making the mirror surface aspherical. This will further enhance the attractiveness of a mirror-based Thomson scattering system.

narihara@nifs.ac.jp

Keywords: Thomson scattering, LHD, aspherical mirror

PACS: 52.70.Kz

1. Introduction

Thomson scattering (TS) diagnostic is a commonly used method for measuring electron temperature (T_e) and density (n_e) profiles in fusion plasma experiments. At present, three types of TS are under operation in the world: LIDAR on JET [1], TV-TS on TEXTOR [2] and YAG-TS on many fusion plasma devices [3-6]. The LIDAR seems to be the ultimate candidate for the future large fusion devices like ITER [7], but with the current technology it lacks necessary spatial resolution; hence a YAG-TS being considered for measuring the edge region, where a finer spatial resolution is needed [7]. For smaller plasma devices, the LIDAR is not suitable for the same reason, and hence TV- and YAG-TS are still necessary for plasma experiments. The spatial resolution of the LIDAR is determined by the time response of a light detector through the light-cone relation, $x=ct$, and hence

the imaging performance is not severely required for the backward light-collection optics based on a mirror system [1]. On the other hand, for TV- and YAG-TS, the imaging performance of light collection optics for an extended object (laser beam across the entire plasma) has significant effects on the spatial resolution, light collection efficiency and the accuracy of the deduced n_e data. For this reason, the light-collection optics for such TS usually adopts a lens system, which has much better imaging performance than a mirror system. However, as fusion devices become larger and the confined plasma becomes hotter, it is required for light-collection-optics to be large in size, to be resistant to neutron radiation and to be free from color aberration for a wider wavelength band, which is much harder to meet for a lens system than a mirror system. With these considerations in mind, we have for the first time developed a YAG-TS system based on a spherical mirror with a reasonable spatial resolution for the large helical device (LHD) [6,8,9]. A multi-segment spherical mirror (assembled area 1.5 m ×1.8 m and radius of curvature ρ= 4.5m) with the center of the curvature located nearly at the center of the view window forms an image of the laser beam of diameter less than 4 mm running along the major radius 2.25m ≦R≦ 5m onto the ends of the arrayed 200 optical fibers of 2 mm in diameter cut at 60°. The LHD-TS, thus configured, has been yielding fairly good *Te* profiles but the n_e data sometimes suffers a systematic error probably because of slight misalignment between the image of laser beam and the end-surface of arrayed optical fibers, both having the almost same transverse size[6]. If the image size of the laser beam, which is largely determined by the spherical aberration, can be reduced by some means, it will be greatly helpful for solving this problem and will further enhance the attractiveness of a mirror-based TS. In this paper, we show numerically that it can really be done by finely adjusting the inclination of each hexagonal small mirror, which is equivalent to making the mirror surface aspherical.

2. Light Collection Optics of The LHD-TS

Figure 1 schematically illustrates the light collection optics of the LHD-TS [6]. The front view of the 4O-port is shown in an inset. Key ingredients are: the laser beam, the view window, the light collection mirror and the fiber array. We setup a Cartesian coordinates (x,y,z) measured in mm unit

with its origin at the center of LHD so that the z-axis coincides with the major radius along which the laser beam runs inwards. The x- and y- axes are setup so that the center of the view window lies on the x=0 plane. As shown in the inset of Fig. 1, a rectangular view window of the effective aperture size of 580×330 mm^2 is located at the "5-oclock" position of the 4O port, the center of which has coordinate $\mathbf{R}_{win}$=(0,870,7356). The light collection mirror is composed of 11 × 12=132 hexagonal mirrors of 88 mm side length and ρ=4500 mm radius of curvature mounted on a spherical concave frame with adjustable screws. The assembled mirror size is ~1.5 m × 1.8 m with the zigzag shaped boundary as shown in Fig. 2. The multi-segment mirror, thus formed, is set so that its longer centerline lies on the x=0 plane with the common center of curvature being at $\mathbf{R}_{cc}$= (0,870,7366). As representative scattering points, we choose 12 points along the laser beam in the region 2250 ≤ R ≤ 5000 with a 250 interval, which are denoted as {$\mathbf{R}_{sct}$ (m); 0≤ m≤ 11}. From each scattering point $\mathbf{R}_{sct}$ (m) we can see through the window a rectangular region on the multi-segment mirror, which can be regarded as a mirror (m-mirror) as shown in Fig. 2. One can note that the different scattering points share largely the same hexagonal mirrors to form their images. The optical axis of the m-mirror is the line passing $\mathbf{R}_{sct}$ (m) and $\mathbf{R}_{cc}$ and its intersection with the m-mirror surface defines the vertex position $\mathbf{R}_{ver}$ (m). Since each scattering point lies on the optical axis, the corresponding image is free from the coma and astigmatism aberrations. The focal point of the m-th scattering point $\mathbf{R}_{focal}$(m) is defined as the position where the spot size formed by the m-mirror is smallest. The focal points {$\mathbf{R}_{focal}$(m);m=0,11} lie on a slightly curved line. The tips of the arrayed fiber are set on the image plane $\mathbf{P}_{image}$ that gives the best-focused image of laser beam. $\mathbf{P}_{image}$ is specified by a point **p**=(0,1129, 8954) on it and its normal vector **n**=(0, 0.94, 0.32). Let rays, starting from $\mathbf{R}_{sct}$ (m) and being reflected at 6 points on an (i,j)-mirror, intersect with the $\mathbf{P}_{image}$ plane at $\mathbf{R}_{image}$(i,j,k,m). The ensemble of points {$\mathbf{R}_{image}$(i,j,k,m)} on the image plane, spot diagrams, for the scattering points 0≤ m ≤ 11thus calculated are shown in Fig. 3. The spots disperse because of spherical aberration plus blurring due to defocusing for some points. In taking into account the finite size of the laser beam, the real image sizes are somewhat larger than those given in Fig.3. Except for the both end-points (R=2250 and R=5000), which are outside of the plasma region, the image of the laser beam is within

the core of the fiber if the optical setting is precise and the laser beam size is small enough.

3. Asphericalization

The spot diagram $\{\mathbf{R}_{image}(i,j,k,6)\}$, for example, is shown with a magnified scale in Fig. 4. The image is composed of 279 points, of which 6 points are formed by the (6,5)-mirror and are marked by square-symbol. As can be noticed, the (6,5)-mirror forms groups of spots localized in space. This suggests us that if we suitably adjust the inclination of the hexagonal mirrors, the spot size will become much smaller. Indeed, for one scattering position, e.g., m=6, it is possible to adjust the inclination of each segment mirror so that its corresponding image points be within 0.3 mm in diameter. This adjustment also reduces the spot sizes of the adjacent scattering points, but it enlarges the image sizes of the other scattering points. Then the problem is to find a combination of mirror's inclination that gives an overall high imaging performance for all the involved scattering points. To this end, we calculate the image $\mathbf{R}_{image}(\delta x, \delta y, i, j, k, m)$ of $\mathbf{R}_{sct}(m)$ formed on the plane $\mathbf{P}_{image}$ by the k-th point on the (i,j)-mirror with its center of the curvature shifted by $(0, \delta x, \delta y)$. The shift δx and δy are scanned from -2 mm to 2 mm with 0.04 mm step. From the set of data $\{\mathbf{R}_{image}(\delta x, \delta y, i, j, k, m)\}$, we first calculate the variance of the image points around the reference point $\mathbf{R}_{ref}(m)$:

$$Var(\delta x, \delta y, i, j, m) = \frac{1}{6}\sum_{k=1}^{6} |\mathbf{R}_{image}(\delta x, \delta y, i, j, k, m) - \mathbf{R}_{ref}(m)|^2 \qquad (1)$$

For a convenience, we choose as $\mathbf{R}_{ref}(m)$ the center of "gravity" of the m-th image formed by the spherical m-mirror (Fig.3). The smaller $Var(\delta x, \delta y, i, j, m)$ will result in a better m-th image. Since we are interested in the overall image performance for all the involved images, the estimate function to be minimized is the summation of $Var(\delta x, \delta y, i, j, m)$ over m scattering points that can be seen through the view window from the (i,j) mirror:

$$H(\delta x, \delta y, i, j) = \sum_{m \in Window} Var(\delta x, \delta y, i, j, m) \quad (2)$$

where 'm ∈Window' means that the m-th scattering point can be seen from the (i,j)-mirror through the view window. The contour plot of $H(\delta x, \delta y, 4, 5)$ in $(\delta x, \delta y)$-space is shown in Fig.5 as an example, which indicates that the best overall imaging performance is obtained when the mirror is inclined so that the center of curvature is shifted by $(\delta x, \delta y)=(0.3, -0.05)$.

Similarly, the inclinations of all mirrors are optimized independently of other mirrors with the result shown by arrow vectors in Fig. 6. The maximum magnitude of deviation $|(\delta x, \delta y)|$ is 1.5 mm. The ensemble of image points, spot diagram, formed by all the involved hexagonal mirrors with the inclination thus optimized are shown in Fig. 7 for the 12 representative scattering points. We can see that this asphericalization reduces the spot sizes appreciably. To be quantitative, we introduce a distribution function defined as

$$F(r) = \frac{\#\text{ of image points outside the circle of radius } r}{\#\text{ of total image points}} \quad (3)$$

The distribution functions for the 12 scattering points with/without the asphericalization are shown in Fig.8. These functions show that the asphericalization improves the overall imaging performance more than twice.

4 Discussions

We have showed that the overall imaging performance can be improved, in principle, more than twice by adjusting the inclination of each hexagonal mirror. In applying this practically, however, several problems seem to arise. The first problem is how to adjust the inclination of the mirrors with the precision of sub-mr, that is, setting $\mathbf{R}_{cc}$ with a sub-mm precision at 4500mm distance ahead. A solution to this problem is to use the same method as that used for adjusting the center of curvature at a fixed point [10]. We set an optical fiber of 0.2 mm in diameter with numerical aperture of 0.37 and a thin lens-less CCD camera in the vicinity of the center of the curvature $\mathbf{R}_{cc}$ so that the image of the end surface of the illuminating fiber is clearly formed by a hexagonal mirror at the center of the

CCD plane. The shift in $\mathbf{R}_{cc}$ by (δx,□ δy) results in the shift in CCD image by 2(δx_c,□ δy_c). We cover with paper sheets all hexagonal mirrors except one to be adjusted. Watching the image on the CCD, which is formed by the uncovered mirror, we rotate two adjust screws so that the image point be on the calculated point. Thus we can make the mirror surface's inclination as we want. The second problem is how to set the tip of the arrayed fiber on the image plane $\mathbf{P}_{image}$. In the present setup, it is difficult to set the fiber holder with the required precision of sub-mm. We envision searching the position (**p**) and orientation (**n**) of the $\mathbf{P}_{image}$ by translating the fiber holder while recording Raman scattered signals, which we call a "sweep-profile". The position (**p**) and orientation (**n**) of the fiber holder are progressively varied so that the sweep-profile for all scattering points become narrowest. The third problem is the stability of the mirror's inclination. To examine this, we intentionally add random errors $\{\delta\mathbf{R}_{cc}\}$ to the optimized setting $\{\mathbf{R}_{cc}(\delta x,□\delta y,i,j)\}$ and calculate the image points. The result shows that $\{\delta\mathbf{R}_{cc}\}$ of merely 0.3 mm r.m.s is large enough to degrade the imaging performance appreciably, implying that a more ridged and precise mirror holder should be newly fabricated.

In this paper, we considered to asphericalize the mirror surface by adjusting the inclination of each hexagonal mirror. Likewise, it may be possible to optimize the surface shape of a solid mirror.

Acknowlegements

This work was supported by the LHD project (NIFS09ULHH502) and by the JSPS-CAS Core-University program in the field of 'Plasma and Nuclear Fusion'.

References

1. Salzmann H, Bundgaard J, Gradd A, Gauers C, et al. 1988, Rev. Sci. Instrum., 59: 1451
2. Barth C J, Meiden H J v d , Oyevaar T, Cardozo N J L. 2001, Rev. Sci. Instrum., 72: 1138
3. Murmann H, Götsch S, Röhr H, Saltzman H, Steuer K H. 1992, Rev. Sci. Instrum., 63: 49414
4. Carlstrom T N, Campbell G L, DeBoo J C, Evanko R. 1992, Rev. Sci. Instrum., 63: 49015
5. LeBlanc B P, Bell R E, Johnson D W, Hoffman D E, *et al*. 2003, Rev. Sci. Instrum., 74: 1659
6. Narihara K, Yamada I, Hayashi H, Yamauchi K. 2001, Rev. Sci. Instrum., 72: 1122
7. Donné A J H, Costley A E, Barnsley R, *et al*. 2007, Nuclear Fusion, 47: S337
8. Narihara K, Yamauchi K, Yamada I, Minami T, *et al*. 1997, Fusion Eng. Des., 34-35: 67
9. Narihara K, Minami T, Yamada I , Yamauchi K. 1995, Rev. Sci. Instrum., 66: 4607
10. Narihara K, Yamada I, Hayashi H, Yamauchi K. 2004, Rev. Sci. Instrum., 75: 3878

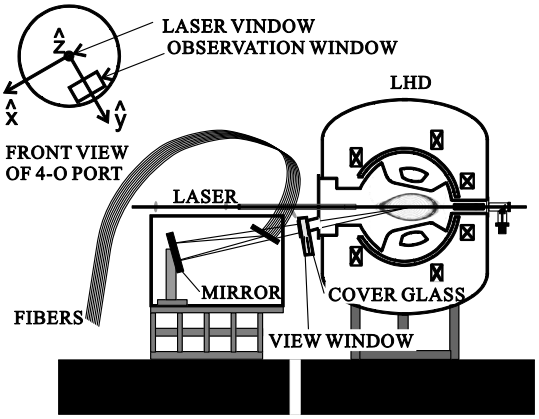

Fig. 1. Light collection optics of the Thomson scattering system installed on LHD. Front view of 4O-port is shown in an inset.

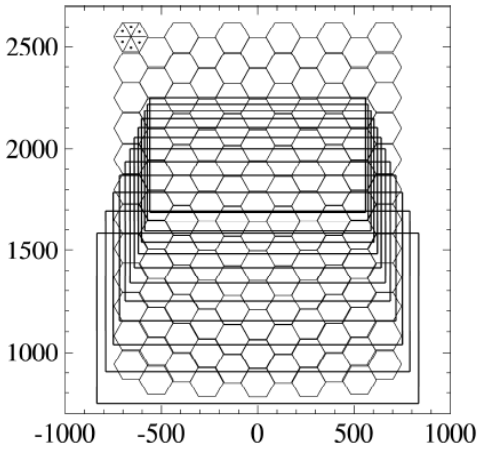

Fig. 2. Front view of the assembled multi-segment mirror composed of 132 hexagonal mirrors. The regions that can be seen through the view window from the 12 representative scattering points are indicated by rectangles. Reflection points on a hexagonal mirror used for calculating spot diagrams are shown on the upper-left mirror.

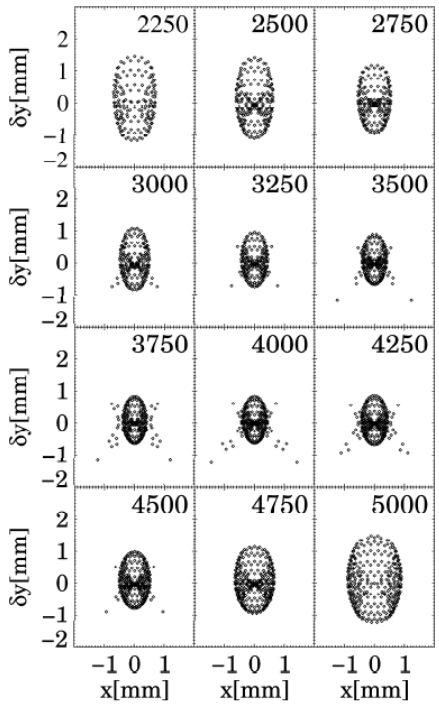

Fig. 3. Spot diagrams on the image plane formed by the spherical multi-segment mirror for the 12 scattering points.

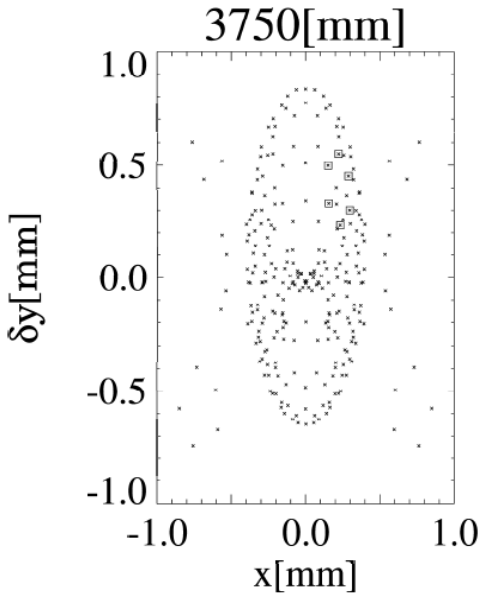

Fig. 4. Magnified spot diagram for the R=3750 scattering point. The image-points formed by the (6,5)-mirror are marked by square-symbol.

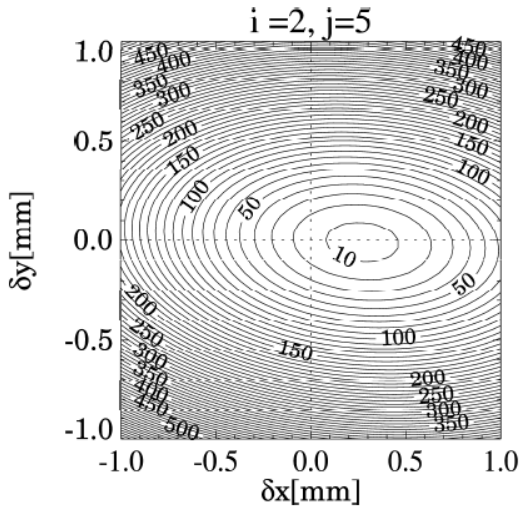

Fig. 5. Contour plot of $H(\delta x,\delta y,2,5)$ in the $(\delta x,\delta y)$-plane.

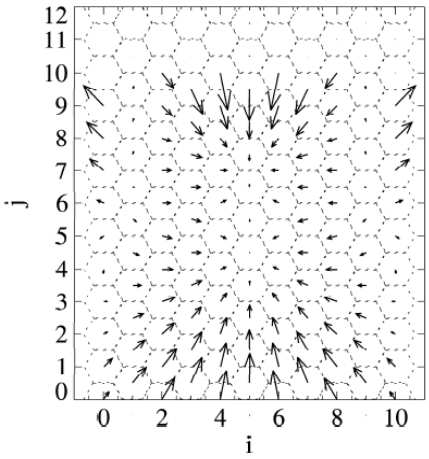

Fig. 6. Distribution of the shift vectors (δx, δy) that gives the overall best imaging performance.

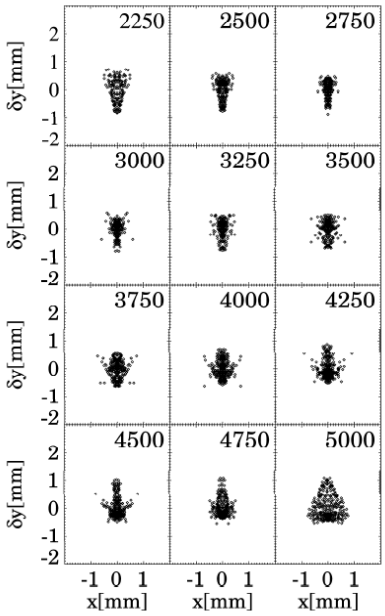

Fig. 7. Spot diagrams obtained by the multi-segment mirror with each mirror's inclination adjusted as shown in Fig.6

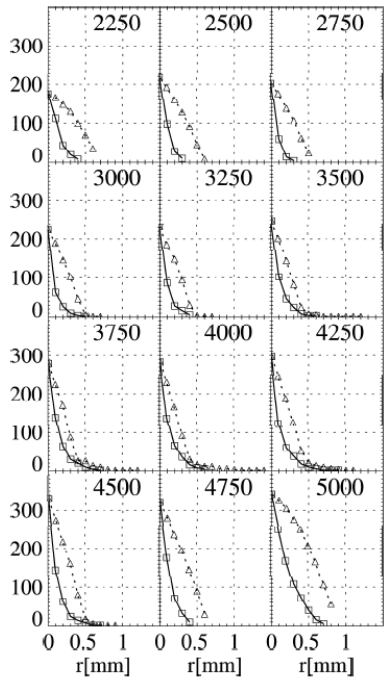

Fig. 8. Distribution functions for the spot-diagrams shown in Fig. 3 (dotted lines) and in Fig. 7 (solid lines), which compare the imaging performance of spherical and aspherical mirrors.

Potential measurement with Heavy Ion Beam Probe in the Large Helical Device

A. Shimizu, T. Ido, M. Nishiura[1)], S. Kato, M. Nakamura, H. Nakano,
M. Yokoyama, K. Toi, Y. Yoshimura, H. Takahashi, S. Kubo, T. Shimozuma,
H. Igami, N. Tamura, LHD Group,

National Institute for Fusion Science, 322-6, Oroshi, Toki, Gifu, 509-5292, Japan
[1)]Graduated School of Engineering, Nagoya University, Furo-cho, 464-8601, Japan

Abstract:
The radial profile of potential in the core region of Large Helical Device (LHD) was measured with Heavy Ion Beam Probe (HIBP). The temporal evolution of radial potential profile was measured and the radial profile of radial electric field was estimated from the differential of the fitting function to experimental data. E_r profiles obtained from experimental data were compared with that from neoclassical calculation. The neoclassical prediction roughly coincides with experimental data. The dependence of sign of E_r measured with experimental data on the electron and ion temperatures was also compared with the neoclassical theory. The fluctuation of potential was measured with HIBP, and the clear peak can be seen in its spectrum at the frequency of the geodesic acoustic mode (GAM). The characteristic of this mode was analyzed.

1. Introduction

In toroidal magnetically confined plasma, the radial electric field E_r is a very important parameter because it makes an effect on transport. In the low collisional regime of helical device, ripple induced diffusion loss is enhanced due to the neoclassical theory. This ripple induced diffusion loss is non-ambipolar, so the radial electric field E_r is determined by the ambipolar condition. This E_r suppresses the enhanced ripple induced diffusion loss, so it is important to study physics of E_r formation in experimental helical devices. In previous experiments in LHD, charge exchange recombination spectroscopy (CXRS) was used to study E_r formation. However, most data were obtained in the outer region of plasma ($\rho > 0.6$). In order to study physics of E_r formation in the core region, Heavy Ion Beam Probe (HIBP) [1] was installed to the Large Helical Device and the radial profile of potential in the core region was measured with HIBP. We investigated E_r in the wide range of plasma parameter space including high ion temperature and high electron temperature plasma in which the E_r measurements by CXRS are difficult. Moreover, HIBP has good temporal resolution as well as good spatial resolution, so the fluctuation of potential (and density) was

measured in LHD. Recent experimental results of potential profile and fluctuation measurements with HIBP are reported in this article.

2. Experimental Setup

The Large Helical Device (LHD) is a helical device, of which maximum magnetic field strength is 3 T, and standard major radius is about 4 m. The magnetic field configuration of LHD can be characterized by the major radius of magnetic axis, R_{ax}, the pitch parameter γ, the quarupole field B_q. In this article, γ and B_q are fixed as the standard one, namely $\gamma = 1.254$, $B_q = 100\%$. By changing the major radius of R_{ax}, the helical ripple is changed and the particle orbit is modified. In general, the heliotron magnetic field configuration has better confinement property in the inward shifted configuration than the outward shifted configuration, because the effective helical ripple becomes small and charged particle orbit is improved.

HIBP system was installed to LHD and has been developed in many years [2-9]. A schematic view of HIBP system in LHD is shown in Fig.1. For an ion source, a target sputtering negative ion source is used to produce negative gold ion. By using the tandem accelerator, the single charged gold ion beam (A_u^+), maximum energy of which is 6 MeV, is generated. The beam is injected to plasma from the lower side port of LHD. This beam is called as the primary beam. The total current of the primary beam is about a few μA. The doubly charged gold ion beam (A_u^{2+}) is formed by the collision with plasma. This doubly charged gold ion beam is called as the secondary beam. In the outside of plasma, the energy of the secondary beam is analyzed. From the energy conservation law, the difference of energy between the initial primary beam and the final secondary beam corresponds to the potential energy at the point where the secondary beam is formed by collision. In order to analyze the energy of the secondary beam, the tandem parallel plate energy analyzer [10], not the standard Proca Green 30 degree analyzer, is used so the required voltage to analyze the energy of 6 MeV beam can be reduced to 120 kV. The three

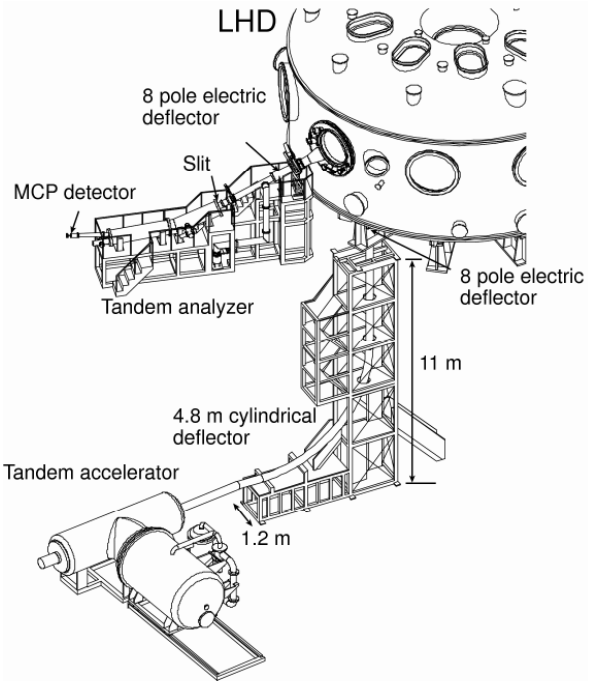

Fig.1 Shematic view of HIBP system on LHD

dimensional orbit of probe beam is controlled by two 8-pole electrostatic deflectors located at the injector and the detector side of diagnostic ports. The amount of detected secondary beam current is a few nA, so the sensitive current detector, micro channel plate (MCP), is used to detect this small current.

3. Experimental Results

In Fig.2, the typical shot is shown, in which the radial potential profile was measured in LHD. The toroidal magnetic field strength, B_t, was 1.5 T, and the major radius of magnetic axis, R_{ax}, was 3.75 m. The plasma was made by electron cyclotron heating (ECH) and sustained by neutral beam injection heating (NBI). Both of NBI lines (NBI#1, #3) are tangential injection and counter-direction. The line averaged density was ramped up from 0.2×10^{19} m^{-3} to 0.5×10^{19} m^{-3} by gas puff control. The central electron temperature was about 2.5 keV in the ECH phase, and 1.0 keV in the NBI phase. In this experiment, the incident angle of probe beam was scanned in 10 Hz so each 0.1 ms of radial potential profile was measured with HIBP. In periods marked by alphabets from A to E in Fig.2, potential profiles obtained from HIBP are shown in Fig.3. In the period A, ECH phase, the plasma potential at the center is positive. And the potential decreases with the increase of the line averaged density. The experimental data of potential profile was fitted with a polynomial function, and the radial electric field E_r was calculated by the differential of this fitting function. In the period A, E_r in the core region is positive. In NBI phase, it is almost zero or just negative.

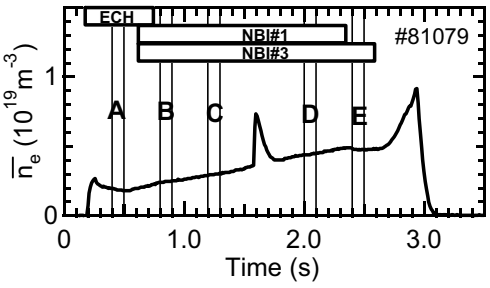

Fig.2 Typical shot in which the radial potential profile was measured with HIBP

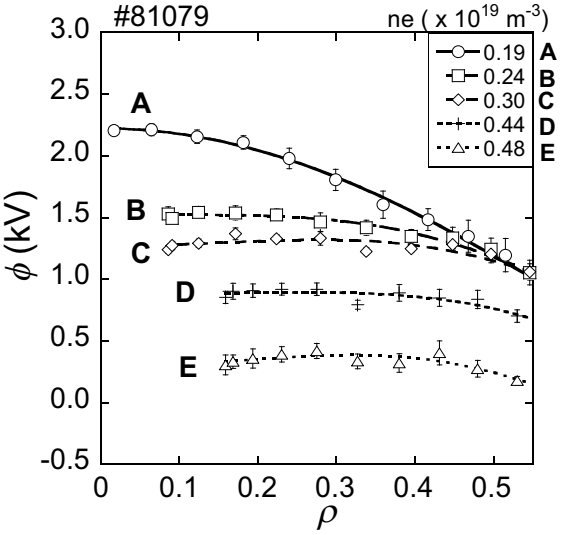

Fig.3 Potential profiles measured with HIBP are shown. Alphabets from A to E correspond to periods in Fig.2.

Obtained radial profiles of electric field were compared with those estimated by GSRAKE code

[11], which calculates E_r profile based on the neoclassical theory. In Fig.4 (a) and (b), results of the comparison for periods A and C are shown respectively. In the period A, in which the line averaged density is about 0.19×10^{19} m^{-3}, the positive radial electric field (so called electron root) is expected from the neoclassical ambipolar condition. This prediction is roughly in agreement with the experiment result in the core region of plasma as shown in Fig.4 (a). In the period C, in which the line averaged density is about 0.3×10^{19} m^{-3}, the negative radial electric field (so called ion root) is expected in the core region of plasma ($\rho < 0.26$) as shown in Fig.4 (b). In the region of $\rho > 0.26$, both of positive and negative electric fields are predicted. Experimental results coincide with the ion root (a negative E_r) in the core region ($\rho < 0.26$), and with the electron root in the outer region ($\rho \sim 0.6$).

The dependence of the sign of measured radial electric field on the electron and ion temperatures was studied and was compared with the neoclassical prediction. Results of this qualitative comparison are shown in Fig. 5. In these figures, plasma parameters in T_e - T_i space are shown. Different symbols are used for positive and negative E_r measured with HIBP at the radial position of $\rho = 0.25$. Solid lines are predicted boundaries from neoclassical theory, which divide the T_e - T_i space into three regions, "Electron root" (positive E_r), "Ion root" (negative E_r), "Multiple root" (both roots). In the calculation to estimate boundaries, parabolic temperature profiles and low density ($\overline{n}_e \sim 0.3$ - 0.5×10^{19} m^{-3}) are assumed. The major radius of magnetic axis, R_{ax}, is 3.6 m for Fig.5(a), 3.75m for Fig.5(b), and 3.9m for Fig5(c). In the case of high T_e plasma with the electron internal transport barrier (e-ITB) [12,13], a positive radial electric field was observed and these shots are in electron root region. If T_e , T_i parameters are in the ion root region, small negative E_r tended

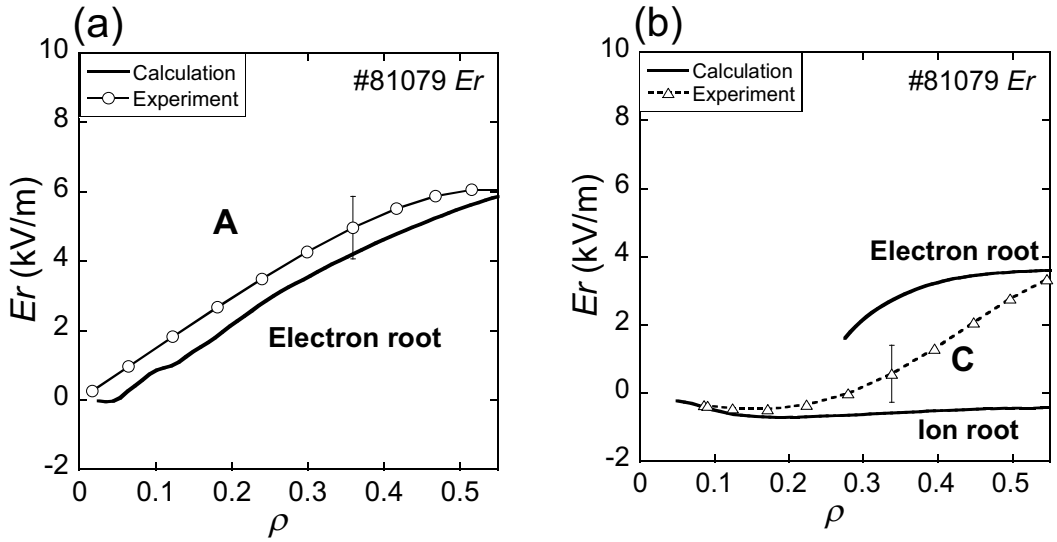

Fig.4 (a) Radial profile of E_r for case A ($\overline{n}_e = 0.19 \times 10^{19}$ m^{-3}) (b) E_r for case C ($\overline{n}_e = 0.3 \times 10^{19}$ m^{-3}) in Fig. 2. Open circle and triangle symbols are experimental data and thick solid lines are theoretical predictions.

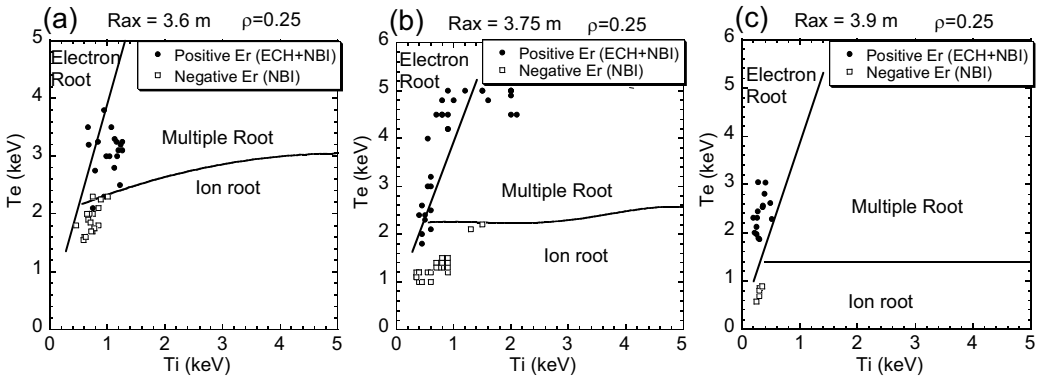

Fig.5 The dependence of the sign of E_r on T_e and T_i is shown. (a) Inward shifted configuration, R_{ax} = 3.6 m (b) R_{ax} = 3.75m (c) Outward shifted configuration R_{ax} = 3.9 m

to be observed. In high T_i shots [14,15], experimental data shows small negative E_r, which corresponds to "Ion root" in the neoclassical context. The theoretical prediction for the dependence of the sign of E_r on temperatures is consistent with experimental results in various magnetic configurations of LHD.

4. Potential fluctuation measurement

HIBP diagnostic system has good temporal resolution, so the fluctuation of potential can be measured. In Fig. 6, temporal evolution of potential is shown with heating methods when the fluctuation was measured with good signal to noise ratio. This plasma was very low density plasma, $\overline{n}_e \sim 0.1 \times 10^{19}$ m^{-3}. In this shot, the plasma was sustained with NBI and co-direction current drive by ECH was applied in the phase from 1.0 to 1.6 s. After turning off ECH, a low frequency coherent mode and other high frequency modes were measured in potential fluctuation. The low frequency coincided with geodesic acoustic mode (GAM) frequency [16]. Mirnov magnetic coil also detected fluctuation of this frequency. Power spectrum density of potential and Mirnov coil fluctuation signals are shown in Fig. 7. Fluctuation around 40 kHz~120 kHz changed its frequency largely with time, and it is considered that the frequency depends on the rotational transform. However, the fluctuation at 20 kHz was almost temporally constant. This frequency coincides with the GAM frequency and this mode was seen more clearly in HIBP potential signal than in Mirnov probe signal. The toroidal mode number of this mode was confirmed to be zero by the analysis of Mirnov probe signal. Theoretically the GAM frequency is proportional to the velocity of compressional wave, therefore to the square root of temperature. The dependence of the observed frequency on the electron temperature was investigated as shown in Fig. 8. The frequency of this mode in experiments is proportional to square root of electron temperature, T_e. Ion temperature, T_i, was less than 1 keV in all shots, so the effect of T_i is considered to be small.

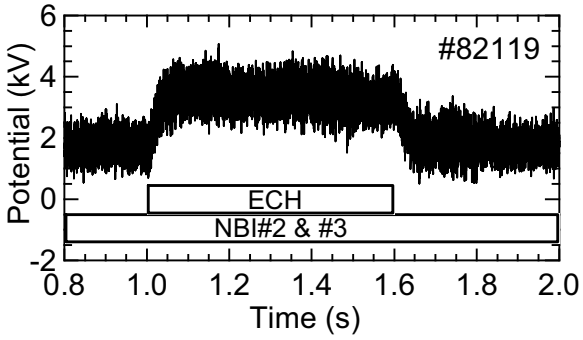

Fig.6 Temporal evolution of potential and heating methods are shown.

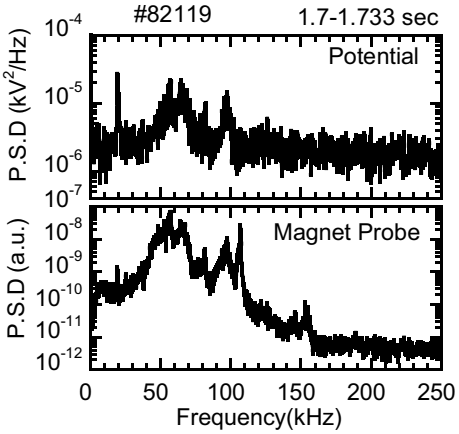

Fig.7 Power spectrum density of potential fluctuation (upper) and Mirnov signal (lower) are shown.

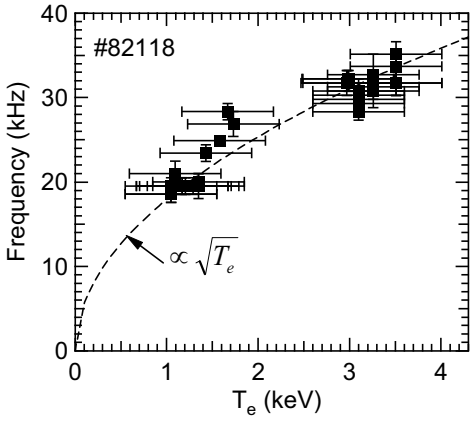

Fig. 8 The dependence of observed frequency on the Te is shown.

Potential fluctuation caused by turbulence has not been observed, because S/N ratio of our HIBP system is not sufficient for turbulence measurement. However density fluctuation caused by turbulence was measured and the amplitude modulation of high frequency fluctuation by low frequency GAM was observed. In the future, the potential fluctuation driven by turbulence will be measured together with the density fluctuation, and the interaction between particle flux and GAM will be studied after the improvement of S/N ratio of our system.

5. Summary

HIBP has been developed to study physics related to the radial electric field in LHD. The temporal evolution of potential profile was measured and the radial electric field was calculated from experimental data. Obtained radial profile of electric field was compared with the neoclassical prediction. The theoretical predictions roughly coincide with experimental data, so it is considered that the ambipolar property of neoclassical theory has a dominant effect on E_r formation in LHD. The dependence of the sign of E_r on the electron and ion temperature was also investigated and experimental results can be explained by the neoclassical prediction qualitatively in various magnetic field configurations of LHD.

Potential fluctuations of coherent modes were measured, and the frequency of one of

those modes was almost temporally constant. The frequency of this mode coincides with GAM frequency. And the dependency of the frequency on the temperature also coincides with the theoretical dependency of GAM frequency.

References

[1] JOBES F. C., MARSHALL J. F., HICKOK R. L., Phys. Rev. Lett. **22** (1969) 1042.

[2] FUJISAWA A. *et al*., IEEE Trans. on Plasma Sci. **22** (1994) 395.

[3] SHIMIZU A., IDO T., NISHIURA M. *et al*., J. Plasma Fusion Res. **2** (2007) S1098-1.

[4] IDO T. *et al*., J. Plasma Fusion Res. **2** (2007) S1100.

[5] IDO T. *et al*., Rev. Sci. Instrum. **77** (2006) 10F523.

[6] SHIMIZU A., IDO T., NISHIURA M. *et al*., J. Plasma Fusion Res. **5** (2010) S1015.

[7] SHIMIZU A., Rev. Sci. Instrum. **81** (2010) 10E138.

[8] IDO T. *et al*., Fusion Sci. Tech. **58** (2010) 436.

[9] IDO T. *et al*., Rev. Sci. Instrum. **79** (2008) 10F318.

[10] HAMADA Y., FUJISAWA A., IGUCHI H., NISHIZAWA A., KAWASUMI Y., Rev. Sci. Instrum. **68** (1997) 2020.

[11] BEIDLER C. D., DHAESELLER W. D., Plasma Phys. Control. Fusion **37** (1995) 463.

[12] IDA K., SHIMOZUMA T., FUNABA H. *et al*., Phys. Rev. Lett. **91** (2003) 085003.

[13] SHIMOZUMA T., KUBO S. *et al*., Nucl. Fusion **45** (2005) 1396.

[14] NAGAOKA K. *et al*., Fusion Sci. Tech. **58** (2010) 46.

[15] IDO T. *et al*., 37th EPS conference on Plasma Physics, 21-25 June , 2010, Dublin, Ireland.

[16] WINSOR N. JOHNSON J. L., DAWSON J. M., Phys. Rev. Lett. **11** (1968) 2448.

Far-infrared Laser Diagnostics on EAST

SHI Nan (史楠), GAO Xiang (高翔), JIE Yinxian (揭银先), ZHANG Shoubiao (张寿彪), ZENG Long (曾龙), WANG Erhui (王二辉), YANG Yao (杨耀), LIU Zixi (刘子奚)

Institute of Plasma Physics, Chinese Academy of Sciences, P.O.Box 1126, Hefei 230031, Anhui, China

Email: nanan@ipp.ac.cn

ABSTRACT: In order to measure plasma electron density profile on the EAST (Experimental Advanced Superconducting Tokamak), a vertical three-channel far-infrared (FIR) hydrogen cyanide (HCN) laser interferometer was developed. The structure, the improvements and the experiment result of this diagnostic system are presented. A five-channel DCN laser interferometer is being developed, some key issues has been overcome, including the economization of working gas, the solution to atmospheric absorption and the application of liquid-helium-cooled detectors. Details of each key issue are described.

KEY WORDS：plasma electron density, FIR laser interferometer, laser power stabilization, atmospheric absorption

1 Introduction

FIR laser diagnostics are widely used on many tokamak devices to determine the distribution of the electron density in the plasma and to follow its temporal evolution [1-5]. The line averaged density in EAST lies in the 0.5-4.0$\times 10^{19}$m^{-3} range. The plasma radius and the distance from the median plane of the plasma to the window are 0.4m and 4.36m, respectively [6]. On the basis of a vertical one-channel interferometer, a three-channel FIR laser interferometer has been developed for EAST to measure plasma electron density profile. The HCN laser (337μm wavelength) is suitable choice as a source. It is a continuous-wave waveguide laser, the discharge length is 3m and the resonator length is 3.4m. The working gas is a gas mixture containing N_2, CH_4 and H_2 in a ratio of 1:1:5. The output power is up to 120mW at 337μm [7-9]. A steady-state output power control system has been designed to stabilize the output power of HCN laser and it has been demonstrated to be effective. Some details of this control system will be described. Now, the space-time distributions of electron density on EAST are derived by asymmetrical Abel inversion [10-12].

In connection with the development of measurements on large tokamaks, such as EAST, multichannel vertical DCN laser interferometer/polarimeter system should be constructed for getting electron density and poloidal current profile simultaneously [13-16]. At present, five-channel FIR DCN laser interferometer is being developed with the position locating at a major radius of R=1.64m, 1.73m, 1.82m, 1.91m and 2.0m. The key issues about the economization of working gas, atmospheric absorption of the 195μm radiations and more sensitive detectors will be presented.

2 Three-channel FIR laser interferometer

Fig.1 shows the optical system of the interferometer. It is a heterodyne laser interferometer with Mach-Zehnder arrangement. The laser beam is divided into a reference beam and three probing beams located at a major radius of R=1.64m, 1.82m and 2.0m. The probing beam traversing a poloidal plasma cross section experience a phase shift and the reference beam through the rotating grating generate a frequency shift for heterodyne detection. The optical signals are received by Triglycine sulfate (TGS) detectors and the detection sensitivity is 1/15 fringe with a temporal resolution of 100μs.

The good stability of the output power is very important to long-term operation for the laser. But in practice, the resonator cavity length is easily influenced by environmental temperature, and the laser is unstable. Conventional solution is to make the oil jacket surround the discharge chamber to keep temperature constant. But there are some defects, such as the frequent oil leakage problem. In order to make this diagnostics system better, it's necessary to take some active precautions to solve this problem and keep the laser stable. The steady-state output power control system aided by Programmable Logic Controller (PLC) has been designed to stabilize the output power of HCN laser.

2.1 Steady-state output power control system for HCN laser

The resonator cavity of the laser consists of a pyrex of 54mm diameter and two plane reflectors against its ends. One of the reflectors is a metal mesh, and the other is a golden glass mirror which can be moved horizontally by means of a micrometer to adjust the cavity length. The oil jacket has been discarded this time. Meanwhile, some changes have been made on this side of the laser: fixing a pulley on the micrometer and fixing another pulley on a stepping motor. One step equals to 0.72°and causes the mirror to move a distance of 1μm correspondingly. Fig.2 shows these details. This is a

closed-loop feedback system. The detected output power signal is converted to voltage, as the feedback signal. According to the decrement of the output power, the PLC makes the judgment to drive the stepping motor to do the corresponding reaction.

The output power under the feedback control is shown in Fig.3. Experiments shows, during six hours, the laser output power is always more than the maximum available power which is defined 80% of the peck value of the output power. The HCN laser is stable and keeps high power. The dashed line represents the control signal. Fig.4 shows the output power without the feedback control. We can see within three hours, the output power has been decreased to the unavailable power which is defined 50% of the peak value. And the laser must be retuned.

By comparison, the steady-state output power control system can repress the output power's downtrend efficiently and make the laser work powerful enough. It is not only instead of oil jacket to settle the power instability, but avoid the experimenters into the EAST hall per 2-3 hours to retune the cavity length.

2.2 Data processing and experimental result

Fig.5 is a waveform of ohmic heating plasma discharge NO.20897 on EAST, with I_P the plasma current, V_P the loop voltage, and HCN1-HCN3 the measured laser phase shift. The reversed signal is due to the phasemeter 0-5V corresponding phase shift 0-2π. Fig.6 is evolution of the averaged electron density. Through asymmetrical Abel inversion, three dimensional diagram of the space-time distribution of electron density on EAST is derived in Fig.7.

3 Key issues of multichannel FIR DCN laser interferometer

The vertical five-channel FIR laser interferometer is being tested. The DCN laser source is also a continuous-wave waveguide laser. It has a similar structure to the HCN laser, but uses a different working gas. After optimization of various parameters, such as the ratio of N_2,CD_4,D_2 and He gas mixture, the discharge current, the pressure, and the new LaB_6 cathode, the laser output power is up to 200mW at 195μm and continuous discharge time is more than 30 days [17-18]. There are some key issues about this diagnostic system and they will be described in the following subsections. Up to now, the center-trace beat frequency has been detected.

3.1 Working gas mode conversions for saving CD_4

The working gas of DCN laser, especially the CD_4, is often difficult to acquire and the Tokamak operation is pulse discharge. The gas flow of the CD_4 should be cut off between two discharges for

economical reason. Therefore, two gas working modes have been confirmed: one mode with the CD_4 as the operating mode (N_2, CD_4, D_2 and He gas mixture) and the other without CD_4 as the non-operating mode (N_2 and He gas mixture). The gas mode should be shift to non-operating mode during the discharge interval and shift to operating mode before discharge beginning. The experiments have been conducted to simulate the mode conversions during EAST discharges. It was supposed that there were six discharges during two hours, and each discharge lasted for 1min. In the interval, the gas mode was non-operating mode, and the output signal was noise power. Fig.8 (a) shows this simulated result. From this result, we can see clearly that laser's output power declined gradually along with the incremental times of gas mode conversions and could never restore the initial peak value.

For keeping the laser power stable near the maximum available power, the power must be retuned after each conversion. Because of the similar structure to the HCN laser, the steady-state output power control system used on HCN laser also used on DCN laser, but with some control parameter changes. After each conversion from non-operating mode to operating mode, the control system will be started up 2min to retune the output power. Fig.8 (b) shows this improved experiment. The decomposition chart is presented in Fig.8 (c). As a result, a large amount of working gas has been saved, the use of the CD_4 and D_2 has been decreased by near 80%.

3.2 Atmospheric absorption of the DCN laser radiation

The ambient humidity of EAST hall is very high (normal relative humidity above 50%). The strong absorption by water vapour in atmosphere of the 195μm laser must be considered. During the testing experiment, such observation was measured. The general expression for the power P(z) received at a distance z from the output laser power is $P(z)=P_0\exp(-\alpha z)$, given by J.L.Bruneau et al [19], where P_0 is the laser power at the window, α is the atmospheric absorption coefficient. The laser power at the window is 108mW, at a constant temperature of 295K with the relative humidity 50%. If z=6m, the P(z)=45mW and α=0.21. If z=12.5m, the P(z)=10mW and α=0.23. For FIR laser interferometer on EAST, the optical distance is up to 20m and the power signal is attenuated approximately 99%. Frozen dehumidified technology had previously been used and the relative humidity had been declined to 30%. But there is no power signal even if using the InSb detectors (see 3.3). At present, the low- dew point rotary dehumidifier has been used. The relative humidity has been down to 10%, and the beat frequency has been detected. As future plan, the disadvantages of strong absorption by atmosphere may be further eliminated by using a hollow waveguide with dry air or

nitrogen.

3.3 Liquid-helium-cooled detector (InSb)

Owing to the long light path and the strong atmospheric absorption, the detected signal attenuated quickly. So, more sensitive detectors must be used. The liquid-helium cooled detectors InSb combining low noise equivalent power (NEP) with fast response have been as the preferred. Compared with TGS detectors, InSb detectors may have 1500 times the optical response and have NEPs two orders of magnitude better than TGS [20].

4 Conclusion

Multichannel FIR HCN laser interferometer has reliably been used on EAST to give the mean electron density and space-time distribution. Five-channel DCN laser interferometer is being developed and at present, some key issues have been resolved. We firmly believe that the whole system will soon be successful. Meanwhile, a study on two-color submillimeter-wave laser is in progress. It is expected in the years to come, the FIR interferometer/polarimeter system could be constructed. This work was partially supported by the JSPS-CAS Core-University program in the field of ‘Plasma and Nuclear Fusion’. This paper has been supported by National Magnetic Confinement Fusion Science Program (Code number 2010GB106000, and 2010GB106001).

References

[1] Wan Y X, HT-7 team and HT-7U team. 2000, Nucl.Fus 40：1057
[2] Dodel G, 1999, Infrared Physics & Technology 40:127.
[3]Veron D, 1974, Optics Communications 10:95.
[4] Xu Q, Gao X, Jie Y X, et al. 2008, Plasma Science and Technology 10:519
[5]Veron D, 1979, Infrared and Millimeter Wave 2:67, Academic Press, New York, K.J. Button
[6]Gao X and the EAST team. 2008, Physics Letters A.372:2286
[7] Gao X, Lu H J, Guo L Q et al. 1995, Rev.Sci.Instrum. 66:139
[8] Jie Y X, Gao X, Cheng Y F et al.2000, International Journal of Infrared and Millimeter Waves 21: 1375-1380.
[9] Jie Y X, 2008, Study of density behaviors on HT-7 tokamak.[PhD]. Institute of Plasma Physics, Chinese Academy of Sciences. X.R. Zhan.
[10] Barr W L, 1961, Journal of the Optical Society of America 52:885
[11]Yasutomo Y, Miyatak K., Himeno S I et al. 1981, IEEE Trans. Plasma Sci. 9: 18
[12] Gao X, and Guo Q.L, 1990, Infrared and Millimeter Waves 11:1399
[13]Jie Y X, Gao X., Liu H Q et al. 2003, International Journal of Infrared and Millimeter Waves 24:2079
[14] Gao L, Gao X,.Hu X W et al. 2004, International Journal of Infrared and Millimeter Waves 25:891

[15] Veron D and Belland P, 1978, Infrared Physics 18:465
[16] Xu Q, Gao X, Jie Y X et al. 2008, Plasma Devices and Operations 17: 16
[17]Liu H Q, Gao X, Jie Y X et al. 2004, International Journal of Infrared and Millimeter Waves 25: 649
[18] Asif M, Gao X, Jie Y X et al. 2004, International Journal of Infrared and Millimeter Waves 25:808
[19] Bruneau J L, Belland P and Veron D, 1978, Optic Communications 24:259
[20] Xu Q, 2009, Study of far infrared laser diagnostic on the EAST tokamak.[PhD]. Institute of Plasma Physics, Chinese Academy of Sciences. Zhan X R.

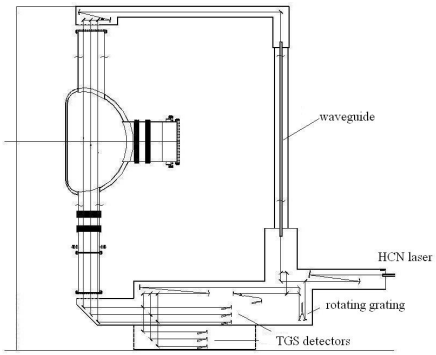

Fig1. Schematic of optical elements and beams arrangement (not to scale) on EAST-not to scale

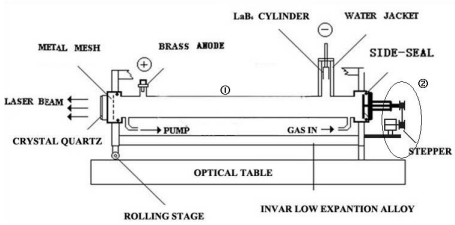

Fig 2. Schematic diagram of the discharge-pumped HCN laser with the improvements（□ discard the oil jacket □ fix the stepping motor）

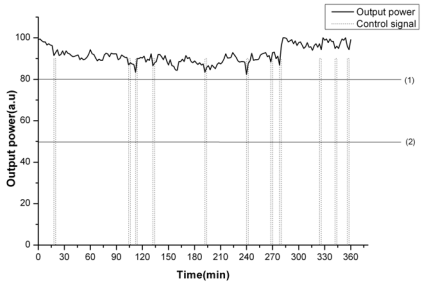

Fig.3 The observation of the output power of the HCN laser under the feedback control （（1）is the maximum available value, (2) is the unavailable value）

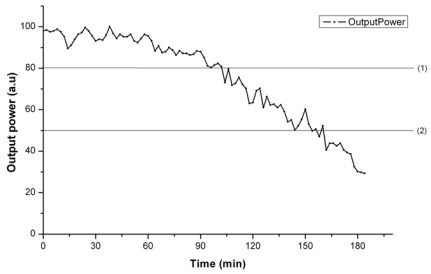

Fig.4 The observation of the output power of the HCN laser without the control （（1）is the maximum available value, (2) is the unavailable value）

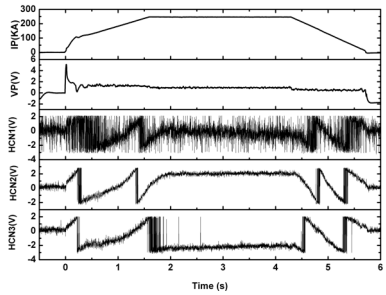

Fig.5 A waveform of ohmic heating plasma discharge on EAST (NO.20897)

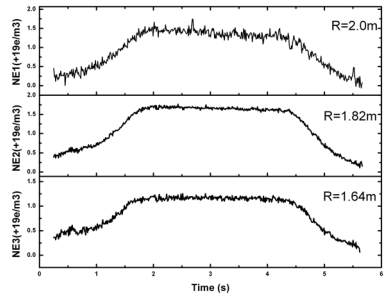

Fig.6 The averaged electron density by data processing (NO.20897)

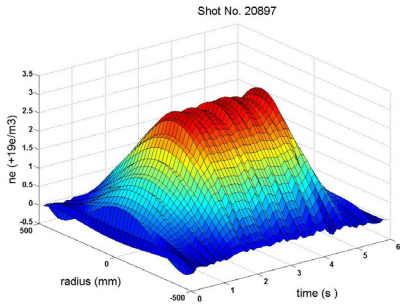

Fig.7 The space-time distribution of electron density by asymmetrical Abel inversion

(a)

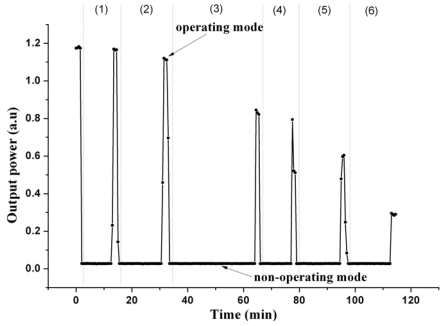

(b)

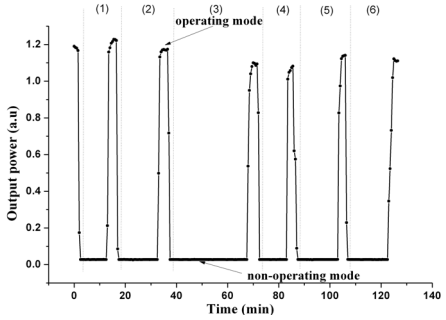

(c)

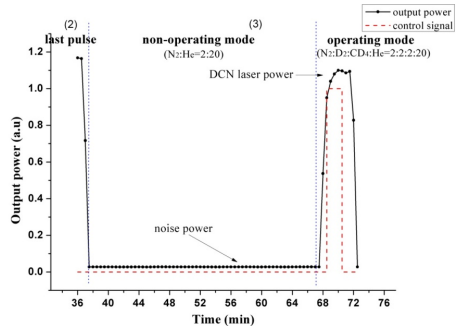

Fig.8 (a) The observation of the output power of the DCN laser with gas mode conversion without control. (b) the output power with control. (c) the decomposition chart of each simulated discharge with the control.

EAST 远红外激光诊断

摘要：为了更好的测量 EAST 托卡马克装置中等离子体电子密度，建立了三道 HCN 远红外激光干涉仪。着重介绍了干涉仪的结构、改进以及诊断测量结果。五道 DCN 激光干涉仪正在进行最后的调试，一些关键性的问题已经被解决，包括基于节省 CD_4 工作气体考虑的气体模式转化，对长期困扰的空气吸收问题的应对方法，高灵敏探测器的使用等等。

关键词：等离子体电子密度， 远红外激光干涉仪， 激光功率稳定性，空气吸收

Study of electron thermal transport on EAST superconducting tokamak

Xiaofeng Han*, Junyu Zhao, Qing Zang, Xiaoqi Xi, Yanmin Duan
and EAST Teams

Institute of Plasma Physics, Chinese Academy of Sciences,
P.O.Box 1126, Hefei, Anhui 230031,P.R.China

E-mail: hxf@ipp.ac.cn

Improved electron confinement plasma produced by lower hybrid current drive (LHCD) has been obtained on the EAST superconducting tokamak, where the plasma current is sustained with the lower hybrid wave. The energy confinement time increases from 22.6 ms (Ohmic phase) to 33.2 ms (LHCD phase). The confinement factor H_{89} increases from 0.79 (Ohmic phase) to 1.3 (LHCD phase). The electron parameters profiles evolution and electron thermal transport coefficients are assessed primarily by using the data of Thomson scattering diagnostic and FIR laser interferometer. Electron heat diffusivity coefficient χ_e profile was estimated during both the ohmically-heated plasma and the LHCD plasma by analyzing the electron power balance. The thermal diffusivity of electron became obviously lower in the LHCD phase. The relationship between χ_e and the energy confinement time τ_E was studied in this paper. The role of the weak magnetic shear is invoked to partly explain the improved confinement by stabilizing the turbulence. This work was partially supported by the JSPS-CAS Core-University program in the field of 'Plasma and Nuclear Fusion'.

Preparation of W/Cu functionally-graded materials by combustion synthesis melt-casting under ultra-high gravity

P. L. Mai[1, 2], S. B. Guo[1], G. H. Liu[1], S. L. He[2], Y. H. Ling[3], and J. T. Li[1]

[1] Technical Institute of Physics and Chemistry, Chinese Academy of Sciences.

[2] Department of Physics, Capital Normal University,

[3]Tshinghua University

Email: lijiangtao@mail.ipc.ac.cn

Abstract

W/Cu functionally-graded materials were prepared by combustion synthesis melt-casting under ultra-high gravity. In the casted W/Cu samples, a clear gradient in chemical composition exists, showing an increasing W/Cu ratio from the top to the bottom. Each W/Cu sample can be divided into three areas, which are pure Cu, Cu-rich W/Cu alloy, and W-rich W/Cu alloy, respectively. The ultra-high gravity has a complex effect on the melt-casting process. A stronger ultra-high gravity filed can accelerate the phase separation but will cause more drastic turbulence in the melts, and thus moderate ultra-high gravity is appropriate to reduce residual Al_2O_3 in the W/Cu ingots.

I. Introduction

Tungsten (W) is the best candidate for plasma-facing components in the International Thermonuclear Experimental Reactor (ITER) or other fusion reactors, owing to its high melting point and high sputtering threshold [1,2]. For such applications, W is generally joined to a copper (Cu) heat sink in order to promote the heat dissipation. However, there is a severe mismatch between the thermal expansion coefficients of W and Cu ($\alpha_W=4\times10^{-6}$/°C, $\alpha_{Cu}=18\times10^{-6}$/°C), which will cause large thermal stress during the fabrication and service of W/Cu composites. When W/Cu mock-ups are exposed to high heat loads (e.g. 5-20 MW/m^2), the thermal stress can cause cracking, delamination, or detachment at the interface and thus reduce the lifetime of the W/Cu components [3-6].

For the accommodation of thermal stress, an effective solution is to prepare functionally-graded materials with gradually-varying compositions and structures. W/Cu functionally-graded materials can be fabricated by several ways such as powder metallurgy and melt infiltration. For powder metallurgy, the bonding of W and Cu by hot isostatic pressing (HIP) has been developed [7]. For

melt infiltration, a porous graded W skeleton is first formed, then Cu melt is poured into the W skeleton, and finally a W plate is welded onto the graded specimen to produce a W/Cu functionally-graded material with a chemical composition transition from pure Cu to pure W. Both the above methods require extensive heat-treatment and long processing time.

This paper reports an alternate method of combustion synthesis melt-casting under ultra-high gravity to prepare W/Cu functionally-graded materials. In this method, highly-exothermic aluminothermic reactions and ultra-high gravity field are coupled [8-10], offering a facile route to fast fabrication of W/Cu materials. The phase separation and microstructure evolution of the W/Cu samples are discussed with a special attention to the effect of the ultra-high gravity field.

II. Experimental

Commercial Al, CuO, and W powders were used as raw materials. The starting powder was prepared by homogeneously mixing 80wt% (2Al+3CuO) thermite with 20wt% W. The powder was pressed into a 30mm compact under a pressure of 10 MPa and loaded in a graphite crucible. Then, the crucible was mounted into an equipment to perform combustion synthesis melt-casting under ultra-high gravity, as illustrated in Figure 1.

The reaction chamber of the equipment for combustion synthesis was evacuated to a vacuum of <300Pa. An ultra-high gravity field was induced by centrifugation with an acceleration of 600-1200g, where g means the gravitational acceleration. By passing an electric current through a tungsten coil closely above the sample, combustion reaction was triggered. During the reaction, a large amount of heat was produced and made the products melted. In the ultra-high gravity field, the Al_2O_3 ceramic and W/Cu metal melts were separated because of their density difference. After the solidification of the melts, bulk ceramic (Al_2O_3) and metal (W/Cu) ingots were obtained. The W/Cu ingot was separated from the ceramic part and then machined and polished for later characterizations.

The bulk density was measured according to the Archimedes principle. The phase composition was identified by X-ray diffraction (XRD; D8 Focus, Bruker, Germany) with a step of 0.02^o and a scanning rate of 6^o/min. The microstructure was examined by scanning electron microscopy (SEM; S-3400, Hitachi, Japan), and the elemental analysis was performed by energy dispersive spectroscopy (EDS; INCA, Oxford Instrument, UK).

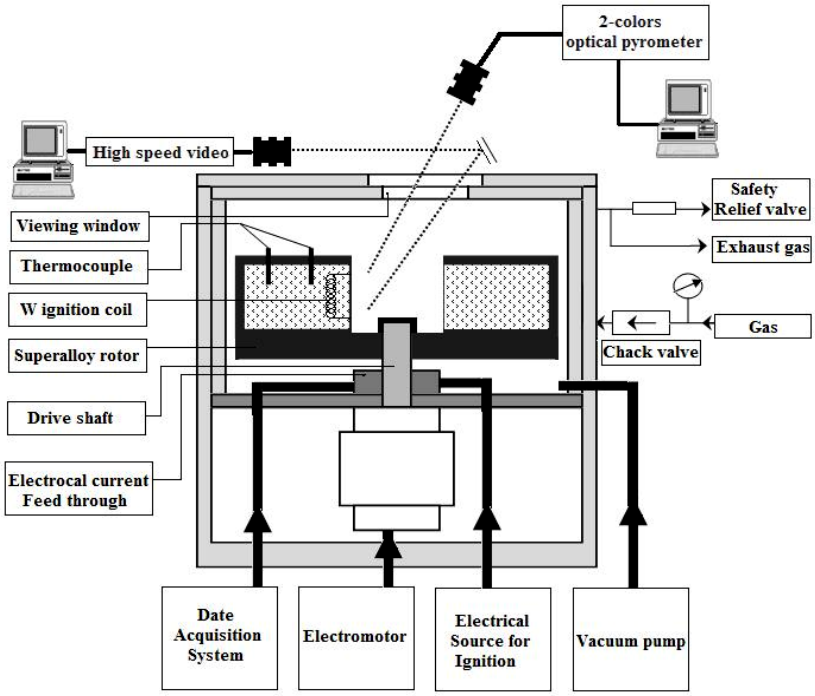

Figure 1. A sketch map of the equipment for combustion synthesis melt-casting under ultra-high gravity

III. Results and discussion

Figure 2 shows the photos for the top and bottom surfaces of a W/Cu sample. There are many large cavities at the top surface, and the bottom surface has a dense structure. Figure 3 shows the side view of a cross section of the sample. From the top to the bottom, the color varies from brown to silver-gray, indicating a change in chemical composition. This composition change is further verified by EDS analysis, which shows an increasing W/Cu ratio from the top to the bottom of the sample. That is to say, there is a clear chemical composition gradient in the W/Cu sample.

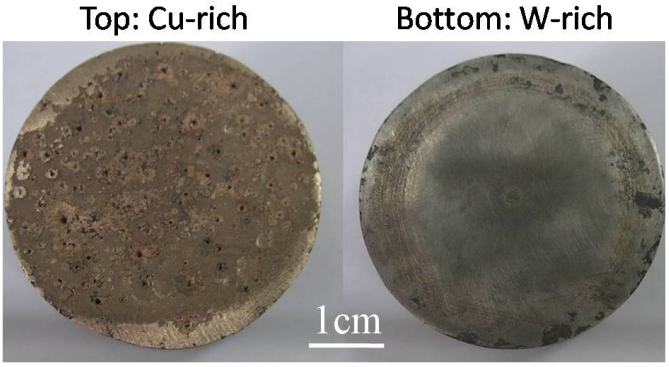

Figure 2. Photos for the top and bottom surfaces of the W/Cu sample.

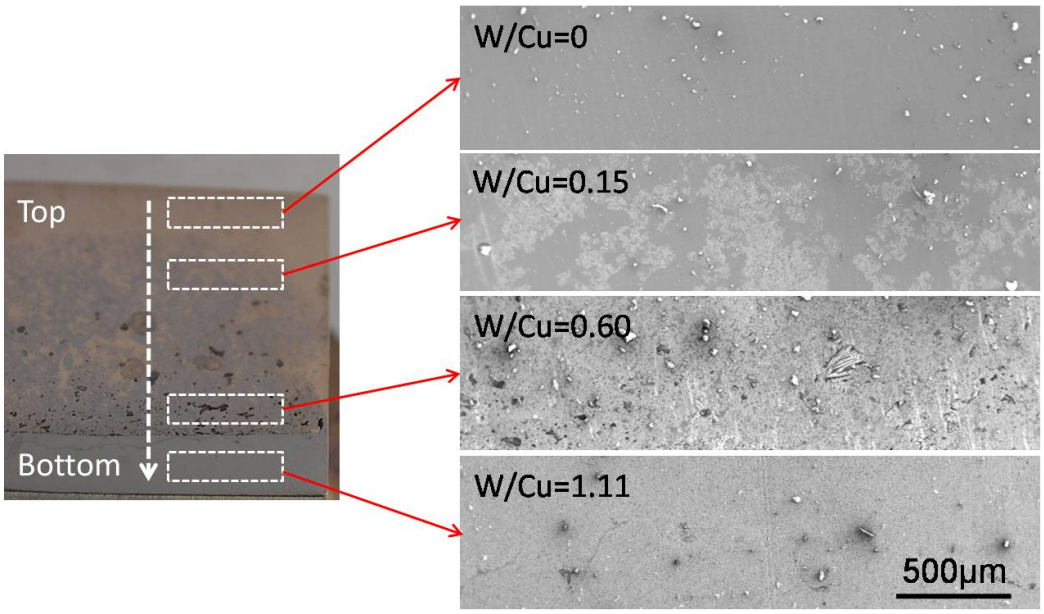

Figure 3. SEM images and W/Cu ratios for different areas of the W/Cu sample.

The formation of the composition gradient in the W/Cu sample should be attributed to the large difference between the densities of W and Cu. The density difference leads to the settling of W particles in Cu melt and thus the separation of the two elements. In this way, W element is concentrated at the lower part of the sample and the upper part has a higher Cu content. The settling of W in Cu melt can be greatly enhanced in the ultra-high gravity field compared with common gravitational field. For this reason, ultra-high gravity condition offers the opportunity for the fast preparation of W/Cu functionally graded materials by combustion synthesis melt-casting.

From the above results, the formation mechanism of W/Cu materials by combustion synthesis melt-casting is proposed as follows. At first, the aluminothermic reaction between Al and CuO takes place. In this reaction, a large amount of heat is created and the resultant Cu and Al_2O_3 are melted. Under ultra-high gravity, the light Al_2O_3 melt is separated from the Cu melt and finally forms a ceramic ingot. The heavy W particles settle in the Cu melt and go to the lower part of the sample. A part of Cu melt fills in the gaps among the W particles to produce a W/Cu ingot. The other part of Cu melt stays between the Al_2O_3 layer and the W/Cu layer and forms a pure Cu ingot after solidification.

According to the chemical composition and microstructure, the casted metal ingot can be divided into three areas from the top to the bottom, which are pure Cu, Cu-rich W/Cu alloy, and W-rich W/Cu alloy, respectively. In the Cu-rich area, W particles are dispersed in continuous Cu matrix. In the W-rich area, W particles are integrated by Cu melt, resulting in a characteristic microstructure of liquid-phase sintering, as shown in Figure 4.

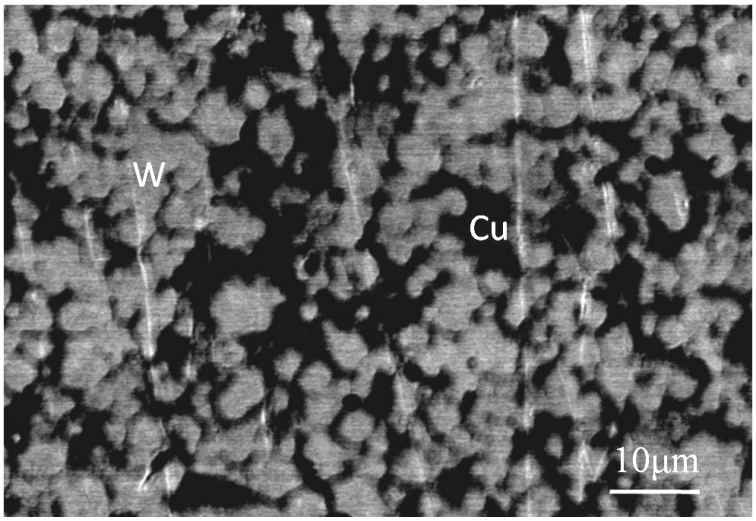

Figure 4. SEM image for the W-rich part of the W/Cu sample.

During the combustion synthesis melt-casting process, the combustion reaction goes very quickly and thus the lifetime of melts is short. In such short time, the separation between the ceramic and metal phases is hard to fully complete, even under ultra-high gravity. In this case, some Al_2O_3 particles remain in the W/Cu ingot, which is verified by SEM observation, as shown in Figure 5. The content of residual Al_2O_3 in the W/Cu ingot is affected by the ultra-high gravity field. Figure 6 shows the chemical compositions of the W/Cu samples prepared with different ultra-high gravity levels. It is found that, the effect of the ultra-high gravity is complex, and there is no simple linear relation between the Al_2O_3 content and the ultra-high gravity level. Moderate ultra-high gravity level helps to reduce the content of residual Al_2O_3 in the W/Cu ingot, and lower or higher ultra-high gravity level can cause the increase of Al_2O_3 content.

The complex effect of ultra-high gravity can be explained from two aspects. On one hand, the phase separation due to density difference can be accelerated by enhancing the ultra-high gravity field. On the other hand, however, stronger ultra-high gravity will lead to more drastic turbulence in the melts, which has a negative effect on the phase separation. Because of the two reasons, too low or too high ultra-high gravity levels are not favorable, and moderate ultra-high gravity is appropriate for the reduction of Al_2O_3 content.

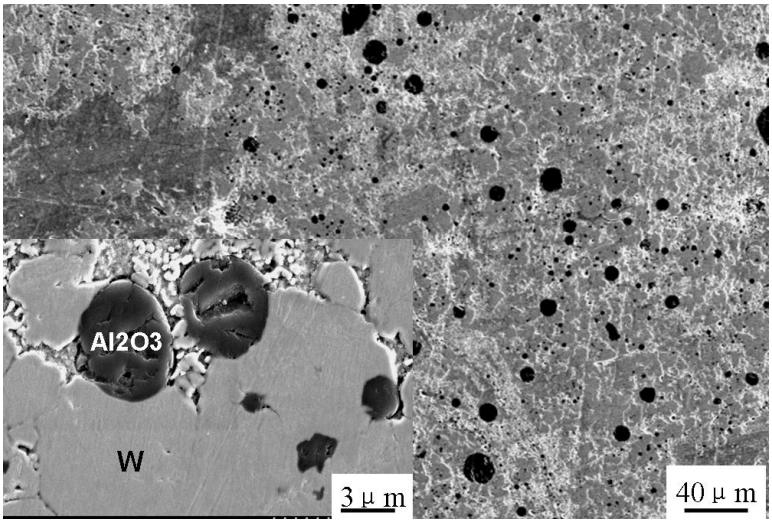

Figure 5. SEM image showing Al_2O_3 particles remaining in the W/Cu ingot.

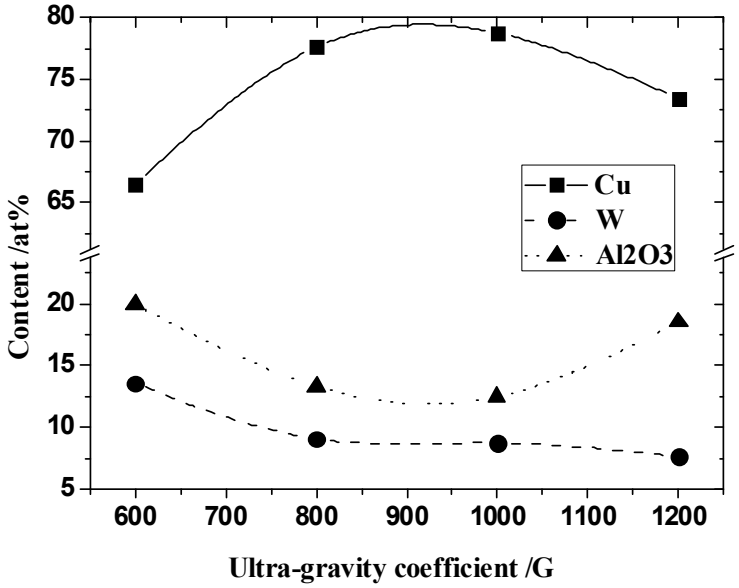

Figure 6. Chemical compositions of the W/Cu samples prepared with different ultra-high gravity levels.

IV. Conclusion

W/Cu functionally-graded materials have been prepared by combustion synthesis melt-casting under ultra-high gravity. In the casted W/Cu samples, a clear gradient in chemical composition exists, showing an increasing W/Cu ratio from the top to the bottom. Each W/Cu sample can be divided into three areas, which are pure Cu, Cu-rich W/Cu alloy, and W-rich W/Cu alloy, respectively. The ultra-high gravity has a complex effect on the melt-casting process. A stronger ultra-high gravity filed can accelerate the phase separation but will cause more drastic turbulence in the melts, and thus moderate ultra-high gravity is appropriate to reduce residual Al_2O_3 in the W/Cu ingots.

Acknowledgements

This paper has been supported by National Magnetic Confinement Fusion Science Program (Code number 2010GB106000, Branch No. 2010GB106003). This work was partially supported by the JSPS-CAS Core-University program in the field of'Plasma and Nuclear Fusion'.

References

[1] I. Smid, M. Akiba, G. Vieider, L. Plochl. J. Nucl. Mater. 258-263 (1998) 160.
[2] R. Andreani, E. Diegele, R. Laesser, B. Schaaf. J. Nucl. Mater. 329-333 (2004) 20.
[3] M. Onozuka, S. Hirai, K. Kikuchi, Y. Oda, K. Shimizu. J. Nucl. Mater. 329-333 (2004) 1553.
[4] J. Linke, R. Duwe, A. Gervash, R. Qian, M. Roedig, A. Schuster. J. Nucl. Mater. 258-263 (1998) 634.

[5] I. Smid, M. Akiba, G. Vieider, C. Ploechl. J. Nucl. Mater. 258-263 (1998) 160.
[6] Y. Nemoto, A. Hasegawa, M. Satou, K. Abe. J. Nucl. Mater. 283-287 (2000) 1144.
[7] S. Saito, K. Fukaya, S. Ishiyama, K. Sato. J. Nucl. Mater. 307-311 (2002) 1542.
[8] J. Pei, J. Li, G. Liu, K. Chen. J. Alloy Comp. 476 (2009) 854.
[9] L. Mei, P. Mai, J. Li, K. Chen. Mater. Lett. 64 (2010) 68.

Irradiation effect on W surface with stress confinement under focus microwave plasma bombardment

LING Yun-Han[1*], LI Jiangtao[2], WANG song[1], CHEN Shilei[1]

[1] *Laboratory of Advanced Materials，Tsinghua University，Beijing 100084，P.R.China;*

[2] *Technical Institute of Physics and Chemistry，Chinese Academy of Sciences，Beijing 100190, P.R.China*

W/Cu functionally gradient material (FGM) is a promising candidate for plasma facing component (PFC) used in ITER divertor due to its high heat capacity as well as excellent sputtering resistance. We have previously reported that such kind of FGM had very good thermal shock resistance. However, the irradiation effect of such composite is still not very clear. In order to investigate the effect of thermal stress on the irradiation damage of tungsten, bi-layered W/Cu composites with different residual stress distribution were designed and fabricated, and their irradiation behavior was investigated by focus H_2/He plasma manipulated in a microwave plasma device. The irradiated microstructures were characterized by FESEM and AFM; and the microscopic mechanism of irradiation damage of stress confined specimen was studied by the slow positron annihilation technique and X-ray diffraction. Finally UV-Vis spectroscopy and four-probe resistivity tester were applied to measure the photoelectric properties of bombarded samples. The results will provide some insight on the thermo-mechanical failure of PFC with stress confinement in the future operation. This work was partially supported by the JSPS-CAS Core-University program in the field of ‘Plasma and Nuclear Fusion’.

*Corresponding author. Tel.: +86 10 62772856; fax: +86 10 62771160.
E-mail address: yhling@mail.tsinghua.edu.cn

Relative calibration of SXR detector array

CHEN Yebin (陈晔斌)[1] ， HU Liqun (胡立群)[2]，CHEN Kaiyun (陈开云)[2]，Li Bo (李波)[2]，
Tang Yuxiang (唐雨翔)[2]

[1] University of Science and Technology of China, Hefei 230031, China

[2] Institute of Plasma Physics, Chinese Academy of Sciences, Hefei 230031, China

e-mail:" chenyebin@ipp.ac.cn"

Abstract A calibration system of SXR detectors was established. The system employed a standard luminance source which is working in visible spectral instead of a soft- x-ray source. With this system we studied the detector arrays which were used four experimental campaigns on EAST tokamak in previous experiments. Reduction of spectrum averaged efficiency of the array had been observed. Comparing results with the new detector, we also found aging progress could improve the coherency of the array.

Keywords：relative calibration, photodiode array, oft-x ray system

PACS: 52.70.La

1. Introduction

Soft x-ray camera is an important diagnostic for tokamak plasma. The soft x-ray system could be used to provide the 2D topology structure of the magnetic surface in a poloidal cross section with tomography technology [1,2]. It allows the study of MHD activity and plasma shape with a fast time response. For such usage, It is common that several cameras are employed to view plasma cross-section simultaneously. Therefore it is obvious that the relative efficiency of the detectors would influence the precision of the tomography result. To decrease such errors, a calibration system was established to select uniform detector. Since Fe^{55} [3] source is unavailable and its short half life period would influence the comparability of the calibration results during a long period, the system employed standard luminance source which is working in visible spectral instead of a soft- x-ray source as a light source.

The system had been used to calibrate the detectors of the SXR system which were mounted on the EAST tokamak machine in previous experiment campaigns. The tested detectors presented in this paper are Hamamatsu S4111-35Q photodiode arrays. Reduction of spectrum averaged efficiency had been observed.

Comparing the results with the new detector, we also found aging progress could improve the coherency of the array.

2. Diode efficiency and Calibration system

2.1. Diode efficiency

The spectrum averaged efficiency [4] for the detector is:

$$<\eta>_v = \frac{\int \eta(v)\tau(v)w(v)dv}{\int w(v)dv} \quad , \tag{1}$$

Where $w(v)$ is spectral power distribution, $\tau(v)$ is attenuation of the ' filter' which contains the doped zone and the passivation zone and assuming that the thickness of the two layer are all known, $\eta(v)$ is the efficiency of the diode for a fraction of monochromatic radiation which depends on the thickness of depletion zone and the substrate.

Then photocurrent I is given by

$$I = JS = \frac{e_0}{E_{pn}} <\eta>_v S \ , \tag{2}$$

where S is area of the detectors and it is a constant.

2.2. Calibration system

The light source of the calibration system is the most important part. Synchrotron radiation [5] and Fe^{55} are always play the role of the source of a calibration system for SXR detector. Considering the convenience of using, the Fe^{55} radioactive source is used more often. While purchasing a radioactive source takes a long time, and it is imminent to calibrate the detector arrays of the SXR system, a standard luminance source was selected to play the role of the source of the calibration system.

We purchased a standard luminance source from EVERFINE PHOTO-E-INFO CO., LTD. And the type of the standard luminance source is SLS-5000. In wave length range of 380 nm to 780 nm the luminance had been tested by the manufactory. The test report shows that the luminance gradually approaches zero as the wave length comes to 380 nm, it comes to peak when the wave length is around 700 nm and the luminance is about 1/9 of the peak luminance when the wave length is 780 nm. The unevenness of the brightness is less than 1% at the window of the

standard luminance source except the edge of the window. The diameter of the window is 36 mm. A piece of frosted glass was covered on the window. In order to eliminate the distribution which is caused by direction angle; the detector array is mounted closed to the window of the standard luminance source. We blackened the inner wall of the bracket to eliminate the influence from the reflection.

An acquisition system was set up. The acquisition contains 48 amplifiers, and the magnification of the amplifiers were normalized to 2.2×10^6. One acquisition card collects the signals in three groups. And the acquisition system passes the signal to the computer and save them in the computer.

3. Calibration of the detector arrays

To test the method and the system, we calibrated three arrays using this system. One of the three arrays is a new one. They were named as used array A and used array A. The left two arrays are used ones. It was named as new array. They were mounted on the EAST tokamak in 2005 and were removed in 2009, they experienced four experiment campaigns.

The test result is show in **Figure. 1**. For each array, when it comes to the edge of the array the coherence turns worse. This is caused by the unevenness at the edge of the window of the standard luminance source. The result shows that the spectrum averaged efficiency reduced 5.8% after the arrays experiencing four experiment campaigns.

Variance is employed here to denote the coherence of the array:

$$\mathrm{var}(X) = E((X - \mu)^2), \tag{3}$$

where μ is the average intensity of the detectors on each array.

The variance is an overall evaluation for the array. It is obvious that the coherence would be better if the variance was smaller for an array. The variances for the three arrays (used array A, used array B and new array) are 0.0042, 0.0043 and 0.0132 successively. It is obvious that the coherency of the new array is worse than the coherency of used arrays. This result shows that limited aging progress can improve the coherency of a photodiode array.

(Figure. 1)

To validate the rationality of the result above, there are two approaches. The first is that compare the efficiency of one array at its very first and very last experiment on EAST tokamak under the same experimental conditions. But it is not easy to find out two shots that operated under the same conditions. Meanwhile most of the first campaign of experiment on EAST tokamak has been deleted, so it is impossible to compare the efficiency of one array at its first and last tokamak experiment. And the second is that compare the efficiency of a new array and an used array at the same point of time during one shot. And in the experiment campaign in 2009, a new array was mount in the tokamak while the used one was not been removed. So the data can be carried out to validate the rationality of the result.

The two arrays were mounted on the same horizontal window, and they were on the other side of the middle plane. The intensity distribution of the two arrays is shown in **Figure. 2**. The average reduction about 23% of the spectrum averaged efficiency.

(Figure. 2)

This result validates the feasibility of the calibration system, since it indicates that after experiencing four experiment campaigns the efficiency of the detectors have been reduced. The result also the reduction of spectrum averaged efficiency is not consistent with the result getting from the calibration system, and this is a divinable phenomenon. Because $\eta(\nu)$ in eq (1) not only depends on the property of detectors but also depends on the frequency of the light.

4. Result and discussion

The calibration system could be used to relatively calibrate SXR detector arrays. The system could be used to study the reduction of spectrum averaged efficiency of the array. And the system could also observe the coherency of the detector array.

Meanwhile since the source does not work in soft-x ray spectrum, the calibration result would have some difference with the result using a source working in soft-x ray spectrum. This would influence the precision of the result.

The test results show that the unevenness at the edge of the window causes problems, so another standard luminance source is needed. The even area's size of the window of the standard luminance source has to be bigger than the size of the detector arrays which would be tested. To

distinguish the difference between the results using the two different sources, the study of the difference between using a standard luminance source and a soft-x ray source would be helpful.

Acknowledgments

This work is supported by the National Nature Science Foundation of China with a grant number 10935004, and it's also supported partially by the core university program between China and Japan. It's a pleasure for the author to thank EAST group for their supports to this work.

References

[1] Chen Kaiyun, *et a.* 2009, *Plasma Sci. Technol.* 11: 472

[2] R.S. Granetz, P. Smeulders. 1988, Nucl. Fusion, 28: 457

[3] A. W. Edwards, H. -U. Fahrbach, R. D. Gill, et al. 1986, Rev. Sci. Instrum. 57: 2142

[4]M. Anton, M. J. Dutch, H. Weisen. 1995, Rev. Sci. Instrum. 66: 3762,

[5] B. Alper, S. Dillon, A. W. Edwards. 1997, Rev. Sci. Instrum. 68: 778

Figure.1: The intensity for the detectors on the three arrays. The blue stars indicate the new array, the red and green stars indicate the tow used arrays. For each array, when it comes to the edge of the array the coherence turns worse. This is caused by the unevenness at the edge of the window of the standard luminance source.

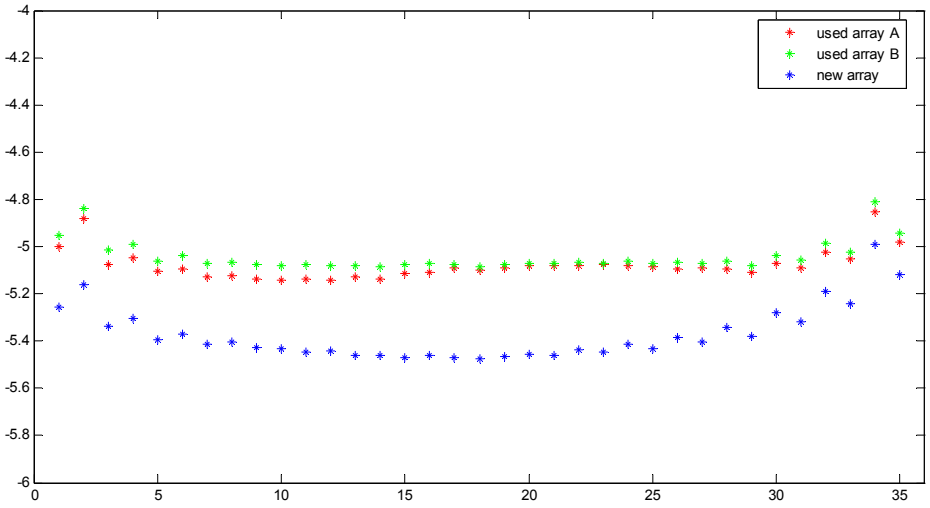

Figure.2: The distribution of intensity of the two arrays. The red stars indicate the new array, and the green stars indicate the used array. There is an error channel caused by the amplifier, and it is channel 12.

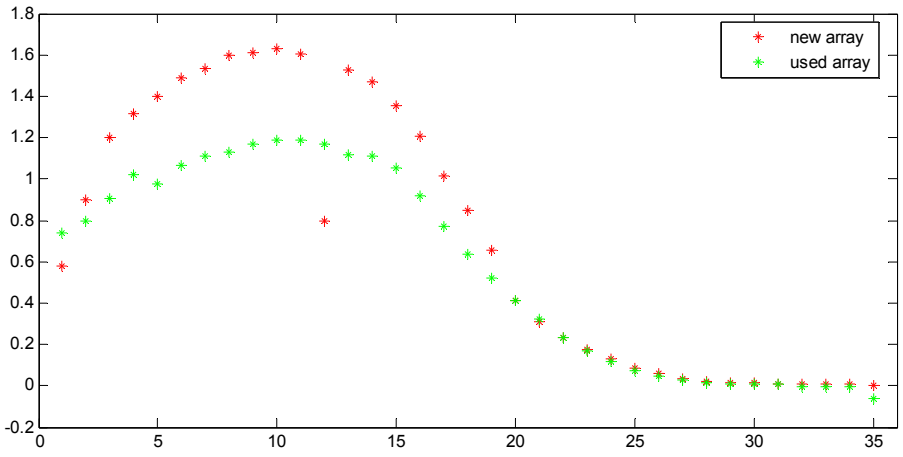

软-x 射线探头阵列的相对标定

陈晔斌 1 ，胡立群 2，陈开云 2，李波 2，唐雨翔 2

[1] 中国科学技术大学，合肥，邮编 230031

[2] 中科院等离子体物理研究所，合肥，邮编 230031

摘要：我们搭建了一个软-x 射线探头阵列的相对标定系统。这个系统采用一个工作在可见光波段的标准亮度光源代替软-x 射线光源作为系统的光源。我们用这个系统研究了再以前的实验中被安装在 EAST 托卡马克上的探头阵列。我们发现那些已经用了四轮放电实验的探头阵列的探测效率明显降低了。同时我们也发现在一定程度上的老化过程有助于改善探头阵列的一致性。

关键词：相对标定，探头阵列，软-x 射线系统

Measurement of neutron flux in the primary stage of EAST deuterium plasma experiment

ZHONG Guoqiang (钟国强)，HU Liqun (胡立群)，Li Xiaolin (李晓玲)

Institute of plasma physics, Chinese academy of sciences, Hefei 230031, China

Email: gqzhong@ipp.ac.cn

Abstract: Five channels of time-resolved neutron flux monitor system have accomplished construction by ^{3}He proportion counter and ^{235}U fission chamber. That was be used for study neutron emission behavior at the initial stage of deuterium plasma experiment on EAST tokamak. At the condition of ohmic discharge, more of photo-neutrons production with low density during the plasma current ramp-up stage. Just increase the central chord average of electron density over $2.0\times10^{19}m^{-3}$, photo-neutron could be availably elimination. The power of lower hybrid wave (LHW) feed-in plasma excess a threshold has ideal effective for reduce loop voltage and photo-neutron, which power strong enough and plasma background parameter higher case that more fusion neutron production. Flux monitor system detected plenty of fusion neutrons during the Ion-cyclotron resonance frequency (ICRF) valid heating plasma.

Keywords: neutron flux, plasma diagnostic, tokamak

PACS: 52.70.Nc, 52.55.Fa

1. Introduction

At present, Experimental Advanced Superconducting tokamak (EAST) mostly operated on deuterium plasma. Sometimes experiment of puffing ^{4}He gas discharge that hopes to reduce hydrogen remains in the first wall of silicon carbide graphite. Adopt iso-flux of magnetic surface control and lower hybrid wave current diver, the plasma current attain to 0.9 MA with double null divertor configuration. At the prophase of experiment on EAST, ICRF and LHW were important approach to auxiliary heating plasma. Fast wave components of ICRF accelerated the minority ion of H and ^{3}He by resonance, through collision that the fast minority ion transfer energy to heating bulk ion. An important precondition for minority heating model was lower than 10% of n_H/n_D ratios. Also, we could change toroidal field and frequency of wave to feasible mostly of RF power

absorbed by second harmonic in plasma. A part of fast wave transformation to ion bernstein wave (IBW) when it frequency satisfy alfven resonance at the range of deuterium second harmonic. IBW approach landau damping and collision between ion and electron to separate heating electron and ion. In addition, fast wave could be direct absorbed by electron thought damping and TTMP effect. At the recently campaign of high parameter experiment on EAST, injection ICRF appears distinct heating effect. LHW were major be used to current driver, but also have valid electron heating effect. The central electron temperature approximately increases fifty percent during strong power of LHW heating on EAST.

Neutron diagnostic along with high power of auxiliary heating system utilize in magnetic confinement fusion experiment become important. At percent, neutron diagnostic of tokamak experiment mostly contain time resolve neutron yield monitor, two dimensions of neutron emission profile measurement (2D neutron camera), neutron spectrometers and activation system [1]. Make use of neutron yield and energy measurement result were capable of get some information such as neutron slowly time, ion temperature and diffuse ratios, fast ion velocity distribution and fusion power. These can be used to do research aspect as neutron yield scale rate, auxiliary heating mechanism, MHD behavior and material radiation damage of first wall. Further more investigation of n_T/n_D in plasma core and fast ion confine and transport by 2D neutron camera. Start project of ITER and existing large scale of tokamak such as JET, TFTR, JT-60U equipment consummate neutron diagnostic system [2]. Begin stage of deuterium plasma experiment on EAST, ion temperature not high enough, have lower yield of DD fusion neutron but more photo-neutron birthed by γ-n reaction. So the neutron diagnostic major contain flux time-resolve monitor and development compact spectrum measurement system on EAST.

2. Experiment setup

EAST is the first construct and success operation of full superconducting tokamak with double null divertor configuration in the world. That research subjects were plasma physics under steady-state condition and advanced operation model explore. The device engineering design parameter are toroidal field B_t=3.5T, major radius R=1.7m, minor radius a=0.4m, maximal elongation $\kappa \approx 1.9$, plasma current I_p=1MA. Up to now, EAST was employed 2MW with 2.45GHz frequency of lower hybrid wave current diver system and 4.5MW with 25 to 110MHz frequency of ion-cyclotron resonance heating system. Over twenty species of diagnostic had been

adoption, they relation with neutron behavior study are mostly contain time resolve neutron flux monitor, γ-ray (hard X-ray) and bremsstrahlung diagnosis, plasma current and loop voltage measurement, electron cyclotron emission diagnosis, n_H/n_D and carbon impurity monitor, plasma density and temperature diagnosis.

Five channel time-resolve neutron flux monitor system basis on four ^{3}He proportion counters and one ^{235}U fission chamber. These two large sizes of ^{3}He counters have high thermal neutron sensitivity up to 133 cps/nv and another two counters are 15cps/nv. The ^{235}U fission chamber made by 1.4 gram highly enriched uranium with 1.16cps/nv of thermal neutron sensitivity [3]. All detectors operate on pulse model that ^{3}He counter and ^{235}U fission chamber maximal count rate are $6\times10^4 s^{-1}$ and $5\times10^5 s^{-1}$ respectively. Five centimeter of polyethylene covers with these detectors for fast neutron moderator [4]. Detectors assembled with their moderator calibration by 2.45MeV atom accelerator neutron source at the nuclear physics laboratory of PeKing University. The Large ^{3}He and ^{235}U fission chamber absolute detection efficiency approximately are 6% and 0.2% respectively. Time resolution of the neutron flux monitor system can be optional in 1-10ms, ordinarily experiment set as 5ms [5]. Employed BC-501A liquid scintillators constructed a local direction neutron strength measurement system that adopt pulse shape technology to n/γ discrimination, which could been detect gamma ray at the same time. A 2inch diameter and length of BGO ($Bi_4Ge_3O_{12}$) scintillator detector installed with the BC-501A in a same collimator that used for γ -ray strength and energy measurement.

The neutrons diagnostic system arrangement in EAST device hall has been demonstrated on **Figure.1**, as follows. Label two higher sensitive ^{3}He detectors with #1 and #2, they are position on outside E and D ports of tokamak device about 9 meter far from plasma core. Lower sensitive ^{3}He detectors of #3 and #4 outside the E port far from plasma core about 5 meters. The ^{235}U detector label as #5 was position on outside the C port distance plasma core approximate 4 meters.

3. Experiment results and analysis

3.1 Ohmic plasma experiment

At the initial stage of deuterium plasma experiment on EAST, more photo-neutrons product in lower density of ohmic discharge. Three shot of ohmic discharge with double null divertor configuration are display on **Figure.2**. The plasma current I_p=500kA and loop voltage V_{loop}=0.7V at flat are similar in these shot. But central electron density of chord even is different that were

$1.0\times10^{19}m^{-3}$, $1.5\times10^{19}m^{-3}$, $2.0\times10^{19}m^{-3}$ respectively. Shots No:29854 at the stage of plasma ramp-up, plenty of fast electrons bring by lower density that shows on electron cyclotron emission (ECE) signal. Loop voltage higher than 1.2V on this stage as that fast electrons were accelerated to high energy of runaway electron [6]. It bring heavy strength of hard X-ray (γ-ray) that lead these signals measurement by CdTe, NaI(Tl), BGO were very strong. High energy of γ-ray (hard X-ray) and electron could been through (γ, n) , (e, e′ n) reaction produce photo-neutron [7], so a lot of neutrons are counted by ^{3}He and ^{235}U detectors. Increase the density to $1.5\times10^{19}m^{-3}$ like No:29861, runaway has been restrained , γ-ray (hard X-ray) emission and photo-neutron yield quickly decrease. When the density over $2.0\times10^{19}m^{-3}$, photo-neutron occupy less ratios in total neutron yield that can been ignored.

3.2 LHW experiment

Injection LHW power exceeds a threshold have observably effect to decrease loop voltage in the period of deuterium plasma experiment on EAST. Shot of No:28075 was LHW heating experiment that displayed on **Figure.3**. Basic parameter of this shot were plasma current Ip=300kA, central electronic density of chord even $ne=1.0\times10^{19}m^{-3}$. At the stage of current ramp-up, launch into 400kW of LHW, the loop voltage reduce from 1.4V to 0.4V. Lower density brings runaway and hard X-ray emission were rapid depress [8]. Less of photo-neutron and fusion neutron produced cause of lower ion temperature (～0.6keV) and density, so time resolve neutron flux count rates very lower due the LHW injection.

Increase background plasma parameter and LHW power in shot of No: 29880 divertor plasma shows on **Figure.4**. This shot parameter were plasma current I_p=800kA, central electronic density of chord even $n_e=1.6\times10^{19}m^{-3}$, LHW power P_{LHW}= 1MW. Loop voltage under 0.6V and electronic density exceed $1.5\times10^{19}m^{-3}$ during the RF wave injection. Runaway and hard X-ray emission slightly, so photo-neutron rate of production is very low. At this time, ^{3}He counter and ^{235}U chamber measurement the neutron flux signal rise relation with plasma density and current that condition fusion neutron occupation more share.

3.3 ICRF heating experiment

Attempt to change experiment condition more times during ICRF heating on EAST. At the situation of higher density, lower n_H/n_D and RF antenna near plasma obtain distinct heating effect. Shot No:30337 was double null divertor configuration discharge shows on **Figure.5**, plasma

current Ip=450kA, central electronic density n_e= $2.9\times10^{19}m^{-3}$, $n_H/n_D\approx10\%$. Auxiliary heating powers contain 1.5MW of 27MHz ICRF and 450kW of LHW. At the ICRF heating stage impurity emission, electronic density, loop voltage and Ha emission not distinct fluctuate, at the same time neutron flux and central soft X-ray emission quickly enhance. Furthermore, ECE signal obvious increase, plasma store energy adds to 10kJ, central temperature raise 0.2keV. BGO detector measurement high energy of γ-ray (hard X-ray) increase a little but neutron flux increase about ten times [9]. According as foregoing experiment result to estimate that fusion neutrons occupy domination at this moment. These neutrons mostly produce by bulk deuterium ions DD reaction and fast ions reactive contribution. The ICRF efficacious heating plasma in this shot can be evidence by neutron flux and other diagnosis signals.

4. Conclusion

The time resolve neutron flux monitor system basis on 3He proportion counter and 235U fission chamber was success operation on each condition of EAST plasma experiment and obtain valuable result. Generally deuterium plasma without auxiliary heating have low yield for DD fusion neutron and besides, more photo-neutron produce with central electronic density of chord even under $1.0\times10^{19}m^{-3}$. LHW can restrain photo-neutron generate when the power over 400kW. In addition, heighten the LHW power and background plasma parameter, more fusion neutron has been observation. At the time of n_H/n_D fewer than 10% and density over $2.5\times10^{19}m^{-3}$, obtain distinct effective of ICRF heating that approved by neutron flux monitor.

Acknowledgments

We would like to express our appreciation to the members of EAST team, especially members of the Tokamak Physics Experiment Division. The plasma experiment works supports and helpful discussions by Computer Application Research Division and RF Heat Diversion. We also acknowledge Dr. Gao Xiang , Dr. Zhu Yubao and Wan Baonian for help in this work.. This work was partially supported by the JSPS-CAS Core-University program in the field of ‘Plasma and Nuclear Fusion’.

REFERENCES

[1] O.N.Jarvis. 1994, Plasma phys. Control. Fusion, **36**:209

[2] B.Wolle. 1999, Physics Reort, **312**:1

[3] T.Hayashi,T.Nishitani, M.Ishikawa. 2004, Rev.Sci.Instrum, **75**: 3575

[4] A.J.Peuttung. 2000, Nuclear Instruments and Methods in Physics Research A, **443**:400

[5] Zhu YB, Chen JQ, Li GM. 2004, Rev.Sci.Instrum, **75** :4284

[6] H.Knoepfel, S.J.Zweben. 1975, Physical Review Letters, **35**:1340

[7] D.Harder, R.Mehling. 1970, Physics Letters, **32B**:610

[8] Z.Y.Chen, B.N.Wan, S.Y.Lin, et al. 2006, Nuclear Instruments and Methods in Physics Research A, **560**:558

[9] Z.Y.Chen, B.N.Wan, S.Y.Lin, et al. 2006, Physics Letters A, **351**:413

Figure.1 Neutron diagnostics system arrangement on EAST tokamak (a) A bird's-eye view (b) A poloidal cross-section view.

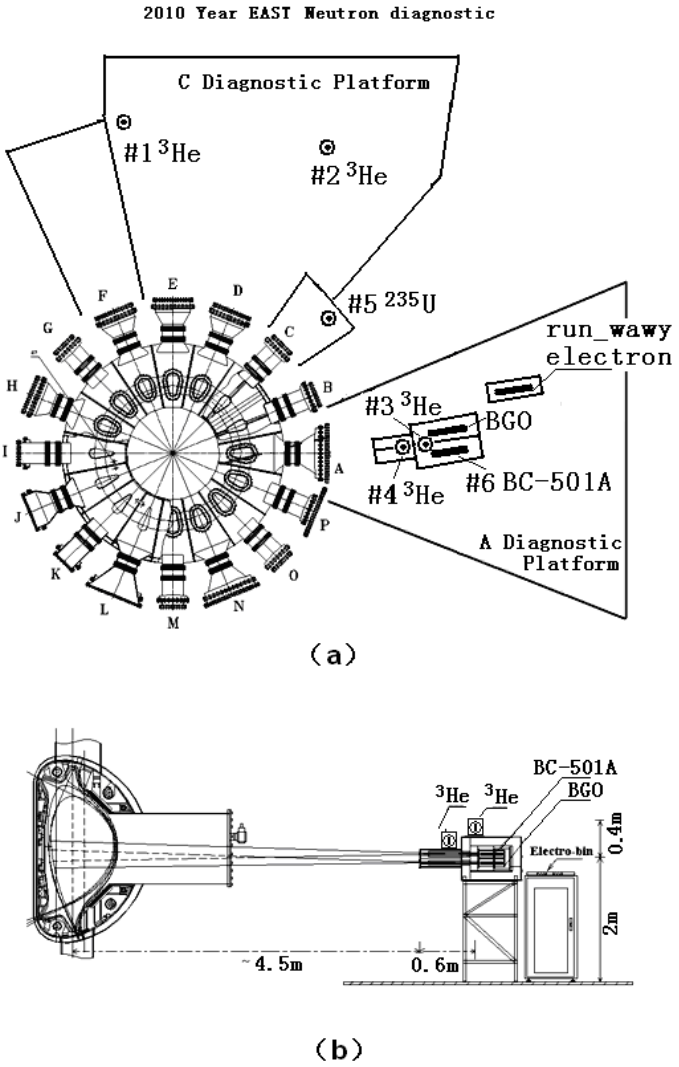

Figure.2 Ohmic heating deuterium plasma experiment in different central electronic density of chord even, No: 29854 n_e= 1.0×$10^{19}$$m^{-3}$, No: 29861 n_e= 1.5×$10^{19}$$m^{-3}$, No: 29644 n_e= 2.0×$10^{19}$$m^{-3}$.

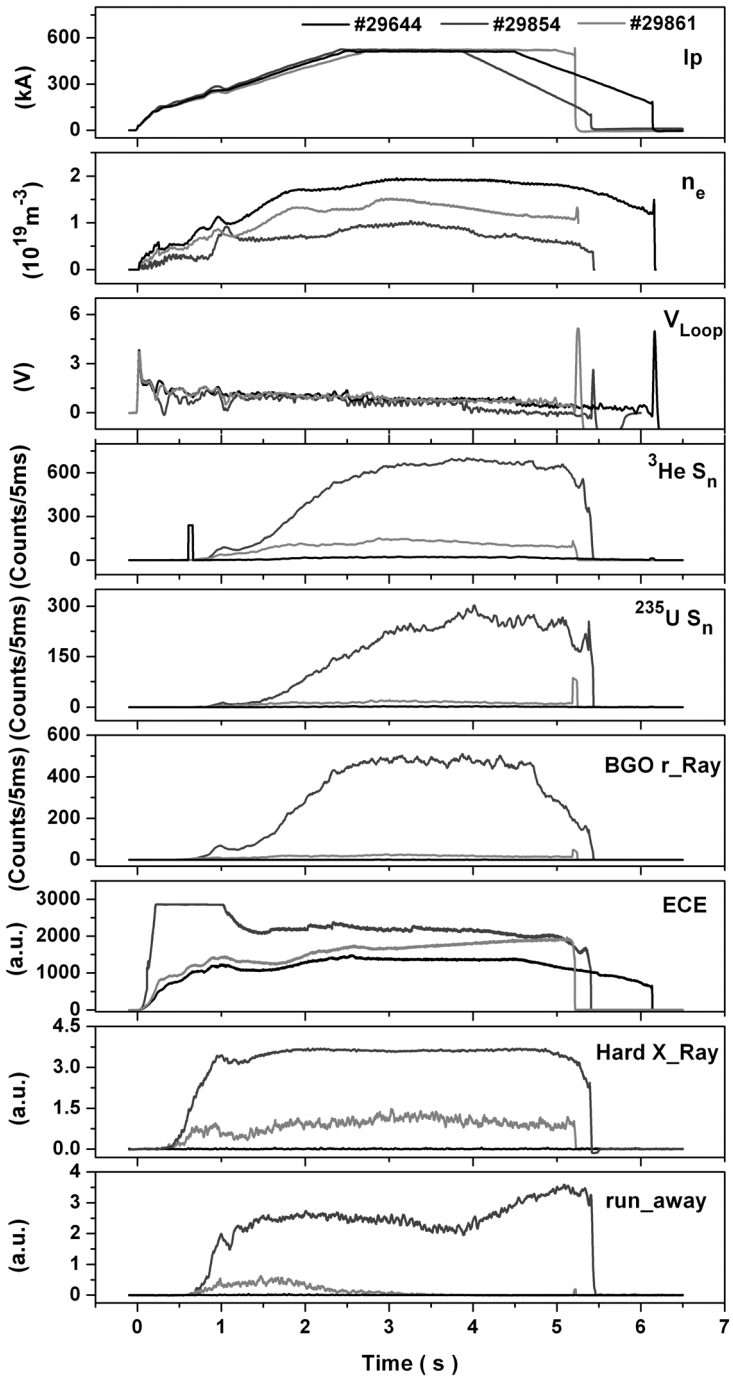

Figure.3 Lower power of LHW experiment of No:28075, ^{3}He Sn and ^{235}U Sn are neutron flux measurement by ^{3}He counter and ^{235}U fission chamber respectively. LHW power P_{LHW}= 450kW.

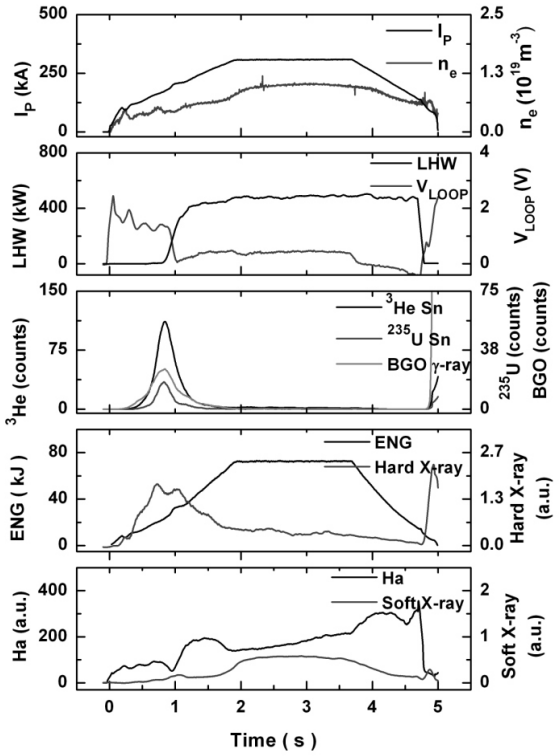

Figure.4 Higher power of LHW experiment of No:29880, ^{3}He Sn and ^{235}U Sn are neutron flux measurement by ^{3}He counter and ^{235}U fission chamber respectively. LHW power P_{LHW}= 1MW.

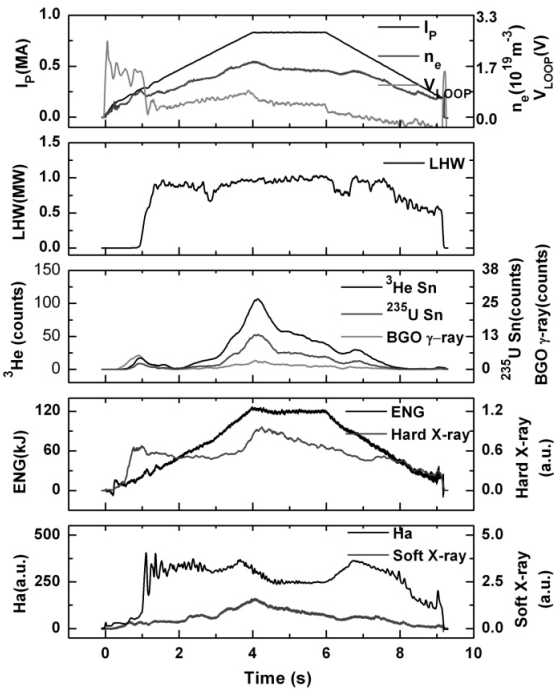

Figure.5 ICRF heating experiment of No:30337, P_{ICRF}=1.5MW, P_{LHW}=600kW. I_P=450kA, central electronic density of chord even $n_e = 2.9\times10^{19}m^{-3}$.

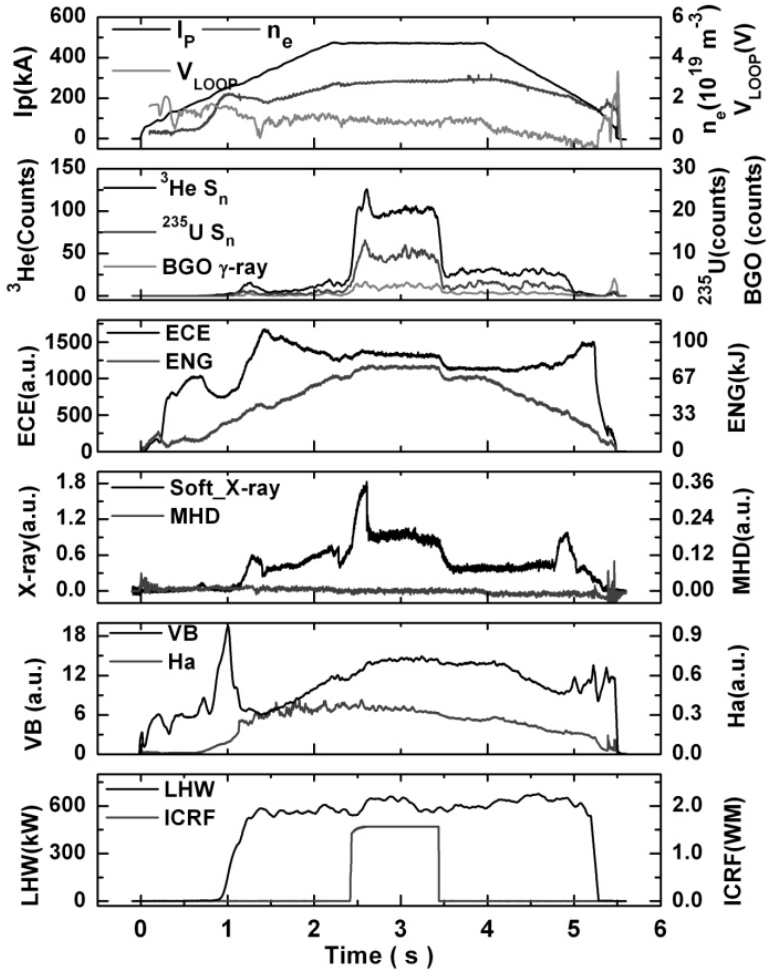

Improvement of plasma performances using carbon pellet injection in Large Helical Device

Shigeru MORITA[1,2)], Motoshi GOTO[1,2)], Kenichi NAGAOKA[2)], Chunfeng DONG[2)], Hangyu ZHOU[2)], Zhengying CUI[3)], Yunbo DONG[3)], Xiang GAO[4)], Katsumi IDA[1,2)], Katsunori IKEDA[1)], Osamu KANEKO[1,2)], Shiyao LIN[4)], Haruhisa NAKANO[1)], Masaki OSAKABE[1)], Ryuichi SAKAMOTO[1,2)], Yasuhiko TAKEIRI[1,2)], An TI[4)], Katsuyoshi TSUMORI[1)], Mikiro YOSHINUMA[1,2)] and LHD experiment group

[1)]National Institute for Fusion Science, Toki 509-5292, Gifu, Japan
[2)]Graduate University for Advanced Studies, Toki 509-5292, Gifu, Japan
[3)]Southwestern Institute of Physics, Chengdu 610041, China
[4)]Institute of Plasma Physics Chinese Academy of Sciences, Hefei 230031, China

Abstract

A cylindrical carbon pellet with a size of 1.2-1.8mm and a velocity of 100-300m/s has been injected in Large Helical Device for the purpose of efficient fueling based on its deeper deposition instead of H_2 gas puffing and ice pellet injection. Electron density increment of Δn_e=10x10^{13}cm^{-3} is successfully obtained by single carbon pellet injection without plasma collapse. Typical density and temperature of the ablation plasma of the carbon pellet are examined by spectroscopic method, e.g., 6.5x10^{16}cm^{-3} and 2.5eV for CII, respectively. The confinement improvement up to 50% compared to ISS-95 stellarator scaling is clearly observed in relatively low-density range of n_e=2-4x10^{13}cm^{-3} and high ion temperature of $T_i(0)$~6keV is also observed with internal transport barrier at n_e=1.2x10^{13}cm^{-3}. These improvements largely exceed the values appeared in usual hydrogen gas-puffed discharges

1 Introduction

In Large Helical Device (LHD) experiments on hydrogen ice pellet injection have been extensively carried out for the improvement of the plasma performance in addition to the increase of the density limit in neutral-beam heated discharges[1], since the discharges can be easily maintained because of the absence of the current-driven instability. The LHD discharge has also considerable robustness against impurity buildup. The discharge operation up to the global power balance limit defined by the radiation loss is basically possible in LHD[2]. This robustness seen in the LHD discharges also permits the injection of a variety of impurity pellets[3]. For example, the carbon pellet injection with cylindrical shape of $1.8\text{mm}^{L}\times 1.8\text{mm}^{\phi}$ is possible showing the density rise of $10\text{x}10^{13}\text{cm}^{-3}$, and the high-Z pellet injection is also successful for double-structure molybdenum and tungsten pellets[4]. In particular, the carbon pellet has a special merit that the penetration depth in high-temperature plasmas is much longer than the hydrogen ice pellet. It indicates that the particle deposition into the central column of plasmas is possible even for single pellet injection. In this paper, experimental results on the improvement of plasma performances using the carbon pellet in LHD are reported with electron and density parameter measurements of the carbon ablation cloud.

2 Impurity pellet injector

The impurity pellet injector[5] consists of a pellet gun with a rotatable disk and three differential pumping systems, as shown in Fig.1. One hundred pellets can be loaded in the disk and is accelerated by pressurized He gas of 15 atm. Two types of the pellet gun and acceleration tube are prepared, which permit the acceleration of the pellets in different sizes, i.e., 0.3-0.9mm and 1.0-2.0mm. It can be easily replaced according to the experimental purpose. Three fast closing gate valves denoted with V1, V2 and V3 are immediately closed after shooting the pellet with a necessary closing time of 5ms. The He gas leakage to the LHD vacuum vessel can be almost avoided by the differential pumping systems. The vacuum pressure is kept in order of 10^{-9}torr at the M3 chamber. The pellet velocity is measured at M1, M2 and M3 chambers using He-Ne laser, two sets of narrow slits and solid state detector in each of them.

The pellet velocity, V_p, is measured at a He gas pressure of 18atm and an opening time of the acceleration valve of 1.4ms, as shown in Fig.2. The horizontal axis means a ratio of the cross section, A_p, to the mass, m_p, of the pellet, which can be directly related to the acceleration force of the pellet. The measured velocities are roughly distributed around 200m/s showing a weak dependence of A_p/m_p. Here, we calculate the pellet velocity, $V_p(t)$, at a time, t, after the opening of the acceleration valve using the following equation, which is developed based on the hydrogen ice pellet;

$$V_p(t) = \frac{2C_0}{\gamma - 1}\left\{1 - \left[1 + \frac{(\gamma+1)A_p}{2m_p C_0} P_0 t\right]^{-\frac{\gamma-1}{\gamma+1}}\right\}, \quad (1)$$

where P_0 is the propellant gas pressure, C_0 the propellant gas sound speed and γ the ratio of specific heats[6]. The acceleration length of the pellet is given by

$$L = \int V_p(t)dt = \frac{2C_0}{\gamma - 1}\left\{ t - \frac{m_p C_0}{A_p C_0}\left[1 + \frac{(\gamma+1)A_p P_0}{2m_p C_0} t \right]^{\frac{2}{\gamma+1}} \right\} + \frac{2m_p {C_0}^2}{(\gamma-1)A_p P_0} \quad . \tag{2}$$

The theoretical prediction of the pellet velocity is obtained for the cylindrical pellet by solving the equations, as plotted with solid line in Fig.2. There exists a big discrepancy between the theoretical prediction and the experimental values. In the equation any gap is not taken into account between the ice pellet and the inside of the acceleration pipe. In case of the present impurity pellet, however, the size of the pellet is smaller than the inside diameter of the acceleration pipe, in particular, for the case of smaller pellets. Therefore, the pellet velocities in the present pellet injector are weak functions of the size, the shape and the mass of the pellet. In practice, the velocities distribute between 100 and 300m/s slightly depending on the He gas pressure.

A variety of pellets have been injected into LHD plasmas for observing the plasma response[7]. The results of the pellet injection with atomic numbers of Z=1 (H_2), 6 (C), 13 (Al), 22 (Ti), 26 (Fe), 42 (Mo), 50 (Sn) and 74 (W) are plotted in Fig.3. The largest density rise, Δn_e, closed to 10×10^{13}cm^{-3} is obtained at hydrogen and carbon pellets without plasma collapse. The possible density rise decreases with Z. For elements of $13 \le Z \le 22$ the density rise is seemed to be less than $1\text{x}10^{13}$cm^{-3}. For elements greater than Z=42 the density rise becomes meaningless, indicating only the meaning as spectroscopic use. The discharges denoted with 'marginal' means those in which the plasma performance does not recover quickly after the pellet injection, but the plasma collapse is not appeared. As a result, the carbon is selected as the element for the present study.

3 Electron density and temperature of carbon pellet ablation cloud

The ablation cloud of the carbon pellet injected to neutral-beam heated discharge with line-averaged density of $1.2\text{x}10^{13}$cm^{-3} and central electron temperature of 2.5keV is studied directly by measuring several spectral lines in range of 2000 to 7000Å emitted from the cloud[8]. The line profile of CII ($1s^2 2s^2\, 3p\ ^2P^0$ - $3d\ ^2D$) transition is observed with a high-resolution 1.3m visible spectrometer and analyzed to measure the electron density of the pellet cloud, as shown with solid circles in Fig.4(a). The density in the cloud can be basically analyzed by taking into account the Zeeman splitting, stark broadening and absorption effect of three lines with J=1/2-3/2 transition at λ=7231Å and J=3/2-5/2 and J=3/2-3/2 transitions at λ=7236Å. The stark broadening profile, $I_S(\lambda)$, is approximately expressed by a Lorentzian function of

$$I_S(\lambda) = \frac{\omega}{2\pi} \frac{1}{(\lambda - \lambda_0)^2 + (\omega/2)^2} \quad , \tag{3}$$

where ω is the full width at half maximum (FWHM) and λ_0 the central wavelength of the line. The values of ω can be reported by Goto et al.[8] as a function of electron density. The Doppler broadening is also considered assuming $T_i=T_e=2.5$eV which corresponds to the Doppler half width of 0.153Å. Here, the electron temperature is analyzed by spectroscopic method as described later. The convolution of the Doppler (Gaussian: I_D) and Stark (Lorentzian: I_S) profiles is defined as Voigt profile, I_V.

The Zeeman splitting is calculated in the wavelength shifts and relative intensities assuming the observation chord perpendicular to the magnetic field. The result at

B_t=2T is plotted in Fig.4(b) as π and σ components. The Voigt profile is thus obtained with dotted line in Fig.4(a) taking into account Doppler broadening, Stark broadening and Zeeman splitting. The Voigt profile from the present calculation gives large values compared to the experimental values, although the experimental data can not be explained only by the Doppler fitting shown with dashed line as a matter of course. The absorption effect is therefore considered to explain the discrepancy. The spectral profile with absorption, $I_{abs}(\lambda)$, is evaluated from the spectral profile without absorption[9], $I(\lambda)$, using the following equation of

$$I_{abs}(\lambda) = \frac{I(\lambda)}{\kappa(\lambda)L}\left[1 - \exp(-\kappa(\lambda)L)\right], \quad (4)$$

where $\kappa(\lambda)$ is the absorption coefficient and L the plasma length. Here, the plasma volume, V, is considered to obtain the plasma length as $L=V^{1/3}$. The experimental data are fitted again under consideration of the absorption effect as plotted with solid line in Fig.4(a). It is obvious that the present calculation included the absorption effect can well explain the experimental profile. Thus, we finally obtain the density of $n_e=6.5\times10^{16}cm^{-3}$ and the plasma volume of $5.3cm^3$ for the pellet ablation cloud.

The Saha-Boltzmann equation with level populations is given by

$$\frac{N_q(p)}{g_q(p)} = \frac{1}{2g_{q+1}(1)}\left(\frac{h^2}{2\pi m_e kT_e}\right)^{3/2} \exp\left[\frac{\chi_q(p)}{kT_e}\right] n_e N_{q+1}, \quad (5)$$

where $N_Z(p)$, $g_Z(p)$ and $\chi_Z(p)$ are volume-integrated population, statistical weight and ionization energy of level p of the ion in charge state q, respectively, and p=1 denotes the ground state. The electron temperature can be determined from the equation, when the level population of ions in the ablation plasma is expressed by local thermodynamic equilibrium (LTE). The volume-integrated populations normalized by their statistical weights are plotted in Figs.5(a) and (b) for CII and CIII excited levels, respectively. The electron temperature is finally determined to be 2.5eV and 3.0eV by the least-squares fitting indicated with solid line for CII and CIII ions, respectively, since the density and plasma volume are already determined from the spectral profile. These plasma parameters of the pellet ablation cloud reasonably certificates the particle deposition at the plasma core with the density profile change after the pellet injection.

4 Plasma performances after carbon pellet injection

The confinement of LHD discharges is studied by injecting large carbon pellets with sizes of 1.2-1.8mm. The maximum size of the cylindrical pellets which can maintain the discharge without plasma collapse is $3.4^{\phi}mm\times3.4mm^{L}$ for H_2 ice pellet and $1.8^{\phi}mm\times1.8mm^{L}$ for carbon pellet under P_{in}~10-18MW. Larger pellets of 3.8mm for H_2 and of 2.0mm for carbon were tried, but the smooth operation of discharges was a little difficult. The maximum plasma stored energy, W_p, which is observed after carbon pellet injection at plasma axis position of 3.6m, divided by the absorption power is summarized in Fig.6 by comparing with H_2 gas puffing and ice pellet injection. In order to delete the effect of different input power ($5\le P_{NBI}\le18MW$) the vertical axis is normalized by power dependence appeared in the Stellalator scaling[10] of

$$\tau_E = 0.079a^{2.21}R^{0.65}P_{abs}^{-0.59}n_e^{0.51}B^{0.83}(\iota/2\pi)^{0.4}, \quad (6)$$

where the value of $\iota/2\pi$ is the rotational transform at 2/3 radius. The data for the H_2 pellet include multi-pellet injection, whereas those for the carbon pellet are obtained

from single-pellet injection. The favourite operational range is therefore different for both pellets (C: 2-4x10^{13}cm^{-3}, H_2: 4-10x10^{13}cm^{-3}). In LHD the confinement improvement has been observed so far compared to the ISS95-scaling[11]. It is indicated as "1.5×ISS95" which means 1.5 times as large as the ISS-95 scaling. The present data from the carbon pellet injection reveals the good confinement property in the relatively low-density range.

The radial ablation profile can be well controlled by the carbon pellet by adjusting the discharge operation scenario, although the control is difficult for single H_2 ice pellet injection due to the short penetration depth. The difference between the two pellets is essentially based on their different sublimation energies, i.e., 0.005eV for solid hydrogen and a few eV for carbon. When the neutral beam power is reduced at the carbon pellet injection, the entire central deposition is possible. Here, it should be pointed out that any global instability is not occurred whereas the T_e profile becomes extremely hollow at the central deposition of the carbon pellet. Therefore, the improvement of the confinement in the carbon pellet injection basically originates in the density profile control in addition to the efficient fuelling.

The energy loss processes after the carbon pellet injection are essentially the ionization and the radiation loss. The ionization loss is the total summation of ionization energies necessary for ionizing the carbon up to C^{6+}. The radiation loss is practically equal to the electron excitation loss which is determined by the total summation of collisional excitation in each change state of the carbon ions. The radiation loss energy is a function of ionization speed of the carbon ions ablated from the pellet cloud, which largely depends on the temperature response after the pellet injection. When the total ionization time from C^0 to C^{6+}, Δt_{ion}, is estimated to be order of 1ms, the radiation loss energy is roughly 150kJ at the carbon pellet injection with Δn_e=5x10^{13}cm^{-3}. It is clear that the radiation loss energy, W_{rad}, is much larger than the ionization energy, W_{ion}, e.g., W_{rad}/W_{ion}~5 at Δt_{ion}=1ms. In brief, the discharge goes to the collapse if the radiation loss energy exceeds the plasma stored energy.

In LHD three negative-ion-source based neutral beams with high beam energy of 180keV are installed tangential to the torus in addition to a positive-ion-source based neutral beam with low beam energy of 40keV. The positive neutral beam installed perpendicular to the torus is mainly used as diagnostic tool for the ion temperature measurement and the confinement study of energetic ions. The cylindrical carbon pellet with a size of 1.4mm^{L}x1.4mm$^{\phi}$ is injected to the neutral beam heated plasma with relatively low input power of 12MW to make the pellet deposit to the central plasma region because the carbon pellet ablation is extremely sensitive to the heat flux of high-energy ions brought by the neutral beams[12]. Typical discharge waveform is shown in Fig.7. After the pellet injection the neutral beam power is increased to the maximum level of 16-18MW. The density is quickly increased and reaches the peak density of 5x10^{13}cm^{-3} within 50ms after the carbon pellet injection. The central electron temperature gradually recovers with the density decay and reaches considerably high electron temperature of $T_e(0)$=4keV at 300ms after the pellet injection. This value clearly exceeds the electron temperature appeared in normal hydrogen discharges. The diamagnetic energy meets the maximum value at earlier time compared to the electron temperature. The radiation loss power is kept at considerably low level (P_{rad}<1MW) even in the phase of carbon pellet injection. The sawtooth-like behavior

seen in the radiation loss signal is affected by the fast neutrals originated in the positive neutral beam.

The ion temperature differently behaves from the electron temperature[13]. It still increases after the electron temperature meets the maximum value and keeps a constant value. The central ion temperature reaches the maximum value of $T_i(0)$=5.6keV with the central density of $n_e(0)=1.6\times10^{13}cm^{-3}$ (line-averaged density: $n_e=1.3\times10^{13}cm^{-3}$) at t=2.4s after 600ms of the pellet injection, at which the density decay is already finished. Here, it is noticed that the density at t=2.4s is still high compared to the original density before the pellet is injected. It is believed that the carbon ions remain in the plasma as a recycled particle.

The ion temperature profiles after the carbon pellet injection interestingly behave at the interior of half radius, as shown in Fig.8(a). The gradient of the ion temperature is seemed to change at R=4.2m suggesting an internal transport barrier (ITB) formation[14,15], whereas three electron temperature profiles shown in Fig.8(b) are similar each other having no sudden change in the radial gradient. The ion transport is considerably improved at the plasma center. For example, the ion thermal diffusivity, χ_i, at ρ=0.25 is reduced to one-third at t=2.37s compared with that in normal discharges without ITB as seen at t=2.01s. The reduced value of $\chi_i=2.2m^2/s$ during the ITB formation is close to the neoclassical value of $\chi_i=2.0m^2/s$.

A large toroidal rotation velocity[16], which is mainly brought by the momentum input of the tangential NBIs, is also observed during the ITB formation, as shown in Fig.8(c). The central rotation velocity reaches 100km/s at t=2.41s, which corresponds to one-third of the thermal velocity of carbon ions. The reduction of the parallel viscosity is also observed during the ITB formation, i.e., $\mu\sim3m^2/s$, which is close to the χ_i. At present, the relation between the reduced ion thermal diffusivity and the appeared large toroidal rotation is entirely unclear.

5 Summary

The carbon pellet has been used for the experiments of LHD. After the carbon pellet injection it is observed that the plasma confinement is improved in density range of $2\text{-}4\times10^{13}cm^{-3}$ and the reduction of the ion thermal diffusivity, of which the value is close to the neoclassical one, is also observed with the appearance of the ITB formation. The carbon pellet injection reported in this paper has fully demonstrated the importance as the experimental tool in LHD.

Acknowledgements

The authors acknowledge all members of LHD experiment group for their technical supports and fruitful discussions. This work was partially carried out under the LHD project financial support (NIFS09ULPP527). This work was also partially supported by the JSPS-CAS Core-University program in the field of 'Plasma and Nuclear Fusion'.

References

1 Sakamoto R, et al. 2009, Nucl. Fusion, 49: 085002
2 Morita S, Goto M, et al. 2003, Nucl. Fusion, 43: 899
3 Morita S, Dong C F, Goto M, Kobayashi M, et al. to be published in Plasma Fusion Research
4 Katai R, Morita S, et al. 2007, Jpn. J. Appl. Phys., 46: 3667
5 Nozato H, Morita S, 2003, Rev. Sci. Instrum., 74: 2032
6 Combs K, 1993, Rev. Sci. Instrum., 64: 1679
7 Morita S, Goto M, et al. 2008, Presented at the 35th EPS Conference on Plasma Phys., 32D-P1.105, Hersonissos, Greece, EPS
8 Goto M, Morita S, Koubiti M, 2010, J. Phys. B, 43: 144023
9 Goto M, Sakamoto R, Morita S, 2007, Plasma Phys. Control. Fusion, 49: 1163
10 Stroth U, et al. 1996, Nucl. Fusion, 36: 1063
11 H.Yamada, R.Sakamoto, J.Miyazawa et al., 2007, Plasma Phys. Control. Fusion, 49: B487
13 Morita S, Shirai Y, et al. 2002, Nucl. Fusion, 42: 876
14 Morita S, Goto M, et al. 2002, Nucl. Fusion, 42: 1179
15 Ida K, et al. 2010, Contributions to Plasma Phys., 50: 558
16 Nagaoka K, et al. 2010, Presented at the 23th IAEA Fusion Energy Conference, EXC/P4-08, Daejeon, Korea, IAEA
17 Morita S, Nozato H, Takeiri Y, et al. 2003, J. Plasma fusion Res., 79: 641

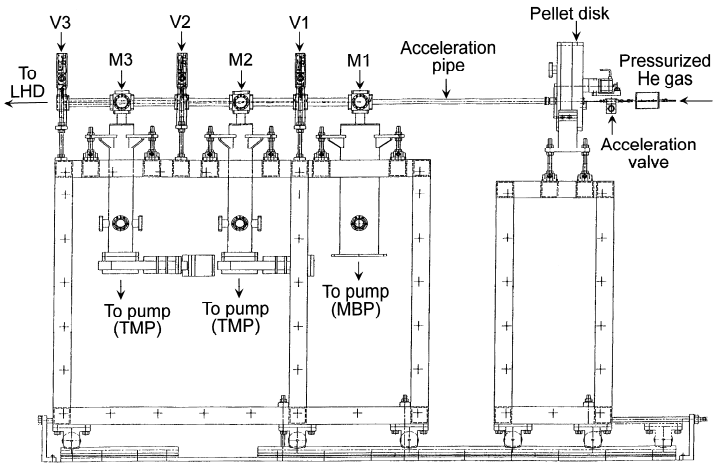

Fig.1 Impurity pellet injector for LHD with three differential pumping system (TMP (300l/s): turbomolecular pump, MBP: mechanical booster pump) separated by three fast closing valves (V1, V2, V3). Pellet velocity is measured at three vacuum chambers (M1, M2, M3) using He-Ne lasers.

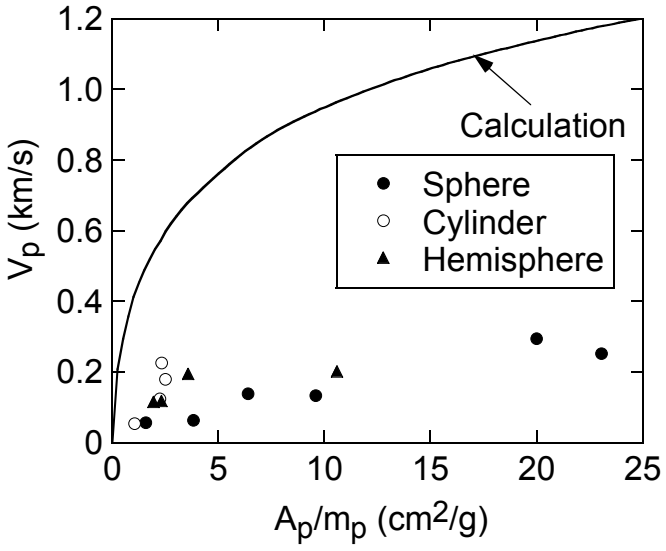

Fig.2 Pellet velocity, V_p, measured at M1 in Fig.1 as a function of ratio of cross section, A_p, to mass, m_p, of spherical, cylindrical and hemispherical pellets. Solid line indicates theoretically predicted pellet velocity.

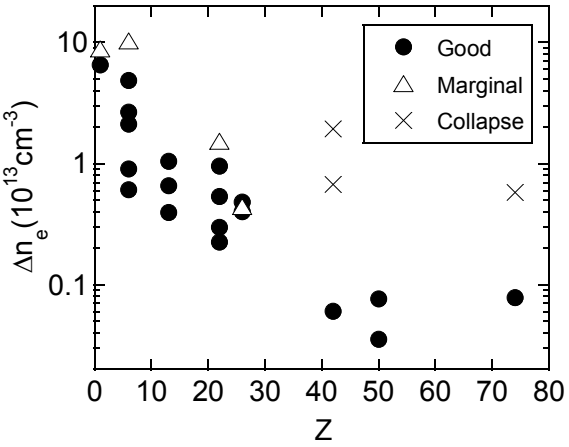

Fig.3 Density rise after single pellet injection in LHD against several elements of hydrogen, carbon, aluminum, titanium, iron, molybdenum, tin and tungsten.

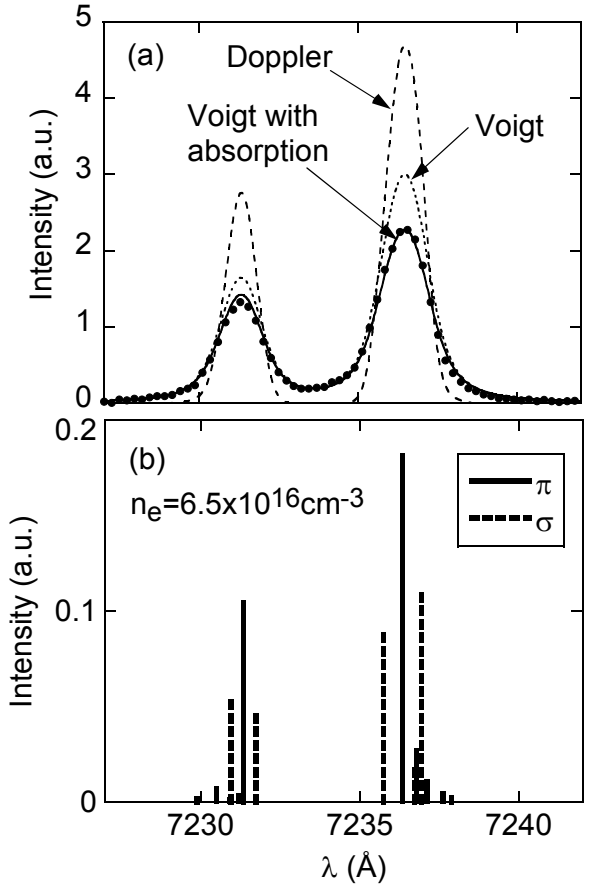

Fig.4 (a) Line profile of CII $2s^2 3p\ ^2P^0$-$3d^2D$ measured from carbon ablation cloud (solid circles). Three fitting curves denote Doppler broadening (dashed), Doppler and Stark (dotted) and Doppler and Stark with absorption (solid). (b) Calculation of Zeeman-split π (solid lines) and σ (dashed lines) components.

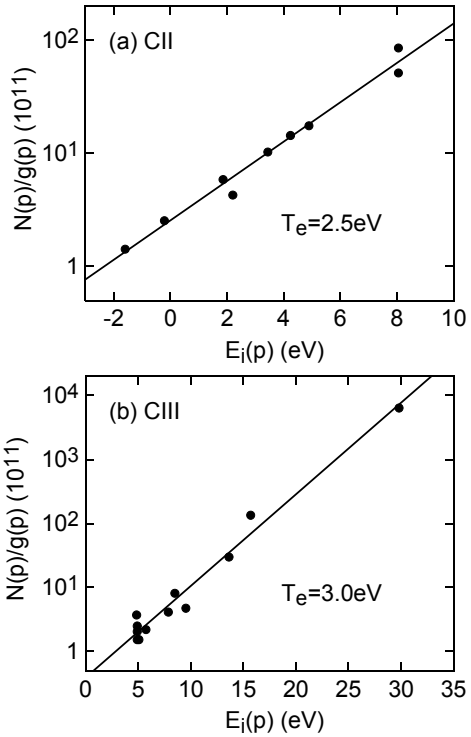

Fig.5 Volume-integrated populations of (a) CII and (b) CIII excited levels normalized by their statistical weights as a function of ionization energy calculated from ionization limit. The fittings of data denoted with solid lines determine electron temperatures through Saha-Boltzmann equation.

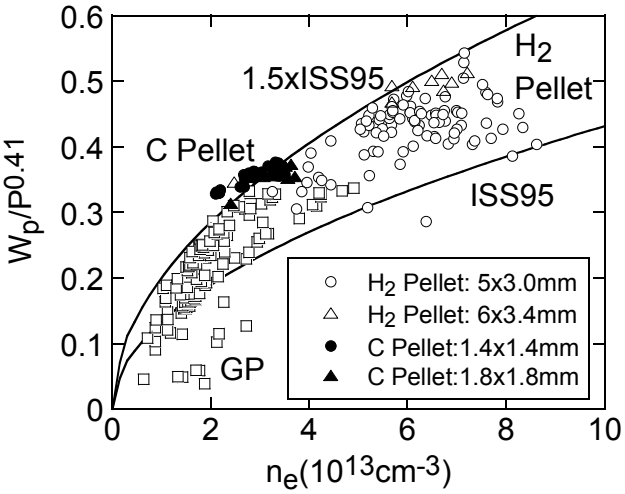

Fig.6 Performance of NBI discharges after carbon single pellet injection (closed triangles and circles) and hydrogen multi-pellet injection (open circles and triangles) as a function line-averaged electron density. Solid line denoted with 'ISS95' indicates international stellarator scaling normalized by input power (Wp [MW], P [MW]). Notation of '5x3.0mm' for H2 pellet means successive five pellet injection with cylindrical size of $3mm^{L}x3mm^{\phi}$, whereas '1.4x1.4mm' for C pellet means only the cylindrical size of $1.4mm^{L}x1.4mm^{\phi}$.

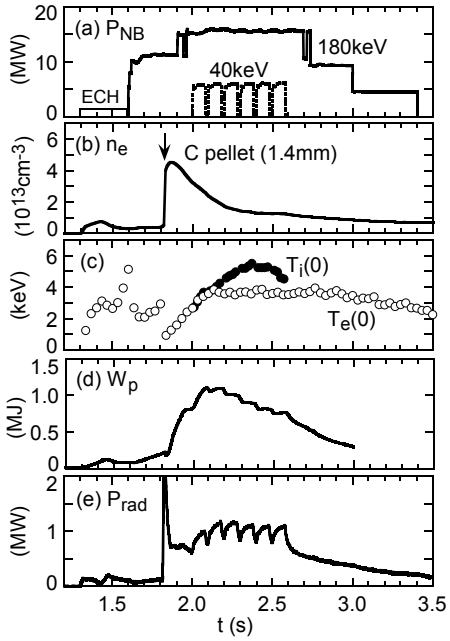

Fig.7 Discharge waveforms of (a) NBI power, (b) line-averaged electron density, (c) central electron and ion temperatures, (d) plasma stored energy and (e) total radiation power. Cylindrical carbon pellet with size of $1.4mm^{\phi}\times1.4mm^{L}$ is injected at t=1.82s as indicated by arrow.

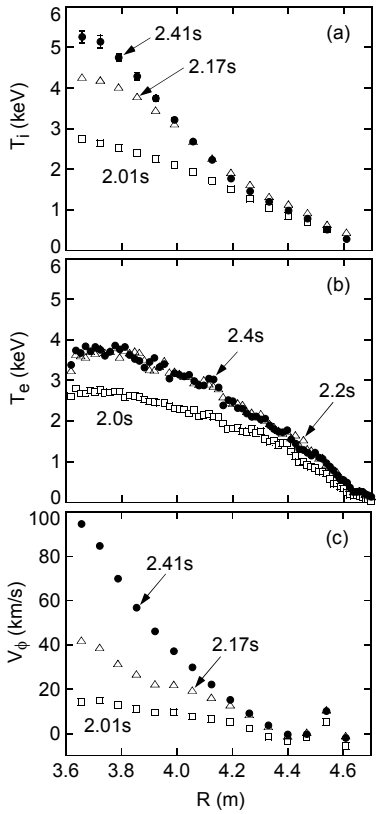

Fig.8 Radial profiles of (a) ion temperature, (b) electron temperature and (c) toroidal rotation velocity after carbon pellet injection at three different discharge times as shown in Fig.7.

Present status of the EAST diagnostics

L.Q. HU, on behalf of EAST diagnostic team and collabrators
Institute of Plasma Physics, Chinese Academy of Science, P.O. Box 1126, 230031, China
Email of the responsible person: lqhu@ipp.ac.cn

Abstract: since the 3rd EAST campaign in 2008, many new techniques have been applied to enhance DN divertor plasma performance, including modification of in-vessel structures and PFCs, iso-flux real-time feedback control, full graphite wall with active water cooling, internal cryo-pump, many significant progress have been achieved. Being a very important step of EAST project, tens of diagnostics were employed for machine operation and protection, plasma control and physics analysis. To accommodate requirement of EAST plasma performance study with upgraded RF injection power up to 4-6MW (both LHCD and ICRF) in the coming two years, new diagnostics are set up to provide various key profiles of plasma parameters not only for the evaluation of the basic plasma performance but also for the understanding of the plasma physics, including 25ch. Thomson scattering system for density and electron temperature, metal bolometry for radiation power, x-ray crystal spectroscopy for ion/electron temperature and plasma rotation velocity, etc. It is expected that these diagnostics would play an important role on data analysis and interpretation based on integrated modeling.

Keywords: plasma diagnostics, tokamak

PACS: 52.70.–m, 52.55.Fa

1. Introduction

EAST (Experimental Advanced Superconducting Tokamak) device is aimed to achieve steady-state high-performance plasma sustained by intensive use of radio frequency heating and current drive, and to study relevant physics and technology. The initial three campaigns were addressed the feasibility of the full superconducting magnets and control algorithm with new features to explore some critical issues relating to steady-state operation with shaped plasma configurations. Since the third campaign in 2008, many new techniques

have been employed to upgrade DN divertor plasma performance, including modification of in-vessel structures and PFCs, iso-flux real-time feedback control, full graphite wall with active water cooling, internal cryo-pump, etc., much significant progress has been achieved [1-4]. Repeatable long divertor plasma discharges with 0.25MA/1minute, 0.25MA/8s fully non-inductive current driven by 1MW LHW had been demonstrated in the 4th campaign last year. In recent 6th campaign, 0.9MA/9s plasma sustained by 1.0MW LHW, and 0.7MA plasma with 2.5MW injected RF power (0.8MW LHW plus 1.7MW ICRF) are obtained. In the meantime, ICRF wave coupling with plasma, LHCD current drive and heating, divertor plasma behavior, plasma initiation with LHW assistant, and different wall conditioning techniques for enhancement of plasma performance and ICRF heating effect have been carried out and studied.

2. Setup of EAST diagnostics

Diagnostic requirements of the EAST are determined by demands of measurement and physics study to characterize the plasma behavior over the full range of conventional plasma parameters, which are varied in different operation scenarios. Basic diagnostics with schematic arrangement illustrated in Fig.1, consist of plasma position and shape, plasma current and loop voltage, vacuum vessel current, electron density, electron temperature, impurity species, various of plasma radiations in different energy range, temperature of the limiter surface and divertor plates, vacuum pressure and mass spectrum, mainly for monitoring and control of machine operation and protection, and description of the basic plasma performance. In the initial two EAST campaigns with full stainless-steel first wall and hydrogen operation gas, about 15 diagnostics were used, except in-vessel diagnostics of magnetic diagnostic, divertor probe and thermocouple, external diagnostics were those used on HT-7 tokamak with some modification of connecting flange and cables due to short of budget. Since the 3rd campaign in 2008, diagnostics have been set up gradually to accommodate EAST features of DN/SN configuration, LHW and ICRF plasma, long pulse discharge, and cover whole region of conventional plasma operation. Until the 5th campaign 2010, diagnostics up to 25 have been employed routinely with extensive function of divertor plasma performance study. In recent campaigns, some key diagnostics focusing on profile of

parameters, such as a Nd:YAG Thomson scattering system [5], a x-ray imaging crystal spectrometer (XCS) [6-7] and a metal bolometer array with newly developed Pt resistor by IPT company, shown in Fig.2, Fig.3 and Fig.4 separately, are applied successfully for evaluation and optimization of the plasma performance, and further for plasma physics understanding. Diagnostics available on EAST tokamak machine is listed in the table 1, in which their function, measurement and purpose are presented, respectively.

3. Basic diagnostics

Magnetic diagnostics involved in plasma equilibrium defining and real-time feedback control were constructed with enough spatial resolution and high accuracy better than 1% for measurement of plasma current and PF coil current with Rogowski coils, and better than 3% for measurement of the poloidal field with magnetic probes and poloidal magnetic flux with flux loops. Combined with a plasma control system (PCS) built in tight collaboration with GA/USA, which is similar to the PCS of DIII-D, real-time EFIT (RTEFIT) for the plasma equilibrium reconstruction and ISOFLUX for the position control of special 8-point on last close magnetic flux surface was realized successfully to obtain DN plasma with elongation κ=1.9/triangurity δ=0.40, SN plasma with κ=1.7/δ=0.64, and to control LHW driven plasma for 63s with ISOFLUX feedback control more than 60s, which already covering all EAST designed configurations. Two groups of Mirnov probes in toroidal direction, each with 38 two-components in poloidal direction with accuracy of 10%, 100 kHz, together with soft x-ray photodiode (PDA) cameras for tomographic reconstruction are used to identify and study MHD instability and other transient electromagnetic behaviors. Plasma store energy is measured by three groups of diamagnetic loop in toroidal direction with an accuracy of 15-20%. Vacuum vessel current and halo current are measured as well for operation safety.

Two tangential visible CCD cameras provide wide-view images coving whole cross-section of the plasma, most area of the inner wall, part of the upper and lower divertor area, movable limiter, ICRF heating and conditioning antenna, and GDC anode, together with one tangential IR CCD camera to constitute an effective inspection way for machine operation, control and protection. A vertical 3ch. far-infrared (FIR) 337-μm HCN laser interferometer is used for measurement of the line average electron density and their feedback control by gas

puffing. The 25ch. multipoint & multipulse Nd:YAG Thomson scattering system for electron temperature and density, a horizontal 15ch. soft x-ray PHA and a horizontal 16ch. ECE for electron temperature, together with two sets of soft x-ray PDA orthogonal cameras (3, each with 35ch.) and two sets of AXUV PDA orthogonal cameras (3, each with 16ch.), and 8 ch. visible bremsstrahlung measurement for effective charge number, have been employed to study core plasma behavior. Edge and divertor plasma, particle recycling and confinement are studied by measuring Ha/Da line radiation distribution with three 35ch. PDA Hα/Dα cameras, in which two cameras view upper and lower divertor region horizontally through a reflecting mirror respectively and one camera views lower dome region from the top port, jointing with fixed divertor Langmuir probes near the divertor target plate and two fast reciprocating probes (2m/s). Combing with fixed Mach probes, fluctuations of potential and density in the plasma boundary like the blob, zonal flow, GAM etc., can be investigated as well. The total spectrum and behavior of the impurity in main plasma, edge plasma and divertor region, and wall conditioning effects are studied by two OSMA (Optical Spectroscopy Multi-Channel Analysis in a spectrum range of 200~1000nm), five UV-VIS monochrometer mainly for CIII, OII, LiI, BI and SiI, two fibre optical spectrometers (200-700nm), and a vertical 18ch. CIII PDA array, while heavy metal concentration and distribution is monitored by the horizontal 15ch. SXS PHA system. One OSMA SP750 with fine resolution 0.02nnm and observation range 5nm consists of 15ch. for main plasma and 15ch. for lower plasma, the other OSMA SP300 with coarse resolution 0.4nnm and observation range 250nm contains 8ch. for main plasma and 8ch. for lower plasma. Distribution of the radiation flux and energy of the fast electron bremsstrahlung emission (FEB) are measured by a tangential hard x-ray array with CdTe detectors, especially for LHCD plasma performance and LHW wave deposition. Runaway behaviors with radiation flux and energy are monitored by a vertical array of NaI(TL) scintillator (1.0-10MeV), a set of tangential system with BGO scintillator (0.5-7MeV) and CdTe (0.3-1.2MeV). Neutron yield and flux measurement are also available using an external 235U fission chamber and four channels of ^{3}He proportion counts detectors, while the spectrum of the neutron is provided by an external liquid BC501 monitor.

4. Diagnostics for key parameters' profile

The high-resolution poloidal and tangential XCSs are implemented on EAST to provide spectrally and spatially resolved images of the plasma on the ion and electron temperature, poloidal and toroidal impurity rotation velocity for all experimental conditions, which are derived from satellite spectra of helium-like argon Ar XVII. Ti, Te and electron density are obtained, the clear toroidal flow with a maximum value of 40 km/s is observed by the XCS for LHCD plasma, and the direction of toroidal flow in core region is consistent with that in edge region measure with the Longmuir probe [6-8]. The upgraded 2D ECE image system with non-spherical (hyperboloid) lens and dual dipole antenna mixers is used to collect the 2nd harmonic of ECE from the core plasma, working well in the frequency ranges of 100~120GHz with the magnetic field 1.4T~2.5T to study core MHD activity and real time fluctuations of the electron temperature. A Pt resistor bolometer array with capability of 14 miniaturized 4ch.-units (IPT-Albrecht GmbH) is setup to measure radiated power and study global and local energy balance.

5. Summary

With actively cooled PFC and SS H&CD, long pulse divertor plasma operation and high performance plasma physics study EAST have been started. For present routine diagnostics, more efforts on diagnostics are needed for accommodate EAST physics requirements, including extending present diagnostics ability, calibration, data interpretation, etc. As the increase of heating power to 4MW, high confinement mode plasma could be achieved, therefore coming physics study will require diagnostics provide reliable and precise data on study of RF physics, rf coupling issues, MHD and control, plasma and surface interaction, ELM-H mode (edge), ITB (weak positive or negative shear) etc. For those purposes, diagnostics toward all key profiles and some of specific measurements for physics understanding are under preparation. Many new diagnostics with upgraded capability, such as 20-channel grating polychromator (GPC) for wide toroidal field, 2D hard x-ray camera with LYSO scintillator, gas puff imaging (GPI), doppler reflectometer, filter scope, CO2 laser scattering and new 32ch. ECE system, are expected to be employed in next EAST campaign to fulfill those physics demands.

Acknowledgments

The author would like to thanks all members of EAST diagnostic group, to all attendee from domestic and international facilities for their contributions to EAST project. This work is undertaken partially under the support of Chinese Nature Science Funds by Grant No. 10935004 and No.10775041, and of the Core University Program on plasma physics between China and Japan.

References:

[1]Baonian Wan, 3rd EAST IAC meeting, Hefei, China, May 14-15, 2009

[2]Baonian Wan, etc., 22nd IAEA Fusion Energy Conference, OV3-4, October 13-18, 2008, Switzerland

[3]Jiangang Li, Yanping Zhao, Jianshen Hu, Xiangzu Gong, Review, R-3, 19th PSI Conference, San Diego, May 24-28, 2010

[4]H.Y. Guo, X. Gao, J. Li etc., Invited, I-8, 19th PSI Conference, San Diego, May 24-28, 2010

[5]Qing Zang, etc., 5th PRC-US Magnetic Fusion Collaboration Workshop, May 5-7, Wuhan, P.R. China

[6]Y.J. Shi, etc., 5th PRC-US Magnetic Fusion Collaboration Workshop, May 5-7, Wuhan, P. R. China

[7]Yuejiang Shi, Fudi Wang, Baonian Wan, Manfred Bitter, Sanggon Lee, Jungyo Bak, Kennith Hill, etc., Plasma Phys. Control. Fusion 52 (2010) 085014.

[8]Baonian Wan, etc., 23nd IAEA Fusion Energy Conference, OV1-2, October 11-16, 2010, Daejeon, Republic of Korea

*Domestic and international collaborators for the EAST: Donghua Univ., South West Institute of Physics, USTC, Tsinghua Univ., Peking Univ.; General Atomic, FRC Austin, PPPL, Tri Alpha Energy in USA; NIFS and JAEA in Japan; Association Euratom-CEA in France, NFRI and KBSI in Korea, etc.

Table 1 Diagnostics available on the EAST machine

Function	Measurements	Purpose
Te profile	TS(25ch.), ECE radiometer, SX PHA GPC, XCS (X-ray crystal spectrum.)	Auxiliary heating effects and optimization profile control, transport and confinement
line-averaged density Density profile	FIR DCN laser interferometer Microwave reflectometer	Fuelling optimization, transport
Ti profile	2-D XCS	Auxiliary heating effects and optimization, confinement
Radiation profile	SXR camera Bolometer, AXUV Tang. HX ray and 2D γ-ray camera Ha/Da array; VB array	Radiation power profile of global plasma, radiation loss mechanism, fast events understanding & control, FEB emission, LHW deposition & coupling, recycling, edge plasma, Divertor behaviors, Zeff profile
Plasma-wall interaction	Tang. visible CCD, IR camera	Deposition of heat load, filament, ripple…
Impurity line radiation, and spectrum	OSMA, UV-VIS, Fiber spectrometer, optical filterscope[#]; SXS spectrum PHA	Impurity species and density, dilution heavy impurity concentration
Runaway behaviors	CdTe+NaI + BGO detector	Run away electron dynamics
MHD instability	Magnetic diagnostics (Mirnov coil) SXR camera, ECEI	Plasma performance, Beta, li, W, Sawtooth and MHD instability
Divertor parameters (Ne /Te profile,	Divertor probe, Mach probe, thermocouple RF probe, Ha/Da, bolometer, …	)ivertor performance optimization, plasma flow, impurity & influx
Neutron flux, spectrum	3He, BC501, fission chamber	Flux, spectrum and emission profile
Vac. P of vessel diver.	Vacuum gauge	Operation scenario optimization, cryo-pump physics
Plasma rotation	XCS	Performance improvement, ML avoidance
q(r) profile	SXR+EFIT reconstruction	Performance improvement….

269

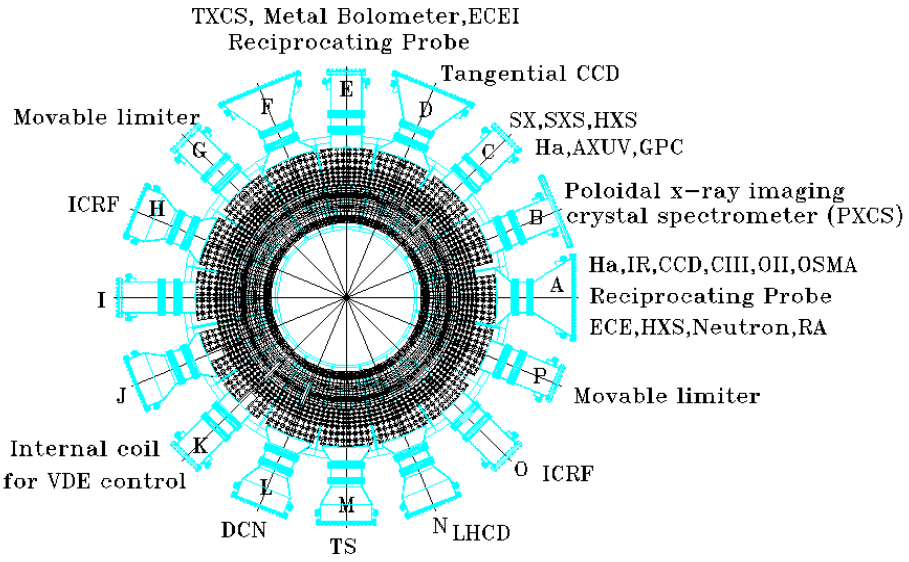

Fig.1 Down view of the EAST diagnostics arrangement

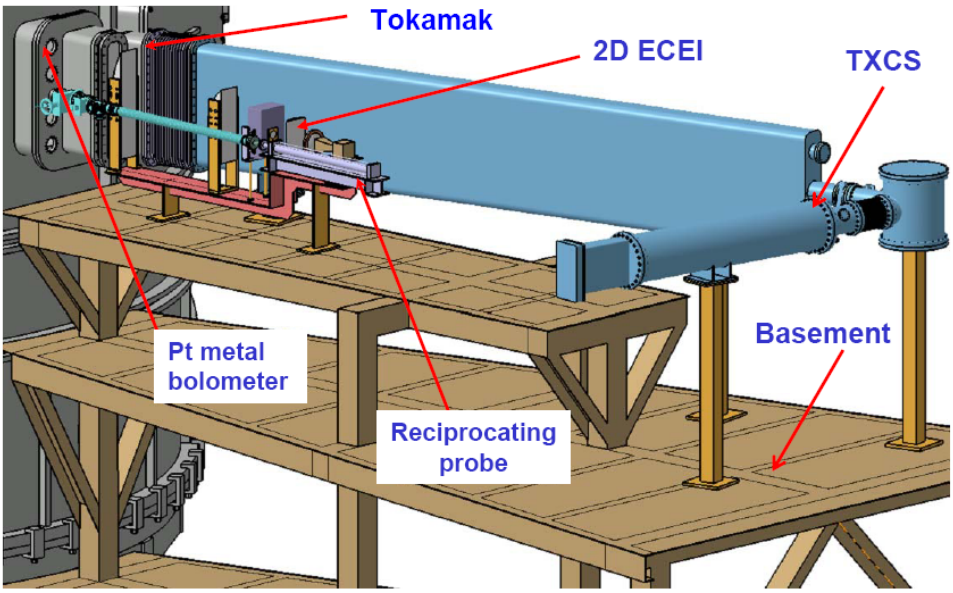

Fig.2 A integration of key diagnostics on window E

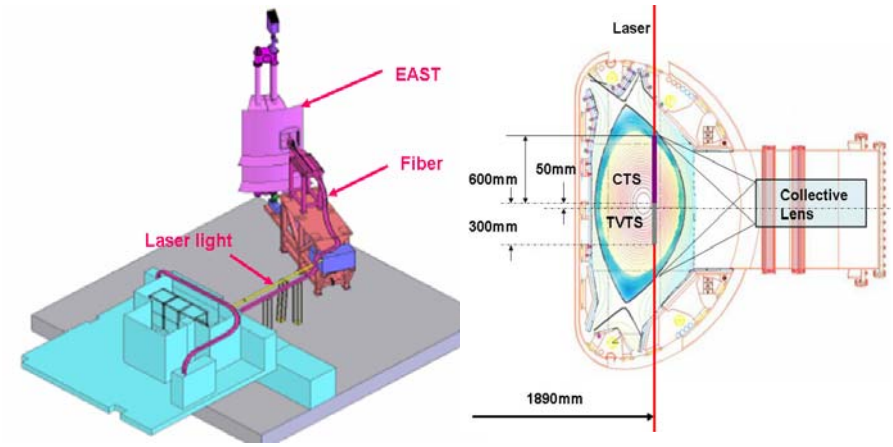

Fig.3 25ch. Nd:YAG Thomson scattering system

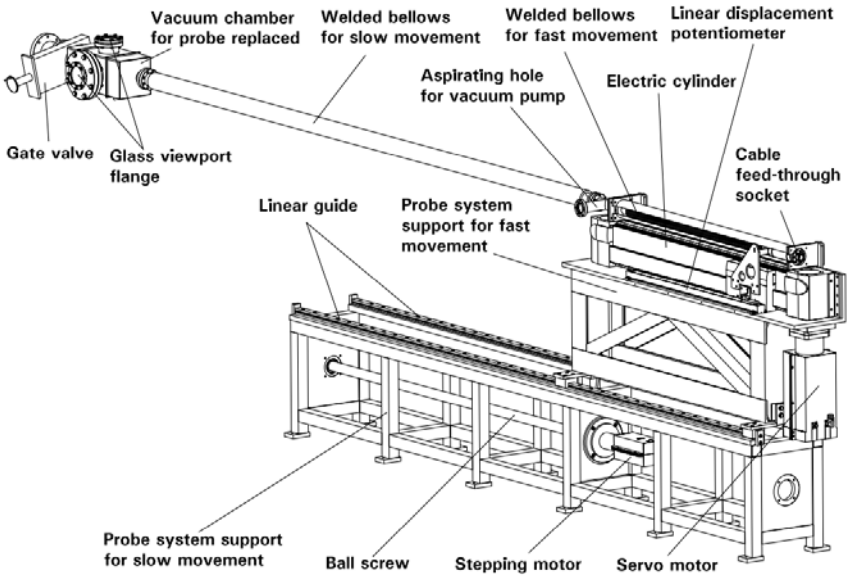

Fig.4 A fast reciprocating probe

Present status of the plasma diagnostics for JT-60SA

K. Itami and JT-60SA team
Japan Atomic Energy Agency, 801-1 Mukoyama, Naka, Ibaraki, 311-0193 Japan
E-mail contact of main author: itami.kiyoshi@jaea.go.jp

1. Introduction

The missions of JT-60SA project are to support ITER as the satellite tokamak and to support DEMO reactor design [1]. The scientific roles of the satellite tokamak are to provide well-diagnosed physics bases and to optimize the operational scenarios for ITER. The main scientific role in support of DEMO reactor design are to provide physic bases for steady state operation in high β_N plasma regimes. In this paper, the plasma diagnostic systems are classified into three categories and the resent status of those diagnostic systems is presented.

2.1 Plasma diagnostic system for machine protection and operation

The first category is the plasma diagnostic systems that are required for the machine protection and safe operation of the JT-60SA plasmas, including the neutron monitors, the visible and infrared TV cameras to monitor the plasma shape and the first wall, the Langmuir probes to identify the divertor equilibrium and D_α emission monitors. The diagnostics systems in this category must work reliably form the first plasma campaign in JT-60SA. Please note that all the magnetic probe diagnostics and thermo couples are defined as the in-vessel component in JT-60SA and these diagnostics are not presented here.

In-vessel visible and infrared camera system is crucially important in the initial plasma experiment after the construction of JT-60SA device. It is planned that the first wall area is almost fully monitored by 8 – 10 cameras which views tangentially the first wall and the plasmas, as shown in Fig. 1.

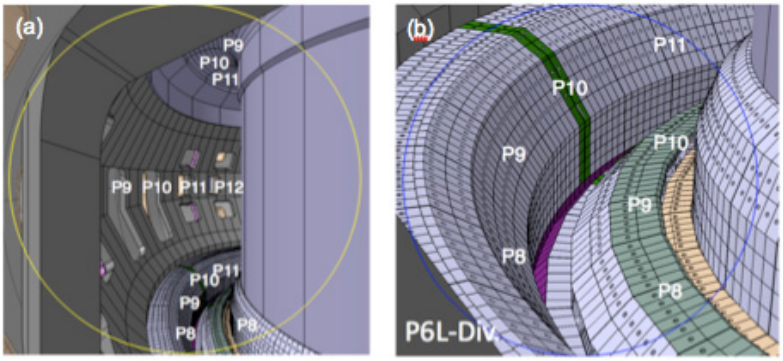

Fig. 1
(a)Field of view from the wide angle camera
(b) Field of view from the divertor camera

The neutron monitor system measures the neutron rate of the deuterium plasmas and that in the neutral beam injection (NBI) systems during conditioning. Since the neutron attenuation by the coils and cryostat is large, three micro fission chambers, installed in the port plug, are used to measure the neutron rate of the plasmas and two fission chambers are used mainly to measure the neutron rate form the NBI systems.

2.2 Diagnostic systems for the fundamental plasma parameters

The second category is diagnostic systems for the fundamental plasma parameters, such as the YAG laser Thomson scattering system for the electron density and temperature profiles, CO2 laser interferometer / polarimeter for line density of the plasma, electron cyclotron emission measurement, charge exchange spectroscopy for ion temperature and plasma rotation profiles, Z_{eff} profile monitor, VUV spectrometer, motional Stark effect polarimeter for the current density profiles and the bolometer.

The JT-60SA aims to sustain the high β_N plasmas above the no wall limit for 100 seconds, which is much longer than the current diffusion time [2]. Simulated profiles of the plasma parameters in the full current drive discharge of JT-60SA is shown in Fig. 2. Current profile is calculated with the assumed density and temperature profiles by ACCOME code.

This plasmas is characterized by high β_N and high bootstrap current fraction with strongly reversed shear profile. In such plasma, profiles of plasma parameters, such as the plasma density, ion and electron temperature, plasma rotation and plasma current density are coupled each other. In order to avoid disruptions by the MHD instabilities and to sustain such high performance plasmas for long pulse, accurate measurement of those parameters by the diagnostic system in this category and sophisticated real time control of those profiles are required.

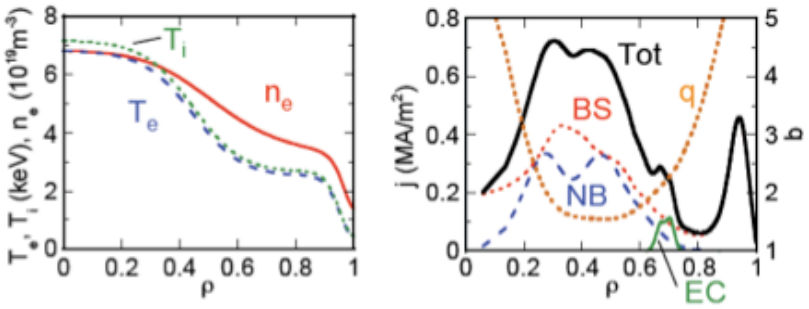

Fig. 2 Profiles in full CD plasma. Parameters are I_p/B_T = 2.3MA/1.7T, f_{BS} = 0.66, β_N = 4.3, H_H = 1.3 with P_{NNB} = 10MW, P_{NB} = 20 MW, P_{EC} = 7MW.

In order to meet this requirement, conceptual design of the Thomson scattering measurement with tangential injection of YAG laser has been made [3]. In JT-60SA, YAG laser beam is injected tangentially from P1 to P8 section on the equatorial plane, three collection optics are arranged in P1 lower oblique, P2 horizontal and P5 horizontal port plugs. The whole radial position in the plasma, from the high field side to the low field side, can be covered by three collection optics, as shown in Fig. 2. The vertical axis of this figure correspond to the radial special resolution. It is assumed that scattered light along the laser beam for each channel is focused on fiber bundles with 4 mm long.

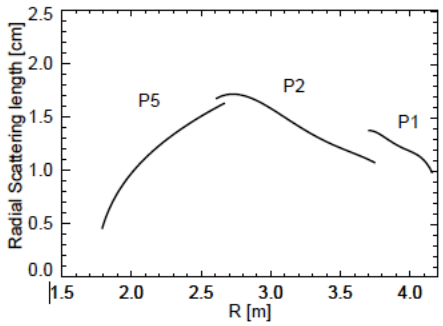

Fig. 3 Radial special resolution of Thomson scattering measurement

2.3 Diagnostic systems for physics understanding

The third category is the diagnostic systems for physics understanding. These plasma diagnostics measure the detailed behaviors of the MHD activities and high energetic particles and fusion products, fluctuations in the plasma and the behaviors of the divertor and scrape-off layer plasmas. The third category includes soft X-ray detector array, neutron emission profile monitor, neutron spectrometer, energetic neutral particle detectors, reflectometer, Li-beam probe, visible and VUV spectrometer for the divertor and neutral pressure gauges.

In the simulation for designing the divertor structure of JT-60SA [4], it has been demonstrated that neutral particle control by gas puffing and divertor pumping, accompanied by the strike point control, are essentially important to promote radiation loss from impurity ions in the divertor plasma and to sustain the detached condition at the strike points. The peak heat flux density must be suppressed on the target plate below 10 MW/m^2 by sustaining such radiative divetor plasma, as shown in Fig. 4 by utilizing two dimensional (2D) profile measurement of the divertor plasma parameters and real time control technique of the divertor plasma.

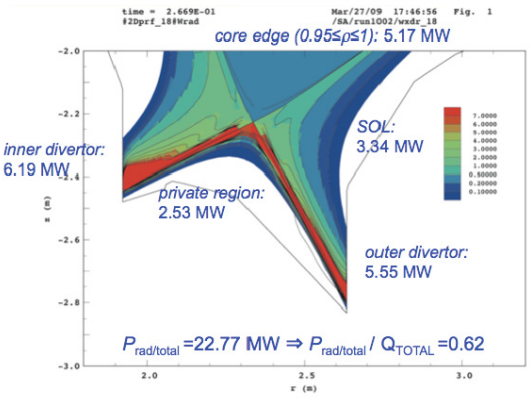

Fig. 4 Radiation profile in the divertor

In order to enable the horizontal viewing chords and 2D tomographic reconstruction of the divertor plasma, the slits in the target area are prepared at the four toroidal locations. Arrangement of viewing chords for visible spectroscopy for the divertor is shown in Fig. 4. Horizontal chords use the target slit at P6 section. The target slit is also assigned for the divertor bolometer at P16. The other slits will be assigned to the advanced divertor diagnostics, such as the divertor Thomson scattering and the retractable material probe, and etc. Feasibility studies of the advanced diagnostics are ongoing in collaboration with the universities in Japan.

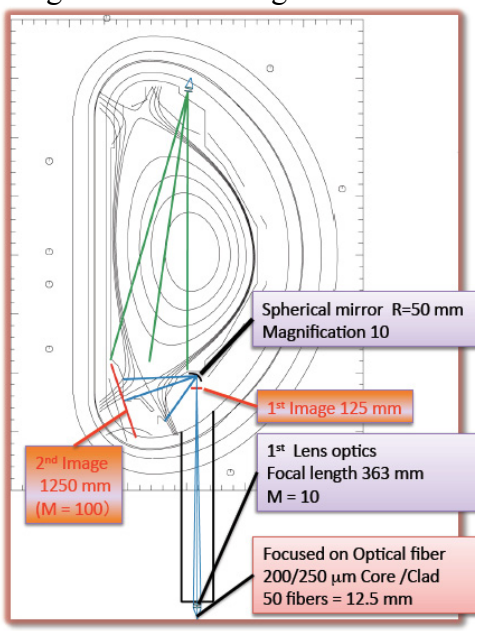

Fig 5
Optical design concept of visible spectroscopy

3. Port plug and vacuum window

Design study of the port plugs and arrangement of diagnostic components inside the port plug progressed significantly in 2010. Port plugs must share the vacuum vessel ports with the in-vessel component such as stabilizing plate, RWM coils, current feeder and water coolant pipes and etc., as shown Fig. 6. Arrangement of vacuum window in the port plug and diagnostic components inside the port plug are studied in detail, so that required field of view is obtained through aperture of the stabilizing plate. R &D activity of the vacuum windows and shutter mechanism d study are ongoing.

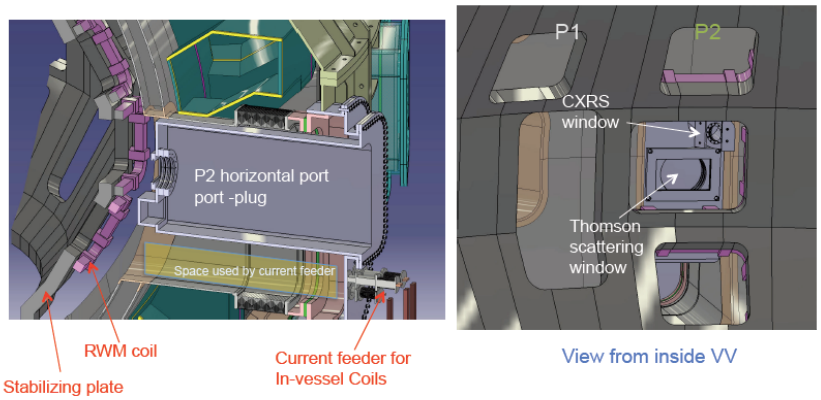

Fig.6
Port plug design for P2 horizontal port

4. Summary

Plasma diagnostic systems in JT-60SA will measure accurate profiles of main plasma and divertor plasma parameters and to provide real-time data for the plasma control system in order to control self-regulating high β_N plasmas for long pulse. Design activity for plasma diagnostics have progressed significantly for port allocation, design of front end component, arrangement of diagnostic systems in the torus hall steadily. Feasibility study of advanced diagnostics has started in collaboration with the universities in Japan. Design study of the port plug and arrangement of diagnostic inside the port plug is significantly progressed in 2010.

Acknowledgement

The presentation was also partially supported by the JSPS-CAS Core-University program in the field of 'Plasma and Nuclear Fusion'.

References

[1] S. Ishida et al., Proc. of the 23rd Fusion Energy Conf., 2010, OV/P-4.

[2] Y. Kamada et al., Journal of Plasma and Fusion Research SERIES Vol. 9 (2010) 641.

[3] H. Tojo et al., Rev. Sci. Instrum. 81, 10D539 2010.

[4] H. Kawashima et al., Fusion Engineering and Design 83 (2008) 1643–1647.

Review of the Low Frequency Collective Modes driven by Energetic Electrons on HL-2A

X.T. Ding, W. Chen, Yi. Liu, Q. W. Yang, X.Q. Ji, G. L. Yuan, Y. P. Zhang, X.Y. Song, Y. Zhou, Y. B. Dong, J. Zhou, X. M, Song, J. Rao, J. Q. Dong, X. R. Duan, and HL-2A team.

Southwestern Institute of Physics, P.O.Box 432 Chengdu 610041, China

E-mail contact of main authors: dingxt@swip.ac.cn

Abstract

The low frequency collective modes driven by energetic electrons on HL-2A, including fishbone and beta induced Alfven eigenmode (e-BAE) instability are reviewed. The experimental results associated with the e-BAE tokamak are observed for the first time in the HL-2A. The new phenomena of the e-fishbone, such as periodic mode frequency jumps and strong frequency chirping observed with higher ECRH power are also presented. The features of the two kinds of the low frequency collective mode are compared each other

1.Introduction

The MHD instabilities driven by the energetic-particle are important for future burning plasma devices, such as ITER and DEMO, because they will affect the alpha particle confinement. The instabilities driven by fast ions, such as fishborn and TAE, have been observed and investigated widely in many fusion devices. Whereas, the modes excited by energetic electrons remain much less studies than energetic ions. Actually, the low frequency collective modes can be driven by the energetic electrons and may affect the confinement of the energetic particles. The energetic-electron behaviors can also provide a contribution for burning plasma research, because their effect on low-frequency MHD modes can be used to simulate and analyze the alpha particles characterized by small dimensionless orbits, which is similar to energetic-electrons in resent tokamak plasma[1]. In the HL-2A tokamak, some low frequency collective modes driven by energetic electrons have been observed both in ohmic and ECRH plasma. The low frequency mode means that their frequency is much lower than TAE. In this paper, the experimental results will be reviewed and the features of the two low frequency collective mode are compared each other

2.Arrangement of the experiments

To investigate the energetic electron behaviors and their interaction with the collective modes, HL-2A (R_{ax} =1.65m, a=0.4 m)[2] is operated in two regimes: the

ohmic discharge with low plasma density and the discharge with high power ECRH. In these discharges, the electron can be accelerated both by the ohmic electric field and ECRH power. The fast electrons should be of asymmetric velocity distributions in the different discharges. In the ohmic discharges, the electrons are accelerated parallel to the toroidal field. In the ECRH discharges, the electrons are accelerated perpendicularly to the field and may become trapped particles. The high power ECRH system has been installed with four 68GHz/500kW/1S gyrotrons. The maximum power is up to 2MW. Both fundamental O-mode and second harmonic X-mode are adopted to inject plasma from the LFS. The ECW power can deposit at different radius both in LFS and HFS through change the toroidal magnetic field.

The collective modes measured by Mirnov probes and soft x-ray detector arrays. The Mirnov probe arrays are arranged around the wall of the device with 18 coils poloidlly and 10 coils toroidally. Five soft x-ray detector arrays are of 100 channels totally. The spatial and temporal resolutions are 2.5 cm and 10us, respectively. Cadmium-telluride (CdTe) detector is used to monitor the lower-energy hard X-ray (HXR) in the energy range of 10-200keV, which can be divided to 10 energy ranges. The nonthermal radiation measured by the ECE were also used to analyze the behaviors of the energetic electrons.

3. The e-fishborn instability on HL-2A

The fishbone activity was firstly observed on PDX [3], then on DIII-D [4]. Strong internal kink mode excited by energetic-electrons, called e-fishbone, was observed firstly in DIII-D[5], subsequently, recorded in other devices including HL-1M[6], FTU[7] and Tore Supra [8], in which the frequency-jump phenomenon was reported during LHCD. The e-fishbone can induce energetic-particle loss, trigger NTMs or ITBs, so it evokes much attention from the scientists, but it is still open problem at present.

The features of the e-fishbone has been identified on HL-2A[9,10]. The e-fishbone can be observed as a burst m/n=1/1 mode during ECRH. It is evident that the structure of the modes is located at the q = 1 flux surface. Its frequency is from several kHz to 15kHz and the frequency increase with the power of the ECRH or the population of the energetic electrons. The modes can be excited by ECRH deposited on both LFS and HFS. The modes occur much more easily during off-axis heating and propagate in the electron diamagnetic drift direction in the laboratory frame of reference.

When the ECRH power exceeds 0.7 MW, the frequency-chirping are very obvious as shown in Fig.1. Figure 1 shows the time evolutions of the HXR energy from 10 to 70 keV, plasma density and soft X- ray frequency spectrum. Abundant

experimental results indicate that the e-fishbone frequencies are higher and provided with up- and down-chirping behaviors, sometimes, also with V-font-style sweeping. The chirping mode is observed at frequency about 10 kHz on the soft X-ray signals.

The mode excitation is correlated with the energetic electrons obviously. The results of the HXR show that the frequency-chirping behaviors are strongly related to the population of the energetic electrons with energy of 30-70keV as shown in Fig.1. The HXR counts increase greatly during ECRH, and the chirping modes are excited when the counts increase to a higher level. The mode frequency increases from $4-8kHz$ to $10-15kHz$ with the HXR counts enhancing in our experiments.

The periodic mode frequency jumps have also been detected for the first time during high power ECRH on HL-2A as shown in Fig.2. It can be found that two modes with different frequencies (one mode is about $5kHz$ and the other mode is about $15kHz$) occur alternately. Before the frequency jump, a frequency down-chirping phenomenon can be observed. These phenomena should be related with the redistribution of the energetic electrons. They are potentially linked to the phase-space-structure formation and q-profile evolution. More investigations are needed to understand the mode excitation and evolution. At present, the space distribution of the energetic electrons is being measured by multi channel CdTe detector.

4.The e-BAE Instability on HL-2A

An instability with a lower frequency than the toroidicity-induced Alfve´n eigenmode (TAE) was initially identified as a beta-induced Alfve´n eigenmode (BAE). The BAE was first observed in DIII-D with fast ions and high beta plasma[11]. Now the instabilities with the frequency features are observed in a wide variety of tokamak plasmas[12-15]. These modes are destabilized by circulating beam ions and they transport circulating beam ions from the plasma core. The BAE seams very complex, because no simple theories match the experimental data, up to now.

A new mode is observed by Mirnov probes and soft X-ray array in either the ohmic or ECRH discharges, when the plasma density is lower than $1.5x10^{19}m^{-3}$ on HL-2A[16]. Figure 3 shows a typical experimental result. Here, the plasma density, ECRH pulse, NBI pulse, magnetic fluctuation signal from Mirnov probes, and its frequency spectrum are shown from the top to the bottom. The frequency of the mode is about 10-23 kHz, which is lower than TAE but proportional to the Alfven velocity. The mode activity exhibits no amplitude bursting or frequency chirping, different from e-fishbone characteristics shown in previous section. The mode frequency is comparable to that of the continuum accumulation point (CAP) of the lowest

frequency gap induced by the shear Alfven continuous spectrum due to finite beta effect. Therefore, the mode can be identified as BAE. In general, the intensity of the mode is weak in ohmic discharges and becomes very strong during high power off-axis ECRH.

The correlation between the excitation of the mode and the behaviors of the energetic electrons is clearly demonstrated. Figure 4 (e) and (f) show the m/n = 3/-1 mode measured by Mirnov probes and its frequency spectra. The energy distribution of the electrons was indirectly measured by hard-x-ray detector with the pulse height analysis. The counts of hard-x-ray photons increase largely during ECRH, as shown in Fig.4 (a-c). Only when the counts of the energetic electrons with 10-40keV increases to a higher level, the mode can be observed.

Figure 5 shows the BAE evolution both in ohmic and ECRH discharges. Here, the plasma density, ECE, ECRH pulse, magnetic fluctuation signal from Mirnov probes, and its frequency spectrum are shown from the top to the bottom. In the ohmic discharge with low density, the initially Maxwellian electron distribution function begins to grow an energetic-electron tail and the circulating energetic electrons effectively contribute to the mode excitation, as shown in Fig.5. When the ECE intensity increase suddenly, indicating that the anomalous Doppler instability (ADI) was excited, it is found that the m/n=3/1 mode disappears at the same time. The ADI causes pitch angle scattering of the energetic electrons and then transfers energy from parallel to perpendicular motion; i.e., the circulating electrons become the trapped electrons primarily. These experimental results indicate that the BAE is related not only with population but also velocity distribution of the fast electrons.

5. Summary and discussion

In the HL-2A tokamak, two kinds of the low frequency collective mode driven by the energetic electrons have been investigated. Their features are different and summarized in the following table:

	e-fishborn	e-BAE	i-TAE
frequency range	4-15kHz	10~23kHz	>100kHz
frequency	$\propto$ n(fast electrons)	$\propto$ Bt/$n^{1/2}$	$\propto$ Bt/$n^{1/2}$
frequency chirping	yes	no	
amplitude	bursting	continuos	continuos
mode number	m/n=1/1	M/n=3/1	

The e-fishborn phnomena are strongly related to the population of the energetic electrons with energy of 30-70keV. The features of frequency-chirping are very clearly observed when the ECRH power exceeds 0.7 MW. The e-fishbone frequencies are higher than that in lower ECRH power and they show up- and down-chirping behaviors, and, sometimes, V-font-style sweeping also. The chirping modes propagate in the electron diamagnetic drift direction in the laboratory frame of reference. The periodic mode frequency jumps have also been detected for the first time during high power ECRH. These phenomena should be related with the redistribution of the energetic electrons.

An energetic-electron-driven BAE is identified for the first time in HL-2A. The mode can be driven by both the barely circulating electrons and trapped electrons via wave particle precession resonance. The mode frequency is proportional to Alfven velocity at fixed thermal ion temperature. The e-BAE excitation is related not only with the population of the energetic electrons, but also their energy and pitch angle.

Acknowledgements

The authors sincerely thank Dr. F. Zonca, Prof. J.Q.Dong for their helpful suggestions and comments. This work was supported by National Natural Science Foundations of China under Grants No. 11005035, No. 10975049. This work was partially supported by the JSPS-CAS Core-University program in the field of‘Plasma and Nuclear Fusion’.

References

[1] Zonca F *et al* **2007** *Nucl. Fusion* **47**, 1588.

[2] X.R. Duan *et al* **2009** *Nucl. Fusion* **49**, 104012

[3] McGuire K *et al* **1983** *Phys.Rev.Lett.* **50** 891

[4] Heidbrink W W *et al* **1994** *Nucl. Fusion* **34** 535

[5] Wong K L et al **2000** *Phys. Rev. Lett*. **85** 996

[6] Ding X T et al **2002** Nucl.Fusion **42** 491

[7] Smeulders P *et al* **2002** EPS Fast MHD Analysis on FTU.

[8] Maget P *et al* **2006** *Nucl.Fusion* **46** 797

[9] Chen W *et al* **2009** *Nucl. Fusion* **49**, 075022

[10] W. Chen et al., **2010**,Nucl. Fusion 50, 084008 .

[11] W.W. Heidbrink et al., **1993**,Phys. Rev. Lett. **71**, 855 .

[12] R. Nazikian et al., **1996**,Phys. Plasmas **3**, 593 .

[13] P. Buratti et al., **2005**.Nucl. Fusion **45**, 1446 .[14] C.Nguyen et al., **2009**,Plasma Phys. Controlled Fusion **51**,095002 .

[15] P. Lauber et al., **2009,** Plasma Phys. Controlled Fusion **51**,124009.
[16] Chen W et al, 23nd IAEA Fusion Energy Conference, **2010**, to be submitted to PRL

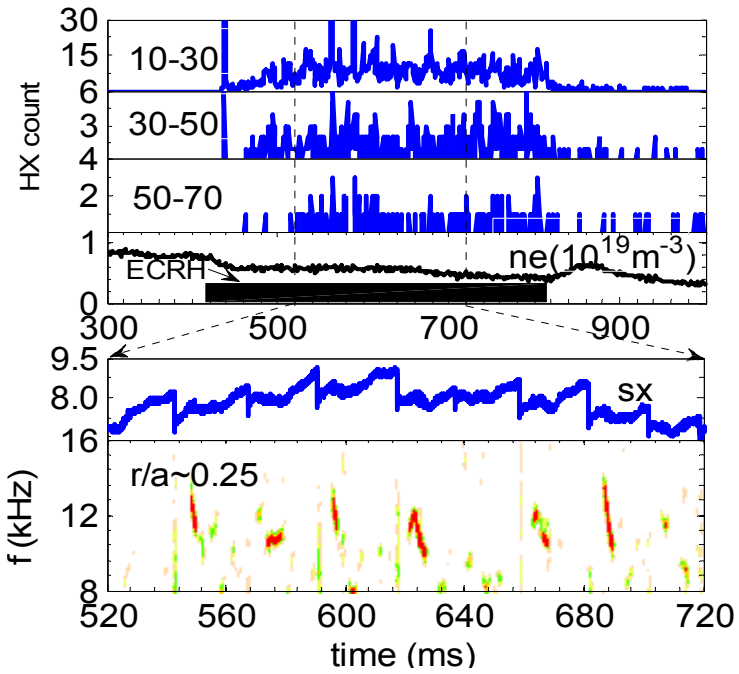

Figure 1 The relation between e-fishborn and energetic electrons
From the top to the bottom, the time evolutions of the HXR energy from 10 to 70 keV, plasma density , ECRH, soft X- ray signal and its frequency spectrum.

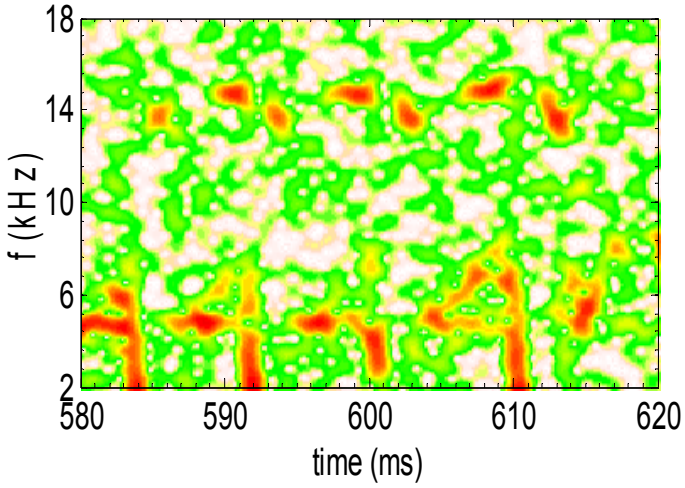

Figure 2 The periodic mode frequency jumps during high power ECRH on HL-2A

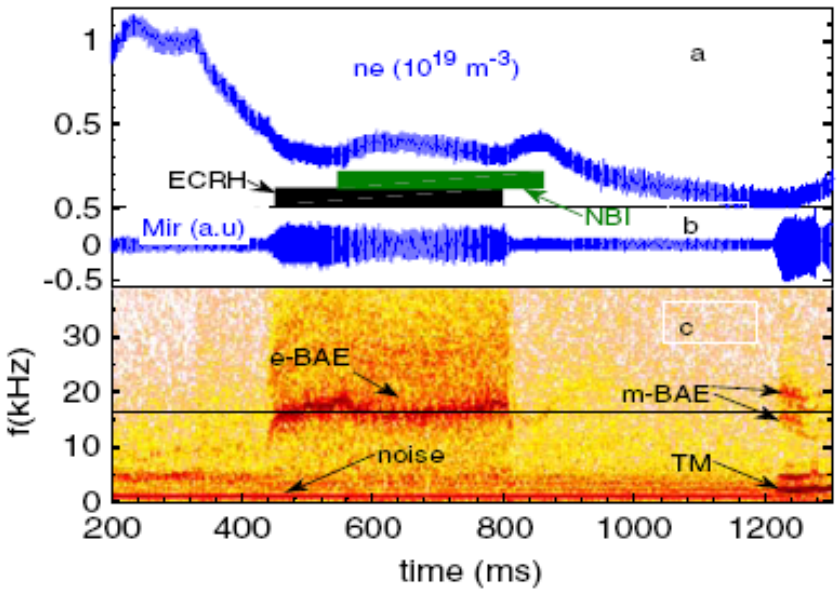

Figure 3 Typical experimental result of the e-BAE.
from the top to the bottom., the plasma density, ECRH pulse, NBI pulse, magnetic fluctuation signal from Mirnov probes, and its frequency spectrum .

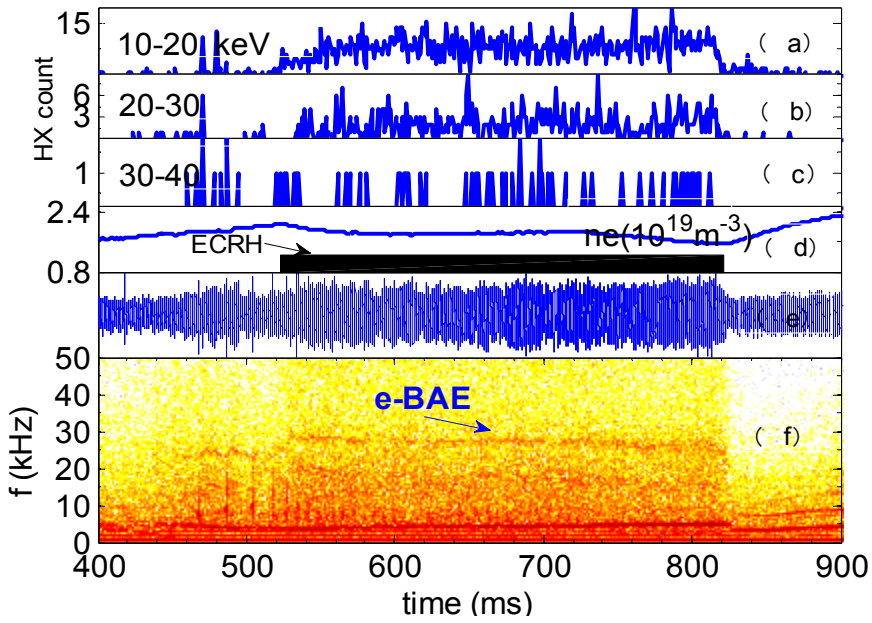

Figure 4 The energy distribution of the electrons measured by hard-x-ray detector with the pulse height analysis indirectly. Figure 4 (a-c) the counts of hard-x-ray

photons during ECRH, (e) m/n = -3/- 1 mode measured by Mirnov probes and (f) its frequency spectra.

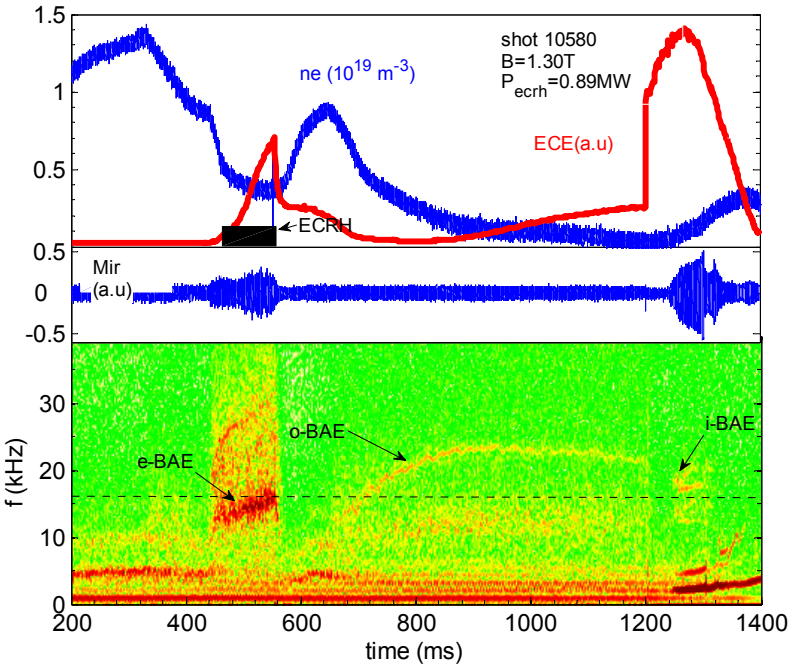

Figure 5 The BAE evolution both in ohmic and ECRH discharges. Here, the plasma density, ECE, ECRH pulse, magnetic fluctuation signal from Mirnov probes, and its frequency spectrum are shown from the top to the bottom.

The diagnostic technique for fast-ions spatial distribution measurement via charge exchange spectroscopy on LHD

T. Ito[1], M. Osakabe[1], K. Ida[1], M. Yoshinuma[1], M. Kobayashi[1], M. Goto[1],
S. Murakami[2], and LHD experimental group

[1]*National Institute for Fusion Science, Toki 509-5292, Japan*
[2]*Department of Nuclear Engineering, Kyoto University, Kyoto 606-8501, Japan*

Spectroscopic investigation for H-alpha lights from reneutralized fast ions via charge exchange process is an useful method to identify spatial density profile of fast ions for each energy range. Tangential viewing geometry is significantly important to observe properties of circulating fast ions in the scheme because this line of sight has a quite large sensitivity for the emitted photon from the reneutralized fast ion in the direction parallel to magnetic field lines compared from the perpendicular viewing geometry. We have successfully identified spatial profile of circulating fast ions on two energy ranges in Large Helical Device(LHD) plasmas which sustained by the three tangential neutral beam injection.

I. INTRODUCTION

For sustaining fusion reaction and heating plasma, fast ions including the fusion-born alpha particle and the externally-injected particle are required to be confined because their loss might ultimately strike a fast wall[1]. In particularly, circulating fast ions are important because they can give their energy and momentum to the fusion plasma for heating and current drive(CD). However, the degradation of fast ion confinement might occur by collective instabilities depending on the fast ion distribution in real or phase space. Therefore, monitoring motion of supra-thermal ions is one of the key issues for understanding fast ion confinement and fast-ion-driven instabilities in high performance fusion devices.

Fast ion charge exchange spectroscopy(FICXS)[2] is applicable to investigate fast ion profiles because of its energy- and spatial-resolved measurement in Large Helical Device(LHD). This diagnostic is one of the active beam spectroscopy based on the analysis of Doppler-shifted spectrum from reneutralized fast ions via charge exchange(CX) processes between the probe beam and the fast ion[3]-[4]. The FICXS diagnostic measures the Doppler shifted Hα spectra from fast neutrals via the CX process between the fast ion and the neutral beam(NB) as a probe beam. This kind of diagnostic can measure the local properties of fast ions for each line of sight(LOS) because the measurement area can be determined by the spatial profile of probe beam

and the observation LOS.

On LHD, various types of Alfvenic phenomena driven by circulating fast ions have been observed[5][6]. To study these modes, we have added the tangential viewing geometry to the FICXS diagnostic and the initial observation of fast ion signal in LHD plasma has been obtained[7]. The previous report shows the validation of the observed fast ion charge exchange(FICX) spectrum compared with the calculation. In this paper, the evaluation of spatial density profile of fast ion for each energy range in the quiet LHD plasma will be presented.

This article is organized as follows. Section II explains the experimental setup of tangential FICXS diagnostic. Section III presents typical observation of FICX spectrum. Section IV shows the evaluation of spatial profile of fast ion density. The conclusion is in section V.

II. EXPERIMENTAL SETUP

The lines of sight(LOS) for tangential FICXS diagnostic on LHD is arranged as shown in Fig. 1. The LOSs is horizontally aligned for measurement of emission from reneutrals in the horizontally-elongated poloidal cross section of LHD plasma at where the diagnostic NB injected. The measurement direction set counter clockwise(CCW) of the torus. The observation area depends on the LOS and the spatial profile of probe beam, so that the region covers from inboard edge of LHD plasma to magnetic axis along the probe beam which radially injected from outboard side to inboard side of the plasma passing through magnetic axis. This corresponds to the major radius R~2.8m to ~3.8m.

For heating and sustaining LHD plasma, three tangential NBIs (NBI#1, NBI#2 and NBI#3) are utilized and then these are main sources of circulating fast-ions. The injection direction of NBI#1 and NBI#3 are CCW and that for NBI#2 is clockwise(CW). In this viewing geometry, the radial injector(NBI#4) is used as a source of probe beam. Typical injection energies of NB for NBI#1, NBI#2, NBI#3 and NBI#4 are 190keV, 180keV, 180keV and 40keV, respectively. The tangential NBIs have a negative ion source and the radial one has a positive ion source. The probe beam injected by radial NBI has three major energy components, which neutrals with full acceleration energy, one-half of acceleration energy and one-third of acceleration energy, different from the tangential NB having almost monoenergy because of the different acceleration structures for each injector.

The observed Hα lights are collected and are transferred by the bundled 41channels optical fibers with 200μm core diameter to the single spectrometer (BUNKOKEIKI/HTP-400E)[8]. The spectrometer has a grating number of 2160/mm, focal length of 400mm and the f-number of 2.8. Observation range of wavelength can be changed by controlling grating angle. No filter is placed in the optics because the wavelength range of the spectrometer is narrow enough to separate a contribution of bulk Hα light from the CX observation domain where we interested in. Finally, the collected lights are recorded by the charged-coupled device(CCD) as a spatial- and wavelength-resolved image.

A modulation of the probe beam is required to observe passive emission because the

tangential FICXS diagnostic does not have any background LOS. The exposure time of the measurement is limited by the operation of mechanical shutter of CCD and its minimum time is 150 ms, while the sampling interval is set to 300 ms.

III. TYPICAL OBSERVATION

The typical discharge waveforms for the tangential FICXS measurement are shown in Fig. 2. The magnetic axis and the magnetic field strength are R_{ax}=3.8m and B_t=1.5T. The direction of magnetic field was set to CCW. The measurement was performed by the switching-on(t=3.85s) and –off(t=3.55s) of probe beam with 39.5keV during the plasmas are sustained by NBI#1(190.5keV) and NBI#2 (164.3keV). The background level is kept by the stationary NB injection and the control of constant electron density.

Figure 3(a) shows the typical shape of the spectrum measured when the probe beam turned on(active) and off(passive). The noise level measured before start of the discharge is also shown in the figure. The several impurity lines are observed both in the active and the passive spectra, and their species have not been identified, yet.

The result of background subtraction between the active and passive spectrum is shown in fig. 3(b). Wavelengths and intensities of the impurity lines are expected to be the same level so that almost impurity lines and visible bremsstrahlung component can be completely removed to extract a pure FICX component caused by the probe beam injection. In this case, the measured spectral range was set between 661.5nm to 666.2nm for focusing CCW-circulating particles with the energy range between ~30 to ~110keV. Because of the observation geometry, the FICX Hα light due to NBI#1 and NBI#2 can be intrinsically identified as in the wavelength of red-shift-side and the blue-shift-side, respectively. Therefore the observed spectra can clearly be identified as from the fast ions produced by NBI#1.

The FICX spectrum is obtained where no great instabilities is observed, so the fast ion velocity distribution can be identified by the comparison between experimental spectrum and calculated one. The evaluated FICX-spectra by using the result of computer simulation code is also shown in Fig.3(b). The simulation for reconstruction of FICX spectrum requires the three essential calculations that are for the reconstruction of equilibrium, for the fast ion velocity distribution function and for the neutral densities for each energy based on the equilibrium. Then their results and the LOS geometry can be used for the evaluation of realistic CX emission. The equilibrium can be found in the database consists of a lot of calculations for LHD configurations derived by the VMEC code. The fast ion distribution function was derived from GNET code[9], which solves the drift kinetic equation in 2-dimensional velocity space and in 3D real space. The NB attenuation profile was calculated by NBATTEN-code[2]. The halo-neutral, which was created by the charge exchange process between bulk-ions and injected neutrals by NBI#4, distribution was evaluated by using 3D neutral transport code (EIRENE-3D code[10]).

As shown in Fig.3(b), the calculated FICX-spectrum and the experimental result are well

agreed for the shape of spectrum. This agreement satisfies that the spatial profile of fast ion velocity distribution based on the realistic equilibrium used for the simulation is reasonable. The absolute value of photon count has not been estimated yet. The measured FICX spectra are contributed by not only the process of collision between the probe beam and the target fast ion(NB-FICX component) but the process between the low energy(several keV) neutrals transported by the probe beam and the fast ion(halo-FICX component). Both NB-FICX and halo-FICX components show similar spectral shape in the region where the wavelengths are greater than 663nm. The halo component becomes slightly larger in the wavelengths less than 663nm because the relative velocity between the halo neutrals and fast-ions become more suitable for CX reaction than that between fast-ions and NB particles.

IV. EVALUATION OF SPATIAL PROFILE

Since both NB-FICX and halo-FICX components contain the information of fast-ions, the signal intensities which are integrated for specific wavelength ranges represent the fast ion densities in certain energy ranges. Thus, the spatial profile of the integrated signal can be used to evaluate the confinement properties of fast ions with different energies on LHD during its slowing down process.

Figure 4(a) shows the spatial profile of LOS for tangential FICXS measurement on LHD, the probe beam attenuation and the equilibrium flux surfaces. The observed spectra shown in Fig.3(b) are obtained in the sight line of #30(R=3.49m). As shown in the figure, the probe beam intensity on the LOS#30 is peaked at ρ=0.15. The full width at half maximum (FWHM) of the probe beam profile on the LOS gives an ambiguity of 0.06 in ρ.

From the FICX measurement, the intensity of FICX component in the specific wavelength range projects an window due to its intensity onto the phase space of fast ion. This profile on the phase space can be considered as a sensitivity of measuring fast ion density for each LOS. Therefore, a spatial profile of intensities of FICX component in the bordered wavelengths indicates a density profile of fast ion with the specific energy range, if the relation between the viewing geometry and fast ion trajectory based on the equilibrium can be assumed to be simple. In this case, we selected two wavelength ranges labeled as A(664.2−665.5nm) and B(662−663nm) as shown in Fig. 3(b). The energies of fast-ions in range-A and -B correspond to about from ~35 to ~55keV and from ~70 to 100keV, respectively. Figure 4(b) and 4(c) show the sensitivities for each NB-FICX component on the tangential viewing geometry at the specific location indicated by the bold cross in Fig.4(a). Fig. 4(d) and 4(e) represent the same plot of Fig. 4(b) and 4(c) for the sensitivities for the halo-FICX component. The wavelength range for Fig. 4(b) and 4(d) corresponds to the range-A, for Fig. 4(c) and 4(e) corresponds to the range-B. In Fig.4(b)-(e), the flux averaged distribution function for this location is shown by green contours.

All of the sensitivity profiles implies that the tangential FICX measurement is fairly sensitive to the FICX component from the fast ion with a small pitch angle (large $\upsilon_{//}$) compared from that with the larger one. These sensitivities has the maximum at the $\upsilon_{\perp}$= 0m/s and they are decrease

due to the increase of $\upsilon_{\perp}$. The $\upsilon_{\perp}$ dependences of the sensitivity are determined by the intensity and the direction of relative energy for the CX reaction by the probe beam and the halo neutral. The charge exchange reaction rate for light hydrogen is maximum at ~35keV for the parallel motion of the related particles. In this case, the full energy of probe beam is 39.5keV and its direction is mostly perpendicular to the plasma. On the other hand, the energy of halo neutral assumed 1keV and its direction is the same as the probe beam. Therefore the sensitivity profile by the halo neutral has the homogeneous energy distribution in the phase space different from the case of probe beam. It seems that the energy of 100keV is the upper limit for Hydrogenic-ions in this observation geometry using the radial-NBI as a probe beam. The use of tangential-NBI (NBI#3) is expected to extend the observable energy range of the measurement since the relative velocity between the fast-ions and probing beam becomes preferable.

Since the measurement range of fast ion energy is intrinsically limited by the viewing geometry, the spatial profile of the extracted FICX component in each wavelength indicates the local distribution of fast ion density. Figure 5 shows the spatial density profile of fast ions derived by the extraction of FICX component from two wavelength ranges A and B. The results of the simulation based on the identified fast ion distribution are also shown in the figure. Because of the uncertainty from the calculation of fast ion distribution, the simulation can not obtain the result outer than R=3.5m. The spatial profiles of fast ion density derived by the simulation and the observation are well agreed for the available region. Both density profile for range-A and –B increase toward the magnetic axis R_{ax}=3.8m except for the small difference between their tendencies. This result implies that the injected NB was deposited near the magnetic axis and then the fast ion confinement probably was not degraded in the slowing-down process.

V. CONCLUSION

A tangential FICXS diagnostic was installed to spatially investigate the confinement properties of parallel fast-ion components on LHD. In the tangential viewing geometry, the FICX component from reneutralized fast ions with energy range up to 100keV are successfully obtained due to the evaluation of fast ion velocity distribution function. By selecting the wavelength range and integrating the spectra for the range, it was shown that the integrated signals well represent the spatial profile of fast ion density in the corresponding energy ranges. Thus, the comparison between the integrated signals in different wavelength ranges will provide us a good knowledge of fast-ion confinement properties during its slowing down process on LHD.

ACKNOWLEDGEMENTS

The support of the LHD experiment group is gratefully acknowledged. This work is supported by the LHD project budget NIFS09ULBB512, NIFS09KLBB301, NIFS09ULBB510 and NIFS09KLBB301. This work also partly supported by the Grant-in-aid for Scientific Research

from JSPS, Nos 18340189, 21360457 and 22860076.

[1] A. Fasoli, *et al.*, Nucl. Fusion **47**, S264(2007)
[2] M. Osakabe, *et al.*, Rev. Sci. Instrum. **79**, 10E519 (2008)
[3] W. W. Heidbrink, *et al.*, Plasma Phys. Control. Fusion **46**, 1855 (2004)
[4] Y. Luo *et al.*, Rev. Sci. Instrum. 78, 033505 (2007)
[5] K. Toi *et al*., Nucl. Fusion 40, 1349(2000)
[6] M. Osakabe, *et al.*, Nucl. Fusion **46**, S911(2006)
[7] T. Ito *et al.*, Rev. Sci. Instrum. 81, 10D327(2010)
[8] M. Yoshinuma et al., Fusion Sci. Technol. 58, 375(2010)
[9] S. Murakami, *et al.*, Fusion Sci. Technol. **46**, 241(2004).
[10] D. Reiter, *et al.*, Fusion Sci. Technol. **47**, 172(2005).

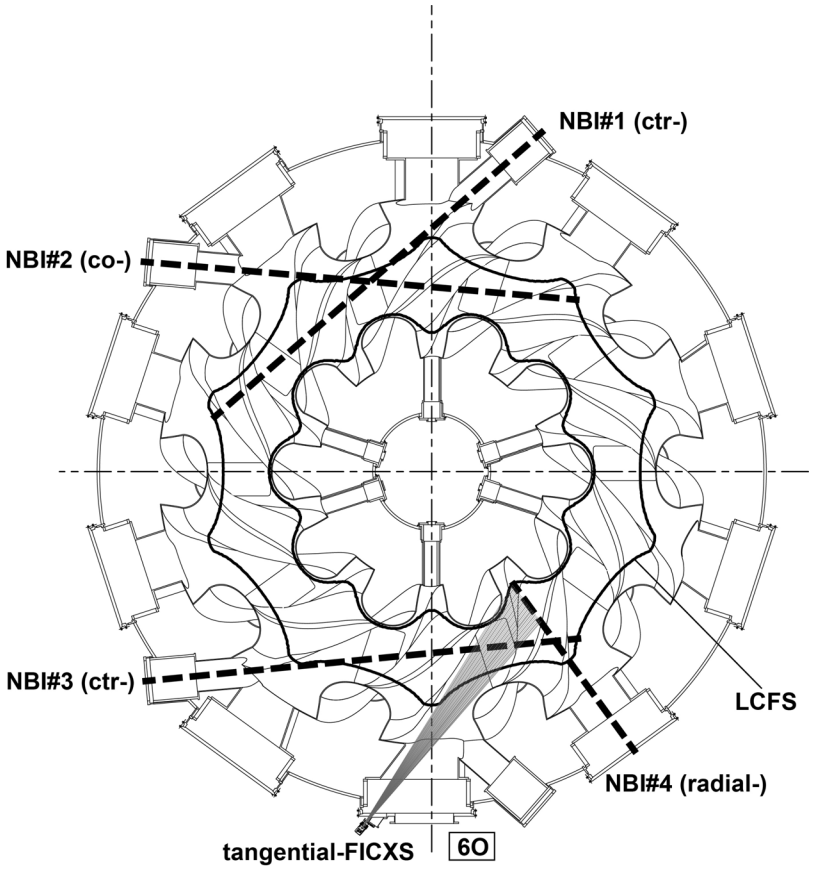

Fig. 1 Hardware apparatus of tangential FICXS diagnostic on the midplane of LHD.

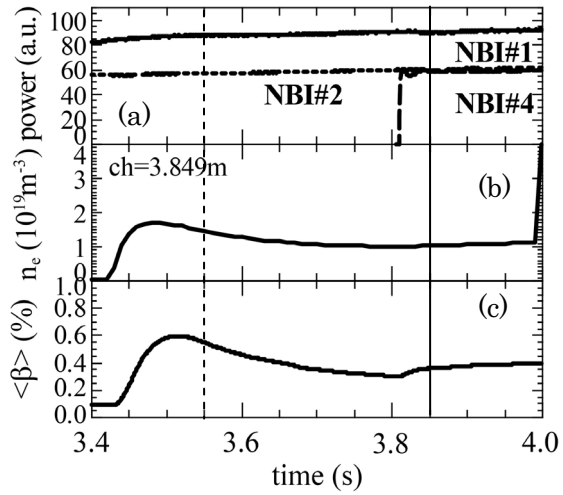

Fig. 2 Waveform of typical discharge for measurement of FICX spectra. (a)Time evolution of NBI power, (b)line-averaged electron density, (c)volume-averaged beta. Vertical broken line and solid line indicate the timings of measurement for background and active signal, respectively.

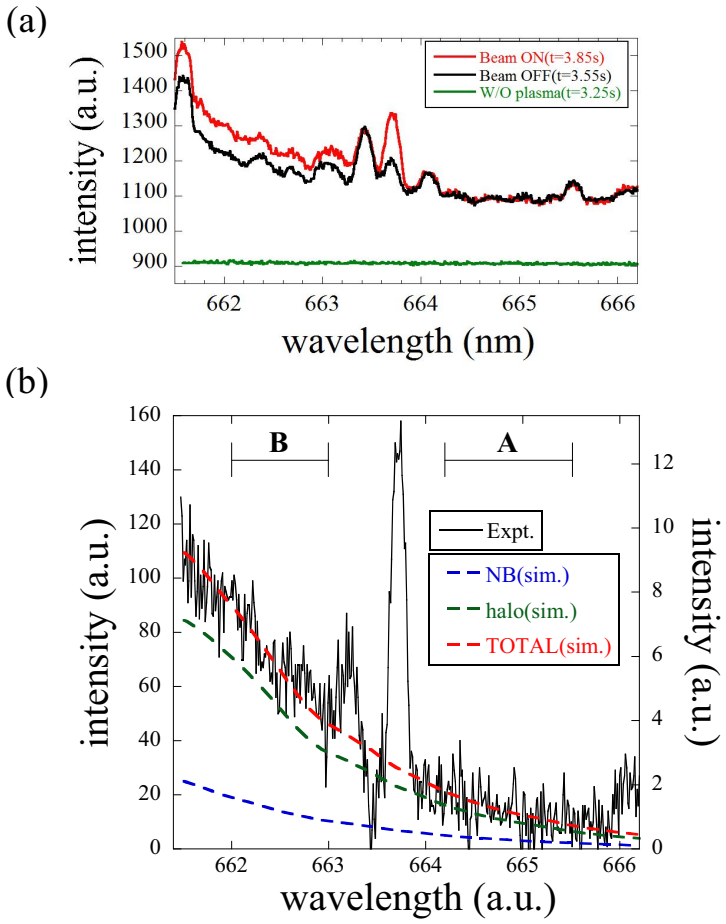

Fig. 3 (a)Example of observed spectrum when the probe beam turned on(t=3.85s) and off(t=3.55s). Noise level(t=3.25s) is also represented. (b)FICX spectrum derived from the background subtraction by using the spectra in the timings t=3.55s and t=3.85s. Thin curve and broken curves indicate the experimental observation and the calculation results, respectively.

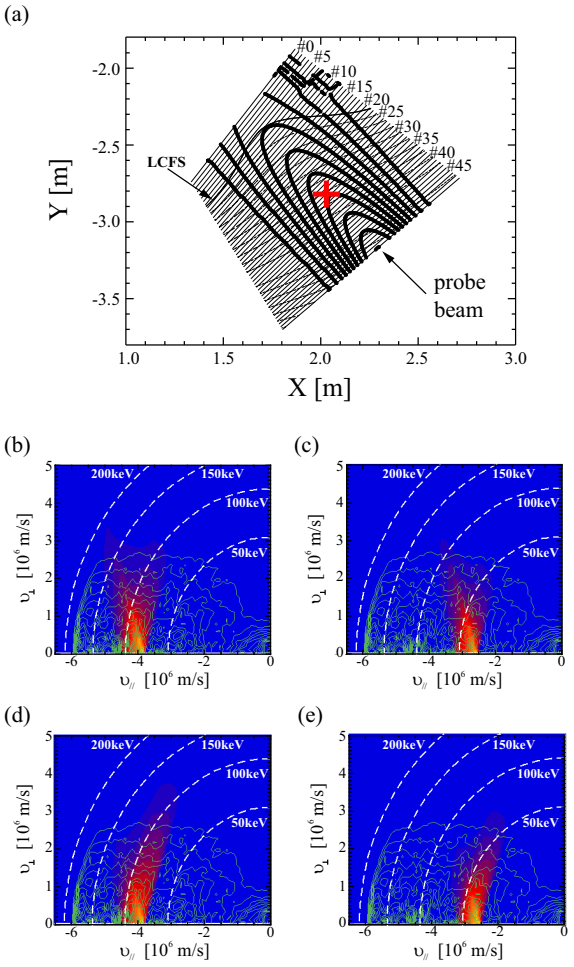

Fig. 4 Measurement range of fast ion velocity corresponding to the specific wavelength ranges. (a)Midplane view of attenuation profile of probe beam on the tangential viewing geometry. The sensitivities of the FICX measurement in the fast ion velocity distribution function for the NB-FICX component((b) and (d)) and halo component((c) and (e)) corresponding to the specific wavelength ranges measured at the specific location indicated by the bold cross in Fig.4(a)

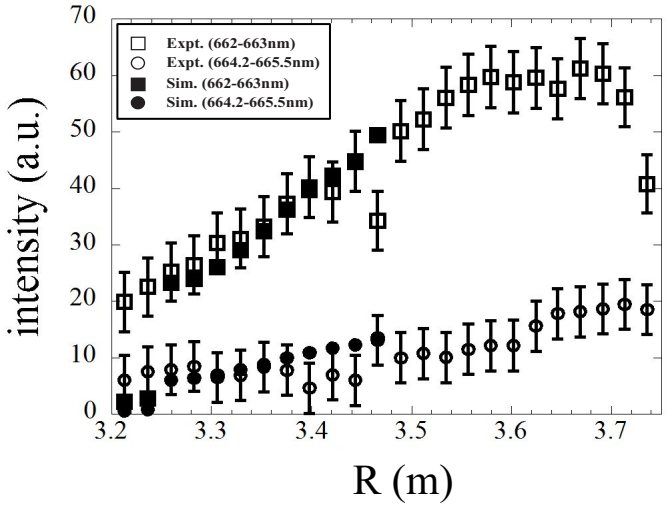

Fig. 5 Spatial intensity profiles of FICX component for each wavelength range derived by the experimental observation and the calculation.

Investigation of some MHD events in the SUNIST spherical tokamak[i]

Long Zeng[ii], [1,2] Zhe Gao,[1] Yi Tan,[1] Wenhao Wang,[1] Huiqiao Xie,[1] Lifeng Xie,[1] Chunhuan Feng,[3] Jian Liu, [3] Long Wang[3], Xuanzong Yang,[3] Yanbin Hu,[4] Fangchuan Zhong[4] and Xiang Gao[2]

1) *Department of Engineering Physics, Tsinghua University, Beijing, China*
2) *Institute of Plasma Physics, Chinese Academy of Sciences, Hefei, Anhui, China*
3) *Institute of Physics, Chinese Academic of Science, Beijing, China*
4) *College of Physics, Donghua University, Shanghai, China*

The IREs, which is characterized by a perturbation of the plasma current I_p, the loop voltage V_{loop}, the $H\alpha$ radiation and the magnetic perturbation dB_p, have been confirmed in the SUNIST experiments. It is found that, the fluctuation before the IREs is characterized by the structure of m =2 / n =1; then it changes to m =4 / n =1 during the IREs; and, after the IREs, the mode number decreases to m =3 / n =1. The analysis of equilibrium parameters evolution during the IREs shows that a positive spike appears in the elongation of the plasma and a negative spike in the plasma poloidal beta. A collapse in the pressure profile is also found corresponding to the occurrence of IREs, which suggests the IREs in the SUNIST are driven by the pressure gradient possibly.

Keywords: IRE, spherical tokamak, SUNIST, SVD, poloidal mode

[i] *This work is supported by the Major State Basic Research Development Program from MOST of China under Grant No. 2008CB717804, NSFC under Grant No. 10535020.*

[ii] EMAIL: *zenglong@ipp.ac.cn*

1. Introduction

In spherical tokamaks (STs), MHD instabilities have different characteristics compared to those in conventional tokamaks. The internal reconnection event (IRE) is one of several unique features observed in STs [1][2][3]. The IREs are known to cause energy and particle losses, but the plasma current is not terminated. Such phenomenon is observed with a spike of plasma current, and in irregular intervals. The IREs are studied experimentally on START [1], MAST [2], TST-2 [3] [4] and other ST devices [5]. The Sino-United Spherical Tokamak (SUNIST) is a spherical tokamak with small aspect-ratio A/a~1.3 and high elongation κ~1.6 [6]. Investigating the IREs in the SUNIST should be necessary. And the motivation of this article is to expound the features of the IREs and to identify the source of instability in the SUNIST.

The structures of this article are as follows. In section 2, magnetic diagnostics system in the SUNIST is introduced, and then the methods of using SVD to analyze MHD mode and using EFIT mode to obtain plasma parameters are also briefly described. Analysis results, including the evolution of MHD mode numbers and plasma parameters, are shown in section 3. The observed impact of the IREs from toroidal field is also discussed in this section. The last section is devoted to the summary.

2. Experimental setup

2.1 Magnetic diagnostics system in the SUNIST

All experimental data in the SUNIST is obtained from magnetic diagnostics system. The system includes a Rogowski coil measuring the total toroidal current in the plasma, 13 flux loops, 15 poloidal pick-up coils and 6 toroidal pick-up coils. Partial locations of the sensors are shown in figure 1.

Magnetic fluctuations are measured by magnetic pickup coils with a frequency response of up to 20 kHz. Especially, the n-coils are located at toroidal angles of θ =

0°, 30°, 120°, 180°, 240°, and 300°. SUNIST reconstructions typically utilize data from a Rogowski coil, 13 loop voltage monitors and 15 integrated poloidal pick-up coils.

2.2 mode analysis by singular value decomposition

Singular value decomposition (SVD) [7] has been used to analyze mode structures in many fusion experiments [8]. Consider a matrix S (M × N), which can be expressed as

$$S = U\Sigma V^T \quad (1)$$

where U (M × M) and V (N × N) are orthogonal matrices and Σ (M × N) is a diagonal matrix. Σ, U, and V are called the singular value, chrono and topo, respectively. Chrono and topo show common waveforms for temporal eigenmodes and spatial eigenmodes, respectively. Time evolutions of each decomposed mode (i.e., chrono) and its spatial distribution (i.e., topo) can be extracted in this way.

2.3 plasma parameters fitted by EFIT model

The EFIT code has been applied to many tokamaks, including DIII-D, JET and JT-60U, full details of which can be found in Ref. [9]. Each implementation has the specific features required to properly model a particular configuration.

For SUNIST plasmas, a reliable basis function set for p' and ff' is

$$p'(\psi) = \alpha_0+\alpha_1\ \psi_N - (\alpha_0+\alpha_1)\ \psi_N^2 \quad (2)$$

$$ff'(\psi) = \beta_0+\beta_1\psi_N - (\beta_0+\beta_1)\ \psi_N^2 \quad (3)$$

where p' and ff' are the plasma pressure gradient and poloidal current functions, respectively. ψ_N is the poloidal flux normalized to the poloidal flux between the plasma boundary and the magnetic axis.

3. Experimental results

3.1 typical discharge

A typical discharge with IREs is shown in figure 2. A positive spike in plasma current and a negative spike in loop voltage are observed. During the IREs, poloidal magnetic fluctuation increase observably. The increase in the emission of Hα

indicates interaction between the plasma and the vacuum vessel due to the loss of the plasma.

3.2 MHD analysis

As mentioned earlier, poloidal and toroidal magnetic fluctuation increase observably during the IREs. Mode number is analyzed using SVD and the evolution is as follows. Before the IREs, poloidal mode number is 2. Then it changes to 4 during IREs. And after the IREs, the number decreases to 3. Meanwhile, the toroidal mode number remains unchanged, n=1.

By changing the toroidal field, we find that the toroidal field sets a threshold for the IREs, which is shown in figure 3. IREs exist only when toroidal field is less than the threshold. dIp/Ip, which is defined the strength of the IREs, don't change clearly when the toroidal field further decreases. It is noticed in figure 3 that Ip changes little although Bt decreases. So the relation between edge safety factor *(*q_a) and the IREs in the SUNSIT are as follows: when q_a is less than 4, the IREs are found during the discharges. The strength of IREs doesn't change clearly when q_a further decreases.

3.3 plasma parameters evolution

Plasma parameters in the SUNIST are fitted using EFIT during the IREs. The results show that corresponding to the spike in plasma current, a positive spike appears in the elongation of the plasma. A negative spike is found in the plasma poloidal beta. Both of them are illustrated in figure 4. The pressure profile of diffent moments (t1, t2, t3, t4 and t5) are shown in figure 5. Before the IREs (from t1 to t2), the pressure profile peaks and the pressure gradient increases. The profile becomes smooth during the IREs (from t2 to t4). And at last, the pressure profile peaks again after the IREs (from t4 to t5). These results show a collapse in the pressure profile is found corresponding to the occurrence of the IREs.

4. Conclusion and Summary

The IREs, which is characterized by a perturbation of the plasma current I_p, the

loop voltage V_{loop}, the $H\alpha$ radiation and the magnetic perturbation dB_p, have been confirmed in the SUNIST experiments. MHD analysis results show the mode number changes observably. It is found that, the fluctuation before the IREs is characterized by the structure of m =2 / n =1; then it changes to m =4 / n =1 during the IREs; and, after the IREs, the mode number decreases to m =3 / n =1.

The analysis of equilibrium parameters evolution during the IREs shows that a positive spike appears in the elongation of the plasma and a negative spike in the plasma poloidal beta. A collapse in the pressure profile is also found corresponding to the occurrence of IREs, which suggests the IREs in the SUNIST are driven by the pressure gradient possibly. The process by MHD simulation shows when such reconnection occurs [10] [11], the pressure gradient along the reconnected magnetic field line causes plasma energy and particle losses. This is consistent with the results from the SUNIST.

Acknowledgements

This work is supported by the Major State Basic Research Development Program from MOST of China under Grant No. 2008CB717804, NSFC under Grant No. 10535020. This work was partially supported by the JSPS-CAS Core-University program in the field of‘Plasma and Nuclear Fusion’.

References

[1] Sykes A, Del Bosco E, Colchin R J, et al. 1992, Nuclear Fusion, 32(4): 694
[2] Sykes A, Akers R J, Appel L C, et al. 2001, Nuclear Fusion, 41:1423
[3] Takase Y, Ejiri A, Kasuya N, et al. 2001, Nuclear Fusion, 41:1543
[4] Ejiri A., Shiraiwa S, Takase Y, et al. 2003, Nuclear Fusion, 43:547
[5] Sabbagh S A, Kaye S M, Menard J, et al. 2001, Nuclear Fusion, 41:1601.
[6] He Yexi. 2002, Plasma Science and Technology, 4(4):1355
[7] Dudok de Wit T, Pecquet A L, Vallet J C, et al. 1994, Physics of Plasmas, 1: 3288.
[8] Kim J S, Edgell D H, Greene J M, et al. 1999, Plasma Physics and Controlled Fusion, 41:1399
[9] Lao L L, John H St, Stambaugh R D, et al. 1985, Nuclear Fusion, 25(11): 1611
[10] Hayashi T, Mizuguchi N, Watanabe T H, et al. 2000, Nuclear Fusion, 40:721.
[11] Mizuguchi N, Hayashi T, Sato T, et al. 2000, Physics of Plasmas, 7:940.

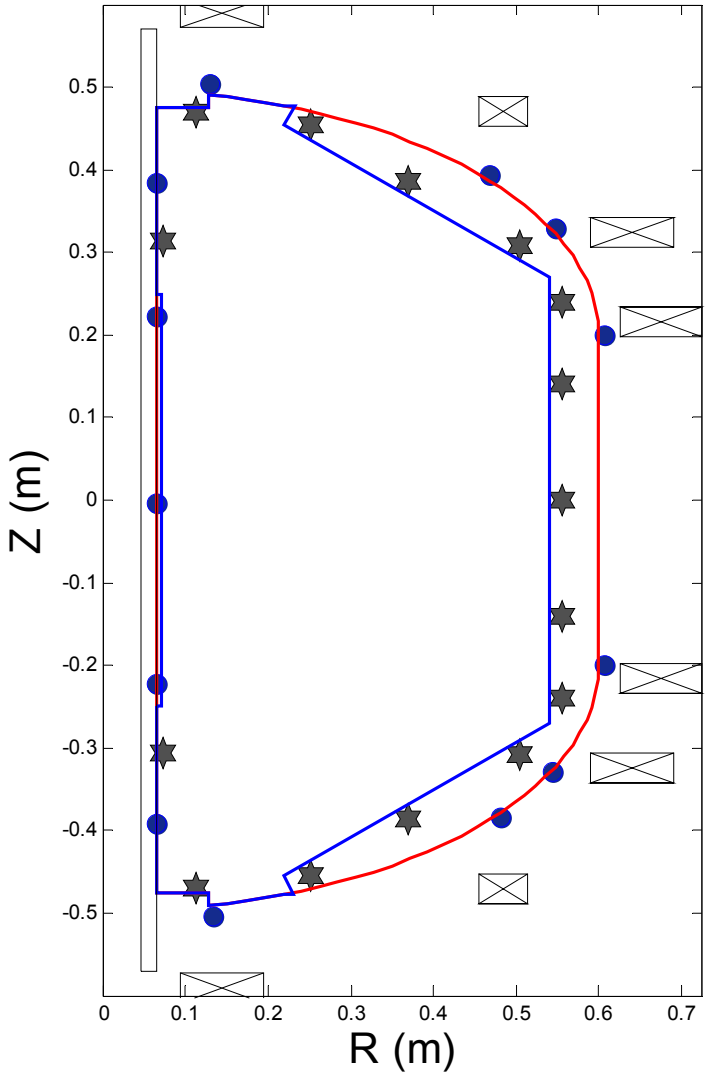

Figure 1 flux loops (●) and poloidal magnetic coils (✡) in the SUNIST.

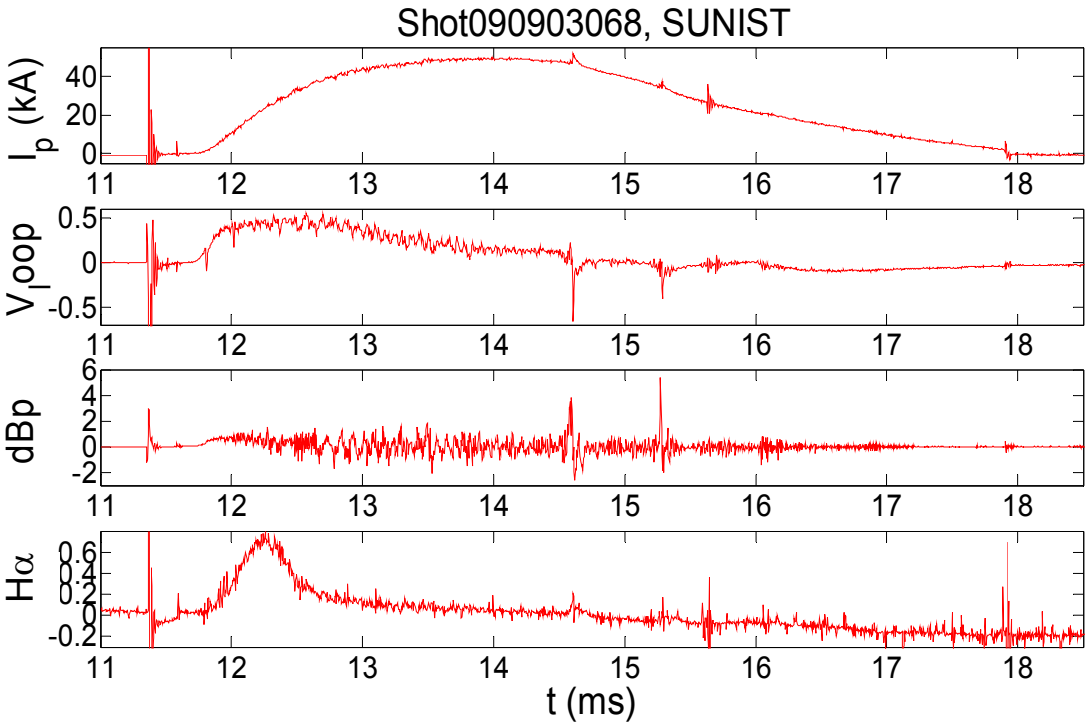

Figure 2 typical discharge waveforms with IREs. (a) Plasma current, (b) loop voltage, (c) signal from a magnetic coil, (d) Hα emission

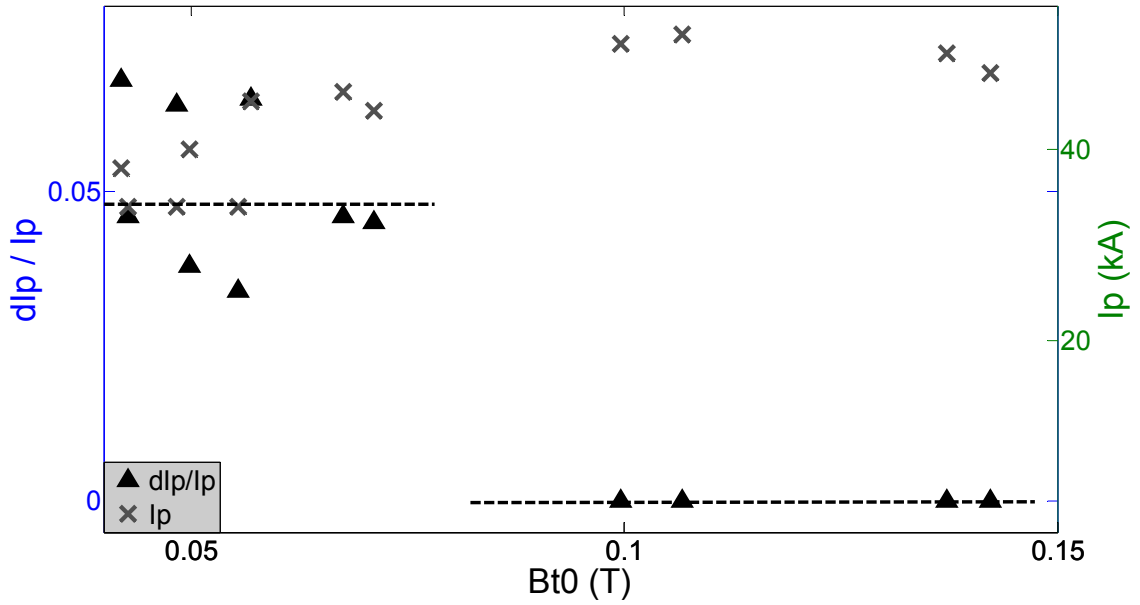

Figure 3 Relation between IREs and B_T

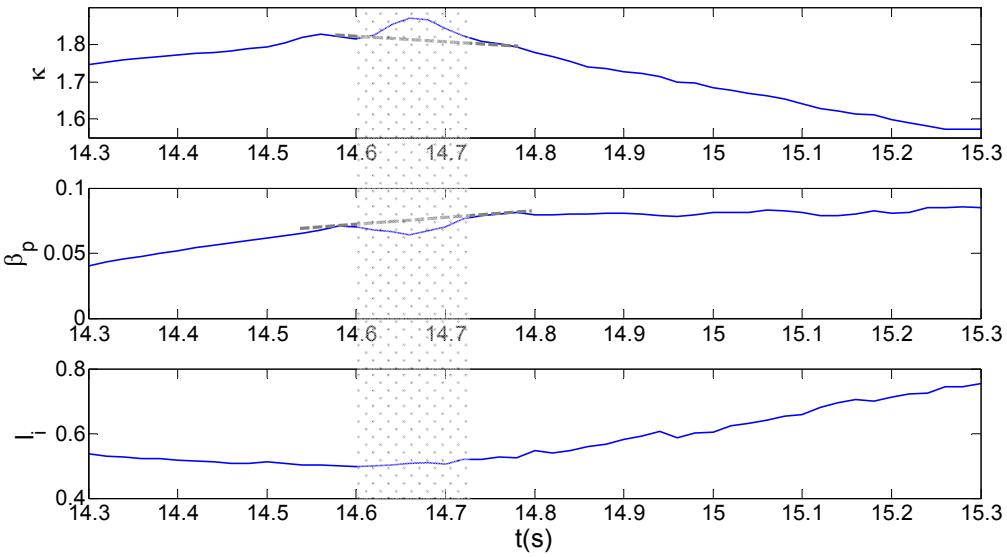

Figure 4 plasma parameters during the IREs

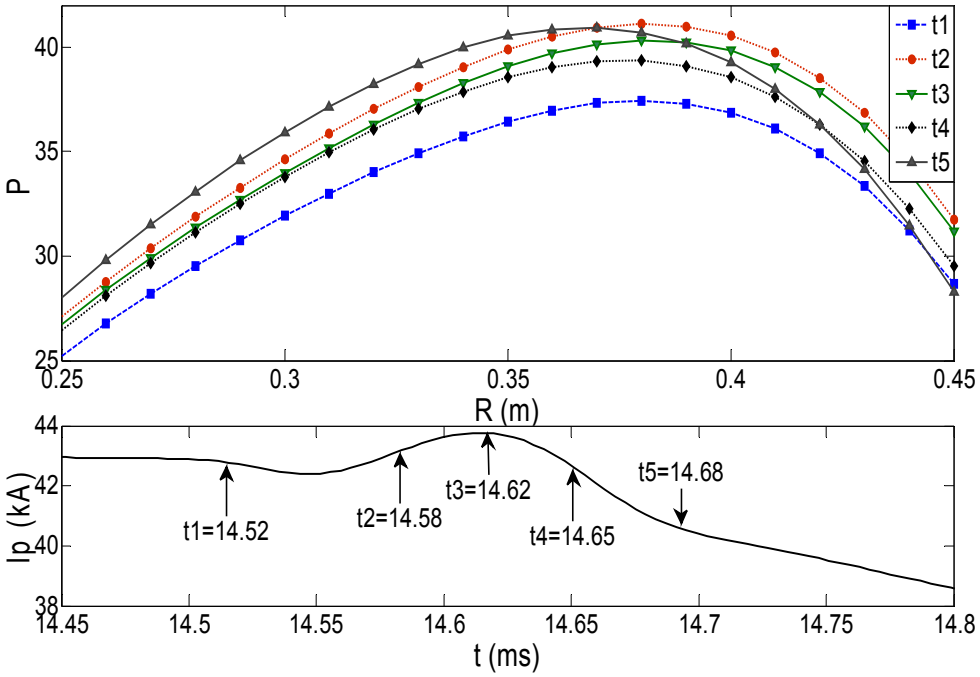

Figure 5 pressure profile during the IREs

ECE Imaging Upgrade and Sawtooth Reconnection on EAST

M Xu [1], X.Y Xu [1], Y.Z Wen [1], C.X Yu [1], J.X Ma [1], J.L Xie [1], B.X Gao [1], T Lan [1], A.D Liu [1], Y Yu [1], Y.H He [1], B.N Wan [2], L.Q Hu [2], X Gao [2], N.C.Luhmann Jr [3], C.W.Domier [3]

[1] CAS Key Laboratory of Plasma Physics, University of Science and Technology of China, Hefei 230026, China

[2] Institute of Plasma Physics, the Chinese Academy of Sciences, Hefei 230031, China

[3] Department of Applied Science, University of California, Davis, California 95616

xum138@mail.ustc.edu.cn

Abstract

A new optical imaging system designed for two dimension (2D) ECEI diagnostics which contains hyperboloid lens are now working well on EAST tokamak. The 16 mixers array elements measure the plasma electron cyclotron emission at 8 frequencies simultaneously, the electron temperature profiles and its fluctuation over an area of 20cm (vertical) by 6cm (horizontal) could then been analyzed. We have been taking results of the sawtooth oscillation in the core plasma of the EAST device. The evolutions of the sawtooth precursor activities on EAST will be given in detail.

I Introduction

In magnetized plasmas, Electron cyclotron emission (ECE) arises from the gyro-motion of electrons at electron cyclotron frequency and its harmonics. In optically thick plasmas, the ECE radiation intensity is known to be proportional to the electron temperature, and as the ECE frequency, which is a monotonically decreasing function of the major radius. Electron Cyclotron Emission Imaging (ECEI) is a two dimensional diagnostic system base on the principle of ECE. Unlike conventional ECE diagnostics which using a single antenna/receiver aligned along a horizontal chord in the direction of the major radius, the ECEI utilized newly developed millimeter wave imaging array which aligned vertically as the receiver/mixers [1-6] and radiation from a vertical chord in the plasma is imaged by lenses onto a detector array. EAST (Experimental Advanced Superconducting Tokamak) is a new full superconductor tokamak, which main physics parameters in deuterium plasma are: I_p = 200-500kA, toroidal field about 2T at R = 1.75m, line averaged density of (1-3)x$10^{19}$$m^3$ and the safety factor of edge is 3-8 with circular configuration in ohm discharge.

This paper primarily focuses on the ECEI upgrade imaging lenses system and the investigation on sawtooth reconnection on EAST tokamak.

.

II Upgrade Optical System Considering

The goal of optics imaging lenses is to achieve the highest possible imaging spatial resolution, namely that the focal plane 3dB spot size and the channel spacing of antenna array be as small as possible. It's easily to use Gaussian Optics to estimate millimeter wave transportation in space. In Gaussian Principle we have:

$$\frac{1}{q(z)} = \frac{1}{R(z)} - \frac{i\lambda}{\pi W^2(z)} \quad (1)$$

$$q(z_2) = \frac{Aq(z_1) + B}{Cq(z_1) + D} \quad (2)$$

Above formula can refer from textbook and detail discussion will be discard. In our Optical System, the primarily materials prepare to using is HDPE (high density Polyethylene), which refractive rate is 1.525[7]. The optical system is primarily to be thought as combination of a series of model lens as figure 1 which suppose that a beam of ray obey Gaussian Optics are

transport from surface P_1 to P_4 across model lens. So we can deduction below transport matrix of model lens from formula (1) and (2):

$$\mathrm{T}=\begin{pmatrix} A & B \\ C & D \end{pmatrix} \qquad (3)$$

In the matrix the component A to D of T is:

$$A=1-\frac{n-1}{n}\frac{d}{|R_1|},\quad B=\frac{1}{n}d,\quad C=-(n-1)\cdot\left(\frac{1}{|R_1|}+\frac{1}{R_2}-\frac{n-1}{n}\cdot\frac{d}{|R_1|R_2}\right),\quad D=1-\frac{n-1}{n}\frac{d}{R_2}.$$

Where n is index of HDPE refraction, d is thickness of model lens, R_1 is curvature radius of surface P_2 and R_2 is curvature radius of surface P_3. T is the Gaussian beam transmit matrix of model lens. It is easily to design ECEI optical system for EAST tokamak according to Gaussian beam tracing technique as formula (3).

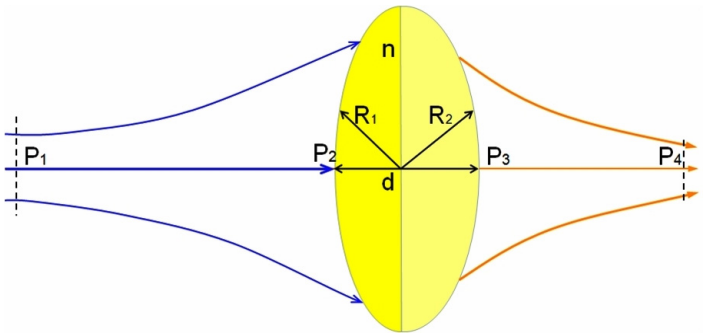

Fig.1 Sketch of Gaussian beam transport on model lens

However, there are some restricted factor is encountered in optical design, the one is the distance between the cores of plasma to diagnostic port window is far away and the other is tokamak diagnostic port window periphery space is restricted. An interval of 2.5 meters between object to imaging, it is difficult to get high spatial resolution and difficulty to avoid of spherical aberration using simple lenses imaging system. So we through increase the amount of lenses to improve spatial resolution and brought into hyperboloid lens to restrain spherical aberration as figure 2. The content of figure 2 is the comparison between optical imaging which having hyperboloid lens and the other is sphere lens is as following: the 1 to 8 of x-axis is meaning that the channel of detect array from center to edge, y-axis is means the size of 3dB spot size or spatial resolution. From figure we see clearly that the two optical systems nearly the same characteristics of spatial resolution for all the channels and 3dB spot size in the core channels 1-3, and the 3dB spot size of hyperboloid lens nearly the same as core channels in the edge channels while the system without hyperboloid lens have tremendous dissimilarity.

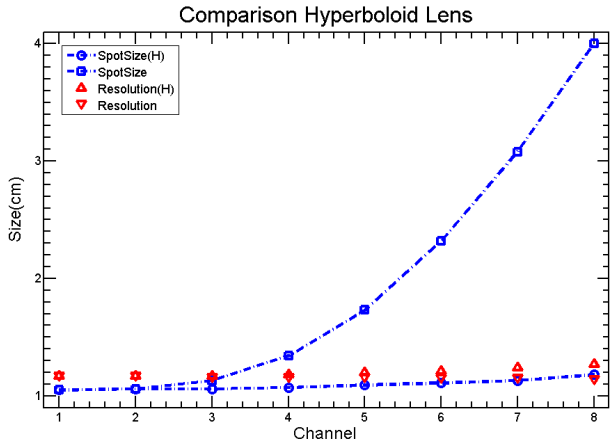

Fig.2 Comparison between Hyperboloid lens and Sphere lens

III Optical Lenses System and Performances

The structure of ECEI upgrade on EAST is as figure 3 and the component of optical imaging system are (at the direction of tokamak radius): Window slab lens, Hyperboloid poloidal lens, Auxiliary poloidal lens, Toroidal lens, Adjust sphere lens and Concave poloidal lens. The merit of this optical imaging system is that it can be divided into two distinct lenses system just through process concave poloidal lens. We define the optical system as name $4P_f$ with concave lens and $3P_f$ without concave lens as figure 4. And the characteristic for $4P_f$ and $3P_f$ are as figure 5 (design result) and figure 6 (Experiment Measurement results). From comparison we can see that the design result is well approved by experiment test and $4P_f$ system is superior to $3P_f$. The focus location may be shifted horizontally via translation the location of adjust sphere lens.

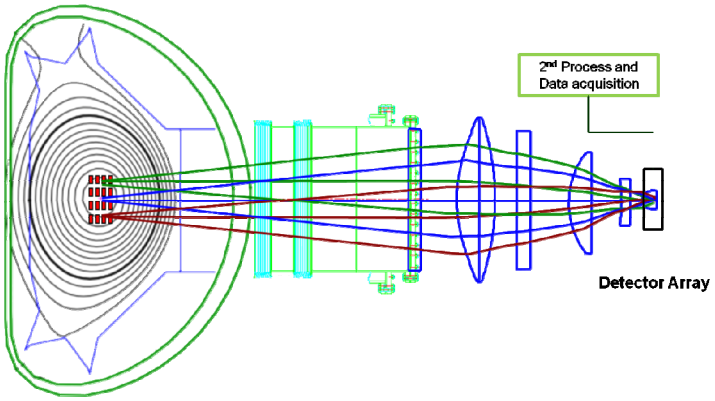

Fig.3 Sketch of Optical System Arrangement on EAST

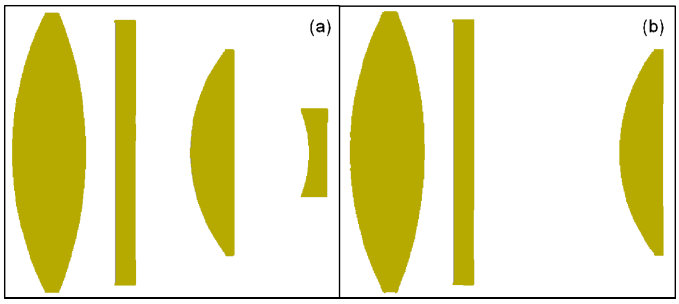

Fig.4 Optical system component of $4P_f$ for (a) and $3P_f$ for (b)

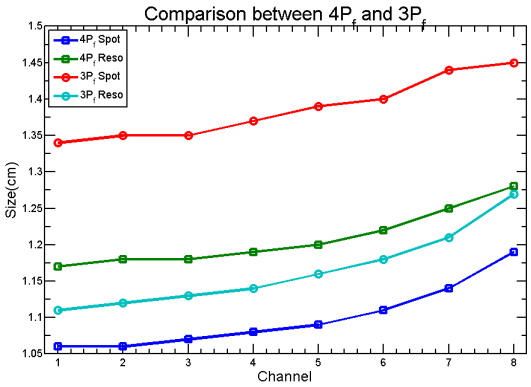

Fig.5 design performance of 4Pf lens and 3Pf lens

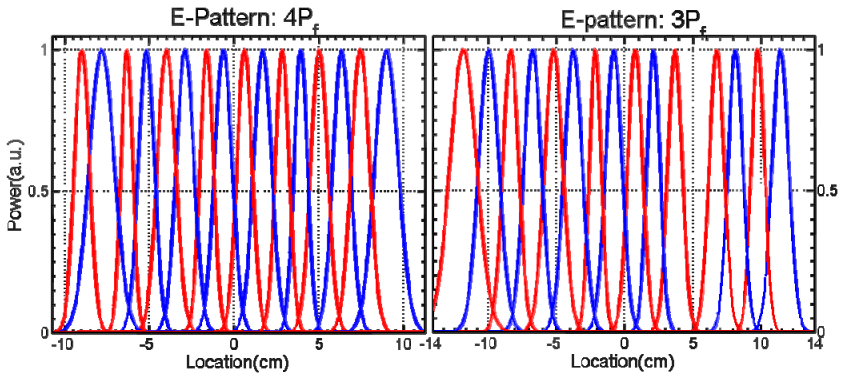

Fig.6 Experiment Measure ECEI focal plane patterns at 102GHz

IV Experiment Result of Sawtooth Reconnection

Sawtooth oscillations are a periodic relaxation process of the plasma temperature, density and other plasma parameters in the central region of a tokamak [8-9], which is characterized by a periodic fast heat loss in the core plasma region, is a well known magnetohydrodynamic (MHD) nonlinear phenomenon in tokamak plasmas. Sawtooth reconnection is investigated in EAST tokamak using ECEI upgrade diagnostic system in this section.

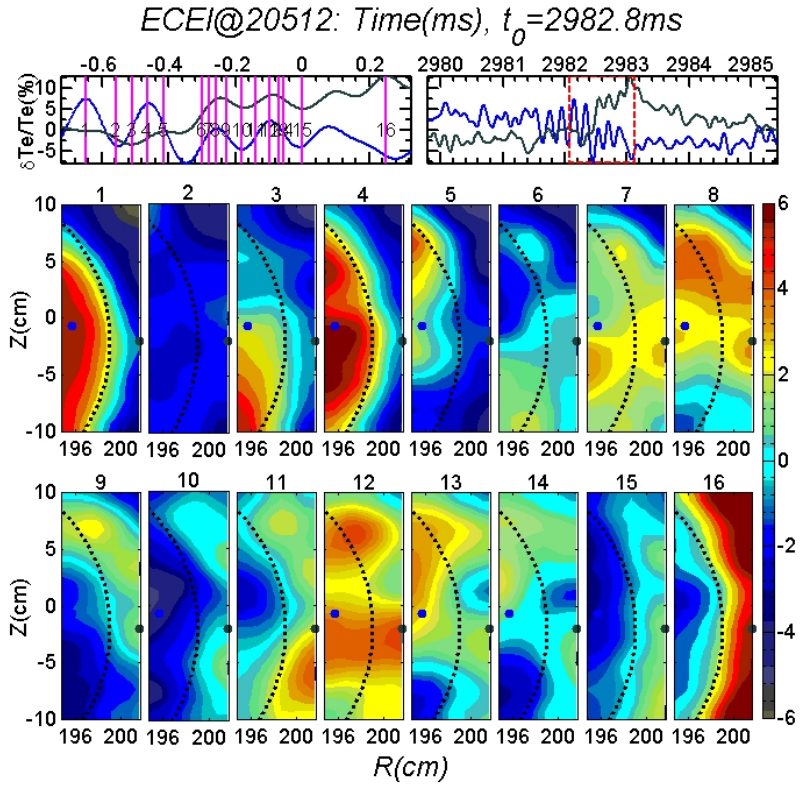

High-resolution single frame images of the time evolution of the hot spot or island (cold spot) while the plasma is rotating along the toroidal direction. During the precursor stage, we can see clearly that when the fluctuation amplitude of Te reaches maximum in frame 4 and a sharp temperature point develops in frame 6 and the reconnection arises subsequently in frame 7. In frame 7 we can see clearly that there have two adjoin hot spot and one still within q~1 radius and the other cross out q~1 radius through reconnection. In frame 9 we can see these two hot spot are cross out q~1 radius. But reconnection not finished and subsequent another reconnection burst in frame 11, we can see the reconnection break two gap in frame 12 and end in frame 15. One sawtooth crash can see in frame 16 that all energy of electron temperature of hot spot is transport from reconnection out of q~1 radius, we can see this reconnection begin from frame 6 and end with sawtooth full crash at frame 16 and this process endures about 400 microseconds for different hot spot for one cycle of plasma rotation.

V Acknowledgment

This work is supported by the National Nature Science Foundation of China under Grant No.10335060, the National Basic Research Program of China under Grant No. 2008CB717800 and Grants from the Ministry of Education and the Academy of Science of P R China, and the CAS-JSPS Core University Program in Plasma and Nuclear Fusion, and by the PRC-US Fusion Cooperation Program (Plasma Physics, Project A-5), the U.S. Department of Energy, Office of Fusion Energy Science.

References

1. R. P. Hsia, W. R. Geck, “ECE imaging array diagnostic development of TEXT-U”. Rev. Sci. Instrum, 66, 834 (1995)
2. B. H. Deng, R. P. Hsia. ”Electron cyclotron emission imaging diagnostic system for Rijnhuizen Tokamak Project”. Rev. Sci. Instrum, 70, 998 (1999)
3. B. H. Deng, C. W. Domier, and N. C. Luhmann, Jr. ” Electron cyclotron emission imaging diagnostic on TEXTOR”. Rev. Sci. Instrum, 72, 368 (2001)
4. C. W. Domier, Z. G. Xia, P. Zhang, and N. C. Luhmann, Jr. “Upgrades to the TEXTOR electron cyclotron emission imaging diagnostic”. Rev. Sci. Instrum , 77, 10E924 (2006)
5. P. Zhang, C. W. Domier et al. “The next generation of electron cyclotron emission imaging diagnostics(invited)”. Rev. Sci. Instrum, 79, 10F103 (2008)
6. Jun, W., Y. Z. Wen, et al. "Optical design of ECEI diagnostic system for HT-7 tokamak." Plasma Science & Technology 6(1): 2166-2171.(2004)
7. J W. Lamb, “Miscellaneous Data on Materials for Millimetre and Submillimetre optics”. International Journal of Infrared and Millimeter waves 17 1997 (1996)
8. S von Goeler, W Stodiek and N Sauthoff. “Studies of Internal Disruptions and m=1 Oscillations in Tokamak Discharges with Soft-X-Ray Techniques”. Phy Rev Lett 33,1201 (1974).
9. J. Wang, X. Xu, Y. Wen, et al.”One-Dimensional Vertical ECEI Diagnostic for HT-7 Tokamak”. Plasma Science and Technology 8, 76 (2006).

Magnetic Configuration Effects on Fast Ion Losses Induced by Fast Ion Driven Toroidal Alfven Eigenmodes in the Large Helical Device

K. Ogawa[2], M. Isobe[1], K. Toi[12], F. Watanabe[3], D. A. Spong[4], A. Shimizu[1], M. Osakabe[1], D. S. Darrow[5], S. Ohdachi[1], S. Sakakibara[1], and LHD Experiment Group[1]

[1]*National Institute for Fusion Science, 322-6 Oroshi-cho, Toki, Japan*

[2]*Department of Energy Science and Engineering, Nagoya University, Nagoya, Japan*

[3]*Graduate School of Energy Science, Kyoto University, Kyoto, Japan*

[4]*Oak Ridge National Laboratory, Oak Ridge, Tennessee, USA*

[5]*Princeton Plasma Physics Laboratory, Princeton University, Princeton, New Jersey, USA*

Abstract

Beam ion losses induced by fast-ion driven magnetohydrodynamic (MHD) instabilities i.e. toroidal Alfvén eigenmode (TAE) are measured with a scintillator-based lost-fast ion probe (SLIP) on various magnetic configurations of the large helical device (LHD). Dependence of the loss fluxes where the energy E and pitch angle $\chi=\arccos(v_{//}/v)$ distribution of the lost fast ions are simultaneously resolved on the magnetic axis position of the vacuum field R_{ax_vac} have been investigated in three typical magnetic configurations of R_{ax_vac}=3.60 m, 3.75 m, and 3.90 m. Dominant losses induced by TAEs were observed in E/χ ~50~190 keV/~40°, ~40~170 keV/~25°, and ~30~190 keV/~30° region for the configurations of R_{ax_vac}=3.60 m, 3.75 m, and 3.90 m, respectively. Lost ion fluxes induced by TAEs clearly depend on the amplitude of TAE magnetic fluctuations, R_{ax_vac} and the toroidal field strength B_t. The losses increase, having the dependence of $(b_{TAE}/B_t)^s$. The power s changes from s=1 to 3 with the increase of the magnetic axis position in finite beta plasmas.

1. Introduction

One of the crucial issues in realizing self-sustained DT burning plasma is that how well fast ions such as alpha particles can be confined. This issue is also important for a reactor-relevant plasma such as ITER [1]. However, significant loss of alpha particles due to fast-ion-driven magnetohydrodynamic (MHD) instabilities such as Alfvén eigenmodes (AEs) [2] excited by alpha particle might give a localized damage onto the plasma facing components. Hence, better understanding of loss process of fast ion due to fast-ion-driven MHD instabilities is required to find a method to control and/or reduce fast-ion losses. Anomalous transport of co-going beam ions due to toroidal Alfvén eigenmodes (TAEs) has been so far recognized in the Large Helical Device (LHD) by an E//B neutral particle analyzer with a tangential line of sight [4]. Recently, TAE-induced beam ion losses were detected by means of a scintillator-based lost-fast ion probe (SLIP) installed at the outboard side of LHD [5]. This paper is devoted to the study of characteristics of energetic ion losses induced by TAE in the various magnetic configurations where neoclassical transport of fast ions due to magnetic field ripple is different.

2. Experimental Setups

There are three negative-ion-based neutral beam (NB) injectors on the LHD and total power more than ~8 MW can be injected having the beam energy of 180~190 keV. In this experiment, one of them tangentially injects NBs in the counter-direction, whereas the others tangentially inject NBs in the co-direction. The beam ion loss from the LHD is measured with an SLIP. The SLIP is essentially a magnetic spectrometer, providing information on the energy E and pitch angles $\chi=\arccos(v_{//}/v)$ of escaping fast ions simultaneously. Here, v and $v_{//}$ indicate the velocity of fast ion and the velocity of fast ion parallel to the magnetic field, respectively. The SLIP installed at the outboard side of LHD is designed to detect co-going

passing or transitional fast ions of which pitch angle and gyroradius are in the ranges of 20–70 degrees and 2–24 cm, respectively, at the detector location [6]. Luminous image produced on the scintillator screen is monitored with a 4×4-photomultiplier tube (PMT) array and an image intensified CMOS camera, simultaneously. Relative sensitivity of PMTs is calibrated with an electro-luminescence sheet emitting a blue-green light, which has uniformity within 10 % error. The energetic ion loss study was carried out in three typical magnetic configurations, i.e. the "inward-shifted configuration" of R_{ax_vac}=3.60 m (R_{ax_vac}: magnetic axis position in the vacuum field), "standard configuration" of R_{ax_vac}=3.75 m, and "outward-shifted configuration" of R_{ax_vac}=3.90 m. In this study, the magnetic field strength B_t was varied from 0.60 T to 0.90 T, where the direction of B_t is in the counter clockwise from the top view of the torus. In these experiments, injected power of the NB injectors was adjusted in each configuration. In all shots of this experiment, TAEs and EPM were excited by beam ions. In these experiment, m~1/n=1 TAE was the dominant energetic ion driven modes, where m and n are respectively poloidal and toroidal mode numbers determined by toroidal/poloidal magnetic probe arrays. The eigenfunction has a peak at the normalized radial position r/a ~0.6. It consists of mainly two m=1 and m=2 Fourier modes, which has opposite polarity each other and odd-parity type TAE [5]. In this paper, experimental studies were carried out, using the TAE amplitude b_{TAE} evaluated by the same magnetic pickup coil placed on the vacuum vessel.

3. Beam Ion Losses induced by TAEs in Various Magnetic Configurations

Characteristics of beam ion losses due to TAEs were investigated in the inward shifted configuration (R_{ax_vac}=3.60 m) at B_t=0.60 T and 0.75 T. In these experiments, three tangential NBs were injected into plasmas. The absorbed total NB powers P_{NB}, averaged fast ion beta $<\beta_{fast}>$, line-averaged electron density $<n_e>$, and magnetic axis position evaluated from the

electron temperature profile measured with Thomson scattering R_{mag} are respectively ~7.9 MW, ~ 1.0 %, ~1.3×10^{19}m^{-3} ,and ~3.86 m at B_t=0.60 T. On the other hand, they are respectively ~ 6.7 MW ~ 0.9 %, ~1.3×10^{19} m^{-3} and ~3.75m at B_t= 0.75 T. The sharp increase in Γ_{SLIP} correlated with TAE bursts was observed in the E/χ ~50~190 keV/~40° region. In Fig.1, the increment of beam-ion loss flux $\Delta\Gamma_{SLIP}$ normalized by the energetic ion content generated by co-injected NB injector ($P_{NBco}\ \tau_{se}$) is plotted as a function of the amplitude of TAE fluctuation b_{TAE} normalized by B_t, where P_{NBco} and τ_{se} indicate absorbed power of co-injected NB and slowing down time of fast ion by electron, respectively. Here, the fast ion loss flux detected with the SLIP is considered to be proportional to co-going fast ion density $\propto P_{NBco}\tau_{se}$, because the SLIP is designed to detect co-going NBs. Here, $\Delta\Gamma_{SLIP}$ is evaluated as the increment of Γ_{SLIP} from that just before each TAE burst. The normalized energetic ion loss flux $\Delta\Gamma_{SLIP}/P_{NBco}\tau_{se}$ increases nearly quadratically with the b_{TAE}/B_t at B_t=0.60 T, while that increases nearly proportional to the b_{TAE}/B_t at B_t=0.75 T. That is, the lower and higher B_t cases respectively indicate diffusive type loss: $\Delta\Gamma_{SLIP}/P_{NBco}\tau_{se} \propto (b_{TAE}/B_t)^2$ and convective one : $\propto(b_{TAE}/B_t)$ [7]. Note that $\Delta\Gamma_{SLIP}/P_{NBco}\tau_{se}$ at B_t=0.75 T is one-order of magnitude lower than that of at B_t=0.60 T, as seen from Fig.1. Enhanced beam ion losses due to TAEs at lower B_t (=0.60 T) are interpreted that TAEs would easily push beam ions into loss cone region expanded in high beta plasmas of $<\beta_{dia}>$~1.7 % with considerable Shafranov shift. On the other hand, the Sharfanov shift in the lower beta plasma (~1.0 %) at B_t=0.75T is appreciably smaller than that at B_t=0.60 T. Small Shafranov shift will lead to shrinkage of the loss cone region. This difference is thought to bring about large diffusive loss in high beta plasmas with large Shafranov shift and low convective loss in lower beta plasmas, even if TAE amplitude is almost same, which can be clearly seen from Fig.1. Note that several data points obtained at highest beta (~1.7 %) strongly deviate from the diffusive loss scaling in the range less than

b_{TAE}/B_t<3.0×10^{-4} T. This can be explained along above discussion based on the extent of loss cone region.

Study on TAE-induced loss was also carried on R_{ax_vac}=3.75 m at B_t=0.60 T and 0.75 T. Here, P_{NB}, $<\beta_{fast}>$, $<n_e>$, and the magnetic axis positions of the finite beta plasma R_{mag} were respectively ~ 6.3 MW, ~0.4 %, ~1.7×10^{19}m^{-3}, and ~3.85 m at B_t=0.60 T, and ~5.5 MW, ~0.3 %, ~1.8×10^{19}m^{-3}, and ~3.90 m at B_t=0.75 T. The plasma beta values at both B_t values were nearly the same as ~1.3 %. The TAE induced losses detected with SLIP was observed in the E/χ ~ 30~190 keV/~30° region. The normalized loss flux $\Delta\Gamma_{SLIP}/P_{NBco}\tau_{se}$ decreases with increase of the magnetic field strength as observed in a previous experiment (Fig.2). The loss flux $\Delta\Gamma_{SLIP}/P_{NBco}\tau_{se}$ increases nearly quadratically with the b_{TAE}/B_t at both B_t=0.60 T and 0.75 T. This tendency corresponds to the characteristics obtained in high-beta plasma at R_{ax_vac}=3.60 m. Note that the magnetic axis position R_{mag} on relatively low-beta plasma (~1.3 %) in the configuration of R_{ax_vac}=3.75 m is comparable with that of the high-beta plasma (~1.7 %) in the configuration of R_{ax_vac}=3.60 m. It may be explained by the loss cone effect. The loss cone of the relatively low-beta plasma in the R_{ax_vac}=3.75 m configuration is similar to that of the high-beta plasma at R_{ax_vac}=3.60 m, because R_{mag} is nearly same in both configurations.

TAE-induced beam ion losses were also studied in the outward-shifted configuration (R_{ax_vac}=3.90 m) at B_t=0.75 T and 0.90 T. Two of NBs were injected into a plasma and the bulk plasma beat was relatively low-beta (~0.7 %). In this experiment, P_{NB}, $<\beta_{fast}>$, $<n_e>$, and R_{mag} are respectively ~4.5 MW, ~0.3 %, ~ 1.0×10^{19}m^{-3}, and ~4.05 m at B_t=0.75 T, and they are respectively ~5.5 MW, ~0.2 %, 1.5×10^{19} m^{-3}, and ~4.00 m at B_t=0.90 T. TAE-induced loss flux was observed in the E/χ ~40~170 keV/~25° region. In this outward-shifted configuration, the losses were clearly observed at higher B_t of 0.90 T, as shown in Fig.3. This result will be

related to the fact that the deviation of beam ion orbits from flux surfaces is considerably large because of large magnetic axis shift, compared with that in the R_{ax_vac}=3.60 m configuration. In contrast to the results of above-mentioned configurations shown in Figs.1 and 2, the normalized loss flux $\Delta\Gamma_{SLIP}/P_{NBco}\tau_{se}$ increases rapidly with the TAE fluctuation amplitude, and is scaled with the higher power of the TAE amplitude, that is, $\propto (b_{TAE}/B_t)^3$ at B_t=0.75 T and B_t=0.90 T. Although this type of losses is inferred to be due to destruction of magnetic surfaces in ref. [7], this dependence also may be explained by loss cone effect. That is, the loss cone in this configuration is wider than that in R_{ax_vac}=3.60 m, and R_{ax_vac}=3.75 m configurations, and fast ions would easily fall into the loss cone. This situation will lead to a stronger dependence of the loss flux on TAE amplitude.

4. Summary

In LHD, time-resolved energy and pitch angle measurements of beam ion losses induced by TAE were carried out in three typical magnetic configurations of R_{ax_vac}=3.60 m, 3.75 m, and 3.90 m, at two different magnitudes of B_t. In all these configurations at B_t=0.60 T to 0.90 T, m~1/n=1 TAE were strongly destabilized and they induced fast ion loss in the range of E/χ ~30-190 keV and χ ~25°-40°. With the increase of the Shafranov shift or magnetic axis position shift R_{mag}, the normalized loss fluxes $\Delta\Gamma_{SLIP}/P_{NBco}\tau_{se}$ increase more rapidly with increase in the relative amplitude of TAE magnetic fluctuations b_{TAE}/B_t. That is, the convective loss character of $\Delta\Gamma_{SLIP}/P_{NBco}\tau_{se} \propto (b_{TAE}/B_t)$ in the plasma with smaller R_{mag} changes via a diffusive type of $\Delta\Gamma_{SLIP}/P_{NBco}\tau_{se} \propto (b_{TAE}/B_t)^2$ in that with large R_{mag}, to a character having stronger amplitude dependence as $\propto (b_{TAE}/B_t)^3$ in the case of largest R_{mag}. This tendency may be consistently explained by effects of the loss cone size.

Acknowledgments

This work is supported in part by the Grant-in-Aid for Scientific Research from MEXT, No. 16082209 and from JSPS No. 21360457, No. 21340175, and No. 22-7912, and the LHD project budget (NIFS09ULHH508). This work was also partially supported by the JSPS-CAS Core-University program in the field of 'Plasma and Nuclear Fusion'.

References

[1] Fasoli A. *et al*., 2007 Nucl. Fusion **47**, S264.

[2] Chen C. Z. and Chance M. S., 1986 Phys. Fluids **29**, 3695.

[3] Chen L., 1994 Phys. Plasmas **1**, 1519

[4] Osakabe M., *et al*., 2006 Nucl. Fusion **46** S911-S917.

[5] Ogawa K. *et al*., 2010 Nucl Fusion **50** 084005

[6] Ogawa K. *et al*. 2009 J. Plasma Fusion Res. Series **8** 655.

[7] Heidbrink W.W. *et al*., 1993 Phys. Fluids B **5**, 2176.

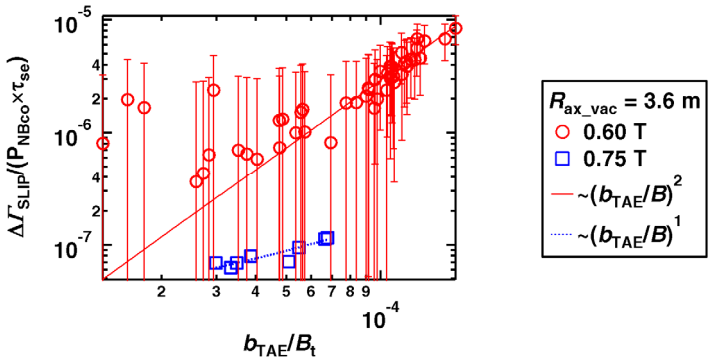

Fig. 1 Dependence of the normalized lost-fast ion fluxes on the magnetic fluctuation amplitude of TAE. The loss fluxes at B_t=0.60 T and 0.75 T are respectively scaled with $(b_{TAE}/B_t)^2$ and $(b_{TAE}/B_t)^1$.

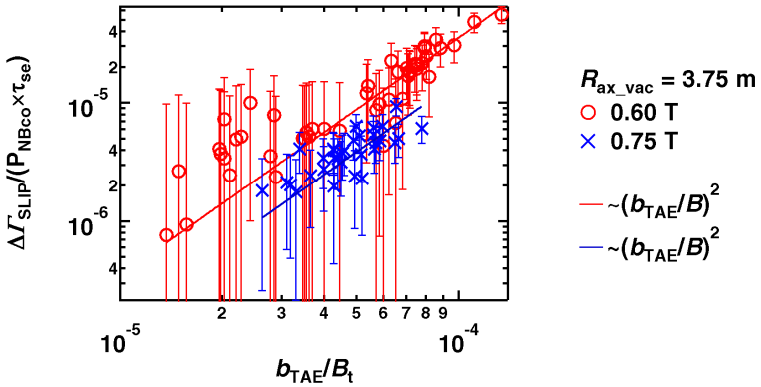

Fig. 2 Dependence of the normalized lost-fast ion flux induced by TAE on the magnetic fluctuation amplitude of TAE. The normalized loss fluxes at B_t=0.60 T and 0.75 T are scaled with $(b_{TAE}/B_t)^2$.

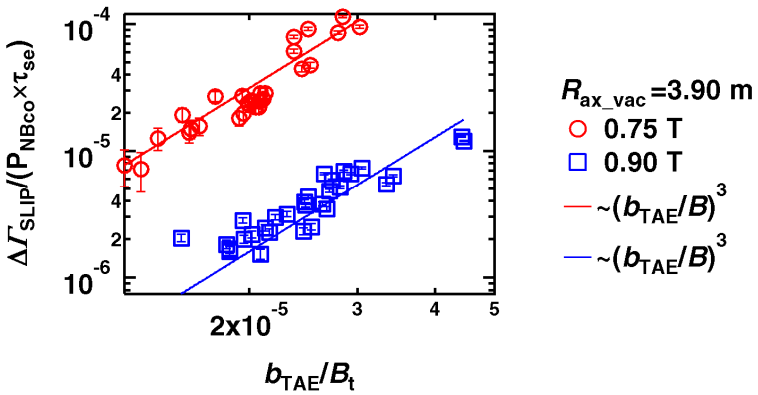

Fig. 3 Dependence of the normalized lost-fast ion flux induced by TAE on the magnetic fluctuation amplitude of TAE. The normalized loss flux on B_t=0.75 T and 0.90 T are scaled with $(b_{TAE}/B_t)^3$.

Experimental study of discharge cleaning on EAST by helicon plasma

C.G.Jin, T.Yu, C.Ye, L.J.Zhuge, S.B.Ge, X.M.Wu

[a] *Department of physics, Suzhou University, Suzhou215006, China*

[b] *The Key Laboratory of Thin Films of Jiangsu, Suzhou University, Suzhou215006, China*

[c] *Analysis and Testing Center, Suzhou university, Suzhou215006, China*

e-mail: nestajcg@126.com

High power steady operation of Experimental Advanced Superconducting Tokamak (EAST), which is an ITER-relevant experimental tokamak would lead to serious plasma-material interactions, wall conditioning must be used to limit impurities release from the wall and tritium inventory retained in the wall. Helicon plasma source is known as efficient generator of uniform and high density plasma. Helicon Wave Plasma (HWP) discharge cleaning was considered as the most promising method for superconducting tokamak. In this paper, HWP cleaning with wave frequency of 13.56 MHz have been performed in presence of permanent toroial magnetic filed (1-2 T) in EAST. Three different antennas were designed for HWP wall conditioning. Influences of working parameters on the HWP cleaning efficiently were investigated. This research is concentrated on experimental study of HWP discharge cleaning, in order to collect more data of wall conditioning and provide science and technology support for the requirement of ITER operation.

This work was partially supported by the JSPS-CAS Core-University program in the field of'Plasma and Nuclear Fusion'.

Study on radial position of impurity ions at core and edge plasmas in LHD using space-resolved EUV spectrometer

Chunfeng DONG[1], Shigeru MORITA[1,2], Motoshi GOTO[1,2] and Masahiro KOBAYASHI[1,2]

[1]Graduate University for Advanced Studies, Toki 509-5292, Gifu, Japan
[2]National Institute for Fusion Science, Toki 509-5292, Gifu, Japan

Abstract

Radial profiles of impurity ions of carbon, neon and iron have been measured from high-temperature plasmas of Large Helical Device (LHD) using a space-resolved extreme ultraviolet (EUV) spectrometer in wavelength range of 60-400Å. The radial positions of the impurity ions are compared with their ionization energies, E_i, and electron temperatures at which the impurity ions are located, T_{eZ}. The impurity ions with $0.3 \leq E_i \leq 1.0$keV are always located in the outside of plasmas, i.e., $0.7 \leq \rho \leq 1.0$, and those with $E_i \leq 0.3$keV exist in the ergodic layer, i.e., $1.0 \leq \rho \leq 1.1$, with a sharp peak edge. It is newly found that the T_{eZ} is approximately equal to the E_i for the impurity ions with $E_i \leq 0.3$keV, whereas the T_{eZ} is roughly half to the E_i for the impurity ions with $0.3 \leq E_i \leq 1.0$keV. It is known the T_{eZ} is considerably smaller than the E_i in the plasma edge and becomes equal to the E_i in the plasma core. Therefore, this result is seemed to originate in the difference of the perpendicular transport between the plasma edge at $\rho \leq 1.0$ and the ergodic layer at $\rho \geq 1.0$. The perpendicular transport is studied with impurity transport simulation code. As a result, it confirm that the difference appeared in the impurity radial positions can be qualitatively explained by different values of the diffusion coefficient, e.g., D=0.2 and 1.0m^2/s, as the typical index of the perpendicular transport.

1 Introduction

Impurity transport is one of the most important subjects in the field of magnetically confined plasma, since the plasma performance is frequently affected by the impurities through radiation loss and the dilution of fuel ions brought by the presence of impurities leads to the decrease in fusion output. The impurity transport has been extensively studied until now in many tokamak [1-3] and helical devices [4-9]. One of special properties in viewpoint of the impurity transport seen in Large Helical Device (LHD) is characterized by the edge magnetic topology. The ergodic layer surrounding the LHD plasma is formed by stochastic magnetic fields with long connection lengths of $10 \leq L_c \leq 2000$m [10], whereas the scrape-off layer in tokamaks is formed by well aligned magnetic fields with short connection lengths of $L_c \leq 100$m. In LHD, therefore, the perpendicular transport becomes important in the ergodic layer in addition to the parallel transport which is mainly dominant in the scrape-ff layer of tokamaks.

Vertical profiles of impurity ions such as carbon, neon and iron have been measured using a space-resolved flat-field extreme ultraviolet (EUV) spectrometer in LHD. The radial positions of each impurity ion are accurately determined at core and edge regions of the LHD plasmas by carefully calibrating the vertical position for each observation chord. The results are correlated with their ionization energies, E_i, and electron temperature at which the impurity ions are located, T_{eZ} for the core and edge impurity ions. In the present paper, the perpendicular transport in the ergodic layer is studied through the analysis on the E_i and T_{eZ}.

2 Experimental setup

The radial profiles of impurity ions studied here are measured from plasmas at magnetic axis position of R_{ax}=3.60m using the space-resolved EUV spectrometer system [11]. The EUV system is illustrated in Fig. 1(a). The EUV spectrometer is installed on LHD perpendicular to toroidal magnetic field to observe the radial profiles of impurity ions in wavelength range of 60-400Å. In order to increase the signal quality, the width of entrance silt is enlarged from 30μm to 100μm. A spatial resolution slit of 0.5mm in width is placed in front of the entrance slit. This combination makes favorable spectral and vertical spatial resolutions of 4 pixels, which correspond to $\Delta\lambda$=0.3Å at 100Å and $\Delta\lambda$=0.5Å at 400Å, and ΔZ=15mm, respectively, keeping a good throughput. A back-illuminated charge-coupled device (CCD) with an array of 1024×255 pixels and a size of 26.6×6.6 mm is used to record the spectral line emissions.

The vertical profile of the EUV spectra can be measured with an observation length of 52cm, which roughly corresponds to half size at short axis of the elliptical LHD plasma. It is noted that all the radial profiles of impurity emissions studied here are taken from the upper half at horizontally elongated plasma cross section of the elliptical LHD plasmas, as shown in Fig. 1(b). A spectral observation range, which is determined by the CCD horizontal size of 6.6 mm, is a large function of wavelength, e.g., 35Å at λ=60Å and 65Å at λ=400Å. In order to take a good time resolution of 200ms a binning mode of the CCD is selected as ΔX=5 pixels, which means that five pixels are summed up and converted into one channel. Although this binning slightly makes the spectral resolution worse, most of

the spectral lines are not blended even in such a relatively worse spectral resolution, since the spectral lines separately exist in the EUV range. The vertical position of each observation chord is accurately calibrated using a series of rectangular-corrugated edge with periodically changed widths. The vertical locations of the initial and final observation chords are shown in Fig.2 as Z_{max} and Z_{min}, respectively. The value of Z_{max}-Z_{min} denotes the observable vertical range in the present EUV system. Here, Z=0 denotes the equator plane at the plasma core. The observable range is a weak function of wavelength having a little wider range at the shorter wavelength side.

3 Radial profiles of impurity ions at core and edge plasmas

The emissions from iron ions have been commonly measured in the EUV range as a typical metal impurity in LHD, although the density of iron ions is negligibly small, i.e., $n_{Fe}/n_e<10^{-4}$. The maximum ionization stage of the iron ions observed in the EUV range is FeXXIV (192.017Å), which has high ionization energy of E_i=2.046keV. Since the iron ions are highly ionized in LHD plasmas, most of the dominant iron emissions in the EUV range are located in the plasma core. Therefore, the radial location of the highly ionized iron ions is a strong function of the electron temperature. In order to confirm the electron density dependence, FeXX (132.85Å) with relatively smaller ionization energy of 1.58keV is selected for the measurement because the iron spectra in higher ionization energies such as FeXXIV are disappeared in low-temperature plasmas. The profiles of FeXX measured from plasmas with two different electron temperatures are compared in Fig. 3(b). The corresponding electron temperature profiles are shown in Fig. 3(a), which are measured by Thomson scattering system. Both profiles are taken from discharges with the same plasma axis position of R_{ax}=3.60m and have similar line-averaged electron densities of 1.4 and 1.3×10^{13}cm^{-3} for cases of $T_e(0)$=2.9 and 1.6keV, respectively. The intensities of both FeXX radial profiles are normalized at the maximum value. As clearly seen in Fig. 3(b), the radial locations of FeXX greatly differ between the two discharges. In the discharge with $T_e(0)$=1.6keV the FeXX is located at ρ=0.24, which is close to the plasma center. In the discharge with $T_e(0)$=2.9keV, on the other hand, the FeXX located at ρ=0.65, which is far from the plasma center. However, it is found that the FeXX from the two discharges are located at the same temperature region of T_e=1.56keV. It indicates that the radial position of the FeXX is close to the ionization energy of E_i=1.58keV, having no dependence on the central electron temperature.

The radial profiles of impurity ions are also a large function of the ionization energy. Figure 4(a) shows the radial profiles from iron ions in different charge states. Since the ionization energies of the three iron ions are largely different based on the charge states, i.e., E_i=0.46keV for FeXV (284.147Å), E_i=1.58keV for FeXX (132.85Å) and E_i=2.05keV for FeXXIV (192.017Å), their radial profiles distribute over a wide range of the plasma. The FeXXIV emission can be observed when the electron temperature is increased up to 3keV, whereas the FeXV emission is always observable. Here, it is noticed that the emission intensity from impurity ions existing in the plasma center is relatively weak because of the small emission volume. An enough expansion of the emission volume is necessary for the observation of impurity ions locating at the plasma center such as FeXXIV.

The radial profiles from impurity ions of CVI (2×33.73Å), CV (2×40.268Å),

NeVIII (88.09Å), NeVII (106Å) and CIV (312.4Å) existing in the plasma edge are also successfully observed with excellent spatial resolution. The results are shown in Fig. 4(b) with expanded horizontal scale of $0.7 \leq \rho \leq 1.2$. It is also clearly seen that all the ions are located in different radial positions depending on their ionization energies, i.e., CVI: E_i=0.59keV, CV: E_i=0.39keV, NeVIII: E_i=0.24keV, NeVII: E_i=0.21keV and CIV: E_i=0.064keV. The carbon is only a dominant intrinsic impurity in LHD, which is mainly transferred through divertor legs from divertor plates made of carbon (see Fig. 1(b)) and the neon is externally introduced by gas puffing. The CIV is practically the lowest ionization stage in carbon ions existing in the ergodic layer. The intensity of CIII (386.2Å) is not usually visible in the present EUV spectrometer. The CV and CVI are located at ρ=0.92 and 0.87, respectively. On the other hand, the CIV, NeVII and NeVIII are located beyond ρ=1 which indicates the last closed flux surface (LCFS). This means that those ions stay in the ergodic layer, which consists of stochastic magnetic fields, surrounding the main plasma of LHD defined by the LCFS.

4 Analysis on radial positions of edge impurity ions

The radial positions of impurity ions existing in the plasma edge ($0.8 \leq \rho \leq 1.0$) and in the ergodic layer ($1.0 \leq \rho \leq 1.1$) are analyzed with the ionization energy. The ionization energy of impurity ions are plotted against their radial positions, as shown in Fig. 5 (a). The spectral lines emitted from the plasma edge and the ergodic layer are named as Group I and Group II, respectively. The location of impurity ions moves outwardly with decreasing E_i. When the E_i is reduced to 0.3keV, the impurity ions stay in the ergodic layer. These ionization energies are correlated with the electron temperature at which the impurity ions are located, T_{eZ}. The result is shown in Fig. 5(b). The solid line denotes the relation of $T_{eZ}=E_i$. From the figure we notice the presence of two different correlations. The impurity ions at Group I, , i.e., CV, CVI, FeXV and FeXVI, indicates the relation with $T_{eZ}<E_i$. The ratios of T_{eZ}/E_i distribute around one-half. Calculating the impurity transport code with usually used common transport parameter, typical ratio of T_{eZ}/E_i is given as one-third for impurity ions existing in the plasma edge and as unity for impurity ions existing in the plasma center. Since the ionization rare coefficient for impurity ions in lower ionization stages is still high even in $T_e<E_i$, the impurity ions are ionized before arriving at the radial location of $T_e=E_i$. However, the impurity ions in higher ionization stages located at the plasma core are ionized at $T_e=E_i$, because the ionization rate coefficient is relatively small at $T_e<E_i$. Therefore, the experimentally obtained ratios seen at FeXX of Fig.3 and Group I of Fig.5 are almost reasonable.

On the other hand, we find the other group (group II) located in the ergodic layer of $1.0 \leq \rho \leq 1.1$, which has the relation of $T_{eZ}=E_i$, such as CIV, NeV, NeVII and NeVIII. The result on the group II can not be understood from the knowledge on the commonly studied impurity transport. It strongly suggests a different perpendicular transport in the ergodic layer.

In order to understand the relation of $T_{eZ}=E_i$ in the Group II, the edge carbon transport is analyzed using the impurity transport code as a function of inward convective velocity, V, and diffusion coefficient, D. The relative shift of radial positions of carbon ions

is plotted in Figs. 6(a) and (b) as a function of V and D, respectively. As seen in Fig. 6(a), the radial positions of CIII and CIV do not entirely depend on V, although those of CV and CVI is a large function of V. The result basically originates in the different temperature dependence of the ionization rate coefficient. The vale of V experimentally observed in the previous study[4] is indicated with a shaded square hatch in Fig.6(a). Therefore, the effect of V on the radial position is practically small. However, the radial positions of CIII and CIV can be a large function of D as well as CVI, as shown in Fig. 6(b). In LHD the value of D is known to be $0.2m^2/s$ in the previous study[4]. The radial position of CVI does not move so much even if the value of D changes near $0.2m^2/s$. In the ergodic layer the perpendicular transport is large due to the stochastic magnetic fields and the diffusion coefficient is a typical index to express the perpendicular transport. Although the global value of D in the ergodic layer has not been yet studied at present, it is believed to be in range of $1\text{-}10m^2/s$. If D is assumed to be $1m^2/s$ for CIII and CIV, the radial positions of them can be inwardly shifted by 1-2cm. This inward shift of the radial position makes the T_{eZ} larger. The large diffusion coefficient, which suggests the enhanced perpendicular transport in the ergodic layer, can qualitatively explain the large T_{eZ} seen in the group II of Fig. 5(b).

5 Summary

The radial profiles of impurity ions have been excellently observed from high-temperature LHD plasmas using the space-resolved flat-field EUV spectrometer. The radial positions are analyzed with E_i and T_{eZ}. We newly found that the impurity ions existing in the ergodic layer have the relation of $T_{eZ}=E_i$, whereas the edge impurity ions usually have the relation of $T_{eZ}=1/3\times E_i$. The large value of T_{eZ} can be quantitatively explained by adopting a large diffusion coefficient in the ergodic layer. However, the stochastic magnetic field in the ergodic layer is very complicated. In order to analyze the data quantitatively, the use of three dimensional edge transport code is necessary.

Acknowledgements

This work was partially supported by the JSPS-CAS Core-University program in the field of 'Plasma and Nuclear Fusion'.

References

1 Ghendrih P, Grosman A, Capes H. 1996, Plasma Phys. Controlled Fusion, 38: 1653
2 Dux R. 2003, Fusion Science and Technology, 44: 708
3 Chen H, Giannella R, Hawkes N, et al. 2001, Plasma Phys. Controlled Fusion, 43: 1
4 Nozato H, Morita S, Goto M, et al. 2004, Phys. Plasma, 11: 1920
5 Nozato H, Morita S, Goto M, et al. 2006, Phys. Plasma, 13: 092502
6 Chowdhuri M, Morita S, Kobayashi M, et al. 2009, Phys. Plasma, 16: 062502
7 Zhou H Y, Morita S, Goto M, Dong C F. 2010, J. Appl. Phys., 107: 053306
8 Kobayashi M, Feng Y, Morita S, et al. 2008, Plasma and Fusion Research, 3: S1005
9 Burhenn R, Baldzuhn J, Brakel R, et al. 2004, Fusion Science and Technology, 46: 115
10 Ohyabu N, Watanabe T, Ji H, et al. 1994, Nucl. Fusion, 34: 387
11 Dong C, Morita S, Goto M, et al. 2010, Rev. Sci. Instrum., 81: 033107

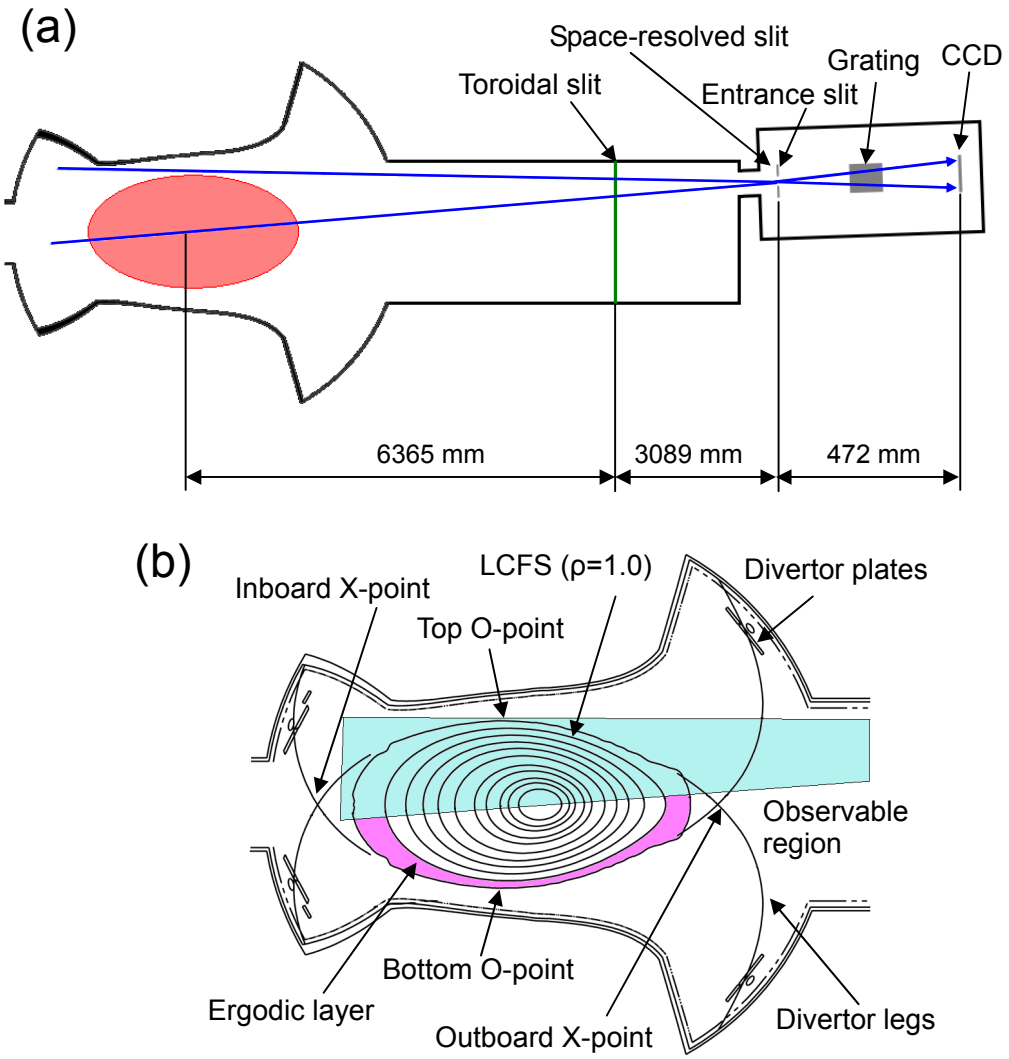

Fig. 1 (a) Space-resolved flat-field EUV spectrometer system and (b) cross section of LHD plasma.

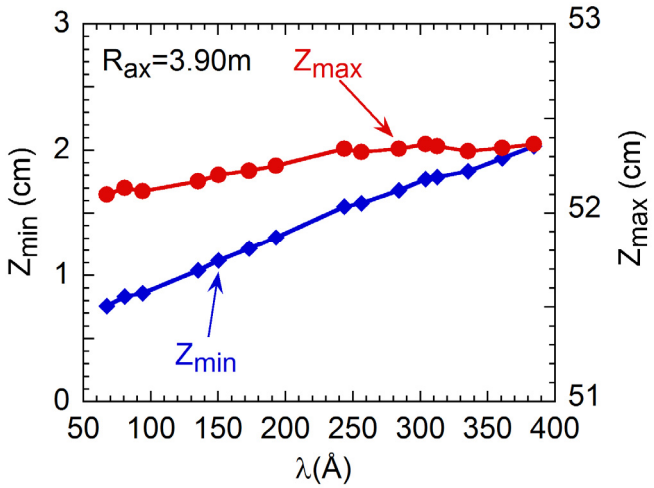

Fig. 2 Observable vertical range of EUV spectrometer system. Values of Z_{min} and Z_{max} mean the top and bottom observation chord when upper half of elliptical LHD plasma is measured.

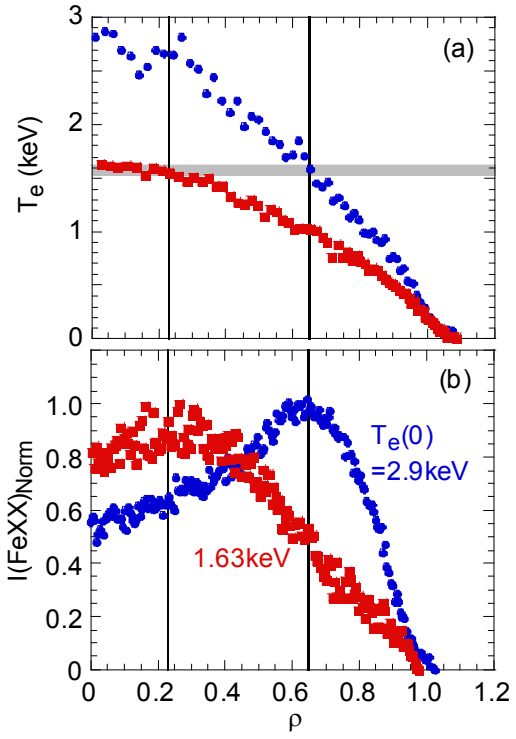

Fig 3. (a) Electron temperature profiles and (b) radial profiles of FeXX (132.85Å) at different electron temperatures as shown in (a).

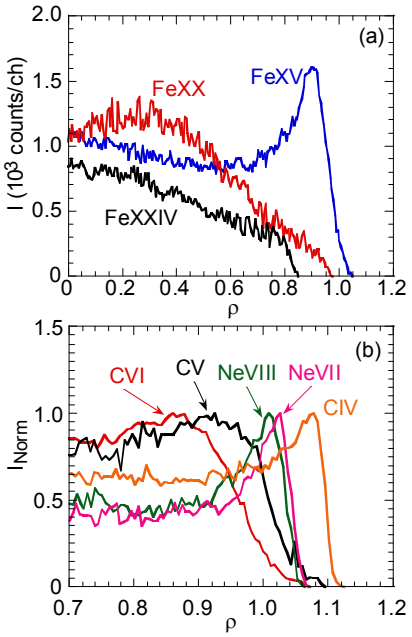

Fig. 4 (a) Radial profiles of (a) iron impurity ions in different charge states at plasma core and (b) carbon and neon impurity ions in different charge states at plasma edge and ergodic layer.

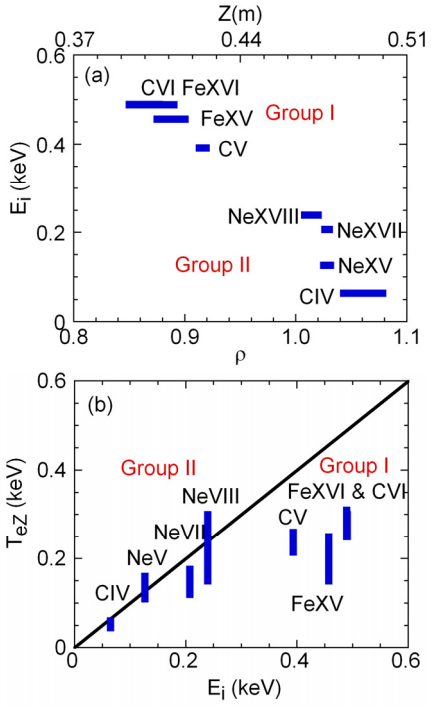

Fig. 5 (a) Ionization energies of impurity ions as a function of normalized plasma radius and (b) electron temperature at which the impurity ions are located as a function of ionization energy. Magnetic surface data in vacuum (β=0%) are used in plotting vertical positions of Z in upper horizontal axis of (a).

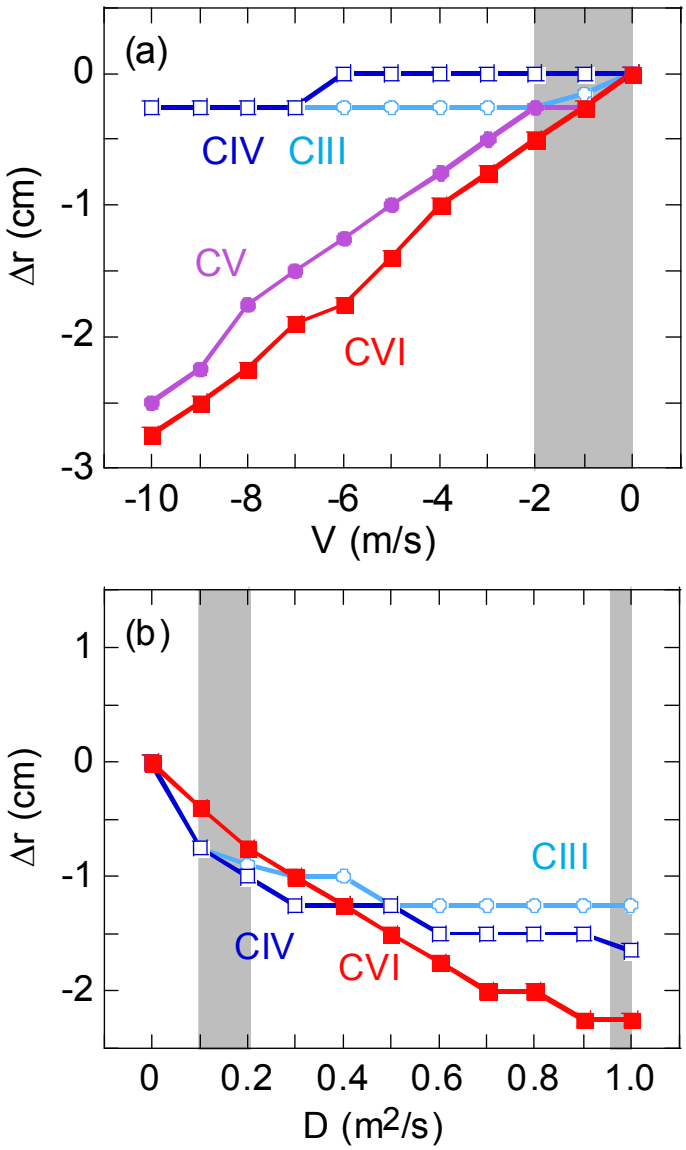

Fig. 6 Radial shift of impurity positions as a function of (a) inward velocity and (b) diffusion coefficient for carbon emissions of CIII to CVI.

Generation and suppression of runaway electrons in EAST LHCD experiments

ZHOU Ruijie(周瑞杰)[1], HU Liqun（胡立群)[1], LU Hongwei (卢洪伟)[2]，LI Erzhong （李二众)[1]，LIN Shiyao（林士耀)[1], XU Ping（许平)[1] ,ZHANG Ling（张凌)[1]

[1] Institute of Plasma Physics, Chinese Academy of Sciences, Hefei 230031, China

[2] Department of Physics, Donghua University, Shanghai 201620, China

e-mail:" rjzhou@ipp.ac.cn"

Abstract In lower hybrid current drive (LHCD) experiment of EAST tokamak in the spring of 2010, the process in which fast electrons transform to runaway electrons was observed, and this process was analyzed according the primary generation mechanism of runaway electrons. Simultaneously, the way how LHW affect the secondary generation mechanisms was studied. It is found that when the power of LHW is low, fast electrons can be accelerated to runaway electrons, but when the power is high enough, fast electrons can not transform to runaway electrons anymore. For the secondary generation mechanisms, even if LHW enhance the primary generation process of runaway electrons, it effectively suppressed the secondary generation process.

Keywords: runaway electron, LHW, generation mechanism, suppression

PACS: 52.59.Px

1. Introduction

In the experiments of Tokamak nowadays, there always exist runaway electrons in plasma. It's a very common phenomenon in plasma physics. The disruption of plasma or low density discharge will create a considerable amount of runaway electrons. The energy of these runaway electrons can reach as high as tens of MeV. So once they loss control, they can cause serious damage to the vacuum vessel and are a potentially dangerous source of hard X-ray[1-2]. Especially for large tokamak like ITER, the damage will be more serious[3]. On the other hand, runaway electrons can carry a substantial amount of the plasma current and may have beneficial effects on plasma confinement.

Lower hybrid waves are routinely used to drive currents in tokamak plasma non-inductively[4]. In LHCD experiment, when the resonance condition is fulfilled, LHW will generate fast electrons through parallel electron Landau damping[5]. These fast electrons can carry current efficiently. The energy of these fast electrons are much higher than the bulk electrons, they can act as a seed population of runaway electrons. And the same time, due to the feedback control of the current, the injection of LHW will reduce the loop voltage. Generally, the loop voltage will not reduce to zero, and there always exist some loop voltage. Runaway electrons are very sensitive to loop voltage, and the change of loop voltage will affect the behavior of runaway electrons significantly. In different condition, the injection of LHW will enhance or suppress the generation of runaway electrons. What we want to do is to find out the mechanisms how LHW enhance or suppress the generation of runaway electrons, and then suppress the generation of runaway electrons by using LHW to protect the first wall of tokamak

In theory, two runaway electron generation mechanisms are known: Primary generation (often called the Dreicer process) and Secondary generation (the avalanche process).

The presence of a toroidal electric field (E) in a tokamak gives rise to the phenomenon of electron runaway. An electron in the plasma experiences a force equal to F_e=-eE and a drag force resulting from Coulomb interactions with plasma ions and electrons. Since the close Coulomb collision frequency between charged particles is much lower than distance Coulomb collision frequency, the contribution of the close Coulomb collision can be neglected. Then the drag force (F_d) is conveniently written in the form:

$$F_d = m_e v \nu_{coll}(v) \tag{1}$$

Where $\nu_{coll}(v)$ is the collision frequency. For a test electron moving much faster than thermal electrons, $\nu_{coll}(v)$ has a v^{-3} dependence and is for a Maxwell distribution approximated by:

$$\nu_{coll}(v) = \frac{e^4 n_e \ln\Lambda}{4\pi\varepsilon_0^{\,2} m_e^{\,2} v^3}(2 + Z_{eff}) \tag{2}$$

Here $\ln\Lambda$ is the Coulomb logarithm, Z_{eff} is the effective charge number of the ions[6].

Electrons with velocities exceeding the critical velocity:

$$v_{crit} = \sqrt{\frac{c^3 n_e \ln\Lambda(2+Z_{eff})}{4\pi\varepsilon_0{}^2 m_e E}} \tag{3}$$

at which F_d balances F_e are continuously accelerated and are called 'runaway electrons'. Runaway electrons have therefore a kinetic energy of at least W_{crit}:

$$W_{crit} = \frac{1}{2} m_e v_{crit}{}^2 = 2.2(2+Z_{eff}) \frac{n_e[10^{19} m^{-3}]}{E[V/m]} keV \tag{4}$$

The electric field for which a thermal electron will run away is called the critical field E_{crit} given by:

$$E_{crit} = \frac{c^3 n_e \ln\Lambda Z_{eff}}{4\pi\varepsilon_0{}^2 m v_{th}{}^2} = \frac{4 Z_{eff} n_e [10^{19} m^{-3}]}{T_e[keV]} \tag{5}$$

As long as the electric field E applied to the plasma is much smaller than this critical field, the distribution function of the electrons stays close to a Maxwell and only an exponentially small fraction of the electrons will run away. This is the primary generation mechanisms, and it's also the basic generation mechanism of runaway electrons. Runaway electrons generated under the primary mechanism are accelerate mainly by the loop voltage, and there parallel momentum with respect to the magnetic field is much larger than the perpendicular momentum, $p_{\|} \gg p_{\perp}$.

Apart from the primary generation, a second generation mechanism of runaways exists[7-9]. Already existing runaway electrons can kick thermal electrons into the runaway region by close Coulomb collisions. If the confinement time of runaway electrons is long enough, close collisions can make the velocity of the bulk electrons overcome the critical energy, and already existing runaway electrons can keep at the runaway region. This process will be like an avalanche, the number of runaway electrons will increase by exponential growth, and it will greatly enhance the runaway production rate. This is the secondary generation mechanism of runaway electrons. Note that in the introduction of the primary generation mechanism only the distance Coulomb collisions were taken into account. Distance Coulomb collision can only result in slight variations in the momentum, both the direction and the magnitude. But close Coulomb collision can significantly change the momentum. When the loop voltage is high the secondary mechanism will be more easy to take place, and as a result of the close collisions, the secondary electrons can have relatively

large perpendicular momentum, $p_{\perp} \gg p_{\parallel}$.

2. Experimental Setup

EAST is a fully superconducting tokamak with major R of 1.84m and minor radius a of 0.48m. Its objective is to study physical issues of the advanced stead-state operation modes and to establish technology basis of fully superconducting tokamak for future reactors[10]. A LHW power of up to 1.5MW at 2.45GHz is available in EAST. There are many diagnostic systems can be use to study the behavior of runaway electrons, such as electron cyclotron emission (ECE) system, fast electron bremsstrahlung (FEB) system, runaway diagnostic system[11].

When runaway electrons leave the plasma, they intersect the material of the limiter or the first wall. The slowing down of the electrons will cause a considerable amount of bremsstrahlung. Because of the relativistic energies of the runaways, the X-ray is emitted in the direction of the incident electrons[12]. After the emitted photons leave the limiter, they can pass through the vacuum vessel and other machine components in the path to the detectors. By measuring this X-ray, the behavior of those runaway electrons can be studied. In EAST tokamak, we have detectors aligned tangentially to the orbit of those runaway electrons, and the same time, we also have detectors aligned vertical to the orbit. The schematic view of this runaway diagnostic system is shown in figure 1. Those detectors are shielded with lead cylinders, and a large amount of lead is used to collimate the X-ray. Also, to get rid of the effect of the magnetic field, all detectors are surrounded with soft iron.

(Figure.1)

In LHCD experiment of EAST tokamak in the spring of 2010, LHW with different power to enhance or suppress the generation of runaway electrons are studied.

A typical LHCD discharge is shown in figure 2. The plasma current is 200kA, the line averaged density is $2.0\times10^{19} m^{-3}$. In this condition, there is only few run away electrons with relatively low energy. The process in which fast electrons transform to runaway electrons can be studied. The plasma was started by Ohmic heating, and when the current went to the flat-top phase, LHW was injected. At first, 100kW LHW was injected at 2.5s. By climbing for 400ms, the power hold steady at 2.9s. 300ms later, the power of LHW increased to 220kW at 3.2s. At last the LHW was turned off at 3.5s. The way how LHW with different power affect the behavior of runaway

electrons can be studied in only one discharge.

(Figure.2)

3. Results and Discussion

In LHCD discharge as shown in figure 2, there was only few runaway electrons duel to high density and low current. When LHW was injected into the plasma, it will drive lots of thermal electrons to fast electrons, and the overall effect of these fast electrons is driving toroidal current. The loop voltage will reduce due to those current driving by LHW. In this LHCD discharge, the loop voltage was changed from 0.9V to 0.35V after 100kW LHW was injected; when the LHW power increased to 220kW, the loop voltage dropped to 0.15V; the loop voltage increased to 0.7V after LHW was turned off. Runaway electrons are very sensitive to the loop voltage, so it will affect the behavior of runaway electrons significantly when LHW is injected. In figure 2, signal RA1 and RA2 represent thick-target bremsstrahlung at the first wall when runaway electrons leave the plasma and hit them, and RA1 get signal from a detector aligned tangentially and RA2 aligned perpendicularly. After LHW was injected, those two signals have great difference.

(Figure.3)

Figure 3 is the count spectrum of signal RA1. We can see at the beginning of the discharge the count is very little. The signal increase rapidly after 100kW LHW is injected. But it reduce rapidly also after 220kW LHW is injected. Until the end of the discharge, the signal increase by exponential growth. During the LHCD phase, the loop voltage reduces and both the current and density keep constant. Based on the primary generation mechanism of runaway electrons, the critical energy of runaway electrons W_{crit} will change greatly. Put the effective charge number of the ions Z_{eff}, density and loop voltage into formula (2.4), we can get the evolvement of the critical energy along with time. The result is shown in figure 4.

(Figure.4)

From the evolvement of the critical energy along with time as shown in figure 4, we can see the critical energy of runaway electrons is about 300keV before LHW was injected, and signal RA1 reflects there only existed little runaway electrons. After LHW is injected, the loop voltage will reduce and the effective charge number will increase, so the critical energy of runaway electrons

will increase rapidly. The higher the LHW power, the higher the critical energy. In this discharge, the critical energy of runaway electrons increased to 500keV after 100kW LHW was injected. As the power of LHW rose to 220kW, the critical energy of runaway electrons increased to more than 1MeV. The critical energy reduced back to 300keV after the LHW was turned off.

(Figure.5)

The energy of fast electrons driving by LHCD system in EAST tokamak is in the range of 50keV-60keV, and those fast electrons will accelerate by the loop voltage to get more energy. If the loop voltage is high enough or the time fast electrons being accelerated long enough, the energy of those fast electrons will get over the critical energy and run away. So those fast electrons can be a seed population of runaway electrons. During the LHCD phase, the evolvement of the energy of runaway electrons along with time in signal RA1 is shown in figure 5. We can see the signal increase step by step during 100kW LHW phase, 2.9s-3.2s. Most of the runaway electrons have energy about 500keV, and there have lots of runaway electrons whose energy were above 500keV. At this time, the critical energy for electrons to run away is about 500keV as can be seen in figure 4. So electrons with energy more than 500keV will run away. However, the loop voltage was low and the confinement time of runaway electrons wasn't long enough, so runaway electrons can't be accelerated to a very high energy. Most of them with energy about 500keV, and then they lost and leave the plasma and intersect the material limiter or the first wall.

When the power of the LHW increased from 100kW to 220kW, the signal RA1 reduced step by step form 3.2s to 3.5s. The loop voltage will reduce as the power of LHW increase. The critical energy of runaway electron increased rapidly to more than 1MeV as can be seen in figure 4. Here the loop voltage was only 0.15V, so electrons can't be accelerated to more than 1MeV. We can see from figure 5 that there nearly have no electrons with energy more than 1MeV before 220kW LHW was injected, so after the power of the LHW was increased to 220kW and the critical energy increased to more than 1MeV, there almost no electrons can get over the critical energy, and no more runaway electrons will be produced. Even for already existing runaway electrons, they will decelerate in this condition.

After the LHW was turned off, the loop voltage increased and the effective charge number reduced, and then the critical energy reduced back to 300keV. At this time, a great mount of electrons can get over the critical energy. Because there were so many fast electrons and the loop

voltage was high, the secondary generation mechanism of runaway electrons will dominate. As we can see in figure 3, the signal RA1 increased by exponential growth at this phase.

(Figure.6)

On the contrary, signal RA2, representing thick-target bremsstrahlung perpendicular to the limiter, give us a different trend as shown in figure 6. We can see in figure 6 signal RA2 rose to the most high point during the current ramp up phase, and it began to reduce as the current went to the flat top phase. When LHW was injected into plasma, signal RA2 reduce to lower region. The higher the LHW power, the lower the signal. After LHW was turned off, the signal also increased by exponential growth.

As we have mentioned, runaway electrons generated under the primary mechanism are accelerate mainly at the action of loop voltage, and there parallel momentum with respect to the magnetic field is much larger than the perpendicular momentum, $p_{\|} \gg p_{\perp}$ but as a result of the close collisions, the secondary electrons can have relatively large perpendicular momentum, $p_{\perp} \gg p_{\|}$. So signal RA2 can reflect the information of runaway electrons generated under the secondary mechanism. In the current ramp up phase, the secondary mechanism was easier to take place for high loop voltage and bad plasma confinement, and the signal RA2 will increase. In the current flat top phase, the secondary mechanism was suppressed for low loop voltage and good plasma confinement, and the signal RA2 will reduce. When LHW was injected into plasma, it will reduce the loop voltage, so the secondary mechanism will be suppressed further, and the signal RA2 will reduce further also. After LHW was turned off, the secondary mechanism will dominate the generation process of runaway electrons, the avalanche of the number of runaway electrons resulted in the exponential growth of signal RA2.

Compared figure 3 and figure 4, we can see the primary generation mechanism of runaway electrons can be enhance under low power LHW though the secondary mechanism can be suppress; and for high power LHW both this two mechanism can be suppress very well. It need be noted that after the LHW was turned off, runaway electrons will increase greatly. This phenomenon is not what we expect.

4. Conclusion

In conclusion, for low power LHW, lots of fast electrons were accelerated above the critical

energy (~500keV) by the loop voltage in discharge No 17590, and runaways were enhanced due to the primary mechanism. For high power LHW, the primary generation mechanism was suppressed as a result of the relatively high critical energy (~ 1MeV) in this discharge. No matter low power LHW or high power LHW, the secondary generation mechanism was suppressed very well. After LHW was turned off, however, both primary and secondary generation mechanism were enhanced.

Acknowledgments

This work is supported by the National Nature Science Foundation of China with a grant number 10935004. This work was partially supported by the JSPS-CAS Core-University program in the field of 'Plasma and Nuclear Fusion'. It's a pleasure for the author to thank EAST group for their supports to this work.

REFERENCES

[1] Gill R D. 1993, Nuclear Fusion, 33:1613

[2] Yoshino R, Kondoh T, Neyatani Y, et al. 1997, Plasma Physics and Controlled Fusion, 39:313

[3] Martin-Solis J R, Esposito B, Sa´nchez R, et al. 1999, Physics of Plasmas, 6:238

[4] Fisch N J. 1978, Physical Review Letters, 41:873

[5] Wesson J. Tokamaks. New York: Oxford university press Inc., Third edition, 2003, 258 - 290

[6] Jaspers R. Relativistic runaway electrons in tokamak plasmas, PhD thesis. Netherlands: Eindhoven University of Technology, 1995

[7] Besedin N T, Pankrotov I M, 1986, Nuclear Fusion, 26:807

[8]Parail V V, Pogutse O P, 1986, Reviews of Plasma Physics, 11

[9] Jayakumar R, Fieischmann H H, Zweben S J, 1993, Physics Letters A, 172:447

[10] Wu S T. 2006, An Overview of the EAST Project. Presented at the 24th Symposium on Fusion Technology (SOFT), No. PL2-O-146, Warsaw, Poland

[11] Gao X. 2007, Overview of Diagnostic System in the EAST Tokamak. Present at the 12th Conf. on High Temperature Plasma Diagnostics, Zvenigorod, Moscow region, Russia.

[12] Von Goeler S, Stevens J, Bernabel S, et al. 1985, Nuclear Fusion, 25:1515

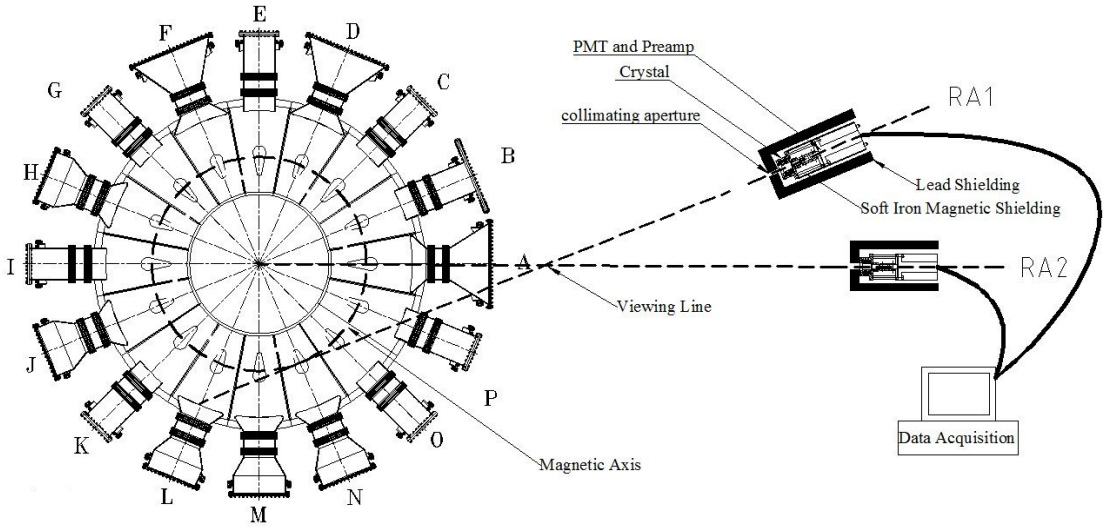

Figure.1: The schematic view of runaway diagnostic system on the EAST Tokamak

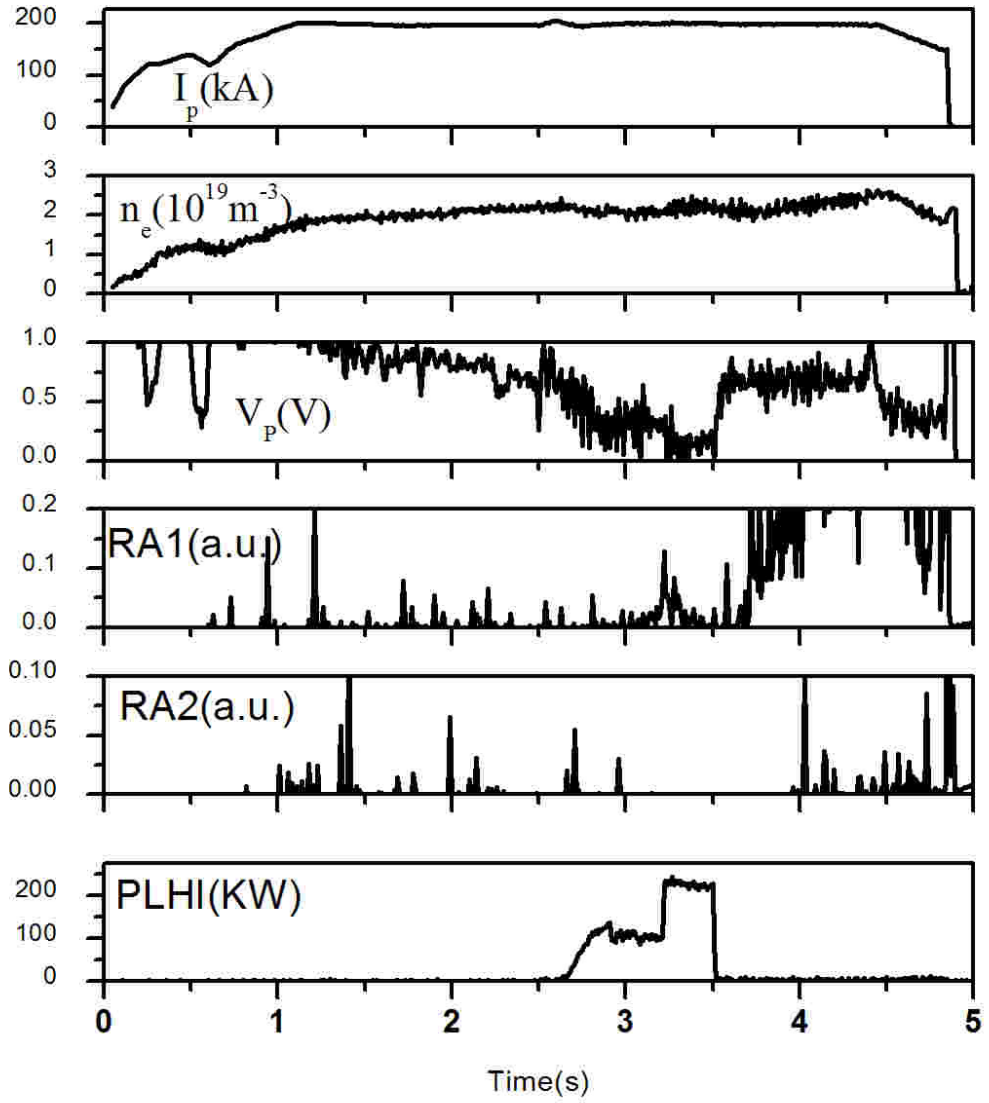

Figure.2: Waveforms of LHCD discharge No 17590. I_p is the plasma current, n_e is the centre line averaged density, V_p is the loop voltage, RA1 is the tangential thick-target bremsstrahlung caused by runaway electrons, RA2 is the perpendicular thick-target bremsstrahlung caused by runaway electrons, PLHI is the LHW power.

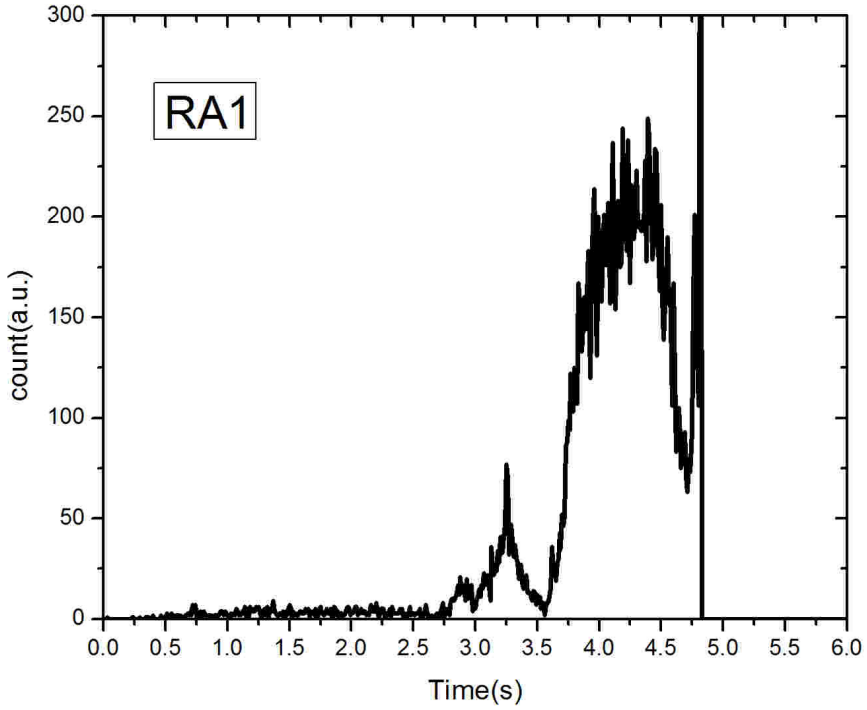

Figure.3: Count spectrum of signal RA1 for discharge No 17590

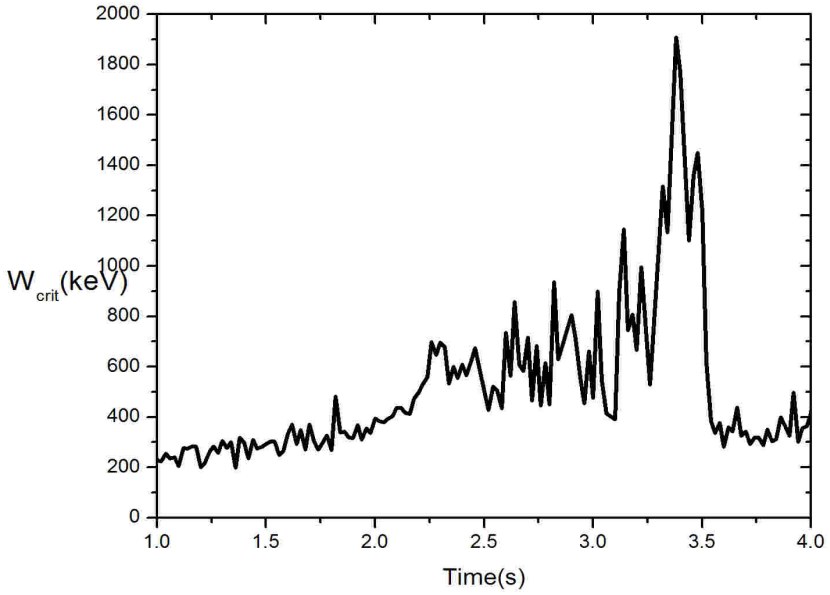

Figure.4: Evolvement of the critical energy of runaway electrons for discharge No 17590

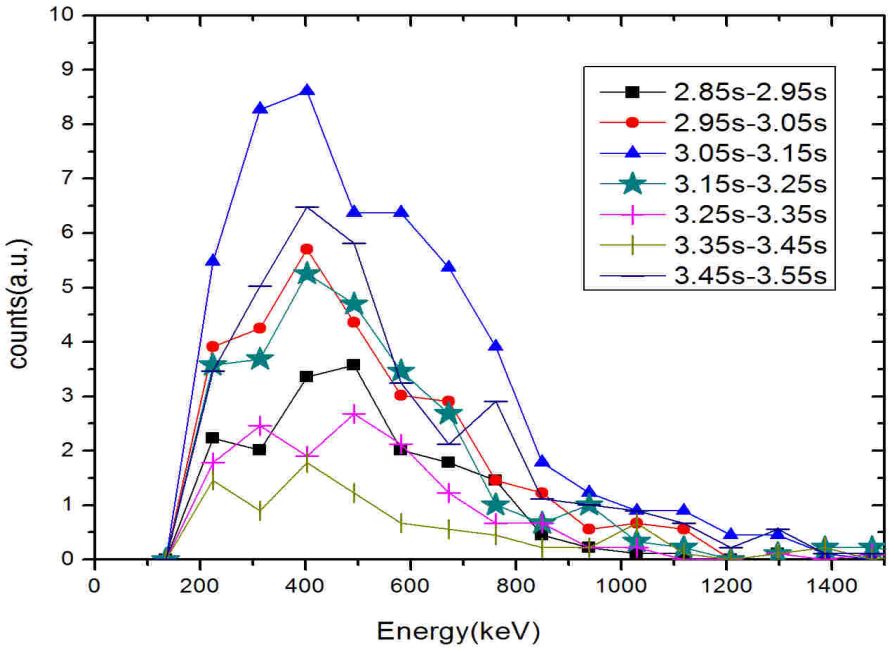

Figure.5: Evolvement of the energy of runaway electrons in signal RA1 from 2.85s to 3.55s

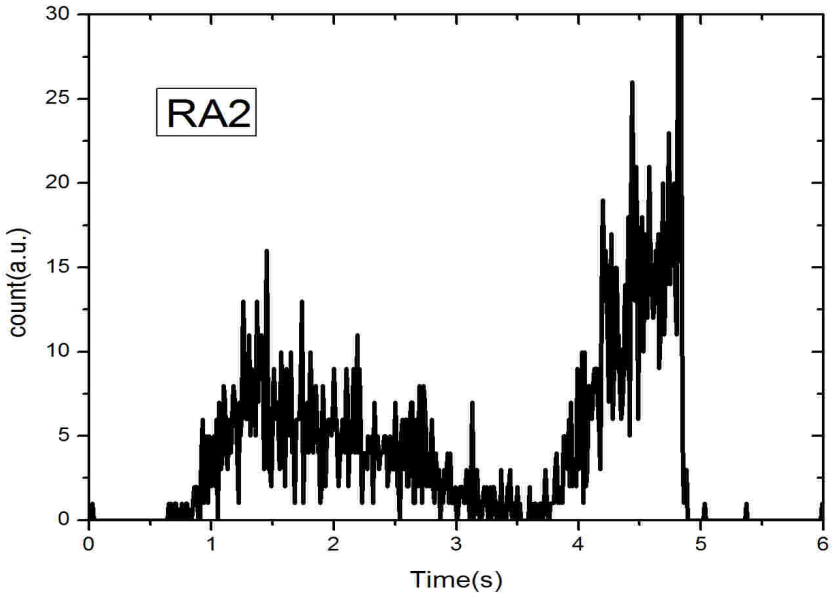

Figure.6: Count spectrum of signal RA2 for discharge No 17590

Development of the High-Throughput Transmission Grating Spectrograph for the TV Thomson Scattering Diagnostics on EAST Tokamak

Shinichiro KADO（門信一郎）Xiaoqi XI[1] (席晓琦) and Junyu ZHAO[1] (赵君煜)

School of Engineering, The University of Tokyo, Bunkyo, Tokyo, 113-8656, Japan
[1]Institute of Plasma Physics, Chinese Academy of Sciences (ASIPP), Hefei, China

High-throughput spectrograph employing the transmission grating was developed in order to apply to the laser Thomson scattering (LTS) system for EAST tokamak. Photographic lens 1.4 in F-number (F/#) for a collimator optics can collect all photons from the input optical fiber 0.3 in numerical aperture located on the optical axis. An F/1.2 camera optics enabled the complete collection over the visible diffracted component. We recognized that the optical arrangement using transmission grating gave rise to multiple reflection ghost (MRG) spectra, and formulated the principle of MRG. Then, the possible countermeasures against MRG were implemented. In order to reject the stray light at the laser wavelength of 532 nm, holographic notch filter was installed inside the spectrograph. The dispersion of the spectrograph was deduced and compared with that obtained from the He I line spectra measured for the helium glow discharge cleaning plasmas of the EAST tokamak.

1. Introduction

Laser Thomson scattering (LTS) has been regarded as a reliable electron temperature measurement, since it detects Maxwellian temperature of the velocity distribution function. LTS was developed in 1960s [1] and has been sophisticated as the laser and detector technologies improve.

Conventional system employs the high-power single-pulse ruby laser (694.3 nm) and photo-multiplier tube (PMT). Nowadays, the modern types of the LTS in the fusion research can be categorized into the following 3 schemes: YAG-LTS using repetitive Nd-YAG laser 1064 nm in wavelength and high-quantum efficiency avalanche photodiode (APD) detector [2], Television - Thomson Scattering (TVTS) detecting spatial profile using Television (i.e. CCD detector for the visible wavelength) usually combined with a gated image intensifier (I.I.) [3, 4], and LIDER (LIght Detection And Ranging) making use of time-of flight to yield spatial resolution [5].

The first author has been applied the TVTS using a frequency doubled visible (VIS) Nd-YAG laser (wavelength of 532 nm, the pulse energy of about 400 mJ, 10 Hz in repetition rate and 7 ns for pulse duration) aiming at the low temperature detached recombining plasmas in MAP-II (material and plasma) divertor simulator at the University of Tokyo [6-9]. Bright double monochromator (F-number is 2) equipped with a stray light rejection rod at the wavelength domain, called Rayleigh block, and data accumulation technique, achieved the measurement of low temperature plasmas below 0.1-eV [10-11].

Based on the experience in the MAP-II device, we designed the TVTS system on EAST (Experimental Advanced Superconducting Tokamak) device in Hefei, China [12]. Major and minor radii are 1.7 and 0.4 m, respectively. The target electron density in the EAST tokamak is typically in the same order as that of MAP-II [13], so that the similar scattered photon fraction can be expected. However, the electron temperature in the core region can be up to several keV and that of the edge plasma will be 50-100 eV. Therefore, we need the spectrograph that is designed to cover these temperature ranges.

In EAST tokamak, YAG-LTS system using fundamental frequency (1064 nm) has been developed for the purpose of high repetition diagnostics [14,15]. The TVTS, on the other hand, is regarded as the alternative diagnostics, sharing at least initially the same optics as the YAG-LTS system. Although the I.I. has no sensitivity in the fundamental frequency, its second harmonic frequency (532 nm) is usable. It

should be noted that the synchronized gating with the laser pulse of approximately 10 ns among 100 ms dead time (10 Hz) is indispensable to avoid strong background plasma radiation. The merit in using TVTS is the capability of measuring the velocity distribution function, while eliminating the effect of the line spectra, bremsstrahlung and blackbody radiation from the chamber wall. On the other hand, a primal demerit is the shortage of photons, because the power is reduced to about half at the second harmonic generator (SHG) crystal and the photon flux become further half at the SH frequency compared with that at the fundamental frequency with the same power. Moreover, the quantum efficiency of I.I. is considerably smaller than that of avalanche photo diode (APD) detectors.

In this paper, we thus developed a high-throughput spectrograph to collect as many photons as possible from high numerical aperture optical fiber in the entrance slit over the diameter of the I.I. at the exit port. In §2, we described the design of the spectrograph. The multi-reflection ghost (MRG) that is distinctively appears in the transmission grating system was investigated in § 3. The coupling optics between image intensifier (I.I.) and the electron multiplying charge-coupled device (EMCCD) detector was evaluated in §4. Experimental evaluation of the spectrograph was described in § 5 and the expected photon number transferred to the spectrograph was calculated in § 6. Finally we concluded our paper with summary and future prospects in § 7.

2. Optical designs of the spectrograph

2.1 Key parameters for the optical design of the TVTS system on EAST.

In designing the spectrograph, the following conditions were considered.

1) Frequency-doubled Nd:YAG laser with the wavelength of 532 nm is used.
2) Numerical aperture (NA) of the fiber is NA≥0.3.
3) Detector diameter is 25-26 mm
4) Optical fiber array with the core/clad diameters of 0.8/0.83 mm is used.
5) Detectable electron temperature T_e is 50 eV - several keV
6) Stray-light rejection technique, such as Rayleigh block or the notch filter.

Because the scattered spectra expands full visible range(T_e = 2 keV, 90º detection angle at 532 nm probe beam), low dispersion bright spectrograph is suitable.

2.2 Selection of the imaging optics for the spectrograph

In order to make full use of the solid angle of input fiber at the entrance slit, F-number or F/#, defined as $F = f / D$, where f and D denote the focal length and diameter of the lens, respectively, needed to be optimized. For example, for the system with standard quartz fiber with NA = 0.2 (F/2.45), F/2 optics had been sufficient, where $NA = \sin(\tan^{-1}(1/2F))$. Recently, however, higher NA such as 0.3 (F/1.59) for quartz fiber or 0.38 (F/1.22) for the polymer/plastic clad quartz core fiber has been available.

Because the size of the detector is 26 mm, the required reciprocal linear dispersion can roughly be evaluated to be (720-380)/26 ~ 13 nm/mm. Then, the possible candidate of the photographic lens and the groove frequency suitable to our specifications are listed in Table 1. Here, the reciprocal linear dispersion was calculated assuming the simple grating equation in which normal incidence and the detection plane normal to the diffracted light at 532 nm was adopted. Considering the collection of photons from the NA > 0.3 fiber, the system with f = 85 mm or with f = 50 mm lens is preferable.

Table 1 Candidates of the optical elements

f [mm]	g [gr/mm]	disp. [nm/mm]	available F/#
200	300	14.0	2.8
135	490	14.6	2-2.8
105	600	15.0	2
85	720	15.1	1.2 - 1.4
50	1200	12.8	1.2

In the imaging optics consisting of two lenses, such as collimator and camera optics in the spectrograph, the off-axis light introduced in the fiber having the finite slit height suffers a strong

Table 2. Example of the optical system evaluated in the present work. F number of the photographic lenses adopted for the collimator and camera optics were 1.4 and 1.2, respectively. The focal length for both lenses are 85 mm.

	Ref. Grating + notch filter box	Trans. Grating + notch filter box	Trans. Grating +built-in notch filter
0 mm(center)	100% (NA=0.3)	100%(NA=0.3)	100% (NA=0.3)
13.2 mm	0 % (44% at 5.8 mm)	43%	54 %
Notch system:	Box: 2 x *f*50 F/1.2	Box : 2 x *f*50 F/1.2) : Filter or Rayleigh block	inside the spectrograph

vignetting effect caused by the distant location between the collimator and camera optics inside the spectrograph. The minimal distance between lenses is determined by the physical interference between them.

First, we considered applying a conventional reflection grating, but with a photographic lens, which we have used in TVTS experiments of low temperature plasmas in MAP-II divertor simulator [6], and in a beam emission spectroscopy in LHD[16, 17]. However, we found that the use of the reflection grating would not meet abovementioned requirement.

Roughly speaking, when the distance between the lenses is equal to their focal length f, the ray introduced from the off-axis position at the height D/2 passing through the center of the first lens cannot enter the second lens. When the distance is $2f$, all rays from the height of $D/2$ having the F-number of f/D completely vignetted at the second lens.

The results of the ray-tracing calculation for several cases assuming the simple thin lens are shown in Table. 2.

When using the reflection grating, the minimum distance for the short focus lens, such as $f = 85$, is approximately 400 mm due to the geometrical interference. In this case, we found that it was impossible to transmit the fiber at the height corresponding to the detector radius of 13 mm.

It should be noted that the use of spherical or toroidal mirror is further difficult to achieve the low-F number spectrograph.

Therefore, we determined that we should evaluate the transmission grating with which the distance between the pair of lens can be minimized. The similar system has been applied to the plasma diagnostics such as TVTS [18] or the charge exchange recombination spectroscopy (CHARS) [19]. However, the spectrograph designed in the present works includes considerable number of improvement or optimization for our purpose.

In addition, if the notch filter or the Rayleigh block has to be located outside the spectrograph as in ref. [18], we need an additional imaging optics, which may also enhance the vignetting effect. Therefore, we designed the spectrograph such that the notch filter mechanism is equipped inside it. This built-in filter structure further improved the transmittance of the off-axis light entered at the 13.2 mm high at the entrance slit up to about 54 %. This fraction represents the situation where the all photons passing through the collimator optics can be delivered to the detector. However, the case of using external notch system with Rayleigh block can be still left as an optional candidate for the low-temperature detection system, such as divertor Thomson scattering, because the notch band of the notch filter is broader than that of the scattered spectra from the edge plasmas.

Figure 1 shows the schematic drawing of the designed optical arrangement. It should be noted that because the transmission grating of the groove frequency higher than 720 nm/mm is not commercially available at the moment, the system with $f = 50$ mm lens cannot apply. Therefore, we applied the photographic lens having the focal length f of 85 mm and F/1.4 for the collimator optics, whereas that with $f = 85$ and F/1.2 is adopted for a camera optics to collect dispersed photons at the grating. The use of F/1.2 lens for the camera optics enables the complete collection of visible photons from the on-axis (central) fiber with NA =0.3, even after the diffraction.

Eventually, the optical length between the collimator and camera optics can be reduced to 88.5 mm even allowing the space for several additional filters.

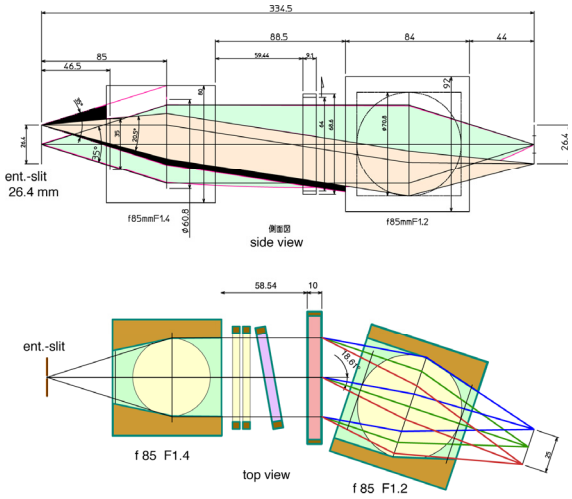

Fig.1. Finalized design of the spectrograph. (a) side view parallel to the slit, and (b) top view perpendicular to the slit.

2.3 Dispersion of the transmission grating spectrograph

Grating equation of the transmission grating with the grating constant d for the light of the wavelength λ having the finite incident angle α is written as,

$$d(\sin(\alpha)+\sin(\theta-\alpha)) = m\lambda \quad (1)$$

where, θ is the diffraction angle measured from the optical axis. α represents the rotation angle of the grating normal (GN) from the optical axis. The integer m denotes the diffraction order. It should be noted that the rotation of the grating would not affect the angle of the undiffracted ray, because θ = 0 for m = 0. In the same manner, even though α is changed, the modification of θ for the diffracted ray is negligibly small, although not zero.

The angular dispersion can be derived by taking derivative of the grating equation (1) with respect to θ as,

$$d\lambda/d\theta = (d/m)\cos(\theta-\alpha) . \quad (2)$$

Geometrical arrangement of the detection plane can be written as

$$f\tan(\theta) = x_0 , \quad (3)$$

where x_0 is the displacement at the image plane normal to the incident and zeroth order rays. However, because the image needs to be recorded on the x plane normal to the diffracted ray of interest, the distances on the x and x_0 planes are related by the equation, $\Delta x = \Delta x_0/\cos(\theta)$, which would usually be negligible for long-focal length monochromator [20].

From this equation, we have

$$dx/d\theta = (f/\cos^2(\theta))/\cos(\theta) = f/\cos(\theta) . \quad (4)$$

Therefore, the reciprocal linear dispersion at the x plane can be written as,

$$d\lambda/dx = (d/m)\cos(\theta-\alpha)\cos(\theta)/f \quad (5)$$

Furthermore, it is worthwhile to note that when θ = α, the Eq.(5) is reduced to

$$d\lambda/dx = (d/m)\cos(\theta)/f , \quad (6)$$

which is equal to the case of the normal incidence, α = 0 and detection at x_0 plane.

Theoretical prediction of the reciprocal linear dispersion on the plane normal to the diffracted ray for α = 22.52°, λ = 532 nm, m = 1, f = 85, yielded 15.0937 nm/mm.

2.4 Finalized design parameter

Finally, we applied the following basic design parameters.

i) f = 85 photographic lenses: F/1.4 for collimator and F/1.2 for camera optics.
ii) Transmission grating of the groove frequency 720 g/mm.
iii) Incident angle of 22.52° which corresponds to the 1st order diffracted light of 532 nm.
iv) Detection: normal to the 1st order diffracted light at 532 nm.
v) Stray light rejection: Holographic notch filter (Semrock NF03-532E-67-D) 17 nm in notch band width at 532 nm, 67 nm in diameter and 2 mm thick.

vi) Optional multi-notch-band filter (Semrock NF01-488/647-33.7-D) 33.7 mm in diameter and 3.5 mm thick to avoid contamination of strong H_α (D_α) and H_β(D_β) spectra between the entrance slit and the collimator optics.

vii) These optical filters can be replaced with dummy filter made of BK7 glass with the same thickness, in order to keep the same optical length.

The fiber diameter of 0.8 mm corresponds to 12 nm when $|d\lambda/dx|$=15 nm/mm which is the instrumental width for fully opened entrance slit. This width is equal to the scattered electron Doppler broadening in FWHM of 23 eV for orthogonal observation of the laser path.

Due to the notch filter v), the measureable lower temperature is limited to approximately 47 eV even without considering the slit width.

3. Multi-Reflection Ghost in the transmission grating system.

We have identified that a kind of ghost spectra appears. The principle is shown in Fig. 2.

The transmission grating produces the back-diffraction component apart from the normal diffractions as shown in Fig. 2. A part of the back-diffracted light is further reflected by the optical components in front of the grating. When the perfect/partial reflection occurs in the collimated section or at the image plane including the entrance slit of the spectrograph, then those lights trace the similar path to the main ray and are imaged on the detection plane. We thus termed it as multiple reflection or multi-refection ghost (MRG).

The equation of the MRG produced at the entrance slit is formulated as follows:

$$\sin\alpha+\sin(\theta_1-\alpha)=\lambda/d \quad (7)$$

$$\sin\alpha+\sin(\alpha-\psi)=m_1\lambda/d \quad (8)$$

$$\sin(\alpha-\psi)+\sin(\theta_2-\alpha)=m_2\lambda/d \quad (9)$$

By taking (7)+(8)-(9),

$$2\sin\alpha+\sin(\theta_1-\alpha)-\sin(\theta_2-\alpha)=(1+m_1-m_2)\lambda/2d=m'\lambda/2d . \quad (10)$$

At $\theta_1=\theta_2$, 1st order light and the ghost overlap, namely,

$$2\sin\alpha=m'\lambda/d \quad (11)$$

In order to examine this MRG model, we performed an experiment with a simple optical arrangement in the University of Tokyo. Photographic lens (Nikon *f*135 *F*/2.8, i.e. *D* = 48mm, NA=0.18) both for collimator and camera optics and a 600 grooves/mm (d=1.67 x 10^{-6} m) grating 50 x 50 mm^2 in dimension were adopted. Dispersed spectra were recorded using Nikon D90 digital camera in 8-bits JPEG format.

The angle at which the first order light coincides with the MRG was measured by rotating the grating mount. The results for H I (656.285 nm) and Hg I (546.073 nm) were shown in Fig. 3. The solid lines show the theoretical values of

$$\alpha=\sin^{-1}(m'\lambda/2d) \quad (12)$$

allowing m' be real.

As shown in Fig. 3, the predicted angles by the Eq. (12) with integer m' were reproduced by the experiment. The reason why the MRG appears slightly below the main diffraction image in the photo is

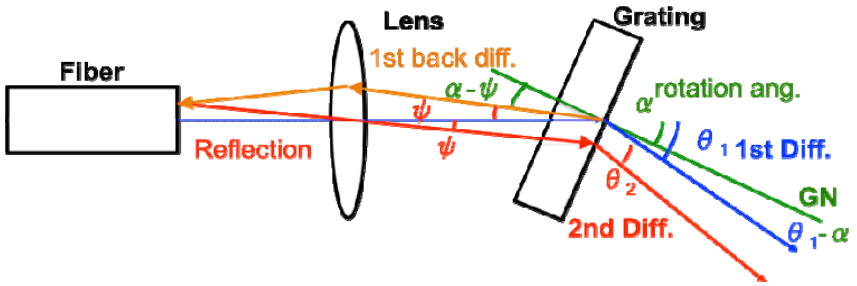

Fig.2. Principle of emerging multi-reflection ghost (MRG) in the transmission grating system.

(a) (b)

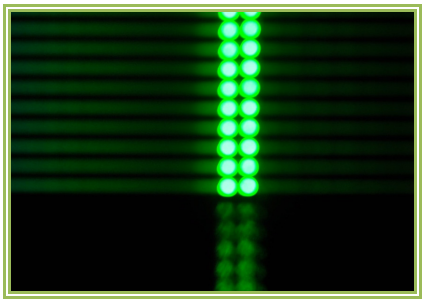

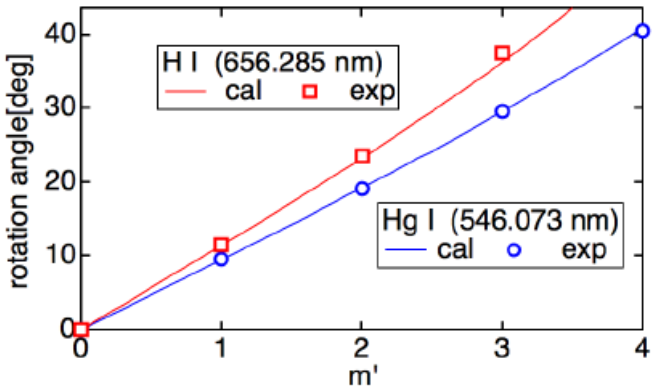

Fig.3. Experimental verification of MRG model. (a) MRG image for Hg I (546.0731nm) when the rotating angle satisfies eq. (11). (b) Comparison with the experiments.

that the grating and fiber surfaces were not perfectly parallel to each other. This fact may also support the effectiveness in the adoption of the inclinable grating in the actual spectrograph.

4. Coupling optics between I.I. at the exit slit and the CCD detector

We have chosen the following items as the detection hardware:

i) Image intensifier (I.I.) - Photek MCP125
- 25mm in effective diameter.
- Bialkali photocathode (single)
- Gate range 25 ns - 89 μs

ii) EMCCD: ANDOR IXON 885 CAMERA
Active Pixels: 1004 x 1002
Pixel Size (WxH) 8 x 8 μm
Image Area: 8 x 8 mm

In order to couple the aperture of the I.I. 25 mm in diameter with the CCD area 8 mm in dimension, the magnification M = 1/3 is required.

For this purpose, we proposed the following optics:

iii) 30 mm F/1.4 lens (Sigma; adaptable for APS-C size 23.4×16.7mm^2, Nikon mount).

iv) Macro adapter ring 8 mm in thickness (Nikon, PK-11A; with this combination, aperture should be opened mechanically) [21].

The shortest focal distance for this lens is 0.4 m. Therefore, the macro adapter ring is necessary to image with 1/3 magnifications. We tried several types of products and found that the ring of 8 mm high can achieve the requirements.

The author proposes a practical evaluation using scales. The image data can be processed separately by Red, Green, and Blue layer. Followings are the example of the criteria that can be deduced from this scheme.

a) Brightness and vignetting effect appear in the intensity of the data in the pixel areas photographing the white object, such as the white paper illuminated by the fluorescent lamp.

b) Black scales correspond to the dips of the one-dimensional contrast. Therefore, defocused area can be identified by the shallower dip.

c) Monochromatic aberrations can be detected by the asymmetry of the dips.

d) Chromatic aberration can be appeared qualitatively as the difference in RGB distribution.

e) Resolution can be evaluated by the ratio of the width of the dip to the pitch between the dips.

Figure 4 shows the images of the scale recorded using Nikon digital camera D90. DX(APS-C) CMOS detector of 4288x2848 pixels having 23.6 x 15.8 mm^2 in dimension is used. Figures 4(a) and (b) are those for the focal length set to infinity and 0.4 m, respectively. The area corresponding to the present Andor CCD, 8x8 mm^2, is indicated by the squire. A slight distortion in the outer area can be observed. However, inside the 8x8 mm^2 rectangle, the distortion is negligible.

As one can see, field of view can be adjusted between 22 and 31 mm (M = 2.750 - 3.875). In order to further suit the magnification rages, approximately M = 2.500 - 3.125 (field of view of 20 - 25 mm, we are now considering to attach a close-up lens, such as the Kenko No.1 which is convex lens of f = 1000 mm, designed to screw in on the front end of the camera lens, just like filters [22],

Figure 5 shows the numerical data for the horizontal cross section about the scale position of Fig. 4 (a).

In the field of optical instruments, Modulation Transfer Function (MTF) chart is used to evaluate the spatial resolution of the optics. However, the chart which covers all the field of view is not available all the time, all the places. Moreover in the practical application for a given lens, the criteria of the usability would be ambiguous.

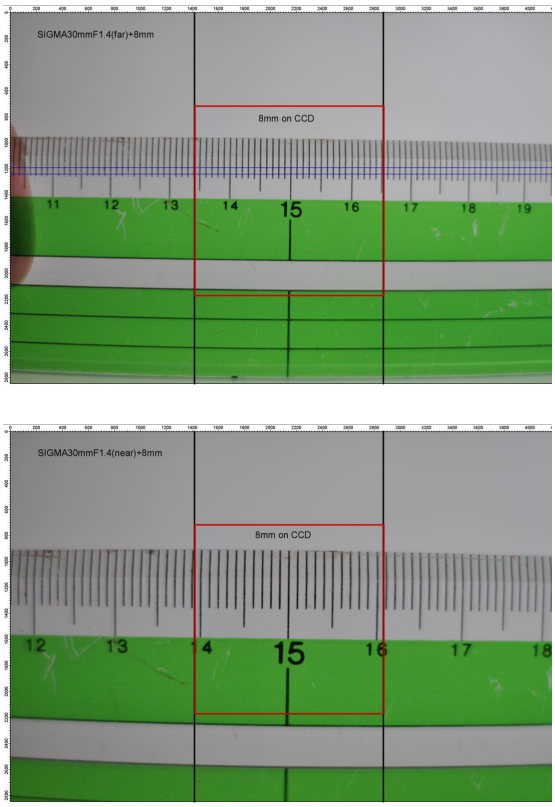

Fig.4. Scale image of the alternative system with f30mm F/1.4 and 8 mm ring. (a) focus to infinite (b) to 0.4 m (minimal).

One can see in Fig. 5 that both the focus and aberration seems good. The difference between the layers for R, G, and B colors were not observed. Even though the phosphor screen emits monochromatic light, the chromatic aberration of the optics can modify the focus when one adjust the focus under the room light.

We measured the phosphor screen of I.I. 26 mm in diameter by the EM-CCD with the pixel size of 8 μm and confirm that, in the present setting on November 2010, the image of the phosphor corresponded to 1030 pixels, namely, the magnification 26 / (1030 x 0.008) = 3.15534.

5. Property of the High-throughput Spectrograph

In the actual situation, the MRG can occur at every optical component though the refection could be a small part of the incident light.

There are several ways to mitigate the disturbance caused by the MRG. Firstly, if a strong component crucially superposes the emission line of interest with small intensity, the location of MRG at the wavelength spectra can be shifted by rotating the grating in the dispersion direction, unless m' = 0. Secondly, MRG can be shifted to the slit direction

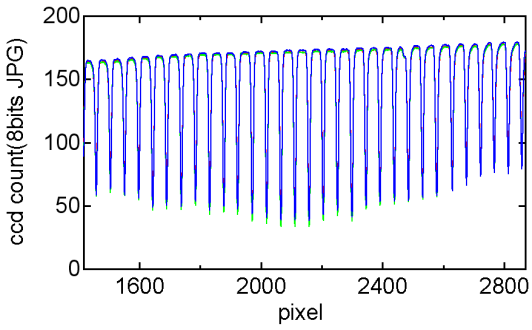

Fig. 5 Numerical data at the position of the scale in the jpeg picture for Fig. 4(a).

by inclining the grating towards perpendicular to the dispersion direction.

As mentioned above, the reflection at the surface of the input fiber array produces the brightest MRG because of the mirror-like perfect reflection, the inside surface of the entrance slit of the spectrograph was blackened. Our spectrograph in the present work adopts these functions.

Figure 6 shows the MRGs observed by intentionally inputting the strong light at 532 nm close to the saturation level of the 16-bits CCD detector (ANDOR Newton 26 μm/pixel, 1024 x 512 pixels). The many of these were identified which optical component can produce them. However, the intensity of most of the MRG due to the partial reflectance was approximately at most 1/1600 of the 1st order light. This might not cause serious effect in the analysis, even without using the inclined grating.

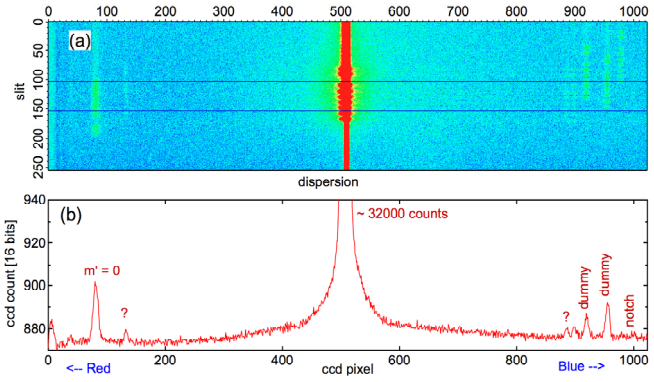

Fig.6. Weak MRGs observed in the developed spectrograph. (a) Images measured for α = 16º, fiber core diameter of 250 μm. (b) Profiles of the averaged over 50 pixels in the slit direction.

The reciprocal linear dispersion can be determined experimentally by the line spectra. We used the He glow discharge cleaning plasma in EAST vacuum chamber (7/Nov./2010) and measure He I spectra using the system for the EAST TVTS, as shown in Fig. 7. Slit width was set to 200 μm to increase the wavelength resolution and obtain the peak of the line spectra. Note that for the LTS diagnostics, slit width corresponds to full fiber diameter of 800 μm to increase the photon counts.

From the correspondence between the pixel number and the wavelength, we determined the scaling equation of the spectrograph as

$$\lambda = c_0+c_1p+c_2p^2 \qquad (13)$$

where $\{c_0, c_1, c_2\} = \{751.11, -0.38744, -3.0771\text{x}10^{-6}\}$ with p as the pixel number of the EMCCD.

Therefore, the reciprocal linear dispersion was determined experimentally as

$$|d\lambda/dp| = c_1+2c_2p \sim 0.38744 \text{ nm/pix.} \qquad (14)$$

Because $dx/dp = 8$ μm, we have $|d\lambda/dx| = 48.43$ nm/mm. Furthermore, considering the magnification of the coupling optics between I.I. and EMCCD of 3.155, the measured reciprocal linear dispersion of the spectrograph is 15.35 nm/mm (accuracy is approximately 1.6 % compared with the theoretical calculation). Instrumental width, measured when the slit width is narrowed to 200μm, is 6.57 nm (FWHM) , which corresponds to 3.9 eV electron Thomson scattering spectra for 90 degree detection angle. Considering the notch band with of 47 eV electron temperature, practical lowest detectable temperature when the photon number is sufficient is about 50 eV.

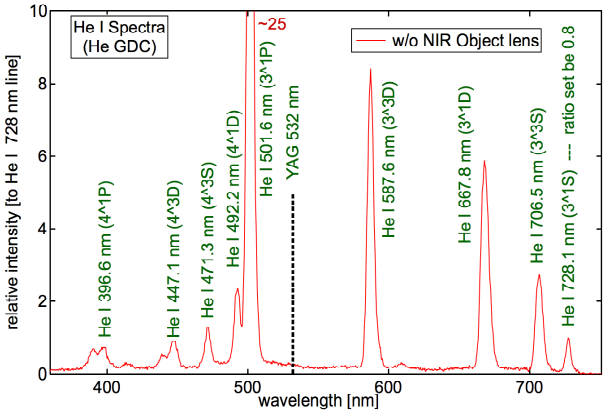

Fig.7. Visible He I spectra observed for He GDC plasma of EAST. Slit width was set to 200 μm. Data was obtained without notch filter and object lens. Intensity was not calibrated, therefore the unit was [relative CCD count] normalized to the peak value of the 728.1 nm line spectrum.

6. Evaluation of the photon number in EAST tokamak.

Generally speaking, in the TVTS system, collecting photons requires huge number of optical fibers and the optical arrangement to make full use of them need quite complicated configuration [23]. However, the present system configuration is rather simple and straightforward evaluation can apply.

The photon number per pulse scattered in the detection solid angle dΩ can be evaluated, for the polarization yielding the maximum intensity and for 90 degree detection, as

$$\Delta N_{photon} = r_e^{\,2}[I_{in} A \Delta t] n_e L d\Omega / h\nu, \tag{15}$$

with the electron classical radius,

$$r_e = \frac{e^2}{4\pi\varepsilon_0 m_e c^2} = 2.82 \times 10^{-15} m, \tag{16}$$

where, n_e is the electron density in m^{-3}, I_{in} is the probe laser intensity in W/m^2, A and L are the cross section of the beam and the interaction length in m, respectively, yielding scattering volume of AL. When the spot size of the viewing chord is smaller than A, the collection efficiency is degraded. Therefore, the ideal case demands the focusing of the laser at the center of the observing area. Δt is the pulse length of the laser. Therefore, square bracket [] denotes the pulse energy in J/pulse.

For the solid angle $d\Omega$ much smaller than hemisphere can be interpreted using the optical parameters of the F number and magnification M (= images at fiber / at plasma) as

$$d\Omega = \frac{\pi}{4} \frac{1}{F^2 (1+1/M)^2} = \frac{\pi}{4} \frac{1}{F_{eff}^{\,2}} = \pi (NA)^2, \tag{17}$$

where F_{eff} is the effective F- number of the imaging optics: $F_{eff} = F$ for collimated input (object at the infinite distance) and = $2F$ for 1 to 1 magnification. NA denotes the numerical aperture of the object side. Namely, brightness is proportional to the square of NA for the small detection solid angle.

For example, 3 J/pulse 532 nm laser (frequency doubled Nd:YAG Laser), $n_e = 10^{19}$ m^{-3} plasma, L = 3.2 mm and M = 0.25 (namely fiber 0.8 mm in core diameter) collected by NA=0.38 fiber yield about 48000 photons, which can be collected per pulse. These photons are further lost through the spectrograph and detector by about one order of magnitude.

Usually, dΩ is limited by the NA of the fiber, when the diameter of the object lens is sufficiently large. To maximize this performance or the current system, the object lens with the diameter of larger than F/1.4, 180 mm for f = 250 plus height corresponding to the fiber channel is required. The fiber channel can be summed up to 3 channels within the desirable spatial resolution of 10 mm along the laser path in the plasma and the repetition of the laser may enhance the signal to noise ratio. It is also possible to bin the pixels along the wavelength direction. In this procedure it is possible to remove the line spectra unless it is too large to saturate the well of the CCD.

7. Summary and Future plans

We have developed the f = 85 mm, F/1.4 spectrograph for the visible TVTS system on EAST tokamak. By employing transmission grating, the distance between the collimator and camera optics was achieved to be shorter than the case using conventional reflection grating. As a result, the vignetting effect of the off-axis light was mitigated to a considerable extent. Notch filter to reject stray light at the probing laser wavelength of 532 nm can be located between the imaging optics inside the spectrograph.

MRG caused by the transmission grating system was identified and the formula to describe MRG due to the reflection at the input fiber was derived. For a practical application, several functions to avoid MRG were prepared. Then, the MRG was found to be sufficiently small in the actual situation.

The reciprocal linear dispersion was determined from the He I spectra during the He glow discharge cleaning of the EAST chamber wall.

Finally the photon flux expected to transmit to the spectrograph was evaluated.

At present the application of the spectrograph to the EAST device is ongoing. This spectrograph is useful as the low-dispersion visible spectrograph even without laser. We measured the EAST discharge

with lithium droplet conducted on 8-9 /Nov. /2010, and identified the very bright signal of atomic and singly ionized lithium, Li I ($1s^2 2s\ ^2S$ - $1s^2 2p\ ^2P$; 670.8 nm) and Li II ($1s2s\ ^3S$ - $1s2p\ ^3P$; 548.5 nm), respectively. These lines were sometimes brighter than D_α line, which drew further attention/caution in the application of SHG for the LTS diagnostics. In the present situation, we use the object lens with near-infrared (NIR) coating, which is designed for the YAG-TS at 1064 nm. Due to this coating, the transmittance of the visible line especially below 550 nm has degraded to a great extent. We confirmed it by measuring GDC using the lens and compare with the result without the object lens. Therefore, we need to replace the object lens with a proper one in the future.

Acknowledgements

We acknowledge Bingjia Xiao in ASIPP for the help in launching and organizing this collaboration. We acknowledge Yohei Iida in the University of Tokyo for providing a ray-tracing code. We acknowledge Mizuki Okada for the test-stand experiments on MRG. We also acknowledge Keita Kamiyama at Bunko-Keiki co. for the discussion about the optical arrangement of the spectrograph. This work was supported partially by the Dean of significant funds of the Hefei Institute of Physical Science of Chinese Academy of Sciences No. O75FD46131, and partially by the JSPS-CAS Core-University program in the field of 'Plasma and Nuclear Fusion'.

References

[1] N.J. Peacock, D.C. Robinson, M.J. Forrest, P. Wilcockand V.V. Sannikov, Nature **224**, 448 (1968)
[2] H. Rohr, K.-H. Steuer, G. Schramm, K. Hirsch, H. Salzmann, Nucl. Fusion, **22**, 1099 (1982).
[3] N. Bretz, D. Dimock, V. Foote, D. Johnson, D. Long, and E. Tolnas, Appl. Opt. **17**, 192 (1978).
[4] D. Johnson, D. Dimock, B. Grek, D. Long, D. McNiell, R. Palladino, R. Robinson and E. Tolnas, Rev. Sci. Instrum. **56**, 1015 (1985).
[5] H. Salzmann, K. Hirsch, P. Nielsen, C. Gowers, Gadd, M. Gadeburg, H. Murmann and A. Schrodter, Nucl. Fusion, **27**, 1925 (1987).
[6] A. Okamoto, S. Kado, S. Kajita and S. Tanaka, Rev. Sci. Instrum. **76** (2005) 116106.
[7] F. Scotti, S. Kado, A. Okamoto, T. Shikama and S. Tanaka, Plasma Fusion Res. 1, **54-56** (2006).
[8] F. Scotti, S. Kado, A. Okamoto, T. Shikama, Y. Kuwahara, K. Kurihara, K-S. Chung and S. Tanaka, Plasma Fusion Res. **2**, S1110(2007).
[9] S. Kado and F. Scotti, Proc. 13th International Symposium on Laser-Aided Plasma Diagnostics, Takayama, Japan, 2007. (NIFS-PROC-68, ISSN 0915-6348), General Talk 3.
[10] Flippo Scotti and Shinichiro Kado, J. Nucl. Matter. **390-391**, 303-306 (2009).
[11] F. Scotti, master thesis dissertation, the University of Tokyo (2007).
[12] X. Gao and the EAST team, Physics Letters A **372**, 2286-2290(2008).
[13] S. Kado, Y. Iida, S. Kajita *et al*., J. Plasma Fusion Res. **81** (2005) 810.
[14] Yang Li , Wan Baonian , Zhao Junyu , Hu Qingsheng , Jia Yanqing , Xi Xiaoqi , Han Xiaofeng and Zang Qing , Plasma Sci. Technol. **12** 284, (2010)
[15] Zang Qing , Zhao Junyu , Yang Li , Hu Qingsheng , Jia Yanqing , Zhang Tao , Xi Xiaoqi , S. H. Bhatti and Gao Xiang, Plasma Sci. Technol. **12** 144 (2010)
[16] S. Kado, T. Oishi, M. Yoshinuma and K. Ida, Rev. Sci. Instrum. **81**, 10D720 (2010).
[17] T. Oishi, S. Kado, K. Ida, M. Yoshinuma, H. Nakano and K. Yamazaki , Rev. Sci. Instrum. **81**, 10D719 (2010).
[18] T. Munsat and B. LeBlanc, Rev. Sci. Instrum. **70**, 775 (1999).
[19] Ronald E. Bell, Rev. Sci. Instrum. **75**, 4158 (2004).
[20] S. Kado, J. Plasma Fusion Res. **83**, 176 (2007). [in Japanese]
[21] http://www.nikon-image.com/jpn/products/lens/accessory/close-up/ring.htm
[22] http://www.kenko-tokina.co.jp/imaging/eq/mc123.html [in Japanese]
[23] H. J. van der Meiden, S. K. Varshney, C. J. Barth, et al., Rev. Sci. Instrum. **77**, 10E512 (2006).

Optical design of TV Thomson scattering on EAST Tokomak

Xiaoqi Xi[1], Junyu Zhao[1], S. Kado[2], Xiang Gao[1], Qing Zang[1], Qingsheng Hu, Xiaofeng Han[1], Xingxing Dai[1], Jianhua Yang[1], Mengting Li[1], Ling Zhang[1]

[1]Institute of Plasma Physics, Chinese Academy of Science, China

[2]School of Engineering, the University of Tokyo, Japan

Email: xixq@ipp.ac.cn

Abstract A TV Thomson scattering system has been designed and built on EAST tokamak. It incorporates a second-harmonic(532nm) Nd:YAG laser, a transmission grating spectrometer instead of a conventional one, and a detector based on an second generation image intensifier combined with an electron multiplying charge coupled device(EMCCD), which provides a short exposure time for background light reduction as well as optimum signal to noise ratio(SNR). It is designed to measure electron temperatures between 100eV and 5keV at 10 spatial points with ~10mm resolution while the fiber used allows a resolution down to 3.3mm and spatial points up to 90. The magnification and f number of the collection lens, the diameter and numerical aperture of the fiber, the entrance and exit slit area and f number of the spectrometer are designed interactively to maximize light throughput, with also beam quality taken into account. We measured the conversion factor (counts/photon) of the detection branch from the fiber to the EMCCD using a standard lamp, while both spatial and spectral binning was performed. From the comparison between the input radiation photons and the estimated scattering photons with EM gain applied, the system detection capability for $n_e = 2\times10^{19}\ m^{-3}$ was verified.

Key words: TV Thomson scattering, etendue, image intensifier, EMCCD

1 Introduction

TV Thomson scattering system, which gains the name from the television-like detectors placed after a spectrometer for receiving an two-dimensional image, is originally developed in 1967 on PLT as a relatively simple setup to perform the

spatial-resolution-oriented electron temperature and density measurements for the observation of confinement-related structures, while the study of dynamics of these structures is also realized in 2006 on TEXTOR due to a high temprol resolution. In this article, the design considerations, the system setup, and the detection capability verification of the recently built TV Thomson scattering system on EAST is discussed.

2 Optical design considerations

In general, the characteristic of weak scattering of radiation is the most concern in the design of a TS system. However, in TV Thomson scattering system on EAST, a laser operating at second-harmonic is used for the present operation, which gives only 1/4 of photons at the fundamental wavelength. Therefore, it's more necessary in the optical design to avoid further loss of the amount of radiant power transferred from the source to the detector.

After the laser beam being focused into the plasma, the following optical elements are often involved to deal with the scattering signal: collection lens for imaging scattering beam onto fiber, delivery fiber bundle, slit and optics in the spectrometer. Change of the image can be schematically seen in Fig.1. Basically, the aim of those designed optics is: to match a long narrow image onto a circular photocathode after dispersed by the spectrometer, while maximizing the light collected and maintaining the acceptable image quality.

Before getting started with the optical design, it's necessary to be aware of the design limits: length from the laser beam in plasma to the window of the collection port is ~1200mm (object length); available diameter for the collection lens is ~500mm; available numerical aperture (NA) of fiber <0.39; available diameter of the image intensifier is ~25mm, and also to take cost into account.

The first process is shown in Fig.2. Scattering photon flux collected by collection lens is proportional to the collection solid angle Ω, which is approximately given by

$$\Omega \approx S/L_o^2$$

when tan Ω ~ sin Ω ~ (radians), where L_o is the object length and f, S is the focal length and the area of the collection lens, respectively. It is almost determined by the space limits mentioned before, so does the collected photons.

Etendue characterizes the ability of an optical system to accept light. It's a function of the area of the emitting source and the collection solid angle:

$$G \approx S_o \Omega_o$$

and it's the same for the source and the image

$$G \approx S_o \Omega_o = S_i \Omega_i$$

When working with fiber optics

$$G \approx \pi S_i (NA)^2$$

Therefore, G of the scattering source is also determined.

In the second fiber collection process:

First, G of the fiber and lens needs to be matched:

$$\pi S_i (NA)^2 = S_i \Omega_i = S_o \Omega_o$$

Then, in order to use less fiber for collecting the same scattering area, which will further enlarge the scattering length one spectrometer can measure, fiber with larger NA needs to be applied, as shown in Fig.3.

Once the NA is chosen, the area of the fiber is also determined. At the same time, focal length of the lens f is also determined.

The design principle is similarly when in the third process.

3 System setup

Laser and injection optics

Due to the relatively low quantum efficiency of CCD detectors in near infrared region and also to make full use of the existing laser source, we employ the Nd:YAG laser operating at second harmonic (532nm,2.3J,1Hz/10Hz,0.5mrad), which is currently in use in 25channel Thomson scattering system operating at the fundamental wavelength of 1064nm. Transmission mirrors are highly reflective at

both wavelengths with a damage threshold above the laser energy density.

Collection lens

In the initial operation of ~100mm scattering length along the laser beam, a single lens will be used for evaluation. The f number is f/8 with a magnification of ~0.25.

Fiber bundle

The NA and core/clad ratio of the fiber bundle are 0.39 and 0.8/0.83mm, respectively, which matches both the collection lens and the scattering width of ~3.5mm in plasma and allows the spatial resolution down to one fiber of scattering length of ~3.3mm.

The configuration of fiber bundle is designed to change conveniently the measuring position for now and reserve for the further development. Two independent parts are connected with SMA connectors. For the input side, there are 90 fibers and 10 alignment fibers with a length of 15m. For the output side, there are 30 fibers for one spectrometer with a length of 3m. All fibers are buffer stripped for higher spatial resolution. Fibers could be binned in the software of the detector to get more signals at the cost of decrease of spatial resolution.

Alignment fibers, as shown in Fig.4, together with the motorized target, monitor and motorized fiber holder, is designed to avoid the optical misalignment.

Spectrometer

A high throughput transmission grating spectrometer which matches both the 30 fibers and the detector to collect as more as light will be used for spectral analysis, providing enough spectral resolution and good stray light and background light reduction with fine notch filters.

Detector

The detector system is based on a second generation image intensifier of 25mm diameter combined with an EMCCD of 8×8mm of image area, which provides a short exposure time for background light reduction as well as an optimum SNR

when the signal is lower than the readout noise. And they are coupled with a camera lens to obtain better image quality and for the convenience of changing CCD or image intensifier to improve the SNR .The frame rate of the EMCCD is 31.5 frames per second and can increase to at least 185 when binning is performed. Gain and gate are remotely controlled by adjusting the voltage and the gate width of a pulse/delay generator, respectively.

4 Detection capability verification

Before the design parameters of all the system parts are determined, number of detected photoelectrons per scattering length per 10^{19} of plasma density is repeatedly compared with TV Thomson scattering on TEXTOR, to make sure the detector are sensitive enough.

To identify the required photon detection capability, firstly, we evaluate the Thomson scattering photons per pulse per scattering length based on the designed parameters above before the spectrometer, as shown in Fig.5. And the calculation shows that the number of the incoming photons to the collection optics is approximately 200 /nm.

Then, a standard lamp (Deuterium and tungsten halogen lamp)is connected at the collection fiber, in order to compare under the actual measurement condition, we assumed the exposure time of 20ns and 0.8mm diameter fiber as shown in Fig.6. and the incoming photons to the detection fiber are approximately 200 /nm. So this situation is similar to that in the scattered photons per shot. This figure can be used to evaluate the criteria of the detection limit. If one detects the signal of the standard lamp, then one can detect the TS signal for a single shot. Initial results show that TS signal is detectable by the current optics by binning the pixels corresponding to one fiber diameter in the spatial direction.

5 Preparation

Before operation during the discharge, some work has been done to ensure the system is well prepared for the experiment: the gate of image intensifier and that

of the EMCCD is synchronized with a pulse/delay generator. The TS signal pulse and the acquisition pulse is synchronized. Plasma background has been measured first, with gate of about 40ns and all amplifying methods that might be used applied. And the result shows that the background signal is far lower than the dynamic range.

6 Summary

It is designed to measure electron temperatures between 100eV and 5keV at 10 spatial points with ~10mm resolution while the fiber used allows a resolution down to 3.3mm and spatial points up to 90. We are planning to perform the experiment in this campaign, with a single collection lens to check the signal intensity. If the photons are not enough, the accumulation techniques may improve the SNR.

ACKNOWLEDGMENTS

The authors would like to appreciate A. J. H. Donné and H. J. van der Meiden (FOM-Institute for Plasma Physics Rijnhuizen) , C. L. Hsieh (General Atomics) for useful suggestions and Bingjia Xiao (Institute of Plasma Physics) for organizing and launching the collaboration.

This work was funded by the National Nature Science Foundation with Contract Nos. 10675126 and 10375068. This work was partially supported by the JSPS-CAS Core-University program in the field of'Plasma and Nuclear Fusion'.

[1]S. Kado, F. Scotti, X. Xi and J. Zhao, Proc. JSPS-CAS Core University Program Seminar, 4-7 Nov.2008, Lijiang, China, NIFS-PROC-77 pp.221-225(2009)

[2]N. Bretz, D. Dimock, V. Foote, D. Johnson, D. Long, and E. Tolnas, Appl. Opt. 17, 192 (1978)

[3]R. Scannell, M. J. Walsh, P. G. Carolan, et al, Rev. Sci. Instrum. 79, 10E730(2008)

[4]C. J. Barth et al., Rev. Sci. Instrum. 72, 1138 (2001)

[5]H. J. van der Meidan, R. S. Al, C. J. Barth, et al, Rev. Sci. Instrum. 79, 013515, (2008)

[6]H. J. van der Meiden, S. K. Varshney, C. J. Barth, et al, Rev. Sci. Instrum. 77,

10E512 (2006)
[7] J. Sheffield, Plasma Scattering of Electromagnetic Radiation (Academic, New York, 1975)
[8]M. J. Walsh, E. R. Arends, P. G. Carolan, et al, Rev. Sci. Instrum. 74, 1663(2003)
[9] M. Walsh, N. J. Conway, M. Dunstan, et al, Rev. Sci. Instrum. 70, 742 (1999)
[10]D. Johnson et al., Rev. Sci. Instrum. 57, 1810 (1986)
[11]M. Yu. Kantor, C. J. Barth, D. V. Kouprienko, and H. J. van der Meiden, Rev. Sci. Instrum. 72, 1159 (2001)
[12] D. W. Johnson et al., Rev. Sci. Instrum. 72, 1129 (200l)
[13] M. N. A. Beurskens et al., Rev. Sci. Instrum. 68, 721 (1997)

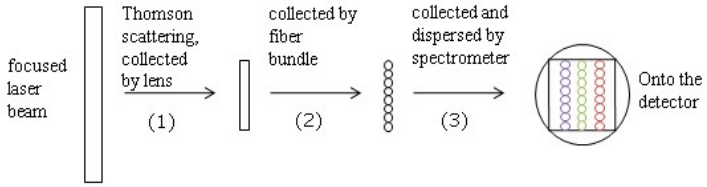

Fig. 1. Change of the light signal from the source to the detector. There are three main design process: (1) scattering photon collection; (2) fiber collection; (3) spectrometer collection and delivery.

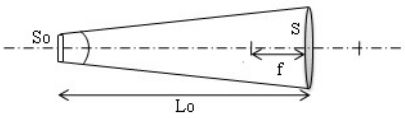

Fig. 2. Scattering signal is collected by a collection lens. S_o represents the area of the scattering source.

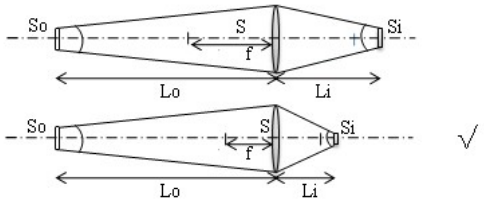

Fig. 3. Fiber collection process.

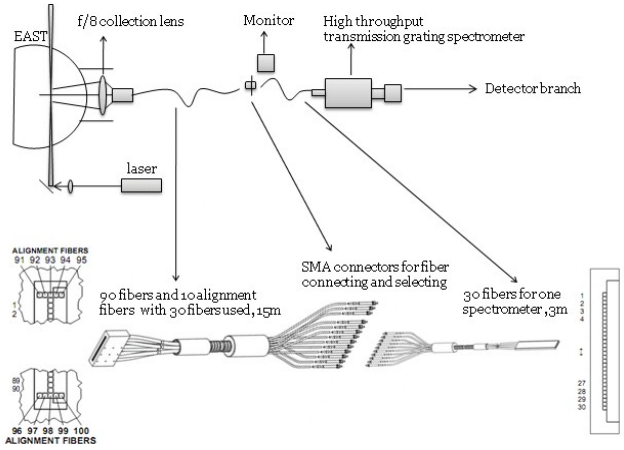

Fig. 4. System setup overview.

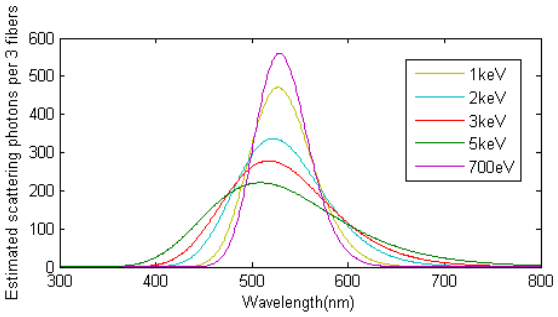

Fig. 5. Estimated scattering photons at different electron temperatures per 3 fibers.

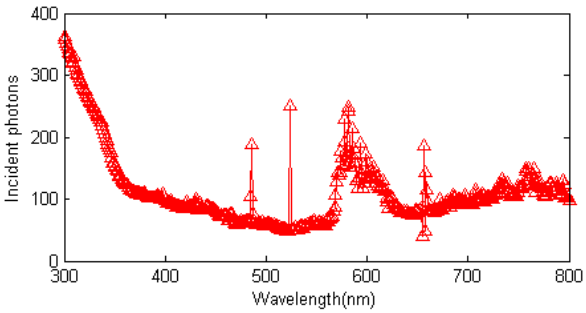

Fig. 6. Input photons of the standard lamp with reasonable counts in the detector.

Measurement of the electron Bernstein wave emission with one of the power transmission lines for ECH in LHD

IGAMI Hiroe[1], IDEI Hiroshi[2], KUBO Shin[1], YOSHIMURA Yasuo[1], SHIMOZUMA Takashi[1] and TAKAHASHI Hiromi[1],

[1]National Institute for Fusion Science. 509-5292, Toki, Japan

[2] Research Institute for Applied Mechanics, Kyushu Univ., 816-8580, Kasuga, Japan

Abstract

Possibility of the measurement of radiated waves derived from the thermally emitted electron Bernstein wave (EBW) has been numerically investigated on the assumption of a super dens core plasma generated in the large helical device (LHD). The EBW that is thermally emitted in the electron cyclotron resonance (ECR) layer may couple with the electromagnetic wave and be emitted to the vacuum via the EBW-extraordinary-ordinary (B-X-O) mode conversion process. We consider using one of the transmission lines for electron cyclotron heating (ECH) in the LHD as a receiving system of the emission. It has been derived that the measurement of the waves in the fundamental cyclotron frequency range does not provide information in the core region of the plasma since the emission region is near the their upper hybrid resonance layer outside the last closed flux surface (LCFS). On the other hand, measurement of the waves in the second harmonic frequency range provides information of the core region. It means successfully measurement of waves in the second harmonic frequency range emitted from extremely high dens core plasma indicates the possibility of the second harmonic ECH by the EBW in the core region with the same aiming and polarization.

Keywourds : LHD, electron cyclotron heating (ECH), electron Bernstein wave (EBW), high density plasma

PACS : 52.35.Hr, 52.50.Sw, 52.70.Gw

1 Introduction

With progress of high density operations in fusion-relevant plasma devices, electron ECH/ECCD by the EBW has been expected as promising substitutes for ECH/ECCD by normal electromagnetic propagation modes in plasmas. In the LHD the achievable central electron density has exceeded 1.2 $\times 10^{21}m^{-3}$ with the formation of the super dens core plasma (SDC) [1]. For ECH/ECCD in LHD, 77GHz millimeter wave is now mainly used, however the achieved highest central electron density is about 16 times as high as the cutoff density of the cutoff density of 77GHz ($7.35 \times 10^{19}m^{-3}$). In the previous papers [2][3], for launching of 77GHz millimeter wave from the existing horizontal launcher for ECH, we investigated the possibility of ECH by the EBW excited via the ordinary-extraordinary-EBW (O-X-B) mode conversion process in a high density plasma where the density profile is parabolic and the central electron density is $1.0 \times 10^{20}m^{-3}$. For a fixed magnetic axis, R_a=3.75m, several cases of central magnetic filed strength B_t such as 2.0, 2.2, 2.4, 2.6 T were considered there. In each case, the EBW can be excited by optimization of the aiming of the launching antenna however the excited EBW is mainly absorbed outside ρ=0.8 where ρ is the normalized minor radius as soon as it is excited in the upper hybrid resonance (UHR) layer. The UHR layer and the Doppler-shifted cyclotron resonance layer are located near the last close flux surface (LCFS).

When the SDC plasma is generated, since the plasma density profile spreads outside the LCFS, the UHR layer and the Doppler shifted ECR layer of 77 GHz wave may be located outside the LCFS because the helical coil is located near the UHR layer. Therefore effective heating in the core region may not be expected. If we can increase the frequency up to the second harmonic wave range, the position of the UHR layer shifts toward the core regions apart from the helical coil. Power absorption of the EBW near the core region may be expected. However there is no gyrotron of that frequency range now. It is well known that the emission process is the reversed process of the heating process. The thermally emitted EBW connects with the electromagnetic wave via the B-X-O mode conversion process and is emitted to the vacuum. If we can measure this kind of

emissive waves with use of one of the transmission lines for ECH as a receiving system with a certain aiming of the receiving antenna and polarization, it indicates that ECH by the EBW can be performed by launching of millimeter waves with use of the same transmission line with the same aiming and polarization. Measurement of such kind of emitted waves of the second harmonic frequency range may confirm the effectiveness of the second harmonic ECH by the EBW in the SDC plasma.

In this paper we report an example of numerical investigation for measurement of waves in the fundamental and the second harmonic frequency range emitted from a super dens core plasma with one of the transmission lines for ECH in the LHD. In section 2, we shortly introduce the current ECH system in the LHD then we report an example of investigation in section 3. Discussion and summary are presented in section 4.

2 ECH system in LHD in 2010

Figure 1 is a schematic diagram of the ECH system in the LHD in 2010. We use three TOSHIBA 77GHz triode collector potential depression (CPD) gyrotrons, one GYCOM 84GHz diode CPD gyrotron, one 82.7GHz GYCOM diode gyrotron and one 84GHz GYCOM diode CPD continuous wave (CW) gyrotron. The development of 1MW 77GHz gyrotron started in 2006 under the joint program between NIFS and University of Tsukuba. A series of three 77 GHz gyrotrons had been installed in the ECH system for the LHD between 2007 and 2009. The design of the tube has been improved by reference to the previous ones. In 2009, the total power of 77 GHz wave injected into the LHD simultaneously exceeded 3MW with 3 gyrotrons. In September in 2010, the output power of the newest 77GHz gyrotron has achieved 1.9 MW for 0.1 second, 1.8 MW for 1 second and 0.3 MW for 40 minutes operations [4]. Transmission lines connected to 77GHz gyrotrons are evacuated to avoid arcing during high power transmission and cooled by water to inhibit increase of temperature of the transmission line during long pulse operations. Since 2010, we have stopped to use 168 GHz gyrotrons which had been used since 1999.

3. Possibilities of heating/emission-measurement in the SDC plasma with the fundamental and second harmonic EC waves

Figure 2 shows the launching/receiving geometry of antennas installed in the horizontal port. The left antenna (L-antenna) is now can be used for measurement. As shown in figure 3, the range of aiming angle is restricted by the wall of the horizontal port and by the winding helical coil structure. If the O-X-B (B-X-O) mode conversion window appears inside the black region, the emissive waves can be successfully measured by aiming to the mode conversion window. Figure 4 shows the electron density and temperature profiles of a SDC plasma which are used for numerical calculation to investigate possibility of EBW heating/measurement in this paper.

Figure 5 shows the O-X-B (B-X-O) mode conversion rate of 77GHz wave plotted as a function of aiming that is represented by the toridal angle θ_{tor} and tilting angle θ_{tilt} of the quasi-optical mirror antenna. Mode conversion window appears inside the restricted range of aiming. The numerical method to obtain the O-X-B mode conversion rate at the plasma cutoff and the characteristics of propagation and absorption with the ray-tracing calculation are the same as that used in the previous papers [2][3]. In figure 6, the trajectory of the 77GHz wave launched as the O-mode from the L-antenna is projected to the plane sliced at z = 0.38 m where z is the distance from the equatorial plane. As soon as EBW is excited in the UHR layer via the O-X-B mode conversion process, the Doppler-shifted resonance condition is fulfilled and power absorption occurs outside the LCFS. 77GHz wave cannot access the core region of the plasma and if the emission of 77GHz does not contain the temperature information in the core region.

In figure 7, the O-X-B mode conversion rates for waves of the second harmonic range are shown. The O-X-B mode conversion window appears inside the restricted range of aiming similarly to the case of 77GHz. In figure 8, the trajectory of 154GHz wave launched as the O-mode is projected to the plane sliced at z = 0.0 m. It can be seen that the EBW propagates toward the core region after it is excited in the UHR layer and is absorbed inside the LCFS. In figure 9, the normalized local absorbed power is plotted versus the normalized minor radius ρ for various frequencies including

154GHz. The considered aiming of the antenna is the same that is θ_{tor}=-9.2deg., θ_{tilt}=7.4deg.. Since this aiming is the optimized one for 142GHz, the mode conversion rates of another frequencies are not unity. This is why the total absorbed powers integrated along ρ do not reach unity. All of the rays can access the core region where the electron density is more than 2.5 times higher than each cutoff density. The power of EBW is absorbed in the Doppler shifted second harmonic ECR layer where Ω_{ce}/ω is less than 0.5. Where Ω_{ce} is the electron cyclotron angular frequency and ω is the angular frequency of the wave. For the frequency range from 142GHz to 160GHz, power absorption region is distributed from ρ =0.15 to ρ =0.4. This suggests that electron temperature information in this region can be obtained and ECH by EBW can be performed inside ρ =0.4 if we choose this frequency range for the second harmonics heating.

4. Summary

Progress of extremely high density operation in fusion relevant plasma devices like LHD has required ECH by EBW. In LHD, over 1MW power of 77GHz millimeter wave has been able to be launched by one transmission line. However, the fundamental Doppler-shifted ECR layer of EBW excited by launching of 77GHz is outside LCFS when a SDC plasma is produced. The second harmonic Doppler-shifted ECR layer (142-154GHz) is located near the core region. Successful measurement of the second harmonic waves emitted via B-X-O mode conversion process with a transmission for ECH may support to install a 154GHz gyrotron connected to the transmission line in future.

Acknowledgment

This work was mainly performed under the budget codes NIFS10ULRR502 and NIFS10KLRR307. This work was also partially supported by the JSPS-CAS Core-University program in the field of 'Plasma and Nuclear Fusion'

References

[1] Ohyabu N, Morisaki T, Masuzaki S, et al, (2006) *Phys. Rev. Lett*. **97**, 055002

[2] Igami H., S. Kubo., Shimozuma T., et al, (2010) Fusion Science and Technology, **58** 539

[3] Igami H., Ikeda R., Takahashi H. et al, (2009) Plasma Science and Technology **11** 430

[4] Imai T., Kariya T., Minami R. et al, (2010) Proceedings of 23id IAEA Fusion Energy Conference, FTP/P6-12

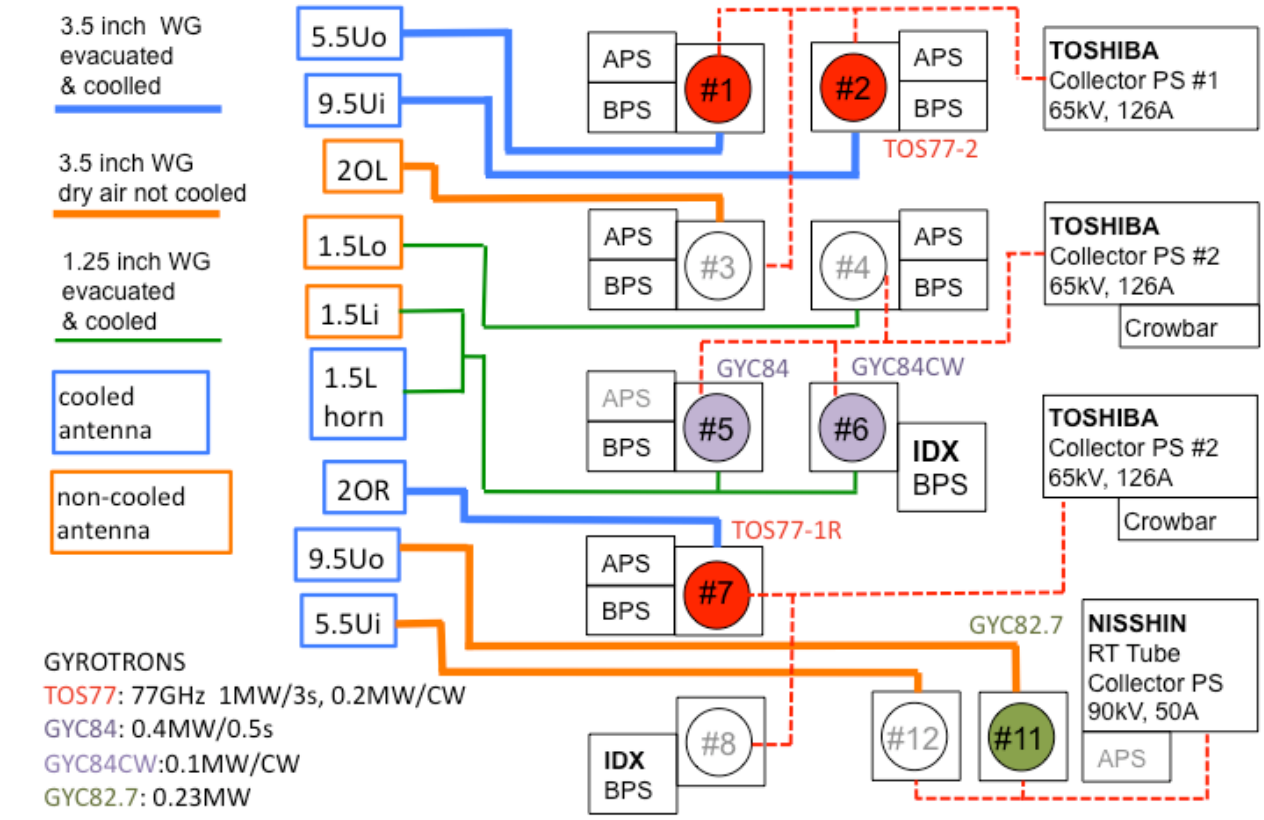

Figure 1 : Schematic diagram of ECH system in LHD in 2010

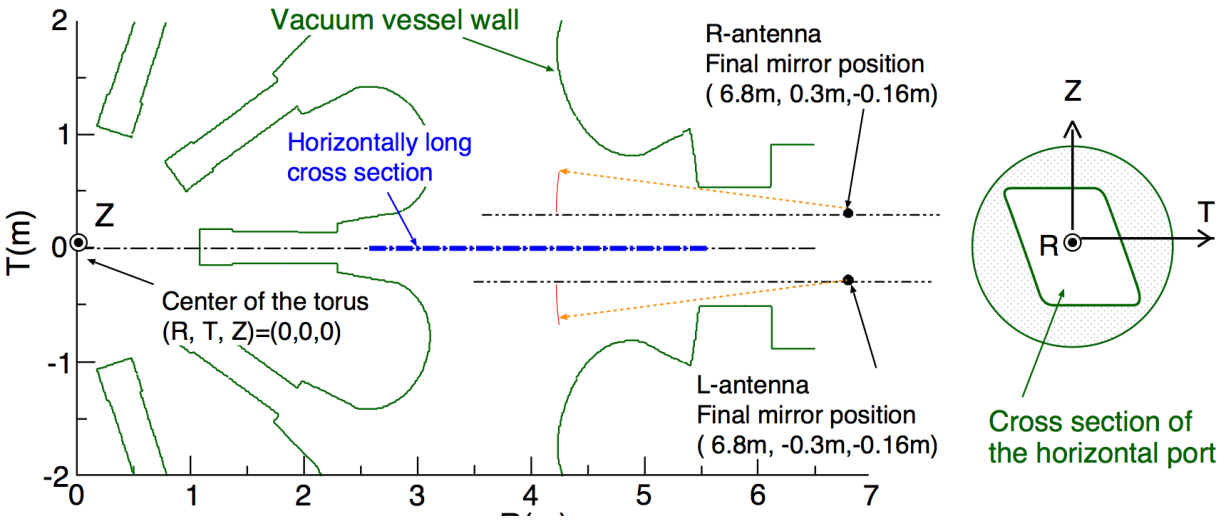

Figure 2 : Slice of the vacuum vessel at the equatorial plane and positions of the final mirrors of antennas installed in the horizontal port of LHD.

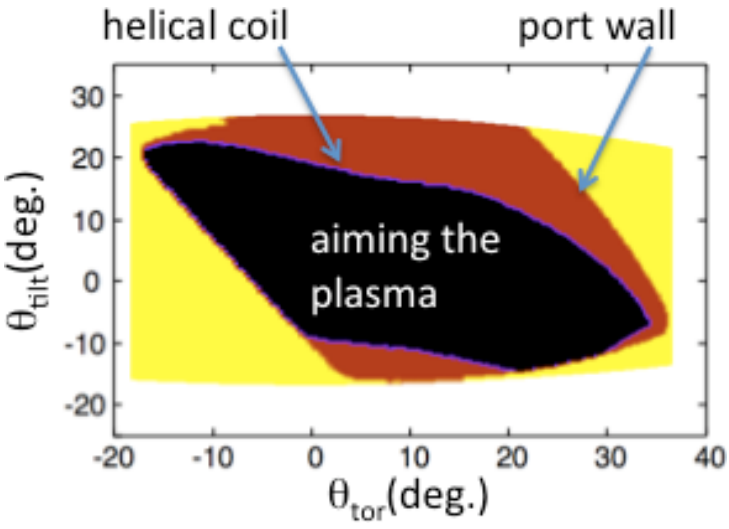

Figure 3: Range of the L-antenna aiming. The aiming area is restricted by wall of the horizontal port and helical coil structure.

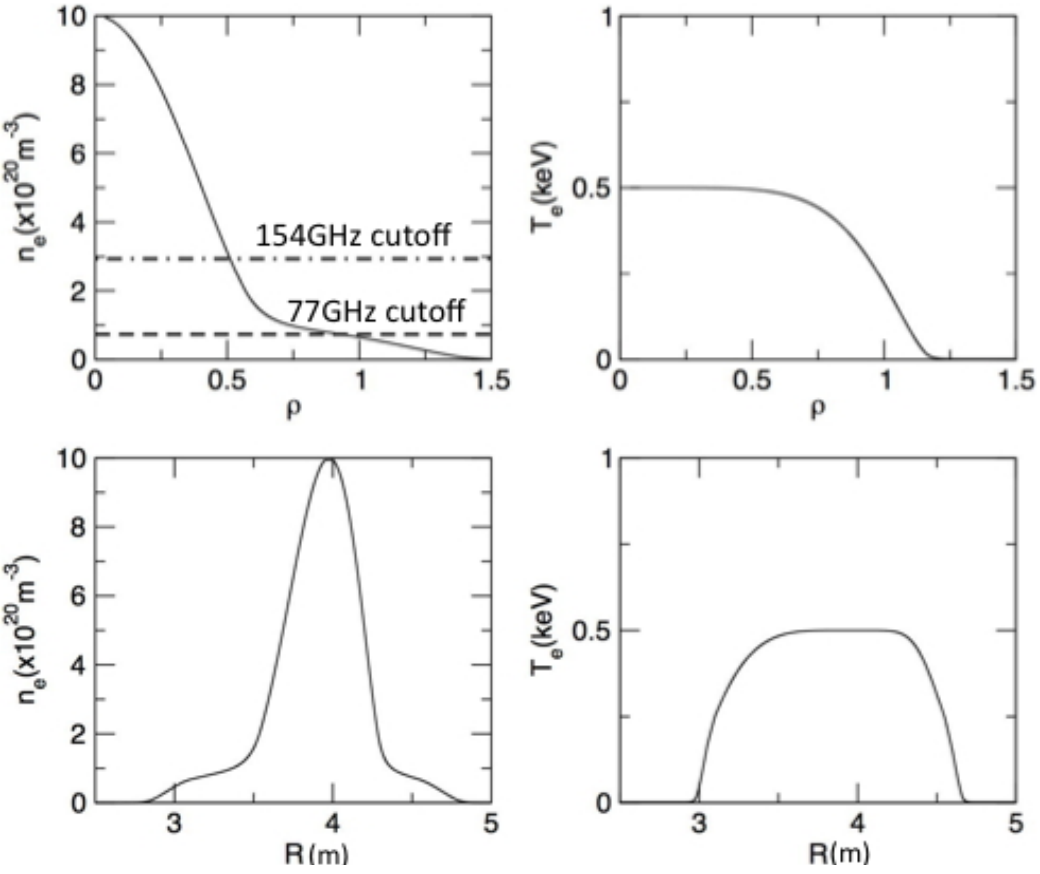

Figure 4 : Profiles of electron temperature and electron density versus normalized minor radius (upper column) and distance from the center of the torus (lower column) used for the numerical investigation in this paper

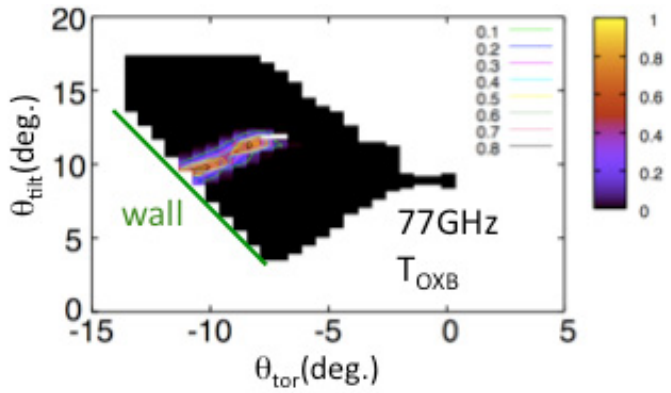

Figure 5: O-X-B (B-X-O) mode conversion rate plotted versus antenna toroidal variation angle and titling angle.

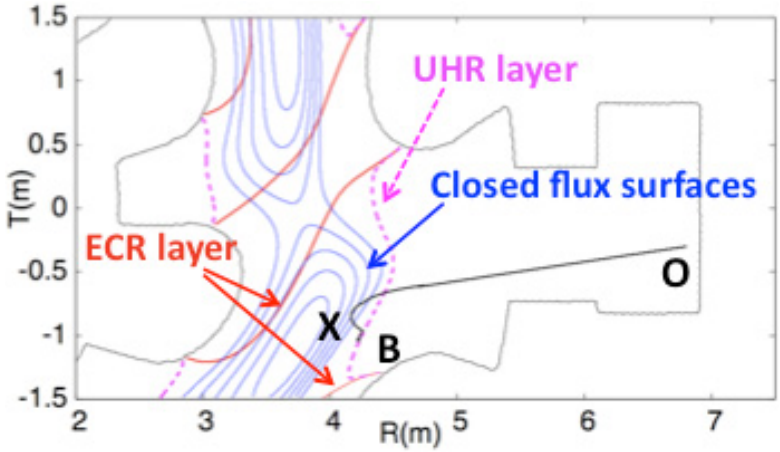

Figure 6: Distributions of the ECR layer and the UHR layer, contours of the closed flux surfaces on the slice at z = 0.38 m. Where z is the distance from the equatorial plane. Projection of the ray of 77GHz wave is also plotted.

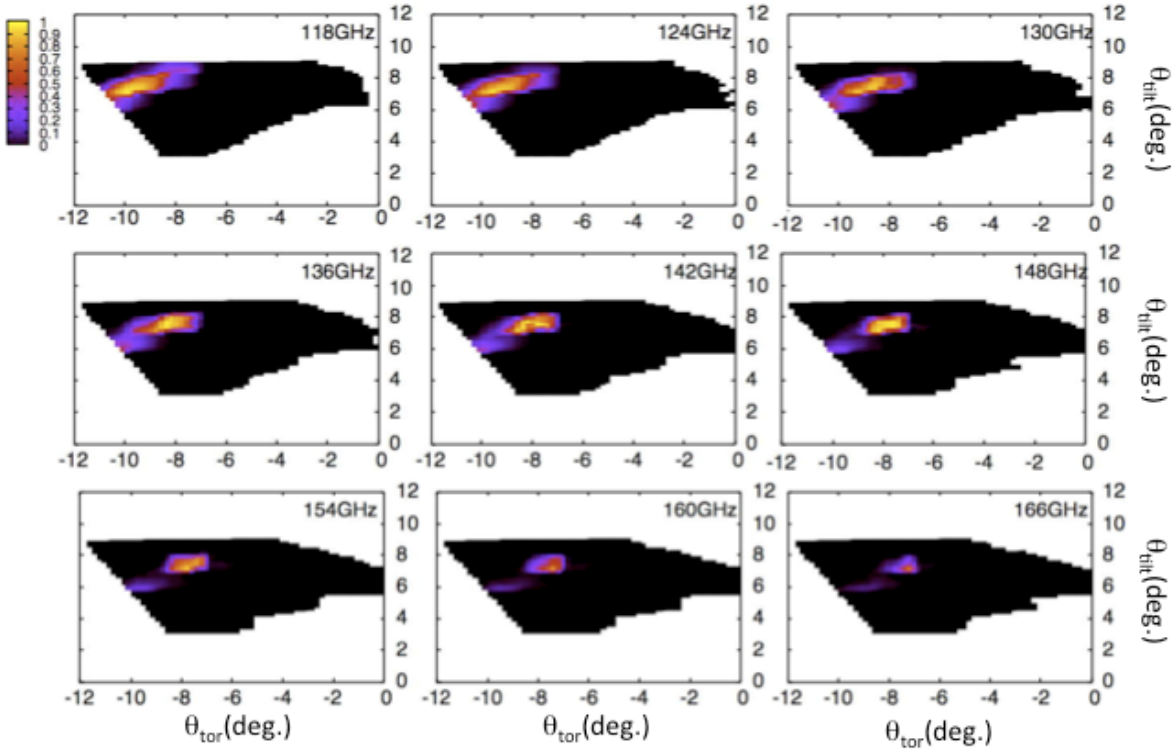

Figure 7: Similar plots to figure 6 for second harmonic frequency range waves.

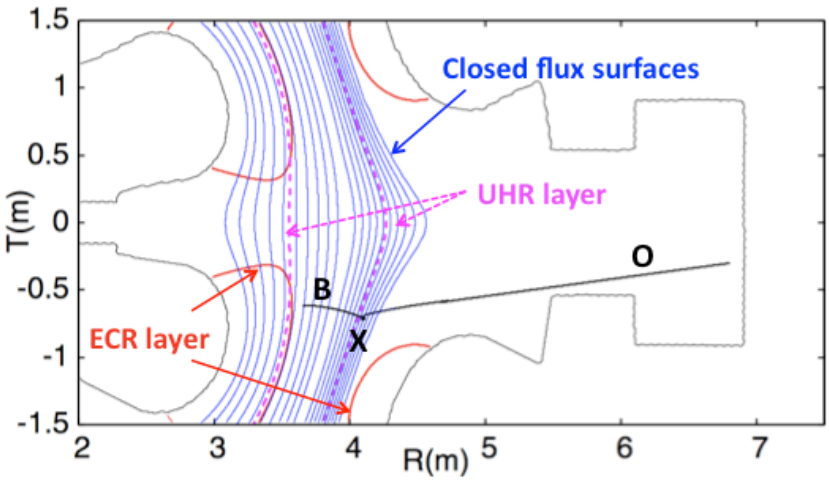

Figure 8: Distributions of the ECR layer and the UHR layer, contours of the closed flux surfaces on the slice at z = 0.0 m. Where z is the distance from the equatorial plane. Projection of the ray of 154GHz wave is also plotted.

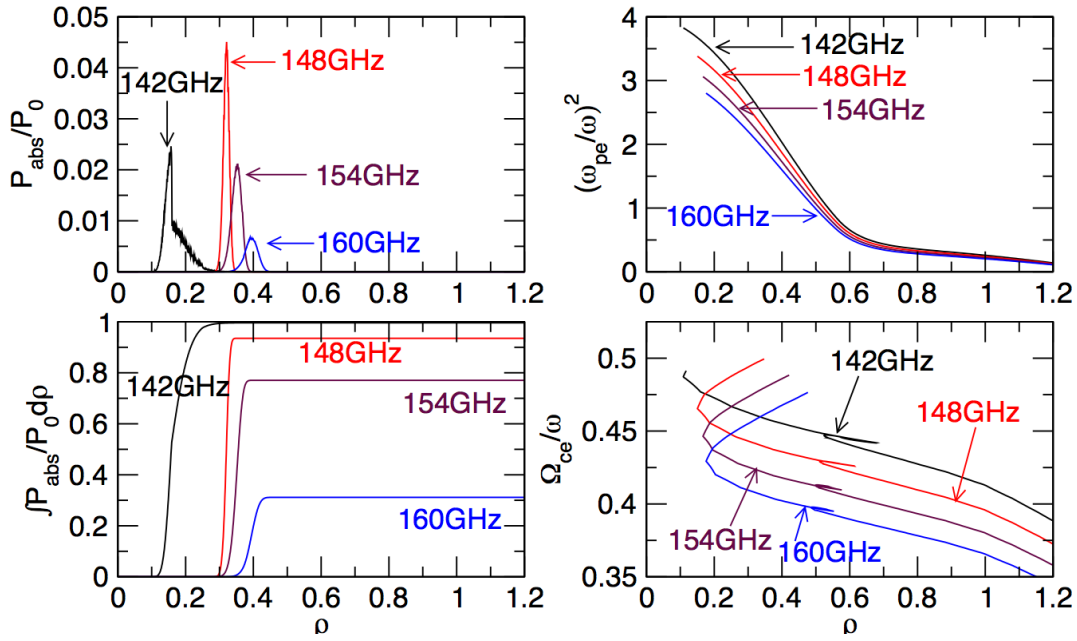

Figure 9: Normalized local absorbed power (upper-left), Normalized total absorbed power integrated along the normalized minor radius ρ (lower-left), square of normalize plasma angular frequency along the ray trajectory (upper-right), normalized electron cyclotron frequency along the ray trajectory (lower-right).

Program of Guilin Workshop

(November 1-4, 2010)

October 31, 2010 (Sunday)

10:30 – 22:30 Registration, Guilin Bravo Hotel (桂林宾馆)

November 1 (Monday)

Session 1 Chair: Prof. X.Gao	08:30	**K.J.Wang** (ASIPP)	**Welcome speech** "Memory of CUP collaboration" (15 min)
	08:45	**K.Toi** (NIFS)	**Memorial talk** "MHD spectroscopy in toroidal plasmas using various MHD instabilities" (60 min)#
	09:45		Group Photo
	Coffee Break 10:00 - 10:30		
Session 2 Chair: Prof. S.Morita	10:30	**G.S.Xu** (ASIPP)	Inversed shear of intrinsic toroidal rotation near the edge of the EAST ohmic plasmas (25 min)
	10:55	**Y.Ikeda** (JAEA)	Present status of JT-60SA project and development of heating systems for JT-60SA (25 min)
	11:20	**L.W.Yan** (SWIP)	Recent results of H-mode experiments in HL-2A (25 min)
	11:45	**K.Hanada** (Kyushu U.)	Recent experiments towards steady state operation of spherical tokamak QUEST (25 min)#
	Lunch Break 12:10 - 13:30		
Session 3 Chair: Prof. X.T.Ding	13:30	**T.Mizuuchi** (Kyoto U.)	Recent progress on plasma control studies for improved confinement in Heliotron J (25 min)#
	13:55	**B.J.Xiao** (ASIPP)	The verification of real time plasma shape reconstruction on EAST (25 min)
	14:20	**T.Maekawa** (Kyoto U.)	Formation of closed flux surface by ECH (25 min)
	14:45	**L.Zhang** (ASIPP)	Neutral density estimate of edge plasma with double null configuration on EAST tokamak (15 min)
	15:00	**S.B.Zhang** (USTC)	The experimental platform of magnetic reconnection in lab plasma (15 min)
	Coffee Break 15:30 - 16:00		
Session 4 Chair: Dr. Y.Ikeda	16:00	**B.J.Ding** (ASIPP)	Recent results of LHCD experiments on EAST (25 min) #
	16:25	**K.Tsumori** (NIFS)	Progress of positive-ion-base NBI for LHD (25 min) #
	16:50	**X.J.Zhang** (ASIPP)	Present status of ICRF system on EAST (15 min)
	17:05	**T.R.Zhu** (Sichuan U)	Study on overall operation features of tokamak plasma with lower hybrid current drive (15 min)
	17:20	**Z.X.Liu** (ASIPP)	Sawtooth suppression by LHCD on HT-7 and EAST Tokamak (15 min)
	17:35	**S.Y.Lin** (ASIPP)	Suppression of runaway electrons during disruption in HT-7 (15 min)
Welcome Reception	18:00 – 20:00 Guilin Bravo Hotel		

Invited talk: 25 min = 22 min presentation + 3 min question;
Oral talk: 15 min = 13 min presentation + 2 min question.

November 2 (Tuesday)			
Session 5 Chair: Prof. K.Toi	08:30	**K.J.Zhao** (SWIP)	Turbulence and zonal flows in edge plasmas of HL-2A tokamak (25 min)
	08:55	**T.Watari** (NIFS)	Gyrokinetic response function of zonal flows (25 min)
	09:20	**Z.X.Wang** (Dalian U. of Tech.)	Magnetic-island-induced ion temperature gradient mode (25 min)
	09:45	**N.Yan** (ASIPP)	Observation of blobs and holes in the boundary plasma of EAST tokamak (15 min)
	Coffee Break 10:00 - 10:30		
Session 6 Chair: Prof. T.Maekawa	10:30	**T.Tukuzawa** (NIFS)	Recent progress of microwave reflectometer for density fluctuation measurements in LHD (25 min)
	10:55	**X.D.Peng** (SWIP)	Basic features on ExB convection nonlinearity in tokamak plasmas (25 min)
	11:20	**Y.Liu** (ASIPP)	The present state of the ECE measurements on HT-7 and EAST (15 min)
	11:35	**L.Wang** (ASIPP)	Study of SOL width in ohmic and LHCD heating double-null divertor plasma on EAST tokamak (15 min)#
	Lunch Break 12:00 - 13:30		
Session 7 Chair: Prof. M.Kwon	13:30	**K.Narihara** (NIFS)	Aspherical light collection mirror for a 200-point Thomson scattering diagnostic installed on the Large Helical Device (25 min)#
	13:55	**A.Shimizu** (NIFS)	Potential measurement with Heavy Ion Beam Probe in the Large Helical Device (25 min)
	14:20	**N.Shi** (ASIPP)	Far-infrared Laser Diagnostics on EAST (15 min)
	14:35	**X.F.Han** (ASIPP)	Multichannel YAG laser TS diagnostics on EAST superconducting tokamak (15 min)
	Coffee Break 15:00 - 15:30		
Session 8 Chair: Prof. T.Watari	15:30	**J.T.Li** (TIPC)	Bulk W-Cu-Fe functionally graded materials prepared by combustion synthesis melt-casting under ultra-high gravity (25 min)
	15:55	**Y.H.Ling** (Tsinghua U)	Irradiation effect on W surface with stress confinement under focus microwave plasma bombardment (25 min)
	16:20	**Y.B.Chen** (ASIPP)	Preliminary work of the ITER type soft x-ray camera (15 min)
	16:35	**G.Q.Zhong** (ASIPP)	Measurement of the neutron flux during the EAST operation primary stage (15 min)
	17:30 – 20:00 Dinner at downtown of Guilin city		

Invited talk: 25 min = 22 min presentation + 3 min question;
Oral talk: 15 min = 13 min presentation + 2 min question.

November 3 (Wednesday)			
Session 9 Chair: Prof.K.Hanada	08:30	**M.Kwon** (NFRI)	Recent experimental results of the steady-state tokamak KSTAR (25 min)
	08:55	**S.Morita** (NIFS)	Improvement of plasma performance using impurity pellet injection in LHD (25 min)
	09:20	**L.Q.Hu** (ASIPP)	Present status of the EAST diagnostics (25 min)
	09:45	**K.Itami** (JAEA)	Present status of the plasma diagnostics for JT-60SA tokamak (25 min)
	Coffee Break 10:10 - 10:40		
Session 10 Chair: Dr. H.S.Cai	10:40	**X.T.Ding** (SWIP)	Low Frequency Collective Modes driven by Energetic Electrons in the HL-2A Tokamak (25 min)#
	11:05	**T.Ito** (NIFS)	The diagnostic technique for fast-ions spatial distribution measurement via charge exchange spectroscopy on LHD (25 min)
	11:30	**L.Zeng** (Tsinghua U.)	Investigation of MHD events in the SUNIST spherical tokamak (15 min)
	11:45	**M.Xu** (USTC)	ECEI upgrading and experiment results on EAST (15 min)
	Lunch Break 12:00 - 13:30		
Session 11 Chair: Prof. T.Mizuuchi	13:30	**K.Ogawa** (NIFS)	Magnetic configuration effect on fast ion losses induced by various MHD instabilities in the Large Helical Device (25 min)#
	13:55	**C.G.Jin** (Suzhou U.)	Experimental study of discharge cleaning on EAST by helicon plasma (25 min)#
	14:20	**C.F.Dong** (NIFS)	Study on radial position of impurity ions at core and edge plasmas in LHD using space-resolved EUV spectrometer (25 min)
	14:45	**R.J.Zhou** (ASIPP)	Generation and suppression of runaway electrons in LHCD experiments in EAST (15 min)
	Coffee Break 15:00 - 15:30		
Session 12 Chair: Prof.K.J.Wang	15:30	**S.Kado** (Tokyo U.)	Development of the High-Throughput Transmission Grating Spectrograph for the TV Thomson Scattering Diagnostics on EAST Tokamak (25 min)
	15:55	**X.Q.Xi** (ASIPP)	Design and development of TV Thomson scattering on EAST tokamak (15 min)
	16:10	**H.Igami** (NIFS)	Measurement of electron Bernstein wave emission with one of power transmission lines for ECH in LHD (25 min)
	16:40	**S.Morita** (NIFS)	Summary report
	17:00	**Xiang.Gao** (ASIPP)	Closing speech
Banquet	18:00 – 21:00 Guilin Bravo Hotel		

Invited talk: 25 min = 22 min presentation + 3 min question;
Oral talk: 15 min = 13 min presentation + 2 min question.

November 4 (Thursday)	
Session 13 Chair: Prof.X. Gao Prof.S.Morita	09:00-12:00 Plenary meeting on future collaboration in the filed of confinement, heating and diagnostics 14:00-17:00 Individual discussions in each category

(END)

List of participants

CAI Huishan
University of Science and Technology of China
,P.R.China
E-mail:hscai@mail.ustc.edu.cn

CHEN Yebin
Institute of Plasma Physics,
Chinese Academy of Sciences
P.O.Box 1126,Hefei,Anhui 230031,P.R.China
E-mail:chenyebin@ipp.ac.cn

DING Bojiang
Institute of Plasma Physics,
Chinese Academy of Sciences
P.O.Box 1126,Hefei,Anhui 230031,P.R.China
E-mail:bjding@ipp.ac.cn

DING Xuantong
Southwestern Institute of Physics
P.O.Box 432,Chendu,Sichuan,610041,
P.R.China
E-mail:dingxt@swip.ac.cn

DONG Chunfeng
National Institute for Fusion Science
322-6 Oroshi-cho,Toki-shi ,Gifu
509-5292,Japan
E-mail:dong.chunfeng@nifs.ac.jp

Dong Shaohua
Institute of Plasma Physics,
Chinese Academy of Sciences
P.O.Box 1126,Hefei,Anhui 230031,P.R.China
e-mail:shdong@ipp.ac.cn

GAO Xiang
Institute of Plasma Physics,
Chinese Academy of Sciences
P.O.Box 1126,Hefei,Anhui 230031,P.R.China
E-mail:xgao@ipp.ac.cn

HAN Xiaofeng
Institute of Plasma Physics,
Chinese Academy of Sciences
P.O.Box 1126,Hefei,Anhui 230031,P.R.China
E-mail:hxf@ipp.ac.cn

HU Liqun
Institute of Plasma Physics,
Chinese Academy of Sciences
P.O.Box 1126,Hefei,Anhui 230031,P.R.China
E-mail:lqhu@ipp.ac.cn

HANADA Kazuaki
Kyushu University
6-1Kasuga-koen Kasuga,Fukuoka,
816-8580,Japan
E-mail:hanada@triam.kyushu-u.ac.jp

IGAMI Hiroe
National Institute for Fusion Science
322-6 Oroshi-cho,Toki-shi ,Gifu
509-5292,Japan
E-mail:igami.hiroe@LHD.nifs.ac.jp

IKEDA Yoshitaka
Japan Atomic Energy Agency
801-1,Muko-yama,Naka-shi,Ibaraki,
311-0193,Japan
E-mail:ikeda.yoshitaka@jaea.go.jp

ITAMI Kiyoshi
Japan Atomic Energy Agency
801-1,Muko-yama,Naka-shi,Ibaraki,
311-0193,Japan
E-mail.itami.kiyoshi@jaea.go.jp

ITO Takafumi
National Institute for Fusion Science
322-6 Oroshi-cho,Toki-shi,Gifu,
509-5292,Japan
E-mail: ito.takafumi@LHD.nifs.ac.jp

JIN Chengang
Suzhou University
Suzhou 215006,P.R.China
E-mail:nestajcg@126.com

KADO Shinichiro
The University of Tokyo
E8-BLDG,7-3-1Hongo,Bunkyo-ku,
Tokyo 113-8656、Japan
E-mail:kado@n.t.u-tokyo.ac.jp

LI Jiangtao
Technocal Institute of Physics and Chemistry
No. 2 Beiyitiao Street, Zhongguancun,
Haidian District, Beijing, P. R. China
E-mail:lijiangtao@mail.ipc.ac.cn

LIN Shiyao
Institute of Plasma Physics
Chinese Academy of Sciences
P.O.Box 1126,Hefei,Anhui 230031,P.R.China
E-mail:linsy@ipp.ac.cn

LING Yunhan
Tsinghua University
Beijing 10084,P.R.China
E-mail:yhling@mail.tsinghua.edu.cn

LIU Yong
Institute of Plasma physics,
Chinese Academy of Aciences
P.O Box1126,Hefei,Anhui,230031,P.R .China
E-mail:liuyong@ipp.ac.cn

LIU Zixi
Institute of Plasma Physics,
Chinese Academy of Sciences
P.O.Box 1126,Hefei,Anhui 230031,P.R.China
E-mail:zxliu316@ipp.ac.cn

MAEKAWA Takashi
Graduate School of Energy Science,
Kyoto University
Yoshida honmachi Sakyou-ku,
Kyoto 606-8501,Japan
E-mail:maekawa@energy.kyoto-u.ac.jp

MIZUUCHI Tohru
Institute of Advenced Energy ,
Kyoto University
Gokasho,Uji ,Kyoto 611-0011,Japan
E-mail:mizuuchi@iae.kyoto-u.ac.jp

MORITA Shigeru
National Institute for Fusion Science
322-6 Oroshi-cho,Toki-shi,Gifu
509-5292,Japan
E-mail:morita.shigeru@lhd.nifs.ac.jp

NARIHARA Kazumichi
National Institute for Fusion Science
322-6 Oroshi -cho , Toki-shi, Gifu
509-5292,Japan
E-mail:narihara@nifs.ac.jp

OGAWA Kunihiro
National Institute for Fusion Science
322-6 Oroshi-cho,Tokishi,Gifu
509-5292,Japan
E-mail:ogawa.kunihiro@lhd.ac.jp

PENG Xiaodong
Southwestern Institute of Physics
P.O. Box 432,Chendu,Sichuan,
610041,P.R.China
E-mail: pengxd@swip.ac.cn

SHI Nan
Institute of Plasma Physics,
Chinese Academy of Sciences
P.O. Box 1126,Hefei,Anhui 230031,P.R.China
E-mail:nanan@ipp.ac.cn

SHIMIZU Akihiro
National Institute for Fusion Science
322-6 Oroshi-cho,Toki-shi ,Gifu
509-5292,Japan
E-mail:shimizu.akihiro@nifs.ac.jp

TOI Kazuo
National Institute for Fusion Science
322-6 Oroshi-cho,Tokishi,Gifu
509-5292,Japan
E-mail: toi.kazuo@LHD.nifs.ac.jp

TOKUZAWA Tokihiko
National Institute for Fusion Science
322-6 Oroshi-cho, Toki-shi ,Gifu
509-5292,Japan
E-mail:tokuzawa.tokihiko@lhd.nifs.ac.jp

TSUMORI Katsuyoshi
National Institute for Fusion Science
322-6 Oroshi-cho,Toki-shi,Gifu
509-5292,Japan
E-mail: tsumori @nifs.ac.jp

WANG Zhengxiong
Dalian University of Technology
No.2 Linggong Road, Ganjingzi District,
Dalian City, Liaoning Province, 116024 ,P. R. China
E-mail: zxwang@mail.dlut.cn

WANG Kongjia
Institute of Plasma Physics,
Chinese Academy of Sciences
P.O. Box 1126,Hefei,Anhui 230031,P.R.China
E-mail: kjwang@ipp.ac.cn

WANG Liang
Institute of Plasma Physics,
Chinese Academy of Sciences
P.O. Box 1126,Hefei,Anhui 230031,P.R.China
E-mail: wliang@ipp.ac.cn

WU Xuemei
Suzhou University
Suzhou 215006,P.R.China
E-mail:xmwu @suda.edu.cn

WATARI Tetsuo
National Institute for Fusion Science
322-6 Oroshi-cho,Toki-shi ,Gifu
509-5292,Japan
E-mail:watari.tetsuo@toki-fs.jp

XI Xiaoqi
Institute of Plasma Physics,
Chinese Academy of Sciences
P.O.Box 1126,Hefei,Anhui 230031,P.R.China
E-mail:xixq@ipp.ac.cn

XIAO Bingjia
Institute of Plasma Physics,
Chinese Academy of Sciences
P.O.Box 1126,Hefei,Anhui 230031,P.R.China
E-mail:bjxiao@ipp.ac.cn

XU Guosheng
Institute of Plasma Physics,
Chinese Academy of Sciences
P.O.Box 1126,Hefei,Anhui 230031,P.R.China
E-mail:gsxu@ipp.ac.cn

XU Ming
University of Science and Technology of China
Hefei, Anhui Province 230026
P. R. China
E-mail:xum138@mail.ustc.edu.cn

YAN Longwen
Southwestern Institute of Physics
P.O.Box 432,Chendu,Sichuan,
610041,P.R.China
E-mail:lwyan@swip.ac.cn

YAN Ning
Institute of Plasma Physics,
Chinese Academy of Sciences
P.O.Box 1126,Hefei,Anhui 230031,P.R.China
E-mail:yanning@ipp.ac.cn

ZENG Long
Tsinghua University
Beijing 10084,P.R.China
E-mail:zenglong@ipp.ac.cn

ZHANG Ling
Institute of Plasma Physics
Chinese Academy of Sciences
P.O.Box 1126,Hefei,Anhui 230031,P.R.China
E-mail:zhangling@ipp.ac.cn

ZHANG Shoubiao
Institute of Plasma Physics
Chinese Academy of Sciences
P.O.Box 1126,Hefei,Anhui 230031,P.R.China
E-mail:bszhang@ipp.ac.cn

ZHANG Xinjun
Institute of Plasma Physics
Chinese Academy of Sciences
P.O.Box 1126,Hefei,Anhui 230031,P.R.China
E-mail:xjzhang@ipp.ac.cn

ZHAO Kaijun
Southwestern Institute of Physics
P.O.Box 432,Chendu,Sichuan,
610041,P.R.China
E-mail: kjzhao@swip.ac.cn

ZHONG Guoqiang
Institute of Plasma Physics
Chinese Academy of Sciences
P.O.Box 1126,Hefei,Anhui 230031,P.R.China
E-mail:gqzhong@ipp.ac.cn

ZHOU Ruijie
Institute of Plasma Physics
Chinese Academy of Sciences
P.O.Box 1126,Hefei,Anhui 230031,P.R.China
E-mail:rjzhou@ipp.ac.cn

ZHU Tingru
Shichuan University
,Sichuan,
,P.R.China
E-mail:zhouy@swip.ac.cn